Experimental Approaches to the Corey-Bakshi-Shibata and Dakin-West Reactions as Model Systems for Machine Learning Applications in the Small-Data Regime

---



Dissertation zur Erlangung des Doktorgrades

der Naturwissenschaftlichen Fachbereiche

(Fachbereich 08 – Biologie und Chemie)

der Justus-Liebig-Universität Gießen

vorgelegt von

Oliver Simão Pereira

aus Oberursel

1. Gutachter: Prof. Dr. Peter R. Schreiner
2. Gutachter: Prof. Dr. Richard Göttlich

Die vorliegende Arbeit wurde im Zeitraum von Juni 2022 bis Juni 2026 am Institut für Organische Chemie der Justus-Liebig-Universität Gießen unter der Anleitung von Herrn Prof. Dr. Peter R. Schreiner, Ph.D. durchgeführt.

Eidesstattliche Erklärung und Erklärung zur Nutzung Künstlicher Intelligenz (KI)

Ich erkläre: Ich habe die vorgelegte Dissertation selbstständig und ohne unerlaubte fremde Hilfe und nur mit den Hilfen angefertigt, die ich in der Dissertation angegeben habe. Alle Textstellen, diewörtlich oder sinngemäß aus veröffentlichten Schriften entnommen sind, und alle Angaben, die aufmündlichen Auskünften beruhen, sind als solche kenntlich gemacht. Ich stimme einer evtl. Überprüfung meiner Dissertation durch eine Antiplagiat-Software zu. Bei den von mir durchgeführten und in der Dissertation erwähnten Untersuchungen habe ich die Grundsätze guterwissenschaftlicher Praxis, wie sie in der „Satzung der Justus-Liebig-Universität Gießen zur Sicherung guter wissenschaftlicher Praxis“ niedergelegt sind, eingehalten.

Angaben zu auf KI basierender Hilfen wie ChatGPT oder SchulKI von OpenAI oder Gemini von Google zur Erstellung meiner Dissertation:

☐ Ich habe bei der Erstellung dieses Textes kein KI-Tool verwendet.

☒ Ich habe ein KI-Tool in den folgenden Bereichen eingesetzt:

- ☐ Ideen finden, meine Kreativität anregen
- ☒ Verstehen von Konzepten, Recherche von Fakten und Definitionen
- ☒ Optimierung eines von mir verfassten Textes
- ☐ Erstellen ganzer Textpassagen nach meinen Vorgaben

Verwendete Tools: Gemini (Google) / ChatGPT (OpenAI)

Art der Nutzung: Das Tool wurde zur sprachlichen Überarbeitung und stilistischen Optimierung der englischsprachigen Textpassagen verwendet. Dies umfasste die Korrektur von Grammatik, Rechtschreibung und Zeichensetzung sowie die Verbesserung von Satzbau, Übergängen und Lesefluss. Die wissenschaftlichen Inhalte, Argumentationen und Daten wurden vollständig und eigenständig von mir erarbeitet.

_____ _____

Ort, Datum Oliver Pereira

"*It is better to begin the journey, make some mistakes and correct your course, than to wait until everything is perfect and never even start*"

-James Norbury-

für meine Eltern

Abstract (English)

Predicting enantioselectivity remains a fundamental challenge in asymmetric organocatalysis. While Machine Learning (ML) offers data-driven pathways for catalyst optimization, its application is hindered by data scarcity and publication bias. This work investigates the integration of experimental data into predictive ML models within the small-data regime, using the Corey-Bakshi-Shibata (CBS) reduction and the asymmetric variant of the Dakin-West reaction as model reactions. The primary objective was the development of robust predictive models from limited, unbiased datasets, and to delineate the operational limits of current molecular representations as well as ML algorithms. Initial investigations of the CBS reduction of ketones yielded a graph-based ML model that predicts stereochemical outcomes and identifies promising catalyst precursors. However, the synthesis and investigation of additional precursors, enabled by a newly developed synthetic route, revealed deviations from previous predictions. This demonstrates that the reliability of small-data ML models depends on high-quality datasets and robust analytics to avoid the compensation for empirical artifacts. Further investigations of CBS catalysts into ketimine substrates revealed that an unselective background reaction consistently outpaces the catalyzed pathway. This inherent lack of stereocontrol renders ketimines unsuitable for modeling, making the suppression of the background pathway an essential prerequisite for future work. For the asymmetric Dakin-West reaction, the research strategy prioritized empirical data generation over premature modeling. Through systematic parameter optimization, a comprehensive data set was established, which maps complex structure-activity relationships and provides a solid, high-quality foundation for future ML applications. Ultimately, this work demonstrates that advancing ML-powered catalyst design within the small-data regime depends on the synergy of high-precision experimental data and rigorous analytical validation. By focusing on data quality in addition to increasing data quantity, the operational boundaries of predictive modeling can be pushed to address complex synthetic challenges.

Abstract (Deutsch)

Die Vorhersage der Enantioselektivität stellt nach wie vor eine grundlegende Herausforderung in der asymmetrischen Organokatalyse dar. Zwar bietet maschinelles Lernen (ML) datengestützte Ansätze zur Katalysatoroptimierung, doch wird dessen Anwendung durch Datenknappheit und Publikationsverzerrungen behindert. Diese Arbeit untersucht die Integration experimenteller Daten in prädiktive ML-Modelle im Small-Data-Bereich, wobei die Corey-Bakshi-Shibata-Reduktion (CBS) und die asymmetrische Variante der Dakin-West-Reaktion als Modellreaktionen dienen. Das primäre Ziel war die Entwicklung robuster Vorhersagemodelle aus begrenzten, unverzerrten Datensätzen sowie die Abgrenzung der operativen Grenzen aktueller molekularer Darstellungen und ML-Algorithmen. Erste Untersuchungen der CBS-Reduktion von Ketonen führten zu einem graphbasierten ML-Modell, das stereochemische Ergebnisse vorhersagt und vielversprechende Katalysatorvorläufer identifiziert. Die Synthese und Untersuchung weiterer Vorläufer, die durch einen neu entwickelten Syntheseweg ermöglicht wurde, zeigte jedoch Abweichungen von früheren Vorhersagen. Dies verdeutlicht, dass die Zuverlässigkeit von ML-Modellen im Small-Data-Bereich von hochwertigen Datensätzen und robusten Analysen abhängt, um eine Kompensation empirischer Artefakte zu vermeiden. Weitere Untersuchungen von CBS-Katalysatoren an Ketimin-Substraten zeigten, dass eine unselektive Hintergrundreaktion den katalysierten Reaktionsweg durchweg übertrifft. Dieser inhärente Mangel an Stereokontrolle macht Ketimine für die Modellierung ungeeignet, weshalb die Unterdrückung des Hintergrundreaktionswegs eine wesentliche Voraussetzung für zukünftige Arbeiten darstellt. Für die asymmetrische Dakin-West-Reaktion wurde bei der Forschungsstrategie der Erhebung empirischer Daten Vorrang vor einer verfrühten Modellierung eingeräumt. Durch systematische Parameteroptimierung wurde ein umfassender Datensatz erstellt, der komplexe Struktur-Wirkungs-Beziehungen abbildet und eine solide, qualitativ hochwertige Grundlage für zukünftige ML-Anwendungen bildet. Letztendlich zeigt diese Arbeit, dass die Weiterentwicklung des ML-gestützten Katalysatordesigns im Bereich geringer Datenmengen von der Synergie zwischen hochpräzisen experimentellen Daten und einer strengen analytischen Validierung abhängt. Indem neben der Steigerung der Datenmenge auch der Fokus auf die Datenqualität gelegt wird, lassen sich die operativen Grenzen der prädiktiven Modellierung erweitern, um komplexe synthetische Herausforderungen zu bewältigen.

Publication in Peer Reviewed Journals

O. Pereira,[+] M. Ruth,[+] D. Gerbig, R. C. Wende, P. R. Schreiner, *J. Am. Chem. Soc.* **2024**, *146*, 14576–14586. ([+] These authors contributed equally to this work)

Table of Contents

1 Introduction 1

1.1 Importance of Chirality in Organic Chemistry 2

1.1.1 Role of Chirality in Natural Products and Pharmaceuticals 4

1.1.2 Strategies and Challenges for Accessing Enantiopure Compounds 6

1.2 Principles of Asymmetric Organocatalysis 7

1.2.1 The Energetic Basis of Enantioselectivity 8

1.2.2 Catalyst Activation and Non-Covalent Interactions 10

1.3 The Corey-Bakshi-Shibata-Reduction 12

1.3.1 Origin and Development of the CBS Catalysis 13

1.3.2 Development of Imine or Ketimine Reduction 16

1.3.3 Comparing Ketones and Imines 17

1.4 Dakin-West reaction 19

1.4.1 The Classic Mechanism and Racemization Challenge 19

1.4.2 Asymmetric Catalysis and Peptide Architecture 21

1.5 Machine Learning 23

1.5.1 Molecular Representation and Featurization 23

1.5.2 Machine Learning Workflows and Model Evaluation 24

1.5.3 Data Quality and the Challenge of Publication Bias 26

2 Motivation 27

3 Results and Discussion 29

3.1 Driven Differentiation of Subtle Features 32

3.1.1 Synthesis of Catalyst Precursors 33

3.1.2 Optimization of the Catalytic CBS Reduction 36

3.1.3 Catalyst and Substrate Scope 39

3.1.4 Predictions of the Graph-Based Model 41

3.1.5 Virtual Screening and Experimental Validation 44

3.2 New Synthesis Strategy and Boundaries of the Model 50

3.2.1 Synthesis of Aryl Halide Derivates 51
3.2.2 Synthesis of the Precursor: The Problem 55
3.2.3 Synthesis of the Precursor: The Idea 57
3.2.4 Synthesis of the Precursor: The Solution 58
3.2.5 Experimental Evaluation and Model Boundaries 63

3.3 Extending the Concept of CBS Reduction to Imines 70
3.3.1 CBS-Reduction of Cyclic Imines 72
3.3.2 CBS Reduction of Non-Cyclic Imines 75
3.3.3 Evaluation of Previously Documented Results 79
3.3.4 The Background Reaction 82

3.4 The Dakin-West Reaction Data Collection and Empirical Evaluation 88
3.4.1 Substrate Scope and Synthesis of Reference Racemate 89
3.4.2 Parameter Optimization and Experimental Setup 90
3.4.3 The Catalyst Library and Selection Method 93
3.4.4 Evaluation of Catalytic Performance and Structure Relationships 95

4 Summary 104

4.1 Graph Based Modeling in the CBS Reduction of Butanone 104

4.2 Novel Synthetic Strategy and Re-Evaluation of the Predictive Framework 104

4.3 Expansion of the CBS Reduction to Ketimines and Kinetic Evaluation 105

4.4 Data Generation for the Asymmetric Dakin-West Reaction 105

5 Outlook 107

5.1 Corey-Bakshi-Shibata Reduction 107

5.2 Asymmetric Dakin-West Reaction 109

6 Experimental Part 111

6.1 General Information 111

6.2 Instrumentations and Methods 111

6.3 Part I 112

6.3.1 Synthesis and Analysis of Racemates 112
6.3.2 Synthesis of Brominated Aryl Compounds 125
6.3.3 Synthesis of Catalyst Precursors 126
6.3.4 Reduction Reaction Procedure 139
6.4 Part II 140
6.4.1 Synthesis and Analysis of Racemates 140
6.4.2 Synthesis of the Titration Reagent for *n*-BuLi 142
6.4.3 Synthesis of Brominated Aryl Compounds 143
6.4.4 Synthesis of Catalyst Precursor 144
6.4.5 Updated Reduction Reaction Procedure 148
6.5 Part III 149
6.5.1 Synthesis of Non-Cyclic and Cyclic Imines 149
6.5.2 Synthesis of Catalyst Precursors 162
6.5.3 Catalytical Reduction Reaction Procedure 163
6.6 Part IV 164
6.6.1 Synthesis of Starting Materials 164
6.6.2 Synthesis of Racemic Products 165
6.6.3 List of Peptide Catalysts 169
6.6.4 Remaining Dakin-West reactions 183
7 Analytical Data 184
8 References 256
9 Acknowledgments 274

1 Introduction

The synthesis of chiral molecules is no longer a technical challenge but a requirement in modern chemical research. In biological environments where interactions are governed by inherently chiral macromolecules such as enzymes, proteins and nucleic acids, the spatial arrangement of a small molecule determines its physiological destiny and activity.[1] The significance is reflected in the requirements of modern drug discovery and natural product synthesis where the control of absolute configuration has become a standard for safety and efficacy.[2–4] Therefore, the development of robust methods for enantioselective synthesis remains important in organic chemistry.

Among the strategies developed to address this, transition-metal catalysis and biocatalysis have set high standards. Meanwhile, asymmetric organocatalysis, a concept originally pioneered as "organische Katalyse" (organic catalysis) by Langenbeck in 1927,[5] has emerged as an alternative, characterized by its operational and sometimes structural simplicity, its stability, and the absence of metal contaminants.[6–8] Yet, despite decades of methodical expansion, the field remains reliant on empirical optimization due to the chemical complexity of each catalytic system.

Enantioselectivity is dictated by subtle differences in the free energy of competing diastereomeric transition states ($\Delta\Delta G^{\ddagger}$).[9,10] These energetic margins are frequently the result of an interplay of weak non-covalent interactions and are notoriously difficult to capture, making the rational prediction of stereochemical outcomes a challenge.[11,12] To overcome these limitations, the focus has increasingly shifted towards data-driven approaches in the last decade.[13–16] Machine learning (ML) enables the identification of patterns within high-dimensional data that often go unseen by human intuition and knowledge. By translating molecular structures into suitable machine readable descriptors, it becomes possible to identify hidden patterns that determine stereoselectivity.[17]

This thesis follows this new direction of augmented chemistry by trying to combine experimental data from the Corey-Bakshi-Shibata (CBS) reduction and the Dakin-West reaction with ML models.[18,19] The aim of this work is to explore the use of ML for the prediction of enantioselectivity in asymmetric organocatalysis, by validating the model performance and identifying its limitations. Ultimately, this approach seeks to improve the understanding of the factors governing stereoselectivity, moving toward a more rational and predictive framework for catalyst design.

1.1 Importance of Chirality in Organic Chemistry

Chirality, a phenomenon first discovered by Pasteur in 1848[20] and formally named by Lord Kelvin in 1894,[20,21] is a structural attribute of molecular systems, defined primarily by the absence of an internal mirror plane or an inversion center.[22] A molecule is considered chiral if it cannot be superimposed with its mirror image. This principle is most frequently illustrated by human hands. While they exist as mirror images of one another, no degree of rotation or translation can bring them into perfect congruence. In a chemical context, this dictates that a molecule and its mirror image are two distinct units, termed enantiomers, which possess the potential for different behavior in chiral environments.[23]

In both biological systems and synthetic chemistry, chirality is found in a variety of different structural motifs, as illustrated in Figure 1.[24–26] While point chirality usually originates from a tetrahedral sp^3-hybridized central atom such as carbon or specific heteroatoms with four unique substituents, axial chirality arises from restricted rotation about a chiral axis, e.g., in BINOL or BINAP. [26–28] This is further complemented by helical chirality in twisted frameworks like the DNA double helix or helicenes,[29,30] as well as other more complex motifs such as spiro or planar chirality.[31,32] Among these, however, point chirality remains the most prevalent and synthetically significant form through the construction of a rigid three-dimensional scaffold. The construction and control of these stereogenic centers is the central objective of most enantioselective transformations,[22] including the ones investigated throughout this study.

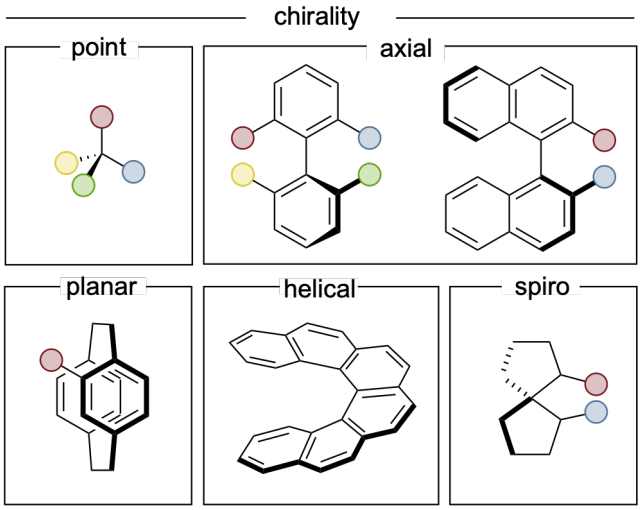


Figure 1: Simplified examples for chiral motifs.

Enantiomers must be distinguished from diastereomers, which are stereoisomers not related as mirror images.[33] Because diastereomers possess different internal spatial relationships between their atoms, they exhibit distinct physical and chemical properties, including varying melting points, solubilities, and chromatographic retention times.[33,34] While the stereochemistry of biomolecules is traditionally described using the relative D/L-system from Fischer,[35,36] the absolute configuration of a molecule is defined by the *R*/*S* nomenclature based on the Cahn-Ingold-Prelog (CIP) priority rules.[37] The practical implications of these configurations are exemplified by the stereoisomers of 2-(methylamino)-1-phenylpropan-1-ol (**1a-d)** in Figure 2.

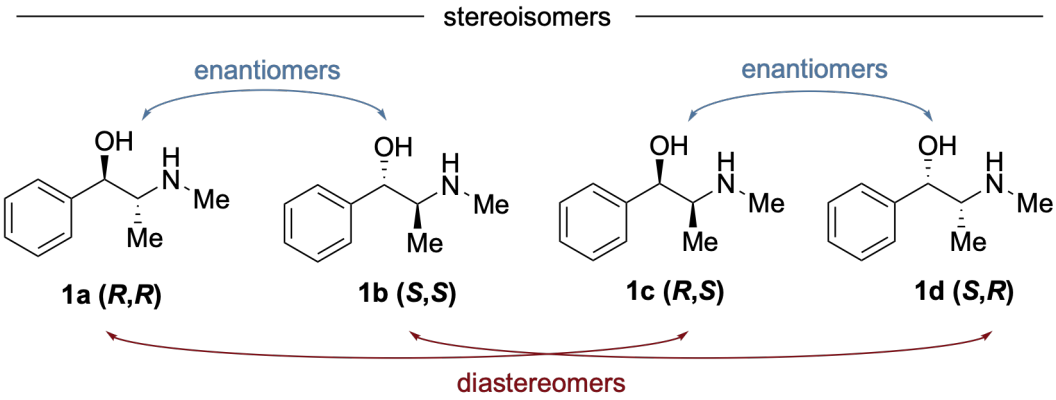


Figure 2: Stereoisomers of 2-(methylamino)-1-phenylpropan-1-ol (**1a-d)** (ephedrine/pseudoephedrine).

In an achiral environment, enantiomers (such as **1c** and **1d**) are physically indistinguishable, as they possess identical boiling points, solubilities, and thermodynamic stabilities.[38] Their only physical difference is the rotation of plane-polarized light, which occurs in equal magnitude but opposite directions. However, this changes in a chiral environment, due to the different spatial interactions with the surrounding chiral medium. When enantiomers interact with other chiral species such as a chiral catalyst or a biological receptor, they form transient diastereomeric complexes. Because these complexes possess different free energies, a thermodynamic differentiation between the two spatial arrangements occurs.[39]

This stereospecific recognition is a decisive factor in biological systems,[1,26] where the human body functions as a highly selective environment.[26,40] The physiological fate of a drug molecule and natural products is directly linked to its absolute configuration, as its spatial orientation determines the nature of its interaction with chiral targets, leading to potentially divergent pharmacological outcomes.[26] These effects are particularly relevant in natural products and

pharmaceutical compounds, where chirality can play a central role in determining biological activity.

1.1.1 Role of Chirality in Natural Products and Pharmaceuticals

The importance of chirality in biological systems is related to the inherent asymmetry of nearly all biomacromolecules, such as enzymes, receptors, and proteins.[1] This structural framework is a consequence of the homochirality of nature, where amino acids predominantly exist as L-enantiomers and sugars as D-enantiomers.[41] Consequently, biological environments function as highly stereospecific chiral media that discriminate between enantiomers based on their spatial orientation.[4]

This discrimination is governed by molecular recognition, where the chiral binding pockets of biological targets provide a specific environment for ligand interaction.[26] Early conceptual models by Fischer (Figure 3) initially described this through the lock-and-key principle, where only a specific chiral isomer fits into the active site of a target.[42] A more refined physical description was provided by Easson and Stedman (Figure 3) with the three-point interaction model, which proposes that a minimum of three simultaneous interactions between a chiral molecule and its environment are necessary to distinguish between enantiomers.[43] Modern understanding, however, views molecular recognition as a dynamic process in which both the chiral molecule and the target can undergo conformational changes, which affects binding affinity and biological activity.[44] These dynamic interactions are based on an interplay of non-covalent forces such as hydrogen bonding, electrostatic and dispersion interactions as well as functional covalent bond formation.[45]

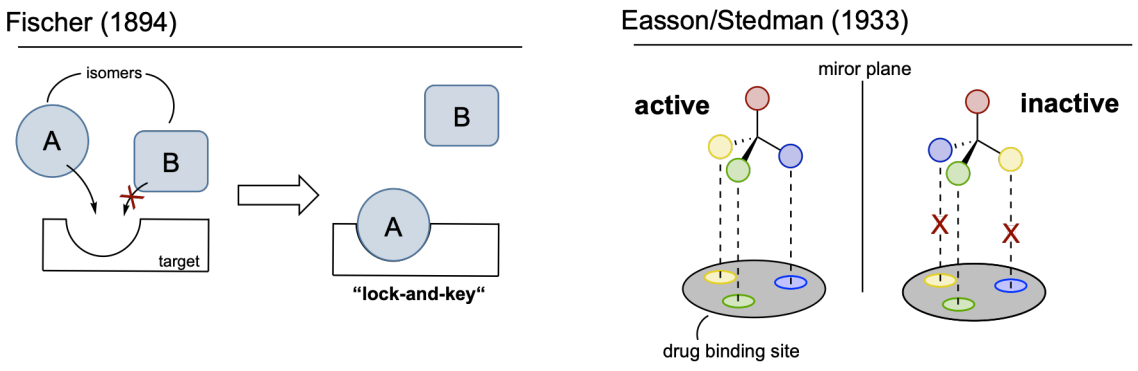


Figure 3: Simplified illustration of Fischer's lock-and-key principle (left). Easson's and Stedman's three-point interaction model (right).

In pharmaceutical applications, stereoselectivity is critical because enantiomers frequently exhibit distinct pharmacokinetic and pharmacodynamic profiles. While one enantiomer provides the desired therapeutic effect, the other can be less active or even inactive. In some cases, the unintended enantiomer is associated with severe toxic side effects.[4] Nevertheless, these differences must be carefully evaluated during drug development to ensure safety and effectiveness. Examples of chiral drugs are summarized in Figure 4. Cases like thalidomide (**2**) and ethambutol (**3**) illustrate the risks associated with a lack of enantiomeric purity in pharmaceutical agents.[4,46,47] In these examples, the wrong enantiomers lead to outcomes such as teratogenic effects or optic nerve damage. In contrast, drugs like levodopa (**5**) and ibuprofen (**4**) show that one enantiomer often exhibits therapeutic activity.[48,49] The other enantiomer is either less active or is converted into the active form within the body. These examples demonstrate that controlling chirality is important for clinical success regardless of the specific biological outcome.

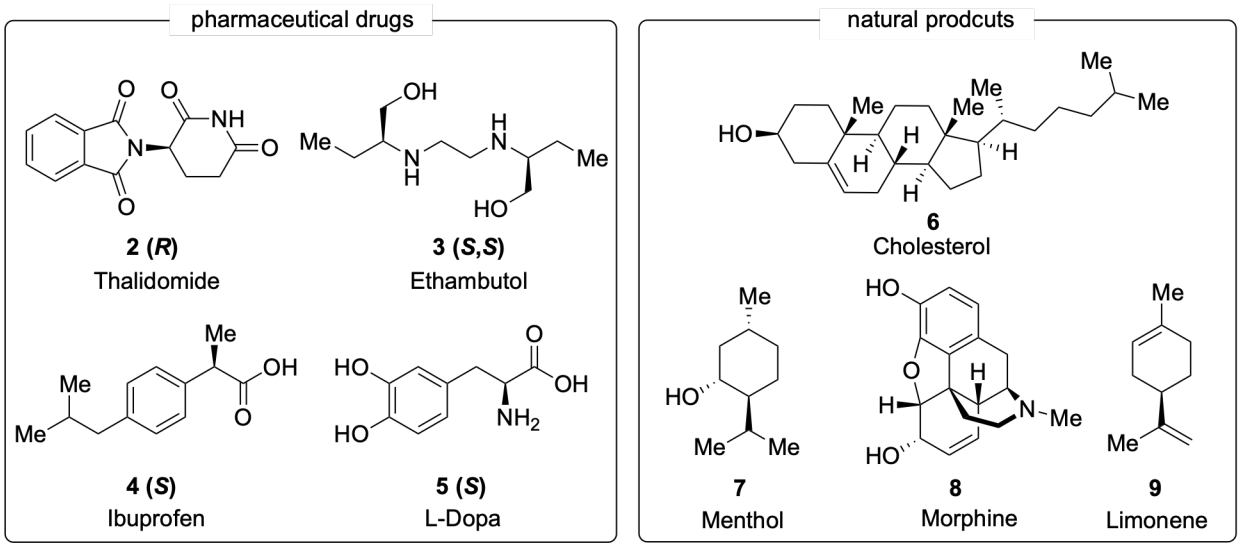


Figure 4: Overview of a small collection of existing pharmaceutical drugs and natural products.

This specificity is evident in natural products which are also shown in Figure 4. Even in simpler molecules, stereochemical differences dictate how we perceive our environment. The human sense of smell distinguishes between the enantiomers of limonene (**9**) as the separate scents of orange and lemon.[50] Similarly, specific forms of menthol (**7**) are responsible for the characteristic cooling sensation on the skin and mucous membranes.[51] In more complex natural products, this significance becomes even more pronounced. Compounds such as cholesterol (**6**) or morphine (**8**) possess multiple stereogenic centers, which theoretically allow for a vast number of

stereoisomers.[52,53] As the number of stereogenic centers (n) increases, the maximum number of potential stereoisomers grows exponentially according to the 2^n rule.[54,55] For a molecule like **6** which contains eight stereogenic centers, this geometric progression results in 256 possible configurations. Yet, nature selectively produces only a single stereoisomer to ensure precise biological functionality.

The metabolic fate of these substances is also influenced by chirality, as enantiomers often follow distinct enzymatic pathways.[56] Such differences in metabolism can significantly alter the overall biological profile and safety of a drug. This metabolic and sensory discrimination, coupled with the requirements of regulatory authorities like the Food and Drug Administration,[57] emphasizes that enantiomeric purity is no longer exclusive but a clinical and biological necessity. However, the transition from recognizing this necessity to its practical realization in the laboratory remains one of the most significant hurdles.

1.1.2 Strategies and Challenges for Accessing Enantiopure Compounds

Chemical reactions typically yield racemic mixtures, in which both enantiomers form in equal proportions. When only a single enantiomer is desired, chemists must apply specific strategies to obtain it in pure form. One commonly used approach is the resolution of racemates,[34] where the mixture is separated into its individual enantiomers. Although widely applied, this method is inefficient from an economic point of view, as it often involves discarding up to half of the synthesized material.[51] This leads to increased production costs and significant chemical waste.

To avoid the problem, chemists often utilize the chiral pool strategy,[58] introduced by Seebach.[59] This method employs enantiopure molecules provided by nature, such as L-amino acids or D-sugars, as starting materials. The primary advantage is that the required stereogenic centers do not need to be constructed from scratch, as they are directly incorporated from the biological precursor. In this work, this strategy is exemplified by the preparation of the catalysts used for the CBS reduction and the Dakin-West reaction. However, the chiral pool is restricted by the limited structural diversity of available natural products.

Another established technique is the use of chiral auxiliaries,[60] pioneered by chemists such as E. J. Corey[61] and D. A. Evans.[62] In this approach an enantiopure directing group is temporarily covalently attached to an achiral substrate to control the stereochemical outcome of the subsequent

reaction. Although this method provides excellent stereoselectivity it requires additional synthetic steps for the attachment and cleavage of the auxiliary and relies on stoichiometric amounts of the chiral directing group.

The limitations of both resolution and the chiral pool and chiral auxiliaries become even more apparent when dealing with complex natural products or highly functionalized compounds. As seen with molecules like cholesterol, the number of potential stereoisomers grows exponentially with each additional stereogenic center. In such cases, neither late-stage separation nor simple starting materials are sufficient to achieve the required stereochemical precision.

These constraints can be bypassed by asymmetric catalysis, which offers a more direct route to enantiopurity. Using small amounts of a chiral molecule to guide the direction of a reaction enables chemists to achieve levels of stereochemical precision that were previously only seen in biological systems. This strategic shift towards catalytic induction provides the necessary framework to overcome the most challenging stereochemical problems in modern molecular design.

1.2 Principles of Asymmetric Organocatalysis

Asymmetric catalysis enables chemists to achieve levels of efficiency and selectivity that are comparable to those of natural systems. The field can generally be divided into several major classes such as transition metal catalysis, biocatalysis, photocatalysis, and organocatalysis.[63–66]

Among the various classes, organocatalysis utilizes the structural and electronic properties of small metal-free molecules to activate substrates and enforce stereochemical control. The immense impact of this field was continuously driven by the creation of diverse catalysts by chemists such as Jacobsen, Schreiner, and Akiyama.[67–70] However the major public breakthrough was achieved when the Nobel Prize in Chemistry in 2021[71] was awarded to B. List and D. W. C. MacMillan for the “development of asymmetric organocatalysis”.[72,73] A major advantage of this approach is the avoidance of often toxic transition metals. This makes organocatalysis particularly attractive for pharmaceutical synthesis, where the removal of toxic trace impurities from final products is a major and costly challenge.[74,75] Beyond safety, these small molecules offer exceptional practical utility as they are generally highly economically viable, typically stable towards air and moisture, and can often be recovered from the reaction mixture.[65,75]

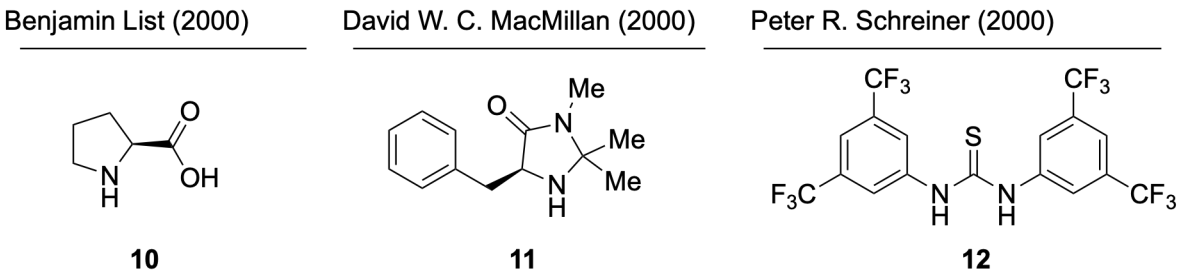


Figure 5: Representative catalysts for asymmetric organocatalysis. The natural amino acid L-proline (**10**) for bifunctional enamine activation used by List (left). First-generation imidazolidinone catalyst **11** for iminium activation pioneered by MacMillan (middle). The achiral thiourea derivative T1 (**12**) introduced by Schreiner representing explicit hydrogen bonding catalysis (right).

Although early organocatalytic systems required high catalyst loadings due to lower reactivity compared to established transition metal catalysts, modern developments have largely overcome this barrier.[76] Nevertheless, successfully applying these systems requires careful optimization. Both reactivity and stereocontrol remain highly sensitive to diverse reaction parameters such as temperature, solvents and subtle structural changes in the substrate.[77,78]

To understand how these small molecules exert stereochemical control under such conditions, it is first necessary to consider the energetic parameters that fundamentally govern enantioselectivity.

1.2.1 The Energetic Basis of Enantioselectivity

Enantioselective catalysis relies on the kinetic differentiation between competing stereochemical pathways. Without a catalyst, the competing pathways to each enantiomer exhibit the same activation energy as seen in Figure 6.[79] However, a selective chiral catalyst can primarily lower one of the activation barriers. Within the framework of transition state theory,[80,81] the ratio of the formed enantiomers is thus determined directly by the difference in Gibbs energy ($\Delta\Delta G^{\ddagger}$) between the corresponding diastereomeric transition states, with the absolute magnitude of $\Delta\Delta G^{\ddagger}$ dictating the degree of selectivity.[82]

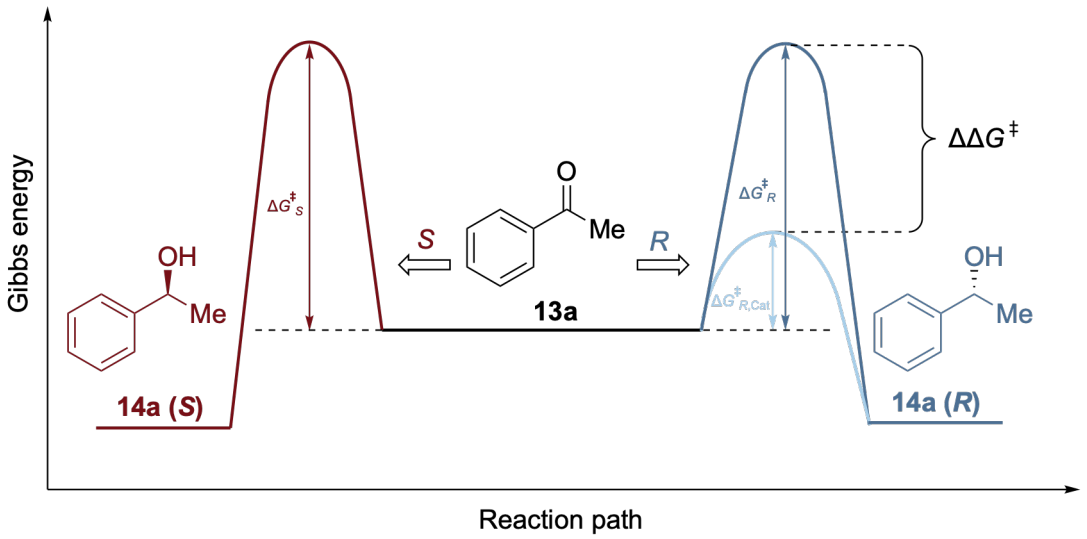


Figure 6: Schematic energy profile of enantioselective catalysis. The final product distribution is determined by the absolute Gibbs energy difference ($\Delta\Delta G^{\ddagger}$) between the competing diastereomeric transition states.

The enantiomeric ratio (*er*) is determined by the ratio of the rate constants of the two competing pathways. By applying the Eyring equation[80] to each pathway, the pre-exponential factors cancel out, yielding an exponential relationship between the *er* and the energetic difference, which is expressed in its logarithmic form [1]:

$$\ln(er) = \frac{\Delta\Delta G^{\ddagger}}{RT} \qquad [1]$$

In this expression, R represents the universal gas constant and T the absolute temperature. This equation provides a direct mathematical connection between the macroscopic, experimentally measurable product distribution and the microscopic free energy disparity between the two competing transition states. Consequently, the energetic margins required for high selectivity are remarkably narrow. For example, at 294 K, a $\Delta\Delta G^{\ddagger}$ of approximately 3.1 kcal mol^{-1} is sufficient to achieve an *er* of 99.5:0.5, which corresponds to an enantiomeric excess (*ee*), defined as the absolute difference between the mole fractions of the two enantiomers, of 99%.[9] To put this into perspective, this energy gap is often smaller than the stabilization provided by a single hydrogen bond or typical London dispersion (LD) forces.[12]

Furthermore, it is crucial to consider that $\Delta\Delta G^{\ddagger}$ is a composite of enthalpic ($\Delta\Delta H^{\ddagger}$) and entropic ($\Delta\Delta S^{\ddagger}$) contributions,[83] as expressed by the Gibbs-Helmholtz relation [2]:

$$\Delta\Delta G^{\ddagger} = \Delta\Delta H^{\ddagger} - T\Delta\Delta S^{\ddagger} \qquad [2]$$

While $\Delta\Delta H^{\ddagger}$ typically reflects differential steric repulsion or electronic stabilization, such as π-stacking or electrostatic interactions, the $\Delta\Delta S^{\ddagger}$ term accounts for changes in molecular degrees of freedom and solvent organization in the transition state. This explains the significant temperature dependence often observed in asymmetric catalysis and highlights that even subtle variations in the molecular environment or reaction conditions can shift the energetic landscape, thereby altering the final stereochemical outcome.[10]

1.2.2 Catalyst Activation and Non-Covalent Interactions

To achieve these energy differences organocatalysts use activation modes to control both the electronic properties and the precise geometry of the transition state. Based on the nature of substrate binding the field of organocatalysis is broadly divided into covalent and non-covalent processes.[77] Non-covalent approaches activate the substrate through weak intermolecular forces such as hydrogen bonding exemplified by the work of Takemoto on bifunctional thioureas and Schreiner on hydrogen bond donors.[68,84] Covalent catalysis on the other hand relies on the formation of transient chemical bonds a principle also shared by the enamine and iminium activation of List and MacMillan (Figure 5).[72,73]

This thesis investigates two distinct covalent activation modes to achieve precise stereochemical control. The first, the CBS reduction,[85] utilizes a cooperative Lewis acid and base interaction to activate the substrate. The second, the Dakin-West reaction,[86] employs and initial nucleophilic acyl transfer to generate reactive intermediates but relies on a chiral Brønsted base to dictate the stereoselectivity in the catalytic cycle. Both mechanisms are described in more detail in the later chapters.

While these electronic interactions establish the fundamental reactivity, the actual stereochemical differentiation is governed by a complex network of secondary non-covalent interactions (NCIs) within the transition state. Recent studies demonstrate that spatial arrangement is controlled by a delicate balance of repulsive interactions, directional hydrogen bonding, and attractive LD forces.[12,87,88]

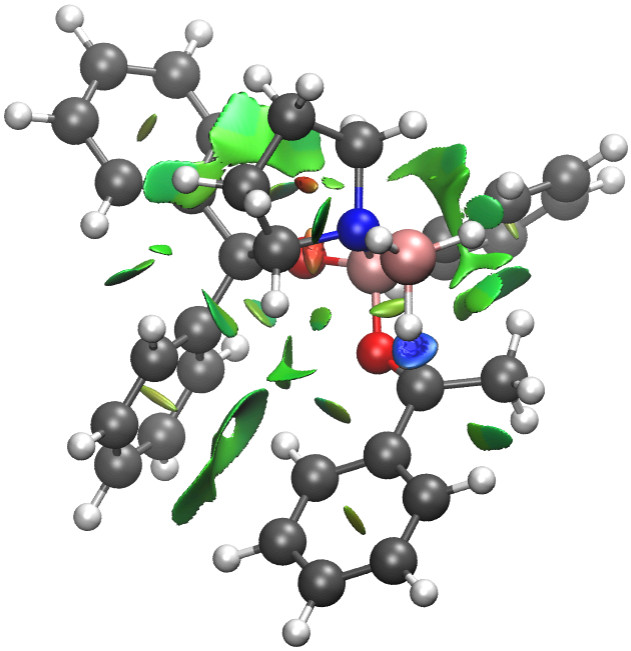


Figure 7: NCI plot of the transition state structure for the CBS reduction, optimized at B3LYP-D3(BJ)/6-311G(d,p). The NCI surfaces are colored according to the sign of the second eigenvalue (λ_2) multiplied by the electron density (ρ). Blue indicates strong attractive interactions (*e.g.*, hydrogen bonds), green represents weak non-covalent interactions (such as LD interactions), and red highlights repulsive interactions.

However, organic frameworks inherently possess significant conformational freedom which results in highly dynamic and flexible transition states. The predictability of the catalytic outcome is severely hindered by this conformational breadth, the competitive influence of the solvent media and the often nonadditive nature of substituent effects. Because of this multivariable complexity structural modifications intended to enthalpically favor one specific pathway are frequently counteracted by unpredictable entropic penalties. Consequently, predicting a precise stereochemical outcome based on physical organic intuition often reaches its limits.[89] To address these challenges, modern ML techniques have emerged as a tool to navigate this high-dimensional chemical space.[14,15] Before exploring these statistical strategies, the following sections will first introduce both mentioned catalytic systems used in this work.

1.3 The Corey-Bakshi-Shibata-Reduction

The CBS reduction is widely recognized for achieving high levels of enantioselectivity in the reduction of prochiral ketones,[90–93] while also being used for other enantioselective reactions such as Diels-Alder reactions or [2+2]-cycloadditions.[94–96] A primary strength of this system lies in the modularity and accessibility of the catalyst. The catalyst is typically synthesized through the combination of prolinol precursor and a borane source, such as BH_3•THF or BH_3•SMe_2. This results in a five-membered heterocycle containing oxygen, nitrogen, and boron, a so-called oxazaborolidine **15** (see Figure 8).

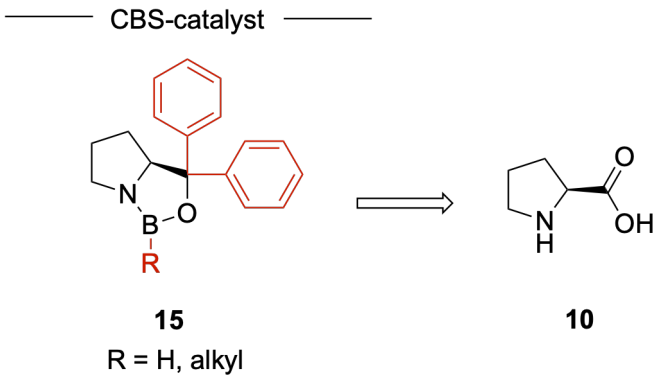


Figure 8: Origin and structural features of the CBS catalyst (**15**). The core scaffold is derived from L- or D-proline with positions for structural derivatization highlighted in red.

The structure of catalyst **15** can be modified in several ways to optimize its reactivity in given reactions (Figure 8). The aryl groups for example, can be varied during the synthesis of the proline precursor. Additionally, the use of different borane species allows for the introduction of various substituents directly on the boron atom.

While the catalyst is defined as a chiral Lewis acid for the reduction of ketones, it possesses a Lewis basic nitrogen atom which is essential for the reaction. This bifunctional nature is important to its efficiency as it enables the simultaneous coordination and activation of both the substrate and the borane reagent.[85] Combined with its mild nature and robust performance, the CBS catalyst provides a reliable method for enantioselective reductions, as evidenced by the extensive research conducted over the last decades.[85]

1.3.1 Origin and Development of the CBS Catalysis

The foundational principles of oxazaborolidine catalysis were established in 1968 when Fiaud and Kagan reported the first asymmetric ketone reduction using a chiral amine borane complex.[97,98] Although yielding only marginal enantioselectivities of 3.6 to 5.0% *ee* this pioneering work inspired subsequent investigations into amine borane reducing agents. A major breakthrough occurred in 1981 when Itsuno and coworkers reported the asymmetric reduction of aromatic ketones (**13a-d**) using stoichiometric amounts of amino borane complexes (**16-19**) achieving enantioselectivities of 60% *ee*.[98] Over the next three years the same group systematically refined this approach developing a enantiopure L-valine derived reagent (**20**) that delivered optical yields of up to >99% *ee*.[99] This optimized reagent became widely recognized within the scientific community as the Itsuno reagent (**20**) serving as the direct precursor to modern oxazaborolidine catalysis (Figure 9).

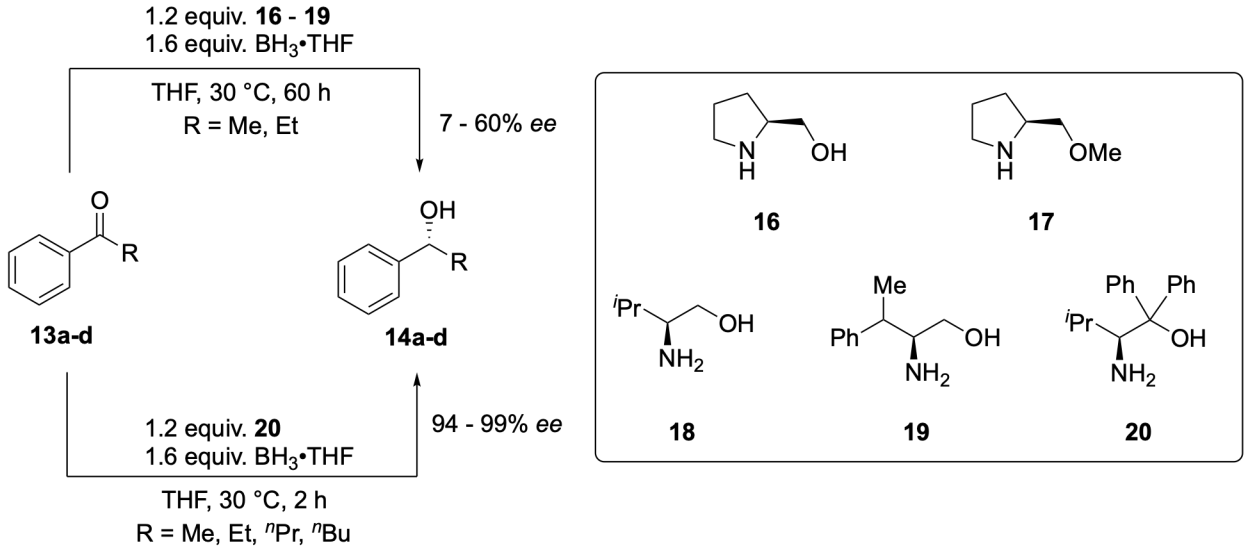


Figure 9: Itsuno's initial studies that led to the development of Itsuno reagent (**20**).

While the Itsuno reagent (**20**) was highly effective, its stoichiometric requirement and limited scope regarding non-aromatic substrates prompted further innovation. In 1987 and 1988, Corey, Bakshi and Shibata solved these limitations by introducing the universally recognized CBS catalyst precursor (**22a**) as seen in Figure 10.[91,92]

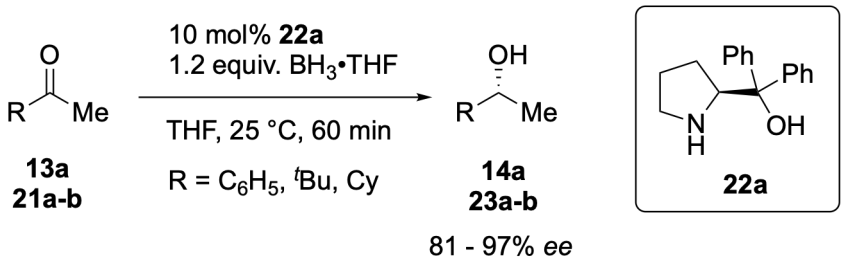


Figure 10: Corey's demonstration of high *ee* achieved in the reduction of the ketones using catalytic amounts of the catalyst precursor (**22a**) and BH3•THF.

They demonstrated that this new system could achieve high *ee* ranging from 81 to 97% *ee* for a diverse array of ketones using only catalytic amounts of oxazaborolidine and proposed a comprehensive mechanistic model (Figure 11).[85,90]

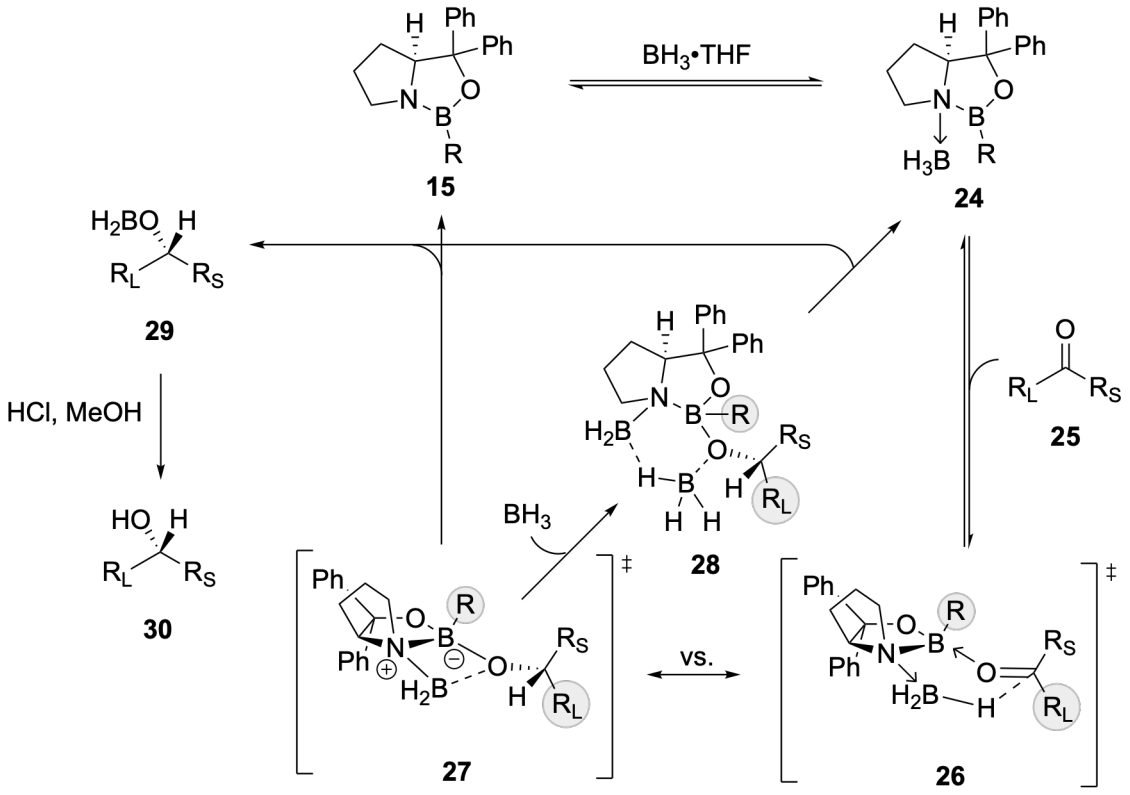


Figure 11: CBS-mechanism proposed by Corey and coworkers for the reduction of ketones.

In their proposed mechanism, the cycle is initiated by the coordination of the Lewis acidic borane to the Lewis basic nitrogen atom of oxazaborolidine **15**. This step enhances the Lewis acidity of the boron center while simultaneously activating BH_3 (**24**) to become a more potent hydride donor.[85] Subsequently, the carbonyl oxygen atom of ketone **25** coordinates to the activated boron

atom that enables the stereo-defining hydride transfer to yield **29** through transition state **26** and **27** (Figure 11).

The stereochemical outcome of this hydride transfer was originally rationalized through a purely steric approach. In this model the spatial arrangement of the substrate is dictated by the relative sizes of its large (R_L) and small (R_S) substituents. To minimize steric strain with the catalysts substituents the substrate aligns in a boat-like transition state (**26**). Within this framework repulsion between the catalysts boron substituent and the large ketone substituent is considered the decisive factor for enantiocontrol.[85] Following the hydride transfer the cycle proceeds to form a stable alkoxyborane (**29**) intermediate while regenerating the catalyst. This intermediate remains unreactive until the final aqueous work-up releases the enantiomerically enriched alcohol (**30**).

Over the next decade extensive optimizations established the CBS reduction as a highly robust synthetic method.[85] The synthetic utility of these chiral oxazaborolidines was further expanded in the early 2000s when Corey applied the structural motifs to asymmetric Diels-Alder and enantioselective [2+2]-cycloaddition reactions.[96,100]

While further studies were conducted in the 21st century, no fundamental shifts in the understanding of the system were established. This changed in 2021 when Schreiner and coworkers proposed a different mechanistic perspective based on computational and experimental evidence.[87]

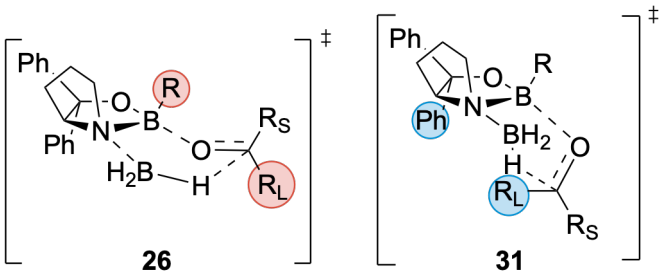


Figure 12: Comparison of the Corey (**26**) and Schreiner (**31**) transition state models for the enantioselective reduction of ketones catalyzed by the CBS catalyst.

They suggested that the reaction eventually proceeds *via* a chair-like transition state (**31**) in which the aryl substituents of the catalyst play a fundamentally different role (Figure 12). Schreiner demonstrated that attractive non-covalent interactions, specifically LD interactions, are essential

for stabilizing this transition state. In this framework, the large aryl groups of the catalyst act as dispersion energy donors (DEDs) that actively engage in attractive interactions with the substituent of the substrate, thereby competing with traditional steric repulsion.

1.3.2 Development of Imine or Ketimine Reduction

In contrast to the reaction with ketones, the history of asymmetric imine reductions within this period followed a more complex and narrower path. Two years after Corey's initial reports, Cho and Chun were the first to evaluate both the Itsuno and CBS systems for the reduction of imines.[101] However, their studies revealed that the CBS catalyst (**24**) was less effective than the Itsuno-reagent (**33**) for the substrates (**32a-g**) shown in Figure 13. Furthermore, stoichiometric amounts of the reagent were required to suppress background reactions. It was also noted that cyclic imines (**37**) could not be reduced by any of the reagents shown, and that *N*-substituted alkyl ketimines, such as **35** and **36**, performed poorly (9 or 14% *ee*) even when utilizing the Itsuno reagent (**33**).

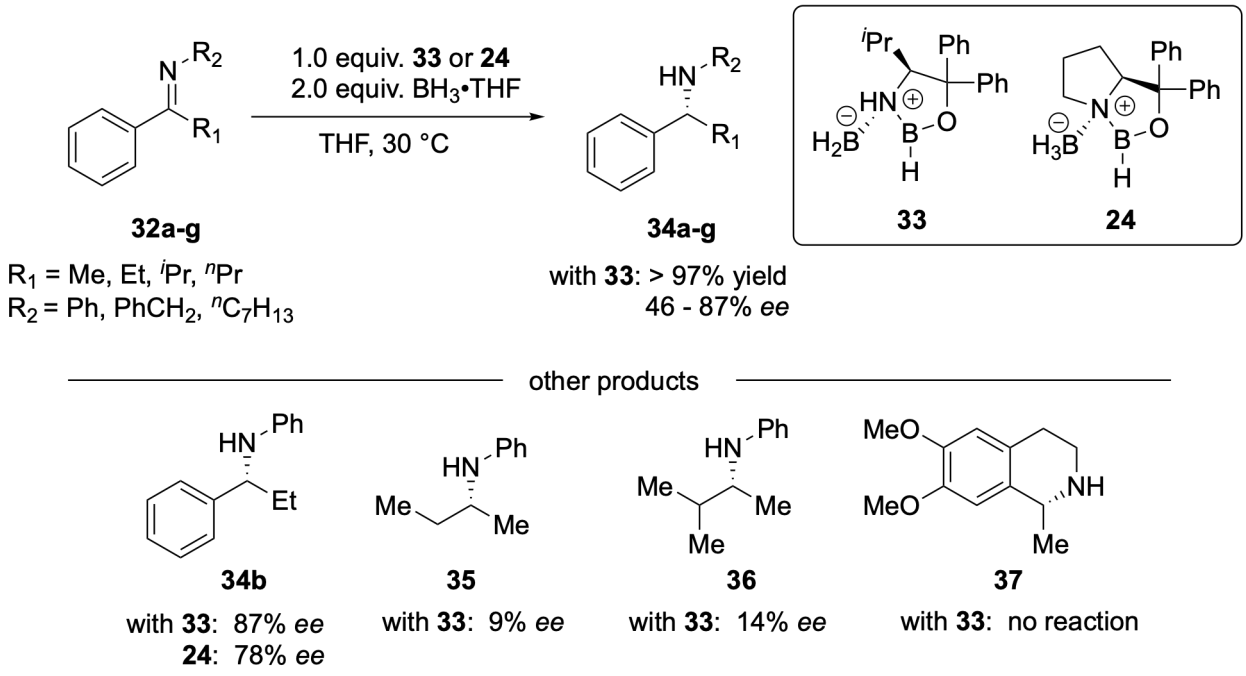


Figure 13: The Itsuno reagent (**33**) outperforms the CBS catalyst (**24**) in the reduction of imines. Additional evaluated substrates are depicted while cyclic derivatives proved unreactive.

In a follow up study from 1992 (Figure 14),[102] Cho and Chun demonstrated that the CBS catalyst could, in fact, be used in catalytic amounts (10 mol%) to reduce imines to the corresponding amine **34b** (92% yield, 70% *ee*), even surpassing the performance of the Itsuno reagent under catalytic

conditions (95% yield, 66% *ee*). However, they did not capitalize on this finding and instead suggested the continued use of the Itsuno reagent in stoichiometric amounts. This was due to the fact that the stoichiometric Itsuno reagent still provided better *ee*.

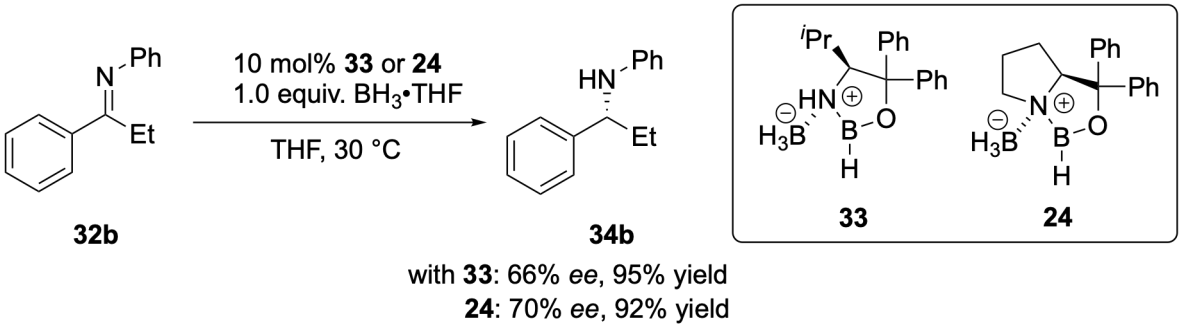


Figure 14: Demonstration that both the Itsuno reagent (**33**) and the CBS catalyst (**24**) can be employed in catalytic amounts for the reduction of imines. Under these conditions the CBS catalyst (**24**) exhibits better performance compared to the Itsuno reagent (**33**).

In the following years, only a few groups independently explored the potential of a catalytic imine reduction using the CBS catalyst. In 1996, Uneyama reported the reduction of α-imino esters with a moderate enantioselectivity of 63% *ee*.[103] This was followed by a 2004 study which demonstrated that the choice of reducing agent could influence the stereochemical configuration of the products.[104] Specifically, while the use of BH_3•THF yielded the (*R*)-enantiomer, the use of catecholborane resulted in the (*S*)-enantiomer, which the authors explained through a conceptual transition state model.

Notably, in 2003, research temporarily returned to the use of stoichiometric amounts of the chiral reagent, highlighting some unexplained challenges within the system but also showing that cyclic imines could after all be reduced as well.[105] It was not until 2011, that the catalyst could be utilized in catalytic amounts for the enantioselective reduction of sultams.[106] Apart from a computational study in 2020 describing a possible transition state for the imine reduction,[107] further developments remained limited. When compared to the rapid evolution of ketone reductions, the progress in imine systems appears significantly less developed and remains largely unexplored.

1.3.3 Comparing Ketones and Imines

The different behavior of imines during asymmetric reduction originates from their altered bond polarization compared to ketones. According to the principles of bond polarity, ketones are characterized by a strongly polarized C=O bond due to the high electronegativity of oxygen

($\chi = 3.44$).[108] This facilitates a rigid and predictable coordination to Lewis acidic centers, which is essential for the organized transition states established in CBS-type reductions.[87,90] In contrast, the C=N bond in imines is less polarized because nitrogen is less electronegative ($\chi = 3.04$).[108] This implies that the nitrogen atom holds its lone pare less tightly, making it a stronger Lewis base, which facilitates non-catalyzed background reactions.[109] This uncatalyzed pathway often proceeds *via* direct coordination of the imine nitrogen to the achiral reducing agent, producing racemic mixtures and thereby inevitably lowering the *ee* of the catalytic process. Furthermore, nitrogen introduces an additional substituent (N-R), leading to the existence of *E*/*Z* isomers.[109] This creates multiple, competing possible coordination modes that can destabilize the complex required for high stereocontrol.

The synthetic motivation for overcoming these challenges lies in the nature of the resulting products. While ketone reduction yields secondary alcohols, the asymmetric reduction of imines provides direct access to chiral secondary amines. These amines serve as indispensable building blocks in the synthesis of complex molecular architectures, particularly in pharmaceutical and bioactive compounds.[110] To achieve high enantioselectivity despite the high reactivity of the imine substrate the catalytic system must be optimized to suppress background pathways while maintain the selectivity of the CBS catalytic cycle.

1.4 Dakin-West reaction

The Dakin-West reaction which is thermodynamically driven by the release of carbon dioxide, is an organic transformation that converts α-amino acids (rac-**38)** into their corresponding α-acetamidoketones (rac-**40**). Originally reported in 1928 by H. D. Dakin and R. West,[86] this method relies in principle on the reaction of an amino acid with an anhydride (**39**) in the presence of a nucleophilic base, as illustrated in Figure 15.

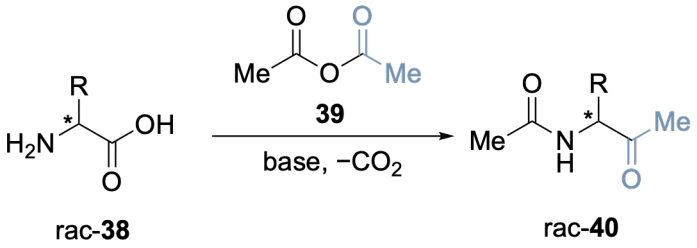


Figure 15: The Dakin-West reaction. The functional group undergoing transformation is highlighted in blue.

Over the decades this method has evolved into a versatile strategy for generating synthetic building blocks as it provides direct access to bifunctional motifs.[111] This versatility stems from several practical advantages, most notably its efficiency as a one-pot procedure running under relatively mild conditions. Furthermore, the scope of the reaction is remarkably broad, as it is not strictly limited to primary α-amino acids but can also be applied to secondary amino acids and simple carboxylic acids.[86,111] A notable historical application is Woodward's synthesis of Strychnine in 1954,[112] which successfully utilized this method to construct a key intermediate towards this bioactive natural product.

Despite its recognition as a robust technique for assembling specific structural motifs, a major historical limitation was the lack of a stereoselective version. This limitation was overcome in 2016 by the Schreiner group.[113] Through the use of peptide catalyst bearing a π-methylhistidine as catalytically active moiety they established absolute stereocontrol bringing this classic reaction firmly into the era of asymmetric synthesis.

1.4.1 The Classic Mechanism and Racemization Challenge

Understanding the inherent stereochemical challenges of this method requires a detailed examination of its mechanism (Figure 16).

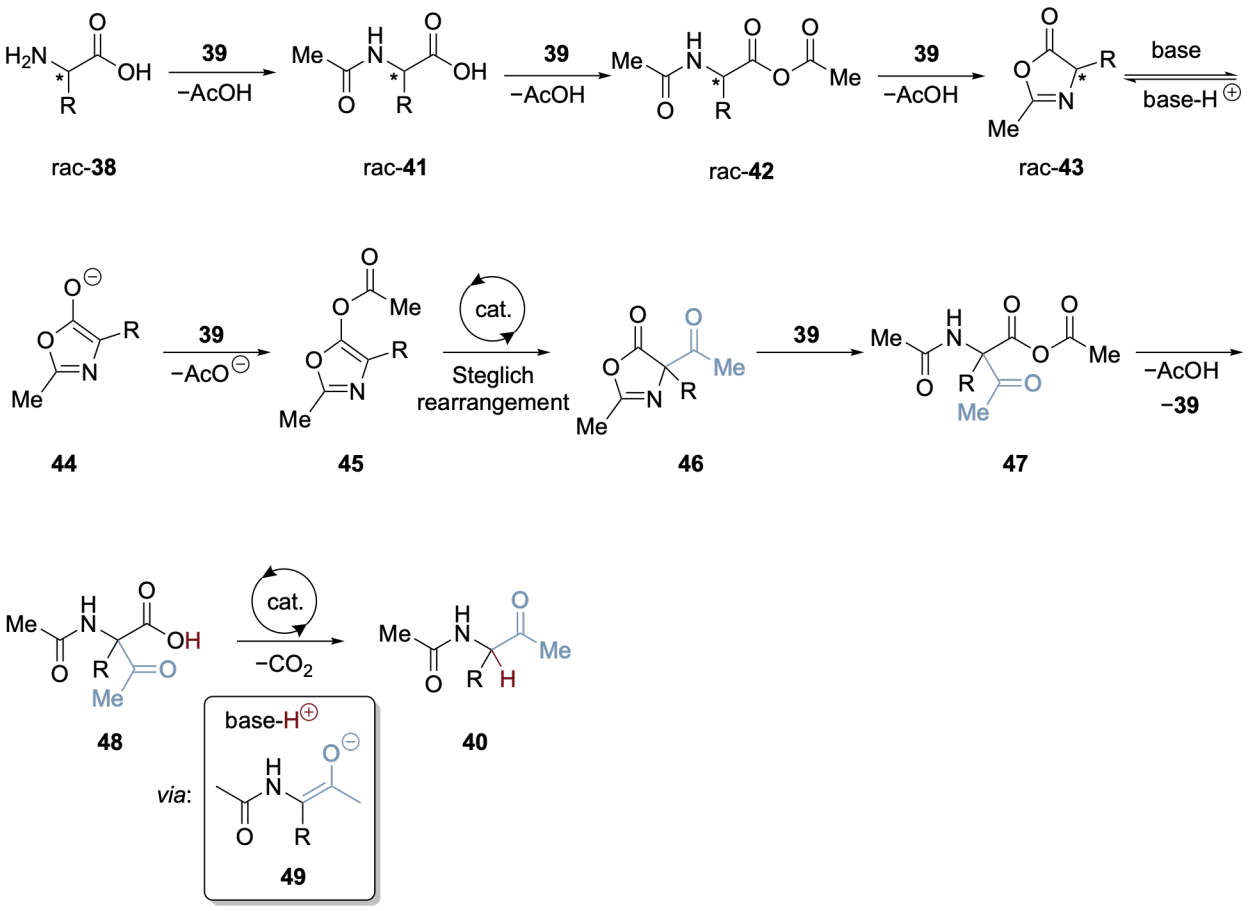


Figure 16: Proposed mechanism for the Dakin-West reaction.

The reaction proceeds through a well-defined but complex sequence of acylation events that release acetic acid in every single step, resulting in the formation of an azlactone intermediate (rac-**43**), also known as an oxazolone.[19] The reaction begins with the initial nitrogen acylation of the amino group (rac-**38**), followed by activation of the carboxyl group through formation of a mixed anhydride (rac-**42**). Subsequent cyclization yields the azlactone intermediate (rac-**43**). The existence of these highly reactive species including the mixed anhydride (rac-**42**) and the azlactone (rac-**43**), was experimentally validated through advanced mass spectrometric investigations.[114] In the presence of a base, rac-**43** is then deprotonated to form a resonance-stabilized enolate (**44**), which then undergoes further acetylation by the anhydride. The typical product arises from carbon acetylation a process heavily favored by the Steglich rearrangement.[115] This crucial O- to C-acyl transfer is driven by nucleophilic catalysts such as DMAP, which efficiently convert any oxygen acetylated species (**45**) into the required thermodynamically favored carbon acetylated intermediate (**46**). Subsequent ring opening by acetic acid yields a β-keto acid derivative (**48**) after

transacylation, which undergoes rapid decarboxylation through an enolate intermediate (**49**) to form the final product (**40**).

The issue regarding stereocontrol is that the original stereochemical information of the starting amino acid is completely lost during the reaction sequence. For this reason, racemic starting materials can be employed. The initial loss of stereochemical information occurs upon the deprotonation of the azlactone. Furthermore, following the final decarboxylation, the system forms a second, highly reactive enolate species in which the final protonation is unselective, resulting in a racemic product mixture.[19]

1.4.2 Asymmetric Catalysis and Peptide Architecture

The use of synthetic oligopeptides for asymmetric acyl transfer reactions has been significantly advanced by the studies of Miller and coworkers.[116] While these peptide-based catalysts are well established for various transformations, the Schreiner group demonstrated that standard motifs, such as the established D-Pro-Aib-turn fail to induce high stereoselectivity under the Dakin-West conditions.[113] To solve this problem, they designed a tripeptide catalyst **50** (Figure 17) that achieves an *ee* ranging from 11 – 58 % across different substrates.[113]

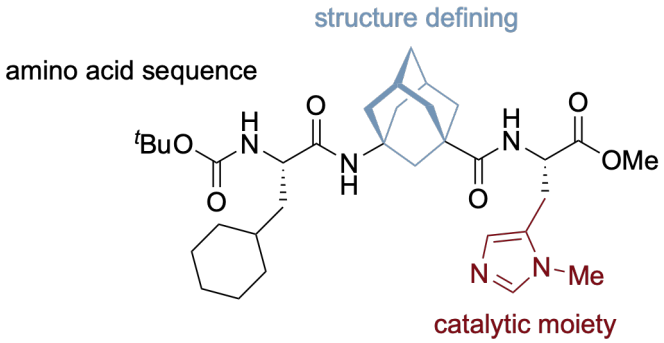


Figure 17: The catalyst **50** employed by Schreiner *et al.* for the enantioselective Dakin-West reaction.[113]

Catalyst **50** contains a C-terminal π-methylhistidine residue and an adamantane-derived amino acid as structural motifs. While the bulky adamantyl group serves as a structural turn to define the steric boundaries of the catalytic pocket, the π-methylhistidine (pmh) fulfills a dual role as the catalytically active moiety (Figure 18). Initially pmh acts as a nucleophilic Lewis base to facilitate the acetyl transfer. Later in the catalytic cycle, pmh functions as a Brønsted base by accepting a proton and temporarily storing it during the decarboxylation step. This proton is subsequently

delivered back to the enolate intermediate in an enantioselective reprotonation step which simultaneously regenerates the catalyst for the next catalytic cycle.[113]

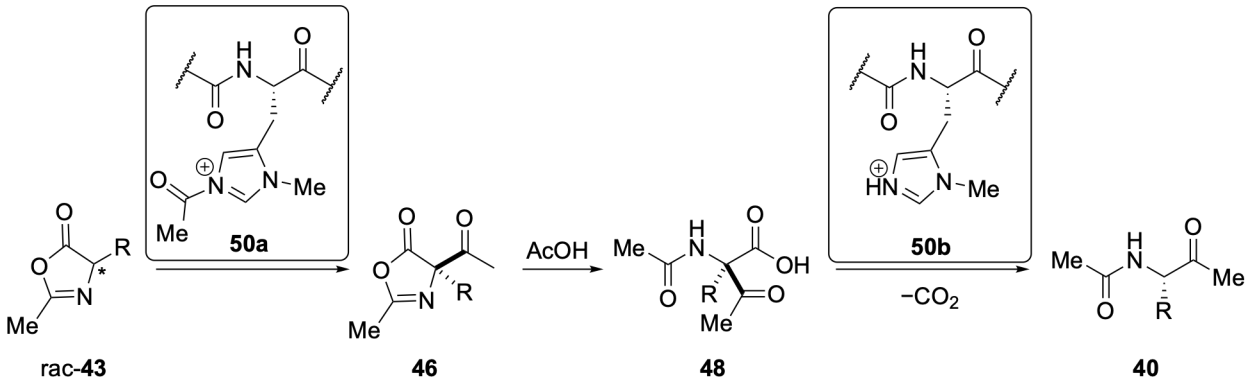


Figure 18: Proposed mechanism by Schreiner *et al.* for the tripeptide catalyst (**50**) in the Dakin-West reaction.[113]

The combination of both motifs ensures the formation of a specific pocket. The ultimate facial selectivity is dictated by a delicate interplay of specific interactions: As depicted by the proposed transition state model by Schreiner and coworkers in Figure 19, the hydrogen bonding anchors the reactive enolate intermediate into a defined position. Within this locked geometry, a cyclohexylalanine residue acts as a key DED.[113] Attractive LD forces between the cyclohexyl moiety of the catalyst and the substrate side chain then govern the facial approach. Confined in this geometric arrangement, protonated pmh delivers its proton exclusively to one face of the enolate, resulting in the observed enantioselectivity.

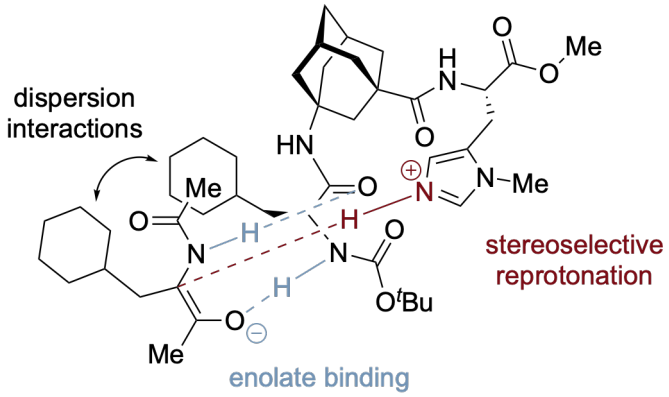


Figure 19: Proposed transition state model by Schreiner *et al.* illustrating the interactions between substrate and catalyst that govern asymmetric induction.[113]

1.5 Machine Learning

As established in the previous chapters the stereochemical outcome of asymmetric transformations such as the CBS reduction and the Dakin-West reaction relies on an intricate interplay of non-covalent interactions.[87,113,117] Because the balance of these interactions creates a multidimensional problem achieving the desired experimental outcome it is often highly challenging and difficult to predict. While mechanistic considerations and computational tools are valuable for understanding these patterns, they remain either limited in scope or are time consuming and difficult to apply across diverse reaction spaces.[118] Consequently, data driven approaches like ML have become an efficient alternative to evaluate these parameters and accelerate molecule development.[119]

As a subfield of artificial intelligence ML offers the algorithmic foundation for recognizing complex patterns within a dataset.[120] Unlike traditional programming with rigid rules, these algorithms autonomously extract mathematical relationships from the provided data.[119] To leverage these capabilities, however, chemical structures must be translated into machine readable formats.[121,122]

1.5.1 Molecular Representation and Featurization

Molecular representations can generally be classified according to their dimensional complexity as seen in Figure 20. One-dimensional text-based approaches like SMILES encode molecules as linear strings.[123] While computationally highly efficient due to their simplicity, they are insufficient for asymmetric catalysis because they completely neglect spatial geometry. Two-dimensional representations such as molecular fingerprints offer a more structural perspective by converting atomic neighborhoods into numerical bit vectors.[124,125] However, this mathematical compression frequently loses critical stereochemical information.[126] To capture the true spatial environment three-dimensional quantum chemical descriptors derived from density functional theory are often utilized.[15] Although these parameters accurately map the intricate electronic environment, calculating them across large datasets demands excessive computational resources and is therefore time consuming.

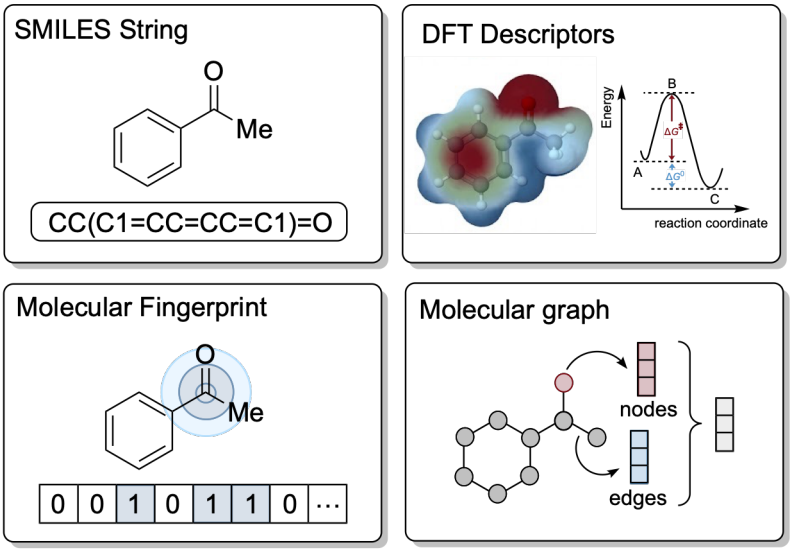


Figure 20: Evolution of molecular representations across different dimensional complexities. The depicted approaches include one-dimensional SMILES strings, two-dimensional topological graphs, and molecular fingerprints, as well as three-dimensional quantum chemical descriptors.

To avoid these limitations topological molecular graphs have emerged as a prominent alternative representation.[127] Within this framework atoms act as nodes containing essential chemical features while bonds act as edges specifying the interaction type. However, modeling a catalytic reaction usually involves separating the substrate and catalyst into separate graphs. Because this separation obscures the crucial non-covalent interactions that dictate stereoselectivity accurately representing the active catalytic complex remains a significant challenge.[128]

1.5.2 Machine Learning Workflows and Model Evaluation

To capture the relationship between molecular structure and chemical reactivity, modern models are categorized learning into unsupervised, semisupervised, and supervised learning.[129] While unsupervised algorithms aim to identify hidden clusters within unlabeled data and semisupervised approaches combine small amounts of known data with vast uncharacterized datasets, the prediction of catalytic performance hitherto relies entirely on supervised learning. In this approach the algorithm maps featurized inputs such as molecular graphs directly to precise experimental outputs like the *ee* or differences of Gibbs energies of activation ($\Delta\Delta G^{\ddagger}$). By continuously minimizing the prediction error during the training process, the model extracts complex connections and correlations within the data with the goal of accurately evaluating the performance of untested catalysts.

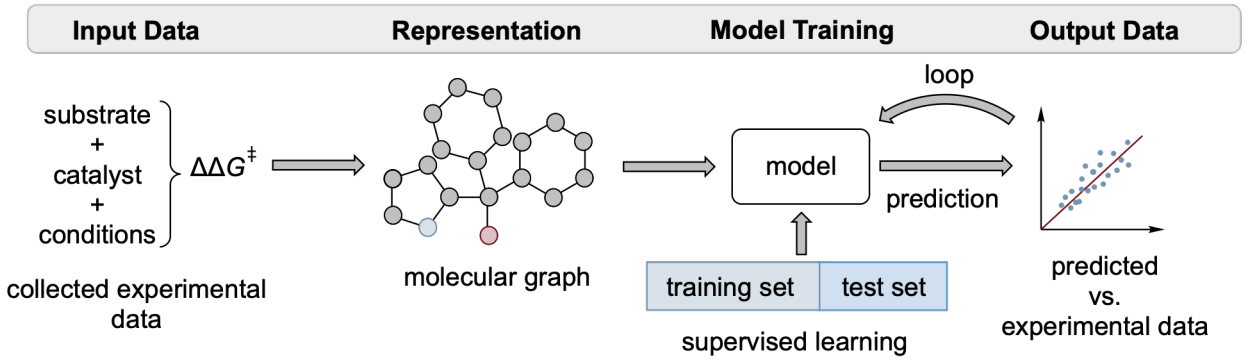


Figure 21: Schematic representation of a simplified ML workflow for predicting transition state energy differences ($\Delta\Delta G^{\ddagger}$).

The architecture of the predictive model dictates how this chemical information is processed. Traditional ML algorithms including random forests support vector regression and gradient boosting machines typically evaluate molecules as flat numerical arrays.[130] While effective for recognizing general trends this linear approach often struggles to differentiate minute spatial variations. In contrast graph neural networks natively process the intricate topology of chemical structures.[131] Through a mathematical mechanism known as message passing, each atom iteratively exchanges information with its direct neighbors.[127] This process allows the network to autonomously build a comprehensive representation of the chemical environment surrounding a reaction center.

Training highly complex algorithms inevitably introduces the risk of overfitting, where a model memorizes training examples rather than learning generalized principles.[132] To prevent predictive failure on novel molecules, datasets are conventionally divided into independent training and test subsets.[133] While a simple random split is often sufficient for large datasets, it can become statistically unreliable when dealing with limited data.[134] In such cases, general cross-validation techniques are implemented. These methods iteratively partition the data into different training and testing sets, ensuring that the model is evaluated on multiple different subsets to provide a robust assessment of its overall generalizability.[133]

Recent landmark studies in asymmetric catalysis have demonstrated the practical value of these optimized workflows. For instance, the research group of Denmark successfully employed data-driven models to predict the stereochemical outcome of chiral phosphoric acid-catalyzed reactions.[13] By analyzing extensive virtual libraries, their algorithms successfully identified highly selective catalyst candidates that were subsequently validated through experimental

synthesis. Similarly, Sigman and co-workers pioneered the use of three-dimensional molecular descriptors combined with ML to accurately predict enantioselectivity across diverse transition metal-catalyzed transformations.[15] Furthermore, foundational work by Doyle and collaborators showcased that sophisticated algorithms can reliably evaluate multidimensional reaction parameters to predict general catalytic performance across broad chemical spaces.[135] Such works confirm that when correctly implemented, ML advances from a theoretical framework to a powerful predictive tool in modern synthetic chemistry.

1.5.3 Data Quality and the Challenge of Publication Bias

The predictive performance still remains strictly constrained by the quality of the training data. Unlike computer vision models that are trained on millions of data points, asymmetric catalysis is short on data. Generating experimental data requires time consuming synthesis and precise analytical quantification which limits typical high-quality datasets.[119] As a result, the primary bottleneck in chemical ML is no longer algorithmic complexity but the lack of robust standardized experimental data.

This underlying challenge is further amplified by publication bias within the scientific literature. Since publications historically favor successful outcomes, the available literature is saturated with highly enantioselective systems while negative results are rarely reported.[136] For a predictive model however, these failed reactions are also valuable. An algorithm cannot map the true stereochemical boundaries if it is exclusively trained on optimal configurations: It must learn from poorly performing reactions to identify the specific properties that cause a selective pathway to fail. Relying solely on published literature therefore creates an artificially shifted database leading to models that cannot generalize to novel substrates.[136]

To overcome these constraints constructing custom standardized datasets is essential. The predictive success ultimately scales with data quality and uniform distribution rather than pure quantity. Conducting targeted reactions under identical conditions including those expected to perform poorly ensures that the dataset provides an accurate representation of the chemical space.[16,135] The synergy of high-quality unbiased data generation and advanced algorithmic processing ultimately provide the framework to systematically address complex challenges in asymmetric catalysis.

2 Motivation

Modern synthetic methods now enable the synthesis of more compounds in a single year than in nearly two centuries of previous chemical history.[137,138] However, the development of new asymmetric catalysts remains difficult because predicting the general catalyst performance and the subtle network of interactions within the diastereomeric transition states of substrate and catalyst is highly complex.[12,117,139] Since large-scale computations are often time-consuming for regular use,[118] complex reaction patterns remain difficult to grasp using human intuition alone. Therefore, new strategies for catalyst optimization are required.

Data-driven approaches like ML offer a way to recognize these intricate patterns within experimental datasets.[129] Yet, applying these tools to synthetic chemistry faces the fundamental challenge of data insufficiency.[140,141] Unlike other fields of artificial intelligence that use millions of data points,[142,143] experimental catalysis operates within a small data regime because generating high-quality stereochemical data is resource-intensive and time-consuming.[15,129,141] Furthermore, the reliance on existing literature is hindered by a publication bias, which favors successful outcomes and leaves out low-selectivity results necessary for a ML model to learn the boundaries of catalytic control.[136,144,145] An objective of this work is therefore to demonstrate how robust predictive models can be developed from limited and unbiased datasets. By shifting the focus from data quantity to data quality, this research aims to establish data-efficient workflows that are directly applicable to practical synthetic challenges.

To evaluate the scope of this approach, two chemical systems with different levels of complexity are investigated. The study begins with the CBS reduction of ketones,[90] which provides a structurally rigid and well-characterized framework to start the initial ML workflows in a controlled environment. Given the extensive knowledge of this reaction,[85] its integration into ML models is expected to be more straightforward than with less well characterized systems. The focus is then further placed on transferring these models to imines. Although the stereoselective reduction of imines is far less explored and presents greater experimental challenges,[101] it is expected to operate within a similar modality. This underlying mechanistic relationship provides a rational basis for adapting the predictive models.

To establish the opposite end of this complexity, the asymmetric Dakin-West reaction is subsequently investigated.[111] While the structurally rigid and mechanistically well-defined CBS

reduction serves as a highly controlled baseline for the initial model, the Dakin-West reaction acts as a stress test for the ML model. This transformation utilizes flexible peptide catalysts capable of adopting a vast number of conformations.[113,146] Given that research into this reaction is still not fully developed,[113] this immense structural complexity creates a significant challenge for molecular representation and requires the algorithm to navigate a highly dynamic conformational space. Capturing the underlying patterns of such a dynamic system evaluates the robustness of the methodology against structural noise. Investigating this challenge aims to reveal whether the framework can be effectively extended to highly flexible catalysts, or if such dynamic systems fundamentally exceed the limits of current representations.

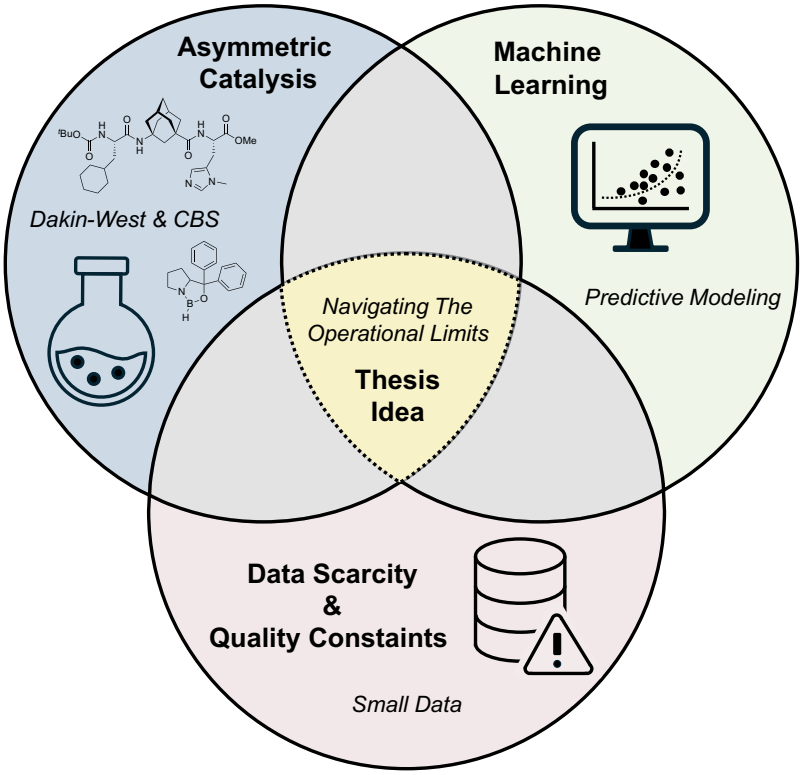


Figure 22: The three research domains in this thesis. The central aim focuses on identifying the operational limits of ML in asymmetric catalysis (CBS and Dakin-West reaction) within restricted data environments.

By contrasting these two reactions, this thesis aims to outline the operational limits of current ML representations in asymmetric catalysis with small data sets. Establishing these boundaries provides the necessary context for the discussion of why models succeed or struggle and evaluates the generalizability of data-driven approaches for synthetic chemistry.

3 Results and Discussion

To ensure a clear overview the discussion of these findings is divided into four main sections.

Section 3.1 introduces a graph-based ML model to solve the 'butanone case' in the CBS reduction. It highlights the workflow, starting with the synthesis of the precursor library, followed by the generation of a predictive model and concluding with the validation of the predictive framework. (The results in this section have been published: O. Pereira,[+] M. Ruth,[+] D. Gerbig, R. C. Wende, P. R. Schreiner, *J. Am. Chem. Soc.* **2024**, *146*, 14576–14586. ([+] These authors contributed equally to this work))

Section 3.2 describes the development of a novel synthetic strategy for accessing bulky CBS precursors and the results obtained that led to the reevaluation of the predictive model introduced in Section 3.1, thereby exploring the intricate relationship between experimental data and algorithmic reliability.

Section 3.3 outlines the attempted expansion of the CBS reduction toward ketimines. It details the combined experimental and computational investigations that uncovered severe kinetic limitations within this substrate class demonstrating why it cannot yet be integrated into the ML frameworks.

Finally, Section 3.4 explores the asymmetric Dakin-West reaction. This section details the experimental efforts undertaken to establish a comprehensive empirical database for this transformation focusing on the systematic optimization of the catalytic parameters and the precise evaluation of the underlying structure-activity relationships.

Part I

Exploring the Corey-Bakshi-Shibata Reduction of Ketones using Machine Learning

3.1 Driven Differentiation of Subtle Features

The initial phase of this work was dedicated to the investigation of the CBS reduction, targeting catalyst **15** to differentiate sterically similar substituents. As seen in Figure 23, **51** represents a difficult case for asymmetric induction due to the minimal difference between its methyl and ethyl groups. We hypothesized that a data-driven approach could reveal structural correlations that are often overlooked in traditional catalyst design.

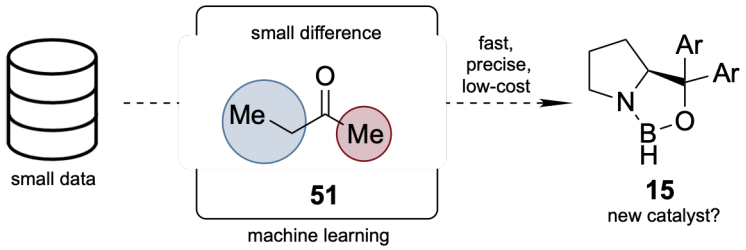


Figure 23: Simplified process of utilizing small data and ML for developing new catalysts.

However, the reliability of any predictive model is tied to the consistency of the underlying experimental data. To avoid the inherent variance of literature-reported values, we aimed to generate an internal dataset under controlled conditions. This required the preparation of a diverse library of catalyst precursors and substrates to probe the influence of different of diverse structural features. Therefore, our investigation started with the synthesis of various precursors.

3.1.1 Synthesis of Catalyst Precursors

For the preparation of the catalyst precursors (**22**), we relied on a four-step protocol starting from L-proline (**10**), following a synthetic procedure established within our research group (Figure 24).[87] This synthetic route allows for late-stage structural diversification by the introduction of various substituents at the carbinol center during the Grignard reaction from **52** to **53**, thereby modifying the steric and electronic properties of the catalyst and building a diverse library. While most of these steps proceed without complications, some steps required optimization to ensure reproducibility and acceptable yields.

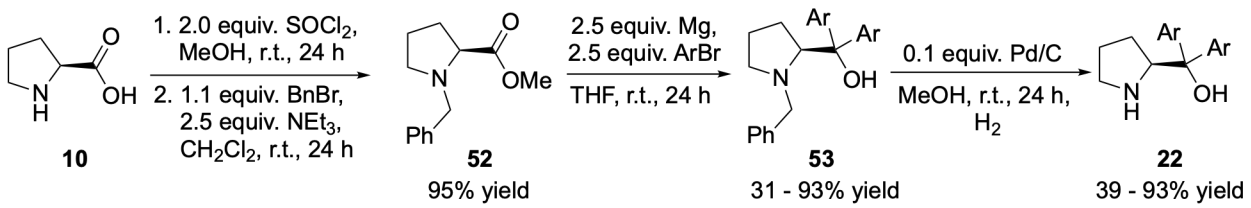


Figure 24: General synthetic protocol for the preparation of various catalyst precursors **22.** The reaction conditions were adapted from Eschmann *et al*.,[87] based on known procedures for the respective derivatives.[147–151]

Upon obtaining the crude product **52**, we observed that immediate purification *via* column chromatography after the removal of the solvent is essential. If stored for more than 24 h prior to purification, **52** starts to form a viscous oil that retains on the silica gel, leading to reduced yields of isolated product. Furthermore, the purified product **52** is noticeably hygroscopic. When stored under ambient conditions, moisture is accumulated which causes problems for the subsequent Grignard reaction as it quenches the Grignard reagent and decreases the yields. Consequently, it is necessary to either dry **52** under reduced pressure overnight prior to use or store it under argon.

A more significant challenge was encountered during the reductive cleavage of the benzyl protecting group to obtain catalyst precursors **22b-g**. Initial attempts utilizing the previously reported conditions yielded only three out of six desired precursors in low yields (Figure 25).

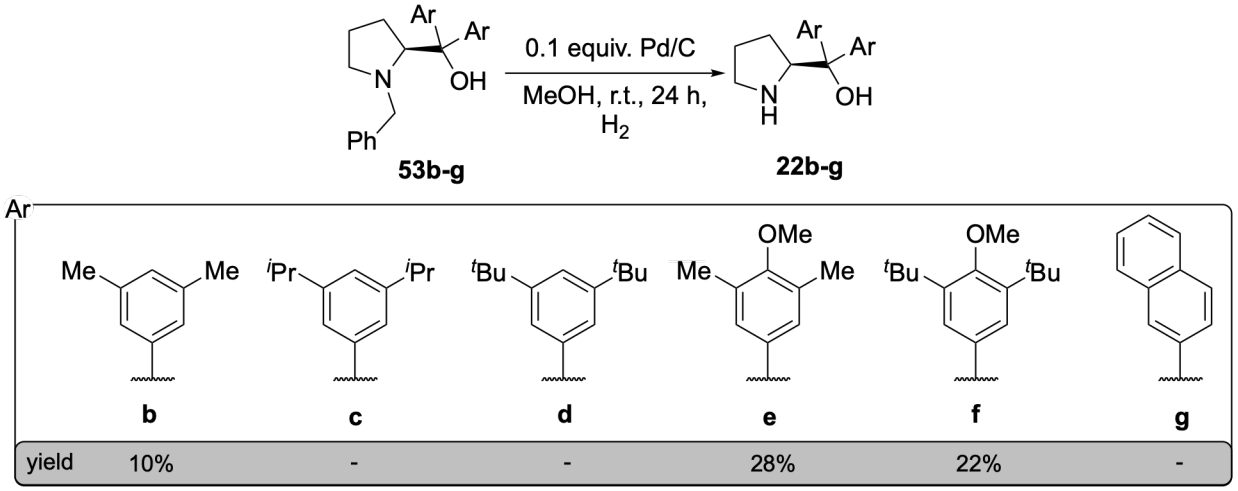


Figure 25: Benzyl deprotection from **53b-g** to **22b-g** using previously reported conditions on a 1.0 mmol scale. While specific derivatives remained inaccessible the isolated compounds are reported with their respective yields.

Extending the reaction times and increasing the temperature, changing the amount of Pd/C used and evaluating various Pd/C sources, such as wet or dry catalysts at different loadings as seen in Table 1, gave similar results as shown in Figure 25. This lack of reactivity can be attributed to catalyst poisoning, as the free lone pair of the tertiary amine of **53** and **22** coordinate to the active

palladium surface,[152] thereby preventing the chemisorption and homolytic cleavage of hydrogen gas. A general approach to circumvent this issue is the addition of Brønsted acids to protonate the amine,[152] yielding a tertiary ammonium species that no longer coordinates to the metal and that allows the palladium surface to activate hydrogen. However, identifying the appropriate acid proved challenging first.

Table 1: Screening of the benzyl deprotection step from **53b** to **22b**.

Entry [a]	Pd/C [equiv.]	Time [h]	Temperature [°C]	**22a** [%] [d]
1	0.1 [b]	24	r.t.	9
2	0.1 [b]	72	r.t.	11
3	0.1 [b]	24	50	0
4	0.2 [b]	24	r.t.	10
5	0.5 [b]	24	r.t.	12
6	0.1 [c]	24	r.t.	10
7	0.1 [c]	72	r.t.	11
8	0.5 [c]	24	r.t.	12

(a) All reactions were performed in MeOH using **53b** on a 1.0 mmol scale. (b) Dry Pd/C was used. (c) Wet Pd/C was used. (d) Yields of **22a**.

The use of a weak acid such as acetic acid proved ineffective, resulting in the recovery of starting material. On the contrary, applying a strong acid like concentrated aqueous hydrochloric acid initiated the deprotection but also induced side reaction, yielding the elimination product **54b-c** as shown in Figure 26, an outcome that could not be improved by varying the stoichiometric equivalents of the acid.

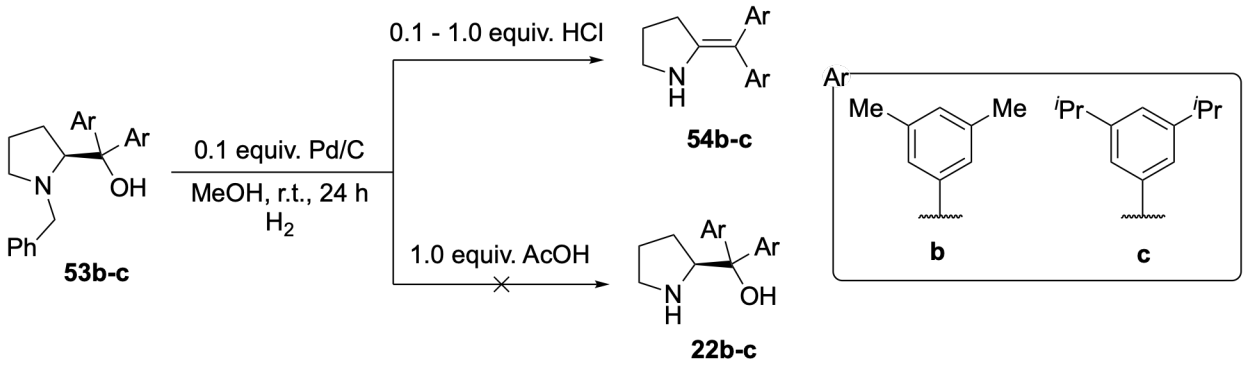


Figure 26: Attempted deprotection of the Benzyl group of **53b-c** using acids as additives. The reaction was performed on a 1.0 mmol scale.

To circumvent this, an acid of intermediate strength was evaluated. The application of TFA mediated the deprotection affording all depicted precursors in good yields (Figure 27). However, given the mentioned elimination to **54** induced by HCl, it was necessary to verify the stereochemical integrity of the resulting amino alcohols **22**. This was crucial as TFA could potentially also trigger a reversible elimination and subsequent water addition, ultimately leading to racemization. We therefore conducted polarimetric measurements on some selected products (**22b-c, 22e-f**), which matched established literature values of optical rotation,[148,149,153] and performed additional chiral HPLC analyses, confirming the absence of the other enantiomer. Through these analyses, we demonstrated that the TFA-mediated hydrogenation facilitates the benzyl cleavage without compromising the enantiomeric purity of the catalysts, thereby establishing a robust protocol for the preparation of various catalysts **22**. We then turned our attention to the optimization of the catalytic reduction conditions.

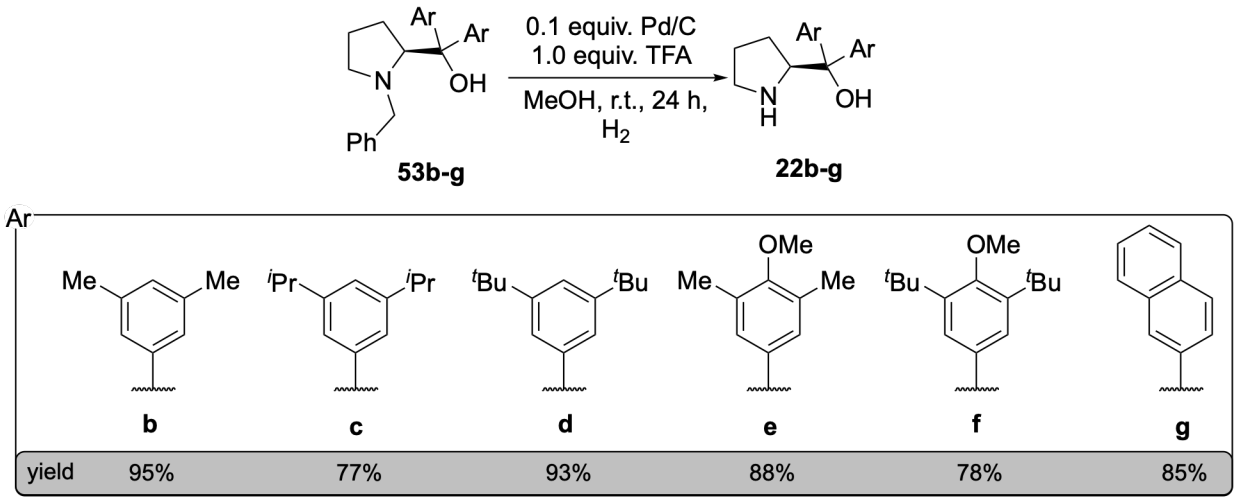


Figure 27: Benzyl deprotection from **53b-g** to **22b-g**. Reaction were performed on a 1.0 mmol scale. The isolated compounds are reported with their respective yields.

3.1.2 Optimization of the Catalytic CBS Reduction

The optimization of the catalytic reaction was driven by two primary objectives, namely reproducing the results established by previous work in the group[73] and exploring conditions to further enhance the overall reaction. For the initial screening, the combination of acetophenone (**13a**) and catalyst precursor **22d** was selected as the model system for optimization. Although **22d** already achieved 91% *ee* with acetophenone (**13a**),[87] it still left a margin for improvement to monitor the effects of varying reaction conditions.

To determine the optimal reaction parameters, we first evaluated the stoichiometry and the type of reductant to use for this reduction. This screening confirmed that a combination of 10 mol% of the catalyst and 1.1 equivalents of the reductant ensure the best outcome, thereby also validating the conditions established in previous work of our group.[87] Furthermore, comparative tests between different borane sources, specifically BH_3•THF and BH_3•SMe_2, showed no noticeable change in the catalytic efficiency, prompting the selection of BH_3•SMe_2 as the reductant for all subsequent reductions.

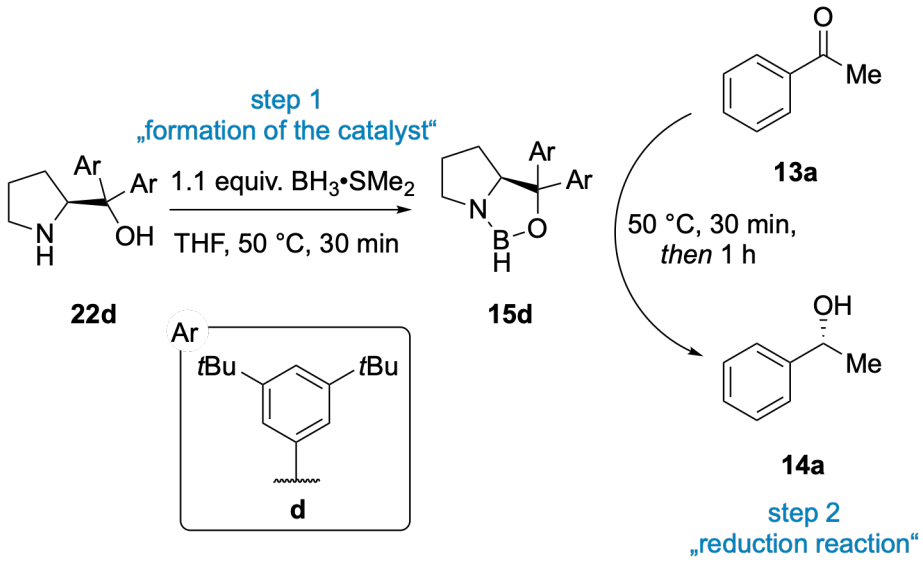


Figure 28: Conditions for the catalytic reduction of ketones (exemplified by **13a**) utilizing a CBS catalyst (exemplified by **15d**).

Our focus then shifted to the optimization of the reaction conditions. As illustrated in Figure 28, the reaction can be divided into two distinct steps. The reaction begins with the *in situ* formation of the oxazaborolidine **15** by combining catalyst precursor **22** with the borane source and is followed by the addition of the ketone substrate. Analyzing these two reaction steps separately allowed us to independently optimize the parameters for the initial catalyst activation and the subsequent enantioselective reduction.

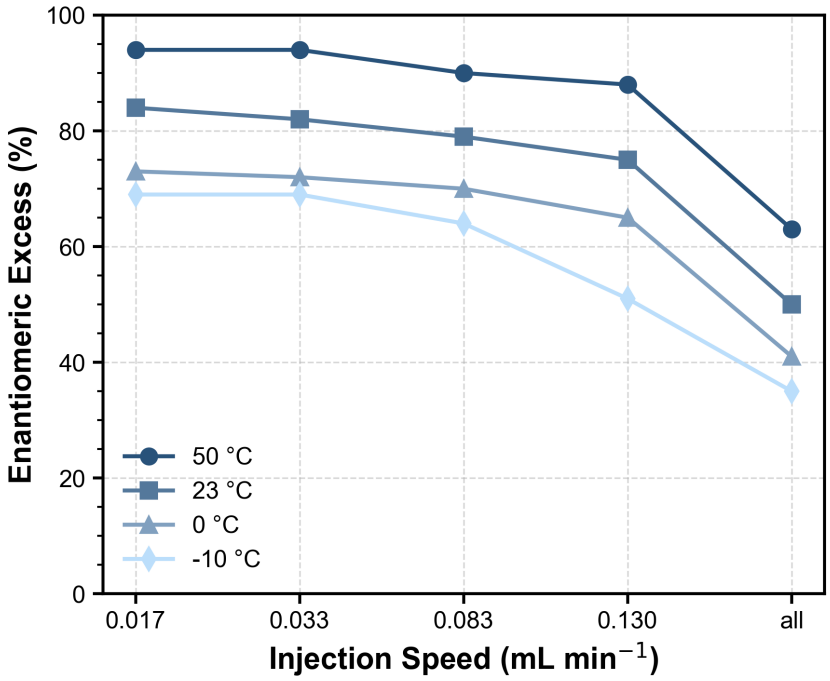


Figure 29: Influence of temperature and injection speed on the *ee* during the CBS-reduction.

Investigating the temperature dependencies revealed distinct trends for each step. While varying the temperature during oxazaborolidine (**15**) formation had no significant impact, the temperature during the second reaction step proved to be a critical parameter. As illustrated in Figure 29, conducting the reaction at 50 °C yielded the best selectivity. This observation is attributed to the inherent tendency of the catalyst to form inactive dimers at lower temperatures.[90,148] At higher temperatures the dimers dissociate and releases the monomeric active catalytic species. Alongside optimizing the temperature, we standardized the injection speed of **13a**. While established literature protocols often achieve high *ee* using dropwise addition,[85,87,90,91] we utilized a syringe pump to ensure the strict reproducibility required for our ML dataset. Maintaining slow addition is crucial to suppress background reduction.[85,154,155] Given that the reaction mixture contains an excess of the borane, rapid addition of **13a** would saturate the active catalyst, thereby forcing the remaining ketone to react with borane. By continuously dispensing **13a** *via* the syringe pump at an injection speed of < 0.03 mL min^{-1}, the effective concentration remains sufficiently low, which preserves the catalyzed pathway. Having concluded the optimization by reaching an *ee* of 93% for **14a** we proceeded to generate the ML dataset by applying these established conditions across our diverse library of catalyst precursors and substrates.

3.1.3 Catalyst and Substrate Scope

The diversity of the catalyst library was governed by the synthetic feasibility of the Grignard reaction. Installing novel groups at the carbinol center was the primary limiting factor, dictating both the number and the structural variations of precursors **22**. Notably, the final precursor library included one specific precursor (**55**) that is not classified as a CBS catalyst. This precursor was included to serve as an "out-of-sample" reference, providing the model with a structurally unique data point that shares identical chemical reactivity while possessing a framework outside the traditional CBS catalyst architecture.

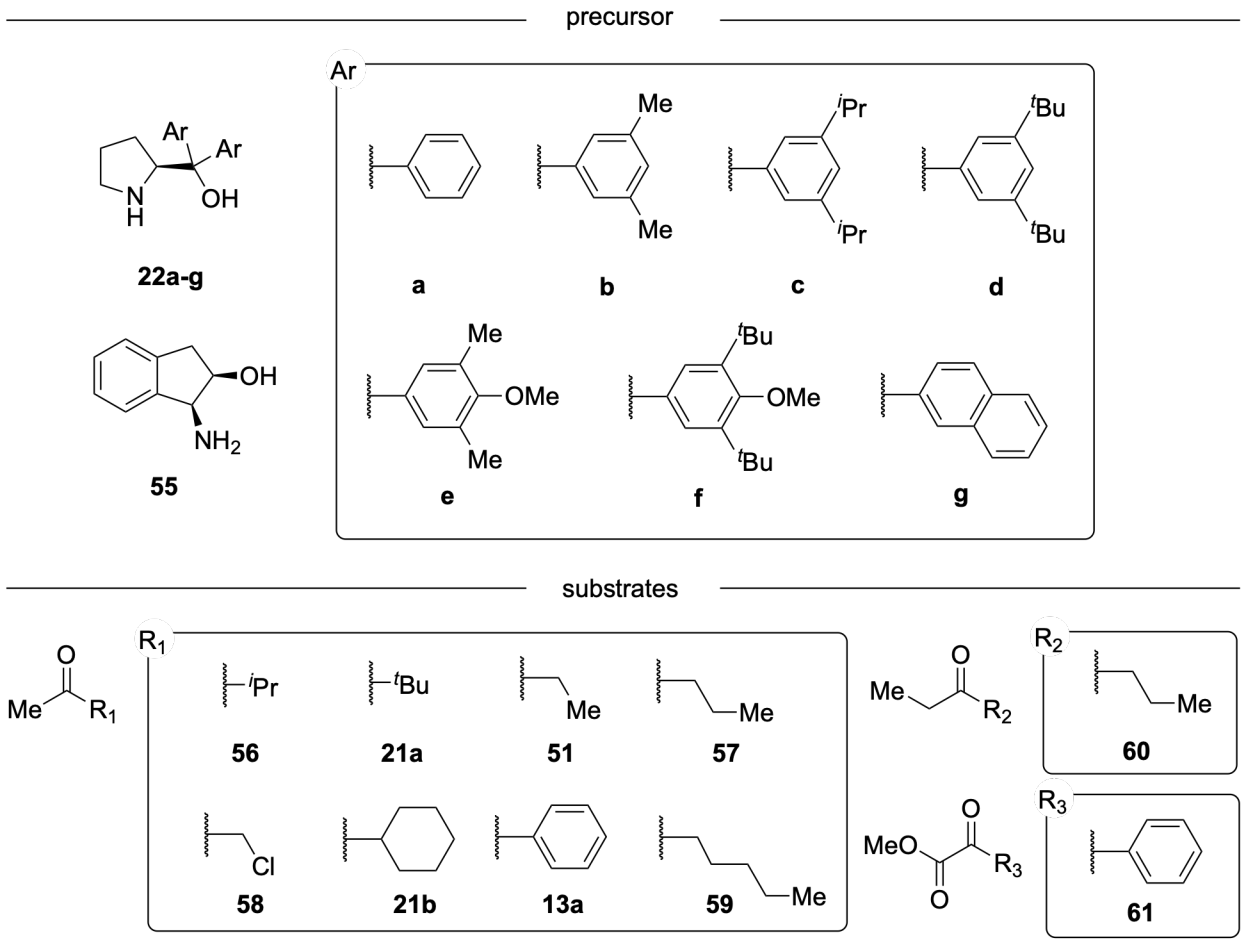


Figure 30: The precursor and substrate scope for the ML model.

Regarding the substrate scope, the selection of ketones was driven by a balance of accessibility and structural variance. We compiled a set of ketones that exhibit distinct differences in both their substitution patterns and electronic behavior. This selection was made to provide the ML model with a broad spectrum of catalysts, ensuring that it learns from multiple structure rather than

memorizing a single substrate class. The complete scope of the catalyst precursors and the respective ketones is depicted in Figure 30.

Generating a meaningful dataset, however, requires a high degree of confidence in the analytical data. While the *ee* of some alcohols could be determined directly *via* chiral GC, several derivatives required an additional derivatization step either with BzCl or Ac_2O to ensure baseline separation. Furthermore, to ensure reproducibility and statistical confidence for the algorithm training, all catalytic reactions were performed in triplicate.

Following the execution of the catalytic reactions, a comprehensive data matrix was compiled and is visualized as a heatmap (Figure 31). Analyzing the *ee* confirmed that the obtained values are in agreement with previously established in-house results, thereby further validating the robustness of the established reduction reaction.

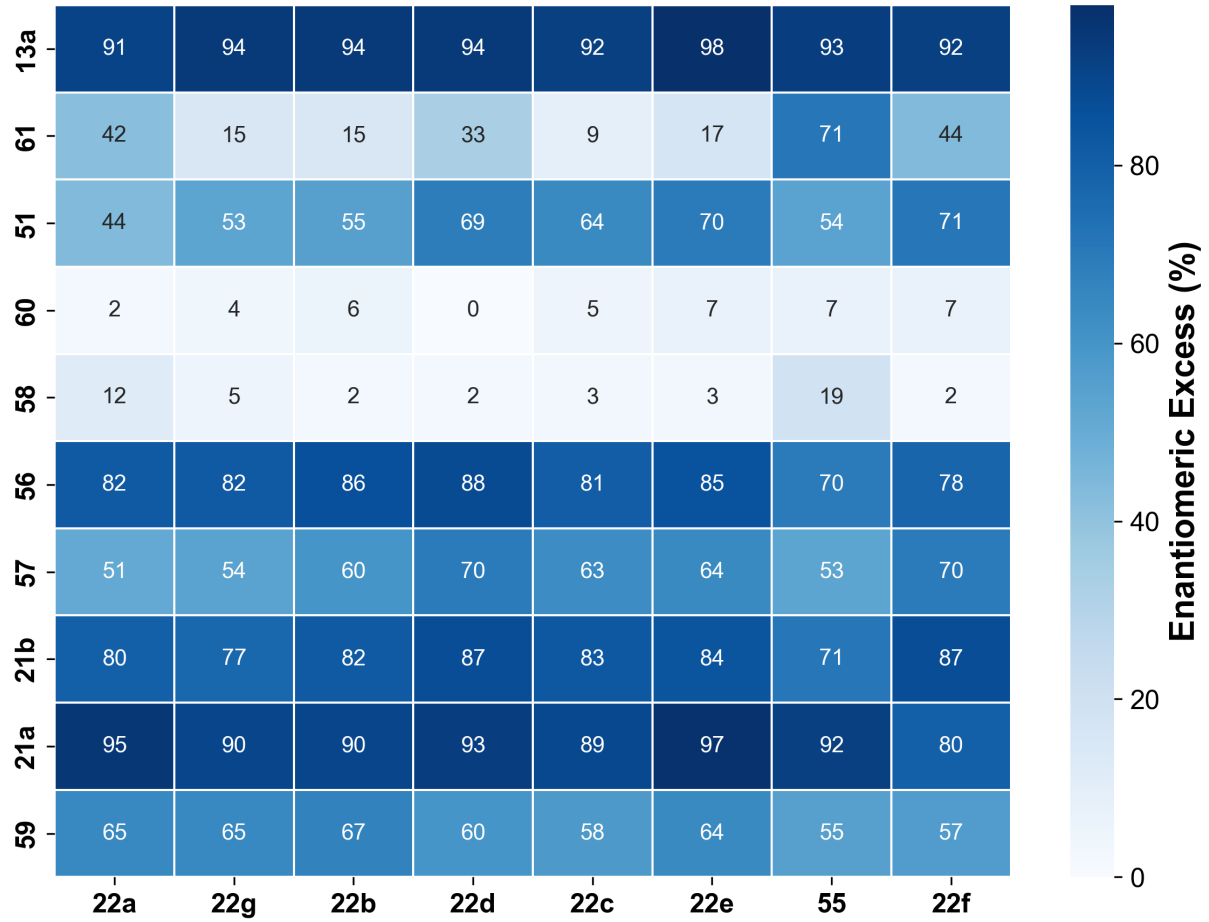


Figure 31: Heatmap illustrating the screening results for the reduction of several ketones utilizing various precursors. Darker blue shades correspond to higher *ee* values while lighter shades indicate lower enantioselectivities.

Evaluating the substrate scope revealed clear structural correlations driven by noncovalent interactions. Ketones featuring bulky DED groups such as **13a** and **21a** consistently achieved high *ee* across all catalysts. Decreasing the polarizability and the steric bulk, as seen for **56** and **21b**, diminishes this stabilizing LD interaction, thus reduces the selectivity slightly to values between 70% and 88% *ee*. The examination of substrates with purely aliphatic chains generally resulted in lower *ee*. This overall decrease is attributed to the high conformational flexibility of linear alkyl chains, which prevents the formation of a well-defined transitions state stabilized by strong, directional LD interactions. While methyl ketones like **57** and **59** maintained selectivities around 50% to 70% *ee*, **60** exhibited a drop of *ee* below 10%. This selectivity loss arises because the ethyl group minimizes the structural contrast between the chains making it difficult for the catalyst to distinguish between the two substituents. Electronic properties also profoundly dictate the reaction outcome. Substrate **58** bearing an electronegative chlorine atom showed poor *ee* for all combinations of catalysts. This occurs because the depleted electron density at the carbonyl oxygen weakens its essential coordination to the Lewis acidic boron thereby favoring the unselective background reaction. Finally, the established protocol proved highly chemoselective. The reduction of the bifunctional substrate **61** yielded the secondary alcohol leaving the ester functionality entirely intact. By mapping these diverse structural electronic and chemoselective nuances the obtained experimental dataset provided the necessary variance to train the subsequent ML model.

3.1.4 Predictions of the Graph-Based Model

To capture the underlying interactions governing enantioselectivity, we chose not to use *ee* as the target variable in our model, but rather the difference in free activation energy ($\Delta\Delta G^{\ddagger}$).[9] While *ee* is the standard experimental metric, it is not an additive property. Subtle noncovalent interactions and steric repulsions present in the transition state impact the activation energy in a linear fashion whereas the resulting percentage values follow a nonlinear relationship. This discrepancy is particularly problematic near the mathematical limit of 100% *ee* where large changes in energy, result in only marginal differences in the observed selectivity. Therefore, all experimentally determined *ee* values were converted into their corresponding $\Delta\Delta G^{\ddagger}$ values *via* the Eyring equation [1] (*vide supra*).[80]

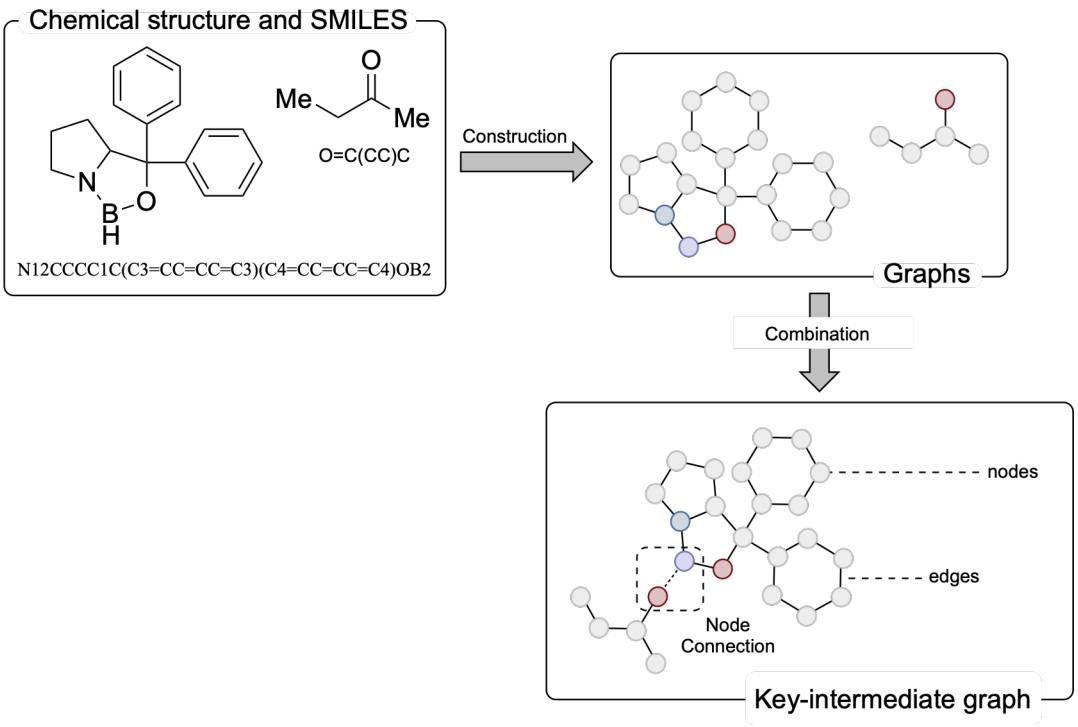


Figure 32: Translation of individual chemical structures into molecular graphs and their subsequent combination into a single key intermediate graph.

The next step was to translate the chemical structures of the catalysts and substrates into a machine-readable format. Traditional computational approaches, such as DFT, rely on three-dimensional spatial coordinates.[127] However, these representations are heavily conformation-dependent and computationally expensive, making them impractical for the efficient evaluation of large datasets. Instead, a two-dimensional graph-based representation was chosen to avoid the challenges of conformational sampling. As seen in Figure 32, molecules are treated as mathematical graphs where atoms act as nodes and chemical bonds as edges.[156] To provide the ML algorithm with sufficient chemical context, each node is embedded with specific atomic features, including the element symbol, formal charge, hybridization state, aromaticity, and absolute configuration. Simultaneously, the connecting edges are futurized with bond type information specifying whether a connection is conjugated part of a ring or constitutes a coordinative bond. However, rather than processing the catalyst and substrate as isolated entities, a "key intermediate graph" was implemented, conceptually building upon the established principles of Condensed Graphs of Reaction[157] and Imaginary Transition Structures.[158] By digitally assembling the catalyst and the ketone into a single, unified graph that mimics the stereodetermining pre-transition state, the model perceives the connectivity and spatial proximity between the catalyst and the ketone. This specific

descriptor generation effectively bridges the gap between computationally inexpensive two-dimensional topology and the complex three-dimensional reality of the reaction, providing a set of structural descriptors.

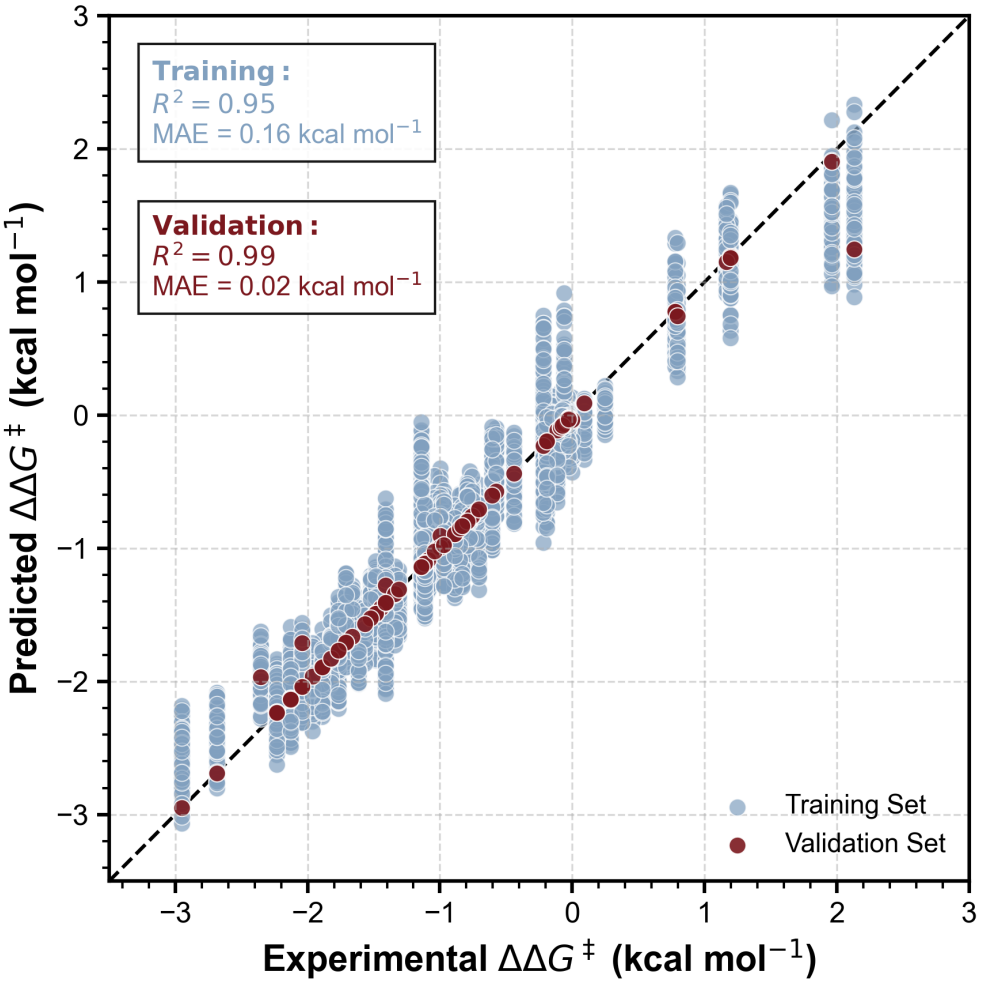


Figure 33: Parity plot comparing the experimentally determined and model predicted difference in free activation energy $\Delta\Delta G^{‡}$. The performance on the training set is depicted in blue yielding an R^2 of 0.95 and a mean absolute error of 0.16 kcal mol^{-1}. The validation set is shown in red demonstrating high accuracy with an R^2 of 0.99 and a mean absolute error of 0.02 kcal mol^{-1}. The dashed diagonal line represents perfect correlation between experiment and prediction.

These assembled graph representations, coupled with their corresponding $\Delta\Delta G^{‡}$ values, were subsequently fed into a Graph Neural Network architecture utilizing a graph attention layer.[159,160] Through global pooling operations, molecular embeddings were generated and subsequently processed by a feed-forward neural network to predict the continuous thermodynamic targets.[161] Given the relatively small size of the curated dataset, mitigating the risk of overfitting was a primary concern. To prevent this and ensure the generalizability of the algorithm, a cross-

validation strategy was implemented. By iteratively partitioning the dataset into training and validation sets, it was ensured that the model was evaluated on reaction combinations it had not encountered during the training phase.

The predictive capability of the optimized graph-based model was then evaluated by comparing the computationally predicted $\Delta\Delta G^{\ddagger}$ values against the experimentally determined targets. As illustrated by the parity plot in Figure 33, the model demonstrated a strong correlation between prediction and experiment and differentiated between high-performing catalytic systems and challenging cases. Achieving an R^2 of 0.95 and a low mean absolute error of 0.16 kcal mol^{-1} confirmed that the key intermediate graph approach correlates the structural representation with the stereochemical outcomes of the CBS reduction. Having established the performance, the focus shifted towards evaluating the predictive power of the model on unseen catalysts in the laboratory especially for substrate **51**.

3.1.5 Virtual Screening and Experimental Validation

We commenced by generating a virtual target library of oxazaborolidine derivatives to serve as input data for predicting the *ee* of **51**. To ensure practical relevance, we aimed to generate only synthetically feasible catalysts. Since the overall structural diversity of the catalyst substituents is dictated by the Grignard reaction, we confined our candidates based on the availability of the corresponding aryl bromides. Evaluating this virtual library provided a list of predicted $\Delta\Delta G^{\ddagger}$ values which were translated back into the corresponding *ee* values here to facilitate an intuitive comparison. From this list, we selected the four specific structures shown in Figure 34. While their high predicted selectivities were the primary selection criterion, we deliberately favored candidates featuring extended and highly polarizable π-systems. We hypothesized that these motifs would act as strong DED. Including these specific extremes provided an excellent opportunity to test whether the algorithm accurately captures the impact of pronounced LD interactions on the overall catalytic performance.

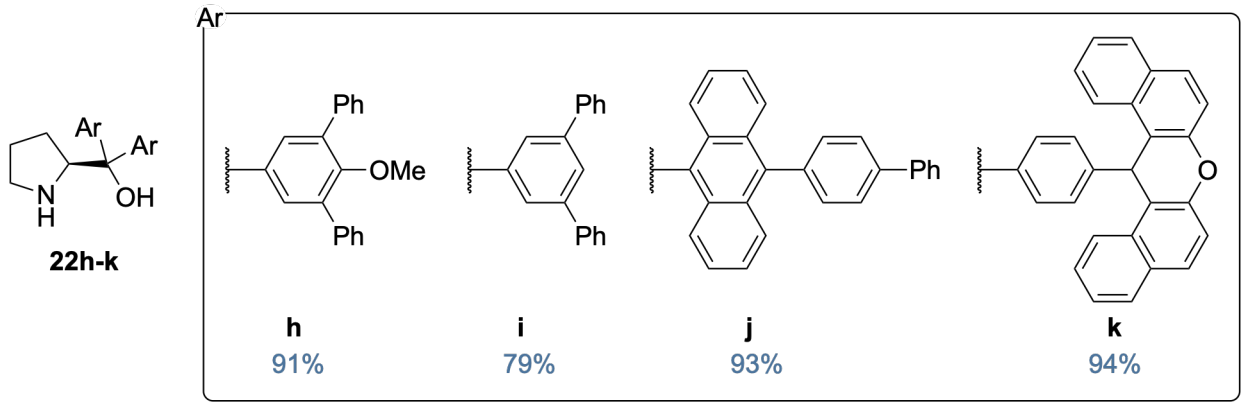


Figure 34: List of catalyst precursor **22** that were chosen to validate the predictions given by the model. The prediction by the model is highlighted in blue.

While the corresponding aryl halides for **22j** and **22i** were commercially available, the precursors for **22h** and **22k** were synthesized. However, during the timeframe of this ML study, efforts to prepare these two targets encountered several synthetic problems. As a result, their completion could not be achieved at that time and prevented us from evaluating these systems. Alternative strategies developed at a later stage allowed the preparation of both structures and the evaluation of the systems but these are discussed in later sections of this work.

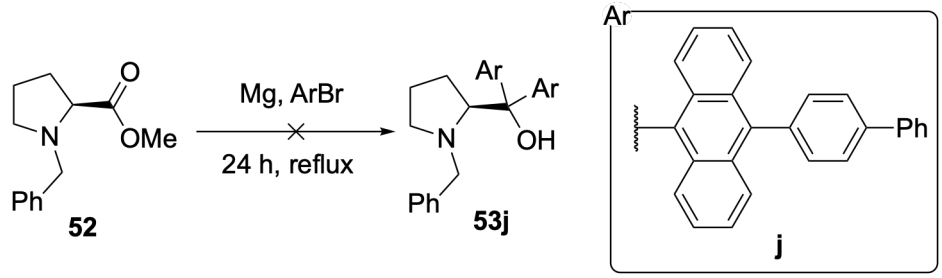


Figure 35: Grignard reaction from **52** to **53j** using Mg.

Next, we attempted the synthesis of catalyst **22j** (Figure 34). To assemble this, we first had to prepare the corresponding precursor **53j** *via* a Grignard reaction (Figure 35). Extensive screening of the reaction conditions, which included variation in Grignard reagent, reagent stoichiometry, and the use of different solvents such as THF, CPME, and Et_2O, failed to yield **53j**. In all attempts, the ester remained unreacted, and aqueous workup merely led to the hydrolysis of the Grignard reagent. The addition of $CeCl_3$ to promote a more nucleophilic Imamoto-type reaction proved equally unsuccessful.[162] Suspecting that the standard Grignard reagent lacked sufficient reactivity for this sterically demanding system, a Turbo Grignard reagent developed by Knochel was

employed.[163] Although this reactive Grignard reagent indicated a reaction, it only resulted in the formation of side products **62j** and **63j**, which were detected *via* mass spectrometry (Figure 36). The formation of **62j** demonstrated that increasing reactivity enabled the initial addition of an aryl moiety. Nevertheless, the emergence of **63j** also revealed that the steric environment surrounding the substrate was simply too congested to allow the attachment of the second aryl group. Further optimization of the reaction conditions proved entirely ineffective to overcome this problem and resulted in the same results as shown before.

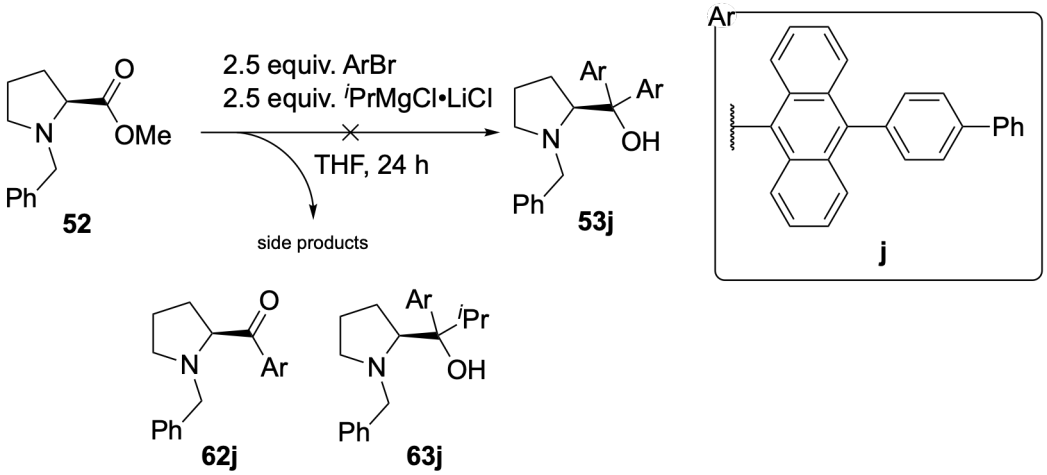


Figure 36: Grignard reaction from **52** to **53j** using ^{i}PrMgCl •LiCl. **62j** and **63j** were observed as major products.

We therefore questioned whether the intrinsic steric bulk of the molecular framework or the substitution pattern of the aryl group was responsible for inhibiting the secondary addition. To evaluate this, the specific aryl bromides **64**, **65**, and **66** shown in Figure 37 were tested in the Grignard reaction.

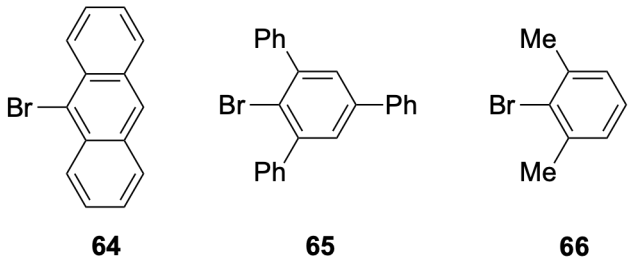


Figure 37: Aryl bromides used for the evaluation of the Grignard reaction with ^{i}PrMgCl •LiCl.

Using substrate **64** in the Grignard reaction reproduced the aforementioned results shown in Figure 38, where only the monosubstituted intermediate and the side product were formed. This

confirmed that the structural framework was already causing significant steric issues on its own. Because all previously synthesized precursors exclusively utilized *meta*- or *para*-substituted aryl bromides and never caused those problems, we suspected that *ortho*-substituents might be the reason for this outcome. To investigate this, we tested substrates **65** and **66** under various conditions. The reactions with substrate **65** showed no signs of conversion, yielding exclusively unreacted starting material. In contrast, subjecting substrate **66** to the reaction conditions resulted in the formation of the monosubstituted intermediate without any trace of the desired product. This outcome clearly indicates that extremely bulky *ortho*-substituents prevent even the initial Grignard reaction while smaller *ortho*-groups permit the first addition but effectively block the second step. Considering these findings, we discontinued all efforts targeting *ortho*-substituted catalyst motifs and focused on solely *para*- or *meta*-substituted products.

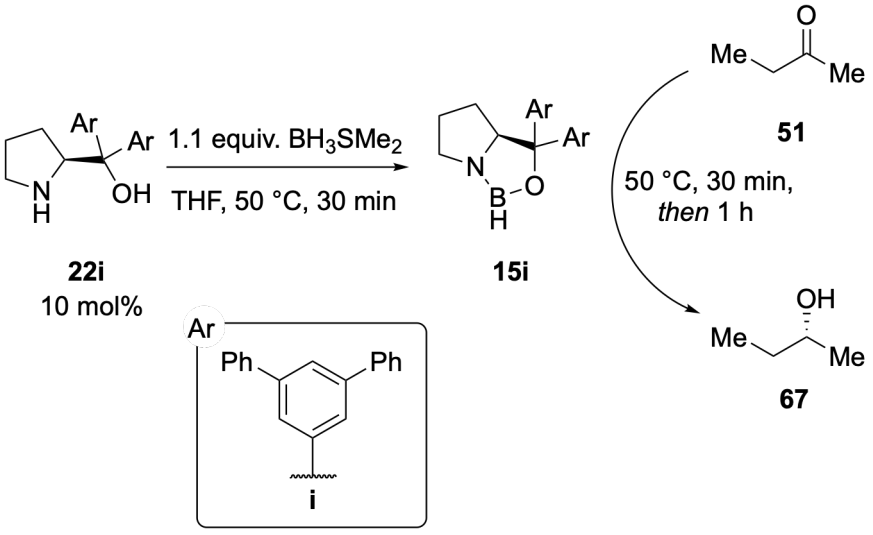


Figure 38: Catalytic reduction using catalyst **15i** to selectively reduce substrate **51** to product **67**.

Despite the synthetic limitations encountered with the previous substrates, the preparation of the final remaining precursor **22i** shown in Figure 34 was achieved. Following the optimization of the reaction parameters detailed in the experimental section, **22i** was isolated in good yield and high purity. With the target structure in hand the focus shifted toward the experimental validation of the ML model. To evaluate the predictive accuracy of the algorithm, five consecutive catalytic reactions were conducted using the established standard conditions as depicted in Figure 38.

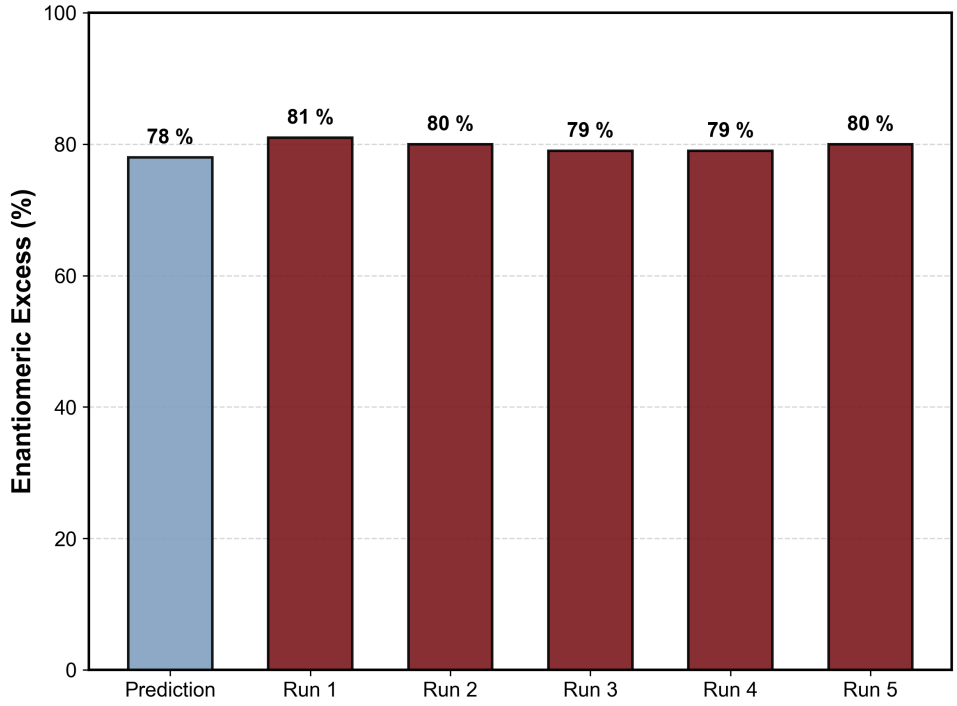


Figure 39: Comparison of the ML predicted *ee* and the initial experimental results obtained from five independent catalytic runs yielding an average *ee* of 80% for the reduction of **51** to **67** *via* **15i**.

The outcomes of these catalytic runs are summarized in Figure 39, demonstrating how the initial experimental measurements aligned with the predictions of our computational model. By determining the mean across all consecutive catalytic reactions, we calculated an average *ee* of 80%. Compared to the previously most selective precursor catalyst **22f** developed in our group, which achieved 72% *ee*, this represented an absolute increase of 8%. Translated into thermodynamic parameters this improvement corresponds to a relative $\Delta\Delta G^{\ddagger}$ increase of 0.27 kcal mol^{-1}. While these evaluations culminated in the publication of this methodology in JACS,[164] we remained eager to further interrogate the overall robustness of our analytical system. We therefore actively sought to expand the scope of the investigated catalysts by exploring novel synthetic pathways as reported in the following sections.

Part II

Novel CBS Catalysts and Boundaries of the Model

3.2 New Synthesis Strategy and Boundaries of the Model

The initial part of this work highlighted the potential of data driven methods for identifying structural correlations in the CBS reduction. However, the practical generation and further expansion of the required experimental dataset was severely hindered by synthetic limitations particularly concerning the preparation of the aryl halides and their corresponding catalyst precursors.

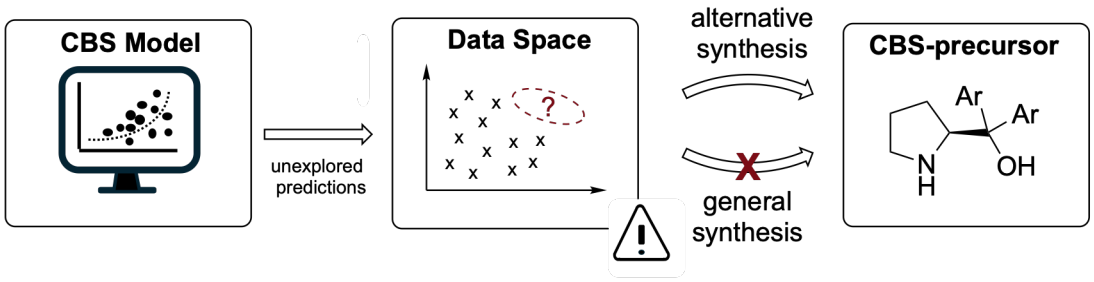
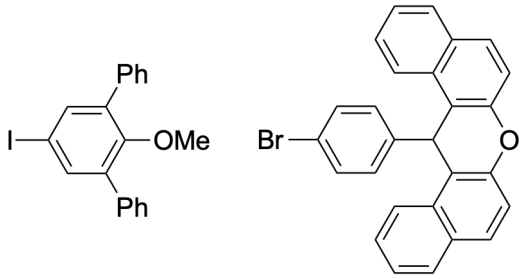


Figure 40: Schematic illustration of the iterative data driven catalyst optimization cycle

As we aimed to further utilize the computational model, expand the catalyst library, and validate the model predictions, we conceptualized a novel synthetic pathway for the synthesis of CBS precursors. This new approach enabled the synthesis of the previously mentioned precursors and allowed for another validation of the computational model. However, these investigations yielded unexpected results that necessitated a fundamental reassessment of the entire framework. To comprehensively discuss these findings and expose the analytical boundaries of our approach the following sections will trace this development back to its initial starting point.

3.2.1 Synthesis of Aryl Halide Derivates

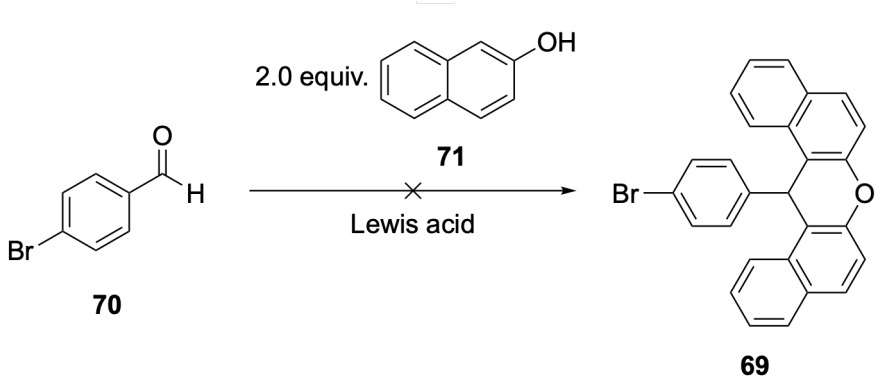
The preparation of specific aryl halides such as **68** and **69** was investigated (Figure 41). While the preparation of **68** was previously conducted by Michael Fuhrmann[165] the present work focused on the development of the xanthene derivative (**69**).



68 **69**

Figure 41: The desired aryl halides **68** and **69** for the synthesis of the corresponding precursor **22**.

Initial attempts to prepare **69** followed literature protocols by Behbahani *et al.*[166] and Cao *et al.*[167] utilizing Lewis acids such as $CuSO_4 \bullet H_2O$ or $FeCl_3$ to catalyze the reaction of 2-naphthol (**71**) and 4-bromobenzaldehyde (**70**) under neat conditions. However, these reported procedures could not be reproduced as they led to thermal degradation and oxidation of the starting material. Consequently, the reaction parameters, such as the solvent ($CHCl_3$ and EtOH) and temperature (r.t. to 90 °C), were systematically modified. Chloroform was initially investigated to enable controlled reflux conditions at lower temperatures to prevent thermal decomposition. However, this adjustment did not lead to the formation of **69**, and only starting materials **70** and **71** were recovered, indicating a lack of reactivity. Ethanol was subsequently employed to evaluate the impact of a polar protic solvent. Under these conditions, we observed the formation of the corresponding acetal as a major side product, which effectively consumed the starting aldehyde. Among all evaluated conditions, solely the reaction utilizing $FeCl_3$ in ethanol at 80 °C yielded faint traces of **69** detectable by mass spectrometry. Nevertheless, the overall conversion remained negligible, and the target compound could not be isolated (Figure 42).



70 **69**

Figure 42: Condensation reaction of **70** and **71** to **69** using Lewis acids.

Due to these results, the synthetic strategy was shifted towards using Brønsted acid as catalysts instead. This approach was chosen because it relies on a similar mechanistic pathway (Figure 43) to those of Lewis acids and it is also shown to work by literature reports for analogous reactions.[169]

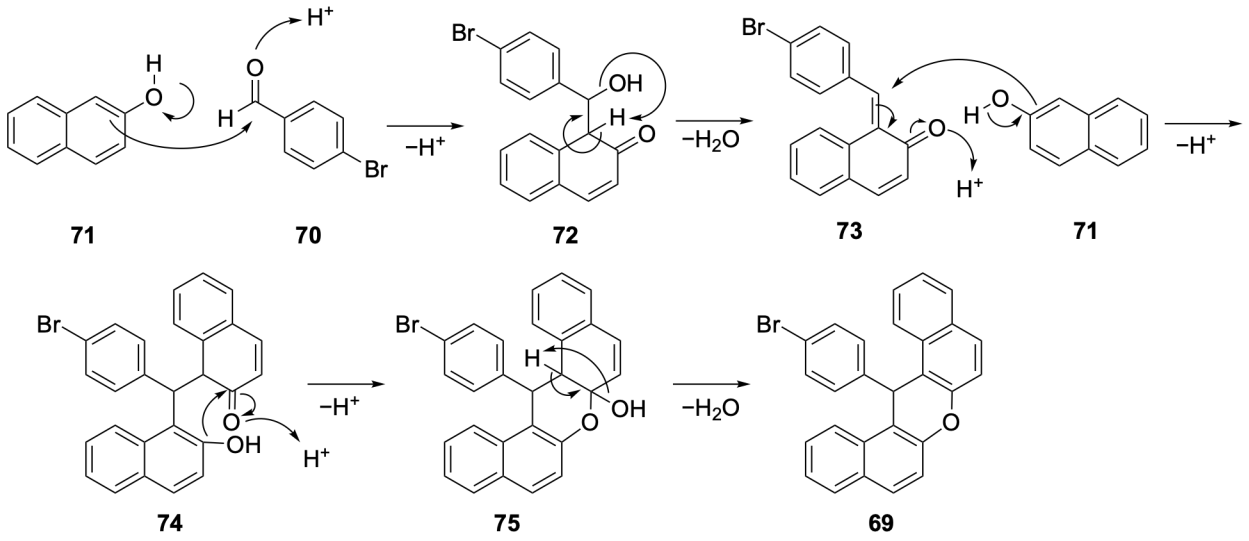
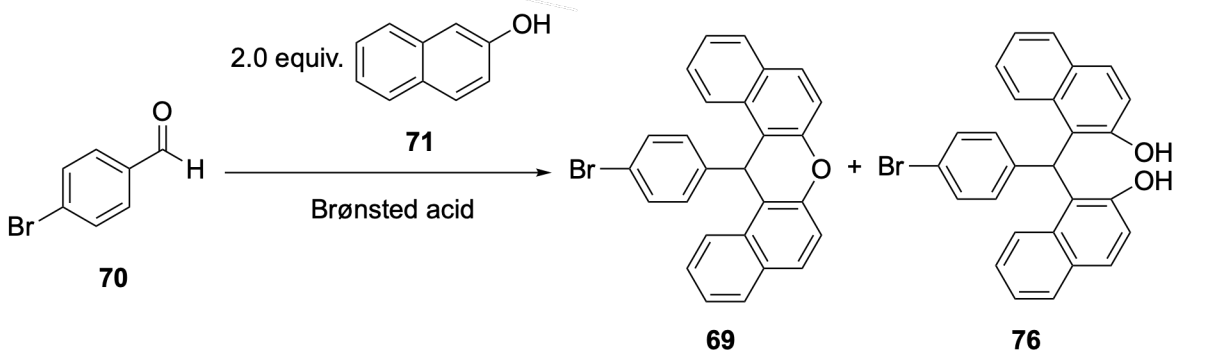


Figure 43: Proposed reaction mechanism for the preparation of **69** using **70** and **71** using Brønsted acids.

The proposed mechanism for this Brønsted acid catalyzed reaction starts with the protonation of **70** which enhances the electrophilicity and enables the nucleophilic attack by **71** to form **72**. The subsequent elimination of H_2O then yields an *ortho* quinone intermediate (**73**) which is nucleophilically attacked by **71** at the conjugated system to form a binaphthyl ketol (**74**). This is followed by an intramolecular cyclization to form a cyclic hemiacetal (**75**) and ends in another condensation step to restore the aromaticity of the system to yield **69**.

The results obtained using Brønsted acidic conditions are summarized in Table 2. The use of HCl in dioxane (Entry 1) yielded traces of the target compound **69**. Switching to aqueous HCl (Entries 2-4) achieved the first isolation of **69** in low yields but led to the formation of **76** as a side product. This observation implies that proton donors are necessary for the reaction, yet an unidentified factor hinders the final cyclization. Investigation of alternative proton donors revealed that weak Brønsted acids, such as citric acid (Entry 5), are completely insufficient to drive this reaction. Conversely, employing another strong acid like H_2SO_4 (Entry 6) resulted in a reactivity profile similar to that of HCl, indicating that simply changing the specific strong acid does not facilitate the final cyclization.

Table 2: Screening of the reaction of **70** and **71** to **69** using Brønsted acids.



Entry [a]	Solvent	Additives [b]	Temperature [°C]	**69** [%] [c]	**76** [%] [c]
1	EtOH	HCl [d]	r.t.	- [e]	0
2	EtOH	HCl	r.t.	3	63
3 [f]	EtOH	HCl	r.t.	4	68
4 [g]	EtOH	HCl	r.t.	4	70
5	EtOH	citric acid	r.t.	- [e]	0
6	EtOH	H_2SO_4	r.t.	4	60
7	Me-C_6H_5	H_2SO_4	r.t.	44	0
8	Me-C_6H_5	pTsOH	r.t.	49	0
9	Me-C_6H_5	pTsOH	115	55	0
10	1,2-DCA	pTsOH	90	92	0

(a) All reactions were conducted on a 2.0 mmol scale for 24 h. (b) 0.1 equiv. (c) Yield. (d) HCl dissolved in dioxane. (e) Traces detected *via* mass spectrometry. (f) With Soxhlet extractor. (g) With molecular sieves (beads 4 Å).

We therefore hypothesized that the solvent must be key to the reaction outcome. EtOH can potentially interfere by stabilizing the intermediates through hydrogen bonding, or, as previously observed, by forming acetals with the starting material, thereby preventing the last condensation and cyclization. The solvent was changed to toluene as a nonpolar solvent (Entry 7), which provided **69** in moderate yields, while the formation of **76** was effectively suppressed. Subsequent experiments (Entry 8) using *p*TsOH showed no significant improvement until the reaction temperature was elevated (Entry 9), leading to a slight increase in yield. The solvent was then changed to 1,2-dichloroethane (1,2-DCA) to provide better solubility and to allow the reaction to be conducted at elevated temperatures. This resulted in 92% yield (Entry 10), demonstrating that the combination of a strong Brønsted acid and a suitable solvent is the key for obtaining good

yields. With **68** and **69** finally obtained, our next step was to synthesize the catalyst precursor **22h** and **22k**.

3.2.2 Synthesis of the Precursor: The Problem

While the synthesis of precursor **22h** was successfully conducted by Michael Fuhrmann following the optimized general procedure (Figure 24) and proceeded without any complications,[165] the preparation of **22k**, proved to be more complicated than initially anticipated. The starting point was again the Grignard reaction with Mg turnings under standard conditions to form **53k** (Figure 44). However, these conditions failed to yield **53k** in any reaction aside from the $CeCl_3$ mediated attempt, in which the product was detected *via* mass spectrometry but could not be isolated.

Modifying other parameters, such as the stoichiometry or the solvent, did not alter the outcome either, resulting merely in the recovery of the starting material alongside the dehalogenated arene formed *via* hydrolysis of the unreacted Grignard reagent upon aqueous workup. This observation alone confirmed that the Grignard reagent was indeed formed, but simply lacked the activity required to attack **52**. We therefore concluded that it was necessary to increase the overall reactivity and subsequently shifted our strategy to utilize Turbo-Grignard as a reagent.

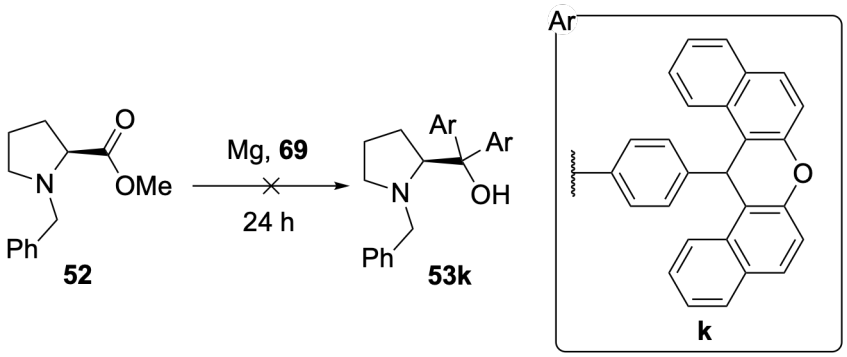
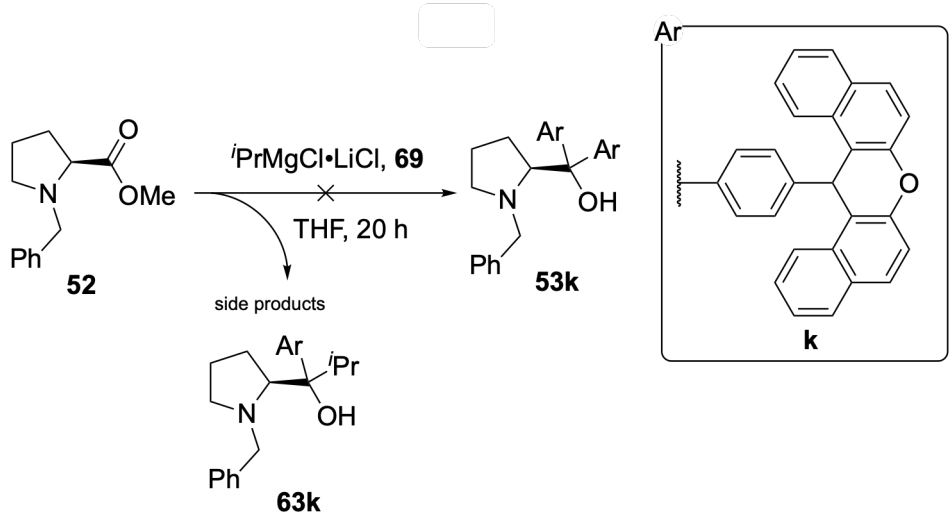


Figure 44: Grignard reaction from **52** to **53k** using Mg and **69**.

However, the implementation of the Turbo-Grignard did not lead to expected results, directly mirroring the complications encountered during our earlier syntheses attempts of *ortho*-substituted precursors. As summarized in Table 3, the reaction outcome was dependent on temperature. Conducting the reaction at lower temperatures (Entry 1 - 3) yielded no conversion and resulted in the recovery of the starting materials. Elevating the temperature (Entry 4) afforded the desired

product once, but led to the formation of side product **63k**. Furthermore, the isolated material lacked analytical purity, contaminated with traces of **63k** that resisted all purification efforts, including standard column chromatography, preparative HPLC, and crystallization. Even the addition of $CeCl_3$ at higher temperatures (Entry 5), intended to increase the electrophilicity of **52** and suppress side reactions, resulted in the formation of side product **63k**, without any detectable traces of the desired compound **53k**.

Table 3: Screening of Turbo-Grignard conditions for the synthesis of **53k**.



Entry [(a)]	Temperature [°C]	Additives	**53k** [%]
1	0	-	0
2	r.t.	-	0
3	r.t.	$CeCl_3$	0
4	70	-	7 [(b), (c)]
5	70	$CeCl_3$	0

(a) All reactions were conducted on a 0.5 mmol scale in THF. (b) Yield, but the product contained inseparable traces of **63k**. (c) The initial result could not be reproduced in subsequent trials.

At this stage, rather than continuing the optimization of an inefficient Grignard reaction, we decided to prioritize a proof of concept for the subsequent step. The objective was to determine whether **53k** would be accessible at all, assuming the coupling of **69** onto **52** could be achieved. Therefore, despite the presence of impurities, **53k** (from Entry 4) was used to evaluate the general viability of the deprotection process.

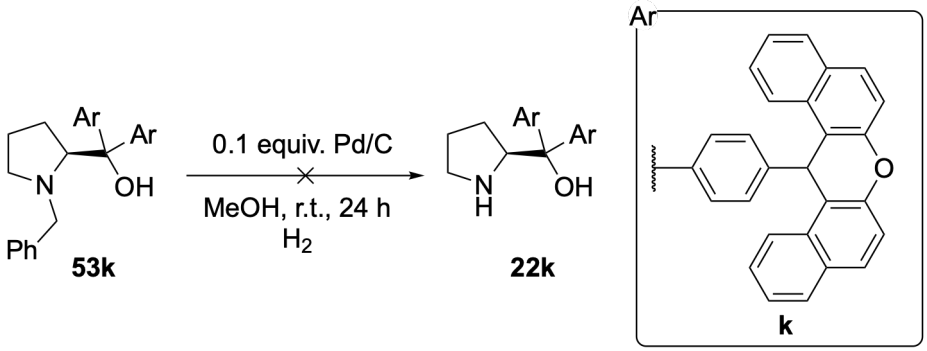


Figure 45: Deprotecting conditions for **53k** to **22k**.

Applying general hydrogenation conditions (Figure 45) resulted in the recovery of the starting material (**53k**). Even when the reaction was repeated at elevated temperatures, the same results were obtained. We attributed this lack of reactivity to the pronounced insolubility of the precursor in methanol, which likely hindered the required interactions for the heterogeneous catalytic process.

Given the complications associated with the Grignard reaction and the solubility problems observed during the deprotection attempts, it became evident that this synthetic route would not provide a viable path for **22k.** Consequently, we concluded that a new strategy was required, which will be discussed in detail in the following section.

3.2.3 Synthesis of the Precursor: The Idea

The first aspect of our revised strategy focused on the replacement of the problematic Grignard reaction by metal-halogen exchange (Figure 46). Since our previous experiments clearly indicated that the Mg lacked the necessary reactivity to reliably attack the electrophile, we shifted our focus to more reactive organolithium reagents.

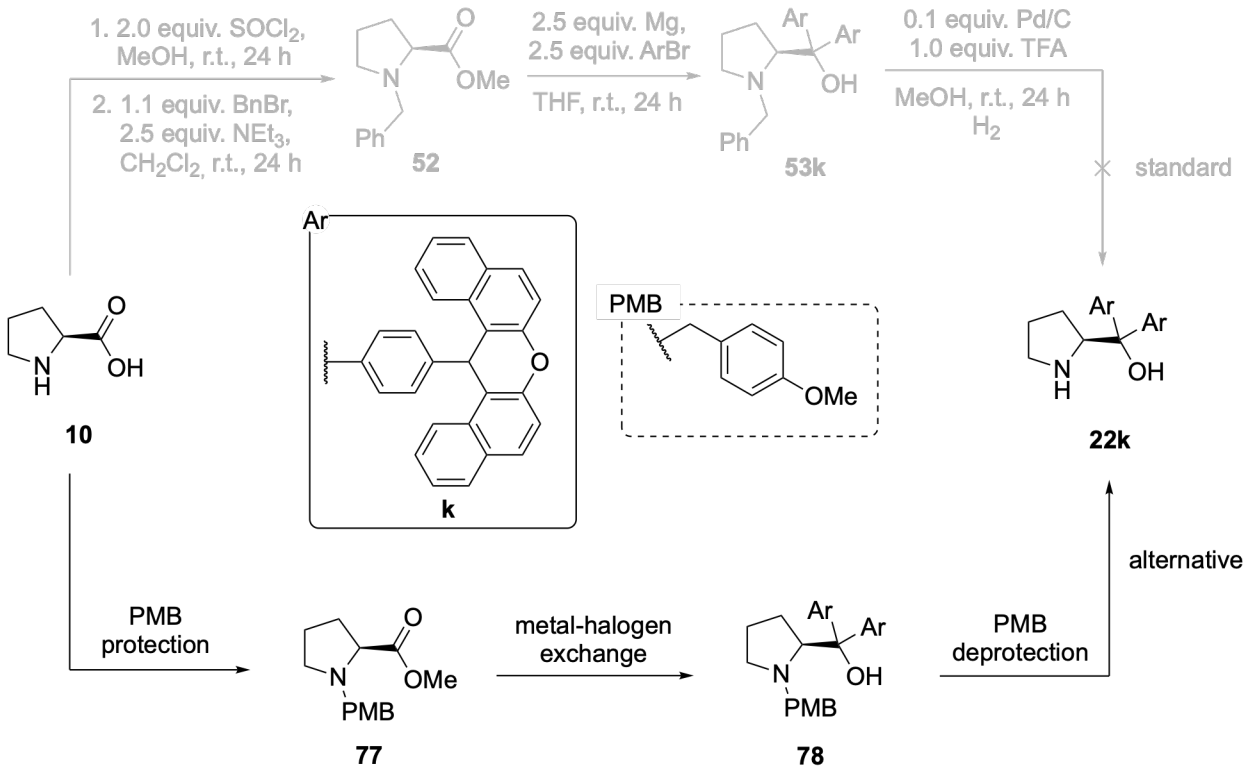


Figure 46: Alternative synthetic pathway for **22k** *via* metal halogen exchange with a modified protecting group. The general approach is illustrated in grey and the new alternative strategy in black.

Parallel to this modification, we opted to replace the benzyl protecting group with a more versatile alternative (Figure 46). Our primary requirement was chemical stability during the organolithium reaction, which precluded the use of nucleophile-sensitive moieties. We also sought a protecting group that provides diverse deprotection pathways beyond catalytic hydrogenation to ensure flexibility in cleaving the group. We selected the *para*-methoxybenzyl (PMB) (**80**) group as it remains inert towards organolithium reagents and allows oxidative or acidic cleavage,[170–172] while its methoxy group simultaneously improves the solubility of the precursor. Consequently, we proposed the synthetic route (Figure 47) and the results of this approach are explained in detail in the following section

3.2.4 Synthesis of the Precursor: The Solution

Analogous to the beginning of the general syntheses, L-proline **10** was initially converted into the corresponding methyl ester hydrochloride (**79**). The PMB-protecting group was then incorporated utilizing 1.1 equivalents of **80**. Although the overall synthesis proceeded without any complications the reaction of **77** only achieved moderate 54 % yield (Figure 47).

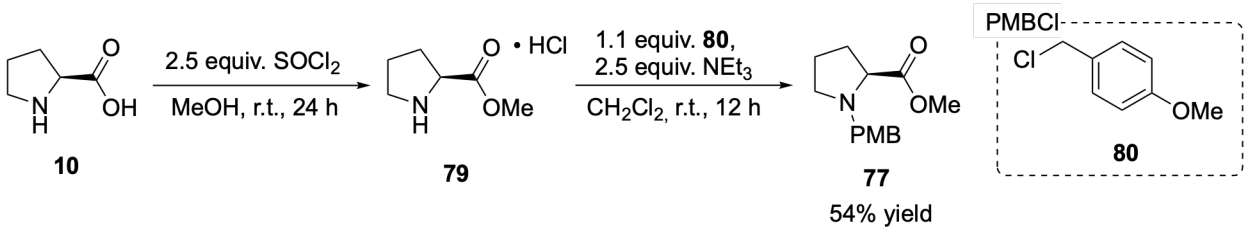


Figure 47: Synthesis of **77** using PMBCl (**80**) after the conversion of **10** to **79**.

Our focus then shifted toward the critical nucleophilic addition step utilizing *n*-BuLi. As a primary assessment, the formation of the organolithium intermediate was investigated because generating this reactive species was an essential requirement for the subsequent nucleophilic attack.

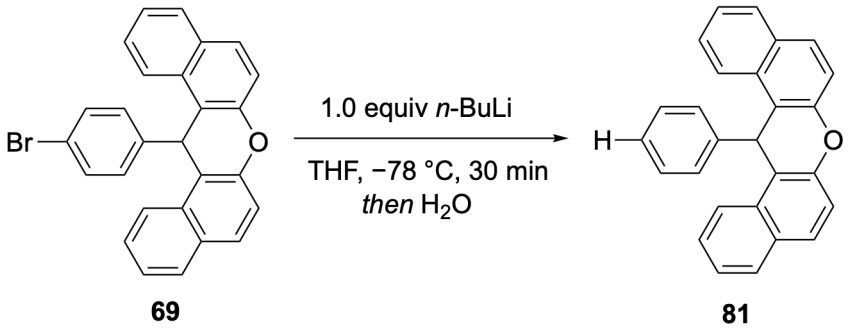
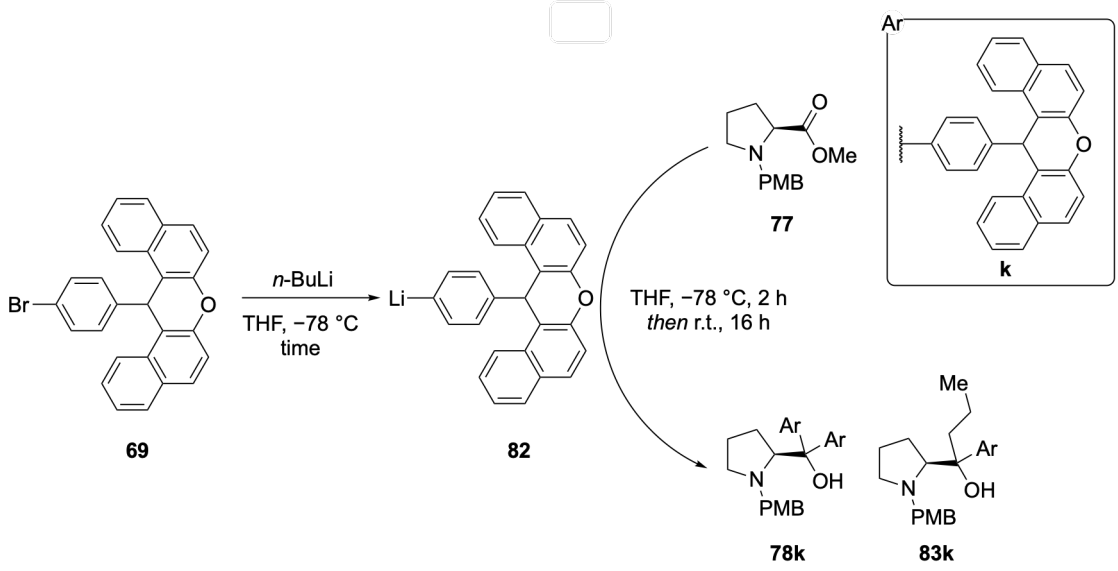


Figure 48: Preliminary experiments to establish the optimal conditions for the lithium halogen exchange.

To verify this, *n*-BuLi was slowly added to a solution of **69** in THF and stirred for 30 min prior to being quenched with H_2O (Figure 48). This confirmed the formation of **81**, demonstrating that the organolithium intermediate was generated efficiently. With the viability of the exchange established, we proceeded with the actual reaction, utilizing this intermediate for the nucleophilic addition to **77** to yield **78k** (Table 4).

Table 4: Screening conditions for the organolithium mediated synthesis of **78k** from **77** and **69**.



Entry [a]	Time [min]	*n*-Buli [equiv.]	**69** [equiv.]	**78k** [%]
1	30	2.5	2.5	- [b]
2	30	2.0	3.0	- [b]
3	30	2.3	2.5	- [b]
4	20	2.3	2.5	32
5	10	2.3	2.5	66

(a) All reactions were conducted on a 1.2 mmol scale. (b) Yield not determined due to formation of **83k**.

The initial reaction resulted in the formation of **78k** as confirmed by mass spectrometry. However, the exact yield could not be determined because side product **83k** formed and their separation was infeasible. Consequently, our primary goal shifted toward optimizing the reaction conditions to completely suppress the formation of **83k**. We realized that the side product predominantly formed when the reaction time for organolithium intermediate formation was prolonged and the stoichiometric ratio of *n*-BuLi to **69** was 1:1. By reducing the preparation time to 20 min and carefully adjusting the stoichiometric amount of *n*-BuLi (Entry 4), we obtained **78** without any side products in 32% yield. Further testing (Entry 5) then revealed that even higher yields could be achieved by minimizing the initial reaction time resulting in a final yield of 66%.

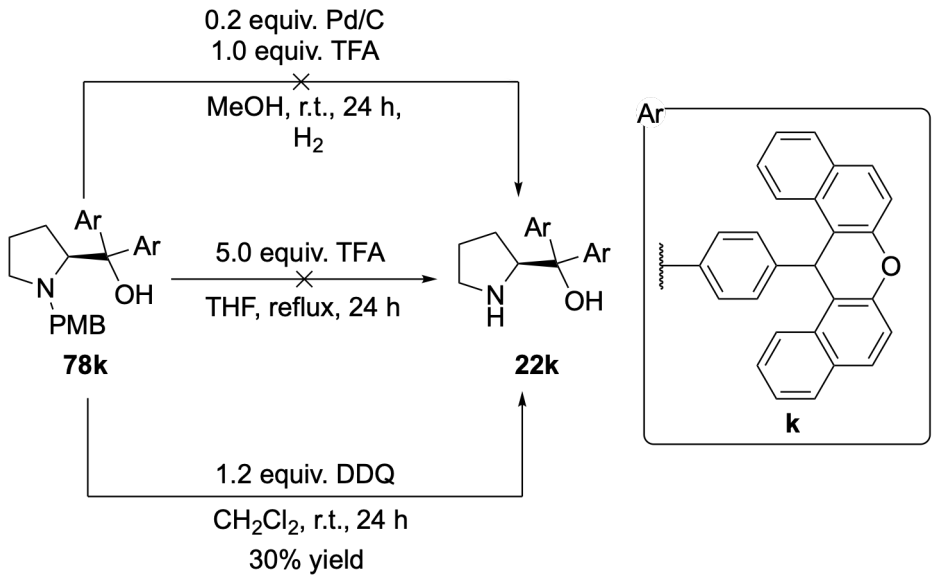


Figure 49: Screening conditions for the PMB deprotection. The reported yields are not absolute due to the constant presence of trapped solvent molecules.

Our focus then shifted toward the removal of the protecting group to form **22k** (Figure 49). Initial deprotection attempts utilizing Pd/C with H_2 in TFA failed to induce any cleavage resulting in the recovery of **78k**. Similarly, subjecting the compound to purely acidic conditions employing 5 equivalents of TFA resulted in no conversion. The deprotection was then achieved *via* oxidative cleavage utilizing 1.2 equivalents of DDQ. However, this reaction was not quantitative and consistently afforded low yields of the crude product.

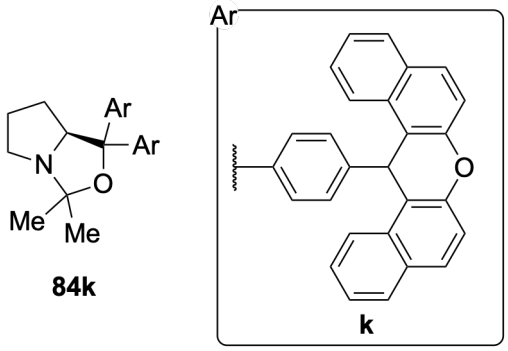


Figure 50: Observation of **84k** during the HPLC purification process using an acetone MeOH and NEt_3 mobile phase mixture.

Classical purification methods such as conventional column chromatography and recrystallization proved completely ineffective necessitating the use of preparative HPLC. During initial purification runs utilizing a mobile phase mixture containing acetone, MeOH, and NEt_3 the formation of side product **84k** was detected *via* mass spectrometry (Figure 50).

To circumvent this issue the mobile phase was changed to a mixture of MeOH, TBME and NEt_3 which prevented formation of **84k** and yielded **22k**.

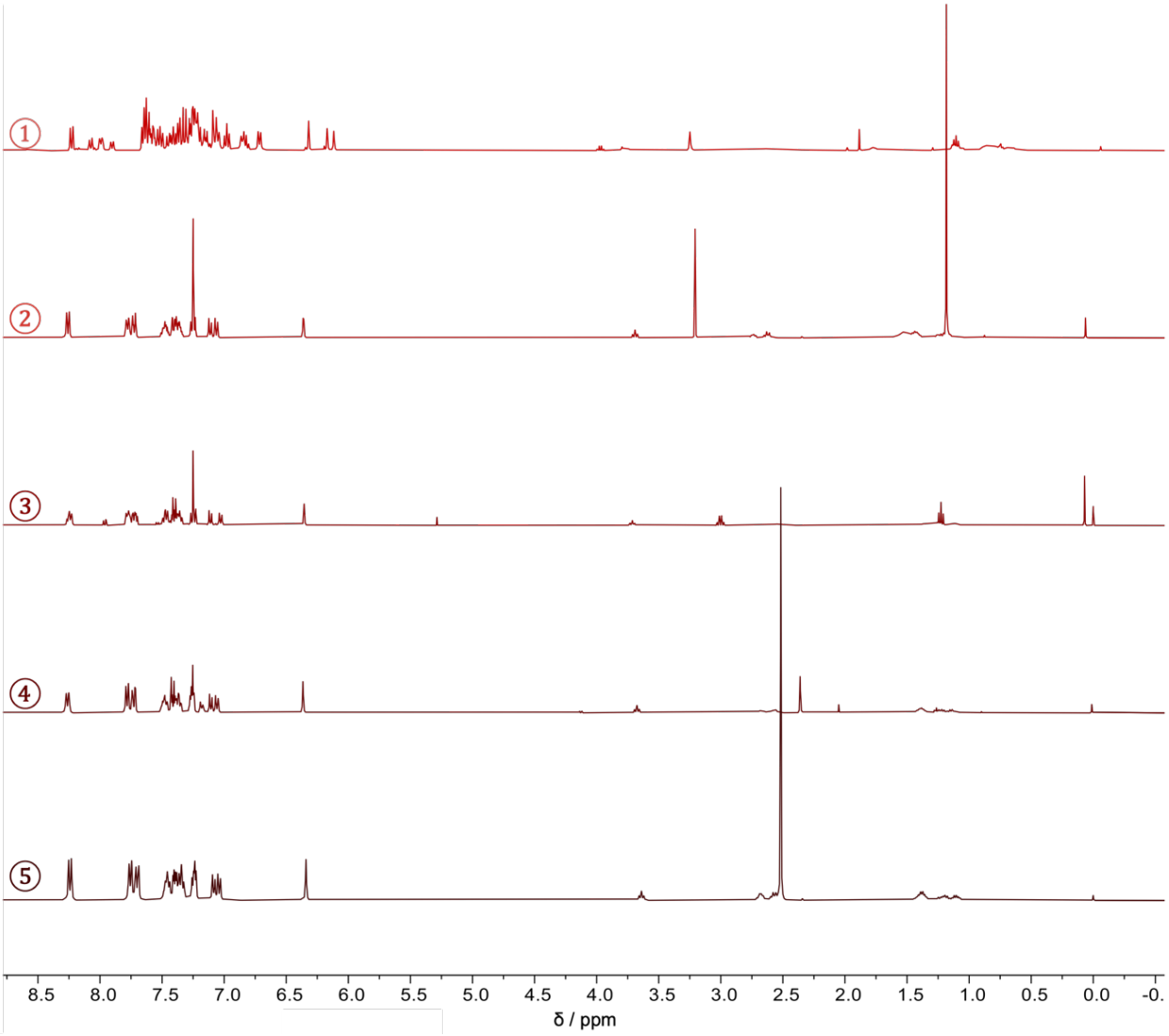


Figure 51: ① Crude NMR spectra before HPLC of **22k**. ② After HPLC using MeOH, TBME, NEt_3 as mobile phase. ③ HPLC product after co-evaporation with CH_2Cl_2. ④ HPLC product after co-evaporation with toluene. ⑤ HPLC product after co-evaporation with DMSO.

Although the chromatographic separation was ultimately successful a major challenge arose during the subsequent solvent removal process, because the purified compound **22k** exhibited a tendency to trap solvent molecules as a solid as shown in the NMR spectra (Figure 51).

Prolonged evaporation attempts of the HPLC fraction failed to remove the residual TBME (Figure 51, ②). Consequently, co-evaporation strategies using various alternative solvents were investigated. The use of CH_2Cl_2 as a co-evaporator unfortunately led to the decomposition of the

product as indicated by the appearance of new unidentified signals in both NMR (Figure 51, ③) and mass spectra. Switching to toluene displaced TBME but resulted in toluene remaining trapped within the sample (Figure 51, ④). Following a final approach, the sample was treated with DMSO and subjected to lyophilization. While this method removed the previous solvent, it led to a final product contaminated with DMSO, highlighting the solvent trapping properties of **22k** (Figure 51, ⑤). We hypothesize that this persistent retention of diverse solvent molecules might be indicative of the compound acting as an exceptionally strong DED. The extended, highly polarizable structural motifs likely engage in substantial LD interactions with the solvent molecules,[12] preventing their complete removal.

Although a completely solvent free solid could not be isolated, the structure of **22k** was confirmed. We therefore decided to proceed with the batch containing toluene. Since toluene is a simple nonpolar solvent, we assumed it would not interfere with the CBS reduction.

3.2.5 Experimental Evaluation and Model Boundaries

The enantioselective performance of **22h** and **22k** for the reduction of **51** was evaluated employing the standardized reduction protocol (Figure 52). However, the results not only revealed significant deviations from the ML predictions, but also proved highly inconsistent during repeated trials as the *ee* values fluctuated between individual runs. Because precise and reproducible experimental data is an absolute requirement for our model, these problems prompted a systematic investigation into the analytical robustness of the reduction of **51** itself.

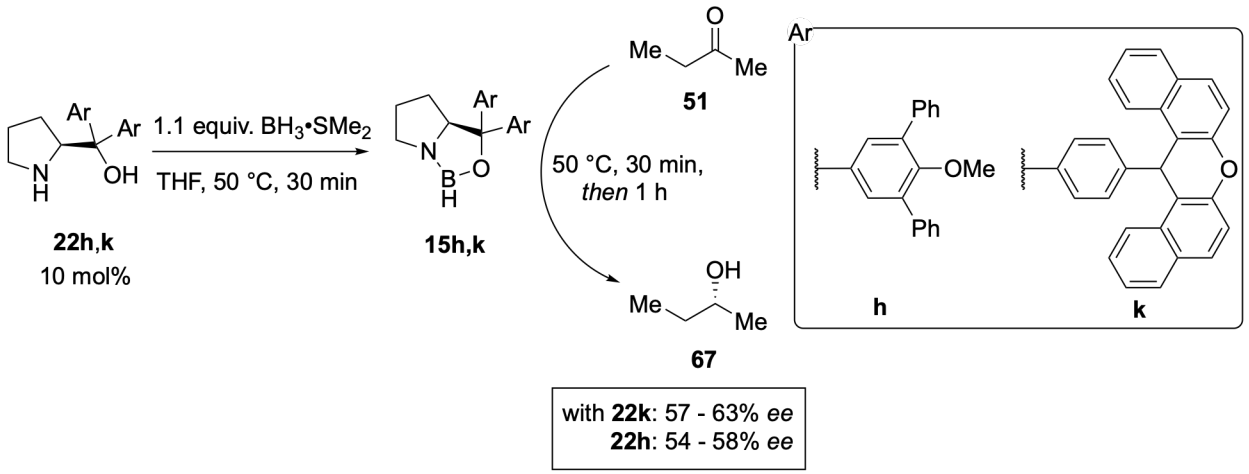


Figure 52: First evaluation of the precursors **22h** and **22k** for the reduction of **51**.

During this process we identified a flaw in the standard workup procedure. To quench the reaction and release the final product, an excess of aqueous acid or water must be added to hydrolyze the formed alkoxy borane. While this aqueous quenching works for most substrates, **67** is highly soluble in water (approximately 290 mg mL^{-1} at 25 °C),[173] which was overlooked in our previous published studies.[164]

A simple estimation of our experimental scale highlights the magnitude of this issue. In a catalytic reduction reaction utilizing 0.4 mmol of **51**, the theoretical quantitative yield of **67** is approximately 31 mg. Quenching this mixture with 5 mL of water, as dictated by the standard protocol,[87,164] introduces a large aqueous volume. Due to the high-water solubility of **67**, the partition equilibrium between the two phases is highly unfavorable for the organic layer. The alcohol partially dissolved in the aqueous phase, leaving only low concentrations of the product in the organic solvent for further derivatization and analysis. When these organic samples are then analyzed by GC-FID, the resulting signals are weak, which can lead to a low signal to noise ratio and complicates reliable peak integration. To resolve these issues, we pursued a dual analytical approach by developing a completely new HPLC strategy and optimizing the existing GC protocol for **67**.

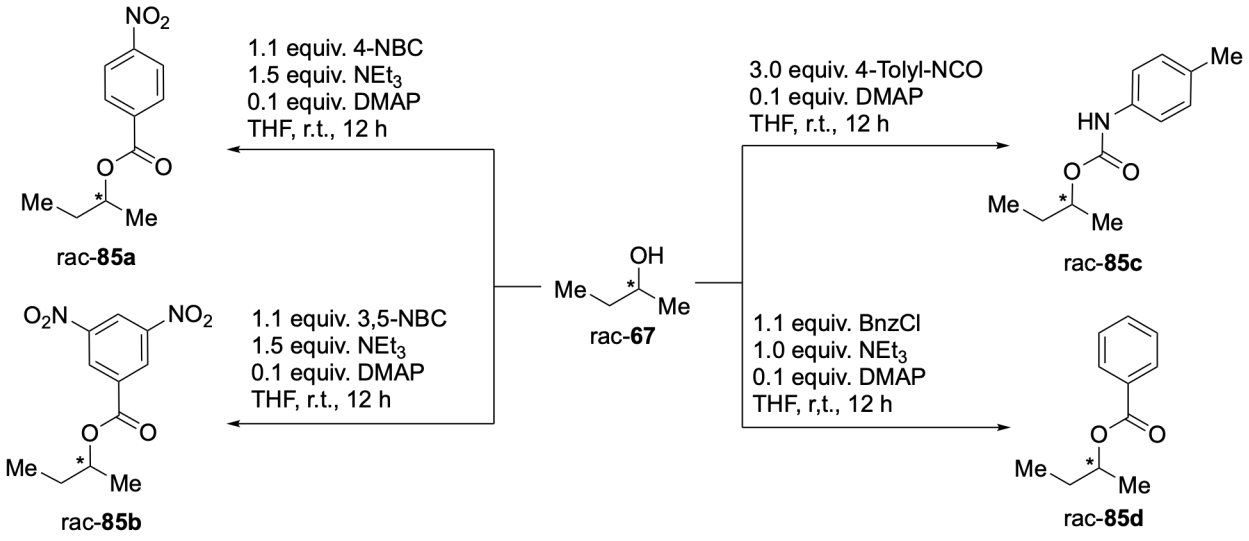


Figure 53: Derivatives screened to achieve perfect baseline separation on the HPLC. **85c** was ultimately selected because it provided the optimal resolution during HPLC analysis.

The HPLC method was specifically employed to overcome these sensitivity limitations by capitalizing on a different mode of detection. In our GC-FID setup, the signal intensity is dictated

not only by the analyte's absolute concentration but also by its specific response factor (i.e., the number of oxidizable carbon atoms). Since **67** lacks a suitable chromophore, it inherently exhibits poor UV absorbance. However, by derivatizing the molecule with a strong chromophore, the molar extinction coefficient is increased, enabling highly sensitive detection even at low analyte concentrations. We screened several potential derivatizing agents, including **85a** and **85b**, but ultimately identified **85c** as the best derivative for achieving optimal baseline separation during HPLC analysis (Figure 53).

In parallel, the gas chromatography protocol was optimized to provide a robust independent verification of these results. To mitigate the loss of the product, we reduced the water content for quenching to 3.0 equivalents which corresponds to merely 21 µL. By minimizing the aqueous volume to such an extent, the partition equilibrium is fundamentally shifted, ensuring that the vast majority of the target compound is retained in the organic phase. Experimental implementation of this refined quenching procedure confirmed our hypothesis. By retaining a high concentration of the product in the organic layer, the subsequent GC measurements exhibited intense signals, eliminating the previous noise interference and enabling precise peak integration.

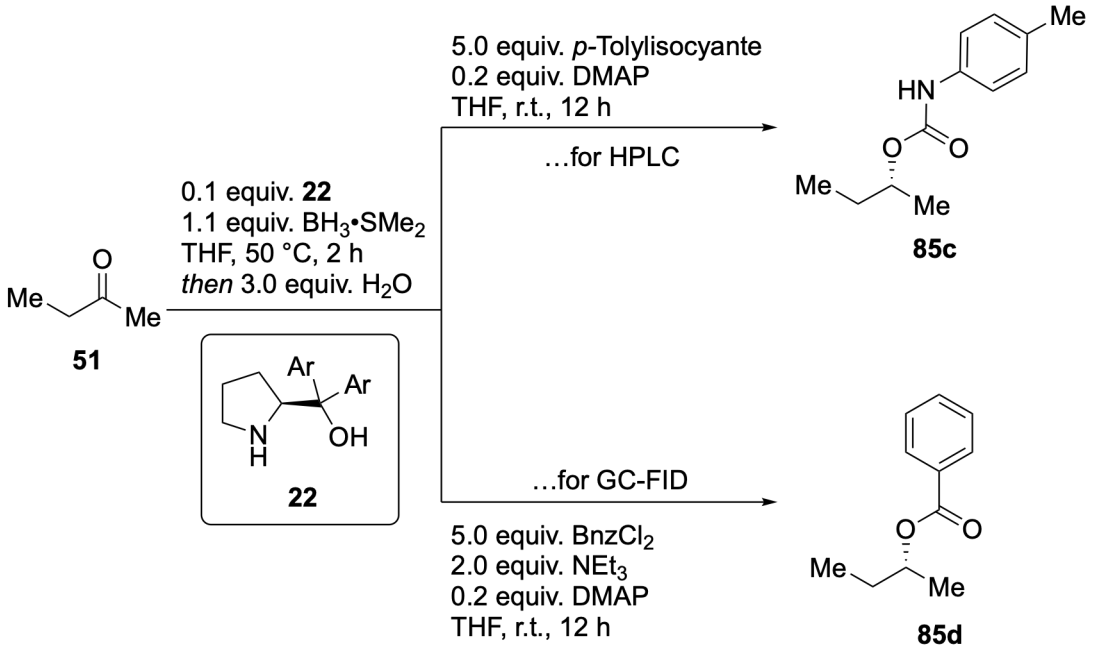


Figure 54: Optimized conditions that enabled the accurate evaluation of the reduction of **51**.

After implementation of both the HPLC method and the optimized GC method (Figure 55), we re-evaluated the aforementioned precursors. Both independent techniques yielded identical and

low *ee*, thereby confirming that the ML model had indeed not accurately predicted the performance of these specific catalysts in the first place.

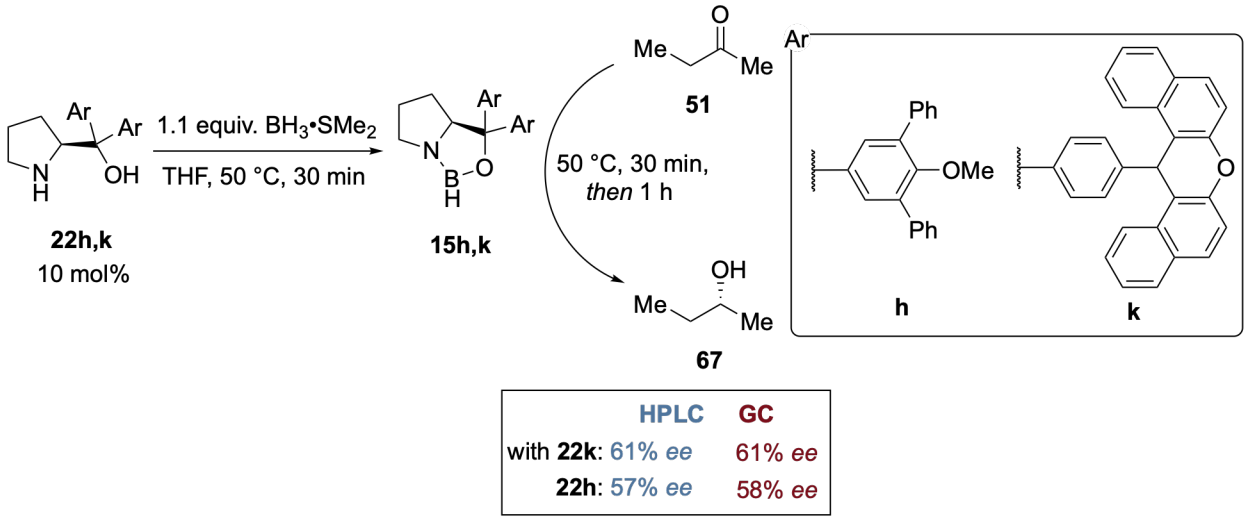


Figure 55: Second evaluation demonstrating consistent results obtained through independent HPLC and GC measurements.

Based on these results and the fact that we had to optimize our analytical strategies, we re-evaluated the majority of the precursors from our previous work with **51**. Applying this to our previously analyzed precursors revealed systematic deviation as in Figure 56. While precursor catalysts **22e** and **22f** exhibit merely marginal deviations between the old GC protocol and our optimized methods, the corrected *ee* for **22i** shows a major discrepancy that definitively exposes the unreliability of the former approach.

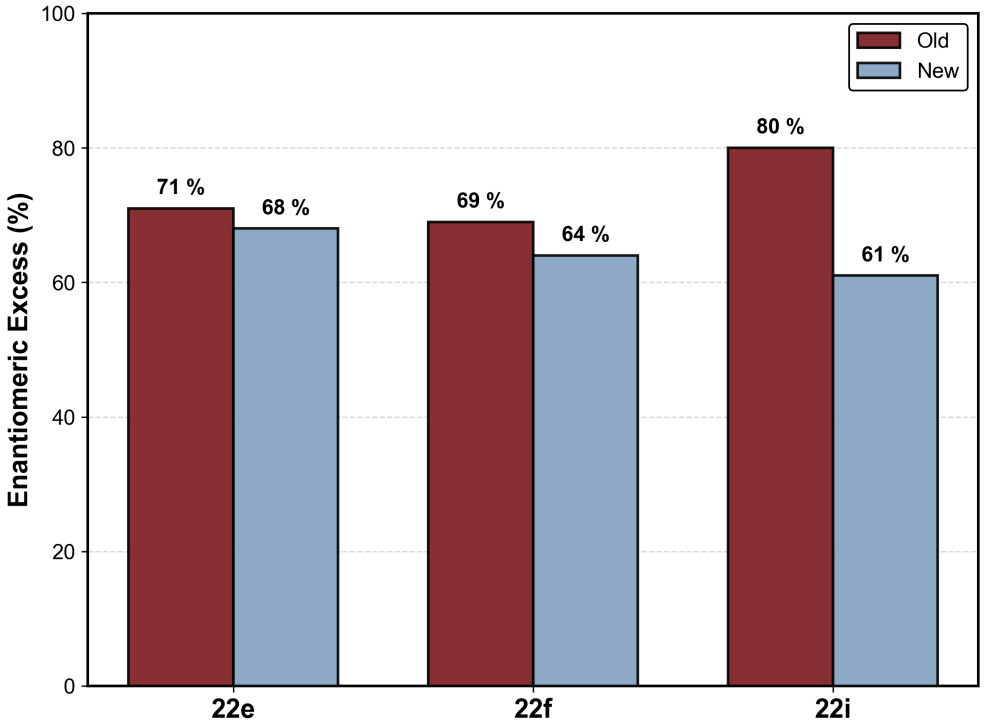


Figure 56: Corrected evaluation of precursors **22e**, **22f**, and **22i** for the reduction of **51**. The figure highlights the fundamental systematic deviation within the previous dataset.

The re-evaluation demonstrates that the predictive capabilities of the current ML model are fundamentally restricted by analytical data integrity and a currently limited understanding of exceptionally bulky catalyst structures. The identification of a systematic error regarding the unquantified loss of the highly water-soluble product during aqueous workup revealed a definitive analytical bias in the initial test data. This flaw highlights that models operating on small datasets are highly susceptible to data quality and cannot mathematically correct for experimental artifacts, making robust analytical protocols the absolute prerequisite for any data driven approach. Beyond these analytical limitations, the complex physical behavior of highly sterically hindered systems requires further investigation. The pronounced difficulty in removing solvent residues from precursor **22k** underscores the true nature of these structures as highly potent DEDs. This intense propensity suggests that these catalysts might undergo unwanted intermolecular dimerization alongside. Since it remains unclear to what extent such aggregation phenomena disrupt the catalytic cycle, subsequent experimental studies must address this uncertainty. Future research should therefore evaluate these specific reactions under adapted conditions, such as elevated temperatures or different solvents, to actively suppress potential dimer formation and conclusively determine the intrinsic catalytic activity of these structures.

Part III

CBS Reduction of Imines

3.3 Extending the Concept of CBS Reduction to Imines

The conceptual framework for this investigation was established following the results of Section 3.1 and prior to uncovering the analytical insights detailed in Section 3.2. Our primary ambition was to further explore the scope of the CBS reduction by applying the predictive model to a novel yet structurally related substrate class. We selected imines as the next logical step since they are nitrogen analogs to the previously investigated ketones. This substrate class provides direct access to chiral amines which constitute valuable building blocks in chemical synthesis.[110,174] Furthermore, their distinct electronic properties and the additional *N*-substituent introduce new chemical features providing an ideal opportunity to test the robustness of our predictive model.

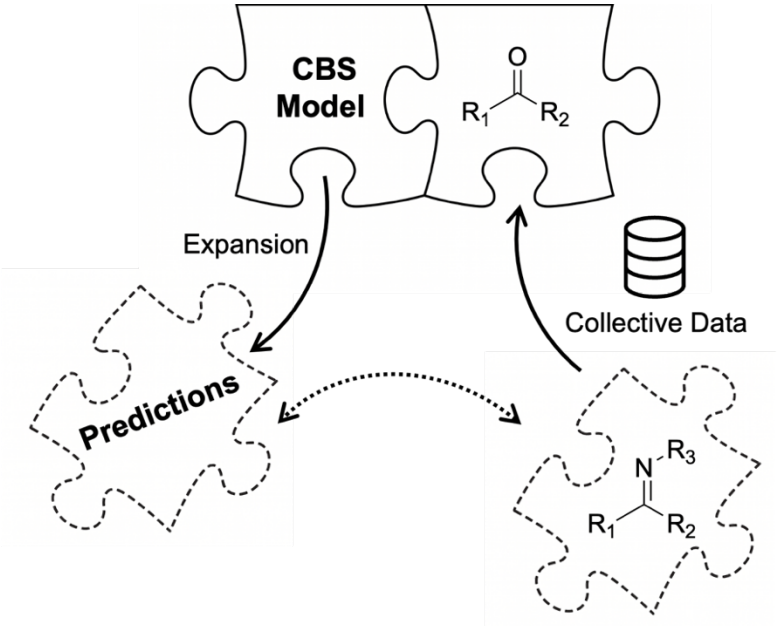


Figure 57: Conceptual framework illustrating the transition from the ketone-based CBS model to the integration of imine substrates.

Although this similarity makes imines an intuitive target, a thorough evaluation of the existing literature revealed a scarcity of experimental data. Our primary ambition was therefore to construct a comprehensive internal database for these reductions and integrate it into our predictive model to establish a unified computational framework. However, during the data collection process, we encountered unexpected challenges and made critical observations regarding the reactivity of this system.

3.3.1 CBS-Reduction of Cyclic Imines

The investigation of imines started with cyclic systems. We chose **86** and **87** (Figure 58) to evaluate the influence of ring size and steric bulk on the reduction. Compound **86** provides an accessible imine bond due to its simple pyrroline ring. In contrast, compound **87** features a larger framework, that acts as a substantial steric obstacle directly next to the reactive center. While **86** was commercially available, **87** was synthesized in two steps from **88** (Figure 59).

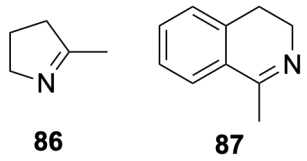


Figure 58: Structures of the investigated cyclic imines **86** and **87**.

The synthesis of **87** started with the acetylation of primary amine (**88**), yielding **89** in 83%. Subsequently, a Bischler-Napieralski cyclization[175] was employed to convert **89** to the cyclic imine (**87**). However, **87** was only isolated in 53% yield as the elevated temperatures caused thermal degradation of **87**, resulting in product loss.

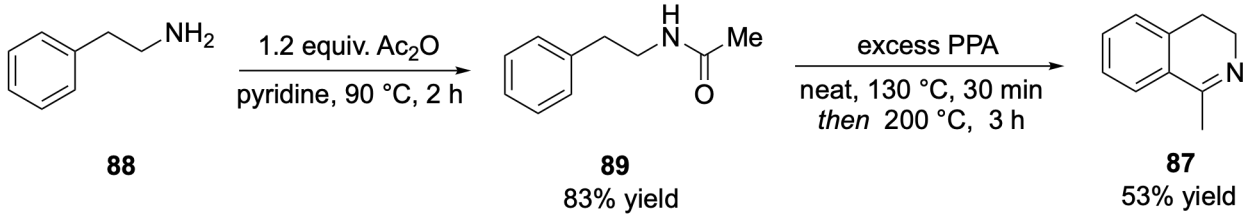


Figure 59: Reaction scheme for the two-step preparation of **87** from **88**.

Our focus then shifted toward evaluating the performance of **86** and **87** under standard CBS reduction conditions. However, attempts to perform the catalytic reductions using precursor **22a** proved unsuccessful, as the formation of the desired products **90** or **91** could not be observed (Figure 60).

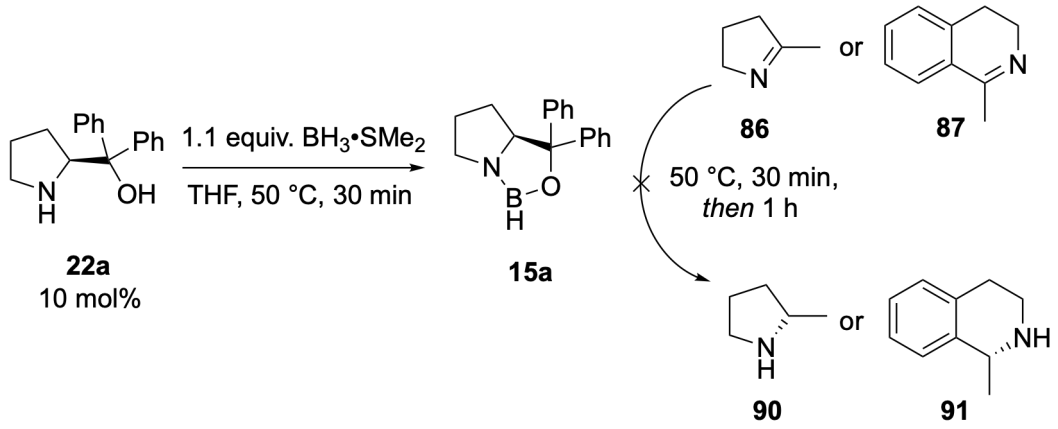


Figure 60: CBS reduction of **86** to **90** and **87** to **91** using precursor **22a** under the standard conditions.

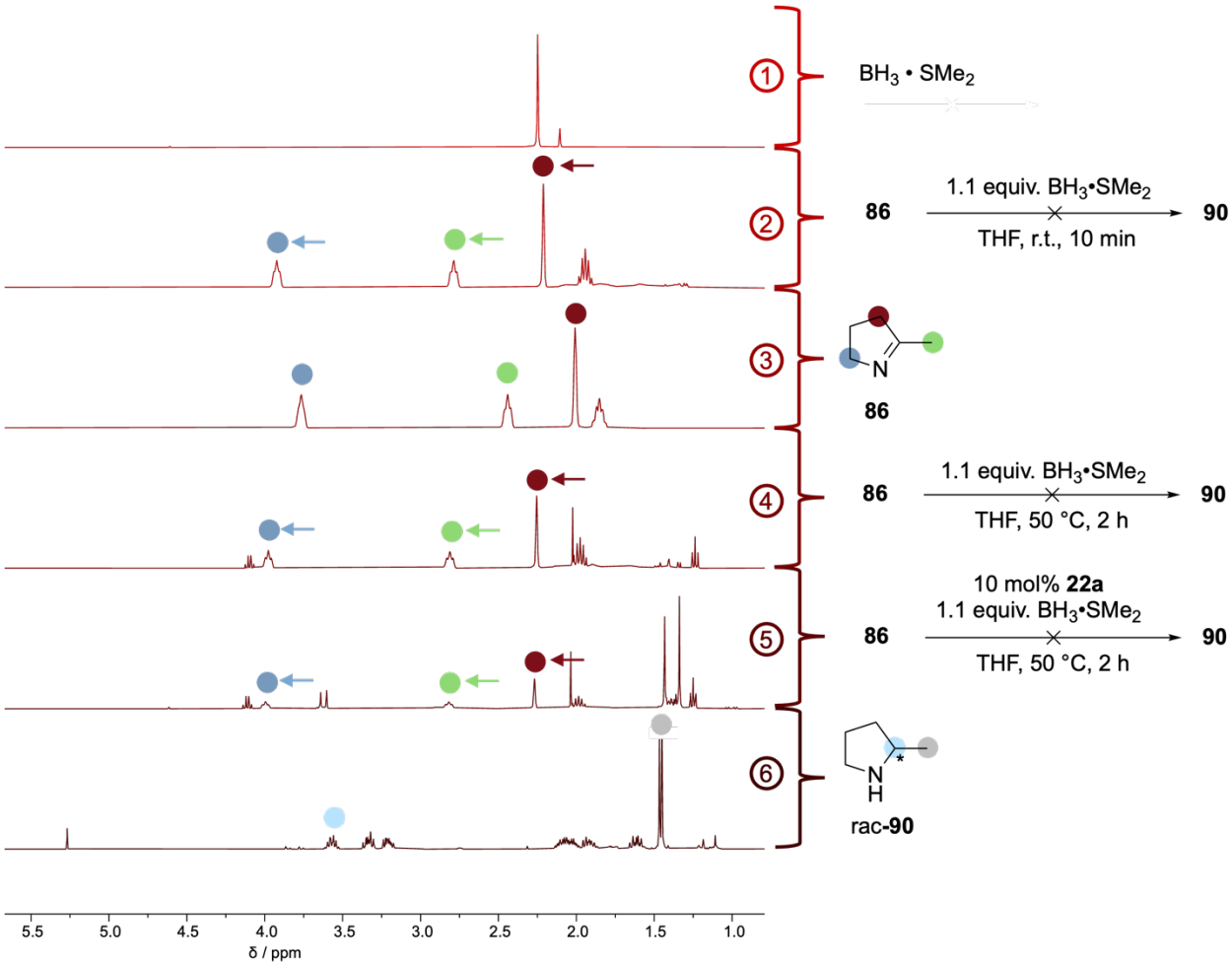


Figure 61: ^{1}H-NMR spectra monitoring the reduction of cyclic imine **86**. The spectral windows are truncated for clarity, as no significant signals were observed below 1.0 ppm and above 5.5 ppm. All spectra were recorded in $CDCl_3$. ① Reference spectrum of the reducing agent BH_3•SMe_2. ② Reaction mixture of **86** and the reducing agent after stirring for 10 min at room temperature. ③ Reference spectrum of **86**. ④ Reaction mixture of **86** and the reducing agent after prolonged stirring at 50 °C. ⑤ CBS reduction of **86** with **22a** under standard conditions. ⑥ Reference spectrum of product rac-**90**.

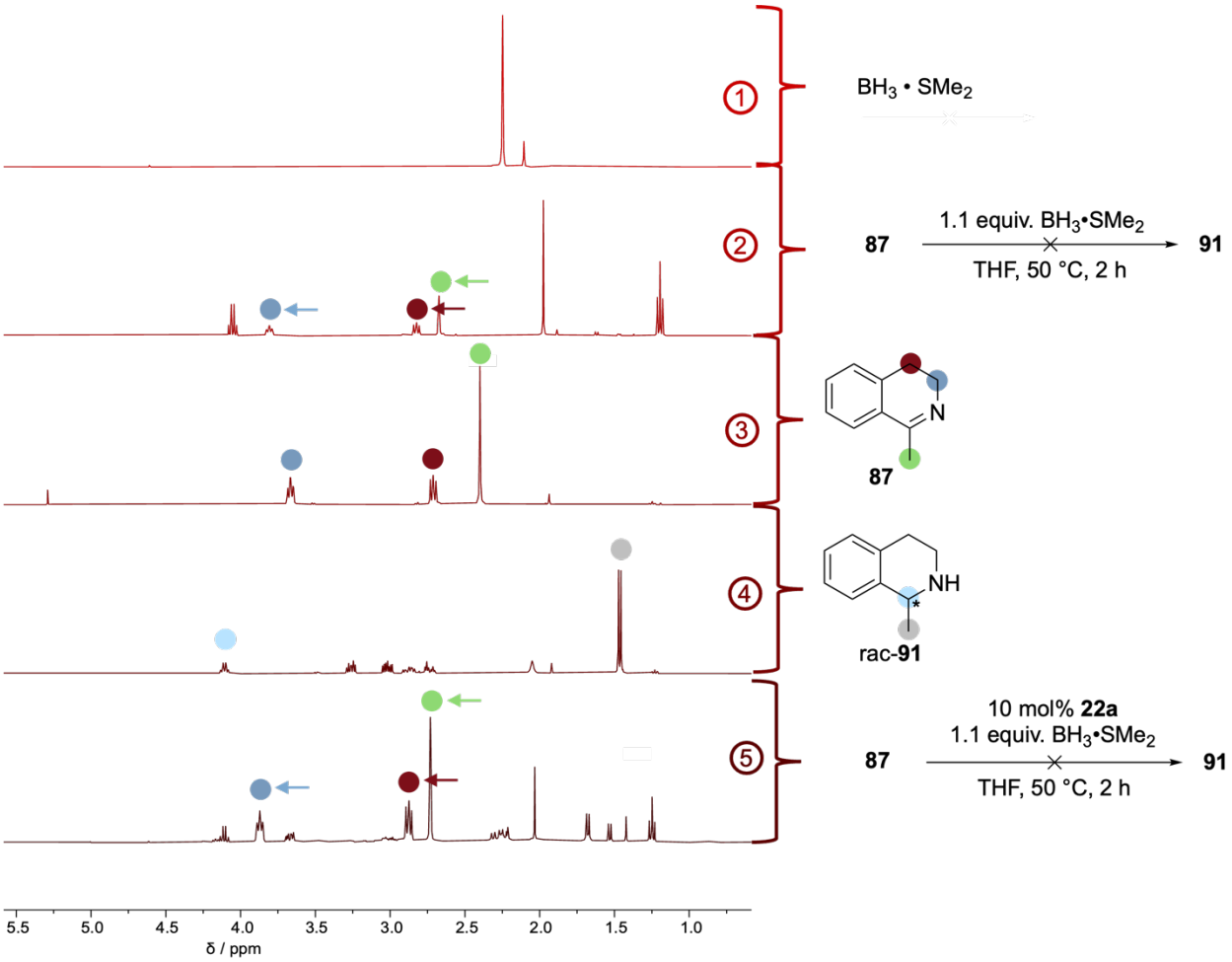


Figure 62: ^{1}H-NMR spectra monitoring the reduction of cyclic imine **87**. All spectra were recorded in $CDCl_3$. The spectral windows are truncated for clarity, as no significant signals were observed below 1.0 ppm and above 5.5 ppm. ① Reference spectrum of the reducing agent BH_3•SMe_2. ② Reaction mixture of **87** and the reducing agent after prolonged stirring at 50 °C. ③ Reference spectrum of **87**. ④ Reference spectrum of product rac-**91**. ⑤ CBS reduction of **87** with **22a** under standard conditions.

To elucidate the problem, an investigation of the reaction was conducted using NMR spectroscopy. The resulting spectra revealed that no reaction had occured in any of the attempts, yielding only unreacted starting material **86** or **87 (**Figure 61 and 62**,** ⑤**)**. However, the respective signals of **86** and **87** exhibited a downfield shift in comparison to the reference spectra (Figure 61 and 62, ③). Further experiments confirmed this trend for both cyclic imines whenever BH_3•SMe_2 is present in the solution and indicating a strong Lewis acid/base coordination between the cyclic imine and the borane species which might deactivate the reducing agent.

We then employed alternative borane sources like BH_3•THF and catecholborane to evaluate their influence on the reaction outcome. Given the higher reactivity, we anticipated that BH_3•THF would

undergo a similar deactivation process to that of $BH_3 \bullet SMe_2$. On the contrary, we expected catecholborane to overcome this limitation due to its steric properties. However, both reducing agents led to the recovery of **86** and **87**, demonstrating that this transformation is infeasible under the investigated conditions. These experimental findings align with early observations by Cho *et al*.[101] who likewise documented the same results using cyclic imines. Although subsequent reports by other groups have suggested that these reductions could be achieved,[105] they remained entirely unsuccessful for us.

3.3.2 CBS Reduction of Non-Cyclic Imines

Following the limitations encountered with cyclic imines the focus shifted toward the exploration of non-cyclic imines using **92** as the model substrate. This strategic choice was motivated by the close structural resemblance to acetophenone (**13a**), synthetic accessibility *via* condensation of simple and readily available substrates (Figure 63) and the good documentation of structurally related molecules in the literature.[101,102]

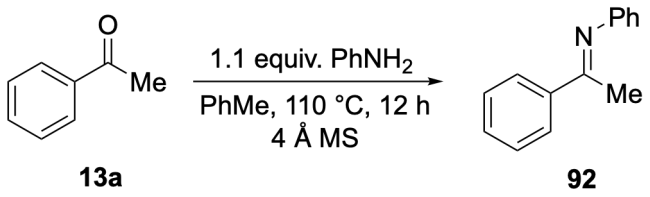


Figure 63: Synthesis of **92** using a condensation reaction of **13a** and aniline with powdered molecular sieves (4 Å).

The initial analysis following the condensation reaction of **13a** and aniline appeared to confirm the isolation of **92**. Operating under this assumption, we prepared what we believed to be the corresponding racemic standard (**93**) for the reduction experiments. Upon initiating the catalytic experiments (Figure 64), we observed promising selectivities that correlated well with reported literature data.[101,102]

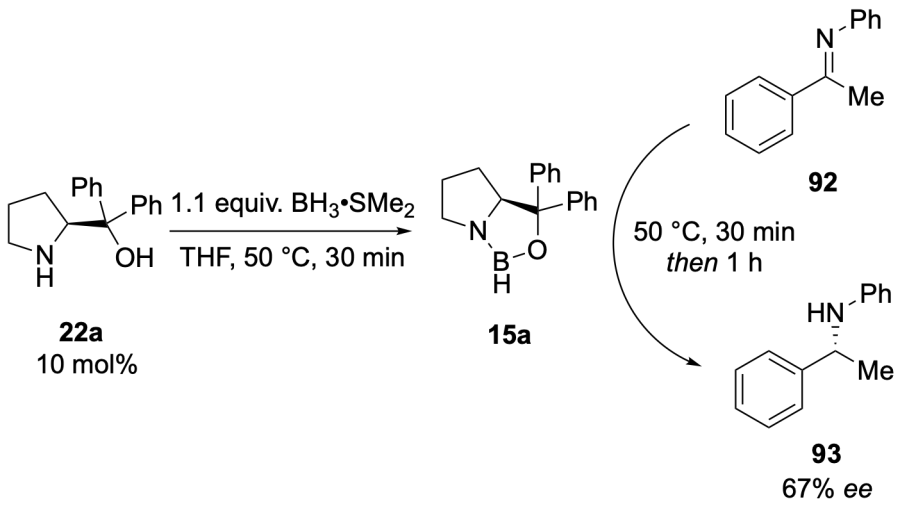


Figure 64: First CBS reduction of **92** using **22a** and achieving comparable results to the literature.

However, this correlation turned out to be a deceptive analytical coincidence. As it was later discovered, the sample predominantly contained the hydrolyzed starting material acetophenone (**13a**), rather than the imine **92**. As a result, the reduction steps generated phenylethanol (**14a**) rather than the desired amine (**93**). Because the HPLC retention times and the observed *ee* of **14a** coincidentally mirrored the expected literature values,[101,102] this critical error remained completely undetected at this early stage.

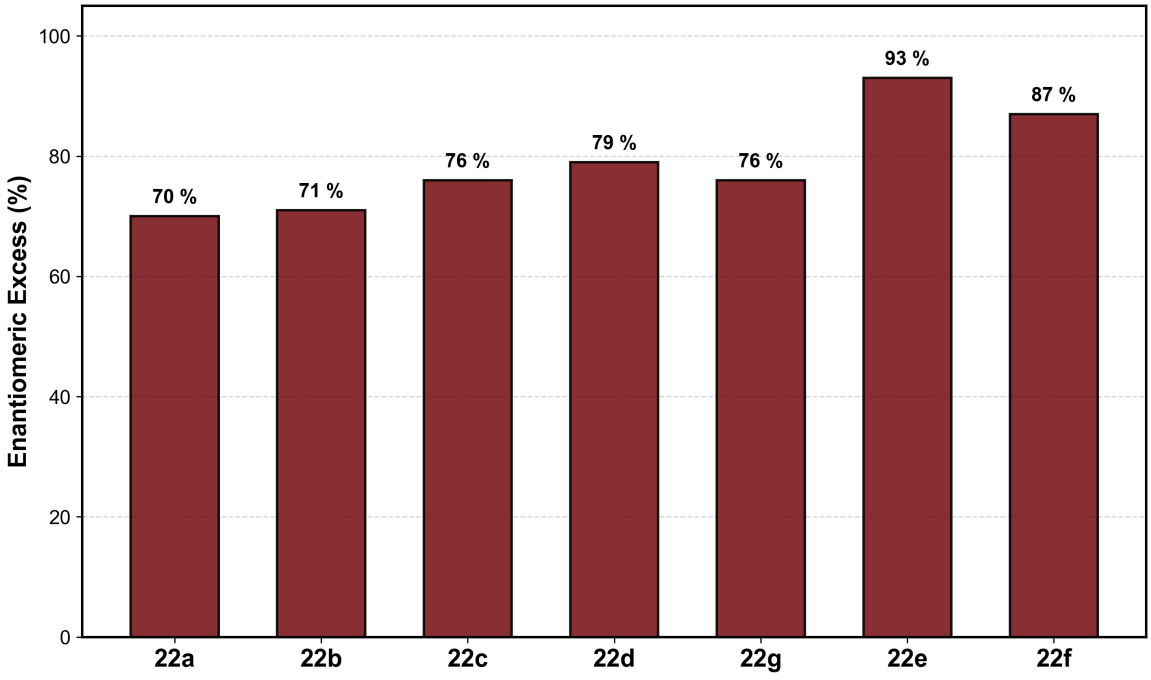


Figure 65: Results of the initial optimization phase using the precursors **22a-g** in the CBS reduction, operating under the assumption that substrate **92** was employed.

Operating under the illusion that we were optimizing the reduction of **92**, we evaluated diverse precursors **22a-g** to determine their influence on the catalytic outcome. As depicted in Figure 65, these investigations revealed a distinct structural trend where the implementation of larger DED groups consistently improved the overall *ee*, effectively mirroring the observations previously made for analogous ketone reductions.[87] Encouraged by these results, we proceeded to further expand the overall substrate scope.

To facilitate this expansion a targeted library of specific derivatives was designed (Figure 66). For instance, **96**, **97**, and **98** were chosen to investigate the influence of electron withdrawing and electron donating substituents on the substrate. Furthermore, **94** was envisioned to evaluate the impact of altered steric demands and to determine the general importance of this nitrogen substituent for the overall reaction. Additionally, **95** and **32b** were tested to assess the effect of incorporating a methylene spacer into the molecular framework when compared to **92**. Given the minimal structural deviation and established status as a literature benchmark the catalytic outcome for **32b** was expected to closely parallel that of **92**.[101,102] In contrast, the more pronounced steric and electronic modifications present in derivatives **94**, **95**, **96**, **97**, and **98** were anticipated to dictate their overall reactivity.

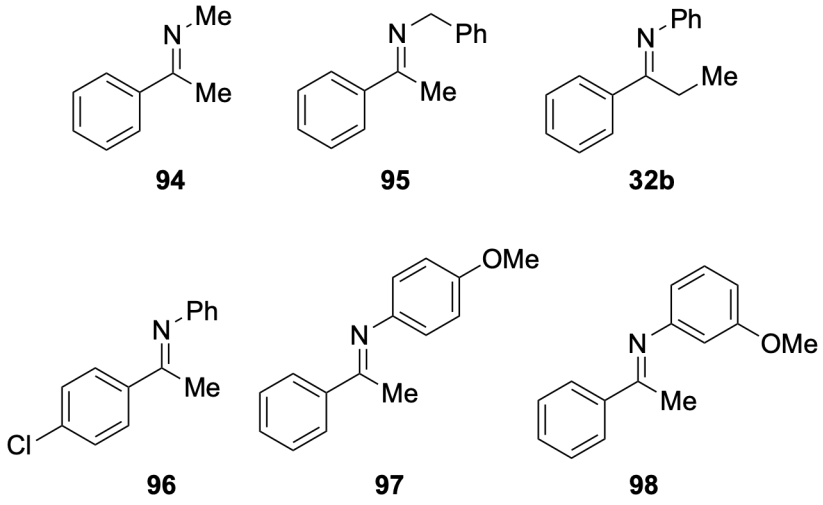


Figure 66: Overview of the synthesized imine substrates utilized for further catalytic investigations.

During the attempt to synthesize these targets utilizing the established condensation shown in Figure 63, we encountered severe experimental inconsistencies. While specific derivatives such as **94**, **95**, **96**, and **97** were isolated in low yields, the synthesis of the other analogues proved unsuccessful. We then discovered that replacing the powdered molecular sieves with beads

circumvented this problem and allowed for the reliable isolation of all targeted imines and the subsequent preparation of their corresponding racemic mixtures for HPLC.

However, upon subjecting the substrates to the catalytic conditions, the results diverged significantly and completely contradicted our structural hypotheses, as all observed selectivities were exceptionally poor, yielding mostly racemic products. Substrate **32b** for example, which was expected to yield comparable results to **92** due to the strucural similarity and previous literature reports,[101] resulted in a racemic mixture. The same observation was made for **96**, and **97**, all of which ultimately yielded only racemic products. The only derivatives that exhibited any measurable *ee* were **94** and **95**, as depicted in Figure 67. While a decrease in *ee* compared to **92** was expected for **94** and **95**, as preliminary computations conducted by Caio Porto suggested that the phenyl moiety on the nitrogen of the substrate engages π-π-stacking interactions with the catalyst framework, the magnitude of this difference could not be explained solely by this effect.

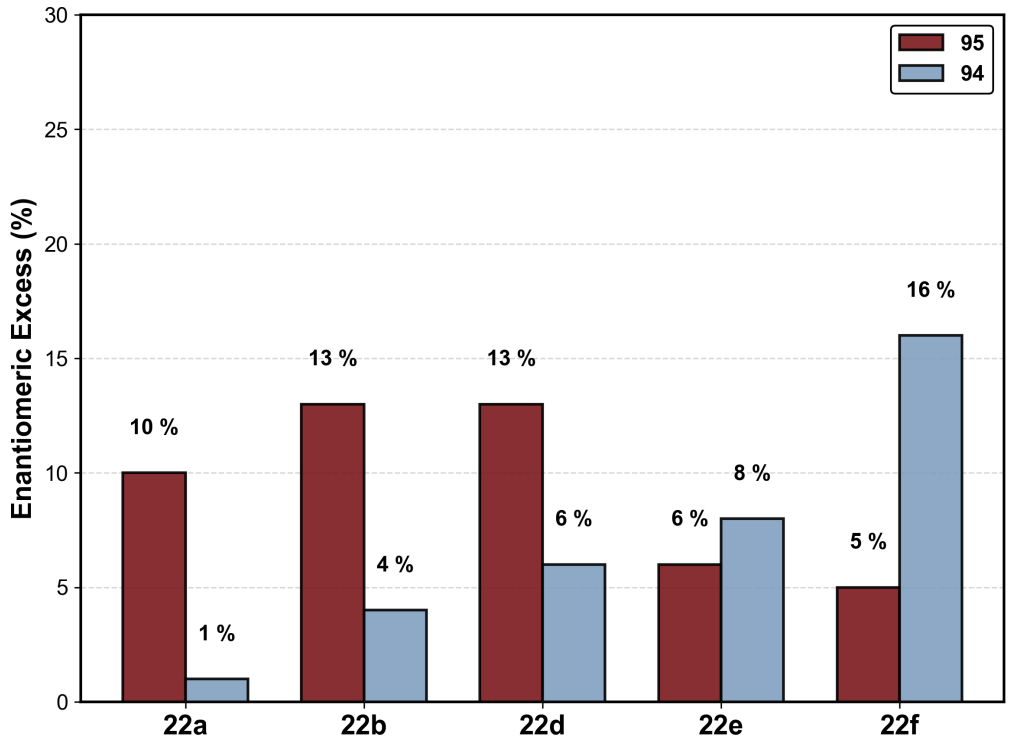


Figure 67: CBS reduction of **94** and **95** using precursors **22a, 22b, 22d, 22e**, and **22f**.

Control experiments to rule out contaminated reagents or inconsistent reaction conditions provided no explanation for this lack of selectivity. Consequently, we systematically investigated alternative sources of error, starting with a rigorous re-characterization of our original model system **92**.

Prompted by the synthetic discrepancies associated with the powdered molecular sieves, we critically re-evaluated the identity of our initial substrate batches. It was at this point we finally confirmed the critical analytical misidentification foreshadowed earlier.

The synthesis of **92** was repeated using molecular sieve beads, affording the true imine in 98% yield. After synthesizing the verified racemic standard **93**, the actual substrate **92** was subjected to the catalytic CBS conditions. Evaluation of the results revealed that, even after extensive optimization of parameters such as temperature, solvents, borane species, and stoichiometries, the reaction consistently yielded a racemic mixture. This outcome perfectly mirrored the results previously observed with the other verified substrates. The only method to achieve any measurable stereoselectivity was to employ the chiral promoter in stoichiometric amounts, which afforded 37% *ee*. Since catalytic enantioselective turnovers could not be realized under these conditions, we shifted our focus toward a critical re-evaluation and reproduction of the established literature procedures.

3.3.3 Evaluation of Previously Documented Results

As a primary starting point, we selected the foundational works of Cho and Chun.[101,102] Since their original reports explicitly utilized the Itsuno reagent (**20**) as a crucial benchmark, we consequently synthesized this reagent to ensure a direct analytical comparison towards the CBS-catalyst. By utilizing L-valine (**99**), the synthesis proceeded without the necessity of amine protection to **20** in moderate yield of 46% (Figure 68).

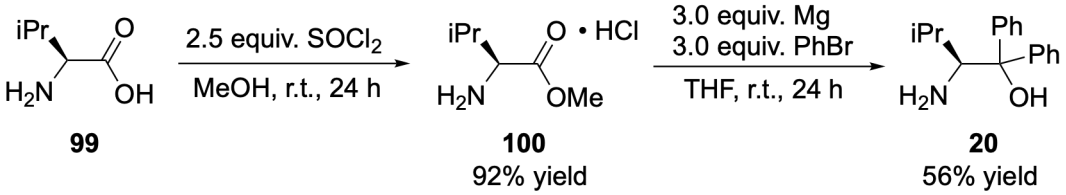


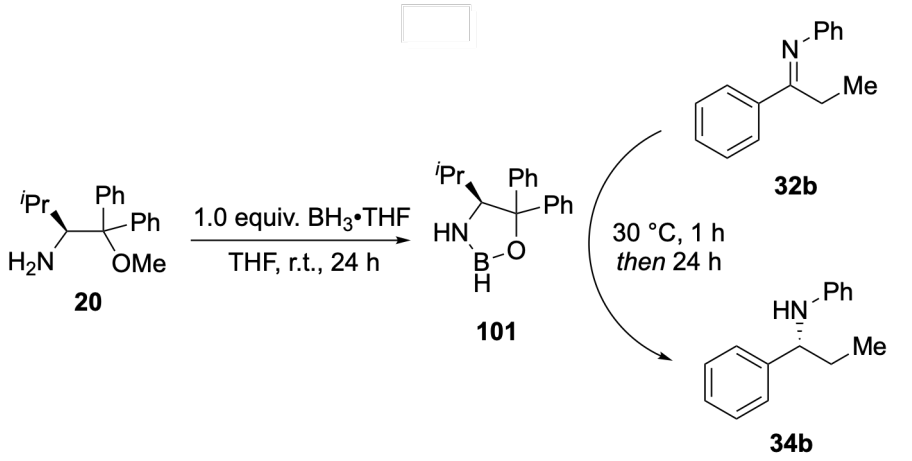
Figure 68: Reaction scheme for the two-step preparation of **20** from **99**.

To ensure the best comparability, we strictly followed the experimental procedures documented previously, employing **32b** as the test substrate, alongside 1.0 equivalents of the BH_3•THF as the reducing agent. Since the original protocol lacked a precise description regarding the exact substrate addition, we decided to conduct the reactions utilizing two distinct experimental setups. The first approach involved the immediate addition of the entire amount of substrate to the reaction

mixture, while the second setup followed our previously established method utilizing a syringe pump for a controlled slow addition. Following the reported 24 h stirring period after the addition of **32b** to the mixture of BH_3•THF and the precursors, the overall catalytic outcomes were evaluated utilizing our established analytical methods.

The evaluations revealed that the direct addition of the substate in all cases yielded (Entry 1 and 3) racemic mixtures, thereby conclusively indicating that a controlled addition is a requirement for any stereochemical induction (Table 5). However, even with slow addition (Entry 2 and 4), the results still deviated from literature data. When employing a catalytic loading of 10 mol% of **20**, we observed an *ee* of merely 10%, which is in stark contrast to the reported value of 66%. Upon utilizing stoichiometric amounts of **20**, the *ee* increased to 40%, which was still considerably lower compared to literature data (87%).[101,102]

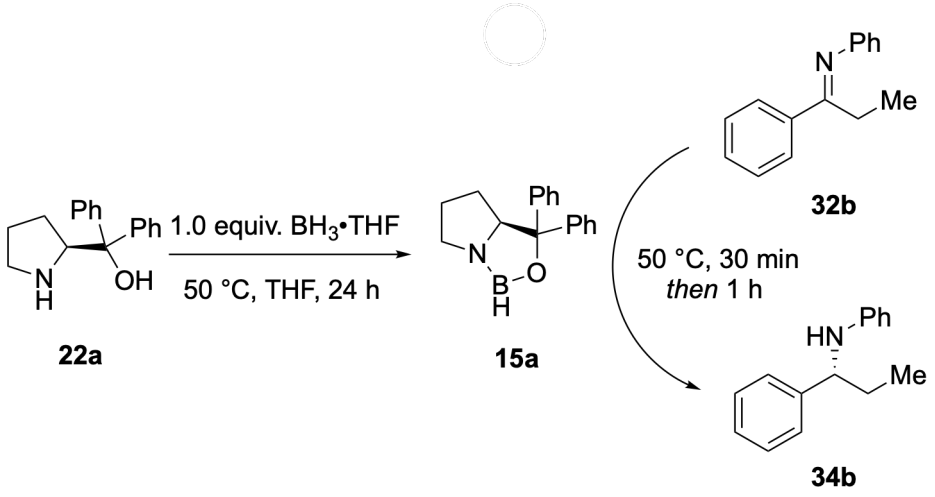
Table 5: Screening of catalytic conditions for the CBS reduction of **32b** to **34b** using catalyst precursor **20**.



Entry [a]	**20** [equiv.]	**34b**$_{Lit}$ [% *ee*] [b]	**34b** [% *ee*]
1 [c]	0.1	66	*rac*
2 [d]	0.1	66	10
3 [c]	1.0	86	2
4 [d]	1.0	87	40

(a) Reactions were conducted on a 0.05 mmol scale. (b) Literature values. (c) Fast addition of **32b** to **101**. (d) Dropwise addition of **32b** to **101**.

Table 6: Screening of catalytic conditions for the CBS reduction of **32b** into **34b** using precursor **22a**.



entry [(a)]	**22a** [equiv.]	**34b**$_{Lit}$ [% *ee*] [(b)]	**34b** [% *ee*]
1 [(c)]	0.1	70	*rac*
2 [(d)]	0.1	70	*rac*
3 [(c)]	1.0	78	3
4 [(d)]	1.0	78	37

(a) Reactions were conducted on a 0.05 mmol scale. (b) Literature values. (c) Fast addition of **32b** to **15a**. (d) Dropwise addition of **32b** to **15a**.

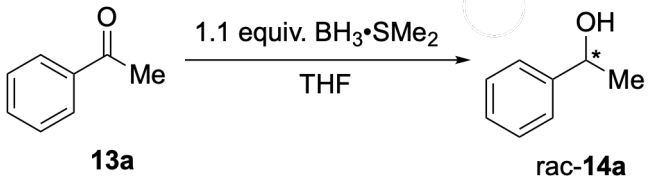
The parallel investigations utilizing **22a** yielded the same results (Table 6). The application of 10 mol% of **22a** resulted in a racemic mixture, whereas the literature reported an *ee* of 70% (Entry 2). Elevating the loading of **22a** to 1.0 equivalents provided 37% *ee* (Entry 4), thereby deviating from the reported 78%. To understand these discrepancies, we hypothesized that differences in ambient labaratory conditions, specifically varying levels of humidity between our facilities and the originating authors location, might exert a decisive influence on the catalytic outcome. To verify both environmental extremes we conducted two control experiments: By deliberately introducing trace amounts of water to the reaction mixture, we attempted to simulate a highly humid environment. However, instead of yielding **34b**, this addition induced hydrolysis of **32b**. Conversely, we executed the entire reduction protocol under strictly anhydrous conditions in a glovebox. This approach yielded the exact same selectivities as observed in our previous trials (Table 5 and 6). Since neither condition provided any measurable improvement, we ruled out moisture as the underlying source.

To rule out the reducing agent as a potential source of error and inspired by the application of catecholborane in the report of Kirton *et al.*,[104] we evaluated various alternative borane sources and batches. Similarly to previous results, these methodical variations provided no measurable improvement and the experimental outcomes remained entirely consistent with our previous unselective results. In a search for alternative mechanistic rationales, we considered the findings of Gschwind *et al*.[176] Their studies on the catalyzed hydrogenation of imines demonstrated that the *Z*-isomer is the reactive species, which is generated *via* photochemical irradiation at 365 nm. Although their catalytic system utilizes chiral Brønsted acids and differs in mechanism, we hypothesized that a similar isomeric dependency might be the underlying cause for our lack of selectivity, as imines predominantly exist as the thermodynamically more stable *E*-isomers in solution.[177] To investigate whether this specific phenomenon also applies to our reaction we attempted to induce an *E*- to *Z*-photoisomerization utilizing the corresponding 365 nm light source. We evaluated various experimental setups, including a 24 h preliminary irradiation of the sample prior to the reduction, alongside continuous irradiation during the actual catalytic event. The original study by Gschwind highlights that the thermal backreaction of the generated *Z*-imine is exceptionally fast at ambient conditions, requiring low-temperature NMR measurements at 180 K to prevent this relaxation and allow for characterization. Due to this rapid thermal back-isomerization at the operating temperatures of our catalytic setup, we were unable to analytically quantify the exact extent of the conversion. Nevertheless, even under continuous irradiation, these photochemical approaches did not yield any measurable improvement in selectivity. As variations of reaction parameters, substrate geometry, and environmental conditions failed to induce any stereoselectivity, we redirected our investigation from these external factors toward the intrinsic kinetic profile of the reduction.

3.3.4 The Background Reaction

To evaluate the extent of the uncatalyzed reaction we monitored the reduction progress of **13a** and **92** across various temperatures *via* GC-MS. Aliquots were systematically extracted from the reaction mixture every 3 min over 2 h to determine the exact time required for complete consumption of the starting material.

Table 7: Monitoring of the uncatalyzed background reduction of ketone **13a** at varying temperatures *via* GC-MS.



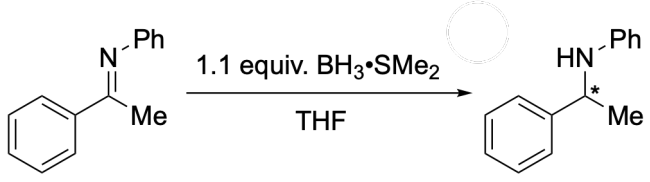
13a rac-**14a**

Entry [a]	Temperature [°C]	Time [min]
1	50	105
2	r.t.	- [b]
3	0	- [b]

(a) Reactions were conducted on a 0.5 mmol scale. (b) The exact time for full conversion could not be determined as the analysis was stopped after 2 h.

The analytical results revealed a kinetic difference between the two substrate classes. While elevated temperatures of 50 °C led to rapid conversion of **92** within nine minutes (Table 8), **13a** exhibited substantially lower reactivity reaching full conversion only after 105 min (Table 7). At lower temperatures, full conversion for **13a** could not be determined, as the reactions remained incomplete within the monitored timeframe (Table 8).

Table 8: Monitoring of the uncatalyzed background reduction of imine **94** at varying temperatures *via* GC-MS.



92 rac-**93**

Entry [a]	Temperature [°C]	Time [min]
1	50	9
2	r.t.	12
3	0	18
4	−78	30

(a) Reactions were conducted on a 0.5 mmol scale.

Since the primary objective of this experiment was the direct kinetic comparison with **92**, the monitoring window was tailored to 2 h and prolonged tracking of **13a** was not evaluated further. Substrate **92** achieved full conversion very rapidly at all tested temperatures (Table 7). While

literature demonstrates that an active background reduction does not universally preclude high stereochemical induction,[178] our system evidently lacks this necessary kinetic differentiation. Ultimately, this rapid, uncatalyzed background pathway offers a highly plausible explanation for the observed lack of selectivity.

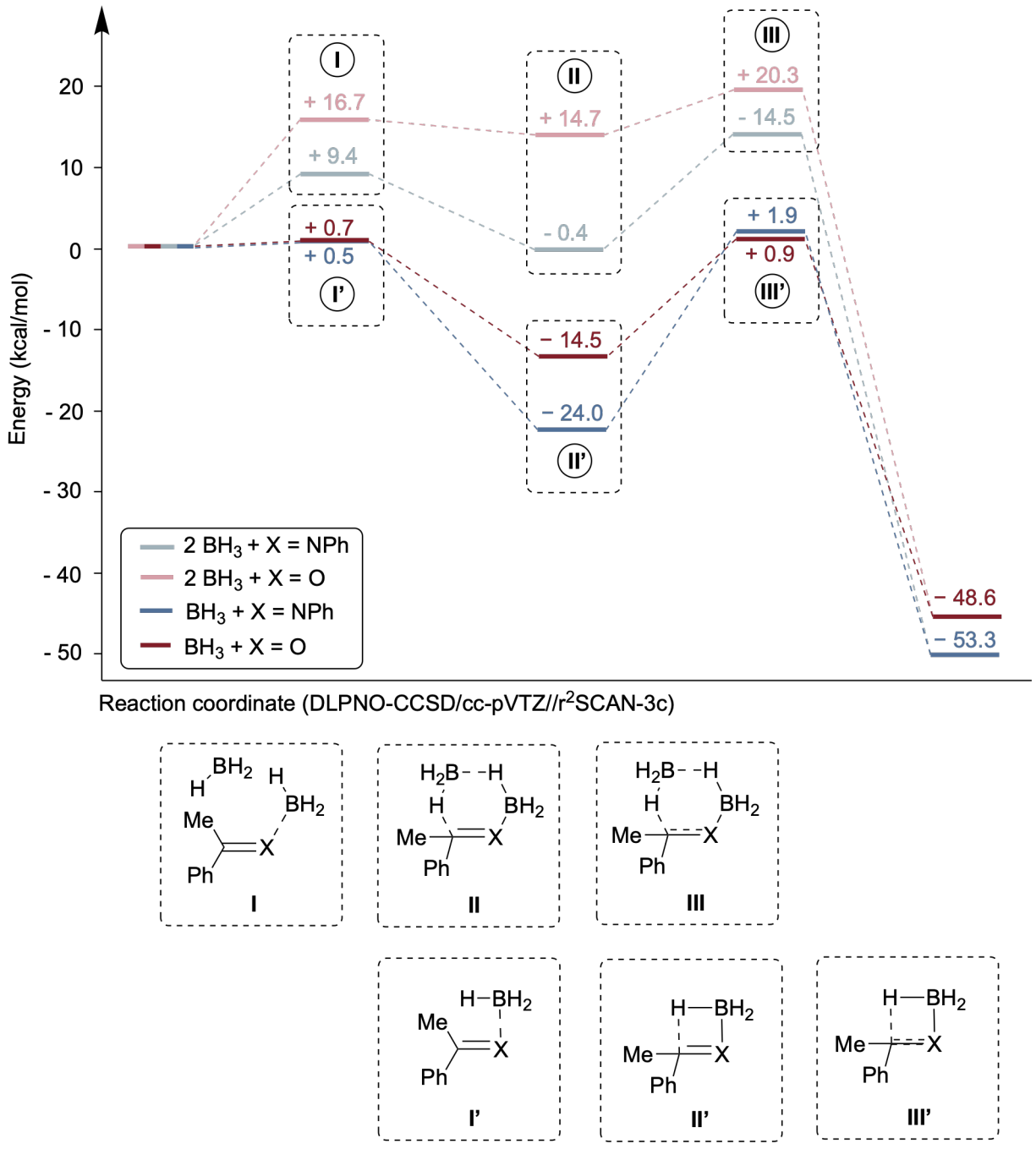


Figure 69: Computed thermodynamic energy profiles for the background reduction. The energetic pathway for the ketone is depicted in red whereas the corresponding imine reduction is highlighted in blue. Both reaction coordinates demonstrate a highly competitive unselective process proceeding via a single BH_3 molecule.

To support these experimental findings, computational studies were carried out by Caio Porto to investigate the thermodynamic energy profiles of both the catalyzed (Figure 70) and the uncatalyzed pathways (Figure 69). The computations revealed a critical mechanistic detail by demonstrating that the uncatalyzed background reaction proceeds through a transition state involving only a single BH_3 molecule, which contrasts with previously proposed mechanisms.[179] For the ketone reduction, the computed effective activation barrier for the catalyzed pathway is 0.1 kcal mol^{-1}(Figure 70, **I**)). This value is comparable to the effective barrier height of 0.9 kcal mol^{-1} (Figure 69, **III'**) computed for the uncatalyzed background reaction. Because these energetic requirements are within a similar range, the catalyzed pathway remains competitive which allows for the achievement of high *ee* depending on the specific catalyst and substrate.

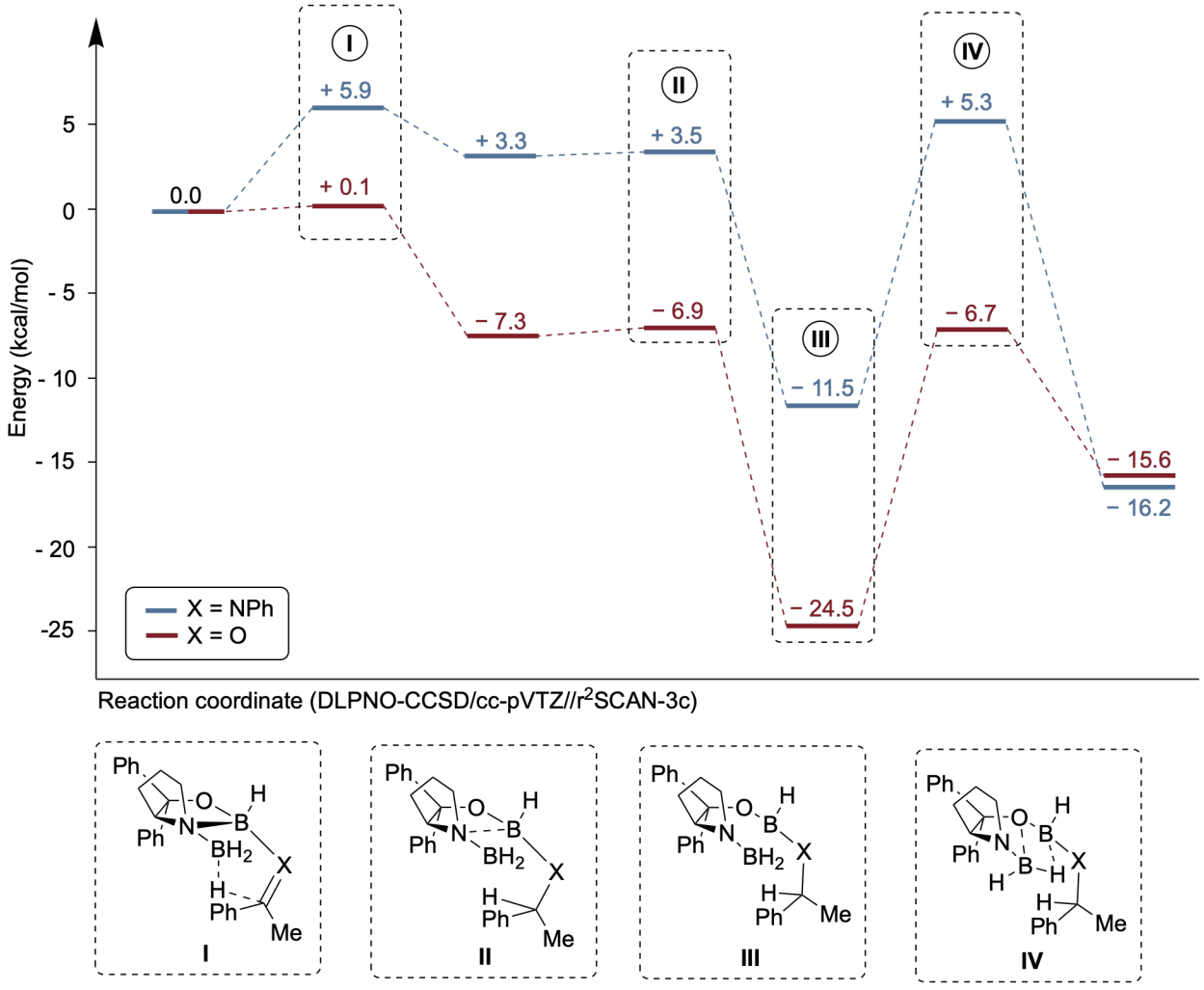


Figure 70: Computed thermodynamic energy profiles for the CBS reduction. The competitive energy profile for the ketone reduction is shown in red while imine pathway is represented in blue illustrating the kinetic disadvantage of the catalyzed imine reduction.

However, the thermodynamic profile for the imine reduction presents a different situation. The computed barrier for the catalyzed imine reduction is 5.9 kcal mol^{-1} (Figure 70, **I**). While this barrier might seem accessible, it has to compete directly with the uncatalyzed background reaction. The computations established that this background reaction features a significantly lower activation barrier of 1.9 kcal mol^{-1} (Figure 69, **III'**) which is similar in magnitude to the ketone background process. Since the catalyzed pathway requires substantially more energy than the unselective background reaction, it becomes highly uncompetitive and the imine is predominantly reduced by the direct uncatalyzed pathway. Therfore, the low selectivity observed in previous experiments and the lack if success in increasing them can be attributed to the fast unselective background reaction that competes with the catalzyed route.

Taking both the experimental and computational data into account, the conclusion is that, under the tested and reported conditions, the direct reduction of the imine is too competitive to be supressed without modifiying and specializing the substrate, which defeats the purpose of showing the broad applicability of the CBS catalyst to imines. For this reason, we discontinued the optimztation of this reaction and did not further pursue this topic.

Part IV

The Enantioselective Dakin-West Reaction

The Dakin-West Reaction Data Collection and Empirical Evaluation

From the very outset of this work, our conceptual design aimed to investigate two different catalytic systems and develop independent predictive models for both. While the previous chapters detailed the CBS reduction, the enantioselective Dakin-West reaction was selected as the second major target to achieve a generalizable model applicable across various substrate classes. Pioneered by our research group, the asymmetric variant of this reaction provides direct access to chiral α-acetamido ketones **40** utilizing rationally designed peptide catalysts. However, as our earlier investigations demonstrated that ML models rely heavily on highly precise and structurally diverse data, especially when working with small datasets, we decided to adapt our approach.

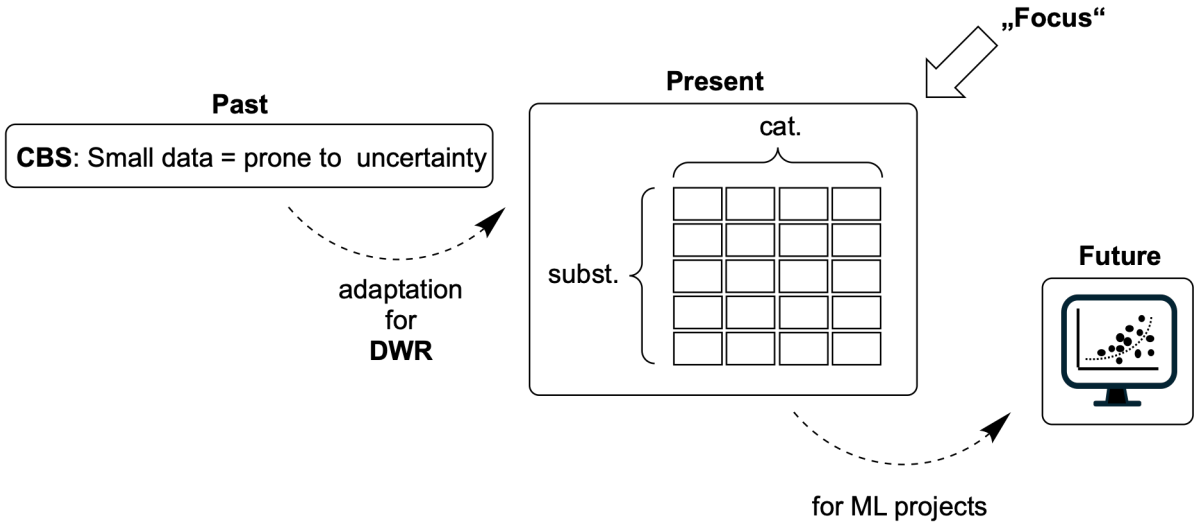


Figure 71: Conceptual shift based on past learnings: Establishing a systematic empirical data collection in the present to ensure robust ML applications in the future.

Rather than training an algorithm on sparse data and risking inaccurate predictions, we focused entirely on generating an experimental dataset for future model applicability. Consequently, this chapter presents the establishment of a defined data collection for this reaction and focuses on the catalytic parameters as well as the analytical evaluation, which will be examined in detail in the upcoming chapters.

3.3.5 Substrate Scope and Synthesis of Reference Racemate

As a preliminary substrate scope, four *N*-acetyl amino acid derivatives (rac-**41a-d**) were chosen for investigation. To enable the determination of the *ee* the corresponding racemic products

(rac-**40a-d**) were synthesized using the conditions shown in Figure 72. Subsequently, chiral GC- and HPLC-methods were developed for the separation of the enantiomers.

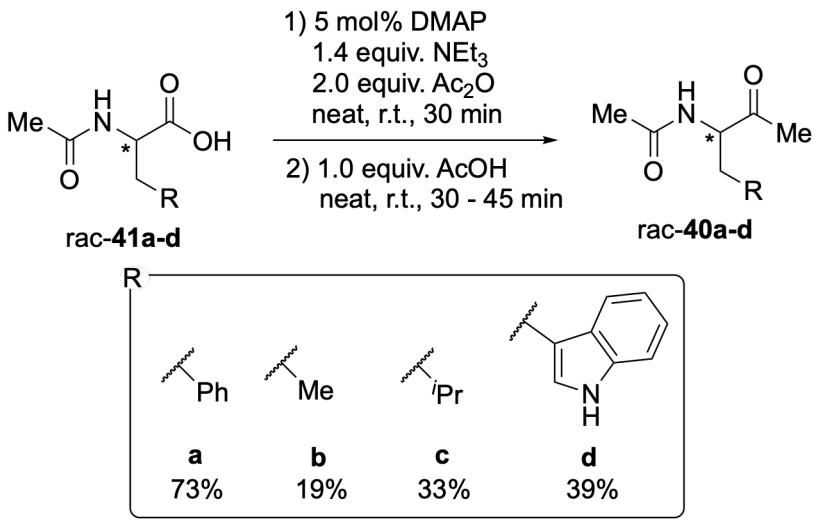


Figure 72: Synthesizing racemic mixtures rac-**40a-d**.

While the synthesis of rac-**40a** proceeded without any complications and afforded the desired product in 73% yield, the other three derivatives resulted in lower yields. For instance, rac-**40b** was obtained in 19% yield, which was caused by the volatile nature of the product that led to evaporation during solvent removal. For the remaining two substrates (rac-**40c-d**), the exact reasons for the diminished yields remain unclear as of yet.

With the racemic references compounds in hand, the focus shifted toward the optimization of the reaction parameters and the catalyst screening. The phenylalanine derivative (**41a**) was chosen as the model substrate for experimental optimization. This system was utilized to refine the reaction conditions and systematically evaluate the catalytic parameters, as detailed in the following section.

3.3.6 Parameter Optimization and Experimental Setup

To initiate this optimization phase, the chiral tripeptide **50** was selected as the catalyst. While this pmh-based catalyst was originally developed in our group for the kinetic resolution of diols,[180] it was subsequently adapted for the enantioselective Dakin-West reaction.[113] The mechanistic complexity of the asymmetric Dakin-West reaction requires a carefully balanced set of reaction conditions to efficiently separate the initial acetylation from the subsequent decarboxylation step.

Since this balance regarding solvents and stoichiometries was already established,[113] a comprehensive rescreening of these variables was not conducted. Instead, the focus was first directed toward refining the practical parameters using rac-**41a** together with **50** (Figure 73). The previously reported 37 % *ee* for this combination provided a reliable foundation for the subsequent optimization.

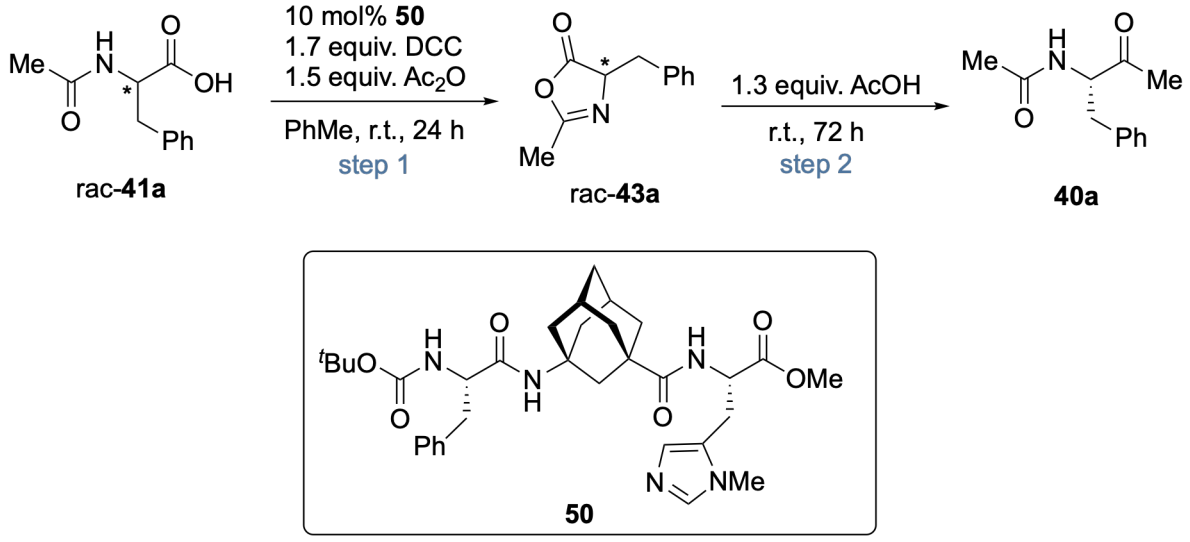


Figure 73: The enantioselective Dakin-West reaction using peptide catalyst **50**.

To evaluate the exact reaction time the progress was monitored *via* GC-MS in the two distinct stages. The first stage was tracked prior to the addition of acetic acid to ensure the complete formation of the intermediate azlactone rac-**43a**. The second stage then monitored the conversion to the final product **40a**. This confirmed an optimal reaction time of 24 h for the initial step and a minimum of 48 h following the acid addition. Notably, prolonged reaction times proved entirely unproblematic as no further side reactions or product degradation were observed. Consequently, an extended stirring period of 72 h was selected as the standard protocol to guarantee complete conversion to **40a**.

Following the optimization of reaction time, we evaluated the conventional activating agents DIC and DCC. The use of DIC generates a soluble urea byproduct, which complicates product isolation and interferes with analytical measurements. The application of DCC affords an insoluble urea derivative, enabling a straightforward purification *via* a short filter column, although the resulting continuous precipitation and carbon dioxide release form a dense suspension that disrupts stirring and causes inconsistent *ee* values. We resolved this physical limitation by performing the reactions

in small GC vials, where the compact dimensions ensured excellent mixing. This practical adjustment allowed us to maintain the purification benefits of the reagent, establishing DCC as the standard coupling reagent for all further investigations.

Furthermore, precise temperature control proved to be an absolute necessity. Initially, the GC vials were placed in a metal block for stability. Prolonged continuous stirring induced unintended heat transfer from the stirrer to the metal block, thus warming the reaction mixture over time. Analysis of these samples revealed that this elevated temperature induced thermal degradation and generated numerous unidentified byproducts which obscured the HPLC chromatograms, making accurate analysis of the *ee* difficult. To resolve this issue, the metal block was replaced with a non-heat-conducting holder ensuring a controlled thermal environment and securing clean analytical data.

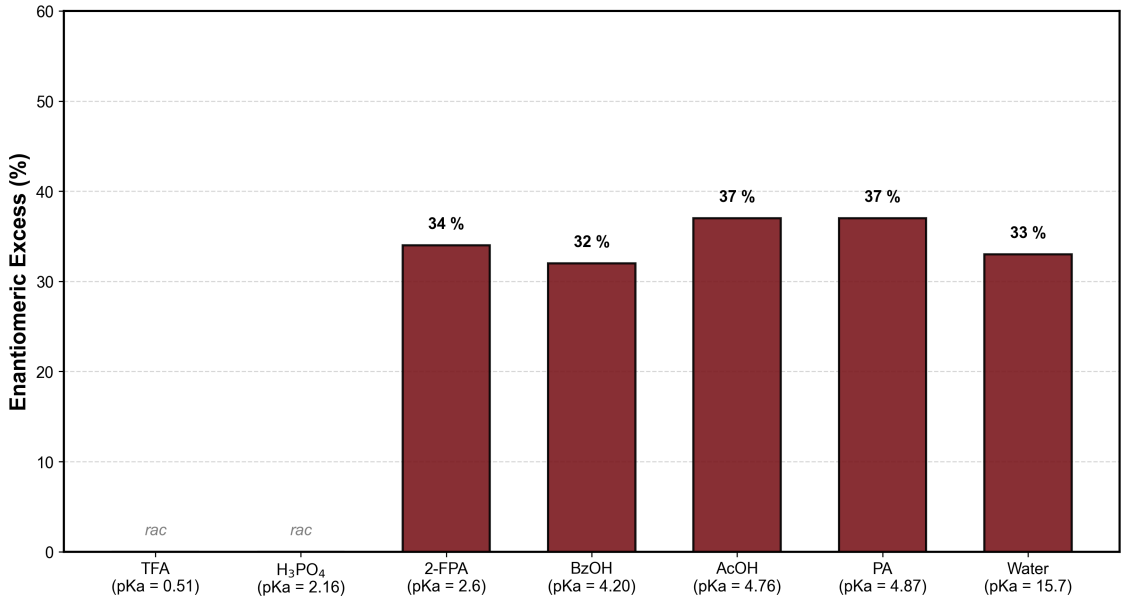


Figure 74: Influence of different acids on the stereoselective decarboxylation/reprotonation steps of the Dakin-West reaction.

Having established the optimized reaction parameters, the role of acidic additives in the second stage was investigated as summarized in Figure 74. Since the decarboxylation is an intrinsic step of the cascade sequence, the addition of the acid primarily governs the subsequent quenching and the stereoselective protonation of the reactive intermediate. The experimental data revealed a defined tolerance threshold regarding acid strength. Strong acids, such as trifluoroacetic acid (TFA) and phosphoric acid (H_3PO_4) suppressed the desired reaction and led to degradation. Conversely, moderately acidic additives, such as benzoic acid (BzOH), acetic acid (AcOH), and

propionic acid (PA) provided consistent stereochemical outcomes ranging from 32% to 37% *ee*. The application of water afforded a comparable 33% *ee*. Both propionic acid and acetic acid emerged as the most effective proton sources. Since acetic acid is already an integral component of the primary reaction mixture, it was selected as the standard additive. Furthermore, the use of acetic acid eliminates the risk of cross reactivity and the formation of undesired mixed anhydrides that would arise from introducing additional acids.

3.3.7 The Catalyst Library and Selection Method

The peptide catalyst library evaluated in this study was synthesized and provided by Jan Metzler. Instead of depicting every single molecule, which would exceed the scope of this chapter, the following section outlines the design concepts and structural modifications exemplified by catalyst **50** (Figure 75). These structural motifs were varied and combined in a modular fashion to explore a highly diverse chemical space. A complete library detailing all individual structures is provided in the experimental section of this work.

A defining characteristic shared across the majority of these catalysts is the incorporation of a rigid adamantyl backbone. This sterically demanding motif is utilized to enforce a dynamic binding pocket [181] and preorganize the flexible peptide chain originating from this conserved foundation targeted modifications were made to probe the structural requirements of the catalytic environment.

These variations included the alteration of the peptide chain length as shown by **106** to investigate the spatial boundaries of the chiral pocket. Furthermore, the optimal topological arrangement was evaluated by shifting the position of specific amino acids within the sequence as demonstrated by **103**. To determine the importance of the exact spatial orientation, stereochemical alterations were applied by substituting distinct L-amino acids with their corresponding D-enantiomers (**105**). Additionally, both the steric environment and the electronic properties of the catalytic unit itself were modified by utilizing alternative protecting groups on the active histidine moiety (**104**). Finally, the overall structural influence of the terminal protecting group was assessed by replacing the standard Boc moiety (**107**). With this library established, the respective peptide catalysts were subjected to further screening.

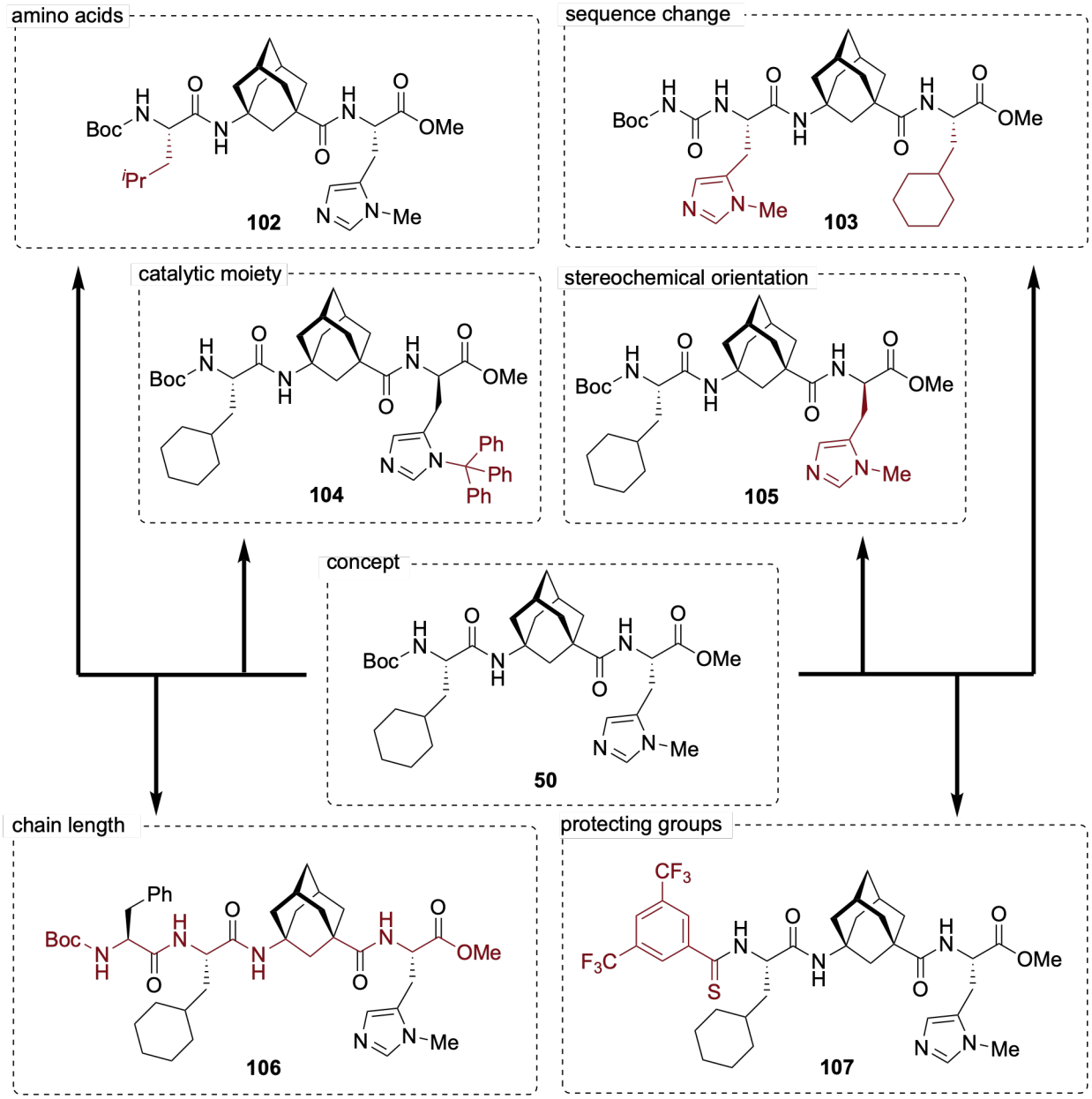


Figure 75: Overview of the structural variations within the peptide catalyst library. The respective modifications are highlighted in red.

3.3.8 Evaluation of Catalytic Performance and Structure Relationships

For the screening, the previously optimized reaction conditions utilizing substrate rac-**41a** were applied to the peptide catalysts (Figure 76). To maintain clarity, this discussion focuses on the essentail aspects of modifications and the catalytic results, while all remaining data points are provided in the appendix.

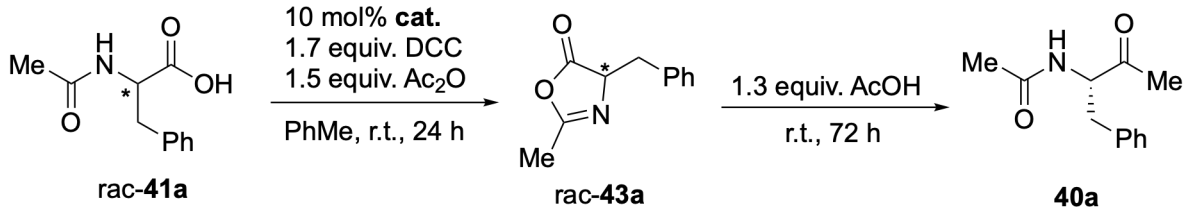


Figure 76: The asymmetric Dakin-West reaction converting rac-**41a** to **40a**.

As illustrated in Figure 77, the role of the catalytically active π-methyl histidine moiety was evaluated through both stereochemical (**105**) and steric modifications (**104**). Inverting the stereogenic center to the corresponding D-enantiomer (**105**) resulted in a drop of 19% *ee* compared to **50**. This indicates that the D-configuration of the π-methyl histidine is important in this specific sequence. The inversion presumably creates a stereochemical mismatch within the catalytic framework, disrupting the optimal spatial alignment of the substrate during the stereodetermining transition state. Furthermore, the steric demand of the imidazole moiety itself proved equally decisive and introducing a trityl-group (**104**) entirely suppressed stereocontrol, yielding a racemic product.

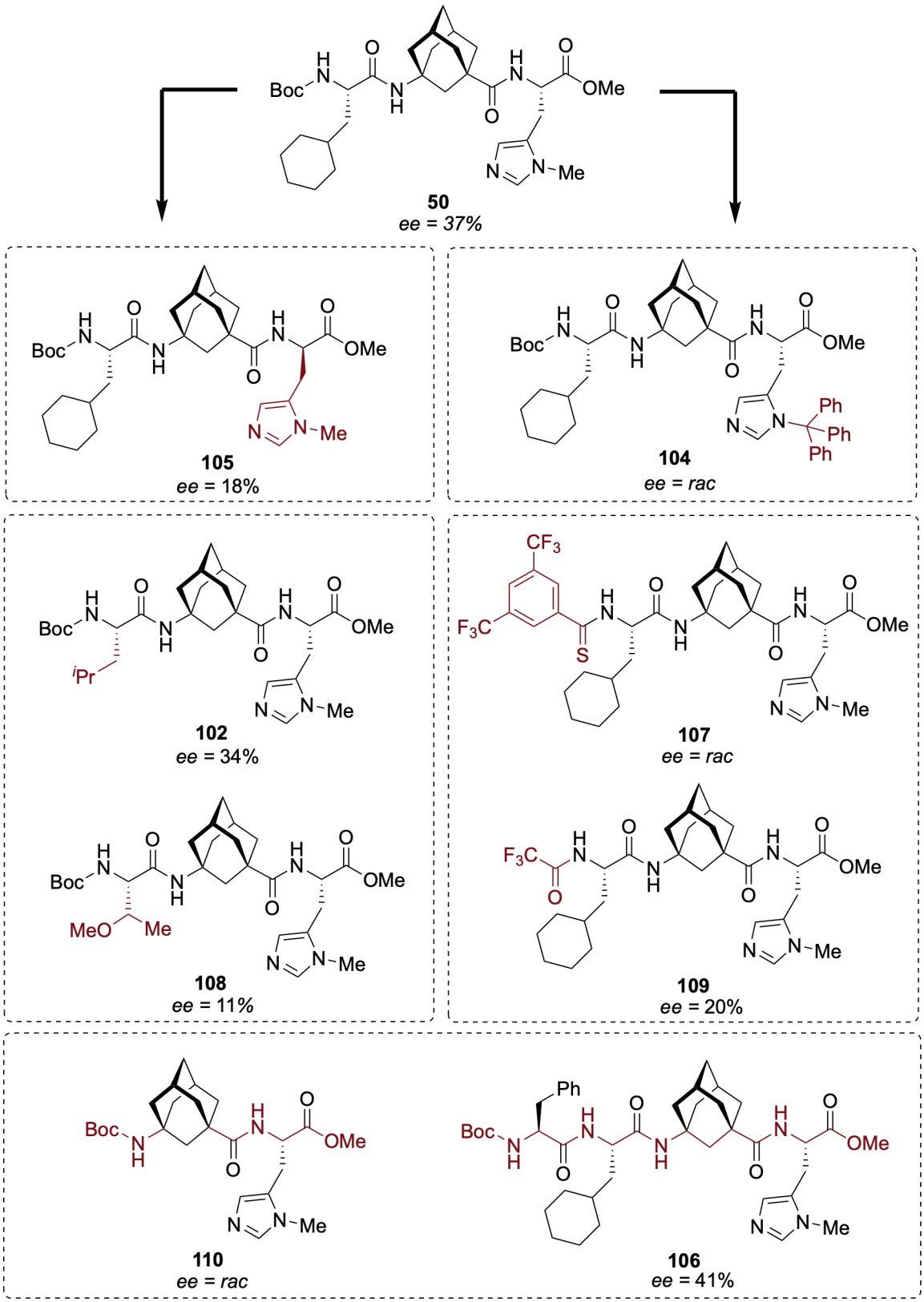


Figure 77: Overview of the catalytic performance of the evaluated peptide library in the asymmetric Dakin-West reaction utilizing substrate rac-**41a**. The respective structural modifications are highlighted in red.

The *N*-terminal protecting group also played an essential role. Replacing the Boc-group with a thiourea moiety (**107**) yielded a racemic product mixture. Substituting the *tert*-butyl-carbamate (**50**) with a less bulky trifluoroacetyl group (**109**) decreased the *ee* to 20%. These results indicate that the stereoselectivity strongly depends on both the steric and electronic properties of the *N*-terminus.

Variations of the adjacent amino acid side chains revealed a highly sensitive structural network. Replacing the cyclohexyl group with an aliphatic leucine side chain (**102**) maintained an *ee* comparable to **50**, whereas incorporating a modified threonine (**108**) reduced the selectivity to 11%. Consistent with previous findings within the group,[113] this highlights the critical role of LD interactions. The polarizable cyclohexyl moiety stabilizes the stereodetermining transition state *via* LD forces. Utilizing smaller or less polarizable residues, such as an *iso*-propyl-group eliminates this stabilization thereby explaining the observed drop in selectivity.

The overall length of the peptide sequence dictated the structural integrity of the catalyst. Truncating the scaffold to the dipeptide **110** led to a complete loss of *ee*, as the absence of the amino acid prevents the formation of secondary structure. In contrast, extending the sequence to a tetrapeptide (**106**) *via* the addition of a phenylalanine residue improved the selectivity to 41% *ee*. This enhancement can likely be attributed to an increased steric shielding or a potential reinforcement of the catalyst's secondary structure, which provides a more rigid and defined environment for the stereoselective step.

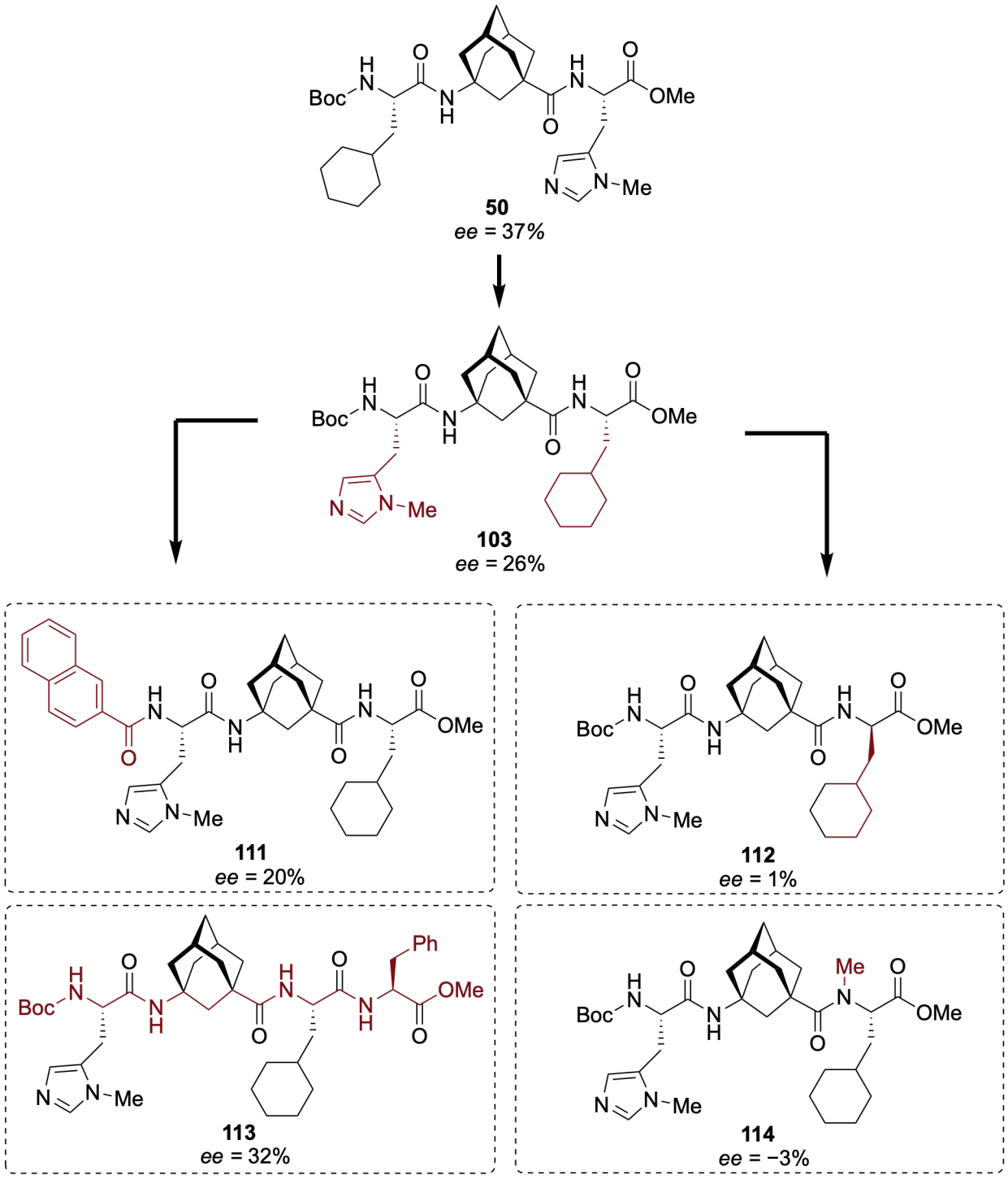


Figure 78: Overview of the catalytic performance of the evaluated peptide library for rac-**41a** in the asymmetric Dakin-West reaction derived from **103**. The respective structural modifications are highlighted in red.

An analysis of the topological arrangement (Figure 78) further aligned with this established previous results.[113] Interchanging the positions of the catalytically active residue and the cyclohexyl moiety (**103**) diminished the *ee* to 26%. The sensitivity of this rearranged framework

was demonstrated by the inversion of the cyclohexyl stereocenter (**112**), which yielded a nearly racemic mixture. Exploring the *N*-terminal protecting group also revealed dependencies. Replacing the Boc-group with a sterically demanding naphthyl-group (**111**) likewise decreased the *ee*. Additionally, *N*-methylation at the nitrogen of ^{A}Gly (**114**) suppressed stereocontrol, indicating that this center is essential for establishing an intramolecular hydrogen bond. Finally extending this specific peptide chain with a phenylalanine residue (**113**) again elevated the *ee* to 32%, which suggests that the expanded scaffold provides additional interaction sites that enable a different binding mode for the enol intermediate.

Building upon **113** (Figure 79), minor structural variations elucidated further electronic and steric requirements. Introducing electron donating groups at the terminal phenylalanine (**117**) led to 33% *ee*, whereas electron withdrawing groups (**115**) decreased the *ee* to 26%, suggesting that increased electron density on the aromatic system strengthens beneficial noncovalent interactions. Modifying the C-terminus to a benzyl ester (**116**) did not alter the stereochemical outcome, indicating that this peripheral position points away from the active site. Reevaluating the cyclohexyl moiety confirmed its indispensable structural role: Replacing this unit with smaller amino acids (**118**) caused a drop in selectivity, while an adamantyl-moiety (**120**) maintained a comparable *ee* to that of **113**. Although the adamantane framework possesses higher polarizability and greater potential for LD interactions, the chiral pocket appears already optimal with a cyclohexyl residue. Additionally, elongating the peptide sequence at the C-terminus (**119**) by attaching an additional phenylalanine residue resulted in an inversion of the *ee*. This shift suggests that extending the scaffold beyond the tetrapeptide stage induces a complete conformational reorganization. Finally, the rigid adamantyl backbone dictates the overall structural integrity of the **113** framework. Replacing adamantyl with a flexible linear alkyl chain (**121**) led to a complete loss of stereocontrol. Conversely, substituting the adamantyl backbone with a cyclohexyl moiety (**122**) restored the *ee*. Catalytic selectivity thus relies on a synergistic interplay between the absolute configuration of the individual stereogenic centers and the general rigidity of the central peptide backbone.

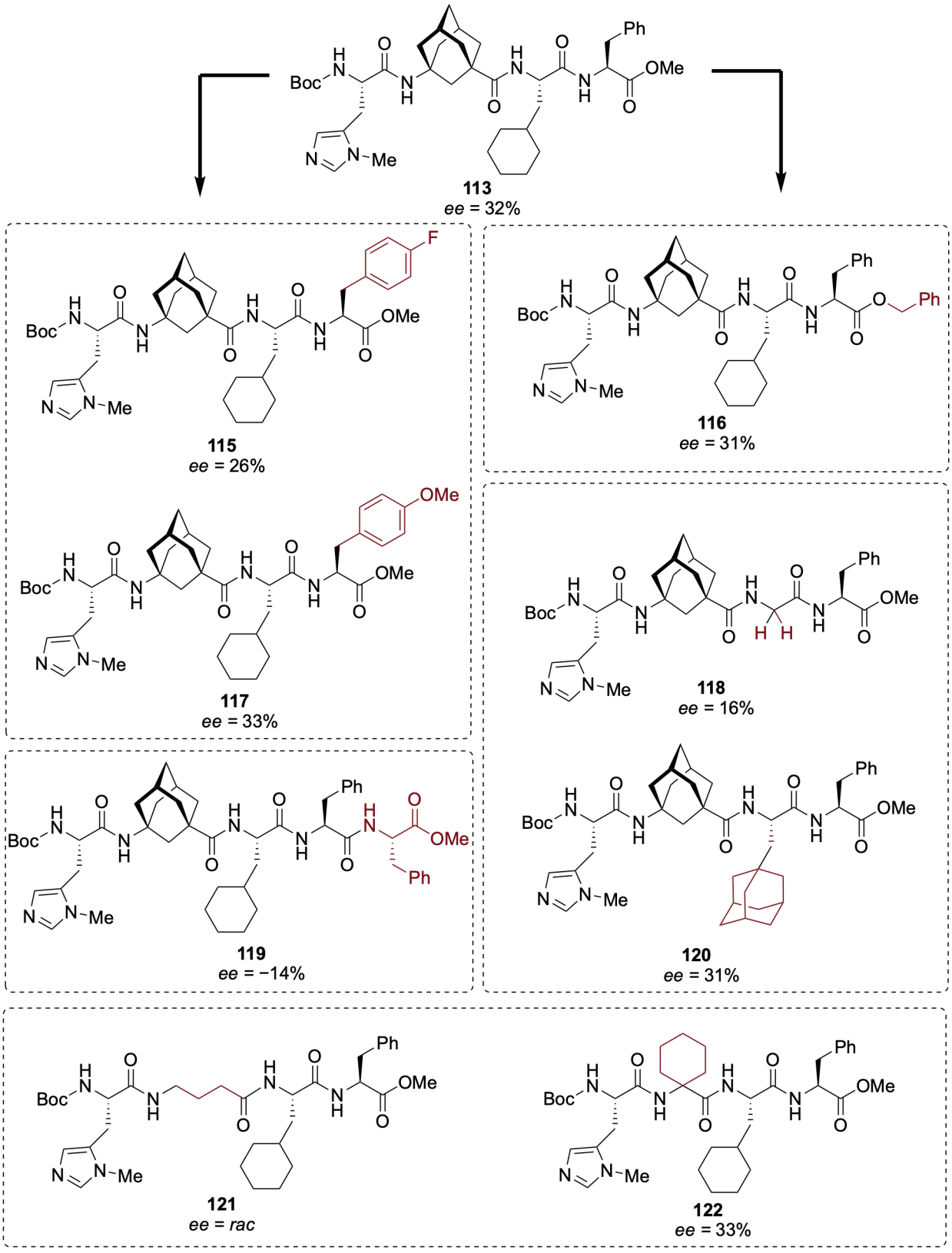


Figure 79: Overview of the catalytic performance of the evaluated peptide library for rac-**41a** in the asymmetric Dakin West reaction derived from **113**. The respective structural modifications are highlighted in red.

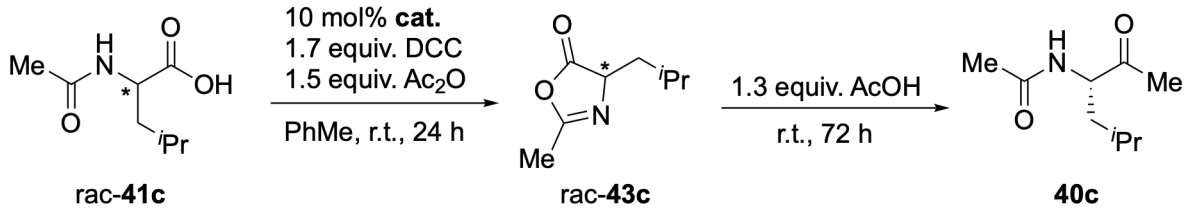


Figure 80: Catalytic performance of the peptide library in the asymmetric Dakin-West reaction converting rac-**41c** to **40c**.

To evaluate substrate specificity and generate a diverse dataset for subsequent ML applications, the screening was extended to substrate rac-**41c** (Figure 80). A comparison of the experimental data revealed a general trend across the majority of the evaluated catalyst library (Figure 81). The application of **41c** resulted in an increase in *ee* compared to rac-**41a**, corroborating previous findings.[113] For instance, **50** increased the *ee* from 37% for rac-**41a** to 57% for rac-**41c**, and **113** showed a comparable enhancement. This pronounced trend is likely driven by the varying capacity of the respective amino acid side chains to engage in stabilizing non-covalent interactions. Specifically, the aliphatic *iso*-butyl group of rac-**41c** is presumed to establish highly effective LD interactions with the peptide catalyst. In contrast, the benzyl group of rac-**41a** appears less capable of this specific dispersion forces within the chiral pocket.

However, distinct outliers deviated from this linear shift. Most prominently, **125** exhibited a complete collapse in selectivity with the aromatic rac-**41a**, yielding a racemic mixture. Yet, when applied to rac-**41c**, an *ee* of 35% was observed (Figure 81). This deviation proves that **125** has not lost its catalytic activity but is highly substrate-specific.

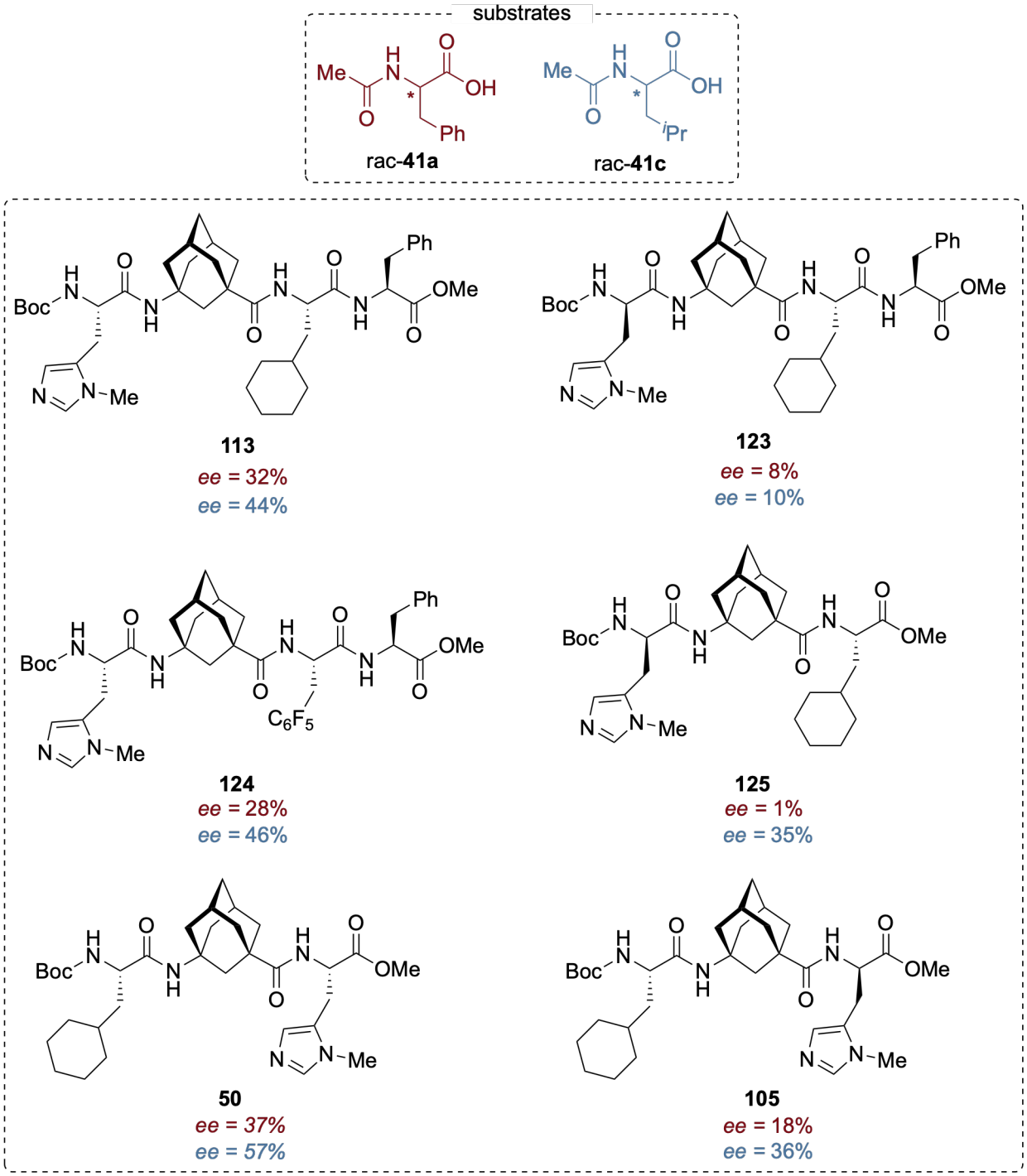


Figure 81: Comparison of the *ee* achieved in the asymmetric Dakin-West reaction of substrates rac-**41a** and rac-**41c**. The data corresponding to rac-**41a** are highlighted in red, whereas those for rac-**41c** are depicted in blue.

Regarding the broader objective of this thesis, this generated data collection serves as the foundational dataset for the subsequent development of predictive ML models. In contrast to the previously evaluated CBS reduction, where data generation was severely restricted by synthetic

bottlenecks, the asymmetric Dakin-West reaction offers a decisive advantage through the sheer volume of accessible peptide catalysts. This dense information matrix, enriched by distinct outliers such as **125**, provides the necessary boundary conditions to prevent statistical models from oversimplifying complex three-dimensional stereoelectronic interactions. To fully exploit this potential and establish a robust framework characterized by maximum chemical diversity, extending this screening process to the remaining substrates remains a critical next step. Whether this systematically expanded library ultimately suffices to construct a broadly applicable predictive model remains to be evaluated in the ensuing investigations.

4 Summary

The research presented in this thesis evaluates the development of an empirical modeling approach for organocatalytic reactions and outlines the process required to establish predictive reliability when working with limited experimental datasets. The following summary presents the key findings across the four main chapters, following the evolution from statistical approaches to the empirical validation required for ML modeling.

4.1 Graph Based Modeling in the CBS Reduction of Butanone

The enantioselective CBS reduction of butanone (**51**) served as the initial system to establish a workflow for small data driven modeling. By synthesizing a defined precursor library and training a graph-based ML model, this phase demonstrated the technical implementation of the data driven workflow. Within this initial dataset, the algorithm reproduced the existing experimental values and predicted precursor **22i** to be a highly selective catalyst for the targeted reduction. To verify this computational prediction, **22i** was synthesized and evaluated experimentally, thereby achieving an average *ee* of 80%, which matched the algorithmic prediction and outperformed the previously reported catalyst precursor **22f**.[87] Due to the prevailing synthetic limitations, further expansion of the precursor library was restricted. Consequently, this represented the optimal achievable outcome and served as the basis for a peer reviewed publication. This first phase therefore provided a computational setup that seemingly depicted the known chemical space without noticeable discrepancies.

4.2 Novel Synthetic Strategy and Re-Evaluation of the Predictive Framework

To rigorously probe the predictive boundaries of the initial model, a novel synthetic pathway for sterically demanding precursors was approached. Through this, the synthesis of **69** was accomplished, which was essential for the synthesis of **22k** *via* a new synthetic route. This precursor was then evaluated together with **22h** against **51**. These experiments revealed significant inconsistencies that contradicted initial ML predictions and triggered a systematic investigation into the analytical methods. This process identified an analytical bias caused by the workup protocol which revealed that the initial algorithmic predictions were based on inaccurate empirical inputs. To restore analytical integrity, a refined method was established. Applying this to **22h**, **22k**, and **22i** provided highly precise *ee* values that accurately reflect the true chemical reactivity. While

these values were lower than initially predicted, this outcome provided a crucial insight for data driven catalysis and proves that the predictive power of algorithms in the small data regime depends entirely on the quality of the underlying empirical data. These findings highlight that establishing robust analytical workflows is the key for building reliable and generalizable predictive models.

4.3 Expansion of the CBS Reduction to Ketimines and Kinetic Evaluation

The expansion of the CBS reduction toward ketimines aimed to evaluate the structural adaptability of the predictive modeling framework to nitrogen containing substrate classes. Experimental investigations revealed distinctly divergent reactivity profiles, where cyclic imines proved incompatible with standard reduction conditions due to a strong Lewis acid/base complex formation. The asymmetric reduction of non-cyclic analogues consistently afforded racemic products, which directly contradicted the high *ee* claimed by previous research groups. Kinetic and computational analyses established that a highly competitive unselective background reduction completely outpaces the catalyzed pathway, bypassing any stereochemical induction and rendering the enantioselective CBS reduction of simple ketimines infeasible. This inherent lack of stereocontrol eliminated this specific substrate class from current data driven modeling efforts and led to the conclusion that alternative catalytic strategies, which effectively suppress the uncatalyzed background reduction, are required for future predictive frameworks.

4.4 Data Generation for the Asymmetric Dakin-West Reaction

Following the constraints identified in the CBS systems, a strategic reorientation was implemented for the asymmetric Dakin-West reaction, prioritizing the rigorous generation of experimental data over premature computational modeling. Through the screening of a structurally diverse peptide catalyst library, a comprehensive data matrix was established that maps complex structure-activity relationships. The experimental evaluation confirmed that enantioselectivity relies on a synergistic interplay between the precise spatial arrangement of the stereogenic centers, the overall conformational rigidity of the catalyst backbone, and stabilizing non-covalent interactions. While comparative substrate screenings corroborated previously established general reactivity trends,[113] the evaluation also highlighted distinct structural outliers, such as **125**. Such catalysts demonstrate a profound substrate specificity dictated by stereochemical mismatches and altered pocket geometries. By capturing both these general trends and subtle structural deviations, this dataset

establishes a robust and comprehensive experimental foundation for future theoretical and computational investigations.

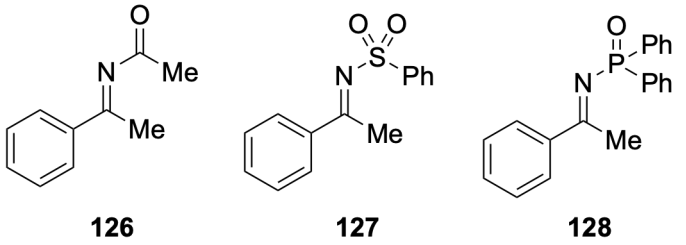
5 Outlook

The findings reported in this thesis open up several scientific avenues for subsequent investigations to expand both the chemical and the computational frameworks. To establish a clear path for the next generation of researchers, the requirements and reaction strategies are outlined along the two main reaction systems investigated.

5.1 Corey-Bakshi-Shibata Reduction

Regarding the enantioselective CBS reduction of ketones, the established ML architecture remains a highly valuable predictive framework. The existing model should be retrained with the new analytically verified dataset, ensuring that the systemic variance introduced is completely eliminated. Once refined, this updated model can be utilized to again perform *in silico* screenings for novel catalyst structures. The most promising candidates, especially those featuring extreme steric hindrance, can be synthesized *via* the novel synthetic route established in the second part of this work. Through the experimental validation of these novel catalyst, we will be able to establish whether the initial mispredictions were exclusively a consequence of the inaccurate dataset or whether algorithmic limitations persist when operating within a small data regime.

The limitations observed in the reduction of ketimines require a targeted optimization of the reaction conditions. The unselective background reaction, driven by the high basicity of the imine nitrogen during the coordination of the free borane,[18,182] currently prevents the establishment of a reliable catalytic reaction. To overcome this obstacle, two pathways are proposed as future solutions. The first proposal (Figure 82) focuses on substrate modification through the introduction of strong electron-withdrawing groups, such as tosyl- (**127**), diphenylphosphinoyl- (**128**), or acyl (**126**) moieties at the nitrogen atom to decrease its basicity.



126 **127** **128**

Figure 82: Proposed structural modifications designed to suppress the unselective background reaction and facilitate the catalyzed CBS reduction of imines.

While this approach offers a viable chemical route to suppress the direct reduction, it shifts the analytical focus of this work. The core objective of the ML workflow is to map and optimize the peptide catalyst library itself. If the algorithm is trained primarily on functionalized derivatives, it will pivot toward substrate optimization. The resulting model would excel at identifying optimal substrate features rather than isolating the subtle structural effects of the catalysts.

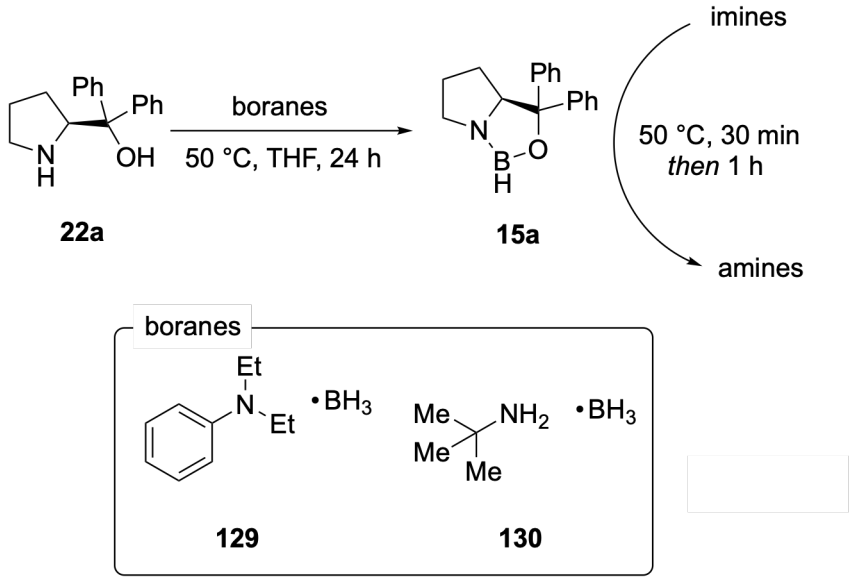


Figure 83: Structures of commercially available amine borane adducts proposed for future experimental validation to determine whether their controlled reactivity can effectively suppress the uncatalyzed background reduction.

Alternatively, a second proposal (Figure 83) for future work involves the optimization of the reducing agent by implementing and testing various alternative borane sources to evaluate their potential on this catalytic reduction. The principle of suppressing uncatalyzed pathways *via* thermodynamically stable "transfer boranes" has been established for ketones using reagents like *N*,*N*-diethylaniline-borane (DEANB) (**129**).[183] It would therfore be interesting to implement DEANB alongside thermodynamically more stable amine-borane adducts such as *tert*-butylamine-borane (**130**).[184] A more controlled and slow release of the reactive borane species for imines could result in higher selectivites. Successfully exploring these specific reagents to establish a reliable basis would provide the experimental data required to either adapt the currently established predictive framework or develop a ML model dedicated to the unique reactivity of these nitrogen containing substrates.

5.2 Asymmetric Dakin-West Reaction

For the asymmetric Dakin-West reaction, the currently generated peptide library provides an essential experimental foundation. To increase the structural diversity and establish a more comprehensive and robust dataset, future work should initially focus on gradually expanding this dataset with a targeted selection of additional substrates **41** and peptide variations under the established optimized conditions.

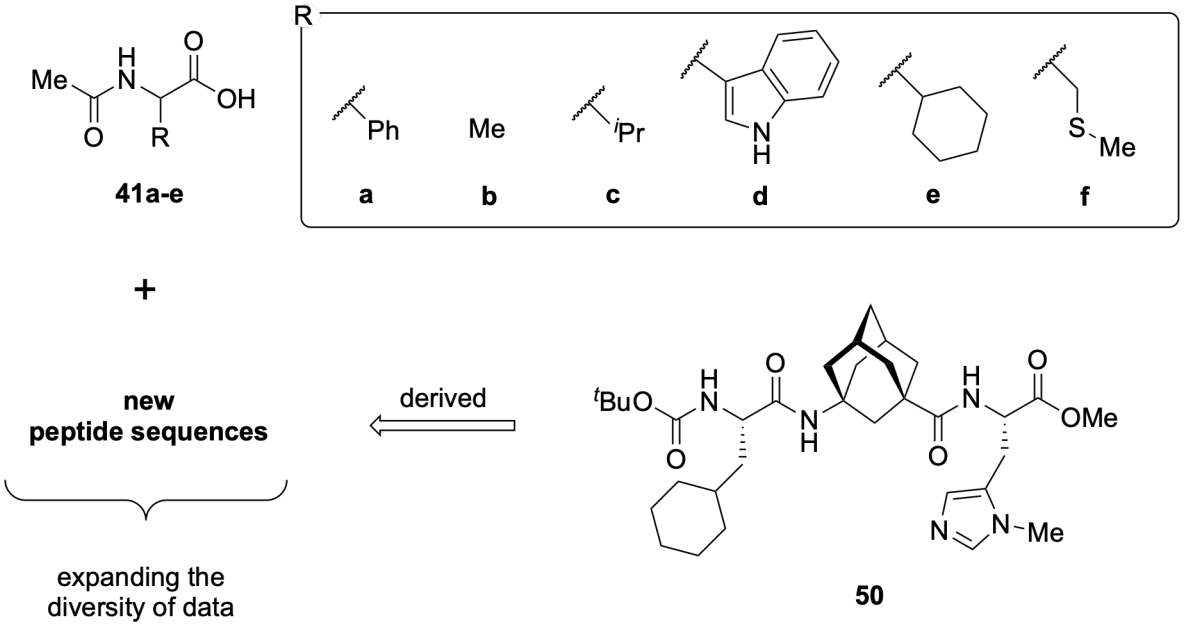


Figure 84: Future steps for the Dakin-West reaction.

Once this expanded library is established, the subsequent phase would involve applying MLalgorithms to extract predictive patterns. In this context, two methods could potentially offer promising predictive capabilities. First, the integration of physics-informed ML strategies might be explored. This involves translating the highly flexible peptide catalysts into computationally derived three-dimensional conformational descriptors, an approach successfully demonstrated for predicting enantioselectivity in complex catalytic systems.[15] Using these descriptors, algorithms such as Support Vector Machines[185] or Random Forests[186] could potentially map the non-linear interactions of steric constraints, electronic properties, and non-covalent interactions (such as LD forces) within the chiral pocket without requiring vast amounts of data.

Second, it could be beneficial to evaluate peptide-specific descriptor systems, such as amino acid z-scales, which mathematically encode the lipophilic, steric, and electronic properties of the

sequence.[187] Combining these physicochemical representations with probabilisitic algorithms like Gaussian Process Regression (GPR)[188] could not only aid in predicting stereochemical outcomes but also provide valuable uncertainty quantification for each prediction. The successful application of these tailored, small-data ML approaches to the expanded empirical matrix could reveal whether a highly interpretable predictive framework can be established to guide future catalyst design.

6 Experimental Part

6.1 General Information

Unless otherwise stated, all starting materials, reagents and catalysts were obtained from commercial suppliers (Acros Organics, BLDPharm, TCI, Alfa Aesar, Merck, Fluka) in the highest available purity and used without further purification. Solvents (*n*-Hex, PhMe, THF, CH_2Cl_2, MeOH, EtOH, Et_2O, EtOAc, DMF) were distilled prior to use. Column chromatography was carried out using Macherey-Nagel silica gel 60 (particle size 0.040 – 0.063 mm). All the CBS reduction, as well as the Grignard and lithium–halogen exchange reactions, were performed in oven-dried glassware under an argon atmosphere

6.2 Instrumentations and Methods

TLC: Conducted on silica-coated plates (Macherey-Nagel, silica gel 60 F254) and analyzed using UV light detection at 254 nm. When necessary, the plate was stained with a PMA or Hanessian stain, followed by careful heating of the plate. For the PMA staining solution phosphomolybdic acid (20 g) was dissolved in Ethanol (200 mL). The Hannessian stain was prepared from cerium sulfate tetrahydrate (1 g), ammonium molybdate (25 g), and concentrated sulfuric acid (25 mL) dissolved in water (250 mL).

NMR: Were acquired at ambient temperature on a Bruker AV 200, AV 400, AV 400HD or AV 600 spectrometers, with ^{1}H-NMR spectra calibrated to the residual proton signal of $CDCl_3$ (δ = 7.26 ppm) and ^{13}C-NMR spectra referenced to the central triplet of $CDCl_3$ (δ = 77.16 ppm). Signal multiplicities were described using the following abbreviations: m (multiplet), s (singlet), bs (broad singlet), d (doublet), t (triplet), q (quartet), quint (quintet), sext (sextett), sept (septet), dd (doublet of doublets), dt (doublet of triplets), and qd (quartet of doublets), td (triplet of doublets), ddd (doublet of doublet of doublets), dq (doublet of quartets), tt (triplet of triplets), tq (triplet of quartets), dquint (doublet of quintets), dtt (doublet of triplet of triplets), dddt (doublet of doublet of doublet of triplets).

MS and HRMS: Mass spectra were recorded on a Bruker Daltonics micrOTOF or an Impact II QTOF mass spectrometer using electrospray ionization (ESI) or atmospheric pressure

chemical ionization (APCI). Samples were prepared as methanol solutions of the corresponding compounds.

Chiral GC: Was carried out on HP-GC 5890 Series II instrument. Chromatograms were evaluated using ChemStation software. The columns used are described in the experimental section.

HPLC: Analytical HPLC measurements were performed on a system equipped with a Dionex P680 pump and a Dionex UVD170U UV detector. Additional detection was carried out using a Shodex RI-101 refractive index detector and an SEDEX 85 LT ELSD. Preparative HPLC separations were performed on a Knauer Azura system equipped with a P6.1L pump, a DAD 2.1L diode array detector, and an ASM 2.2L assistant module. The columns used are described in the experimental section.

IR spectroscopy: Recorded on a Bruker Alpha FTIR spectrometer equipped with a diamond ATR unit.

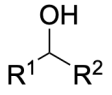
GC-MS: Were performed on an Agilent 8860 GC system coupled to an Agilent 5988B mass selective detector from Agilent Technologies.

EA: Was performed using a Thermo Flash EA 1112 analyzer, with the substances weighed on a Mettler Toledo UMX-2 microbalance prior to analysis.

6.3 Part I

6.3.1 Synthesis and Analysis of Racemates

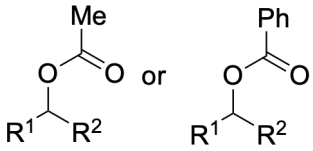
GP1: Synthesis of racemic alcohols



The corresponding ketone (1.0 equiv.) was dissolved in MeOH. At 0 °C, $NaBH_4$ (1.1 equiv. – 1.3 equiv.) was added, and the mixture was allowed to warm to room temperature and stirred for the appropriate time. The reaction mixture was quenched by addition of HCl (1M), and the aqueous layer was extracted three times with EtOAc. The combined organic layers were washed with brine, dried over Na_2SO_4, and the solvent was removed under reduced

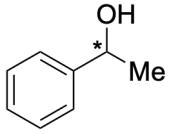
pressure. The crude product was purified by column chromatography (*n*-Hex/EtOAc) to afford the corresponding alcohol.

GP2: Derivatization with BzCl or Ac_2O



For some alcohols whose enantiomers could not be separated by chiral GC, a derivatization approach was employed. The corresponding alcohol was dissolved in THF and Ac_2O (1.1 equiv.) or BzCl (1.1 equiv.) together with DMAP (0.1 equiv.) and NEt_3 (1.1 equiv.) was added to the solution and stirred for the appropriate time. The reaction mixture was then quenched and purified as described above and purified by column chromatography.

1-Phenylethanol (rac-**14a**):



rac-**14a**

Using GP1, $NaBH_4$ (157 mg, 4.16 mmol, 1.0 equiv.) was added slowly at 0 °C to a solution of acetophenone (**13a**) (500 mg, 4.16 mmol, 1.0 equiv.) in 3 mL MeOH. The reaction was then stirred at room temperature for 10 h. After work up and purification *via* column chromatography (*n*-Hex/EtOAc = 3/1), rac-**14a** (477 mg, 3.90 mmol, 94%) was obtained as a colorless liquid.

R_f: 0.42 (*n*-Hex/EtOAc = 3/1).

Chiral GC:

Column:	β-TBDAc
T (Injection + Detector):	250 °C
Flow Rate:	80 mL min^{-1}
Precolumn pressure:	0.8 bar
Initial temperature:	100 °C
Retention time:	(*R*) = 12.51 min
	(*S*) = 13.23 min

Rate [°C min^{-1}]	Temperature [°C]	Time [min]
2.0	140	2.0
20.0	240	3.0

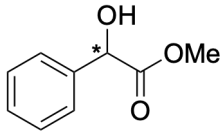
^{1}H NMR (400 MHz, $CDCl_3$): δ/ppm = 7.30 – 7.23 (m, 4 H), 7.23 – 7.16 (m, 1 H), 4.72 (q, *J* = 6.5 Hz, 1 H), 3.20 (s, 1 H), 1.37 (d, *J* = 6.5 Hz, 3 H).

$^{13}C\{^1H\}$ NMR (101 MHz, $CDCl_3$): δ/ppm = 145.87 (C), 128.31 (CH), 127.21 (CH), 125.39 (CH), 70.01 (CH), 25.05 (CH_3).

HRMS (ESI): calcd for $C_8H_{10}O$ $[M+H]^+$: 123.0804; found: 123.0806.

The NMR data are in accordance with those reported in the literature.[189]

Methyl-2-hydroxy-2-phenylacetate (rac-**131**):



rac-**131**

Using GP1, $NaBH_4$ (161 mg, 4.26 mmol, 1.0 equiv.) was added slowly at 0 °C to a solution of methyl-benzoylformate (**62**) (700 mg, 4.26 mmol, 1.0 equiv.) in 5 mL MeOH. The reaction was then stirred at room temperature for 14 h. After work up and purification *via* column chromatography (*n*-Hex/EtOAc = 3/1), rac-**131** (425 mg, 2.56 mmol, 60%) was obtained as a colorless solid.

R_f: 0.31 (*n*-Hex/EtOAc = 3/1)

Chiral GC:

Column:	β-TBDAc
T (Injection + Detector):	250 °C
Flow Rate:	80 mL min^{-1}
Precolumn pressure:	0.8 bar
Initial temperature:	120 °C
Retention time:	(*R*) = 13.49 min
	(*S*) = 15.40 min

Rate [°C min^{-1}]	Temperature [°C]	Time [min]
2.0	160	0.0
20.0	240	3.0

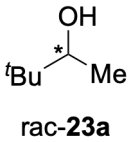
^1H NMR (400 MHz, $CDCl_3$): δ/ppm = 7.45 – 7.30 (m, 5 H), 5.18 (s, 1 H), 3.75 (s, 3 H), 3.51 (bs, 1 H).

$^{13}C\{^1H\}$ NMR (101 MHz, $CDCl_3$): δ/ppm = 174.2 (C), 138.3 (C), 128.7 (CH), 126.7 (CH), 73.0 (CH), 53.1 (CH_3)

HRMS (ESI): calcd for $C_9H_{10}O_3$ $[M+H]^+$: 167.0703; found: 167.0707.

The NMR data are in accordance with those reported in the literature.[190]

3,3-Dimethylbutan-2-ol (rac-**23a**):



rac-**23a**

Using GP1, $NaBH_4$ (207 mg, 5.49 mmol, 1.1 equiv.) was added slowly at 0 °C to a solution of pinacolone (**21a**) (500 mg, 4.99 mmol, 1.0 equiv.) in 3 mL MeOH. The reaction was then stirred at room temperature for 10 h. After work up and purification *via* column chromatography (*n*-Hex/EtOAc = 3/1), rac-**23a** (465 mg, 4.55 mmol, 91%) was obtained as a colorless liquid.

R_f: 0.64 (*n*-Hex/EtOAc = 3/1) [Hanessian Stain].

Chiral GC:

Column:	β-TBDAc
T (Injection + Detector):	250 °C
Flow Rate:	80 mL min^{-1}
Precolumn pressure:	0.8 bar
Initial temperature:	60 °C
Retention time:	(*R*) = 9.89 min
	(*S*) = 10.92 min

Rate [°C min^{-1}]	Temperature [°C]	Time [min]
2.0	60	10.0
20.0	240	3.0

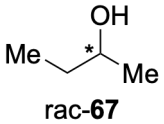
^{1}H NMR (400 MHz, $CDCl_3$): δ/ppm = 3.45 (q, J = 6.4 Hz, 1 H), 1.63 (bs, 1 H), 1.09 (d, J = 6.4 Hz, 3 H), 0.87 (s, 9 H).

^{13}C{^{1}H} NMR (101 MHz, $CDCl_3$): δ/ppm = 75.76 (CH), 35.01 (C), 25.52 (CH_3), 17.98 (CH_3).

HRMS (ESI): calcd for $C_6H_{14}O$ $[M+Na]^+$: 125.0937; found: 125.0941.

The NMR data are in accordance with those reported in the literature.[191]

Butan-2-ol (rac-**67**):



rac-**67**

Using GP1, $NaBH_4$ (577 mg, 15.2 mmol, 1.0 equiv.) was added slowly at 0 °C to a solution of butan-2-one (**51**) (1.00 g, 13.8 mmol, 1.0 equiv.) in 5 mL MeOH. The reaction was then stirred at room temperature for 12 h. After work up and purification *via* column chromatography (*n*-Hex/EtOAc = 3/1), rac-**67** (703 mg, 9.48 mmol, 68%) was obtained as a colorless liquid.

R_f: 0.15 (*n*-Hex/EtOAc = 3/1) [Hanessian Stain].

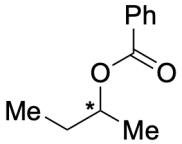
^{1}H NMR (400 MHz, $CDCl_3$): δ/ppm = 3.67 (sext, J = 6.2 Hz, 1H), 1.95 (bs, 1H), 1.51-1.32 (m, 2H), 1.13 (d, J = 6.2, 3 H), 0.89 (t, J = 7.6, 3 H).

^{13}C{^{1}H} NMR (101 MHz, $CDCl_3$): δ/ppm = 69.5 (CH), 32.1 (CH_2), 22.9 (CH_3), 10.0 (CH_3).

HRMS (ESI): calcd for $C_4H_{10}O$ $[M+Na]^+$: 97.0623; found: 97.0630.

The NMR data are in accordance with those reported in the literature.[192]

Sec-butyl benzoate (rac-**85d**):



rac-**85d**

Using GP2, butan-2-ol (rac-**67**) (703 mg, 9.48 mmol, 1.0 equiv.) was dissolved together with DMAP (115 mg, 948 µmol, 0.1 equiv.), NEt_3 (1.06 g, 10.4 mmol, 1.1 equiv). and BzCl (1.47 g, 10.4 mmol, 1.1 equiv.) in 3 mL THF. The reaction was then stirred at room temperature for 12 h. After work up and purification *via* column chromatography (*n*-Hex/EtOAc = 3/1), rac-**85d** (1.00 g, 5.61 mmol, 59%) was obtained as a colorless liquid.

R_f: 0.80 (*n*-Hex/EtOAc = 3/1).

Chiral GC:

Column:	β-TBDAc
T (Injection + Detector):	250 °C
Flow Rate:	80 mL min^{-1}
Precolumn pressure:	0.8 bar
Initial temperature:	60 °C
Retention time:	(*R*) = 35.47 min
	(*S*) = 35.95 min

Rate [°C min^{-1}]	Temperature [°C]	Time [min]
2.0	140	0.0
20.0	240	3.0

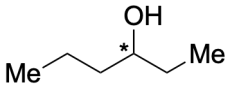
^{1}H NMR (400 MHz, $CDCl_3$): δ/ppm = 8.07 – 8.02 (m, 2H), 7.58 – 7.50 (m, 1H), 7.46 – 7.40 (m, 2H) 4.81 (sext, J = 6.3 Hz, 1H), 1.82 – 1.61 (m, 2H), 1.34 (d, J = 6.3 Hz, 3H), 0.94 (t, J = 7.4 Hz, 3H).

$^{13}C\{^1H\}$ NMR (101 MHz, $CDCl_3$): δ/ppm = 162.5 (C), 134.7 (CH), 130.7 (CH), 129.0 (CH), 128.4 (CH_2), 73.0 (CH), 29.1 (CH_2), 19.7 (CH_3), 9.9 (CH_3).

HRMS (ESI): calcd for $C_{11}H_{14}O_2$ $[M+H]^+$: 179.1066; found: 179.1070.

The NMR data are in accordance with those reported in the literature.[193]

Hexan-3-ol (rac-**132**):



rac-**132**

Using GP1, $NaBH_4$ (491 mg, 12.9 mmol, 1.0 equiv.) was added slowly at 0 °C to a solution of hexan-3-one (**61**) (1.00 g, 9.98 mmol, 1.0 equiv.) in 5 mL MeOH. The reaction was then stirred at room temperature for 12 h. After work up and purification *via* column chromatography (*n*-Hex/EtOAc = 3/1), rac-**132** (834 mg, 8.16 mmol, 82%) was obtained as a colorless liquid.

R_f: 0.34 (*n*-Hex/EtOAc = 3/1) [Hanessian Stain].

Chiral GC:

Column:	β-TBDAc
T (Injection + Detector):	250 °C
Flow Rate:	80 mL min^{-1}
Precolumn pressure:	0.8 bar
Initial temperature:	60 °C
Retention time:	(*R*) = 10.16 min
	(*S*) = 10.69 min

Rate [°C min^{-1}]	Temperature [°C]	Time [min]
2.0	140	0.0
20.0	240	3.0

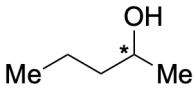
^1H NMR (400 MHz, $CDCl_3$): δ/ppm = 3.51 – 3.42 (m, 1H), 1.50 – 1.22 (m, 6H), 0.92 – 0.81 (m, 6H).

$^{13}C\{^1H\}$ NMR (101 MHz, $CDCl_3$): δ/ppm = 73.2 (CH), 39.3 (CH_2), 30.3 (CH_2), 19.0 (CH_2), 14.2 (CH_3), 10.0 (CH_3).

HRMS (ESI): calcd for $C_6H_{14}O$ $[M+Na]^+$: 125.0936; found: 125.0941.

The NMR data are in accordance with those reported in the literature.[192]

Pentan-2-ol (rac-**133**):



rac-**133**

Using GP1, $NaBH_4$ (571 mg, 15.0 mmol, 1.0 equiv.) was added slowly at 0 °C to a solution of pentan-2-one (**57**) (1.00 g, 11.6 mmol, 1.0 equiv.) in 5 mL MeOH. The reaction was then stirred at room temperature for 14 h. After work up and purification *via* column chromatography (*n*-Hex/EtOAc = 3/1), rac-**133** (345 mg, 3.91 mmol, 33%) was obtained as a colorless liquid.

R_f: 0.20(*n*-Hex/EtOAc = 3/1) [Hanessian Stain].

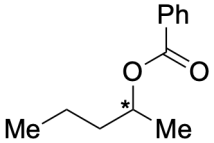
^{1}H NMR (400 MHz, $CDCl_3$): δ/ppm = 3.78 – 3.68 (m, 1H), 2.08 (bs, 1H), 1.46 – 1.25 (m, 4H), 1.13 – 1.09 (m, 3H), 0.87 (t, J = 7.0 Hz, 3H).

^{13}C{^{1}H} NMR (101 MHz, $CDCl_3$): δ/ppm = 67.8 (CH), 41.6 (CH_2), 23.4 (CH_3), 19.0 (CH_2), 14.1 (CH_3).

HRMS (ESI): calcd for $C_5H_{12}O$ $[M+Na]^+$: 111.0780; found: 111.0783.

The NMR data are in accordance with those reported in the literature.[192]

Pentan-2-yl benzoate (rac-**134**):



rac-**134**

Using GP2, pentan-2-ol (rac-**133**) (345 mg, 3.91 mmol, 1.0 equiv.) was dissolved together with DMAP (47.8 mg, 391 µmol, 0.1 equiv.), NEt_3 (435 mg, 4.31 mmol, 1.1 equiv.) and BzCl (605 mg, 4.31 mmol, 1.1 equiv.) in 2 mL THF. The reaction was then stirred at room temperature for 12 h. After work up and purification *via* column chromatography (*n*-Hex/EtOAc = 3/1), rac-**134** (735 mg, 3.82 mmol, 97%) was obtained as a colorless liquid.

R_f: 0.53 (*n*-Hex/EtOAc = 3/1).

Chiral GC:

Column:	β-6-TBDM
T (Injection + Detector):	250 °C
Flow Rate:	80 mL min^{-1}
Precolumn pressure:	0.8 bar
Initial temperature:	80 °C
Retention time:	(*R*) = 61.53 min
	(*S*) = 62.16 min

Rate [°C min^{-1}]	Temperature [°C]	Time [min]
0.0	80	10.0
0.5	120	0.0
20.0	250	3.0

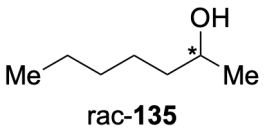
^{1}H NMR (400 MHz, $CDCl_3$): *δ*/ppm = 8.08 – 8.01 (m, 2H), 7.57 – 7.51 (m, 1H), 7.47 – 7.39 (m, 2H), 5.18 (sext, *J* = 6.2 Hz, 1H), 1.80 – 1.67 (m, 1H), 1.64 – 1.53 (m, 1H), 1.51 – 1.36 (m, 2H), 1.34 (d, *J* = 6.2 Hz, 3H), 0.95 (t, *J* = 7.3 Hz, 3H).

^{13}C{^{1}H} NMR (101 MHz, $CDCl_3$): *δ*/ppm = 166.3 (C), 132.8 (C), 132.8 (C), 131.1 (C), 129.6 (C), 128.4 (C), 71.6 (CH), 38.3 (CH_2), 20.2 (CH_2), 18.8 (CH_3), 14.1 (CH_3).

HRMS (ESI): calcd for $C_{12}H_{16}O_2$ $[M+H]^+$: 193.1223; found: 193.1223.

The NMR data are in accordance with those reported in the literature.[194]

Heptan-2-ol (rac-**135**):



rac-**135**

Using GP1, $NaBH_4$ (397 mg, 10.5 mmol, 1.2 equiv.) was added slowly at 0 °C to a solution of heptan-2-ol (**60**) (1.00 g, 8.76 mmol, 1.0 equiv.) in 3 mL MeOH. The reaction was then stirred at room temperature for 12 h. After work up and purification *via* column chromatography (*n*-Hex/EtOAc = 3/1), rac-**135** (851 mg, 7.32 mmol, 83%) was obtained as a colorless liquid.

R_f: 0.35 (*n*-Hex/EtOAc = 3/1) [Hanessian Stain].

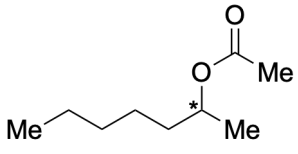
^{1}H NMR (400 MHz, $CDCl_3$): *δ*/ppm = 3.81 – 3.72 (m, 1H), 1.55 (bs, 1H), 1.48 – 1.21 (m, 8H), 1.17 (d, *J* = 6.1 Hz, 3H), 0.88 (t, *J* = 6.7 Hz, 3H).

$^{13}C\{^1H\}$ NMR (101 MHz, $CDCl_3$): δ/ppm = 68.3 (CH), 39.5 (CH_2), 32.0 (CH_2), 32.0 (CH_2), 25.6 (CH_2), 23.6 (CH_3), 22.8 (CH_2), 14.1 (CH_3).

HRMS (ESI): calcd for $C_7H_{16}O$ $[M+Na]^+$: 139.1093; found: 139.1097.

The NMR data are in accordance with those reported in the literature.[195]

Heptan-2-yl acetate (rac-**136**):



rac-**136**

Using GP2, heptan-2-ol (rac-**135**) (851 mg, 7.32 mmol, 1.0 equiv.) was dissolved together with DMAP (89.4 mg, 732 µmol, 0.1 equiv.), NEt_3 (815 mg, 8.06 mmol, 1.1 equiv.) and Ac_2O (822 mg, 8.06 mmol, 1.1 equiv.) in 3 mL THF. The reaction was then stirred at room temperature for 12 h. After work up and purification *via* column chromatography (*n*-Hex/EtOAc = 3/1), rac-**136** (659 mg, 4.16 mmol, 57%) was obtained as a colorless liquid.

R_f: 0.72 (*n*-Hex/EtOAc = 3:1) [Hanessian Stain].

Chiral GC:

Column:	β-6-TBDM
T (Injection + Detector):	250 °C
Flow Rate:	80 mL min^{-1}
Precolumn pressure:	0.8 bar
Initial temperature:	100 °C
Retention time:	(*R*) = 4.05 min
	(*S*) = 4.23 min

Rate [°C min^{-1}]	Temperature [°C]	Time [min]
2.0	120	0.0
20.0	250	3.0

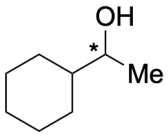
^1H NMR (400 MHz, $CDCl_3$): δ/ppm = 4.81 (quint, J = 6.3 Hz, 1H), 1.95 (s, 3H), 1.62 – 1.34 (m, 2H), 1.31 – 1.17 (m, 6H), 1.13 (d, J = 6.3 Hz, 3H), 0.87 – 0.75 (m, 3H).

$^{13}C\{^1H\}$ NMR (101 MHz, $CDCl_3$): δ/ppm = 170.9 (C), 71.2 (CH), 36.0 (CH_2), 31.6 (CH_2), 25.2 (CH_2), 22.7 (CH_2), 21.5 (CH_2), 20.1 (CH_3), 14.1 (CH_3).

HRMS (ESI): calcd for $C_9H_{18}O_2$ $[M+H]^+$: 159.1379; found: 159.1381.

The NMR data are in accordance with those reported in the literature.[196]

1-Cyclohexlethanol (rac-**23b**):



rac-**23b**

Using GP1, $NaBH_4$ (329 mg, 8.72 mmol, 1.1 equiv.) was added slowly at 0 °C to a solution of 1-cyclohexylethanone (**21b**) (1.00 g, 7.92 mmol, 1.0 equiv.) in 4 mL MeOH. The reaction was then stirred at room temperature for 14 h. After work up and purification *via* column chromatography (*n*-Hex/EtOAc = 2/1), rac-**23b** (789 mg, 6.15 mmol, 77%) was obtained as a yellow liquid.

R_f: 0.52 (*n*-Hex/EtOAc = 2/1) [Hanessian Stain].

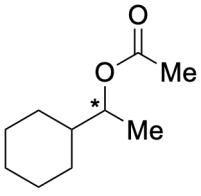
^{1}H NMR (400 MHz, $CDCl_3$): δ/ppm = 3.54 (quint, J = 6.3 Hz, 1H), 1.90 – 1.60 (m, 6H), 1.41 (bs, 1H), 1.31 – 1.16 (m, 4H), 1.15 (d, J = 6.3 Hz, 3H) 1.03 – 0.84 (m, 2H).

^{13}C{^{1}H} NMR (101 MHz, $CDCl_3$): δ/ppm = 72.4 (CH), 45.3 (CH_2), 28.9 (CH_2), 28.5 (CH_2), 26.7 (CH_2), 26.4 (CH_2), 26.3 (CH_2), 20.5 (CH_3).

HRMS (ESI): calcd for $C_8H_{16}O$ $[M+H]^+$: 129.1274; found: 129.1279.

The NMR data are in accordance with those reported in the literature.[197]

1-Cyclohexylethyl acetate (rac-**137**):



rac-**137**

Using GP2, 1-cyclohexlethanol **(**rac-**23b**) (789 mg, 6.15 mmol, 1.0 equiv.) was dissolved together with DMAP (75.1 mg, 615 µmol, 0.1 equiv.), NEt_3 (684 mg, 684 mmol, 1.1 equiv.) and Ac_2O (691 mg, 6.77 mmol, 1.1 equiv.) in 2 mL THF. The reaction was then stirred at room temperature for 11 h. After work up and purification *via* column chromatography (*n*-Hex/EtOAc = 3/1), rac-**137** (910 mg, 5.35 mmol, 87%) was obtained as a colorless liquid.

R_f: 0.70 (*n*-Hex/EtOAc = 3/1) [Hanessian Stain].

Chiral GC:

Column:	β-6-TBDM
T (Injection + Detector):	250 °C
Flow Rate:	80 mL min^{-1}
Precolumn pressure:	0.8 bar
Initial temperature:	80 °C
Retention time:	(*R*) = 23.75 min
	(*S*) = 25.46 min

Rate [°C min^{-1}]	Temperature [°C]	Time [min]
0.0	80	20.0
2.0	120	0.0
20.0	250	3.0

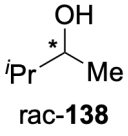
^{1}H NMR (400 MHz, $CDCl_3$): *δ*/ppm = 4.70 (quint, J = 6.3 Hz, 1H), 2.01 (s, 3H), 1.78 – 1.59 (m, 6H), 1.46 – 1.35 (m, 1H), 1.31 – 1.16 (m, 3H) 1.14 (d, *J* = 6.3 Hz, 3H), 1.04 – 0.91 (m, 2H).

^{13}C{^{1}H} NMR (101 MHz, $CDCl_3$): *δ*/ppm = 171.0 (C), 74.8 (CH_2), 42.7 (CH), 26.5 (CH_2), 26.2 (CH_2), 26.1 (CH_2), 21.4 (CH_3), 17.2 (CH_3).

HRMS (ESI): calcd for $C_{10}H_{18}O_2$ $[M+H]^+$: 171.1379; found: 171.1382.

The NMR data are in accordance with those reported in the literature.[198]

3-Methylbutan-2-ol (rac-**138**):



rac-**138**

Using GP1, $NaBH_4$ (483 mg, 12.7 mmol, 1.1 equiv.) was added slowly at 0 °C to a solution of 3-methylbutan-2-one (**56**) (1.00 g, 11.6 mmol, 1.0 equiv.) in 4 mL MeOH. The reaction was then stirred at room temperature for 13 h. After work up and purification *via* column chromatography (*n*-Hex/EtOAc = 3/1), rac-**138** (874 mg, 9.92 mmol, 85%) was obtained as a colorless liquid.

R_f: 0.08 (*n*-Hex/EtOAc = 3/1) [Hanessian Stain].

Chiral GC:

Column:	β-TBDAc
T (Injection + Detector):	250 °C
Flow Rate:	80 mL min^{-1}
Precolumn pressure:	0.8 bar
Initial temperature:	60 °C
Retention time:	(*R*) = 8.05 min
	(*S*) = 8.38 min

Rate [°C min^{-1}]	Temperature [°C]	Time [min]
2.0	100	0.0
20.0	240	3.0

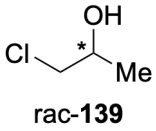
^{1}H NMR (400 MHz, $CDCl_3$): *δ*/ppm = 3.56 (quint, *J* = 6.2 Hz, 1H), 1.67 – 1.54 (m, 1H), 1.42 (bs, 1H) 1.14 (d, *J* = 6.2 Hz, 3H), 0.90 (dd, *J* = 9.0, 6.7 Hz, 6H).

^{13}C{^{1}H} NMR (101 MHz, $CDCl_3$): *δ*/ppm = 73.0 (CH), 35.1 (CH), 20.2 (CH_3), 18.3 (CH_3), 17.9 (CH_3).

HRMS (ESI): calcd for $C_5H_{12}O$ $[M+Na]^+$: 111.0780; found: 111.0783.

The NMR data are in accordance with those reported in the literature.[193]

1-Chloropropan-2-ol (rac-**139**):



rac-**139**

Using GP1, $NaBH_4$ (449 mg, 11.89 mmol, 1.1 equiv.) was added slowly at 0 °C to a solution of 1-chloropropan-2-one (**58**) (1.00 g, 10.8 mmol, 1.0 equiv.) in 3 mL MeOH. The reaction was then stirred at room temperature for 14 h. After work up and purification *via* column chromatography (*n*-Hex/EtOAc = 2/1), rac-**139** (644 mg, 6.81 mmol, 63%) was obtained as a yellow liquid.

R_f: 0.11 (*n*-Hex/EtOAc = 3/1) [Hanessian Stain].

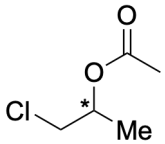
^{1}H NMR (400 MHz, $CDCl_3$): *δ*/ppm = 4.05 – 3.94 (m, 1H), 3.60 (dd, *J* = 11.0, 3.5 Hz, 1H), 3.45 (dd, *J* = 11.0, 7.2 Hz, 1H), 1.27 (d, *J* = 6.4 Hz, 3H).

^{13}C{^{1}H} NMR (101 MHz, $CDCl_3$): *δ*/ppm = 67.8 (CH), 51.7 (CH_2), 20.3 (CH_3).

HRMS (ESI): calcd for C_3H_7ClO $[M+Na]^+$: 117.0077; found: 117.0082.

The NMR data are in accordance with those reported in the literature.[200]

1-Chloropropan-2-yl acetate (rac-**140**):



rac-**140**

Using GP2, 1-Chloropropan-2-ol **(**rac-**139**) (644 mg, 7.31mmol, 1.0 equiv.) was dissolved together with DMAP (89.2 mg, 730 µmol, 0.1 equiv.), NEt_3 (813 mg, 8.04 mmol, 1.1 equiv.) and Ac_2O (820 mg, 8.04 mmol, 1.1 equiv.) in 2 mL THF. The reaction was then stirred at room temperature for 12 h. After work up and purification *via* column chromatography (*n*-Hex/EtOAc = 3/1), rac-**140** (1.11 g, 6.52 mmol, 89%) was obtained as a colorless liquid.

R_f: 0.48 (*n*-Hex/EtOAc = 3:1) [Hanessian Stain].

Chiral GC:

Column:	β-TBDAc
T (Injection + Detector):	250 °C
Flow Rate:	80 mL min^{-1}
Precolumn pressure:	0.8 bar
Initial temperature:	100 °C
Retention time:	(*R*) = 4.12 min
	(*S*) = 6.41 min

Rate [°C min^{-1}]	Temperature [°C]	Time [min]
1.0	120	2.0
20.0	240	3.0

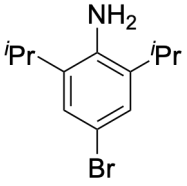
^{1}H NMR (400 MHz, $CDCl_3$): *δ*/ppm = 5.07 – 4.96 (m, 1H), 3.50 (dd, *J* = 5.2, 3.0 Hz, 2H), 2.00 (s, 3H), 1.26 (d, *J* = 6.4 Hz, 3H).

^{13}C{^{1}H} NMR (101 MHz, $CDCl_3$): *δ*/ppm = 170.4 (C), 69.7 (CH), 46.9 (CH_2), 21.2 (CH_3), 17.7 (CH_3).

HRMS (ESI): calcd for $C_5H_9ClO_2$ $[M+H]^+$: 137.0363; found: 137.0367.

6.3.2 Synthesis of Brominated Aryl Compounds

4-Bromo2,6-di-isopropylbenzenamine (141):



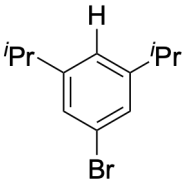
41

Bromine (3.00 mL, 58.6 mmol, 1.04 equiv.) dissolved in 50 mL CH_2Cl_2/MeOH (1:1) was added dropwise to a stirring solution of 2,6-diisopropylaniline (10.6 mL, 56.4 mmol, 1.00 equiv.) in 200 mL CH_2Cl_2 (1:1) at room temperature over 2 h. The solution was stirred for 24 h. The solvents were evaporated, the resulting solid was briefly washed with boiling PE 35-70 and the residue was dissolved in 100 mL CH_2Cl_2. The organic phase was washed with 2M NaOH (2 x 100 mL) and with brine (1 x 100 mL). The organic phase was dried over Na_2SO_4, filtered and the solvent was removed under reduced pressure to give **141** (11.5 g, 44.8 mmol, 79%) as a brown liquid.

^{1}H NMR (400 MHz, $CDCl_3$): δ/ppm = 7.12 (s, 2H), 4.19 (s, 1H), 2.92 (sept, J = 6.7 Hz, 2H), 1.26 (d, J = 6.8 Hz, 12H).

The NMR data are in accordance with those reported in the literature.[201]

1-Bromo-3,5-diisopropylbenzene (142):



142

Sodium nitrite (7.70 g, 112 mmol, 2.50 equiv.) was added in portions to a suspension of 4-bromo-2,6-di-iso-propylbenzenamine (**141**) (11.5 g, 44.8 mmol, 1.00 equiv.) in 90 mL 2M HCl at −5 °C and stirred for 10 min. Subsequently, 50 % H_3PO_2 (49.1 mL, 448 mmol, 10.0 equiv.) was added dropwise to the solution. The reaction mixture was slowly warmed to 3 °C and stirred for 24 h. After that the solution was warmed to room temperature and stirred for another 24 h. The aqueous layer was extracted with CH_2Cl_2 (3 x 100 mL). The combined organic phases were dried over Na_2SO_4, filtered and the solvent was removed under reduced pressure to obtain **142** (10.8 g, 37.3 mmol, 83%) as an orange oil.

R_f: 0.37 (*n*-Hex/EtOAc = 3/1).

^{1}H NMR (400 MHz, $CDCl_3$): δ/ppm = 7.18 (d, J = 1.6 Hz, 2H), 7.00 – 6.96 (m, 1H), 2.85 (sept, J = 7.0 Hz, 2H), 1.24 (d, J = 6.9 Hz, 12H).

$^{13}C\{^1H\}$ NMR (101 MHz, $CDCl_3$): δ/ppm = 151.2 (C), 127.0 (CH), 123.9 (CH), 122.5 (C), 34.2 (CH), 24.03 (CH_3).

HRMS (ESI): calcd for $C_{12}H_{17}Br$ $[M+H]^+$: 241.0586; found: 241.0582.

The NMR data are in accordance with those reported in the literature.[202]

6.3.3 Synthesis of Catalyst Precursors

GP3: Grignard Addition (1) to Benzylproline esters (52)

To a suspension of magnesium (2.5 equiv.) in anhydrous THF under argon a crystal of iodine was added and stirred at room temperature for 30 min. Then 5% of the solution of aryl bromide (2.5 equiv.) in THF was added and the reaction mixture was warmed to 50 °C. As soon as the reaction started, the remaining solution of aryl bromide was added dropwise to the solution. The reaction mixture was refluxed for 1 h and then cooled to 0 °C. To the aryl magnesium bromide suspension, a solution of (*S*)-methyl-1-benzylpyrrolidin-2-carboxylate (**52**) (1.0 equiv.) in THF was added dropwise. The reaction mixture was stirred for appropriate amount of time, monitored by TLC analysis. At 0 °C, saturated NH_4Cl solution was added to quench the reaction. Afterwards the mixture was extracted three times with EtOAc. The combined organic layers were washed with brine and dried over $NaSO_4$. After removing the solvent, the crude product was purified by column chromatography.

GP4: Grignard Addition (2) to Benzylproline esters (52)

To a suspension of magnesium (5.2 equiv.) in anhydrous THF under Argon a crystal of iodine was added and stirred at room temperature for 30 min. Then 5% of the solution of aryl bromide (3.8 equiv.) in THF was added and the reaction mixture was warmed to 50 °C. As soon as the reaction started, the remaining solution of aryl bromide was added dropwise to the solution. The reaction mixture was refluxed for 2 h. To the aryl magnesium bromide suspension, a solution of (*S*)-methyl-1-benylpyrrolidin-2-carboxylate (**52**) (1.0 equiv.) in THF was added dropwise. The reaction mixture was once again refluxed for 20 h and at 0 °C, saturated NH_4Cl was added to quench the reaction. Afterwards the mixture was extracted three times with EtOAc. The combined organic layers were washed with brine and dried over Na_2SO_4. After removing the solvent, the crude product was purified by column chromatography.

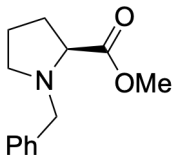
GP5: Hydrogenolysis of Benzyl Group

The benzyl-protected prolinol (**53**) (1.0 equiv.) was dissolved in MeOH and Pd/C (0.2 equiv., 10-20 wt%) as well as TFA (1.0 equiv.) were added. The reaction flask was purged with H_2 and afterwards stirred at room temperature for 48 - 72 h. The mixture was filtered through a pad of Celite and washed with small portions of MeOH. The solvent was removed under reduced pressure, and the residue was dissolved in EtOAc, washed with 2M NaOH and brine and dried over $NaSO_4$. After that the solvent was removed and the crude product was either directly purified by RP-HPLC or recrystallized.

Additional Note

(*S*)-Diphenyl)(pyrrolidin-2-yl)methanol (**22a**) was purchased via TCI, (1*S*,2*R*)-(+)-cis-1-amino-2-indanol and (1*S*,2*R*)-(–)-cis-1-amino-2-indanol (**55**) were purchased from Sigma-Aldrich. Both were recrystallized from *n*-Hex before use.

(*S*)-Methyl-1-benzylpyrrolidine-2-carboxylate (**52**):



52

Esterification and Benzylation: L-proline (**10**) (10.0 g, 88.9 mmol, 1.0 equiv.) was dissolved in 80 mL MeOH and at 0 °C $SOCl_2$ (25.8 g, 217 mmol, 2.0 equiv.) was added dropwise and stirred at room temperature for 24 h. The solvent was removed under reduced pressure and toluene was added and removed under reduced pressure two more times. The crude material was used without further purification for the next step. The crude material was dissolved in 80 mL CH_2Cl_2 and NEt_3 (19.6 g, 193 mmol, 2.5 equiv.) was added. After 15 min the formed precipitate was filtered and washed with CH_2Cl_2. The solvent was removed under reduced pressure and the residue was suspended in 100 mL Et_2O, cooled to 0 °C and BnBr (14.5 g, 85.1 mmol, 1.1 equiv.) was slowly added dropwise. After stirring for 24 h at room temperature the reaction mixture was filtered, washed with small portions of Et_2O, and the solvent was removed under reduced pressure. After column chromatography (*n*-Hex/EtOAc = 3/1) **52** (13.6 g, 62.2 mmol, 71%) was obtained as a yellow oil, which changed to an orange oil upon standing.

$\mathbf{R_f}$: 0.43 (*n*-Hex/EtOAc = 3/1) [CAM].

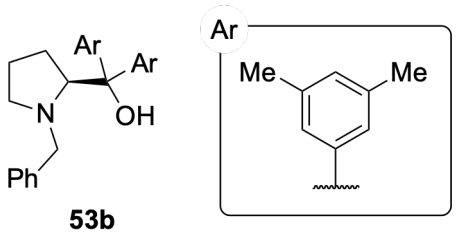
^{1}H NMR (400 MHz, $CDCl_3$): δ/ppm = 7.28 – 7.21 (m, 4H), 7.20 – 7.15 (m, 1H), 3.82 (d, J = 12.8 Hz, 1H), 3.59 (s, 3H), 3.51 (d, J = 12.8, 1H), 3.21 – 3.17 (m, 1H), 3.00 – 2.98 (m, 1H), 2.36 – 2.32 (m, 1H), 2.08 –2.05 (m, 1H), 1.92 – 1.70 (m, 3H).

^{13}C{^{1}H} NMR (101 MHz, $CDCl_3$): δ/ppm = 174.6 (C), 138.3 (C), 129.3 (CH), 128.2 (CH), 127.1 (CH), 65.3 (CH), 58.8 (CH_2), 53.3 (CH_2), 51.7 (CH_3), 29.4 (CH_2), 23.0 (CH_2).

HRMS (ESI): calcd for $C_{13}H_{17}NO_2$ $[M+Na]^+$: 242.1151; found: 242.1153.

The NMR data are in accordance with those reported in the literature.[87]

(*S*)-(1-Benzylpyrrolidin-2-yl)bis(3,5-dimethylphenyl)methanol (**53b**):



53b

Using GP3, (*S*)-methyl-1-benzylpyrrolidine-2-carboxylate (**52**) (2.00 g, 9.12 mmol, 1.00 equiv.) was converted with 1-bromo-3,5-dimethylbenzene (4.22 g, 22.8 mmol, 2.50 equiv.) and magnesium (554 mg, 22.8 mmol, 2.50 equiv.) at room temperature for 20 h. After column chromatography (*n*-Hex/EtOAc = 9/1), (**53b**) (2.44 g, 6.11 mmol, 67%) was obtained as a colorless foam.

R_f: 0.34 (n-Hex/EtOAc = 9/1) [CAM].

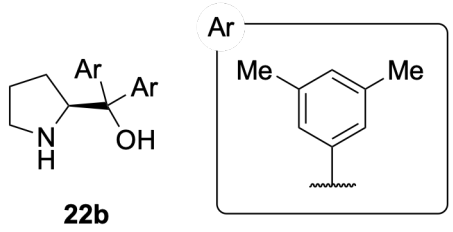
^{1}H NMR (400 MHz, $CDCl_3$): δ/ppm = 7.30 – 7.27 (m, 2H), 7.25 – 7.16 (m, 5H), 7.06 – 7.02 (m, 2H), 6.80 (s, 1H), 6.71 (s, 1H), 4.77 (s, 1H), 3.89 (dd, J = 9.5, 4.5 Hz, 1H), 3.19 – 3.10 (m, 1H), 3.04 – 3.96 (m, 1H), 2.94 – 2.86 (m, 1H), 2.30 (s, 6H), 2.24 (s, 6H) 2.03 – 1.90 (m, 1H), 1.81 – 1.71 (m, 1H), 1.69 – 1.57 (m, 3H).

^{13}C{^{1}H} NMR (101 MHz, $CDCl_3$): δ/ppm = 148.0 (C), 146.6 (C), 140.1 (C), 137.5 (C), 137.4 (C), 128.8 (CH), 128.2 (CH), 128.1 (CH), 128.0 (CH), 126.9 (CH), 123.7 (CH), 123.6 (CH), 78.2 (COH), 71.0 (CH), 60.8 (CH_2), 55.8 (CH_2), 30.0 (CH_2), 24.4 (CH_2), 21.8 (CH_3), 21.7 (CH_3).

HRMS (ESI): calcd for $C_{28}H_{33}NO$ $[M+H]^+$: 400.2635; found: 400.2634.

The NMR data are in accordance with those reported in the literature.[87]

(*S*)-Bis(3,5-dimethylphenyl)(pyrrolidin-2-yl)methanol (**22b**):



22b

Using GP5, (*S*)-(1-benzylpyrrolidin-2-yl)bis(3,5-dimethylphenyl)methanol (**53b**) (500 mg, 1.25 mmol, 1.00 equiv.) was converted with Pd/C (266 mg, 10 wt%, 250 µmol, 0.20 equiv.) and TFA (142 mg, 1.25 mmol, 1.00 equiv.) under H_2 atmosphere for 48 h. After work up and recrystallization (*n*-Hex) (**22b**) (370 mg, 1.20 mmol, 96 %) was obtained as a colorless solid.

R_f: 0.17 (*n*-Hex/EtOAc = 9/1) [CAM].

^{1}H NMR (400 MHz, $CDCl_3$): δ/ppm = 7.12 (s, 2H), 7.02 (s, 2H), 6.80 (s, 2H), 4.68 (t, J = 8.2 Hz, 1H), 2.88 – 2.79 (m, 1H), 2.76 – 2.66 (m, 1H), 2.25 (s, 6H), 2.21 (s, 6H), 2.07 – 197 (m, 1H), 1.97 – 1.87 (m, 1H), 1.86 – 1.75 (m, 1H), 1.70 – 1.62 (m, 1H).

^{13}C{^{1}H} NMR (101 MHz, $CDCl_3$): δ/ppm = 144.0 (C), 143.7 (C), 138.6 (C), 138.0 (C), 129.4 (C), 129.0 (C), 123.4 (CH), 122.9 (CH), 77.4 (COH), 65.9 (CH), 46.6 (CH_2), 26.5 (CH_2), 25.0 (CH_2), 21.6 (CH_3), 21.4 (CH_3).

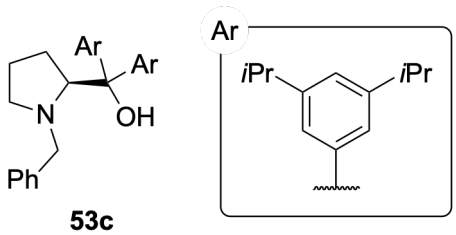
HRMS (ESI): calcd for $C_{21}H_{27}NO$ $[M+H]^+$: 310.2166; found: 310.2167.

EA (%):

	C	**H**	**N**
calculated	81.51	8.79	4.53
determined	81.44	8.70	4.33

The NMR data are in accordance with those reported in the literature.[87]

(*S*)-(1-Benzylpyrrolidin-2-yl)bis(3,5-diisopropylphenyl)methanol (**53c**):



53c

Using GP3, (*S*)-methyl-1-benzylpyrrolidine-2-carboxylate (**52**) (1.00 g, 4.56 mmol, 1.00 equiv.) was converted with 1-bromo-3,5-diisopropylbenzene (**142**) (2.75 g, 11.4 mmol, 2.50 equiv.) and magnesium (277 mg, 11.4 mmol, 2.50 equiv.) at room temperature for 20 h. After column

chromatography (*n*-Hex/EtOAc = 10/1), **53c** (312 mg, 609 µmol, 14%) was obtained as a yellow oil.

R_f: 0.30 (*n*-Hex/EtOAc = 10/1) [CAM].

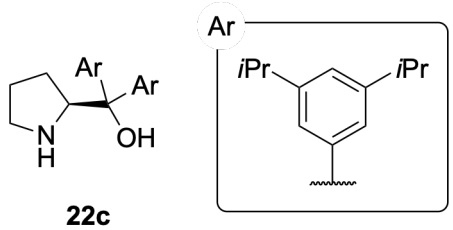
^{1}H NMR (400 MHz, $CDCl_3$): *δ*/ppm = 7.59 (d, *J* = 1.7 Hz, 2H), 7.42 (d, *J* = 1.7 Hz, 2H), 7.29 – 7.15 (m, 3H), 7.14 – 7.06 (m, 2H), 6.96 (s, 1H), 6.89 (s, 1H), 4.96 (s, 1H), 4.09 (dd, *J* = 9.3, 4.8 Hz, 1H), 3.22 (dd, *J* = 92.3, 12.7 Hz, 2H), 3.05 – 2.86 (m, 5H), 2.49 – 2.37 (m, 1H), 2.06 – 1.90 (m, 1H), 1.87 – 1.61 (m, 3H), 1.34 (d, *J* = 6.9 Hz, 12H), 1.29 (d, *J* = 6.9 Hz, 12H).

^{13}C {*1H*} NMR (101 MHz, $CDCl_3$): *δ*/ppm = 148.3 (C), 148.2 (C), 148.1 (C), 146.7 (C), 140.2 (C), 128.7 (CH), 128.1 (CH), 126.8 (C), 123.8 (C), 122.8 (C), 122.3 (C), 121.5 (CH), 121.2 (CH), 78.2 (COH), 71.6 (CH), 60.6 (CH_2), 55.8 (CH_2), 34.4 (CH), 34.4 (CH), 34.3, 29.8 (CH_2), 24.4 (CH_3), 24.3 (CH_3), 24.2 (CH_3), 24.1 (CH_3).

HRMS (ESI): calcd for $C_{36}H_{49}NO$ $[M+H]^+$: 512.3887; found: 512.3885.

The NMR data are in accordance with those reported in the literature.[87]

(*S*)-Bis(3,5-diisopropylphenyl)(pyrrolidin-2-yl)methanol (**22c**):



22c

Using GP5, (*S*)-(1-benzylpyrrolidin-2-yl)bis(3,5-diisopropylphenyl)methanol (**53c**) (320 mg, 625 µmol, 1.00 equiv.) was converted with Pd/C (133 mg, 10 wt%, 125 µmol, 0.20 equiv.) and TFA (71.3 mg, 1.00 mmol, 1.00 equiv.) under H_2 atmosphere for 48 h. After work up and recrystallization (*n*-Hex) **22c** (203 mg, 481 µmol, 77 %) was obtained as a colorless solid.

R_f: 0.17 (*n*-Hex/EtOAc = 3/1) [CAM].

^{1}H NMR (400 MHz, $CDCl_3$): *δ*/ppm = 7.28 (d, *J* = 1.6 Hz, 2H), 7.15 (d, *J* = 1.7 Hz, 2H), 6.87 (dt, *J* = 11.6, 1.6, 2H), 7.73 (t, *J* = 8.3 Hz, 1H), 2.90 – 2.75 (m, 4H), 2.71 – 2.49 (m, 2H), 1.83 – 1.51 (m, 4H), 1.31 – 1.23 (m, 1H), 1.23 – 1.14 (m, 24H).

^{13}C{^{1}H} NMR (101 MHz, $CDCl_3$): *δ*/ppm = 149.0 (C), 148.5 (C), 144.3 (C), 123.1 (CH), 121.9 (CH), 120.9. (CH), 121.3 (CH), 77.8 (COH), 66.1 (CH), 46.5 (CH_2), 34.4 (CH), 26.6 (CH_2), 25.1 (CH_2), 24.5 (CH_3), 24.3 (CH_3), 24.0 (CH_3), 23.6 (CH_3).

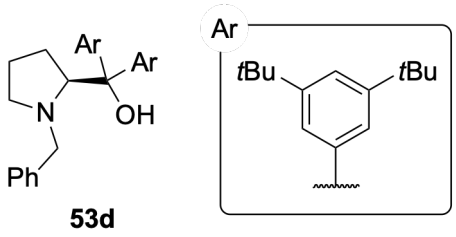
HRMS (ESI): calcd for $C_{29}H_{43}NO$ $[M+H]^+$: 422.3417; found: 422.3419.

EA (%):

	C	H	N
calculated	82.60	10.28	3.32
determined	82.36	10.15	3.08

The NMR data are in accordance with those reported in the literature.[87]

(*S*)-(1-Benzylpyrrolidin-2-yl)bis(3,5-di-*t*buylphenyl)methanol (**53d**):



53d

Using GP3, (*S*)-methyl-1-benzylpyrrolidine-2-carboxylate (**52**) (2.00 g, 9.12 mmol, 1.00 equiv.) was converted with 1-bromo-3,5-di-tert-butylbenzene (6.14 g, 22.8 mmol, 2.50 equiv.) and magnesium (554 mg, 22.8 mmol, 2.50 equiv.) at room temperature for 20 h. After column chromatography (*n*-Hex/EtOAc = 20/1), **53d** (3.60 g, 6.34 mmol, 69%) was obtained as a colorless foam.

R_f: 0.34 (*n*-Hex/EtOAc = 20/1) [CAM].

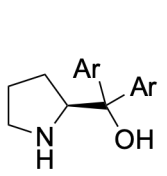
^{1}H NMR (400 MHz, $CDCl_3$): δ/ppm = 7.66 (d, J = 1.8 H, 2H), 7.47 (d, J = 1.8 Hz, 2H), 7.21 – 7.14 (m, 4H), 7.14 – 7.11 (m, 1H), 7.00 – 6.96 (m, 2H), 4.90 (s, 1H), 3.99 (dd, J = 9.3, 4.7 Hz, 1H), 3.17 (d, J = 12.7 Hz, 1H), 2.98 (d, J = 12.7, 1H), 2.94 – 2.87 (m, 1H), 2.40 – 2.29 (m, 1H), 1.92 – 1.80 (m, 1H), 1.72 – 1.57 (m, 3H), 1.31 (s, 18H), 1.26 (s,18H).

^{13}C{^{1}H} NMR (101 MHz, $CDCl_3$): δ/ppm = 150.1 (C), 149.9 (C), 147.6 (C), 146.1 (C), 140.4 (C), 128.7 (CH), 128.1 (CH), 126.8 (CH), 120.3 (CH), 119.9 (CH), 119.9 (CH), 119.8 (CH), 78.4 (COH), 71.9 (CH), 60.5 (CH_2), 55.8 (CH_2), 35.1 (C), 35.0 (C), 31.7 (CH_3), 31.7 (CH_3), 29.8 (CH_3), 24.3 (CH_2).

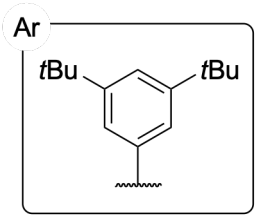
HRMS (ESI): calcd for $C_{40}H_{57}NO$ $[M+H]^+$: 568.4513; found: 568.4517.

The NMR data are in accordance with those reported in the literature.[87]

(*S*)-Bis(3,5-di-*t*butylphenyl)(pyrrolidin-2-yl)methanol (22d):



22d



Using GP5, (*S*)-(1-benzylpyrrolidin-2-yl)bis(3,5-di-^{t}buylphenyl)methanol (**53d**) (500 mg, 880 µmol, 1.00 equiv.) was converted with Pd/C (187 mg, 10 wt%, 176 µmol, 0.20 equiv.) and TFA (100 mg, 880 µmol, 1.00 equiv.) under H_2 atmosphere for 48 h. After work up and recrystallization (*n*-Hex) **22d** (390 mg, 816 µmol, 93 %) was obtained as a colorless solid.

R_f: 0.12 (*n*-Hex/EtOAc = 3/1) [CAM].

^{1}H NMR (400 MHz, $CDCl_3$): δ/ppm = 7.46 (d, J = 1.8 Hz, 2H), 7.37 (d, J = 1.8 Hz, 2H), 7.20 (t, J = 1.8 Hz, 1H), 7.19 (t, J = 1.8 Hz, 1H), 4.24 (t, J = 7.7 Hz, 1H), 3.06 – 2.87 (m, 2H), 1.77 – 1.51 (m, 6H), 1.29 (s, 18H), 1.29 (s, 18H).

^{13}C{^{1}H} NMR (101 MHz, $CDCl_3$): δ/ppm = 150.1 (C), 149.8 (C), 144.7 (C), 120.2 (CH), 120.1 (CH), 120.0 (CH), 120.0 (CH), 77.7 (COH), 46.9 (CH_2), 35.1 (C) , 35.0 (C), 31.7 (CH_3), 31.7 (CH_3), 26.5 (CH_2), 25.6 (CH_2).

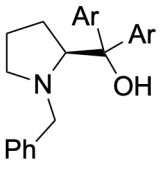
HRMS (ESI): calcd for $C_{33}H_{51}NO$ $[M+H]^+$: 478.4044; found: 478.4049.

EA (%):

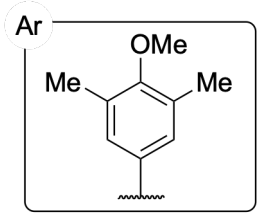
	C	H	N
calculated	82.96	10.76	2.93
determined	82.53	10.20	2.73

The NMR data are in accordance with those reported in the literature.[87]

(*S*)-(1-Benzylpyrrolidin-2-yl)bis(3,5-dimethyl-4-methoxyphenyl)methanol (53e):



53e



Using GP3, (*S*)-methyl-1-benzylpyrrolidine-2-carboxylate (**52**) (2.00 g, 9.12 mmol, 1.00 equiv.) was converted with 1-bromo-3,5-dimethyl-4-methoxybenzene (4.90 g, 22.8 mmol, 2.50 equiv.) and magnesium (554 mg, 22.8 mmol, 2.50 equiv.) at room temperature for 20 h. After column chromatography (*n*-Hex/EtOAc = 10/1), **53e** (1.65 g, 3.59 mmol, 39%) was obtained as a colorless foam.

R_f: 0.20 (*n*-Hex/EtOAc = 9/1) [CAM].

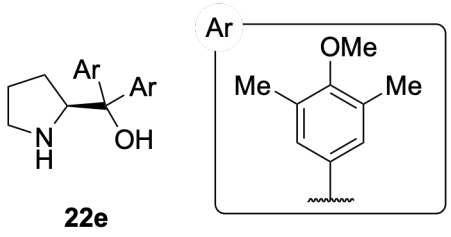
^{1}H NMR (400 MHz, $CDCl_3$): *δ*/ppm = 7.27 (s, 2H), 7.25 – 7.15 (m, 5H), 7.04 – 7.00 (m, 2H), 4.71 (s, 1H), 3.83 (dd, *J* = 9.5, 4.5 Hz, 1H), 3.67 (s, 3H), 3.58 (s, 3H), 3.15 (d, *J* = 12.8 Hz, 1H), 3.03 (d, *J* = 12.8 Hz, 1H), 2.96 – 2.89 (m, 1H), 2.39 – 2.30 (m, 2H), 2.27 (s, 6H), 2.21 (s, 6H), 1.98 – 1.87 (m, 1H), 1.78 – 1.68 (m, 1H), 1.68 – 1.59 (m, 2H).

^{13}C{^{1}H} NMR (101 MHz, $CDCl_3$): *δ*/ppm = 155.5 (C), 155.4 (C), 143.2 (C), 141.9 (C), 140.1 (C), 130.2 (CH), 130.2 (CH), 128.7 (CH), 128.2 (CH), 126.9 (CH), 126.3 (CH), 126.2 (CH), 77.7 (COH), 71.1 (CH), 60.8 (CH_2), 59.8 (CH_3), 59.7 (CH_3), 55.9 (CH_2), 30.0 (CH_2), 24.5 (CH_2), 16.6 (CH_3), 16.5 (CH_3).

HRMS (ESI): calcd for $C_{30}H_{37}NO_3$ $[M+H]^+$: 460.2846; found: 460.2849.

The NMR data are in accordance with those reported in the literature.[87]

(*S*)-Bis(3,5-dimethyl-4-methoxyphenyl)(pyrrolidin-2-yl)methanol (**22e**):



22e

Using GP5, (*S*)-(1-Benzylpyrrolidin-2-yl)bis(3,5-dimethyl-4-methoxy-phenyl)methanol (**53e**) (500 mg, 1.09 mmol, 1.00 equiv.) was converted with Pd/C (231 mg, 10 wt%, 217 µmol, 0.20 equiv.) and TFA (124 mg, 1.09 mmol, 1.00 equiv.) under H_2 atmosphere in 24 h. After column chromatography (CH_2Cl_2/MeOH = 9/1), **22e** (354 mg, 958 µmol, 88 %) was obtained as a solid.

R_f: 0.20 (CH_2Cl_2/MeOH = 9/1) [CAM].

^{1}H NMR (400 MHz, $CDCl_3$): *δ*/ppm = 7.18 (s, 2H), 7.04 (s, 2H), 4.51 (t, *J* = 8.1 Hz, 1H), 3.64 (d, *J* = 1.7 Hz, 6H), 2.81 – 2.73 (m, 1H), 2.67 – 2.57 (m, 1H), 2.21 (s, 12H), 1.98 – 1.87 (m, 1H), 1.86 – 1.65 (m, 2H), 1.61 – 1.51 (m, 1H).

^{13}C {*1H*} NMR (101 MHz, $CDCl_3$): *δ*/ppm = 156.2 (C), 155.8 (C), 140.4 (C), 139.8 (C), 130.8 (C), 130.5 (C), 126.5 (CH), 125.7 (CH), 76.8 (COH), 65.7 (CH), 59.7 (CH_3), 59.6 (CH_3), 46.4 (CH_2), 26.6 (CH_2), 25.1 (CH_2), 16.5 (CH_3), 16.3 (CH_3).

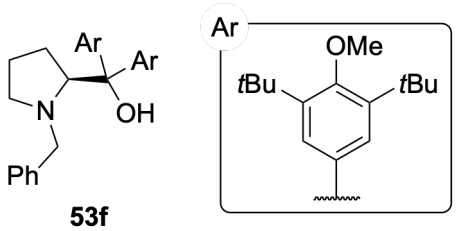
HRMS (ESI): calcd for $C_{23}H_{31}NO_3$ $[M+H]^+$: 370.2376; found: 370.2381.

EA (%):

	C	H	N
calculated	74.76	8.46	3.79
determined	74.30	8.14	3.62

The NMR data are in accordance with those reported in the literature.[87]

(*S*)-Bis(3,5-di-*t*butyl-4-methoxyphenyl)(pyrrolidin-2-yl)methanol (53f):



53f

Using GP3, (*S*)-methyl-1-benzylpyrrolidine-2-carboxylate (**52**) (2.00 g, 9.12 mmol, 1.00 equiv.) was converted with 1-Bromo-3,5-di-*tert*-butyl-4-methoxybenzene (6.82 g, 22.8 mmol, 2.50 equiv.) and magnesium (554 mg, 22.8 mmol, 2.50 equiv.) for 20 h at room temperature. After column chromatography (*n*-Hex/EtOAc = 9/1), **53f** (4.21 g, 6.70 mmol, 74%) was obtained as a colorless foam.

R_f: 0.57 (*n*-Hex/EtOAc = 9/1) [CAM].

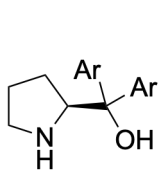
^{1}H NMR (400 MHz, $CDCl_3$): δ/ppm = 7.40 (s, 2H), 7.07 – 6.93 (m, 4H), 6.81 – 6.75 (m, 3H), 4.45 (s, 1H), 3.68 (dd, J = 9.3, 4.6 Hz, 1H), 3.43 (s, 3H), 3.29 (s, 3H), 2.92 (d, J = 12.9 Hz, 1H), 2.84 (d, J = 12.9 Hz, 1H), 2.77 – 2.71 (m, 1H), 1.72 – 1.60 (m, 1H), 3.54 – 1.38 (m, 3H), 1.23 (s, 18H), 1.18 (s, 18H).

^{13}C{^{1}H} NMR (101 MHz, $CDCl_3$): δ/ppm = 157.9 (C), 157.6 (C), 142.6 (C), 142.5 (C), 142.0 (C), 140.6 (C), 140.3 (C), 128.5 (CH), 128.1 (CH), 126.8 (CH), 126.6 (CH), 124.3 (CH), 124.0 (CH), 78.2 (COH), 72.0 (CH), 64.3 (CH_3), 64.2 (CH_3), 60.5 (CH_2), 55.8 (CH_2), 36.0 (CH_3), 36.0 (CH_2), 32.4 (CH_2), 32.3 (CH_3), 32.0 (CH_3), 29.7 (CH_2), 24.5 (CH_2).

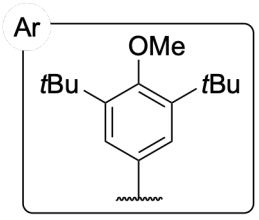
HRMS (ESI): calcd for $C_{42}H_{61}NO_3$ $[M+H]^+$: 628.4724; found: 628.4724.

The NMR data are in accordance with those reported in the literature.[87]

(*S*)-Bis(3,5-di-*t*butyl-4-methoxyphenyl)(pyrrolidin-2-yl)methanol (22f):



22f



Using GP5, (*S*)-bis(3,5-di-tbutyl-4-methoxyphenyl)(pyrrolidin-2-yl)methanol (**53f**) (500 mg, 796 µmol, 1.00 equiv.) was converted with Pd/C (169 mg, 10 wt%, 159 µmol, 0.20 equiv.) and TFA (90.7 mg, 796 µmol, 1.00 equiv.) under H_2 atmosphere for 24 h. After work up and column chromatography (CH_2Cl_2/MeOH = 9/1) **22f** (336 mg, 624 µmol, 78 %) was obtained as a colorless solid

R_f: 0.51 (CH_2Cl_2/MeOH= 9/1) [CAM].

^{1}H NMR (400 MHz, $CDCl_3$): δ/ppm = 7.47 (s, 2H), 7.31 (s, 2H), 4.63 (t, J = 8.2 Hz, 1H), 3.56 (d, J = 2.1 Hz, 6H), 2.76 – 2.54 (m, 2H), 1.84 – 1.52 (m, 4H), 1.40 (s, 18H), 1.35 (s, 18H), 1.26 – 1.17 (m, 1H).

^{13}C{^{1}H} NMR (101 MHz, $CDCl_3$): δ/ppm = 159.0 (C), 158.2 (C), 143.6 (C), 143.1 (C), 138.0 (C), 137.7 (C), 124.3 (CH), 123.6 (CH), 77.8 (COH), 72.0 (CH), 66.2 (CH), 64.2 (CH_3), 64.1 (CH_3), 46.5 (CH_2), 36.1 (CH_3), 36.0 (CH_3), 32.3 (CH_3), 32.2 (CH_3), 26.8 (CH_2), 24.9 (CH_2).

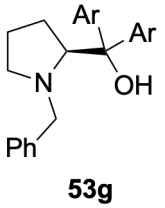
HRMS (ESI): calcd for $C_{35}H_{55}NO^3$ $[M+H]^+$: 538.4255; found: 538.4251.

EA (%):

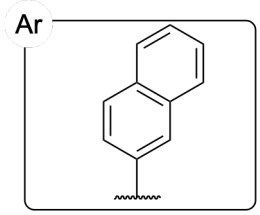
	C	H	N
calculated	78.16	10.31	2.60
determined	77.99	10.01	2.32

The NMR data are in accordance with those reported in the literature.[87]

(*S*)-(1-Benzylpyrrolidin-2-yl)dinaphthylmethanol (53g):



53g



Using GP3, (*S*)-methyl-1-benzylpyrrolidine-2-carboxylate (**52**) (2.00 g, 9.12 mmol, 1.00 equiv.) was converted with 2-bromonaphthalene (4.72 g, 22.8 mmol, 2.50 equiv.) and magnesium (554 mg, 22.8 mmol, 2.50 equiv.) at room temperature in 20 h. After column chromatography (*n*-Hex/EtOAc = 40/1), **53g** (2.20 g, 4.96 mmol, 54%) was obtained as a colorless foam.

R_f: 0.23 (*n*-Hex/EtOAc = 40/1) [CAM].

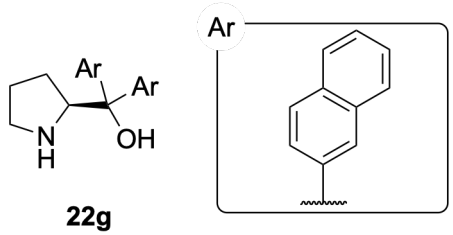
^{1}H NMR (400 MHz, $CDCl_3$): *δ*/ppm = 8.37 – 8.34 (m, 1H), 8.14 – 8.10 (m, 1H), 7.90 – 7.64 (m, 8H), 7.49 – 7.29 (m, 4H), 7.22 – 7.08 (m, 3H), 7.03 – 6.97 (m, 2H), 4.25 (dd, *J* = 9.4, 4.8 Hz, 1H), 3.20 (dd, *J* = 91.3, 12.6 Hz, 2H), 3.01 – 2.94 (m, 1H), 2.48 – 2.38 (m, 1H), 2.13 – 2.01 (m, 1H), 1.94 – 1.84 (m, 1H), 1.78 – 1.63 (m, 2H).

^{13}C{^{1}H} NMR (101 MHz, $CDCl_3$): *δ*/ppm = 145.4 (C), 144.0 (C), 139.6 (C), 133.4 (C), 133.3 (C), 132.2 (C),128.7 (CH), 128.4 (CH), 128.3 (CH), 128.2 (CH), 128.0 (CH), 127.9 (CH), 127.9 (CH), 127.6 (CH), 127.6 (CH), 127.0 (CH), 126.2 (CH), 126.0 (CH), 125.8 (CH), 125.8 (CH), 124.6 (CH), 124.5 (CH), 124.3 (CH), 124.1 (CH), 78.5 (COH), 70.2 (CH), 60.7 (CH_2), 60.6 (CH_2), 55.7 (CH_2), 30.1 (CH_2), 24.3 (CH_2).

HRMS (ESI): calcd for $C_{32}H_{29}NO$ $[M+H]^+$: 444.2322 ; found: 444.2321.

The NMR data are in accordance with those reported in the literature.[87]

(*S*)-Dinaphthalenyl-2-pyrrolidinemethanol (**22g**):



22g

Using GP5, (*S*)-(1-benzylpyrrolidin-2-yl)dinaphthylmethanol (**53g**) (500 mg, 1.13 mmol, 1.00 equiv.) was converted with Pd/C (239 mg, 10 wt%, 225µmol, 0.20 equiv.) and TFA (128 mg, 1.13 mmol, 1.00 equiv.) under H_2 atmosphere for 48 h. After work up and recrystallization (*n*-Hex) **22g** (340 mg, 961 µmol, 85 %) was obtained as a colorless solid.

R_f: 0.21 (*n*-Hex/EtOAc = 1/1) [CAM].

^{1}H NMR (400 MHz, $CDCl_3$): *δ*/ppm = 8.10 – 8.08 (m, 2H), 7.87 – 7.83 (m, 2H), 7.77 – 7.66 (m, 5H), 7.58 (dd, *J* = 8.7, 1.8 Hz, 1H), 7.48 – 7.38 (m, 4H), 4.52 (t, *J* = 7.5 Hz, 1H), 3.10 – 3.05 (m, 1H), 3.04 – 2.99 (m, 1H), 1.82 – 1.71 (m, 3H), 1.66- 1.60 (m, 1H).

^{13}C{^{1}H} NMR (101MHz, $CDCl_3$): *δ*/ppm = 145.5 (C), 142.8 (C), 133.3 (C), 133.2 (C), 132.4 (C), 132.3 (C), 128.4 (CH), 128.3 (CH), 128.2 (CH), 127.8 (CH), 127.6 (CH), 126.2 (CH), 126.0 (CH), 125.9 (CH), 125.8 (CH), 125.4 (CH), 124.5 (CH), 124.1 (CH), 123.9 (CH), 77.7 (COH), 64.1 (CH), 47.0 (CH_2), 26.6 (CH_2), 25.7 (CH_2).

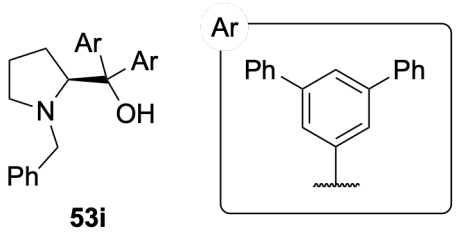
HRMS (ESI): calcd for $C_{25}H_{23}NO$ $[M+H]^+$: 354.1852; found: 354.1855.

EA (%):

	C	H	N
calculated	84.95	6.56	3.96
determined	84.77	6.24	3.82

The NMR data are in accordance with those reported in the literature.[87]

(*S*)-(1-Benzylpyrrolidin-2-yl)bis(3,5-diphenyl)methanol (53i)



53i

Using GP4, (*S*)-methyl-1-benzylpyrrolidine-2-carboxylate (**52**) (2.00 g, 9.12 mmol, 1.00 equiv.) was converted with 1-bromo-3,5-diphenylbenzene (7.05 g, 22.8 mmol, 2.50 equiv.) and magnesium (554 mg, 22.8 mmol, 2.50 equiv.) refluxed for 24 h. After column chromatography (PE35-70/EtOAc = 9/1), **53i** (2.50 g, 3.86 mmol, 42 %) was obtained as a colorless foam.

R_f: 0.20 (PE35-70/EtOAc = 10:1) [CAM].

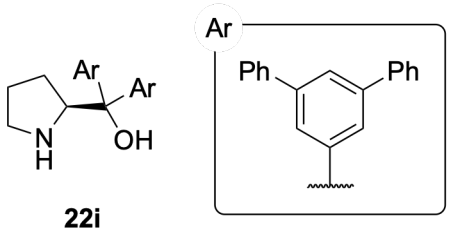
^{1}H NMR (400 MHz, $CDCl_3$): δ/ppm = 8.03 (d, J = 1.7 Hz, 2H), 7.89 (d, J = 1.7 Hz, 2H), 7.68 – 7.56 (m, 10H), 7.48 – 7.41 (m, 8H), 7.39 – 7.32 (m, 4H), 7.20 – 7.13 (m, 3H), 7.07 – 7.02 (m, 2H), 5.12 (s, 1H), 4.21 (dd, J = 9.3, 4.8 Hz, 1H), 3.46 (d, J = 12.7 Hz, 1H), 3.17 (d, J = 12.7 Hz, 1H), 3.05 – 2.98 (m, 1H), 2.49 – 2.40 (m, 1H), 2.14 – 2.02 (m, 1H), 1.98 – 1.88 (m, 1H), 1.79 – 1.64 (m, 2H).

^{13}C{^{1}H} NMR (101 MHz, $CDCl_3$): δ/ppm = 149.2 (C), 147.7 (C), 141.9 (C), 141.7 (C), 141.6 (C), 141.6 (C), 139.7 (C), 128.9 (CH), 128.9 (CH), 128.9 (CH), 128.7 (CH), 128.3 (CH), 127.6 (CH), 127.6 (CH), 127.5 (CH), 127.5 (CH), 127.0 (CH), 124.8 (CH), 124.5 (CH), 124.0 (CH), 123.9 (CH), 78.4 (COH), 71.2 (CH_2), 60.9 (CH_3), 55.9 (CH_3), 30.2 (CH_3), 24.4 (CH_3).

HRMS (ESI): calcd for $C_{48}H_{41}NO$ $[M+H]^+$: 648.3261; found: 648.3266.

The NMR data are in accordance with those reported in the literature.[203]

(*S*)-Bis(3,5- diphenyl)(pyrrolidin-2-yl)methanol (**22i**):



22i

Using GP5, (*S*)-(1-benzylpyrrolidin-2-yl)bis(3,5-diphenyl)methanol (**53i**) (500 mg, 771 µmol, 1.00 equiv.) was converted with Pd/C (164 mg, 10 wt%, 154 µmol, 0.20 equiv.) and TFA (88.0 mg, 711 µmol, 1.00 equiv.) under H_2 atmosphere for 48 h. After RP-HPLC (Eurospher II C18H, 1.0 mL min^{-1}, 95% MeOH, 5% H_2O, 0.05 M acetic acid, retention time = 6.65 min) **22i** (410 mg, 735 µmol, 95%) was obtained as a colorless solid.

R_f: 0.23 (EtOAc) [CAM].

^{1}H NMR (400 MHz, $CDCl_3$): δ/ppm = 7.90 (d, J = 1.7 Hz, 2 H), 7.82 (d, J = 1.7 Hz, 2H), 7.69 – 7.59 (m, 10H), 7.50 – 7.42 (m, 8H), 7.40 – 7.33 (m, 4H), 4.52 (t, J = 6.7 Hz, 1H), 3.08 – 2.88 (m, 2H), 1.88 – 1.65 (m, 4H).

^{13}C{^{1}H} NMR (101 MHz, $CDCl_3$): δ/ppm = 146.3 (C), 142.0 (C), 141.9 (C), 141.7 (C), 141.5 (C), 141.4 (C), 128.9 (CH), 128.9 (CH), 127.6 (CH), 127.5 (CH), 127.5 (CH), 127.5 (CH), 127.4 (CH), 124.9 (CH), 124.7 (CH), 124.0 (CH), 123.6 (CH), 77.6 (COH), 64.9 (CH_2), 47.0 (CH_3), 26.8 (CH_3), 25.6 (CH_3).

HRMS (ESI): calcd for $C_{41}H_{35}NO$ $[M+H]^+$: 558.2791; found: 558.2796.

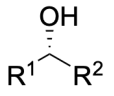
EA (%):

	C	**H**	**N**
calculated	88.29	6.33	2.51
determined	88.14	6.22	2.41

The NMR data are in accordance with those reported in the literature.[203]

6.3.4 Reduction Reaction Procedure

GP6: Catalytic Reduction of Ketones (Previous Version for All Ketones)

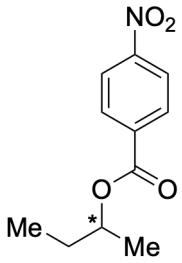


The amino alcohol (0.04 mmol, 0.1 equiv.) was placed in a Schlenk tube. Anhydrous THF (1 mL) and BH_3•SMe_2 (0.44 mmol, 1.1 equiv.) were added, and the mixture was stirred at 50 °C for 1 h. A solution of the ketone (0.40 mmol, 1.0 equiv. in 0.5 mL THF) was then slowly added via a syringe pump over a period of 30 min, after which the reaction mixture was stirred for an additional 120 min at 50 °C. To quench the reaction, 0.5 M citric acid (6.0 mL) was added, and the mixture was extracted with EtOAc (3 × 5 mL). The combined organic layers were washed with brine and dried over Na_2SO_4. After filtration, the solvent was removed under reduced pressure. Using GP2 some alcohols were further derivatized and the crude product was analyzed. This reduction procedure was repeated three to five times.

6.4 Part II

6.4.1 Synthesis and Analysis of Racemates

***Sec*-butyl 4-nitrobenzoate** (rac-**85a**):



rac-**85a**

Butan-2-ol (rac-**67**) (500 mg, 6.75 mmol, 1.0 equiv.) was dissolved in CH_2Cl_2 (3 mL) and 4-nitrobenzoyl chloride (1.38 g, 7.42 mmol, 1.1 equiv.) together with DMAP (82.4 mg, 674 µmol, 0.1 equiv.) and NEt_3 (1.02 g, 10.1 mmol, 1.5 equiv.) was added to the solution and stirred at room temperature for 12 h. The reaction was quenched with 1M HCl (4 mL), extracted with CH_2Cl_2 (3 x 4 mL), washed with brine (5 mL) and dried over Na_2SO_4. The crude was then purified by column chromatography (*n*-Hex/EtOAc = 3/1) to obtain rac-**85a** (755 mg, 3.38 mmol, 50%) as a yellow solid.

R_f: 0.65 (*n*-Hex/EtOAc = 3/1).

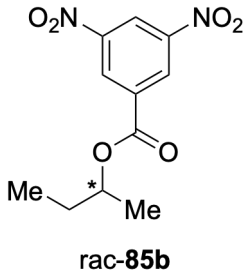
^{1}H NMR (400 MHz, $CDCl_3$): δ/ppm = 8.30 – 7.24 (m, 2H), 8.22 – 8.17 (m, 2H), 6.51 (sext, *J* = 6.3 Hz, 1H) 4.84 (sext, J = 6.3 Hz, 1H), 1.85 – 1.58 (m, 2H), 1.36 (d, *J* = 6.3 Hz, 3H), 0.98 (t, *J* = 7.4 Hz, 3H).

^{13}C{^{1}H} NMR (101 MHz, $CDCl_3$): δ/ppm = 164.4 (C), 150.5 (C), 136.4 (C), 130.7 (CH), 123.6 (CH), 74.3 (CH), 29.0 (CH_2), 19.6 (CH_3), 9.8 (CH_3).

HRMS (ESI): calcd for $C_{11}H_{13}NO_4$ $[M+H]^+$: 224.0917; found: 224.0922.

The NMR data are in accordance with those reported in the literature.[204]

***Sec*-butyl 3,5-dinitrobenzoate** (rac-**85b**):



rac-**85b**

Butan-2-ol (rac-**67**) (500 mg, 6.75 mmol, 1.0 equiv.) was dissolved in CH_2Cl_2 (4 mL) and 3,5-nitrobenzoyl chloride (1.71 g, 7.42 mmol, 1.1 equiv.) together with DMAP (82.4 mg, 674 µmol, 0.1 equiv.) and NEt_3 (1.02 g, 10.1 mmol, 1.5. equiv.) was added to the solution and stirred at room temperature for 12 h. The reaction was quenched with 1M HCl (4 mL), extracted with CH_2Cl_2 (3 x 4 mL), washed with brine (5 mL) and dried over Na_2SO_4. The crude was then purified by

column chromatography (*n*-Hex/EtOAc = 3/1) to obtain rac-**85b** (698 mg, 2.60 mmol, 38%) as a yellow solid.

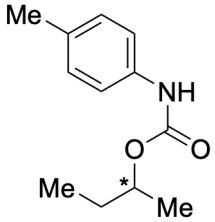
R_f: 0.66 (*n*-Hex/EtOAc = 3/1)

^{1}H NMR (400 MHz, $CDCl_3$): δ/ppm = 9.22 (t, J = 2.1 Hz, 1H), 9.15 (d, J = 2.2 Hz, 2H), 5.21 (sext, J = 6.3 Hz, 1H) 4.84 (sext, J = 6.3 Hz, 1H), 1.87 – 1.67 (m, 2H), 1.41 (d, J = 6.3 Hz, 3H), 1.00 (t, J = 7.4 Hz, 3H).

^{13}C{^{1}H} NMR (101 MHz, $CDCl_3$): δ/ppm = 162.3 (C), 148.6 (C), 134.7 (C), 129.5 (C), 122.3 (CH), 75.9 (CH), 26.9 (CH_2), 19.6 (CH_3), 9.9 (CH_3).

HRMS (ESI): calcd for $C_{11}H_{12}N_2O_6$ $[M+H]^+$: 269.0768; found: 269.0771.

Sec-butyl *p*-tolylcarbamate (rac-**85c**):



rac-**85c**

Butan-2-ol (rac-**67**) (500 mg, 6.75 mmol, 1.0 equiv.) was dissolved in CH_2Cl_2 (4 mL) and 1-isocyanato-4-methylbenzene (2.69 g, 20.2 mmol, 3.0 equiv.) together with DMAP (82.4 mg, 674 µmol, 0.1 equiv.) were added to the solution and stirred at room temperature for 12 h. The reaction was quenched with 1M HCl (4 mL), extracted with CH_2Cl_2 (3 x 4 mL), washed with brine (5 mL) and dried over Na_2SO_4. The crude was then purified by column chromatography (*n*-Hex/EtOAc = 3/1) to obtain rac-**85c** (897 mg, 4.33 mmol, 64%) as a colorless liquid.

R_f: 0.62 (*n*-Hex/EtOAc = 3/1)

Chiral HPLC:

Column:	Chiralpak IB
Flow Rate:	1.3 mL min^{-1}
Run Time:	20 min
Mobile Phase:	80% *n*-Hex. 10% IPA, 10% IPA, 10% TBME
Wavelength:	270 nm
Retention time:	(*R*) = 3.74 min (*S*) = 4.38 min

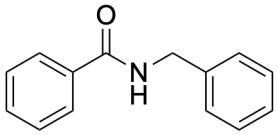
^{1}H NMR (400 MHz, $CDCl_3$): δ/ppm = 7.31 – 7.22 (m, 2H), 7.13 – 7.05 (m, 2H), 6.51 (bs, 1H) 4.84 (sext, J = 6.3 Hz, 1H), 2.30 (s, 3H), 1.71– 1.49 (m, 2H), 1.26 (d, J = 6.3 Hz, 3H), 0.94 (t, J = 7.4 Hz, 3H).

$^{13}C\{^{1}H\}$ NMR (101 MHz, $CDCl_3$): δ/ppm = 153.7 (C), 135.7 (C), 132.9 (C), 129.6 (CH), 118.8 (CH), 73.3 (CH), 29.2 (CH_2), 20.9 (CH_3), 19.6 (CH_3), 9.8 (CH_3).

HRMS (ESI): calcd for $C_{12}H_{17}NO_2$ $[M+H]^+$: 208.1332; found: 208.1333.

6.4.2 Synthesis of the Titration Reagent for *n*-BuLi

***N*-Benzylbenzamide** (**143**):



143

BzCl (6.56 g, 46.6 mmol, 1.0 equiv.) was added at room temperature to a solution of benzylamine (5.00 g, 46.6 mmol, 1.0 equiv.) and NEt_3 (7.08 g, 69.9 mmol, 1.5 equiv.) in 100 mL CH_2Cl_2. The reaction mixture was stirred for 2 h and then washed with 1M HCl (2 x 25 mL) and brine (25 mL). The organic layer was dried over Na_2SO_4 and the solvent was removed under reduced pressure. The residue was recrystallized from 40 mL *n*-Hex/EtOAc (1:1) to afford **143** (7.49 g, 35.4 mmol, 75%) as a colorless powder.

R_f: 0.13 (*n*-Hex/EtOAc = 3/1)

^{1}H NMR (400 MHz, $CDCl_3$): δ/ppm = 7.76 – 7.70 (m, 2 H), 7.45 – 7.39 (m, 1 H), 7.36 – 7.29 (m, 2 H), 7.28 – 7.18 (m, 5 H), 4.53 (d, J = 5.8 Hz, 2 H).

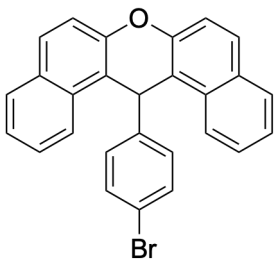
^{13}C {*1H*} NMR (101 MHz, $CDCl_3$): δ/ppm = 167.7 (C), 138.3 (C), 134.4 (C), 131.5 (CH), 128.7 (CH), 128.6 (CH), 127.9 (CH), 127.5 (CH), 127.1 (CH), 44.1 (CH_2).

HRMS (ESI): calcd for $C_{14}H_{13}NO$ $[M+H]^+$: 212.1069; found: 212.1075

The NMR data are in accordance with those reported in the literature.[205]

6.4.3 Synthesis of Brominated Aryl Compounds

14-(4-Bromophenyl)-14*H*-dibenzo[a,j]xanthene (69):



69

A mixture of 2-naphthol (**71**) (2.00 g, 13.8 mmol, 2.0 equiv.), 4-bromobenzaldehyde (**70**) (1.28 g, 6.94 mmol, 1.0 equiv.), and *p*-TsOH (132 mg, 0.06 mmol, 0.1 equiv.) in 1,2-dichlorethane was stirred at 100 °C for 12 h. The solvent was removed under reduced pressure, and the residue was washed with a 3:1 mixture of H_2O/EtOH. The resulting solid was then refluxed in EtOH, filtered and dried to afford **69** (2.80 g, 6.40 mmol, 92%) as a light purple powder.

R_f: 0.55 (*n*-Hex/EtOAc = 3/1).

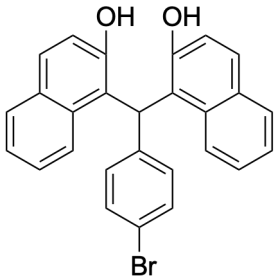
^{1}H NMR (400 MHz, $CDCl_3$): *δ*/ppm = 8.30 (d, J = 8.5 Hz 2 H), 7.87 – 7.75 (m, 4 H), 7.61 – 7.53 (m, 2 H), 7.47 (d, *J* = 8.9 Hz, 1 H), 7.44 – 7.36 (m, 4 H) 7.27 – 7.22 (m, 2 H), 6.45 (s, 1H).

^{13}C{^{1}H} NMR (101 MHz, $CDCl_3$): *δ*/ppm = 148.8 (C), 144.1 (C), 131.7 (CH), 131.4 (CH), 131.2 (CH), 130.0 (CH), 129.2 (CH), 129.0 (CH), 127.1 (CH), 124.5 (CH), 122.5 (CH), 120.3 (CH), 118.1 (CH), 116.8 (CH), 37.6 (C).

HRMS (ESI): calcd for $C_{27}H_{17}BrO$ $[M+H]^+$: 437.0536; found: 437.0539.

IR (ATR, cm $^{-1}$): 3066 (w), 1620, (m), 1589 (m), 1512 (m), 1480 (m), 1235 (s, C-O-C), 824 (s), 738 (s).

1,1'-((4-Bromophenyl)methylene)bis(naphthalen-2-ol) (76):



76

2-Naphthol (**71**) (3.00 g, 20.8 mmol, 2.0 equiv.) and 4-bromobenzaldehyde (**70**) (1.92 g, 10.4 mmol, 1.0 equiv.) were dissolved in a (1:1) mixture of conc. HCl and EtOH (10 mL) and stirred at room temperature for 48 h. Subsequently, saturated $NaHCO_3$ solution (10 mL) was added, and the mixture was extracted with EtOAc (3 x 10 mL). The combined organic phases were washed with brine (10 mL) and dried over Na_2SO_4. The solvent was removed under reduced pressure, and the residue was recrystallized from *n*-Hex to afford **76** (1.47 g, 3.23 mmol, 31%) as a solid.

R_f: 0.26 (*n*-Hex/EtOAc = 3/1).

^{1}H NMR (400 MHz, $CDCl_3$): δ/ppm = 7.91 – 7.85 (m, 2H), 7.84 – 7.78 (m, 2H), 7.74 (d, *J* = 8.8 Hz, 2H), 7.45 – 7.31 (m, 6H), 7.15 – 7.06 (m, 2H), 7.07 – 6.99 (m, 3H), 6.04 (bs, 2H).

^{13}C{^{1}H} NMR (101 MHz, $CDCl_3$): δ/ppm = 152.7 (C), 140.1 (C), 133.6 (C), 132.5 (CH), 130.3 (C), 130.1 (CH), 130.0 (CH), 129.2 (CH), 127.6 (CH), 123.7 (CH), 122.5 (CH), 121.2 (CH), 119.8 (CH), 118.3 (CH).

HRMS (ESI): calcd for $C_{27}H_{19}BrO_2$ $[M+Na]^+$: 477.0460; found: 477.0466.

IR (ATR, cm $^{-1}$): 3218 (br), 1597 (m), 1582, (m), 1514 (m), 1482 (m), 1436 (m), 1234 (s), 1173 (s), 812 (s), 745 (s).

6.4.4 Synthesis of Catalyst Precursor

GP7: Halogen-Lithium Exchange and Nucleophilic Addition to Carbonyl

Aryl bromide (2.5 equiv.) was dissolved in anhydrous THF under argon at –78 °C. Then *n*-BuLi (2.3 equiv.) was added and the reaction mixture was stirred for 10 min at –78 °C. A solution of methyl-1-(4-methoxybenzyl)pyrrolidine-2-carboxylate **77** (1.0 equiv) in THF was added dropwise at –78 °C and stirred at room temperature for the appropriate amount of time monitored by mass spectrometry. At 0 °C, sat. NH_4Cl solution was added to quench the reaction. Afterwards the mixture was extracted three times with EtOAc. The combined organic layers were washed with brine and dried over $NaSO_4$. After removing the solvent, the crude product was purified by preparative HPLC.

GP8: Cleavage of the PMB Protecting Group (1)

The PMB-protected prolinol (**79**) (1.0 equiv.) was dissolved in a mixture of MeOH/ EtOAc (1:1) and moist Pd/C (0.2 equiv., 10-20 wt%) as well as TFA (1.0 equiv.) were added. The reaction flask was purged with H_2 and afterwards the reaction ws stirred at room temperature for 72 h. The mixture was filtered through a pad of Celite and washed with small portions of MeOH. The solvent was removed under reduced pressure, and the residue was dissolved in EtOAc, washed with 2M NaOH and brine and dried over $NaSO_4$.

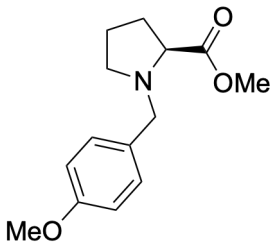
GP9: Cleavage of the PMB Protecting Group (2)

The PMB-protected prolinol (**79**) (1.0 equiv.) was dissolved in CH_2Cl_2 and TFA (5.0 equiv.) was added. The reaction flask was then stirred at room temperature for 24 h. The reaction was quenched with sat. $NaHCO_3$ solution and extracted three times with CH_2Cl_2. The organic phase was then washed with brine and dried over Na_2SO_4.

GP10: Cleavage of the PMB Protecting Group (3)

The PMB-protected prolinol (**79**) (1.0 equiv.) was dissolved in CH_2Cl_2 and DDQ (2.0 equiv.) was added. The reaction flask was then stirred at room temperature for the appropriate time. The reaction was quenched with sat. $NaHCO_3$ solution and extracted three times with CH_2Cl_2. After washing the organic phase with brine and drying over Na_2SO_4 the solvent was removed and the crude was purified *via* preparative HPLC.

(*S*)-Methyl-1-(4-methoxybenzyl)pyrrolidine-2-carboxylate (**77**):



77

Esterification and PMB protection: L-proline (**10**) (2.00 g, 17.3 mmol, 1.0 equiv.) was dissolved in 50 mL MeOH and at 0 °C $SOCl_2$ (5.17 g, 43.4 mmol, 2.5 equiv.) was added dropwise and stirred at room temperature for 24 h. The solvent was removed under reduced pressure and toluene was added and removed under reduced pressure two more times. The crude material was used without further purification for the next step. The crude material was dissolved in 40 mL CH_2Cl_2 and NEt_3 (4.40 g, 43.4 mmol, 2.5 equiv.) was added. After 15 min 4-mehoxybenzyl chloride (**81**) (6.20 g, 43.4 mmol, 2.5 equiv.) was slowly added dropwise at 0 °C. The solution was stirred at room temperature for 12 h and H_2O (20 mL) was added. The aqueous phase was extracted with EtOAc (3 x 25 mL) and the organic phase was washed with brine (25 mL) and dried over Na_2SO_4. The solvent was removed and after column chromatography (*n*-Hex/EtOAc = 5/1) **77** (2.38 g, 9.55 mmol, 54%) was obtained as a yellow oil.

R_f: 0.17 (*n*-Hex/EtOAc = 5/1).

^{1}H NMR (400 MHz, $CDCl_3$): δ/ppm = 7.22 – 7.14 (m, 2H), 6.83 – 6.74 (m, 2H), 3.76 (d, J = 12.7 Hz, 1H), 3.59 (s, 3H), 3.48 (d, J = 12.7 Hz, 3H), 3.17 (dd, J = 8.9, 6.3 Hz, 1H), 2.99 (ddd, J =

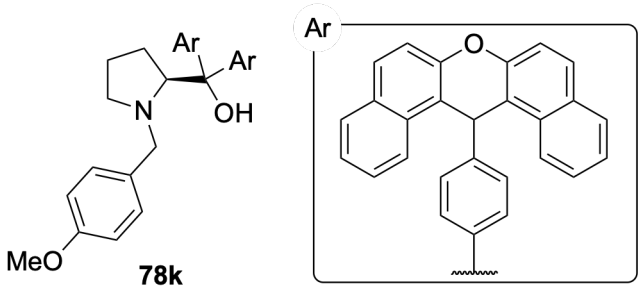
9.6, 7.7, 3.0 Hz, 1H), 2.32 (td, *J* = 8.8, 7.8 Hz, 1H), 2.15 – 2.00 (m, 1H), 1.97 – 1.79 (m, 2H), 1.77 – 1.67 (m, 1H).

^{13}C {*1H*} NMR (101 MHz, $CDCl_3$): *δ*/ppm = 174.4 (C), 158.6 (C), 130.3 (CH) 130.2 (C), 113.4 (CH), 65.0 (CH_2), 57.9 (CH_2), 55.1 (CH_3), 53.0 (CH_2), 51.6 (CH_3), 29.2 (CH_2), 22.8 (CH_2).

HRMS (ESI): calcd for $C_{14}H_{19}NO_3$ $[M+H]^+$: 250.1438; found: 250.1439.

The NMR data are in accordance with those reported in the literature.[206]

(*S*)-Bis(4-(14*H*-dibenzo[a,j]xanthen-14-yl)phenyl)(1-(4-methoxybenzyl)pyrrolidin-2-yl)methanol (**78k**):



78k

Using GP7, 14-(4-bromophenyl)-14*H*-dibenzo[a,j] xanthene **69** (1.00 g, 2.21 mmol, 2.5 equiv.) was dissolved in 16 mL of dry THF, and at −78 °C *n*-BuLi (130 mg, 2.03 mmol, 2.3 equiv.) was slowly added to the solution. After stirring for 10 min at −78 °C, methyl 1-(4-methoxybenzyl)pyrrolidine-2-carboxylate (**77**) (220 mg, 882 µmol, 1.0 equiv.) was added via syringe pump over 30 min. The reaction mixture was allowed to warm to room temperature and stirred for 18 h. After work up and purification via RP-HPLC (Eurospher II C18H, 1mL min^{-1}, 85% MeOH, 15% TBME, 0.5% NH_4Ac, retention time = 8.16 min) **78k** (548 mg, 586 µmol, 66%) was afforded as a colorless solid.

R_f: 0.70 (CH_2Cl_2/MeOH = 9/1).

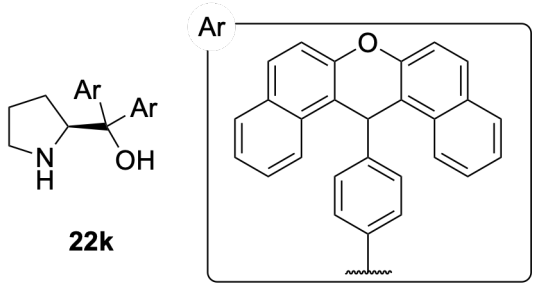
^{1}H NMR (400 MHz, $CDCl_3$): *δ*/ppm = 8.36 – 8.18 (m, 3H), 8.06 (d, *J* = 8.5 Hz, 1H), 7.84 – 7.62 (m, 8H), 7.55 – 7.32 (m, 10H), 7.31 – 7.11 (m, 10H), 7.05 (ddd, *J* = 8.3, 6.8, 1.3 Hz, 1H), 6.54 – 6.45 (m, 2H), 6.43 – 6.35 (m, 2H), 6.31 (s, 1H), 3.80 (s, 3H), 3.38 (dd, *J* = 9.5, 3.3 Hz, 1H), 2.75 – 2.65 (m, 1H), 2.44 (d, *J* = 12.8 Hz, 1H), 2.26 (d, *J* = 12.8 Hz, 1H), 2.11 – 2.00 (m, 1H), 1.64 – 1.48 (m, 1H), 1.41 – 1.23 (m, 3H).

^{13}C{^{1}H} NMR (101 MHz, $CDCl_3$): *δ*/ppm = 158.1 (C), 149.1 (C), 149.1 (C), 148.7 (C), 148.6 (C), 145.5 (C), 143.7 (C), 143.0 (C), 142.6 (C), 131.6 (C), 131.0 (C), 131.0 (C), 131.0 (C), 130.9 (C), 130.9 (C), 129.3 (CH), 128.9 (CH), 128.8 (CH), 128.8 (CH), 128.7 (CH), 128.5 (CH), 128.0 (CH),

127.8 (CH), 126.8 (CH), 126.7 (CH), 126.6 (CH), 126.0 (CH), 126.0 (CH), 124.2 (CH), 124.1 (CH), 122.8 (CH), 122.8 (CH), 122.6 (CH), 122.5 (CH), 118.0 (CH), 117.8 (CH), 117.8 (CH), 117.6 (CH), 117.6 (CH), 117.1 (CH), 117.0 (CH), 113.2 (CH), 77.9 (C), 71.1 (CH), 59.6 (CH_2), 55.6 (CH_2), 55.3 (CH_3), 37.5 (CH), 37.3 (CH), 29.7 (CH_2), 24.3 (CH_2).

HRMS (ESI): calcd for $C_{67}H_{51}NO_4$ $[M+H]^+$: 934.3890; found: 934.3893.

(*S*)-Bis(4-(14*H*-dibenzo9[a,j]xanthen-14-yl)phenyl)8pyrrolidin-2-yl)methanol (**22k**):



22k

Using GP10, (*S*)-bis(4-(14H-dibenzo[a,j]xanthen-14-yl)phenyl)(1-(4-methoxybenzyl)pyrrolidin-2-yl)methanol (**22k**) (500 mg, 535 µmol, 1.0 equiv.) was dissolved in CH_2Cl_2 and DDQ (243 mg, 1.07 mmol, 2.0 equiv.) was added. The reaction mixture was stirred for 40 h. After workup and purification *via* RP-HPLC (Eurospher II C18H, 1 mL min^{-1}, 90% MeOH, 10% TBME, 0.1% TEA, retention time = 14.32 min), **22k** was obtained. The product was further co-evaporated with toluene in an attempt to remove residual solvents. However, complete solvent removal could not be achieved and **22k** (103 mg, approx. 126 µmol, 23%) was obtained as a colorless powder.

R_f: 0.20 (CH_2Cl_2/MeOH = 9/1).

^{1}H NMR (400 MHz, $CDCl_3$): δ/ppm = 8.34 (d, J = 8.6 Hz, 4H), 7.91 – 7.72 (m, 8H), 7.62 – 7.53 (m, 4H), 7.53 – 7.40 (m, 8H), 7.38 – 7.31 (m, 4H), 7.22 – 7.10 (m, 4H), 6.44 (s, 2H), 3.74 (t, J = 7.8 Hz, 1H), 2.85 – 2.73 (m, 1H), 2.72 – 2.64 (m, 1H), 1.54 – 1.41 (m, 2H), 1.36 – 1.26 (m, 1H), 1.23 – 1.12 (m, 1H).

^{13}C{^{1}H} NMR (101 MHz, $CDCl_3$): δ/ppm = 149.0 (C), 149.0 (C), 145.6 (C), 142.7 (C), 142.6 (C), 131.5 (CH), 131.5 (CH), 131.5 (CH), 131.0 (CH), 128.7 (CH), 128.7 (CH), 128.7 (CH), 127.8 (CH), 127.6 (CH), 126.8 (CH), 126.8 (CH), 126.7 (CH), 126.1 (CH), 125.8 (CH), 124.2 (CH), 124.2 (CH), 122.8 (CH), 122.7 (CH), 122.7 (CH), 118.0 (CH), 118.0 (CH), 117.6 (C), 117.5 (CH), 76.6 (C), 64.7 (CH), 46.3 (CH_2), 37.3 (CH), 37.2 (CH), 26.2 (CH_2), 25.1 (CH_2).

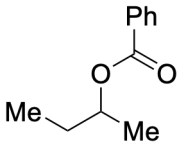
HRMS (ESI): calcd for $C_{59}H_{43}NO_3$ $[M+H]^+$: 814.3315; found: 814.3317.

IR (ATR, cm $^{-1}$): 3314 (w), 3059 (w), 2968 (w), 2871 (w), 1633 (m), 1621 (m), 1592 (m), 1515 (m), 1457 (m), 1432 (m), 1240 (s), 1080 (m), 1018 (m), 804 (s), 741 (s).

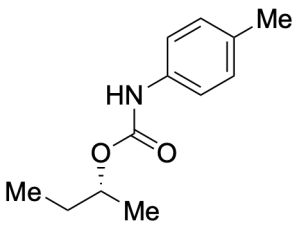
6.4.5 Updated Reduction Reaction Procedure

GP11: Updated Version for the Reduction Reaction of Butan-2-one

The amino alcohol (0.04 mmol, 0.1 equiv.) was placed in a Schlenk tube. Anhydrous THF (1 mL) and BH_3•SMe_2 (0.44 mmol, 1.1 equiv.) were added, and the mixture was stirred at 50 °C for 1 h. A solution of butan-2-one (**67**) (0.40 mmol, 1.0 equiv., in 0.5 mL THF) was then slowly added via syringe pump over a period of 30 min, after which the reaction mixture was stirred for an additional 90 min at 50 °C. The reaction was quenched with water (1.21 mmol, 3.0 equiv.) and subsequently derivatized for HPLC and chiral GC.



85d



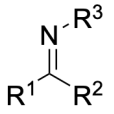
85c

For HPLC analysis, *p*-tolylisocyanate (2.02 mmol, 5.0 equiv.) and DMAP (0.08 mmol, 0.2 equiv.) were added and stirred at room temperature for 12 h. For chiral GC analysis, BzCl (2.02 mmol, 5.0 equiv.), NEt_3 (0.80 mmol, 2.0 equiv.), and DMAP (0.08 mmol, 0.2 equiv.) were added instead and stirred at room temperature for 12 h. The solvent was removed under reduced pressure, and after column chromatography (*n*-Hex/EtOAc) the corresponding derivatized, alcohol was obtained and analyzed by either HPLC or GC as described in the corresponding procedures above.

6.5 Part III

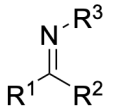
6.5.1 Synthesis of Non-Cyclic and Cyclic Imines

GP12: Synthesis of Non-Cyclic and Cyclic Imines (1)



Molecular sieves (4 Å, beads, 1 g per 1 mmol of ketone) were heated in a two-neck round-bottom flask. The corresponding ketone (1.0 equiv.) and amine (1.0 - 1.1 equiv.) were dissolved in toluene and added to the flask. The reaction mixture was stirred at room temperature for the appropriate time. The reaction was then quenched by addition of sat. $NaHCO_3$, and the aqueous layer was extracted three times with EtOAc. The combined organic layers were washed with brine, dried over Na_2SO_4, and the solvent was removed under reduced pressure. The crude product was further purified either by column chromatography (*n*-Hex/EtOAc with NEt_3) or by fractional distillation to afford the corresponding imine.

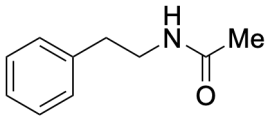
GP13: Synthesis of Non-Cyclic and Cyclic Imines (2)



Molecular sieves (4 Å, beads, 1 g per 1 mmol of ketone) were heated in a two-neck round-bottom flask. The corresponding ketone (1.0 equiv.) and amine (1.1 – 1.5 equiv.) were dissolved in toluene and added to the flask. The reaction mixture was refluxed for the appropriate time. After cooling to room temperature, the reaction was quenched by addition of saturated $NaHCO_3$, and the aqueous layer was extracted three times with EtOAc. The combined organic layers were washed with brine, dried over Na_2SO_4, and the solvent was removed under reduced pressure. The crude product was further purified either by column chromatography (*n*-Hex/EtOAc with NEt_3) or by fractional distillation to afford the corresponding imine.

6.5.1.1 Synthesis of Cyclic Imines

***N*-Phenethylacetamide (89)**:



89

2-Phenylethanamine (**88**) (9.70 g, 80.0 mmol, 1 equiv.) was dissolved in pyridine (8 mL), and Ac_2O (9.81 g, 96.0 mmol, 1.2 equiv.) was added at 0 °C. The reaction mixture was stirred for 3 h at 90 °C and then poured into ice-cold water (10 mL). Subsequently, 1M HCl (3 mL) was added, and the aqueous phase was extracted with EtOAc (3 × 5 mL). The combined organic phases were washed with 8% $NaHCO_3$

solution (5 mL), sat. $CuSO_4$ solution (5 mL), and brine (5 mL), then dried over Na_2SO_4. The solvent was removed and the **89** (10.1 g, 61.9 mmol, 77 %) was obtained as a viscous, colorless liquid.

R_f: 0.10 (*n*-Hex/EtOAc = 5/1).

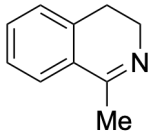
^{1}H NMR (400 MHz, $CDCl_3$): δ/ppm = 7.40 – 7.33 (m, 2H), 7.31 – 7.22 (m, 3H), 6.26 (bs, 1H) 3.55 (q, J = 6.7 Hz, 2H), 2.87 (t, J = 7.12Hz, 1H), 2.00 (s, 3H).

^{13}C{^{1}H} NMR (101 MHz, $CDCl_3$): δ/ppm = 170.9 (C), 138.8 (C), 128.7 (CH), 128.5 (CH), 126.4 (CH), 40.8 (CH_2), 35.4 (CH_2), 23.0 (CH_3).

HRMS (ESI): calcd for $C_{10}H_{13}NO$ $[M+H]^+$: 164.1069; found: 164.1073.

The NMR data are in accordance with those reported in the literature.[207]

1-Methyl-3,4-dihydroisoquinoline (**87**):



87

N-Phenethylacetamide (**89**) (5.00 g, 30.6 mmol, 1.0 equiv.) was stirred with polyphosphoric acid (45 g) for 30 min at 130 °C and subsequently for 4 h at 200 °C. The reaction mixture was treated with 2 M NaOH (500 mL) and extracted with CH_2Cl_2 (3 × 200 mL). The combined organic phases were washed with brine (300 mL) and dried over Na_2SO_4. The solvent was removed to obtain **87** (2.12 g, 14.6 mmol, 48%) as a brown liquid.

R_f: 0.44 (*n*-Hex/EtOAc = 3/1 with NEt_3).

^{1}H NMR (400 MHz, $CDCl_3$): δ/ppm = 7.48 (dd, J = 7.4, 1.4 Hz, 1H), 7.36 (td, J = 7.4, 1.5 Hz, 1H), 7.30 (td, J = 7.5, 1.4 Hz, 1H), 7.21 – 7.15 (m, 1H), 3.67 (ddd, J = 9.0, 5.8, 1.5 Hz, 2H), 2.73 – 2.68 (m, 2H), 2.40 (t, J = 1.5 Hz, 3H).

^{13}C{^{1}H} NMR (101 MHz, $CDCl_3$): δ/ppm = 164.7 (C), 137.5 (C), 130.9 (C), 129.6 (CH) 127.6 (CH), 127.1 (CH), 125.5 (CH), 46.9 (CH_2), 26.1 (CH_2), 23.3 (CH_3).

HRMS (ESI): calcd for $C_{10}H_{11}N$ $[M+Na]^+$: 168.0783; found: 168.0786.

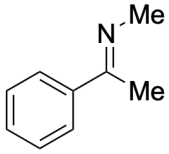
The NMR data are in accordance with those reported in the literature.[208]

Additional

5-Methyl-3,4-dihydro-2H-pyrrole (**86**) was not synthesized but was commercially available from Merck.

6.5.1.2 Synthesis of Non-Cyclic Imines

(E)-*N*-(1-Phenylethylidene)methanamine (**94**):



94

Using GP12, acetophenone (**13a**) (2.00 g, 16.6 mmol, 1.0 equiv.) and methylamine (9.40 g, 33wt% in ethanol, 12.4 mmol, 6.0 equiv.) were dissolved in 6 mL toluene and stirred at room temperature for 48 h. After work up and purification *via* column chromatography (*n*-Hex/EtOAc = 10/1 with NEt_3) **94** (980 mg, 8.22 mmol, 49%) was obtained as a colorless liquid.

R_f: 0.59 (*n*-Hex/EtOAc = 5/1 with NEt_3).

E/Z ratio: 12.5 / 1.

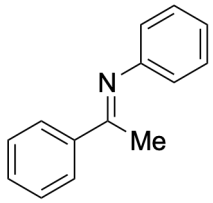
^{1}H NMR (400 MHz, $CDCl_3$): *δ*/ppm = 7.69 – 7.62 (m, 2H), 7.29 – 7.25 (m, 3H), 3.25 (s, 3H) 2.13 (s, 3H).

^{13}C{^{1}H} NMR (101 MHz, $CDCl_3$): *δ*/ppm = 167.1 (C), 141.3 (C), 129.4 (CH), 128.2 (CH), 126.5 (CH), 39.5 (CH_3), 15.1 (CH_3).

HRMS (ESI): calcd for $C_9H_{11}N$ $[M+H]^+$: 134.0964; found: 134.0945.

The NMR data are in accordance with those reported in the literature.[209]

(E)-*N*-(1-Phenylethylidene)aniline (**92**):



92

Using GP12, acetophenone (**13a**) (3.00 g, 24.9 mmol, 1.0 equiv.) and aniline (2.30 g, 24.9 mmol, 1.0 equiv.) were dissolved in 10 mL toluene and stirred at room temperature for 40 h. After work up and purification *via* fractional distillation, **92** (3.40 g, 17.4 mmol, 69%) was obtained as a yellow solid.

R_f: 0.69 (*n*-Hex/EtOAc = 20/1 with NEt_3).

E/Z ratio: 12.5 / 1.

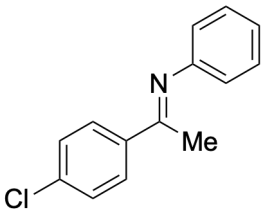
^{1}H NMR (400 MHz, $CDCl_3$): δ/ppm = 8.02 – 7.96 (m, 2H), 7.52 – 7.41 (m, 3H), 7.38 – 7.32 (m, 2H), 7.13 – 7.07 (m, 1H), 6.85 – 6.78 (m, 2H), 2.25 (s, 3H).

^{13}C{^{1}H} NMR (101 MHz, $CDCl_3$): δ/ppm = 165.9 (C), 151.5 (C), 139.5 (C), 130.7 (CH), 129.1 (CH), 128.5 (CH), 127.4 (CH), 123.5 (CH), 119.6 (CH) 17.6 (CH_3).

HRMS (ESI): calculated for $C_{14}H_{13}N$ $[M+H]^+$: 196.1120; found: 196.1125.

The NMR data are in accordance with those reported in the literature.[210]

(E)-*N*-(1-4-Chlorophenyl)ethylidene)aniline (**96**):



96

Using GP12, 4'-chloroacetophenone (2.00 g, 12.9 mmol, 1.0 equiv.) and aniline (1.20 g, 12.9 mmol, 1.0 equiv.) were dissolved in 16 mL toluene and stirred at room temperature for 24 h. After work up and purification *via* column chromatography (*n*-Hex/EtOAc = 10/1 with NEt_3), **96** (1.43 g, 6.23 mmol, 48%) was obtained as a yellow solid.

R_f: 0.63 (*n*-Hex/EtOAc = 10/1 with NEt_3).

E/Z ratio: 5.5 / 1.

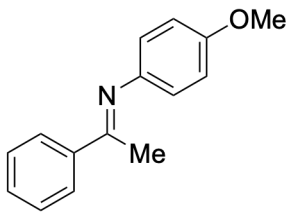
^{1}H NMR (400 MHz, $CDCl_3$): δ/ppm = 7.95 – 7.90 (m, 2H), 7.44 – 7.39 (m, 2H), 7.38– 7.32 (m, 2H), 7.12 – 7.06 (m, 1H), 6.81 – 6.77 (m, 2H), 2.21 (s, 3H).

^{13}C{^{1}H} NMR (101 MHz, $CDCl_3$): δ/ppm = 164.5 (C), 151.4 (C), 138.0 (C), 136.8 (C), 129.1 (CH), 128.7 (CH), 128.7 (CH), 123.6 (CH), 119.5 (CH), 17.4 (CH_3).

HRMS (ESI): calcd for $C_{14}H_{12}ClN$ $[M+H]^+$: 230.0731; found: 232.0732.

The NMR data are in accordance with those reported in the literature.[211]

(E)-4-Methoxy-*N*-(1-phenylethylidene)aniline (97):



97

Using GP13, acetophenone (**13a**) (2.00 g, 16.6 mmol, 1.0 equiv.) and 4-anisidine (2.46 g, 19.9 mmol, 1.2 equiv.) were dissolved in 10 mL toluene and stirred at 130 °C for 48 h. After work up and purification *via* column chromatography (*n*-Hex/EtOAc = 10/1 with NEt_3), **97** (2.45 g, 10.8 mmol, 65%) was obtained as a yellow solid.

R_f: 0.48 (*n*-Hex/EtOAc = 10/1 with NEt_3).

E/Z ratio: 4.5 / 1.

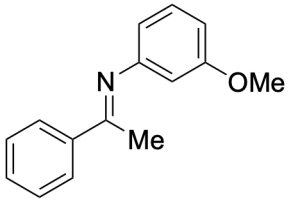
^{1}H NMR (400 MHz, $CDCl_3$): δ/ppm = 8.00 – 7.94 (m, 2H), 7.50 – 7.40 (m, 3H), 6.94 – 6.89 (m, 2H), 6.80 – 6.73 (m, 2H), 3.82 (s, 3H), 2.26 (s, 3H).

^{13}C{^{1}H} NMR (101 MHz, $CDCl_3$): δ/ppm = 166.1 (C), 156.1 (C), 144.7 (C), 139.8 (C), 130.5 (CH), 128.5 (CH), 127.3 (CH), 121.0 (CH), 114.4 (CH), 55.6 (CH_3), 17.5 (CH_3).

HRMS (ESI): calculated for $C_{15}H_{15}NO$ $[M+H]^+$: 226.1226; found: 226.1229.

The NMR data are in accordance with those reported in the literature.[211]

(E)-3-Methoxy-*N*-(1-phenylethylidene)aniline (98):



98

Using GP13, acetophenone (**13a**) (2.40 g, 19.9 mmol, 1.0 equiv.) and 3-anisidine (2.93 g, 23.9 mmol, 1.2 equiv.) were dissolved in 13 mL toluene and stirred at 130 °C for 48 h. After work up and purification *via* column chromatography (*n*-Hex/EtOAc = 10/1 with NEt_3), **98** (2.12 g, 9.33 mmol, 46%) was obtained as a yellow liquid.

R_f: 0.48 (*n*-Hex/EtOAc = 10/1 with NEt_3).

E/Z ratio: 5 / 1.

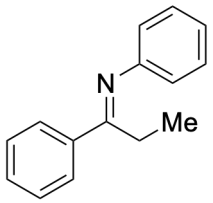
^{1}H NMR (400 MHz, $CDCl_3$): δ/ppm = 8.00 – 7.94 (m, 2H), 7.49 – 7.42 (m, 3H), 7.26 (s, J = 8.0 Hz, 1H), 6.66 (ddd, J = 8.3, 2.3, 1.1 Hz, 1H), 6.41 – 6.36 (m, 2H), 3.81 (s, 3H), 2.25 (s, 3H).

^{13}C{^{1}H} NMR (101 MHz, $CDCl_3$): δ/ppm = 165.7 (C), 160.4 (C), 153.2 (C), 139.5 (C), 130.6 (C), 129.9 (CH), 128.5 (CH), 127.3 (CH), 111.8 (CH), 109.0 (CH), 105.1 (CH), 55.3 (CH_3), 17.5 (CH_3).

HRMS (ESI): calcd for $C_{15}H_{15}NO$ $[M+H]^+$: 226.1226; found: 226.1228.

The NMR data are in accordance with those reported in the literature.[212]

(E)-*N*-(1-Phenylpropylidene)aniline (32b):



32b

Using GP13, propiophenone (3.00 g, 22.3 mmol, 1.0 equiv.) and aniline (3.09 g, 33.5 mmol, 1.5 equiv.) were dissolved in 20 mL toluene and stirred at 120 °C for 30 h. After work up and purification *via* column chromatography (*n*-Hex/EtOAc = 3/1 with NEt_3), **32b** (4.68 g, 14.1 mmol, 63%) was obtained as a orange solid.

R_f: 0.30 (*n*-Hex/EtOAc = 3/1 with NEt_3).

E/Z ratio: 6.3 / 1.

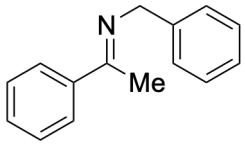
^{1}H NMR (400 MHz, $CDCl_3$): δ/ppm = 7.94 (ddd, J = 7.9, 3.8, 1.8 Hz, 2H), 7.46 (dt, J = 5.6, 1.5 Hz, 3H), 7.35 (tdd, J = 7.4, 2.9, 1.5 Hz, 2H), 7.08 (tdd, J = 6.3, 2.6, 1.3 Hz, 1H), 6.81 (dt, J = 8.4, 1.7 Hz, 1H), 2.68 (q, J = 7.7 Hz, 2H), 1.10 (t, J = 7.7 Hz, 3H).

^{13}C {*1H*} NMR (101 MHz, $CDCl_3$): δ/ppm = 151.7 (C), 138.1 (C), 133.0 (C), 130.4 (CH), 129.0 (CH), 128.6 (CH), 127.7 (CH), 123.1 (CH), 119.2 (CH), 23.6 (CH_2), 13.0 (CH_3).

HRMS (ESI): calcd for $C_{15}H_{15}N$ $[M+H]^+$: 210.1277; found: 210.1278.

The NMR data are in accordance with those reported in the literature.[213]

(E)-1-Phenyl-*N*-(1-phenylethylidene)methanamine (95):



95

Using GP12, propiophenone (2.00 g, 16.6 mmol, 1.0 equiv.) and benzylamine (1.78 g, 16.6 mmol, 1.0 equiv.) were dissolved in 20 mL toluene and stirred at room temperature for 24 h. After work up and purification *via* column chromatography (*n*-Hex/EtOAc = 10/1 with NEt_3), **95** (2.46 g, 11.7 mmol, 70%) was obtained as a yellow liquid.

R_f: 0.63 (*n*-Hex/EtOAc = 5/1 with NEt_3).

E/Z ratio: 12.5 / 1.

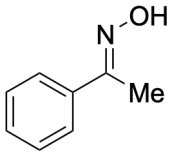
^{1}H NMR (400 MHz, $CDCl_3$): δ/ppm = 7.82 – 7.76 (m, 2H), 7.38 – 7.34 (m, 6H), 7.33 – 7.29 (m, 3H), 7.29 – 7.25 (m, 2H), 7.21 – 7.14 (m, 2H), 4.66 (s, 2H), 2.25 (s, 3H).

^{13}C{^{1}H} NMR (101 MHz, $CDCl_3$): δ/ppm = 166.1 (C), 141.2 (C), 140.6 (C), 129.7 (CH), 128.5 (CH), 128.3 (CH), 127.8 (CH), 126.8 (CH), 126.6 (CH), 55.8 (CH) 15.9 (CH_3).

HRMS (ESI): calcd for $C_{15}H_{15}N$ $[M+H]^+$: 210.1277; found: 210.1278.

The NMR data are in accordance with those reported in the literature.[214]

(E)-Acetophenone oxime (144):



X

Hydroxylamine hydrochloride (1.85 g, 26.6 mmol, 1.6 equiv.), sodium acetate (2.73 g, 33.2 mmol, 2.0 equiv.) and acetophenone (**13a**) (2.00 g, 16.6 mmol, 1.0 equiv.) were dissolved in 80% ethanol and first stirred at room temperature for 30 min and then refluxed for 4 h. The solvent was removed and the crude dissolved in EtOAc (10mL), washed with brine (5 mL) and dried over Na_2SO_4. After removing the solvent **144** (2.00 g, 14.8 mmol, 88%) was obtained as a colorless solid.

R_f: 0.56 (*n*-Hex/EtOAc = 5/1 with NEt_3).

^{1}H NMR (400 MHz, $CDCl_3$): δ/ppm = 7.68 – 7.61 (m, 2H), 7.43 – 7.37 (m, 3H), 2.33 (s, 3H).

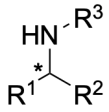
^{13}C{^{1}H} NMR (101 MHz, $CDCl_3$): δ/ppm = 156.1 (C), 136.6 (C), 129.4 (CH), 128.7 (CH), 126.2 (CH), 12.5 (CH_3).

HRMS (ESI): calcd for C_8H_9NO $[M+H]^+$: 136.0756; found: 136.0760.

The NMR data are in accordance with those reported in the literature.[215]

6.5.1.3 Synthesis of Racemic Non-Cyclic and Cyclic Amines

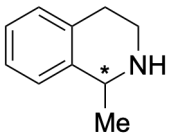
GP14: Synthesis of Racemic Non-Cyclic and Cyclic amines



The corresponding imine (1.0 equiv) was dissolved in MeOH. At 0 °C, $NaBH_4$ (1.2 equiv. – 1.5 equiv.) was added, and the mixture was allowed to warm to room temperature and stirred for the appropriate time. The reaction mixture was quenched by addition of 1M HCl, and the aqueous layer was extracted three times with EtOAc. The combined

organic layers were washed with brine, dried over Na_2SO_4, and the solvent was removed under reduced pressure. The crude product was purified by column chromatography (*n*-Hex/EtOAc with NEt_3) to afford the corresponding amine.

1-Methyl-1,2,3,4-tetrahydroisoquinoline (rac-**91**):



rac-**91**

Using GP14, **87** (150 mg, 1.03 mmol, 1.0 equiv.) was dissolved in 3 mL MeOH and $NaBH_4$ (54.7 mg, 1.45 mmol, 1.4 equiv.) was added at 0 °C. The solution was stirred at room temperature for 23 h. After work up and purification *via* column chromatography (*n*-Hex/EtOAc = 5/1 with NEt_3), rac-**91** (133 mg, 903 µmol, 87%) was obtained as a yellow liquid.

R_f: 0.25 (*n*-Hex/EtOAc = 3/1 with NEt_3).

Chiral HPLC:

Column:	Chiralpak IC
Flow Rate:	1.0 mL min^{-1}
Run Time:	20 min
Mobile Phase:	95% *n*-Hex. 5% EtOAc, 0.25% NEt_3
Wavelength:	270 nm
Retention time:	(*R*) = 11.17 min (*S*) = 12.28 min

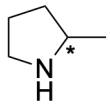
^{1}H NMR (400 MHz, $CDCl_3$): *δ*/ppm = 7.07 – 6.95 (m, 4H), 4.02 (q, *J* = 6.9 Hz, 1H), 3.21 – 3.12 (m, 1H), 2.93 (ddd, *J* = 12.5, 8.7, 4.7 Hz, 1H), 2.78 (dddt, *J* = 16.4, 8.6, 5.4, 1.1 Hz, 1H), 2.64 (dtt, *J* = 16.3, 4.7, 0.9 Hz, 1H), 1.95 (bs, 1H), 1.37 (d, *J* = 6.6 Hz, 3H).

^{13}C {*1H*} NMR (101 MHz, $CDCl_3$): *δ*/ppm = 140.5 (C), 134.8 (C), 129.2 (CH), 128.6. (CH) 126.0 (CH), 125.9 (CH), 51.6 (CH), 41.8 (CH_2), 30.0.3 (CH_2), 22.7 (CH_3).

HRMS (ESI): calcd for $C_{10}H_{11}N$ $[M+Na]^+$: 170.0940; found: 170.0943.

The NMR data are in accordance with those reported in the literature. [216]

2-Methylpyrrolidine (rac-**90**):


rac-**90**

Using GP14, **86** (100 mg, 1.20 mmol, 1.0 equiv.) was dissolved in 3 mL MeOH and $NaBH_4$ (63.7 mg, 1.68 mmol, 1.4 equiv.) was added at 0 °C. The solution was stirred at room temperature for 23 h. After work up and purification *via* column chromatography (*n*-Hex/EtOAc = 5/1 with NEt_3), rac-**90** (880 mg, 10.3 µmol, 87%) was obtained as a colorless liquid.

R_f: 0.54 (*n*-Hex/EtOAc = 5/1 with NEt_3).

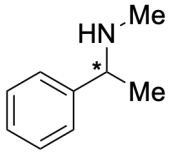
^{1}H NMR (400 MHz, $CDCl_3$): *δ*/ppm = 3.57 (dquint, *J* = 8.9, 6.5 Hz, 1H), 3.34 (dt, *J* = 11.3, 7.5 Hz, 1H), 3.21, (ddd, *J* = 11.4, 8.7, 5.5 Hz, 1H), 2.14 – 1.96 (m, 2H), 1.96 – 1.85 (m, 1H), 1.62 (dt, *J* = 12.7, 8.5 Hz, 1H), 1.46 (d, *J* = 6.6 Hz, 3H).

^{13}C{^{1}H} NMR (101 MHz, $CDCl_3$): *δ*/ppm = 55.9 (CH), 44.7 (CH_2), 32.3 (CH_2), 23.8 (CH_2) 18.0 (CH_3).

HRMS (ESI): calcd for $C_{10}H_{11}N$ $[M+Na]^+$: 108.0783; found: 108.0788.

The NMR data are in accordance with those reported in the literature.[217]

***N*-Methyl-1-phenylethanamine** (rac-**145**):


rac-**145**

Using GP14, **94** (1.00 g, 7.51 mmol, 1.0 equiv.) was dissolved in 9 mL MeOH and $NaBH_4$ (426 mg, 11.26 mmol, 1.5 equiv.) was added at 0 °C. The solution was stirred at room temperature for 24 h. After work up and purification *via* column chromatography (*n*-Hex/EtOAc = 20/1 with NEt_3), rac-**145** (890 mg, 6.58 mmol, 87%) was obtained as a colorless liquid.

R_f: 0.29 (*n*-Hex/EtOAc = 20/1 with NEt_3) [Hanessian Stain].

Chiral-HPLC:

Column:	Chiralpak IA
Flow Rate:	1.2 mL min^{-1}
Run Time:	20 min
Mobile Phase:	85% *n*-Hex. 15% TBME
Wavelength:	250 nm
Retention time:	(*R*) = 5.12 min
	(*S*) = 5.69 min

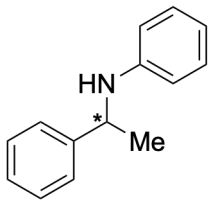
^{1}H NMR (400 MHz, $CDCl_3$): δ/ppm = 7.31 – 7.24 (m, 4H), 7.23 – 7.15 (m, 1H), 3.62 (q, *J* = 6.6 Hz, 1H), 2.25 (s, 3H), 1.34 (d, *J* = 6.6 Hz, 3H).

^{13}C{^{1}H} NMR (101 MHz, $CDCl_3$): δ/ppm = 144.3 (C), 128.4 (CH), 127.11 (CH), 126.6 (CH), 60.1 (CH), 34.06 (CH_3), 23.4 (CH_3).

HRMS (ESI): calcd for $C_9H_{13}N$ $[M+Na]^+$: 158.0940; found: 158.0940.

The NMR data are in accordance with those reported in the literature.[218]

***N*-(1-Phenylethyl)aniline** (rac-**93**):



rac-**93**

Using GP14, **92** (200 mg, 1.02 mmol, 1.0 equiv.) was dissolved in 2 mL MeOH and $NaBH_4$ (50.3 mg, 1.33 mmol, 1.3 equiv.) was added at 0 °C. The solution was stirred at room temperature for 20 h. After work up and purification *via* column chromatography (*n*-Hex/EtOAc = 20/1 with NEt_3), rac-**93** (199 mg, 1.01 mmol, 98%) was obtained as a yellow liquid.

R_f: 0.62 (*n*-Hex/EtOAc = 20/1 with NEt_3).

Chiral-HPLC:

Column:	Chiralpak IB
Flow Rate:	1.2 mL min^{-1}
Run Time:	20 min
Mobile Phase:	88% *n*-Hex. 20% TBME,
	2% IPA, 0.1% NEt_3
Wavelength:	285 nm
Retention time:	(*R*) = 4.08 min
	(*S*) = 4.61 min

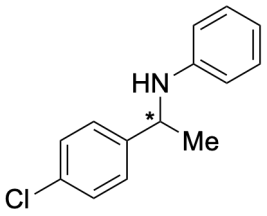
^{1}H NMR (400 MHz, $CDCl_3$): δ/ppm = 7.35 – 7.29 (m, 2H), 7.26 (ddd, J = 7.7, 7.0, 1.3 Hz, 2H), 7.20 – 7.14 (m, 1H), 7.07 – 7.00 (m, 2H), 6.62 – 6.55 (m, 1H), 6.48 – 6.42 (m, 2H), 4.43 (dt, J = 11.5, 6.7 Hz, 1H), 3.95 (bs, 1H), 1.45 (d, J = 6.7 Hz, 3H)

^{13}C{^{1}H} NMR (101 MHz, $CDCl_3$): δ/ppm = 147.4 (C), 145.3 (C), 129.2 (CH), 128.8 (CH), 127.0 (CH), 126.0 (CH), 117.3 (CH), 113.4 (CH), 53.6 (CH) 25.1 (CH_3).

HRMS (ESI): calcd for $C_{14}H_{15}N$ $[M+H]^+$: 198.1277; found: 198.1277.

The NMR data are in accordance with those reported in the literature. [219]

***N*-(1-(4-Chlorophenyl)ethyl)aniline** (rac-**146**):



rac-**146**

Using GP14, **96** (600 mg, 2.61 mmol, 1.0 equiv.) was dissolved in 5 mL MeOH and $NaBH_4$ (108 mg, 2.87 mmol, 1.1 equiv.) was added at 0 °C. The solution was stirred at room temperature for 48 h. After work up and purification *via* column chromatography (*n*-Hex/EtOAc = 10/1 with NEt_3), rac-**146** (458 mg, 1.98 mmol, 75%) was obtained as a yellow liquid.

R_f: 0.42 (*n*-Hex/EtOAc = 10/1 with NEt_3).

Chiral-HPLC:

Column:	Chiralpak IA
Flow Rate:	1.2 mL min^{-1}
Run Time:	20 min
Mobile Phase:	85% *n*-Hex. 15% TBME
Wavelength:	260 nm
Retention time:	(*R*) = 5.02 min
	(*S*) = 5.52 min

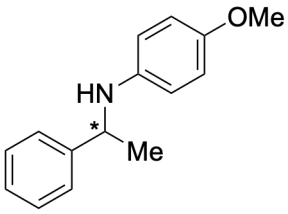
^{1}H NMR (400 MHz, $CDCl_3$): δ/ppm = 7.30 – 7.23 (m, 4H), 7.08 (ddd, J = 8.4, 7.3, 1.2 Hz, 2H), 6.65 (td, J = 7.3, 1.2 Hz, 1H), 6.46 (dt, J = 8.6, 1.2 Hz, 2H), 4.42 (q, J = 6.7 Hz, 1H), 3.92 (bs, 1H), 1.46 (d, J = 6.7 Hz, 3H).

^{13}C{^{1}H} NMR (101 MHz, $CDCl_3$): δ/ppm = 147.1 (C), 143.9 (C), 132.5 (C), 129.2 (CH), 128.9 (CH), 127.3 (CH), 53.1 (CH_2), 25.1 (CH_3).

HRMS (ESI): calcd for $C_{14}H_{14}ClN$ $[M+H]^+$: 232.0887; found: 232.0890.

The NMR data are in accordance with those reported in the literature.[220]

4-Methoxy-*N*-(1-phenylethyl)aniline (rac-**147**):



rac-**147**

Using GP14, **97** (500 mg, 2.22 mmol, 1.0 equiv.) was dissolved in 6 mL MeOH and $NaBH_4$ (125 mg, 3.33 mmol, 1.5 equiv.) was added at 0 °C. The solution was stirred at room temperature for 24 h. After work up and purification *via* column chromatography (*n*-Hex/EtOAc = 10/1 with NEt_3), rac-**147** (367 mg, 1.61 mmol, 72%) was obtained as a colorless liquid.

R_f: 0.37 (*n*-Hex/EtOAc = 10/1 with NEt_3).

Chiral-HPLC:

Column:	Chiralpak IA
Flow Rate:	1.0 mL min^{-1}
Run Time:	20 min
Mobile Phase:	95% *n*-Hex. 5% EtOAc, 0.1% NEt_3
Wavelength:	270 nm
Retention time:	(*R*) = 6.30 min (*S*) = 6.95 min

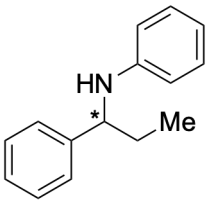
^{1}H NMR (400 MHz, $CDCl_3$): δ/ppm = 7.43 – 7.38 (m, 2H), 7.35 (dd, *J* = 8.5, 6.7 Hz, 2H), 7.29 – 7.23 (m, 1H), 6.75 – 6.70 (m, 2H), 6.53 – 6.49 (m, 2H), 4.45 (q, *J* = 6.7 Hz, 1H) 3.73 (s, 3H), 1.54 (d, *J* = 6.7 Hz, 3H).

^{13}C{^{1}H} NMR (101 MHz, $CDCl_3$): δ/ppm = 152.0 (C), 145.6 (C), 141.7 (C), 128.7 (CH), 126.9 (CH), 126.0 (CH), 114.9 (CH), 114.7 (CH), 55.9 (CH_2), 54.4 (CH_3), 25.2 (CH_3).

HRMS (ESI): calcd for $C_{15}H_{17}NO$ $[M+H]^+$: 228.1382; found: 228.1384.

The NMR data are in accordance with those reported in the literature. [219]

***N*-(1-Phenylpropyl)aniline** (rac-**34b**):



rac-**34b**

Using GP14, **32b** (500 mg, 2.39 mmol, 1.0 equiv.) was dissolved in 6 mL MeOH and $NaBH_4$ (135 mg, 3.33 mmol, 1.5 equiv.) was added at 0 °C. The solution was stirred at room temperature for 20 h. After work up and purification *via* column chromatography (*n*-Hex/EtOAc = 3/1 with NEt_3), rac-**34b** (477 mg, 2.26 mmol, 94%) was obtained as a colorless liquid.

R_f: 0.21 (*n*-Hex/EtOAc = 3/1 with NEt_3).

Chiral-HPLC:

Column:	Chiralpak IB
Flow Rate:	1.2 mL min^{-1}
Run Time:	20 min
Mobile Phase:	88% *n*-Hex. 10% TBME, 2% IPA, 0.1% NEt_3
Wavelength:	270 nm
Retention time:	(*R*) = 3.71 min (*S*) = 4.04 min

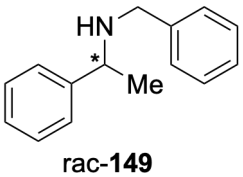
^{1}H NMR (400 MHz, $CDCl_3$): *δ*/ppm = 7.31 – 7.26 (m, 4H), 7.24 – 7.18 (m, 1H), 7.07 (tq, *J* = 7.2, 1.2 Hz, 2H), 6.62 (tt, *J* = 7.3, 1.2 Hz, 1H), 6.54 – 6.48 (m, 2H), 4.22 (t, *J* = 6.7 Hz, 1H), 1.82 (dq, *J* = 13.2, 6.7 Hz, 2H), 0.95 (t, *J* = 7.4 Hz, 3H).

^{13}C{^{1}H} NMR (101 MHz, $CDCl_3$): *δ*/ppm = 147.6 (C), 144.0 (C), 129.2 (CH), 128.6 (CH), 127.0 (CH), 126.6 (CH), 117.2 (CH), 113.4 (CH), 59.9 (CH), 31.7 (CH_2) 10.97 (CH_3).

HRMS (ESI): calcd for $C_{15}H_{17}N$ $[M+H]^+$: 212.1433; found: 212.1435.

The NMR data are in accordance with those reported in the literature.[221]

***N*-Benzyl-1-phenylethanamine** (rac-**148**):



rac-**149**

Using GP14, **95** (600mg, 2.87 mmol, 1.0 equiv.) was dissolved in 8 mL MeOH and $NaBH_4$ (162 mg, 4.30 mmol, 1.5 equiv.) was added at 0 °C. The solution was stirred at room temperature for 24 h. After work up and purification *via* column chromatography (*n*-Hex/EtOAc = 9/1 with NEt_3), rac-**148** (493 mg, 2.33 mmol, 81%) was obtained as a colorless liquid.

R_f: 0.51 (*n*-Hex/EtOAc = 5/1 with NEt_3).

Chiral-HPLC:

Column:	Chiralpak IB
Flow Rate:	1.2 mL min^{-1}
Run Time:	20 min
Mobile Phase:	98% *n*-Hex. 2% IPA, 0.1% NEt_3
Wavelength:	270 nm
Retention time:	(*R*) = 3.53 min (*S*) = 3.68 min

^{1}H NMR (400 MHz, $CDCl_3$): δ/ppm = 7.37 – 7.20 (m, 10H), 3.81 (q, J = 11.5, 6.6 Hz, 1H), 3.66 (d, J = 13.2 Hz, 1H), 3.59 (d, J = 13.2 Hz, 1H), 1.36 (d, J = 6.6 Hz, 3H)

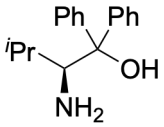
^{13}C{^{1}H} NMR (101 MHz, $CDCl_3$): δ/ppm = 145.7 (C), 140.8 (C), 128.6 (CH), 128.5 (CH), 128.3 (CH), 127.1(CH), 127.0 (CH), 126.8 (CH), 57.6 (CH), 51.8 (CH_2) 25.1 (CH_3).

HRMS (ESI): calcd for $C_{15}H_{17}N$ $[M+H]^+$: 212.1433; found: 212.1425.

The NMR data are in accordance with those reported in the literature.[222]

6.5.2 Synthesis of Catalyst Precursors

(*S*)-2-Amino-3-methyl-1,1-diphenylbutan-1-ol (20):



20

Esterification: L-Valine (**99**) (10.0 g, 85.3 mmol, 1.0 equiv.) was dissolved in 100 mL MeOH and at 0 °C $SOCl_2$ (25.3 g, 213 mmol, 2.5 equiv.) was added dropwise and stirred at room temperature for 24 h. The solvent was removed under reduced pressure and the crude was subsequently used in the following procedure without doing any further analytics. *Grignard Reaction:* To a suspension of magnesium (1.30 g, 53.6 mmol, 3.0 equiv.) in anhydrous THF under Argon a crystal of iodine was added and stirred at room temperature for 30 min. Then 5% of the solution of benzylbromide (8.43 g, 53.6 mmol, 3.0 equiv.) in THF was added and the reaction mixture was warmed to 50 °C. As soon as the reaction started, the remaining solution of benzylbromide was added dropwise to the solution. The reaction mixture was refluxed for 2 h. To the aryl magnesium bromide suspension, a solution of the crude product of the esterification (3.00 g, 17.9 mmol, 1.0 equiv.) in THF was added dropwise. The reaction mixture was once again refluxed for 1 h then stirred at room temperature for 12 h. At 0 °C, sat. NH_4Cl was added to quench the reaction and the mixture was extracted three times with Et_2O. The

combined organic layers were washed with brine and dried over Na_2SO_4. After removing the solvent, the crude product was purified by column chromatography (*n*-Hex/EtOAc = 7/3) and **20** (2.56 g, 10.0 mmol, 56%) was obtained as a colorless powder.

R_f: 0.32 (*n*-Hex/EtOAc = 7/3)

^{1}H NMR (400 MHz, $CDCl_3$): δ/ppm = 7.69 – 7.58 (m, 2H), 7.52 – 7.48 (m, 2H), 7.30 (dt, J = 13.7, 7.5 Hz 4H) 7.23 – 7.11 (m, 2H), 3.85 (d, J = 2.2 Hz, 1H), 1.81 – 1.69 (m, 1H), 0.91 (dd, J = 16.5, 6.9 Hz, 6H).

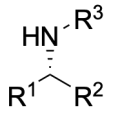
^{13}C{^{1}H} NMR (101 MHz, $CDCl_3$): δ/ppm = 148.1 (C), 145.0 (C), 128.5 (CH), 128.1 (CH), 126.7 (CH), 126.4 (CH), 126.0 (CH), 125.6 (CH), 79.8 (C), 60.3 (CH), 28.0 (CH), 23.1 (CH_3), 16.2 (CH_3).

HRMS (ESI): calcd for $C_5H_{12}O$ $[M+Na]^+$: 256.1695; found: 256.1699.

The NMR data are in accordance with those reported in the literature.[223]

6.5.3 Catalytical Reduction Reaction Procedure

GP15: Catalytic Reduction of imines to amines (Non-Cyclic and Cyclic)



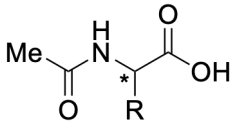
The amino alcohol (0.04 mmol, 0.1 equiv.) was placed in a Schlenk tube. Anhydrous THF (1 mL) and BH_3•SMe_2 (0.44 mmol, 1.1 equiv.) were added, and the mixture was stirred at 50 °C for 1 h. A solution of the corresponding imine (0.40 mmol, 1.0 equiv. in 0.5 mL THF) was then slowly added at room temperature *via* a syringe pump over a period of 30 min, after which the reaction mixture was stirred for an additional 120 min at room temperature. To quench the reaction, 0.5 M citric acid (6 mL) was added, and the mixture was extracted three times with EtOAc (5 mL). The combined organic layers were washed with brine and dried over Na_2SO_4. After filtration, the solvent was removed under reduced pressure and the crude product was analyzed by chiral HPLC analysis.

6.6 Part IV

6.6.1 Synthesis of Starting Materials

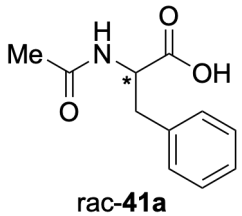
DL-Phenylalanine (rac-**38a**) and DL-alanine (rac-**38b**), as well as *N*-acetyl-DL-valine (rac-**41c**) and *N*-acetyl-DL-tryptophan (rac-**41d**), were obtained from commercial suppliers and were used as received.

GP16 Synthesis of Acetylated Starting Material



The corresponding amino acid (1.0 equiv.) was suspended in methanol, and Ac_2O (2.6 equiv.) was added. The reaction mixture was refluxed for the appropriate time. After cooling to room temperature, the solvent was removed under reduced pressure, and the residue was triturated with EtOAc.

***N*-Acetyl-DL-phenylalanine** (rac-**41a**):



rac-**41a**

Using GP16, DL-phenylalanine (rac-**38a**) (3.00 g, 18.1 mmol, 1.0 equiv.), methanol (9 mL), and Ac_2O (4.82 g, 47.2 mmol, 2.6 equiv.) were heated under reflux for 5 h. After workup rac-**41a** (2.46 g, 11.8 mmol, 65%) was obtained as a colorless solid.

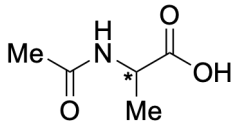
^{1}H NMR (400 MHz, DMSO-d_6): δ/ppm = 12.68 (bs, 1H), 8.19 (d, J = 8.1 Hz, 1H), 7.50 – 6.97 (m, 5H), 4.41 (ddd, J = 9.6, 8.0, 4.9 Hz, 1H), 3.04 (dd, J = 13.8, 5.0 Hz, 1H), 2.83 (dd, J = 13.8, 9.6 Hz, 1H), 1.78 (s, 3H).

^{13}C{^{1}H} NMR (101 MHz, DMSO-d_6): δ/ppm = 173.2 (C), 169.2 (C), 137.7 (CH), 129.0 (CH), 128.2 (CH), 126.4 (CH), 53.5 (CH), 36.8 (CH), 22.3 CH_3).

HRMS (ESI): calcd for $C_{11}H_{13}NO_3$ $[M+H]^+$: 208.0968; found: 208.0972.

The NMR data are in accordance with those reported in the literature.[113]

***N*-Acetyl-DL-alanine** (rac-**41b**):



rac-**41b**

Using GP16, DL-alanine (rac-**38b**) (3.00 g, 33.6 mmol, 1.0 equiv.), methanol (12 mL), and Ac_2O (8.94 g, 87.5 mmol, 2.6 equiv.) were heated under reflux for 6 h. After workup rac-**41b** (2.70 g, 20.9 mmol, 62%) was obtained as a colorless solid.

^{1}H NMR (400 MHz, D_2O): δ/ppm = 4.31 (q, J = 7.3 Hz, 1H), 1.99 (s, 3H), 1.39 (d, J = 7.4 Hz, 3H).

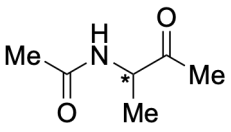
^{13}C{^{1}H} NMR (101 MHz, D_2O): δ/ppm = 176.7 (C), 173.9 (C), 48.6 (CH), 21.4 (CH_3), 16.0 (CH_3).

HRMS (ESI): calcd for $C_5H_9NO_3$ $[M+H]^+$: 132.0655; found: 132.0659.

The NMR data are in accordance with those reported in the literature.[113]

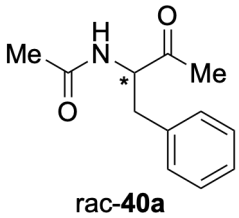
6.6.2 Synthesis of Racemic Products

GP17: Synthesis of Racemic Amino Acid Products



A mixture of the acetylated amino acid (rac-**41**) (1.0 equiv.), DMAP (5 mol%), NEt_3 (1.45 equiv.), and Ac_2O (2.1 equiv.) was stirred at room temperature for the appropriate time. Subsequently, glacial acetic acid (3 mL) was added and the reaction mixture was stirred for an additional time. The solvent was then removed and the residue was dissolved in saturated aqueous $NaHCO_3$ (5 mL) and extracted with $CHCl_3$ (3 x 10 mL). The combined organic phases were washed with 1 M HCl (3 x 10 mL) and brine (10 mL) and dried over Na_2SO_4. Removal of the solvent afforded the crude product, which was purified either by recrystallization

***N*-(3-Oxo-1-phenylbutan-2-yl)acetamide** (rac-**40a**):



Using GP17, rac-**41a** (1.00 g, 4.83 mmol, 1.00 equiv.) was treated with DMAP (29.4 mg, 241 µmol, 5 mol%), NEt_3 (708 mg, 7.00 mmol, 1.45 equiv.), and Ac_2O (985 mg, 9.65 mmol, 2.0 equiv.) and stirred at room temperature for 40 min. Subsequently, glacial acetic acid was added, and the reaction mixture was stirred for an additional 30 min. After workup, the crude product was purified by recrystallization (*n*-Hex/EtOAc = 4:1) to afford rac-**40a** (726 mg, 3.54 mmol, 73%) as a colorless solid.

R_f: 0.35 (EtOAc).

Chiral-HPLC:

Column:	Chiralpak IC
Flow Rate:	1.0 mL min^{-1}
Run Time:	25 min
Mobile Phase:	85% n-Hex. 15% IPA
Wavelength:	245 nm
Retention time:	(*R*) = 17.16 min
	(*S*) = 21.22 min

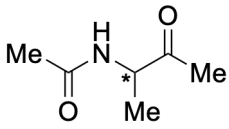
^{1}H NMR (400 MHz, $CDCl_3$): *δ*/ppm = 7.33 – 7.22 (m, 3H), 7.15 – 7.10 (m, 1H), 6.19 (bs, 1H), 4.87 (td, *J* = 7.1, 5.8 Hz, 1H), 3.14 (dd, *J* = 14.0, 6.8 Hz, 1H), 3.04 (dd, *J* = 14.0, 5.8 Hz, 1H), 2.15 (s, 1H), 1.98 (s, 1H).

^{13}C {*1H*} NMR (101 MHz, $CDCl_3$): *δ*/ppm = 206.4 (C), 169.7 (C), 135.9 (CH), 129.2 (CH), 128.7 (CH), 127.2 (CH), 59.6 (CH), 37.2 (CH_2), 28.2 (CH_3), 23.1 (CH_3).

HRMS (ESI): calcd for $C_{12}H_{15}NO_2$ $[M+H]^+$: 206.1175; found: 206.1180.

The NMR data are in accordance with those reported in the literature.[113]

***N*-(3-Oxobutan-2-yl)acetamide** (rac-**40b**):



rac-**40b**

Using GP17, rac-**41b** (1.00 g, 7.63 mmol, 1.00 equiv.) was treated with DMAP (46.5 mg, 381 µmol, 5 mol%), NEt_3 (1.12 g, 11.0 mmol, 1.45 equiv.), and Ac_2O (1.56 g, 15.2 mmol, 2.0 equiv.) and stirred at room temperature for 30 min. Subsequently, glacial acetic acid was added, and the reaction mixture was stirred for an additional 45 min. After workup, the crude product was purified by column chromatographie (EtOAc) to afford rac-**40b** (269 mg, 1.47 mmol, 19%) as a colorless oil.

R_f: 0.15 (EtOAc).

Chiral-GC:

Column:	β-TBDAc
T (Injection + Detector):	250 °C
Flow Rate:	80 mL min^{-1}
Precolumn pressure:	0.8 bar
Initial temperature:	100 °C
Retention time:	(*R*) = 27.03 min
	(*S*) = 28.21 min

Rate [°C min^{-1}]	Temperature [°C]	Time [min]
2.0	180	0.0
20.0	240	3.0

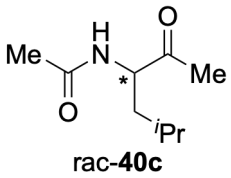
^{1}H NMR (400 MHz, $CDCl_3$): *δ*/ppm = 76.53 (bs, 1H), 4.53 (quint, *J* = 7.1 Hz, 1H), 2.16 (s, 3H), 1.96 (s, 3H), 1.31 (d, *J* = 7.2 Hz, 3H).

^{13}C{^{1}H} NMR (101 MHz, $CDCl_3$): *δ*/ppm = 207.1 (C), 169.7 (C), 54.6 (CH), 26.5 (CH_3), 23.10 (CH_3), 17.42 (CH_3).

HRMS (ESI): calcd for $C_6H_{12}NO_2$ $[M+H]^+$: 130.0862; found: 130.0867.

The NMR data are in accordance with those reported in the literature.[113]

***N*-(5-Methyl-2-oxohexan-3-yl)acetamide** (rac-**40c**):



rac-**40c**

Using GP17, rac-**41c** (1.00 g, 5.77 mmol, 1.00 equiv.) was treated with DMAP (35.2 mg, 288 µmol, 5 mol%), NEt_3 (841 mg, 8.37 mmol,1.45 equiv.), and Ac_2O (1.18 g, 11.5 mmol, 2.0 equiv.) and stirred at room temperature for 30 min. Subsequently, glacial acetic acid was added, and the reaction mixture was stirred for an additional 30 min. After workup, the crude product was purified by fractional distillation under reduced pressure to afford rac-**40c** (358 mg, 1.95 mmol, 33%) as a colorless oil.

R_f: 0.30 (EtOAc).

Chiral-GC:

Column:	β-TBDAc
T (Injection + Detector):	250 °C
Flow Rate:	80 mL min^{-1}
Precolumn pressure:	0.8 bar
Initial temperature:	100 °C
Retention time:	(*R*) = 23.04 min
	(*S*) = 24.33 min

Rate [°C min^{-1}]	Temperature [°C]	Time [min]
2.0	180	0.0
20.0	240	3.0

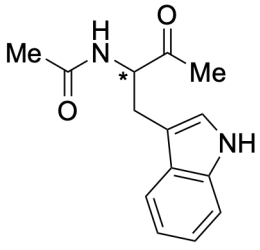
^{1}H NMR (400 MHz, $CDCl_3$): *δ*/ppm = 6.53 (d, *J* = 8.0, 1H), 4.55 (ddd, *J* = 9.7, 7.8, 4.0 Hz, 1H), 2.13 (s, 3H), 1.94 (s, 3H), 1.67 – 1.56 (m, 1H), 1.56 – 1.47 (m,1H), 1.32 (ddd, *J* = 14.0, 9.7, 4.5 Hz, 1H), 0.87 (dd, *J* = 13.1 Hz, 6.45 Hz, 6H).

^{13}C {*1H*} NMR (101 MHz, $CDCl_3$): *δ*/ppm = 207.8 (C), 170.3 (C), 57.3 (CH), 40.1 (CH_2), 27.2 (CH), 24.9 (CH), 23.2 (CH_3), 22.9 (CH_3), 21.7 (CH_3).

HRMS (ESI): calcd for $C_9H_{17}NO_2$ $[M+H]^+$: 172.1332; found: 172.1334

The NMR data are in accordance with those reported in the literature.[113]

***N*-(1-(1*H*-Indol-3-yl)-3-oxobutan-2-yl)acetamide** (rac-**40d**):



rac-**40d**

Using GP17, rac-**41d** (1.00 g, 4.06 mmol, 1.0 equiv.) was treated with DMAP (24.8 mg, 203 µmol, 5 mol%), NEt_3 (595 mg, 5.89 mmol, 1.45 equiv.), and Ac_2O (829 mg, 8.12 mmol, 2.0 equiv.) and stirred at room temperature for 30 min. Subsequently, glacial acetic acid was added, and the reaction mixture was stirred for an additional 30 min. After workup, the crude product was purified by column chromatography (EtOAc) to afford rac-**40d** (391 mg, 1.60 mmol, 39%) as a colorless oil.

R_f: 0.48 (EtOAc).

Chiral-HPLC:

Column:	Chiralpak IC
Flow Rate:	1.2 mL min^{-1}
Run Time:	20 min
Mobile Phase:	80% n-Hex. 20% IPA, 0.15% NEt_3
Wavelength:	280 nm
Retention time:	(*R*) = 9.77 min
	(*S*) = 11.03 min

^{1}H NMR (400 MHz, $CDCl_3$): δ/ppm = 8.35 (bs, 1H), 7.59 (dt, *J* = 7.8, 1.0 Hz, 1H), 7.36 (dt, *J* = 8.1, 0.9 Hz, 1H), 7.20 (ddd, *J* = 8.1, 7.0, 1.2 Hz, 1H), 7.13 (ddd, *J* = 8.0, 7.0, 1.0 Hz, 1H), 6.32 (d, *J* = 6.32 Hz, 1H), 4.95 (td, *J* = 6.7, 5.41 Hz, 1H), 3.37 – 3.19 (m, 2H), 2.14 (s, 3H), 1.95 (s, 3H).

^{13}C{^{1}H} NMR (101 MHz, $CDCl_3$): δ/ppm = 206.9 (C), 170.3 (C), 170.2 (CH), 136.3 (C), 127.7 (C), 122.7 (CH), 122.5 (CH), 119.9 (CH), 118.7 (CH), 115.5 (CH), 110.1 (C), 59.4 (CH), 28.1 (CH_2), 27.1 (CH_3), 23.2 (CH_3).

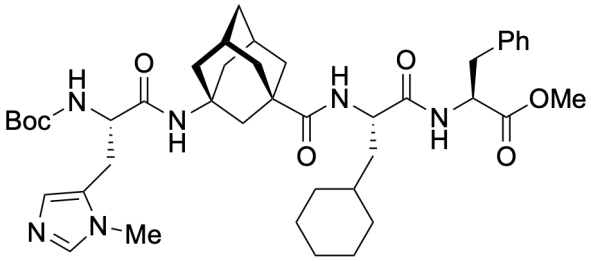
HRMS (ESI): calcd for $C_{14}H_{16}N_2O_2$ $[M+H]^+$: 245.1284; found: 245.1287.

The NMR data are in accordance with those reported in the literature.[113]

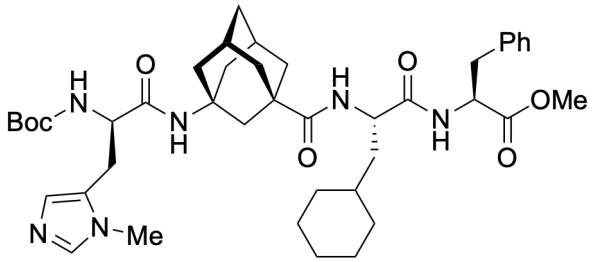
6.6.3 List of Peptide Catalysts

Notification

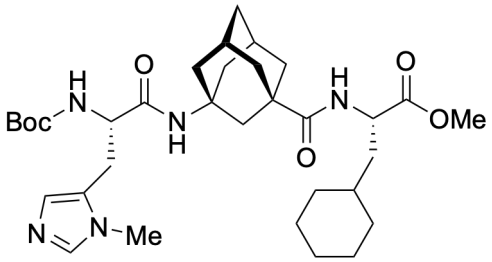
The catalysts were synthesized by Jan Metzler using a multi-step peptide coupling in solution of unmodified and modified amino acids. NMR spectra are not provided. However, all compounds except **178** were employed in the highest available purity.



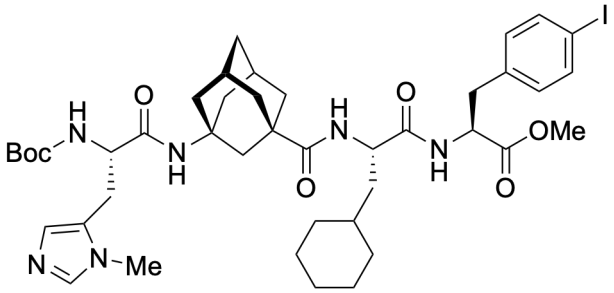
Boc-Pmh-AGly-Cha-Phe-OMe **113**



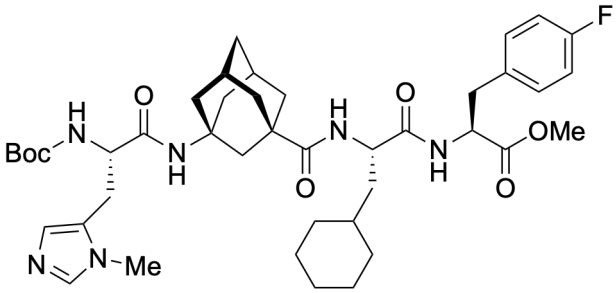
Boc-Pmh-D-AGly-Cha-Phe-OMe **123**



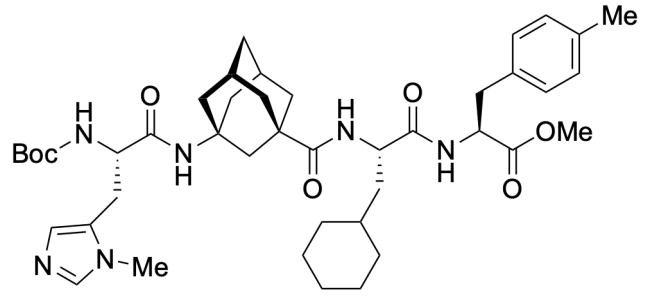
Boc-Pmh-AGly-Cha-OMe **103**



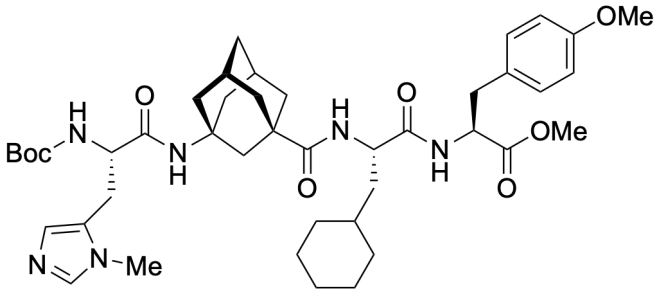
Boc-Pmh-AGly-Cha-(*p*-I)Phe-OMe **149**



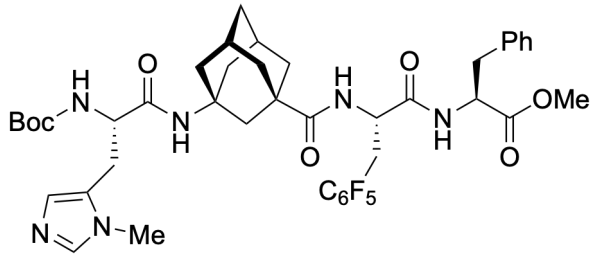
Boc-Pmh-AGly-Cha-(*p*-F)Phe-OMe **115**



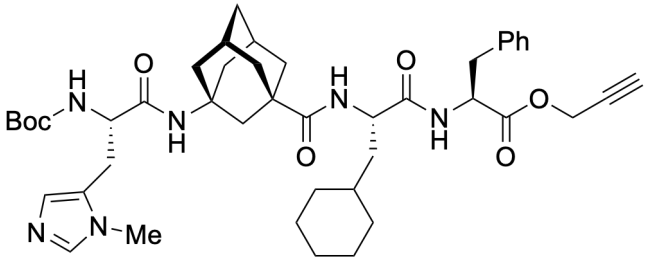
Boc-Pmh-AGly-Cha-(*p*-Me)Phe-OMe **150**



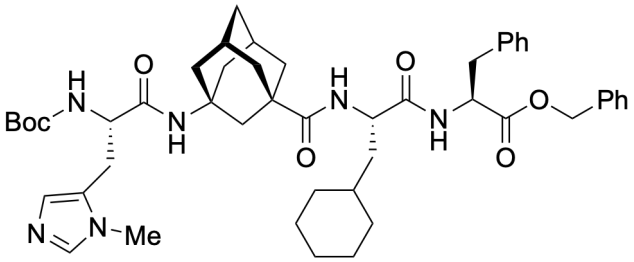
Boc-Pmh-AGly-Cha-(*p*-OMe)Phe-OMe **117**



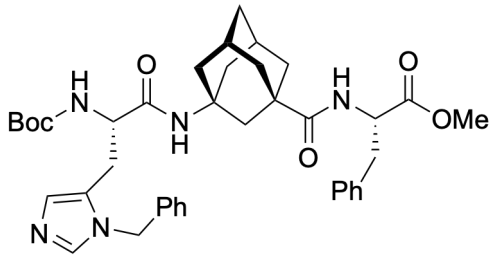
Boc-Pmh-AGly-(F_5)Phe-Phe-OMe **124**



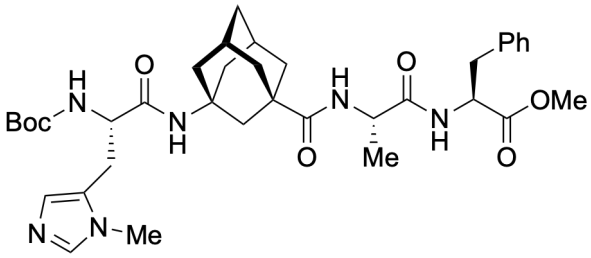
Boc-Pmh-AGly-Cha-Phe-OPg **151**



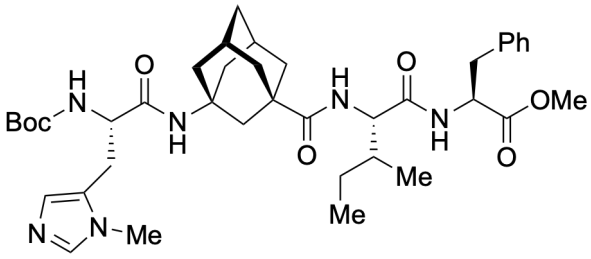
Boc-Pmh-AGly-Cha-Phe-OBn **116**



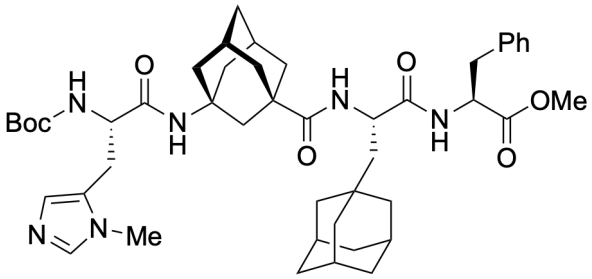
Boc-tBnHis-AGly-Phe-OMe **152**



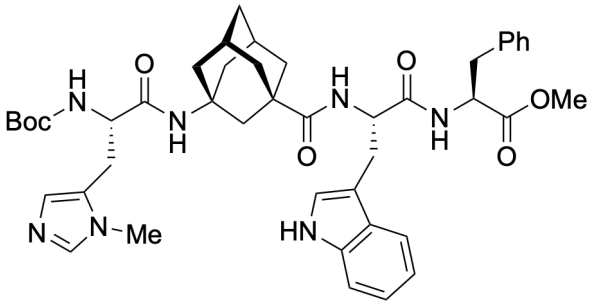
Boc-Pmh-AGly-Ala-Phe-OMe **153**



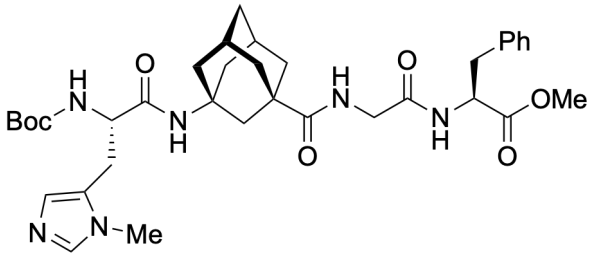
Boc-Pmh-AGly-Ile-Phe-OMe **154**



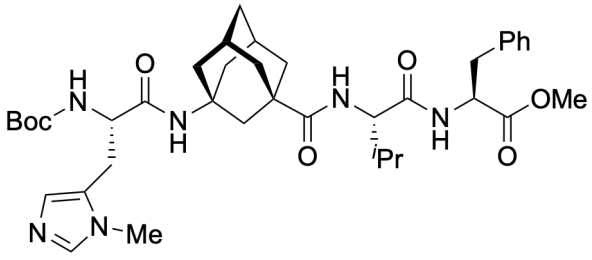
Box-Pmh-AGly-AdAla-Phe-OMe **120**



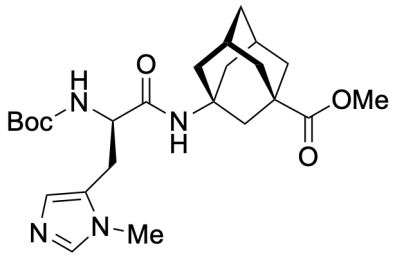
Boc-Pmh-AGly-Trp-Phe-OMe **155**



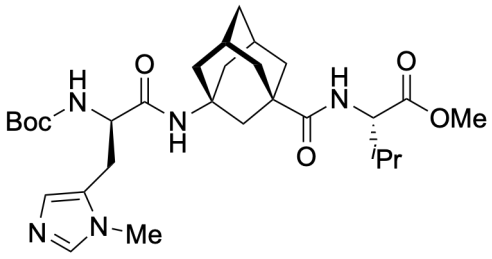
Boc-Pmh-AGly-Gly-Phe-OMe **118**



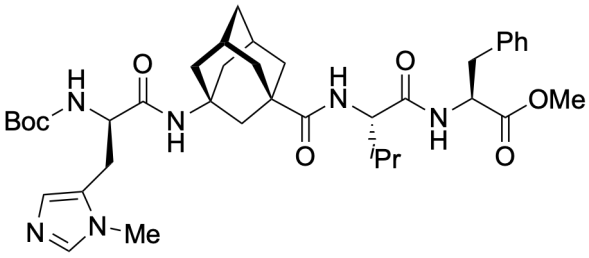
Boc-Pmh-AGly-Val-Phe-OMe **156**



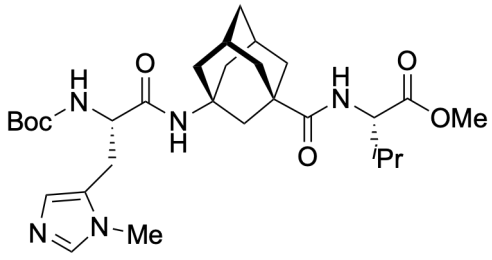
Boc-D-Pmh-AGly-OMe **157**



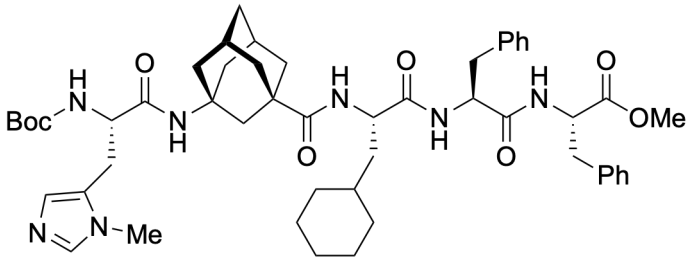
Boc-D-Pmh-AGly-Val-OMe **158**



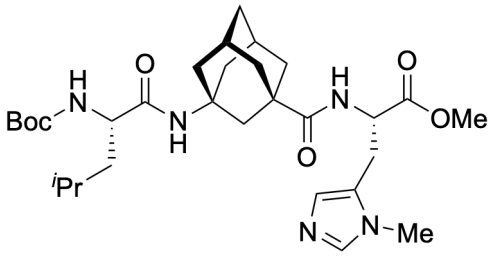
Boc-D-Pmh-AGly-Val-Phe-OMe **159**



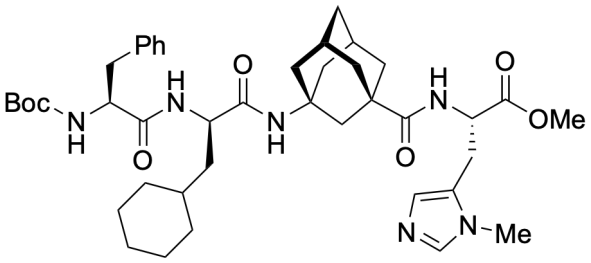
Boc-Pmh-AGly-Val-OMe **160**



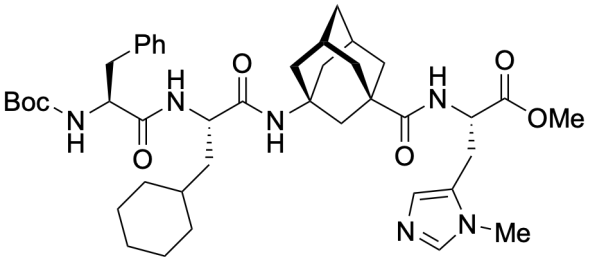
Boc-Pmh-AGly-Cha-Phe-Phe-MeO **119**



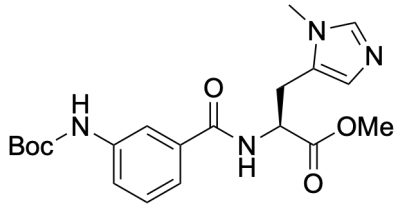
Boc-Leu-AGly-Pmh-OMe **102**



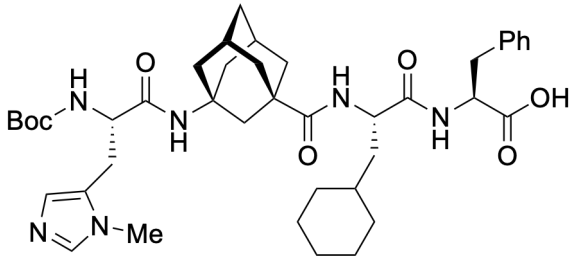
Boc-D-Phe-Cha-AGly-Pmh-OMe **161**



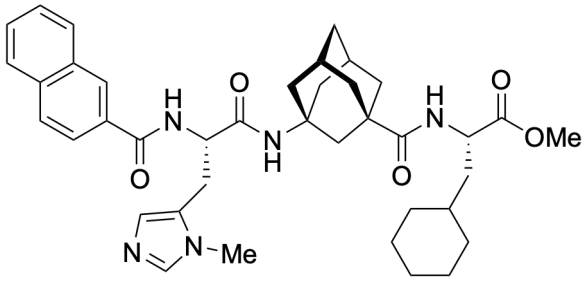
Boc-Phe-Cha-AGly-Pmh-OMe **106**



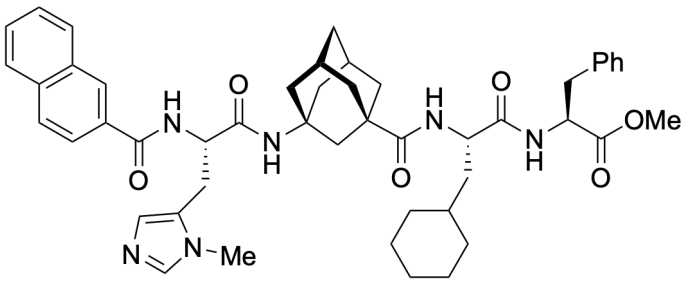
Boc-(*m*Ph)-Pmh-OMe **162**



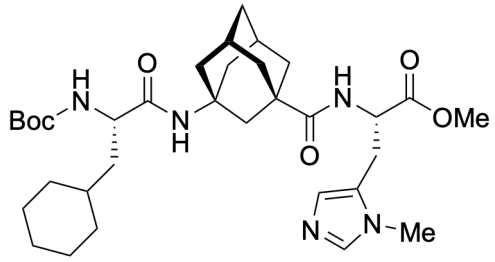
Boc-Pmh-AGly-Cha-Phe-OH **163**



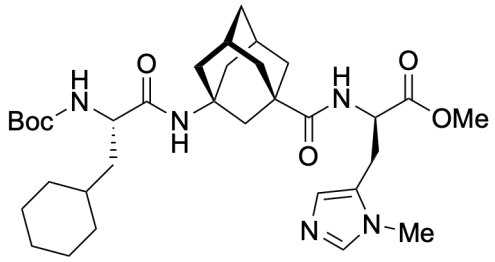
2-Naph-Pmh-AGly-Cha-OMe **111**



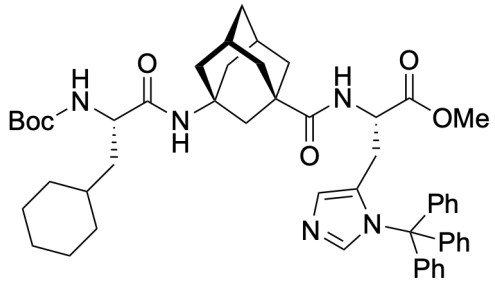
2-Naph-Pmh-AGly-Cha-Phe-OMe **164**



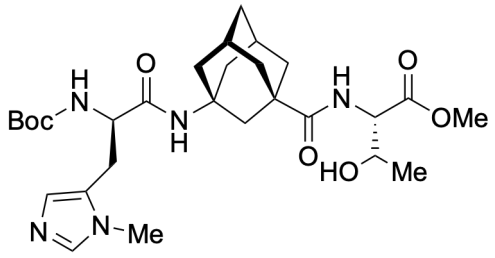
Boc-Cha-AGly-Pmh-OMe **50**



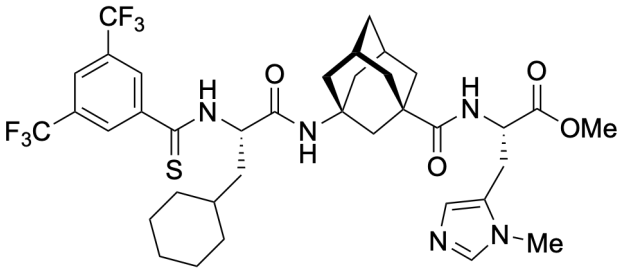
Boc-Cha-AGly-D-Pmh-OMe **105**



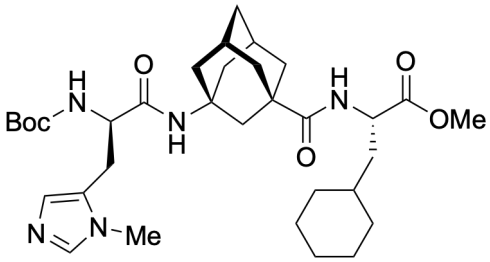
Boc-Cha-AGly-*tau*TrtHis-OMe **104**



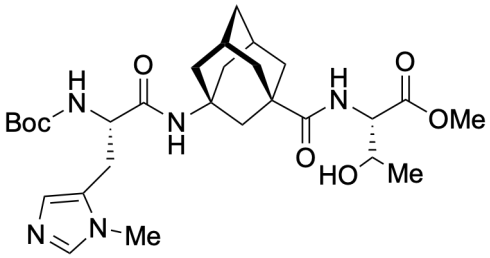
Boc-D-Pmh-AGly-Thr-OMe **165**



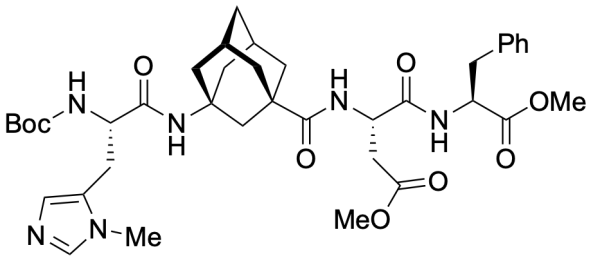
Thiourea-Cha-AGly-Pmh-Ome **107**



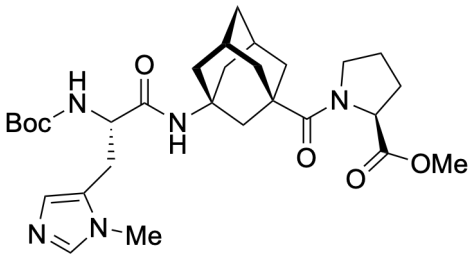
Boc-Pmh-AGly-D-Cha-OMe **125**



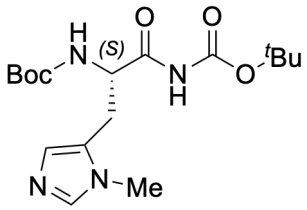
Boc-Pmh-AGly-Thr-OMe **166**



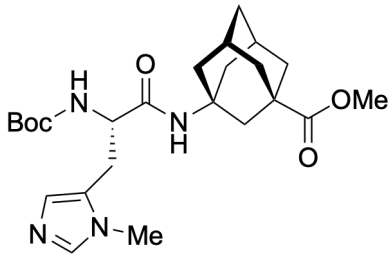
Boc-Pmh-AGly-Asp(OMe)-Phe-OMe **167**



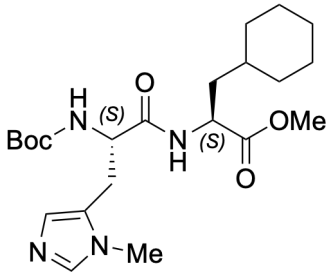
Boc-Pmh-AGly-Pro-OMe **168**



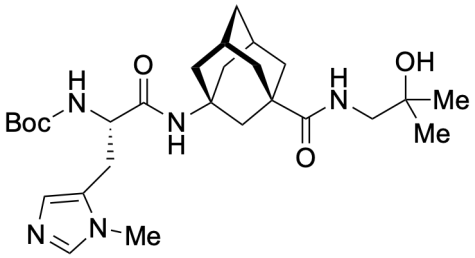
Boc-Pmh-OMe **169**



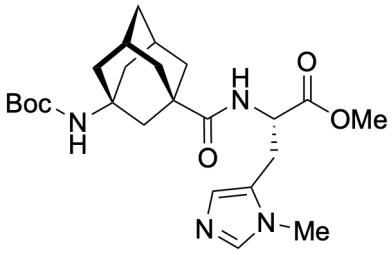
Boc-Pmh-AGly-OMe **170**



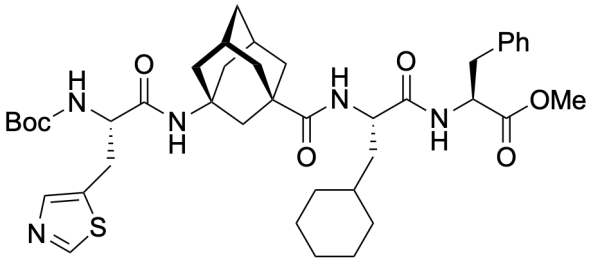
Boc-Pmh-Cha-OMe **171**



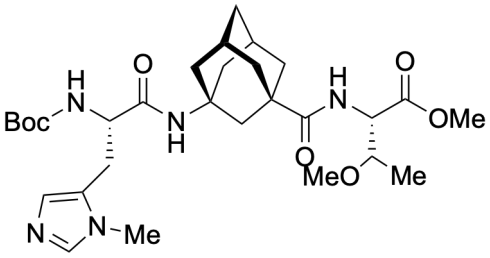
Boc-Pmh-AGly-2-propanol-2-Me-1-amino **172**



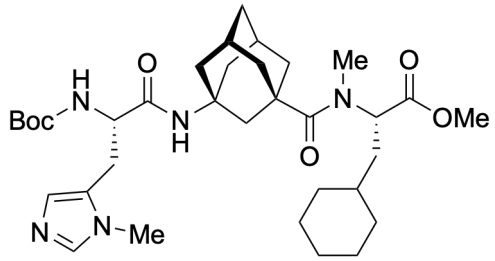
Boc-AGly-Pmh-OMe **110**



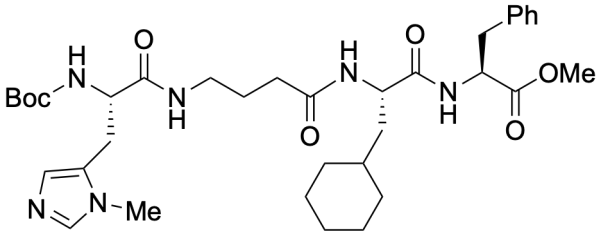
Boc-Thiazol-AGly-Cha-Phe-OMe **173**



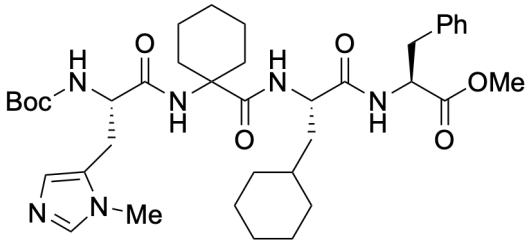
Boc-Pmh-AGly-Thr(OMe)-OMe **174**



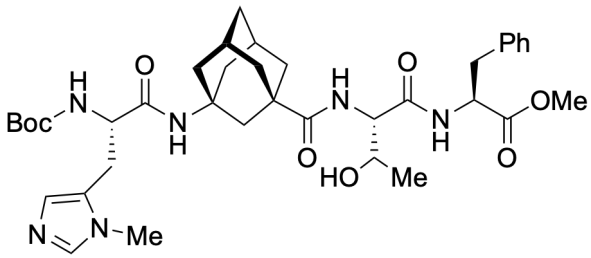
Boc-Pmh-AGly-Cha-N(Me)-OMe **114**



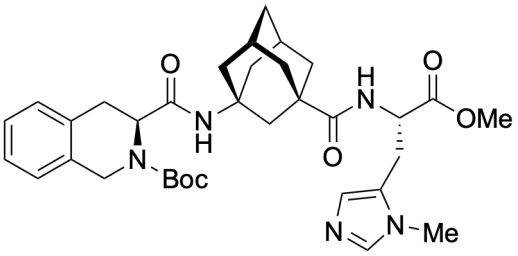
Boc-Pmh-Gab-Cha-Phe-OMe **121**



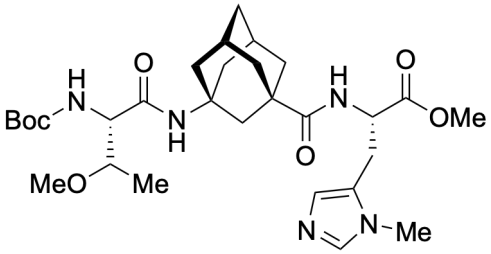
Boc-Pmh-A_6C_6-Cha-Phe-OMe **122**



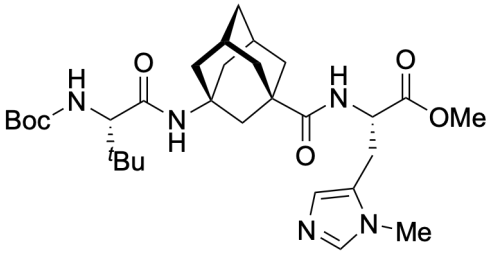
Boc-Pmh-AGly-Thr-Phe-OMe **175**



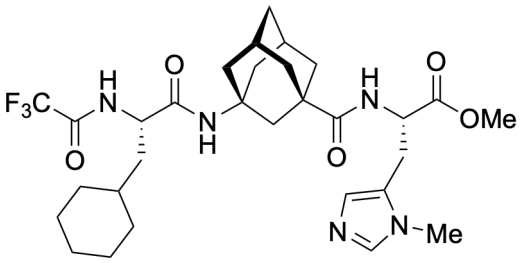
Boc-Tic-AGly-Pmh-Ome **176**



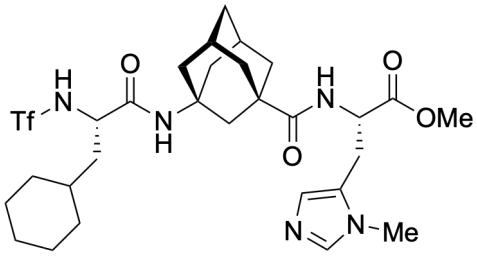
Boc-Thr(OMe)-AGly-Pmh-OMe **108**



Boc-Tle-AGly-Pmh-OMe **177**



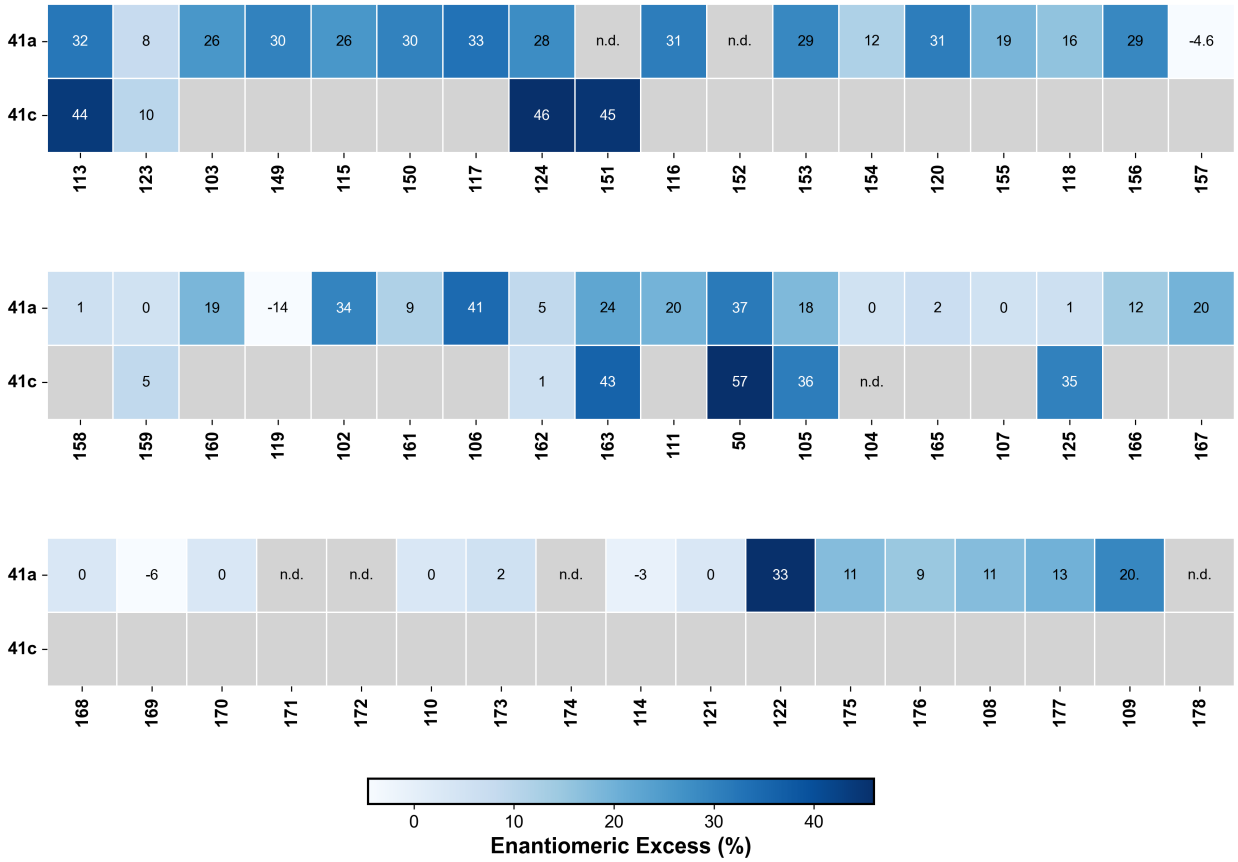
CF_3Ac-Cha-AGly-Pmh-OMe **109**



Tf-Cha-AGly-Pmh-OMe **178**

6.6.4 Remaining Dakin-West reactions

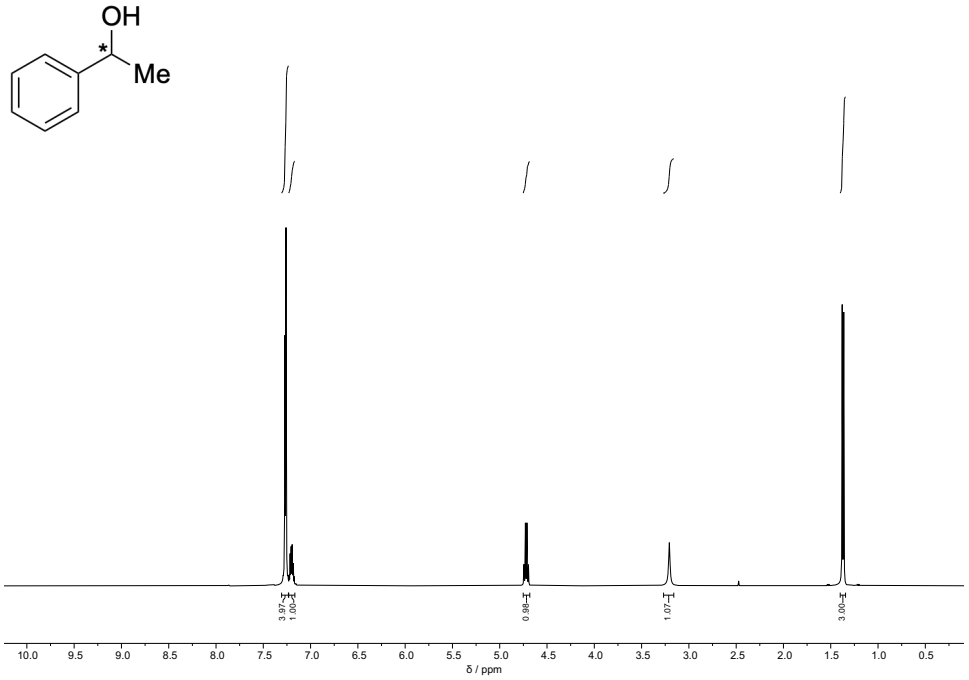
Heatmap illustrating the complete experimental dataset of the asymmetric Dakin-West reaction, mapping the *ee* across the entire peptide catalyst library.



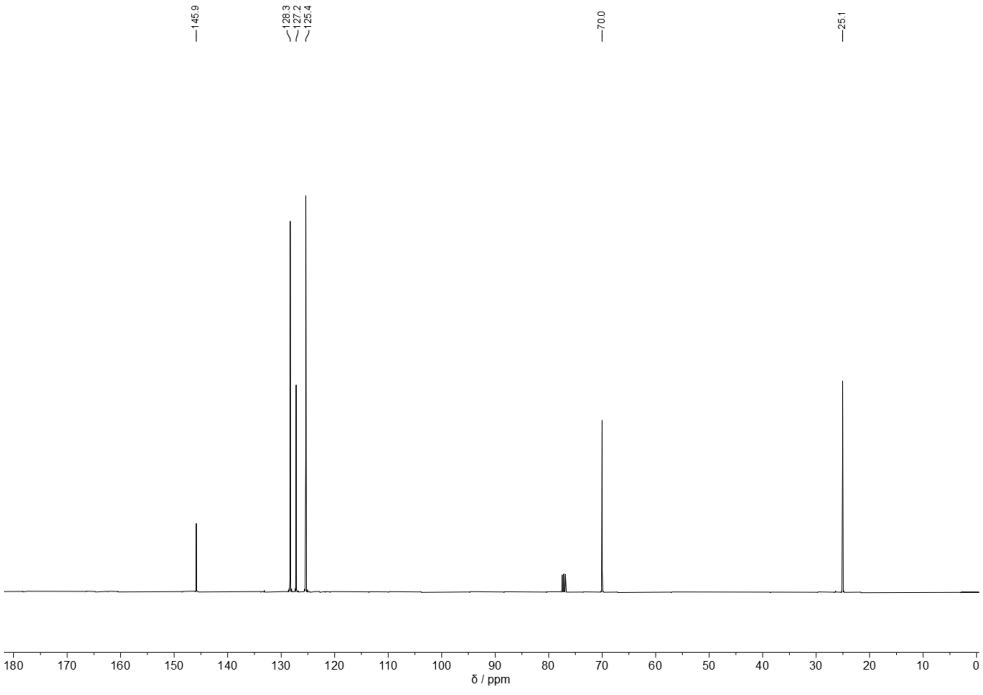
7 Analytical Data

1-Phenylethanol (rac-**14a)**:

^{1}H-NMR (400 MHz, $CDCl_3$):

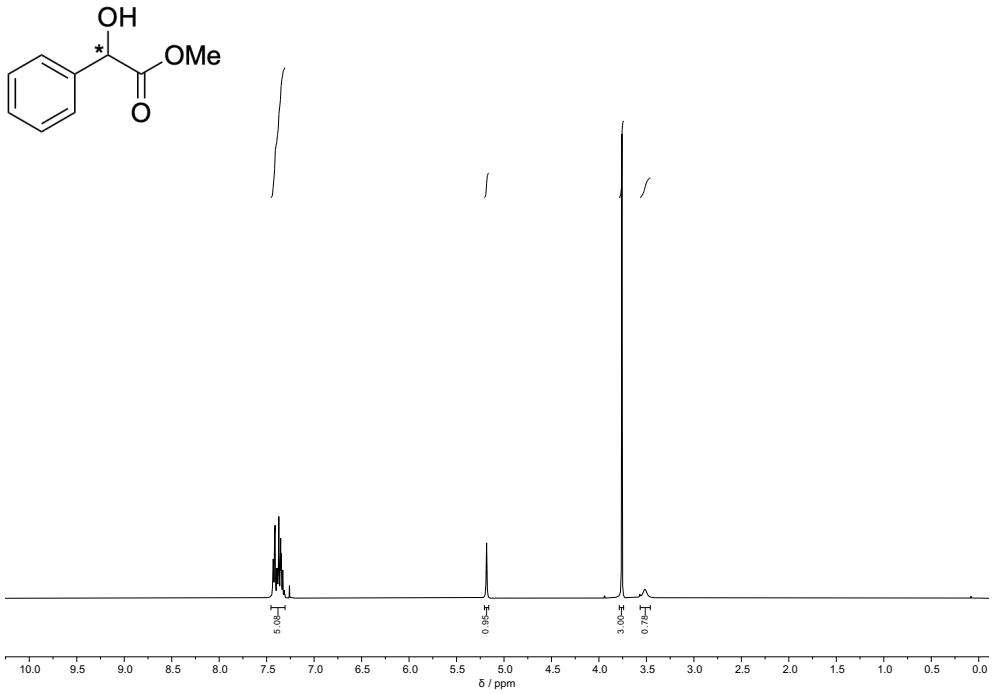


^{13}C-NMR (101 MHz, $CDCl_3$):

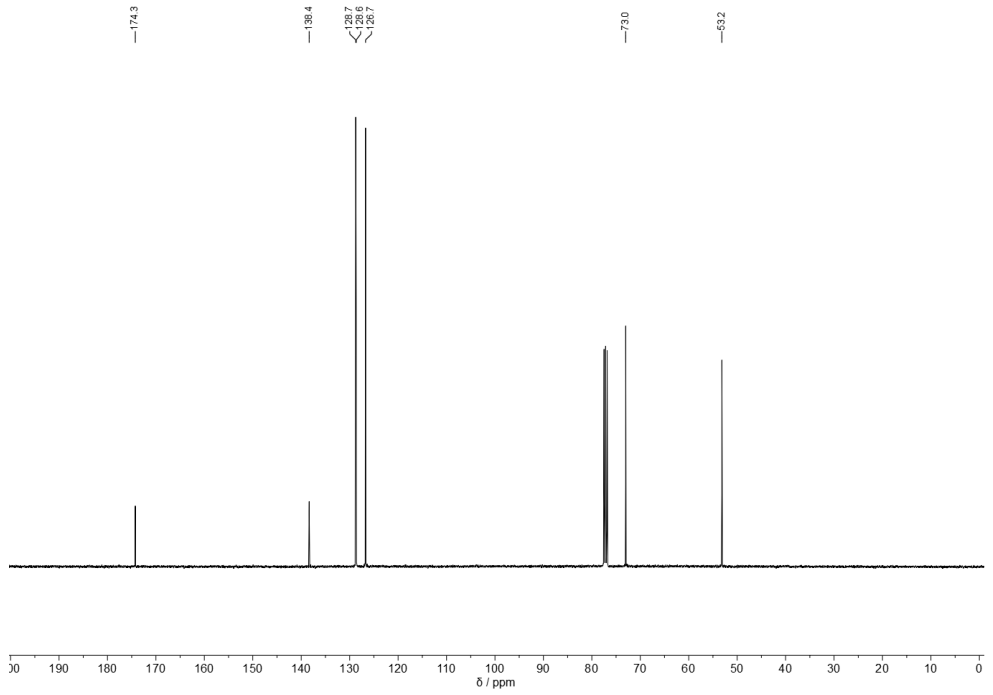


Methyl-2-hydroxy-2-phenylacetate (rac-**131**):

^{1}H-NMR (400 MHz, $CDCl_3$):

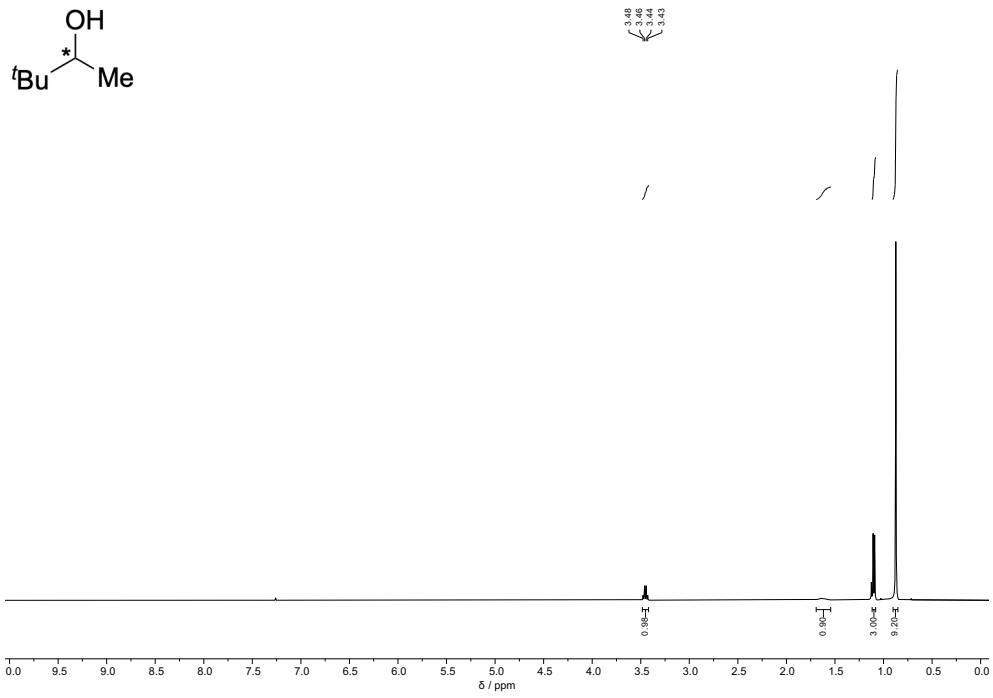


^{13}C-NMR (101 MHz, $CDCl_3$):

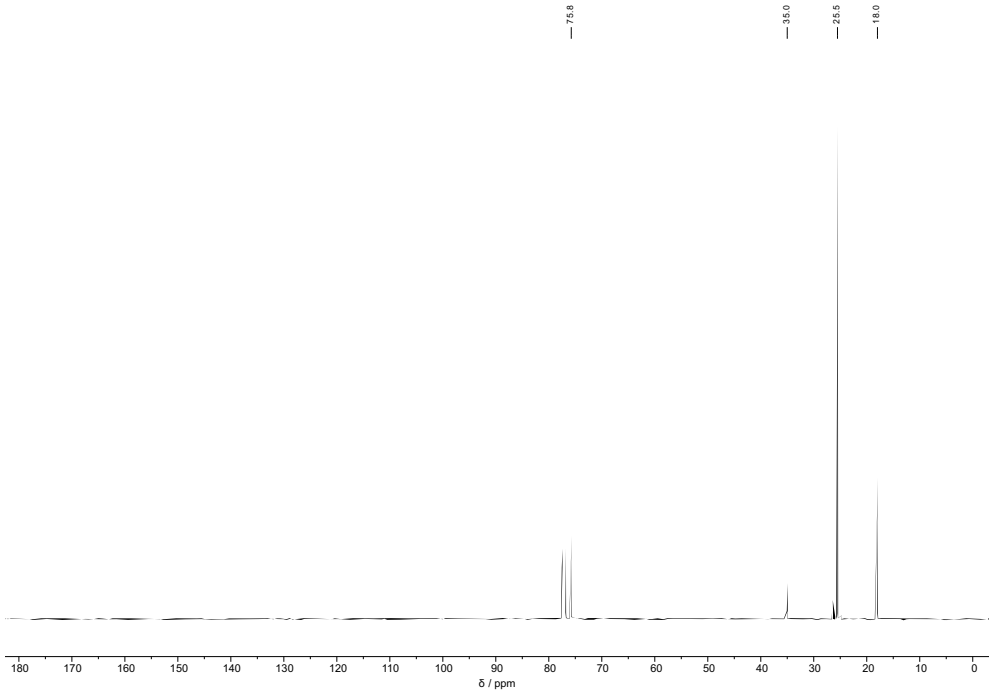


3,3-Dimethylbutan-2-ol (rac-**23a**):

^{1}H-NMR (400 MHz, $CDCl_3$):

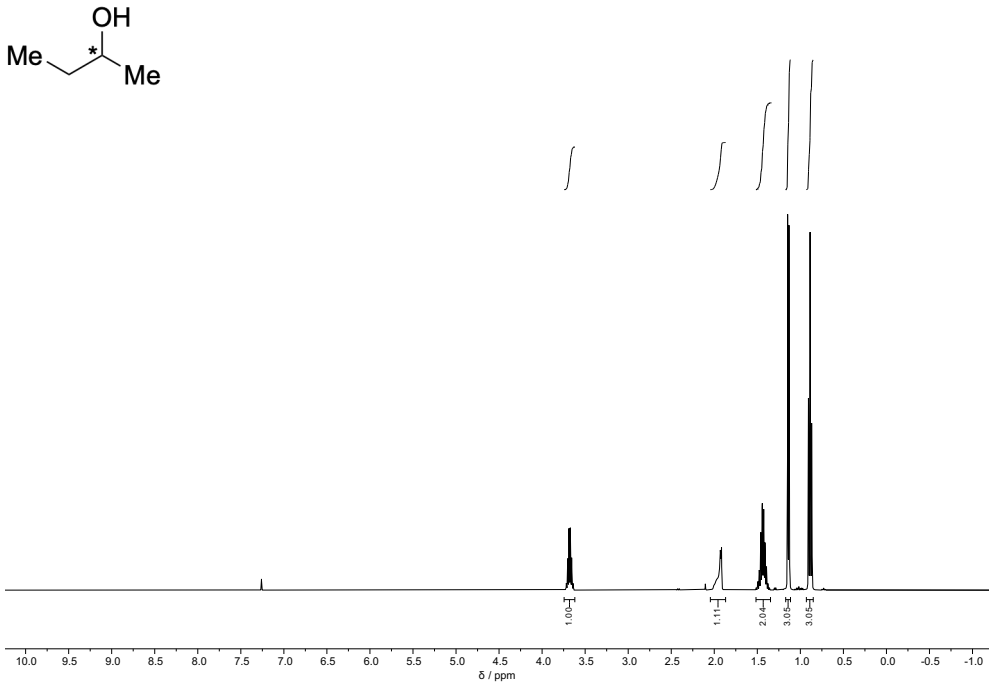


^{13}C-NMR (101 MHz, $CDCl_3$):

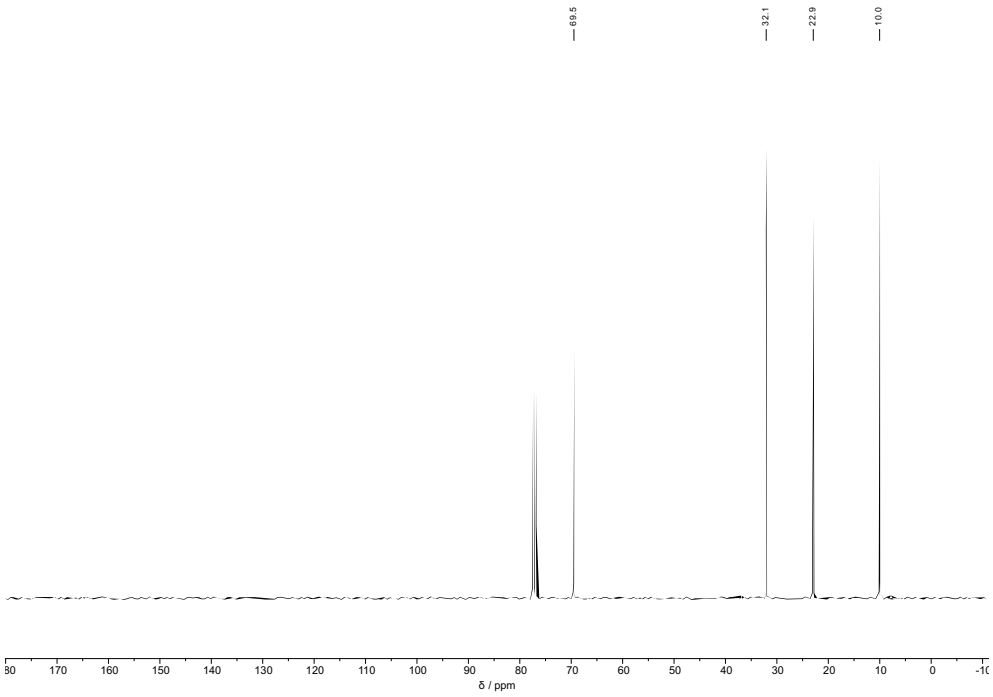


Butan-2-ol (rac-**67**):

^{1}H-NMR (400 MHz, $CDCl_3$):

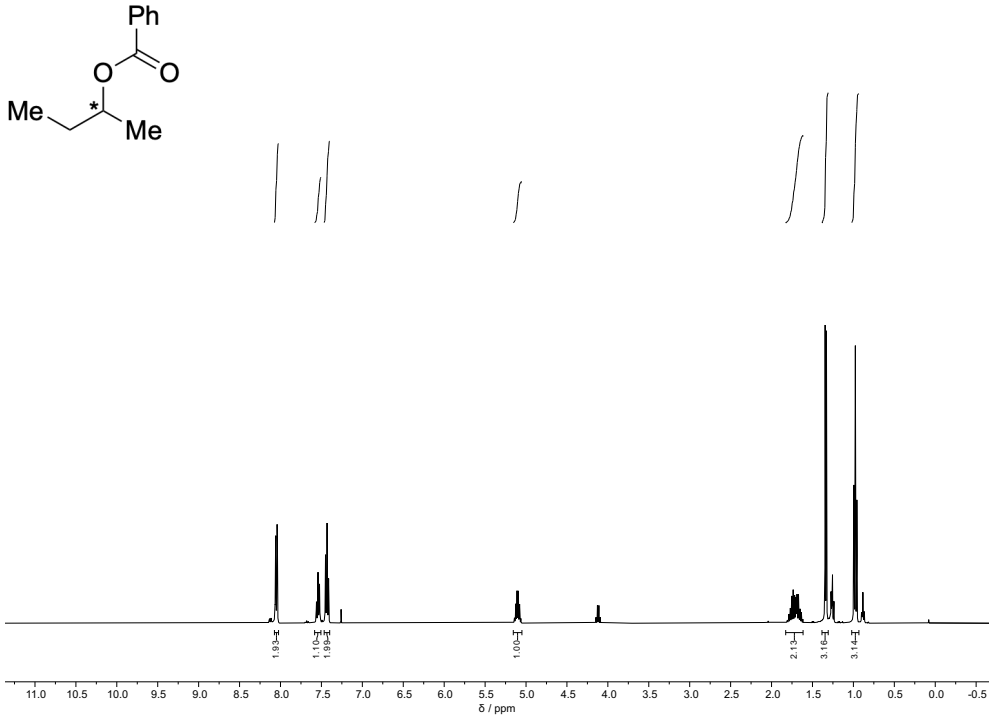


^{13}C-NMR (101 MHz, $CDCl_3$):

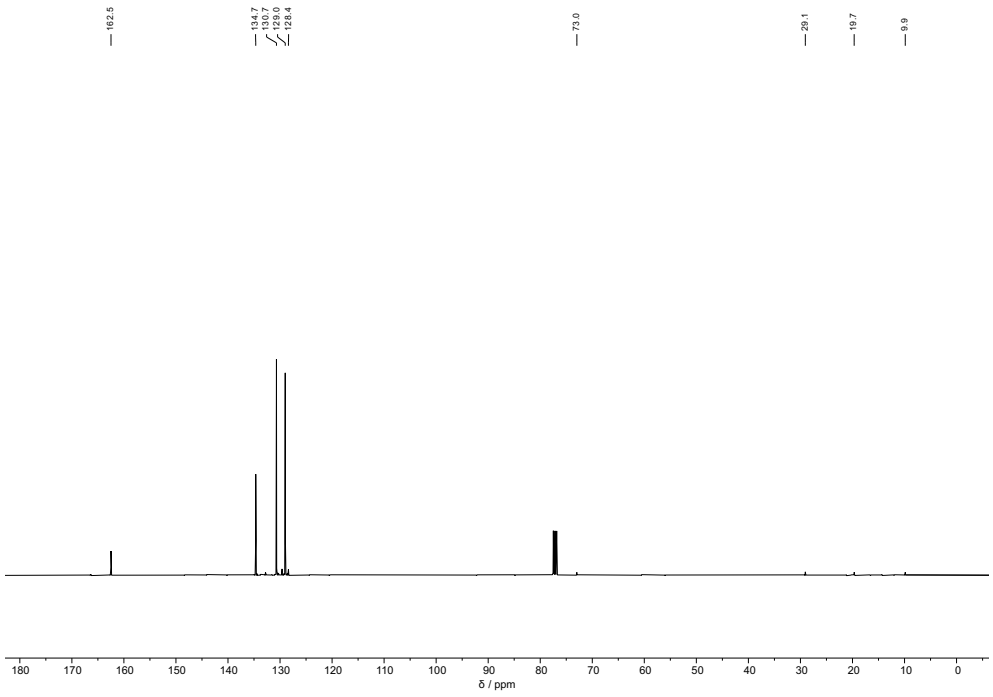


Sec-butyl benzoate (rac-**85d**):

^{1}H-NMR (400 MHz, $CDCl_3$):

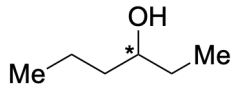


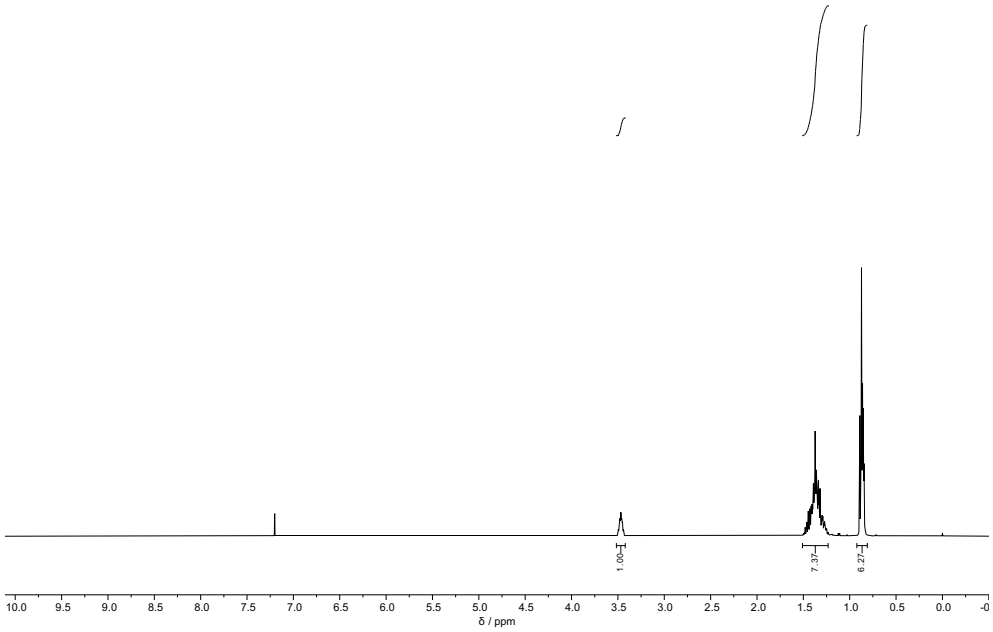
^{13}C-NMR (101 MHz, $CDCl_3$):



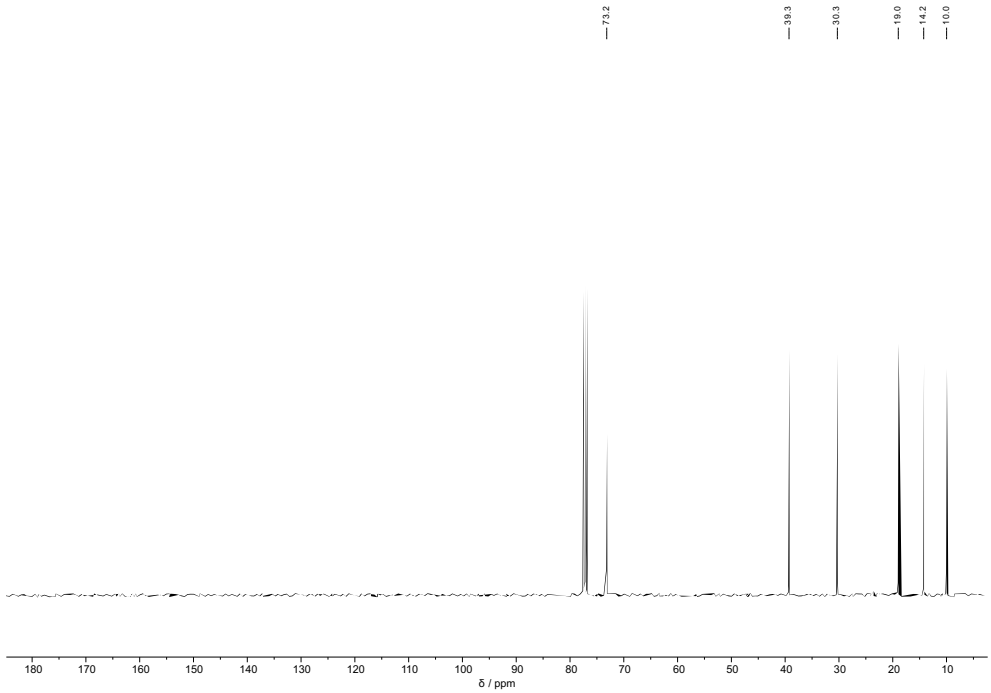
Hexan-3-ol (rac-**132**):

^{1}H-NMR (400 MHz, $CDCl_3$):



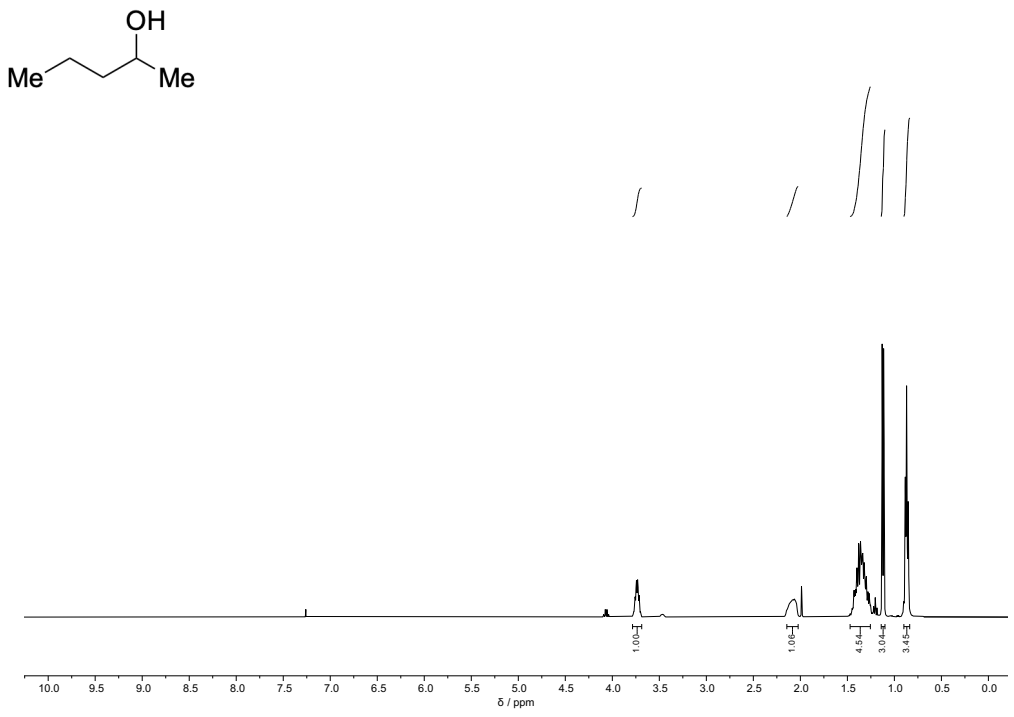


^{13}C-NMR (101 MHz, $CDCl_3$):

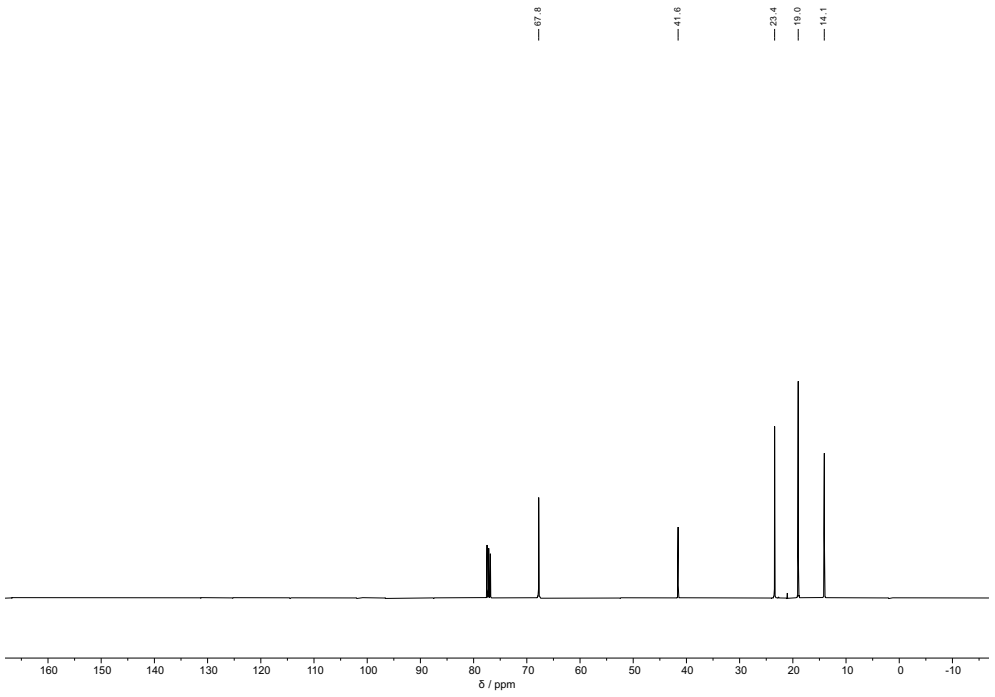


Pentan-2-ol (rac-**133**):

^{1}H-NMR (400 MHz, $CDCl_3$):

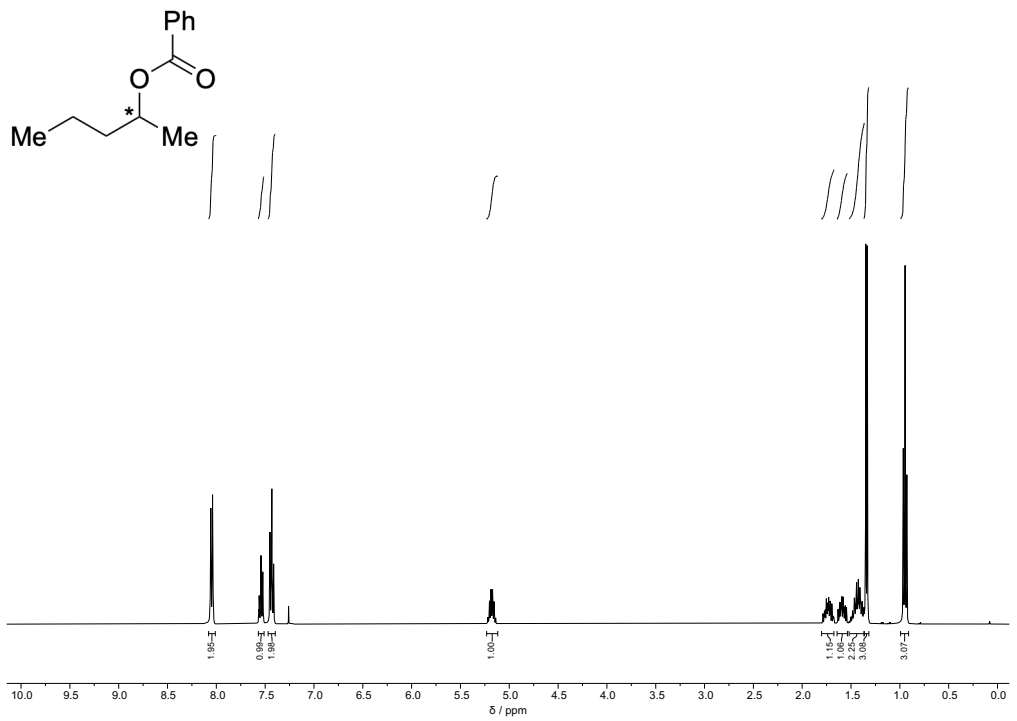


^{13}C-NMR (101 MHz, $CDCl_3$):

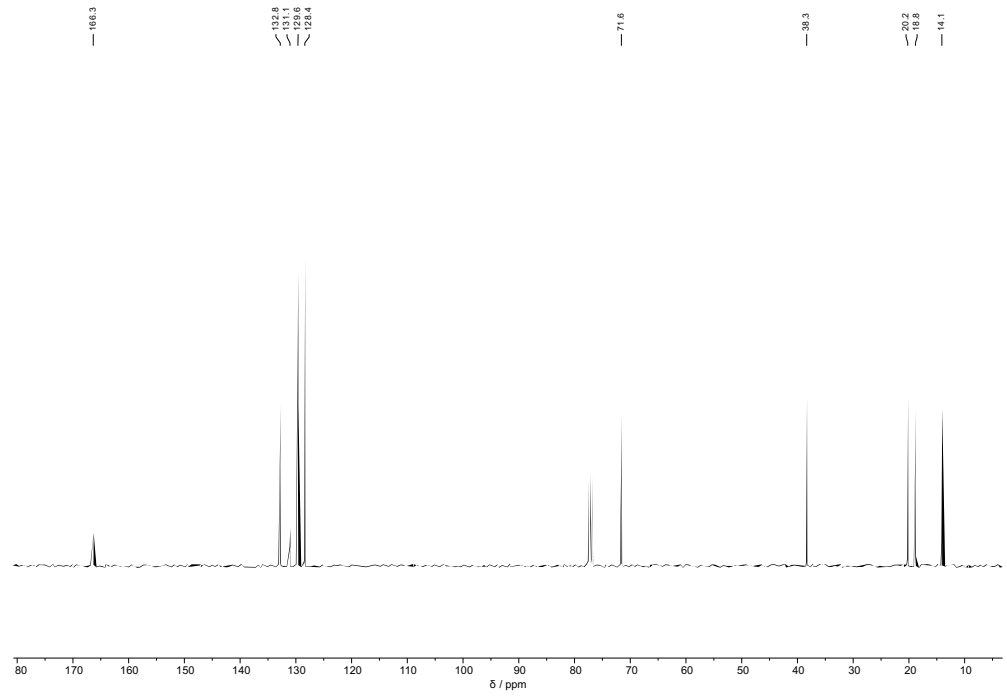


Pentan-2-yl benzoate (rac-**134**):

^{1}H-NMR (400 MHz, $CDCl_3$):

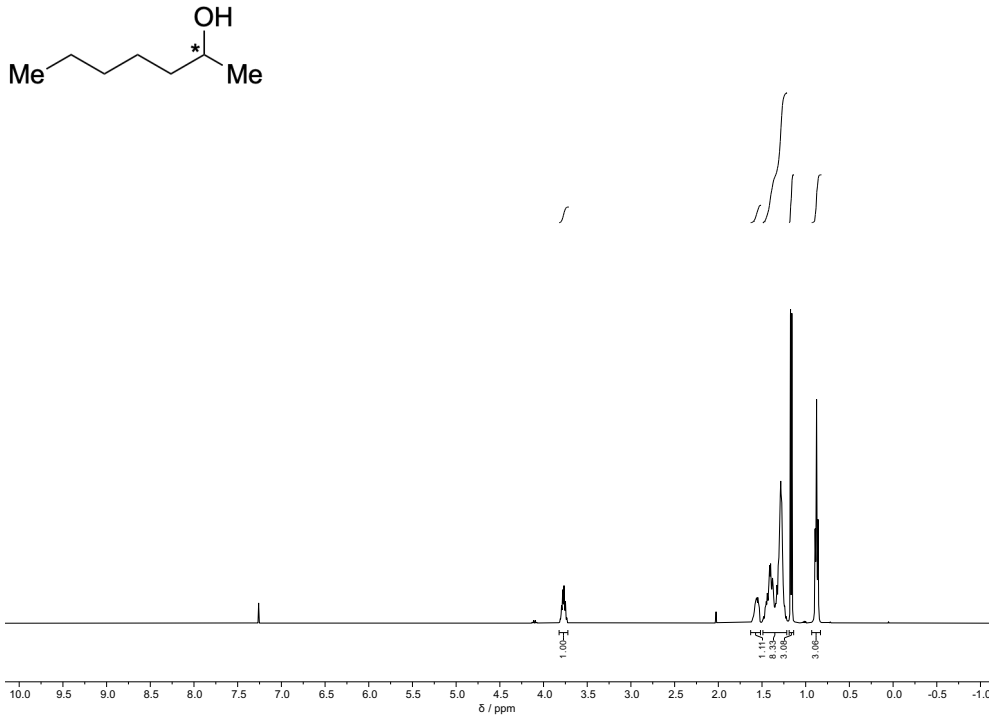


^{13}C-NMR (101 MHz, $CDCl_3$):

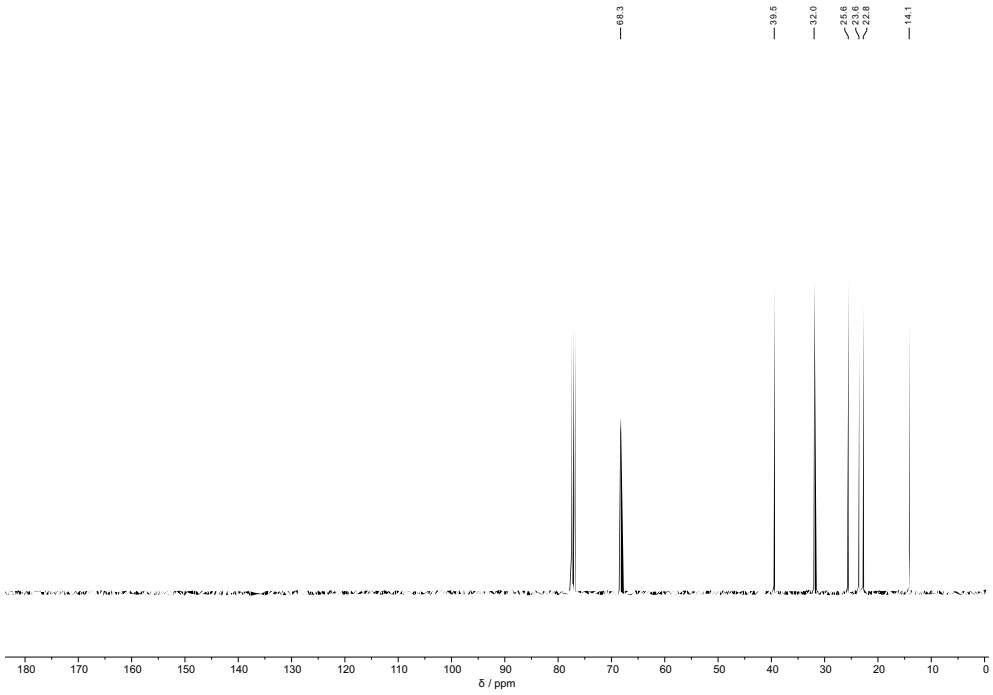


Heptan-2-ol (rac-**135**):

^{1}H-NMR (400 MHz, $CDCl_3$):

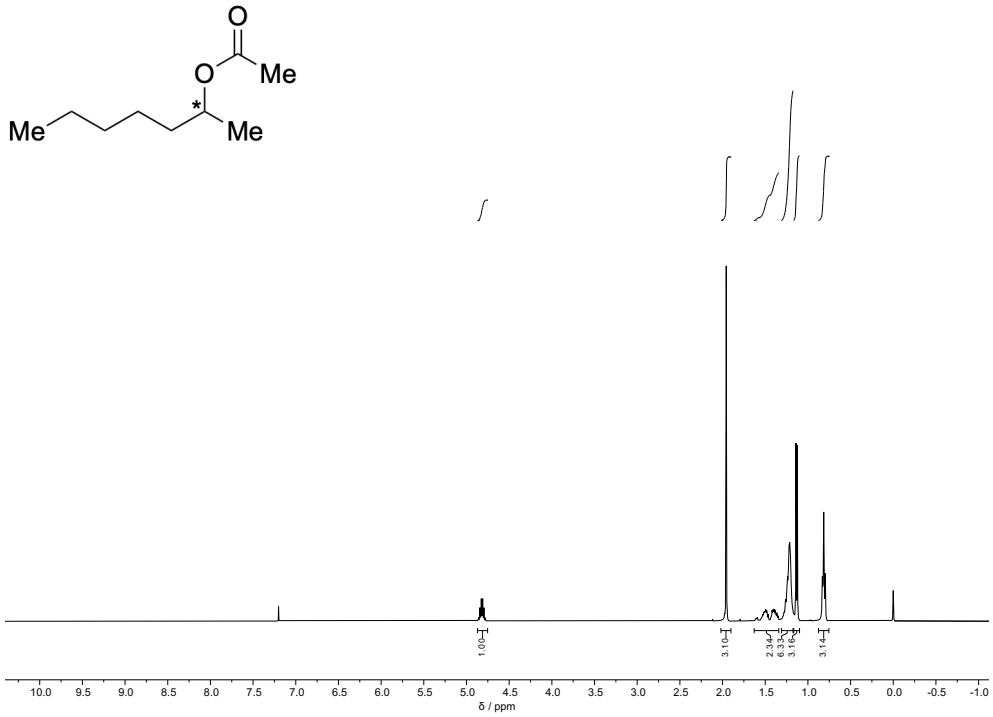


^{13}C-NMR (101 MHz, $CDCl_3$):

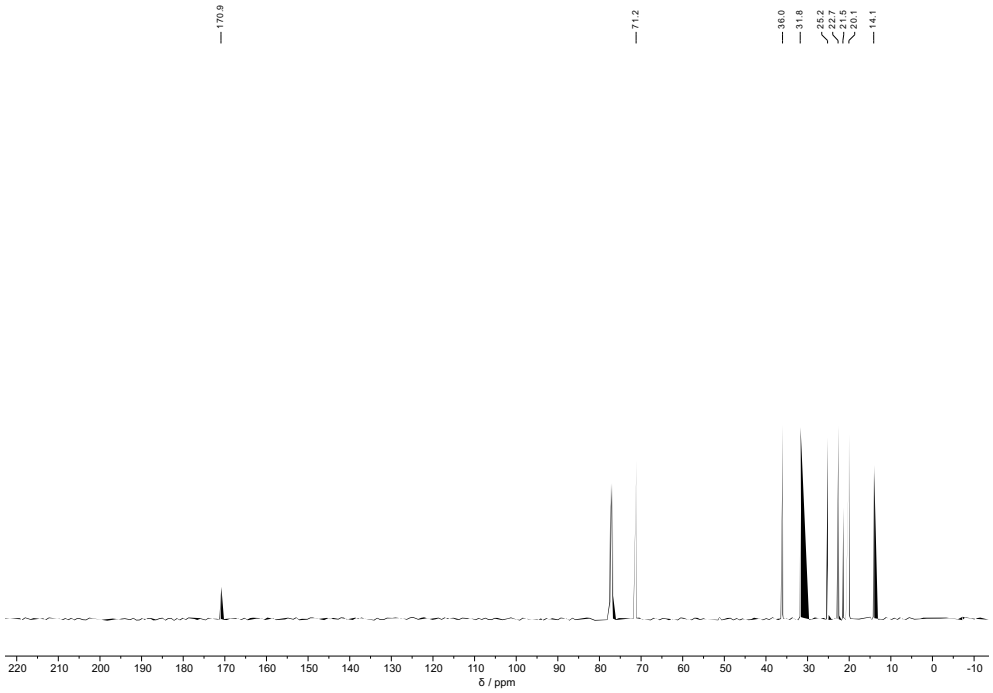


Heptan-2-yl acetate (rac-**136**):

^{1}H-NMR (400 MHz, $CDCl_3$):

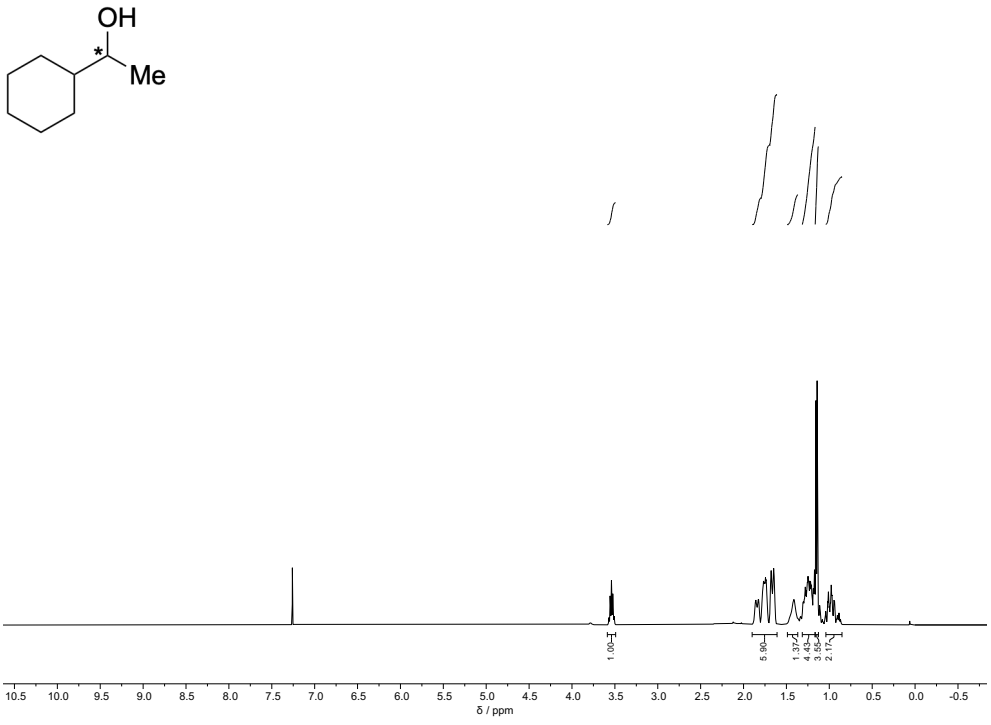


^{13}C-NMR (101 MHz, $CDCl_3$):

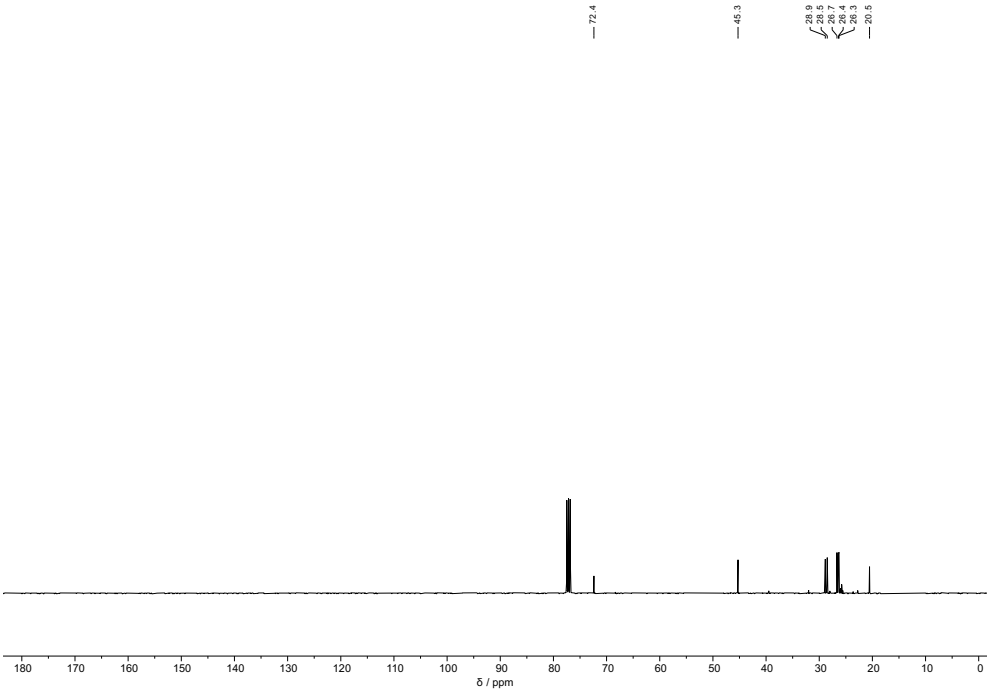


1-Cyclohexlethanol (rac-**23b**):

^{1}H-NMR (400 MHz, $CDCl_3$):

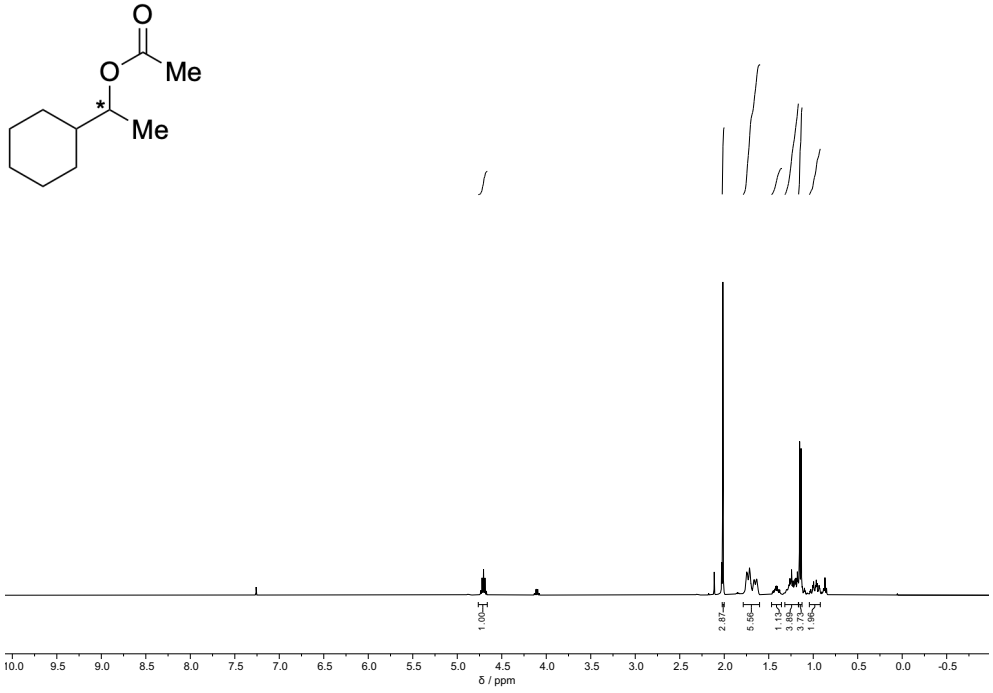


^{13}C-NMR (101 MHz, $CDCl_3$):

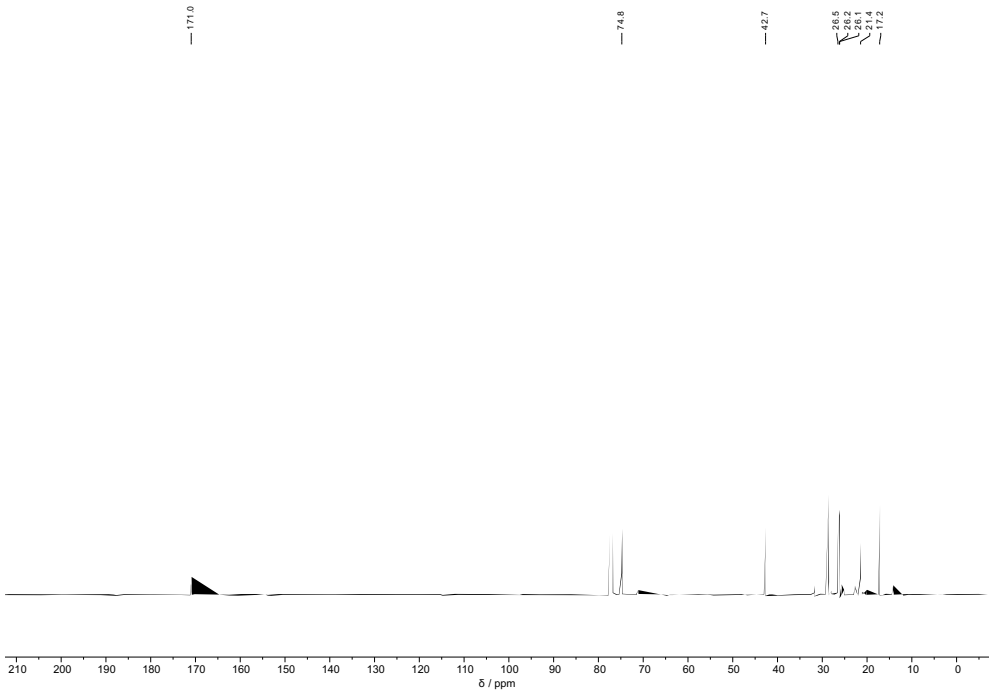


1-Cyclohexylethyl acetate (rac-**137**):

^{1}H-NMR (400 MHz, $CDCl_3$):

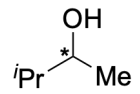


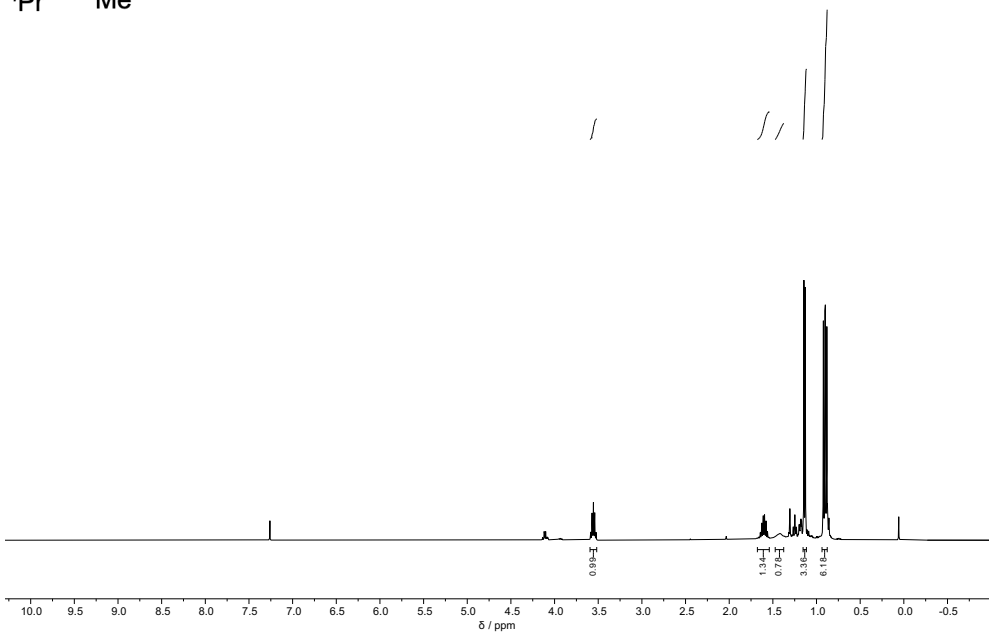
^{13}C-NMR (101 MHz, $CDCl_3$):



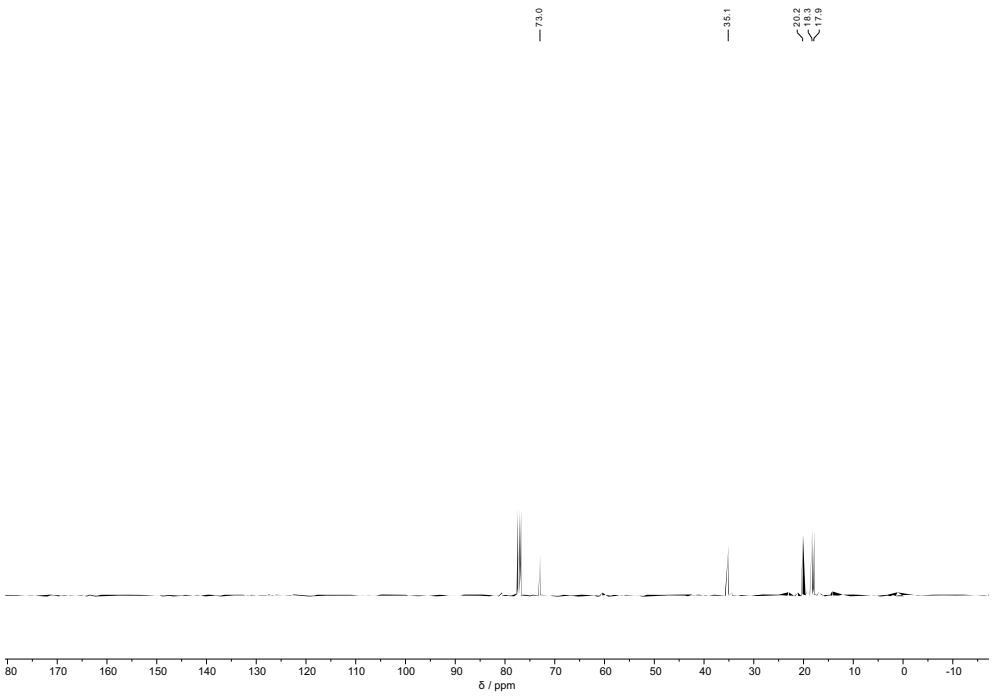
3-Methylbutan-2-ol (rac-**138**):

^{1}H-NMR (400 MHz, $CDCl_3$):



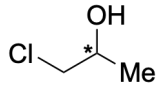


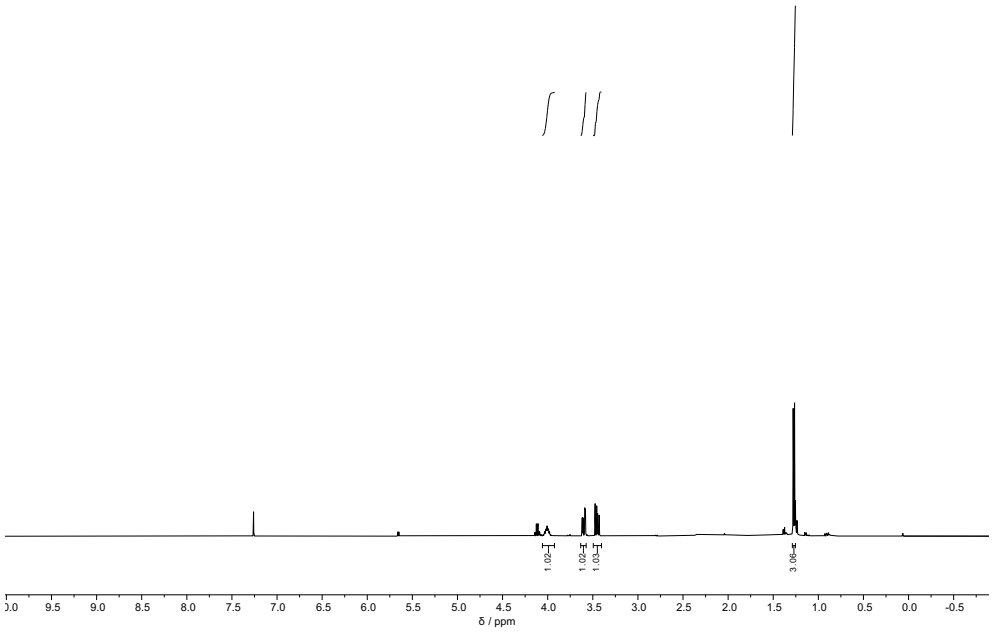
^{13}C-NMR (101 MHz, $CDCl_3$):



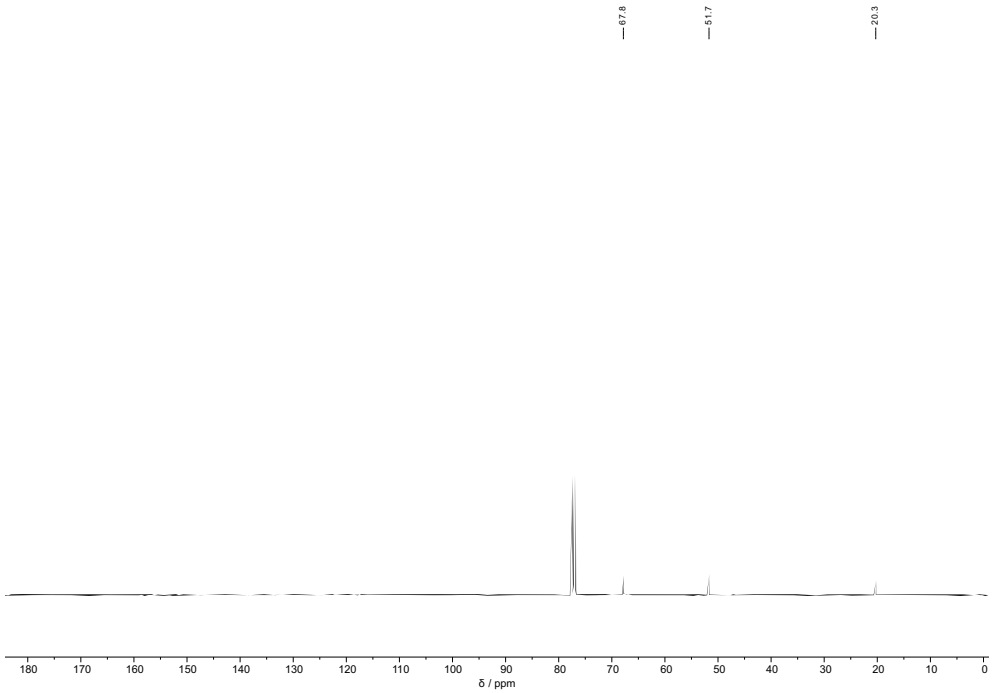
1-Chloropropan-2-ol (rac-**139**):

^{1}H-NMR (400 MHz, $CDCl_3$):



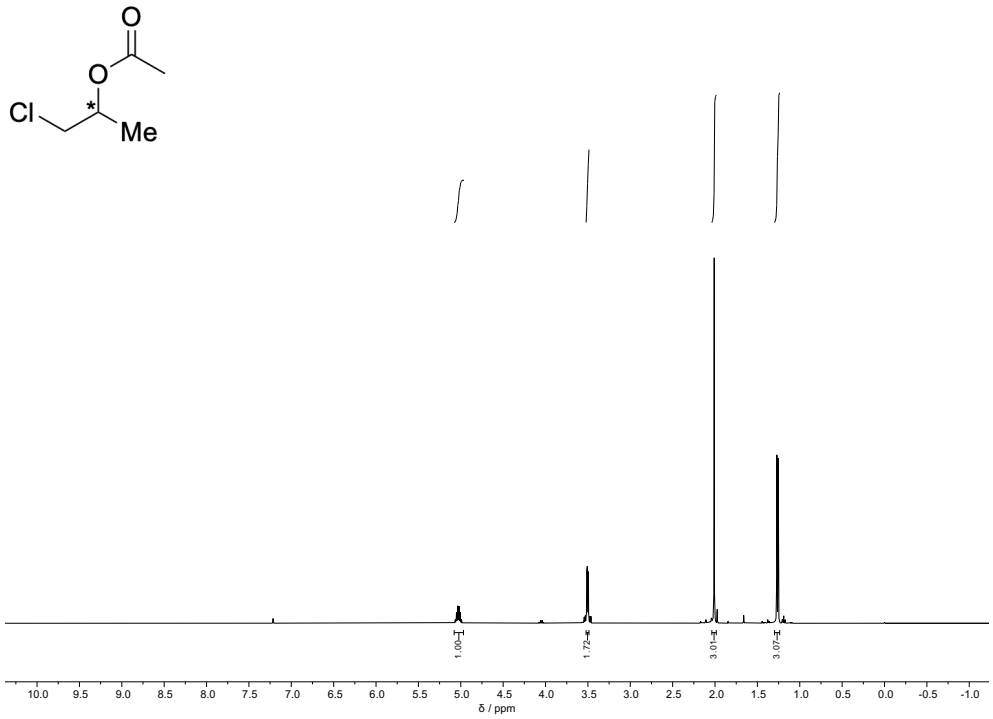


^{13}C-NMR (101 MHz, $CDCl_3$):

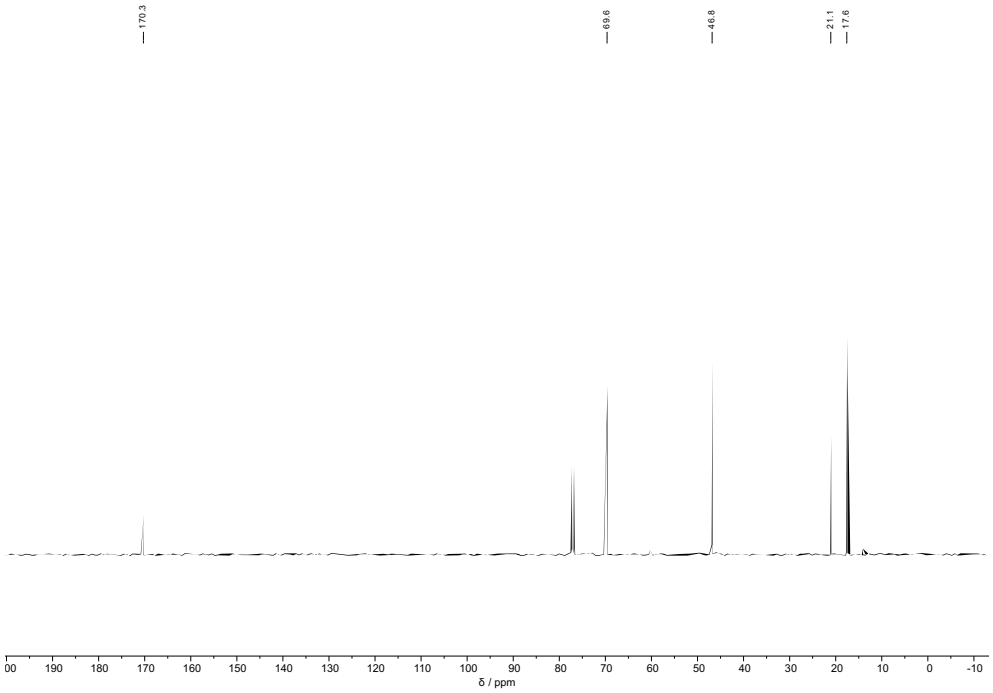


1-Chloropropan-2-yl acetate (rac-**140**):

^{1}H-NMR (400 MHz, $CDCl_3$):

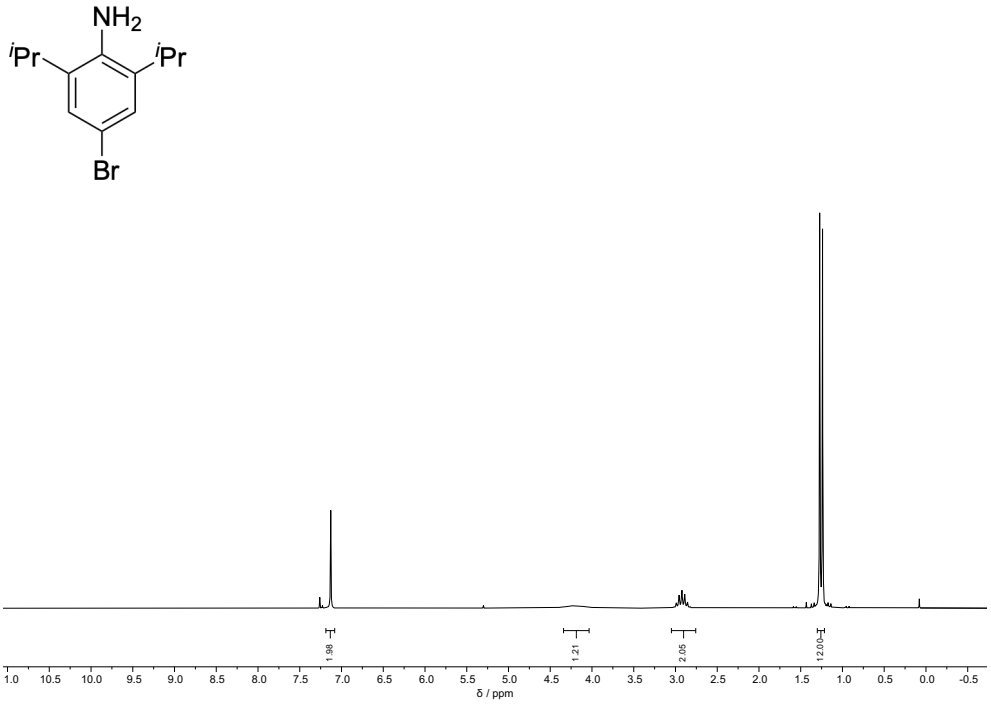


^{13}C-NMR (101 MHz, $CDCl_3$):



4-Bromo2,6-di-isopropylbenzenamine (**141**):

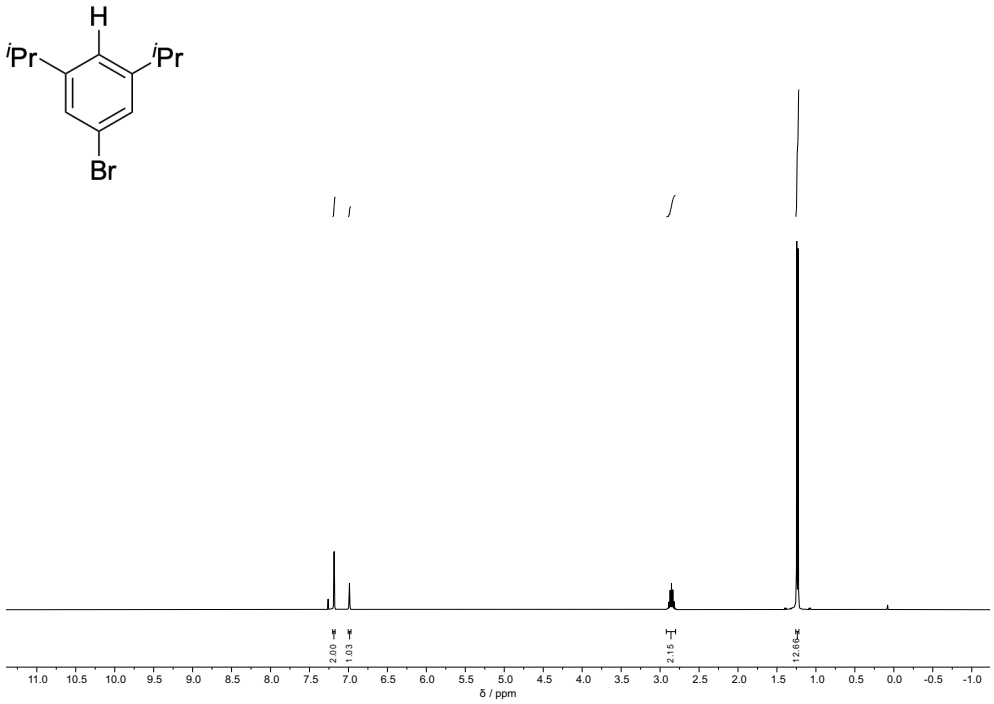
^{1}H-NMR (400 MHz, $CDCl_3$):



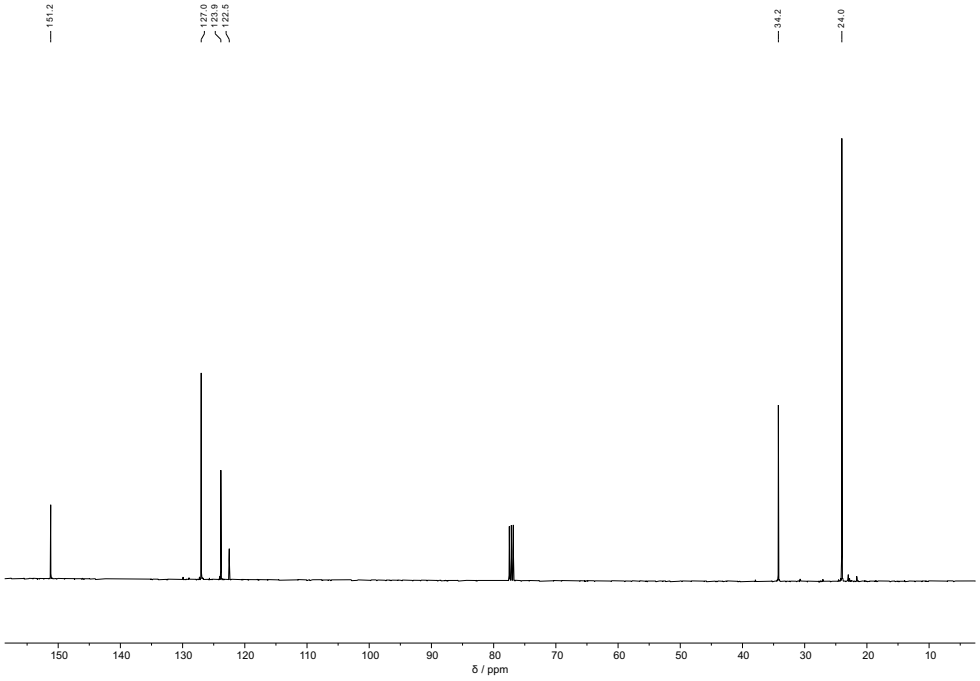
^{13}C-NMR (101 MHz, $CDCl_3$): none

1-Bromo-3,5-diisopropylbenzene (**142**):

^{1}H-NMR (400 MHz, $CDCl_3$):

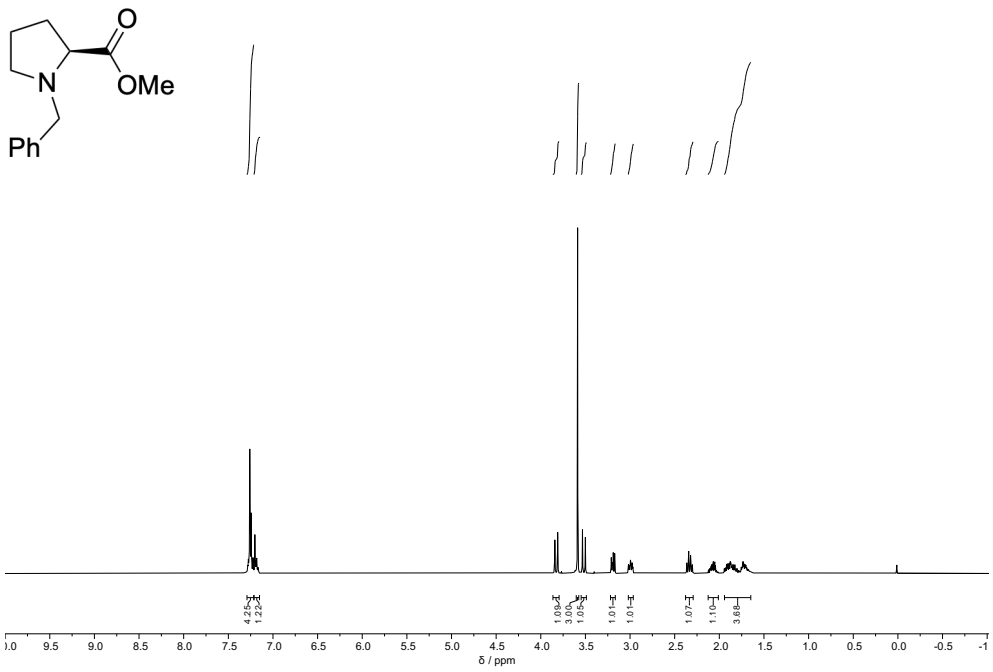


^{13}C-NMR (101 MHz, $CDCl_3$):

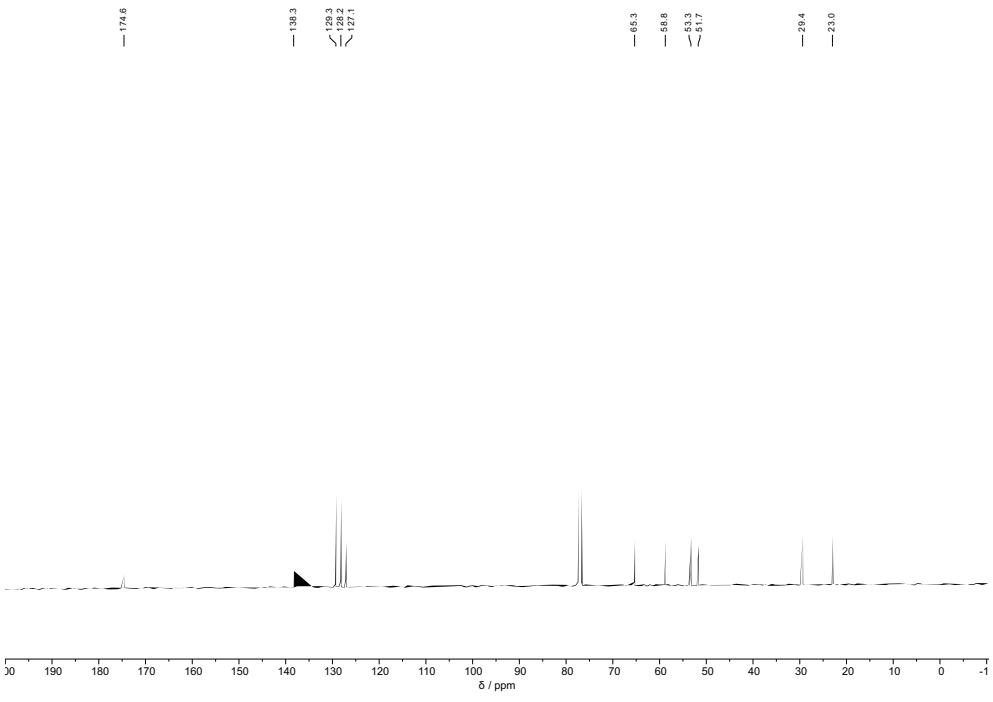


(*S*)-Methyl-1-benzylpyrrolidine-2-carboxylate (**52**):

^{1}H-NMR (400 MHz, $CDCl_3$):

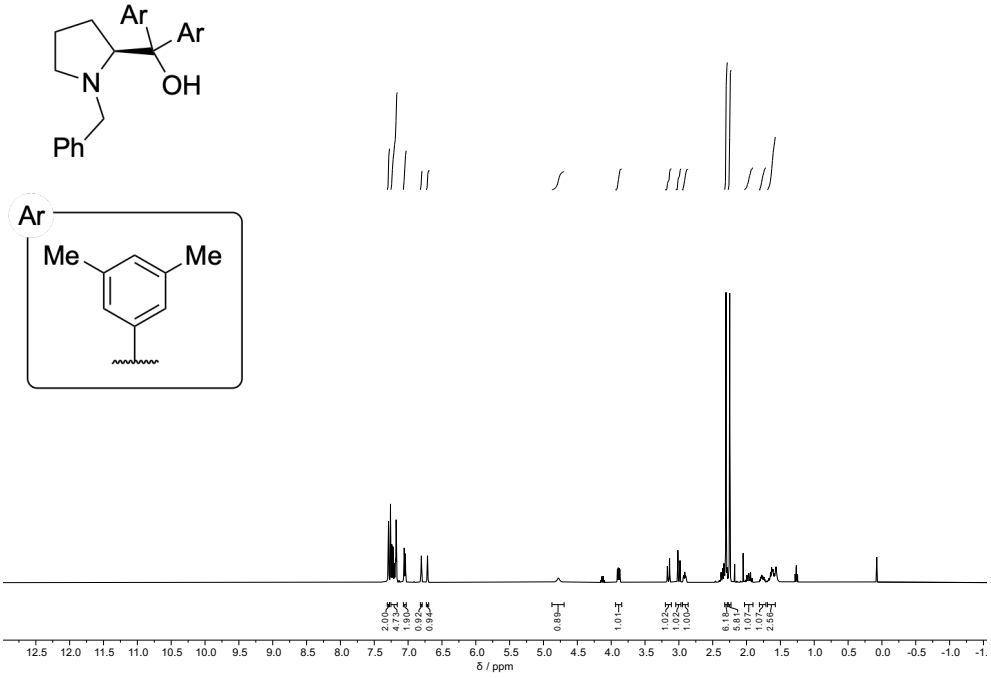


^{13}C-NMR (101 MHz, $CDCl_3$):

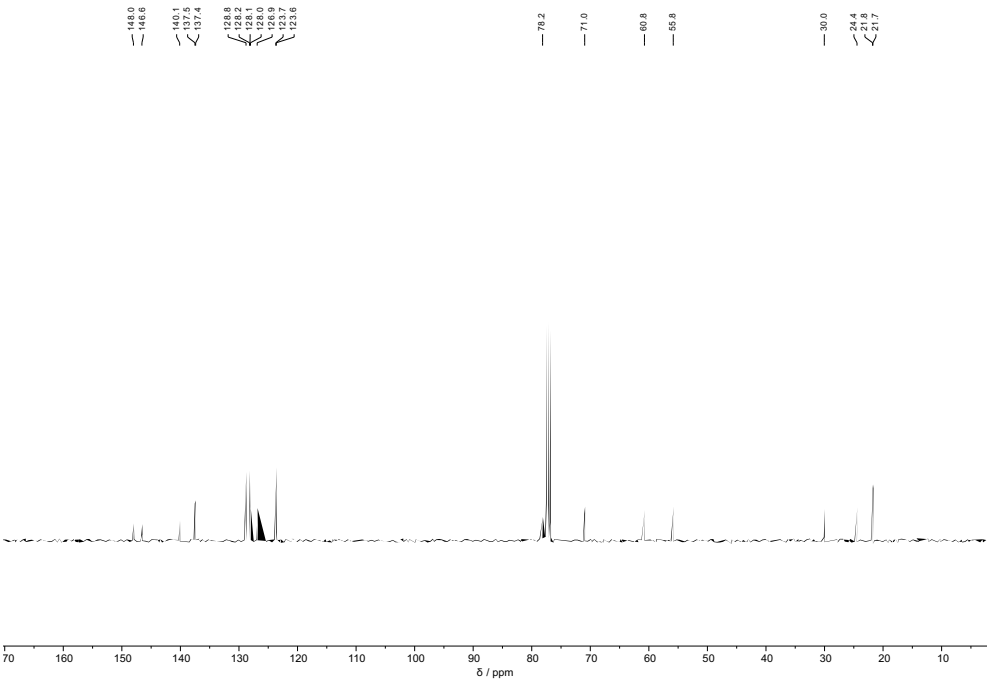


(*S*)-(1-Benzylpyrrolidin-2-yl)bis(3,5-dimethylphenyl)methanol (53b):

^{1}H-NMR (400 MHz, $CDCl_3$):

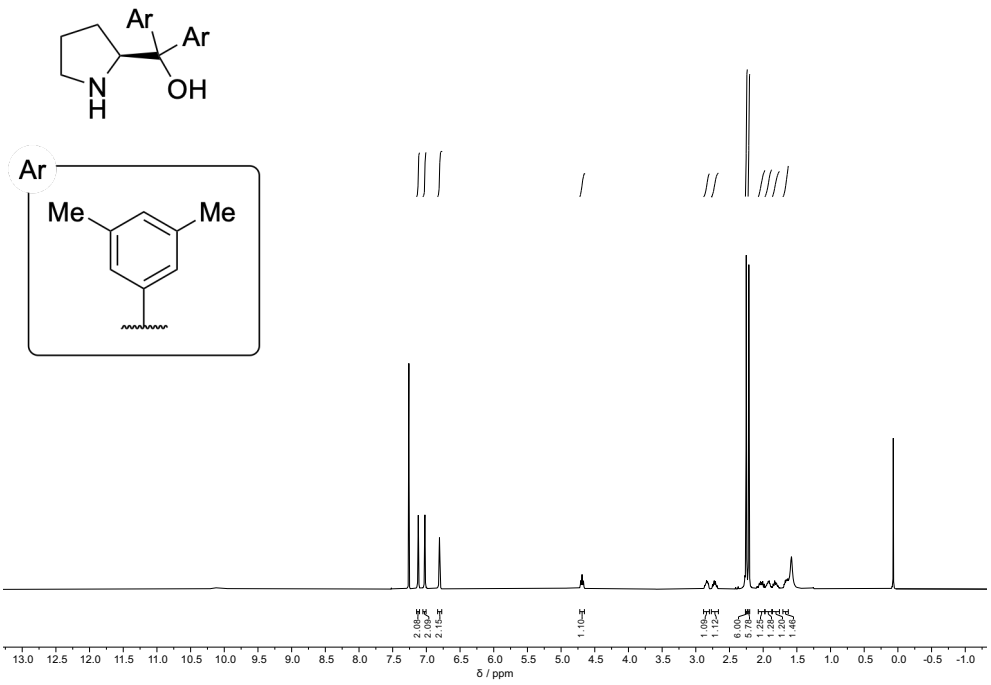


^{13}C-NMR (101 MHz, $CDCl_3$):

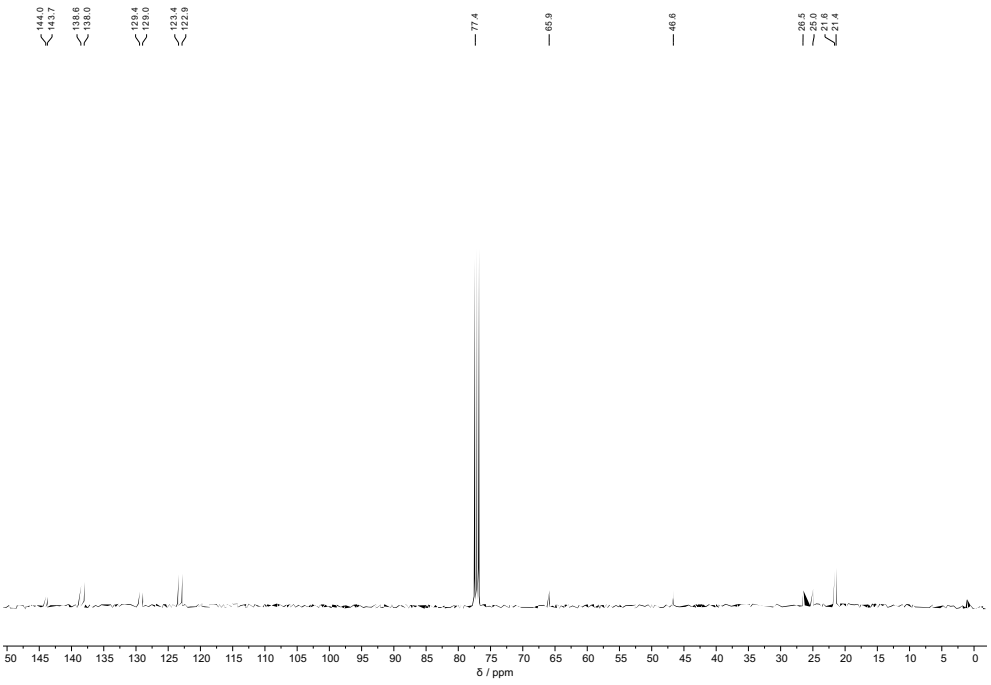


(*S*)-Bis(3,5-dimethylphenyl)(pyrrolidin-2-yl)methanol (**22b**):

^{1}H-NMR (400 MHz, $CDCl_3$):

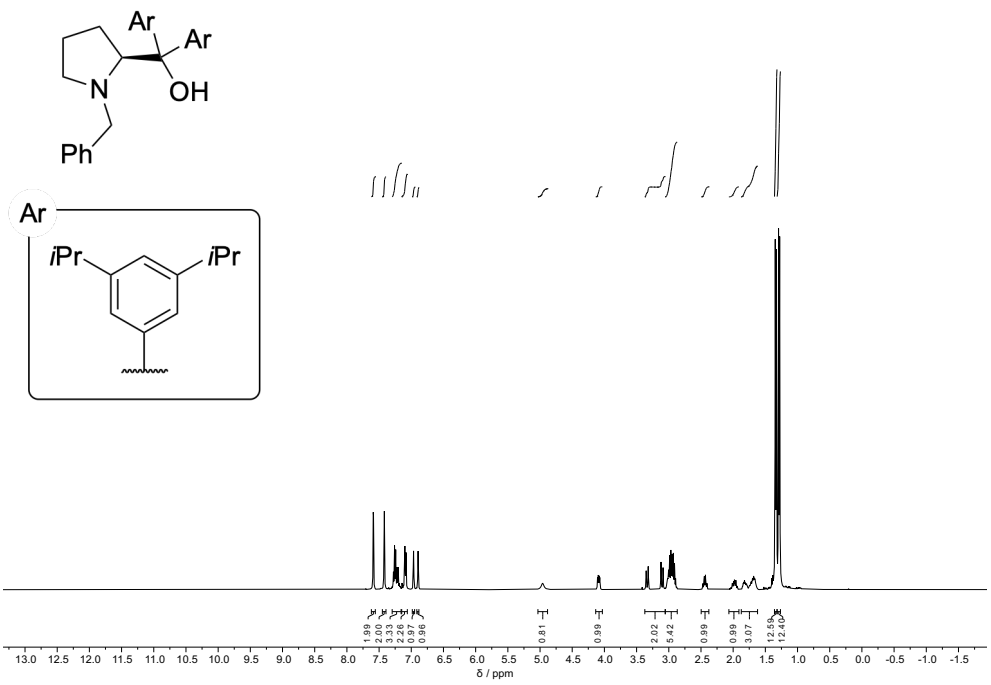


^{13}C-NMR (101 MHz, $CDCl_3$):

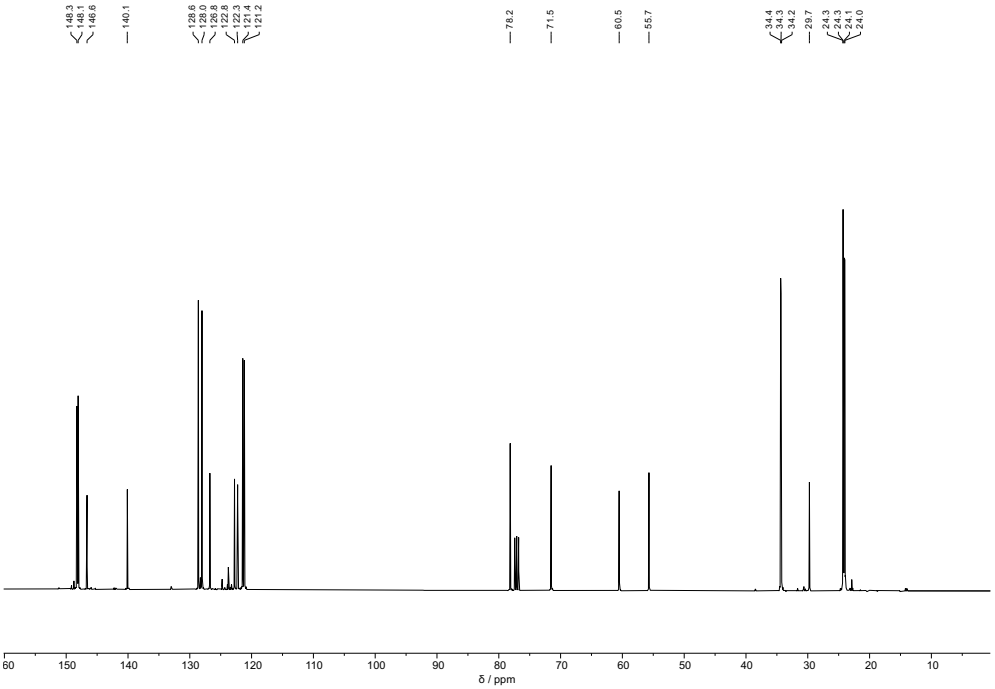


(*S*)-(1-Benzylpyrrolidin-2-yl)bis(3,5-diisopropylphenyl)methanol (**53c**):

^{1}H-NMR (400 MHz, $CDCl_3$):

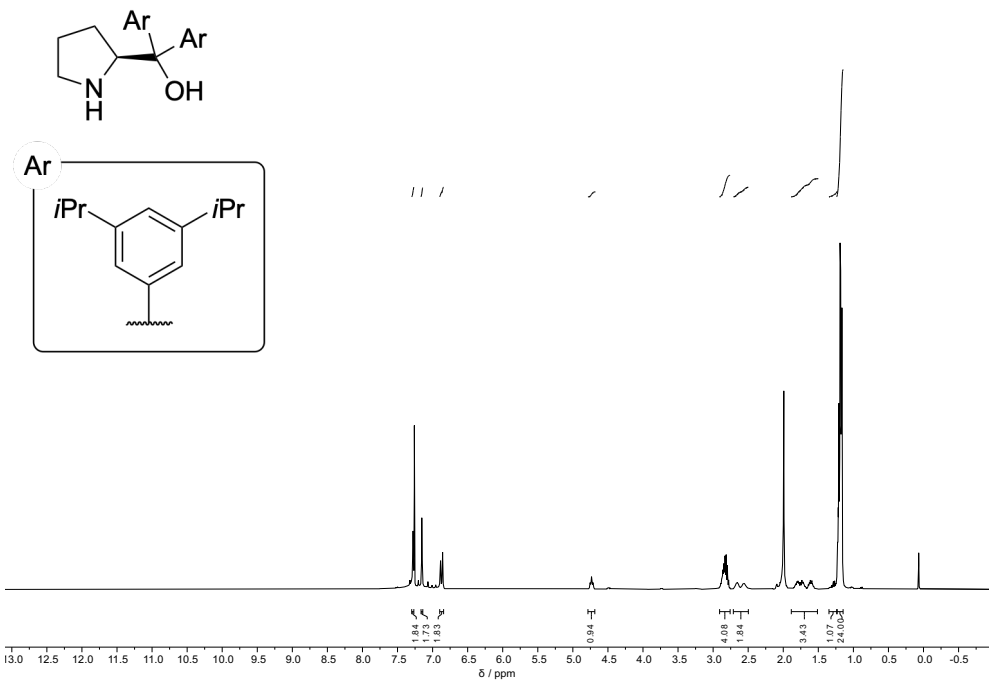


^{13}C-NMR (101 MHz, $CDCl_3$):

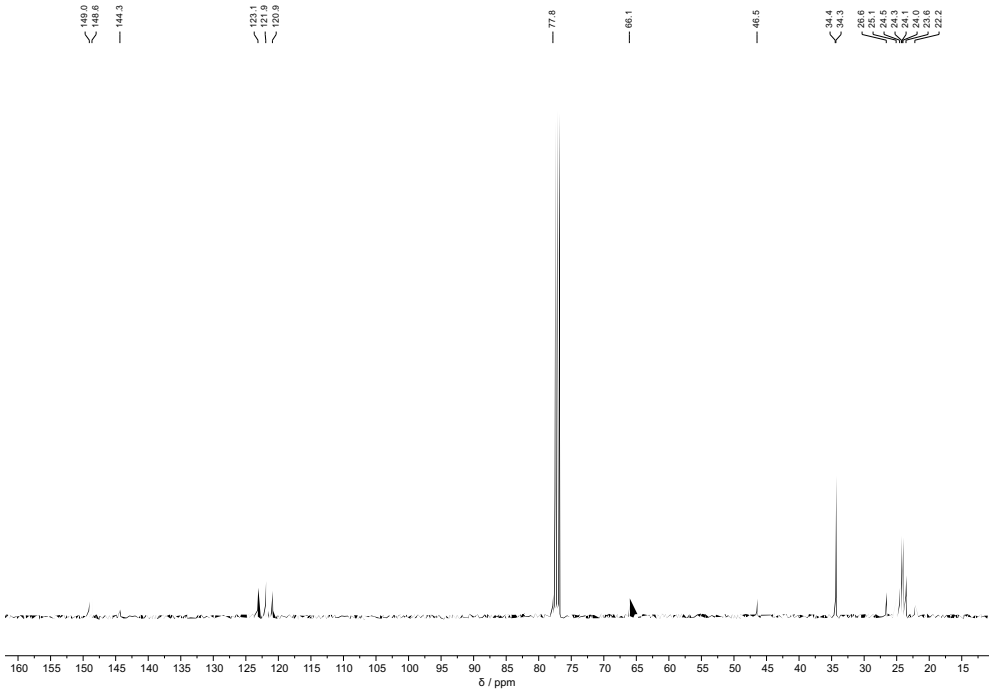


(*S*)-Bis(3,5-diisopropylphenyl)(pyrrolidin-2-yl)methanol (22c):

^{1}H-NMR (400 MHz, $CDCl_3$):

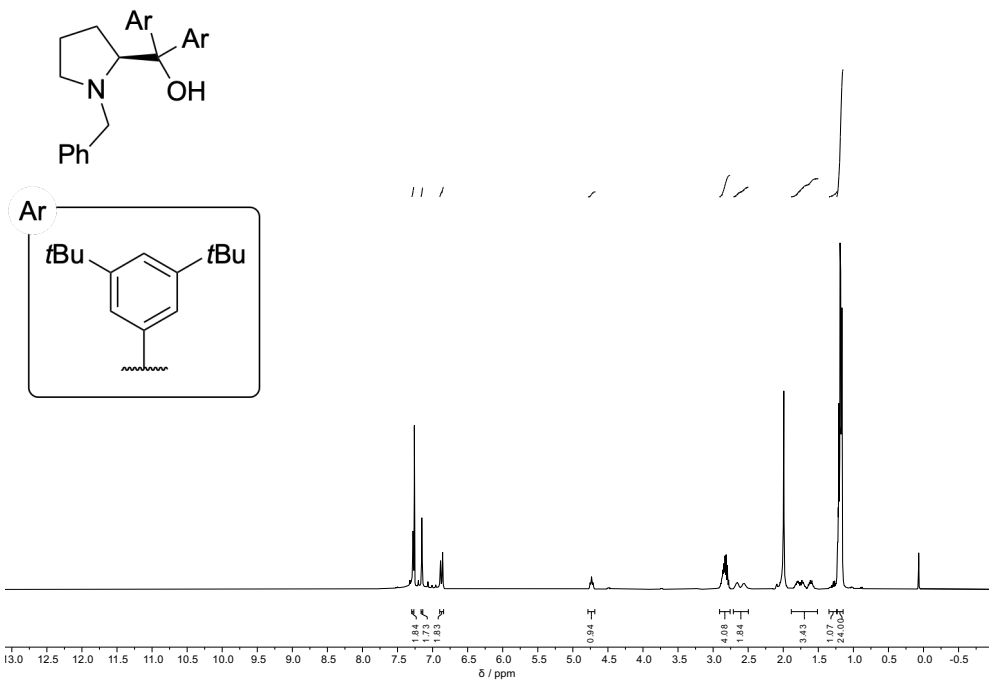


^{13}C-NMR (101 MHz, $CDCl_3$):

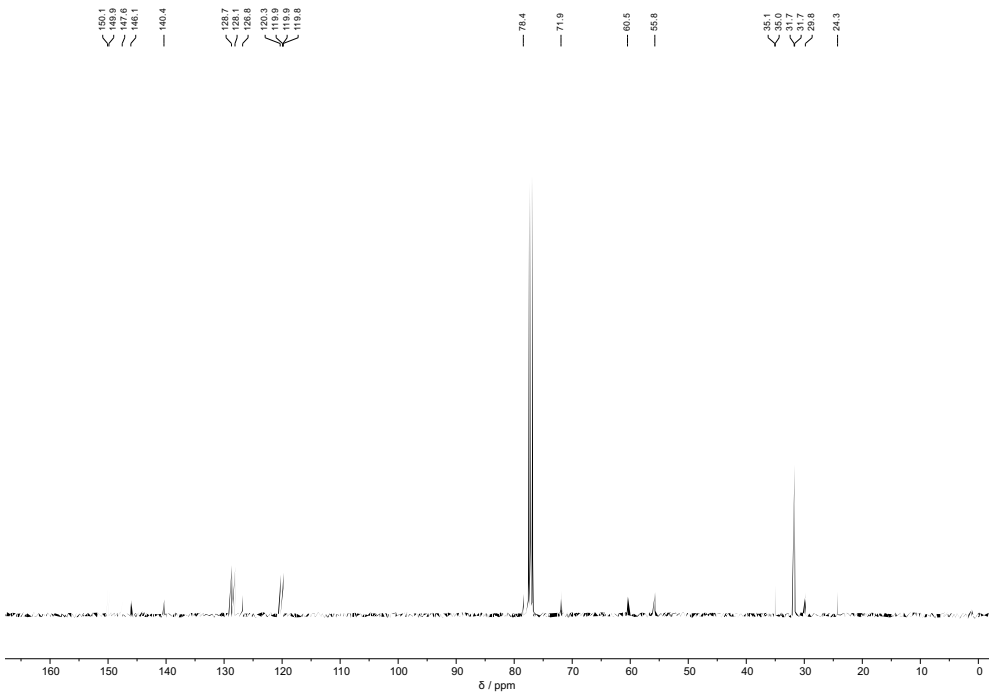


(*S*)-(1-Benzylpyrrolidin-2-yl)bis(3,5-di-*t*buylphenyl)methanol (**53d**):

^{1}H-NMR (400 MHz, $CDCl_3$):

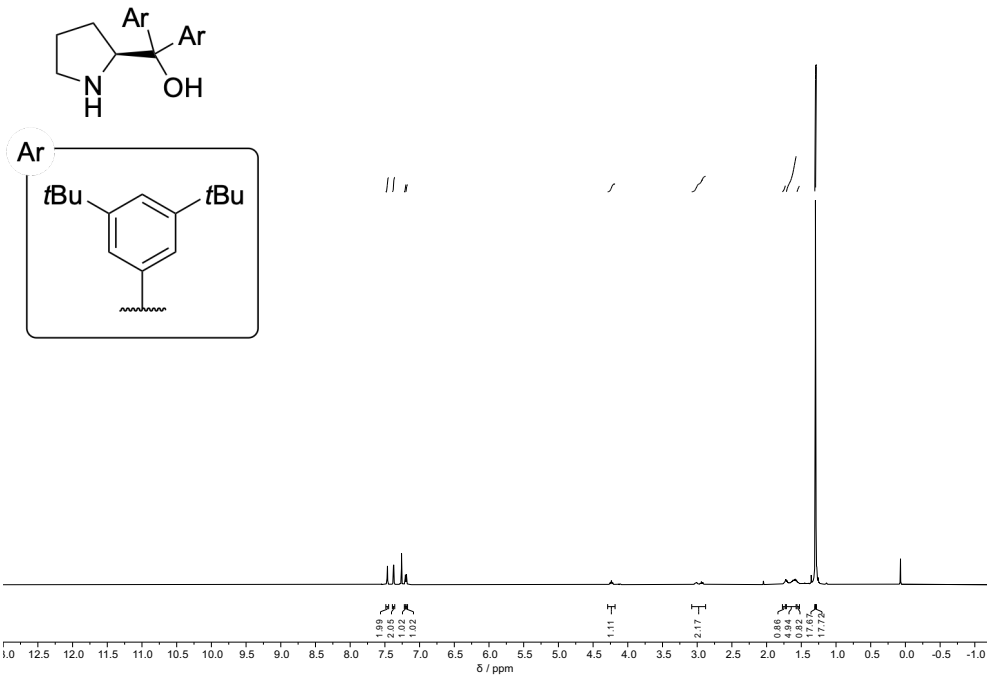


^{13}C-NMR (101 MHz, $CDCl_3$):

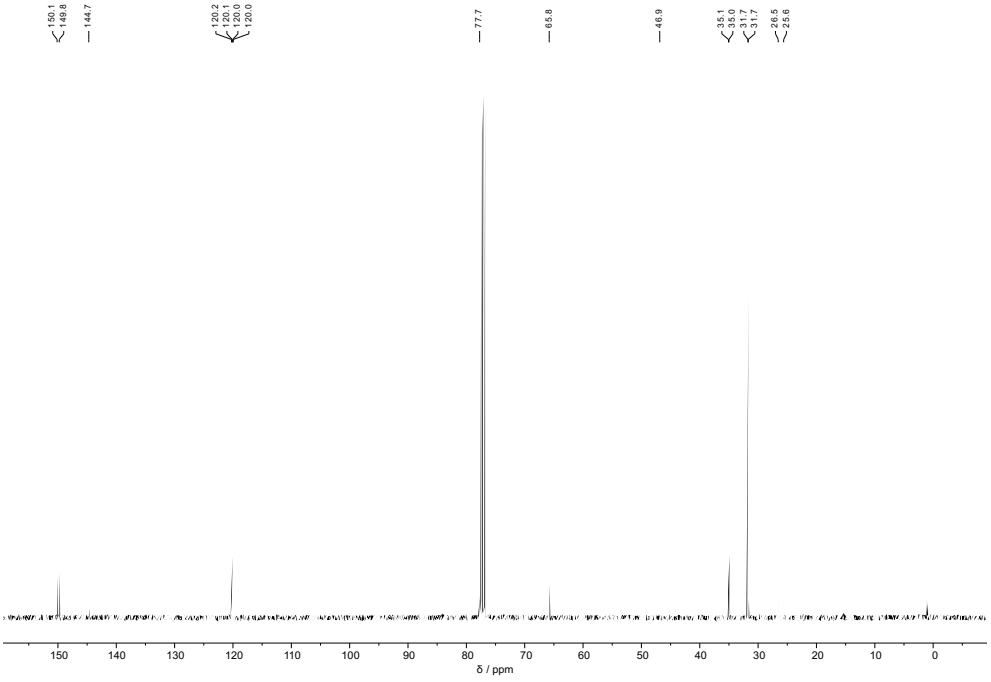


(*S*)-Bis(3,5-di-*t*butylphenyl)(pyrrolidin-2-yl)methanol (22d):

^{1}H-NMR (400 MHz, $CDCl_3$):

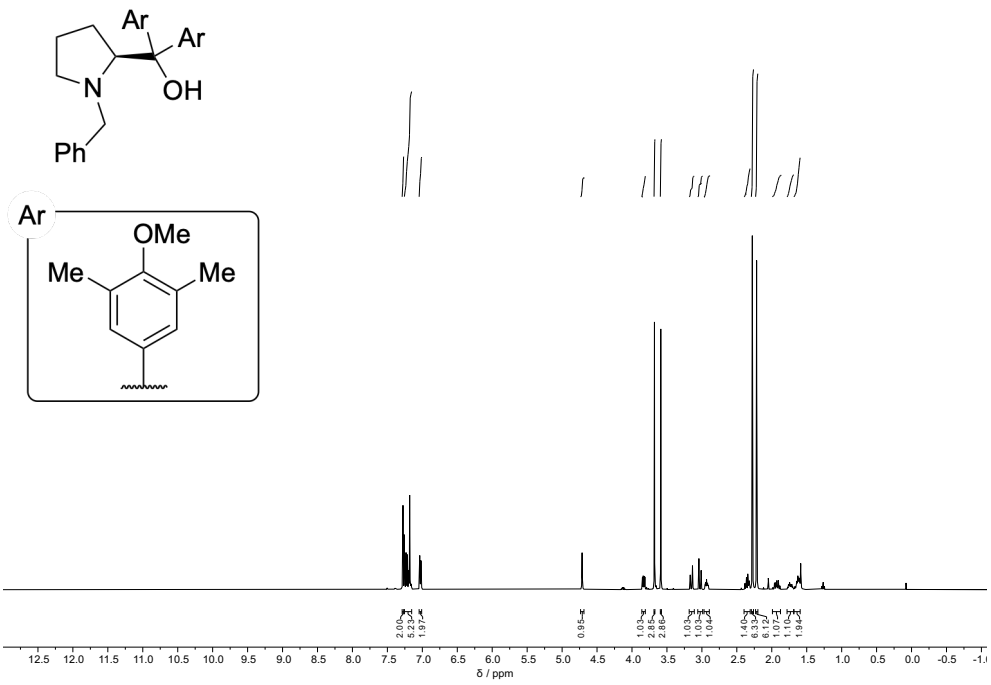


^{13}C-NMR (101 MHz, $CDCl_3$):

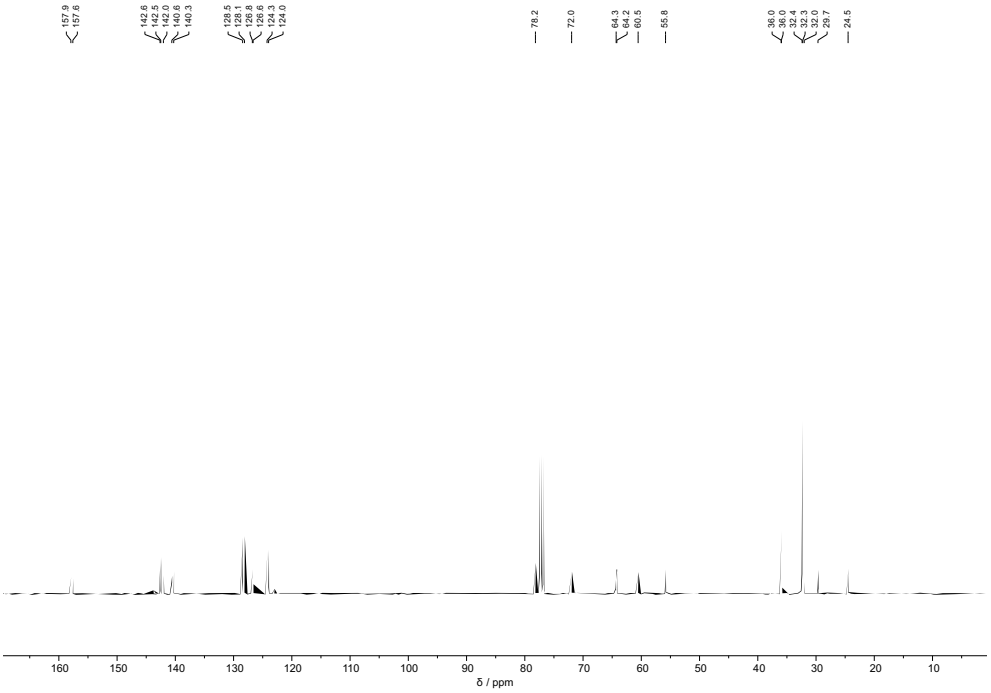


(*S*)-(1-Benzylpyrrolidin-2-yl)bis(3,5-dimethyl-4-methoxyphenyl)methanol (53e):

^{1}H-NMR (400 MHz, $CDCl_3$):

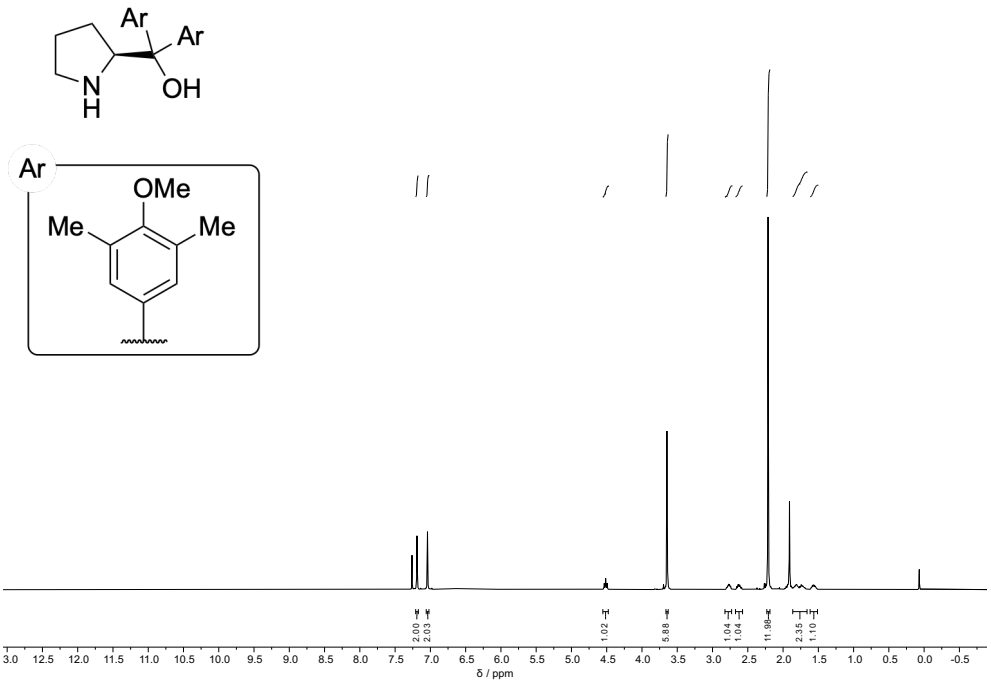


^{13}C-NMR (101 MHz, $CDCl_3$):

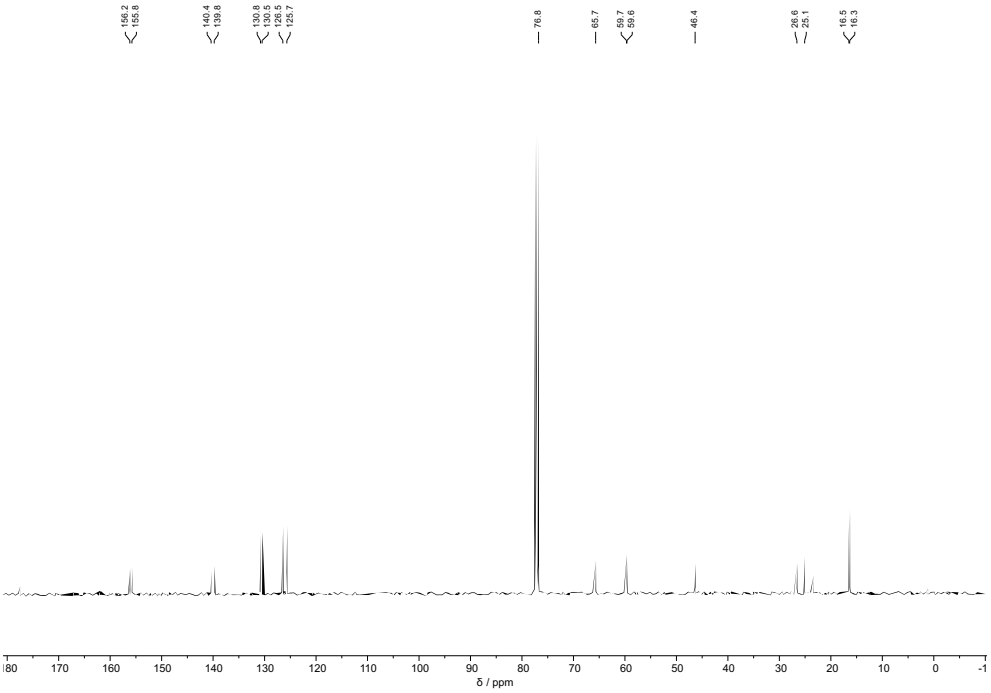


(*S*)-Bis(3,5-dimethyl-4-methoxyphenyl)(pyrrolidin-2-yl)methanol (**22e**):

^{1}H-NMR (400 MHz, $CDCl_3$):

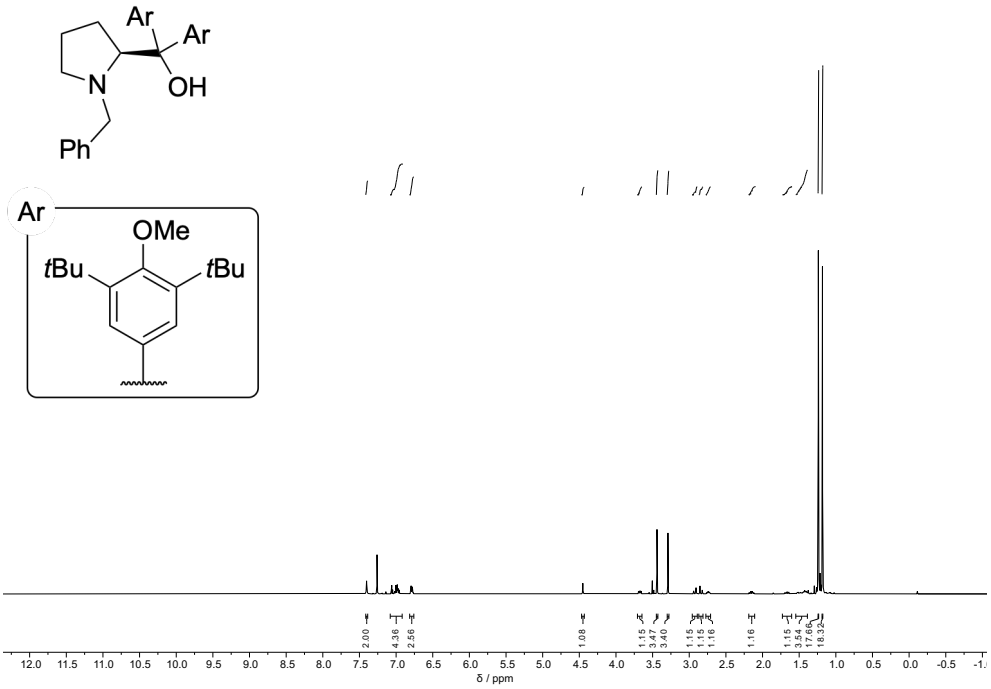


^{13}C-NMR (101 MHz, $CDCl_3$):

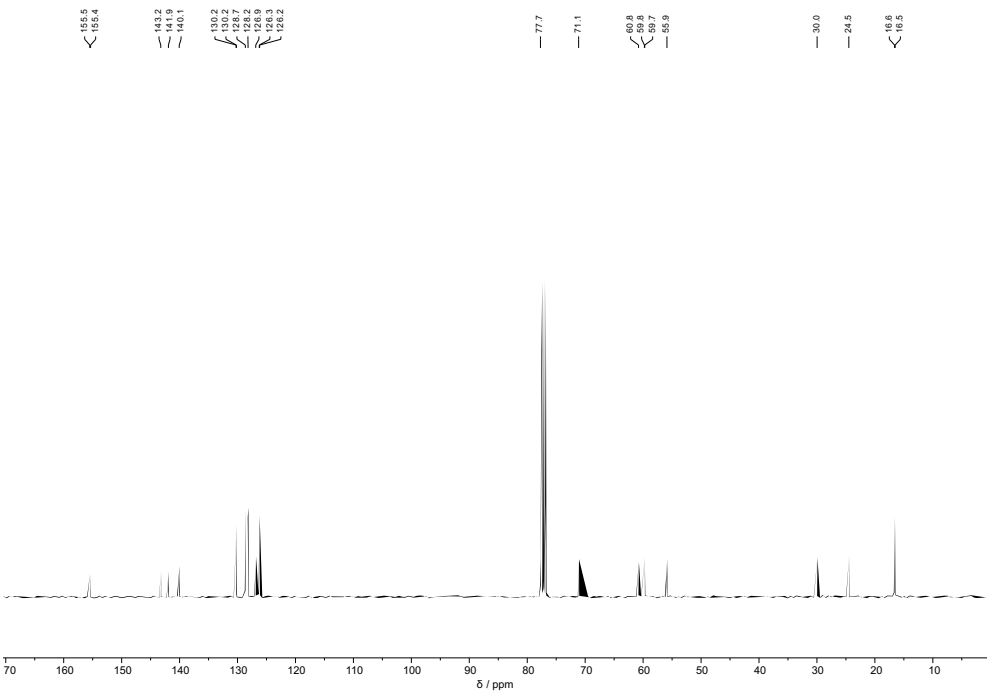


(*S*)-Bis(3,5-di-*t*butyl-4-methoxyphenyl)(pyrrolidin-2-yl)methanol (53f):

^{1}H-NMR (400 MHz, $CDCl_3$):

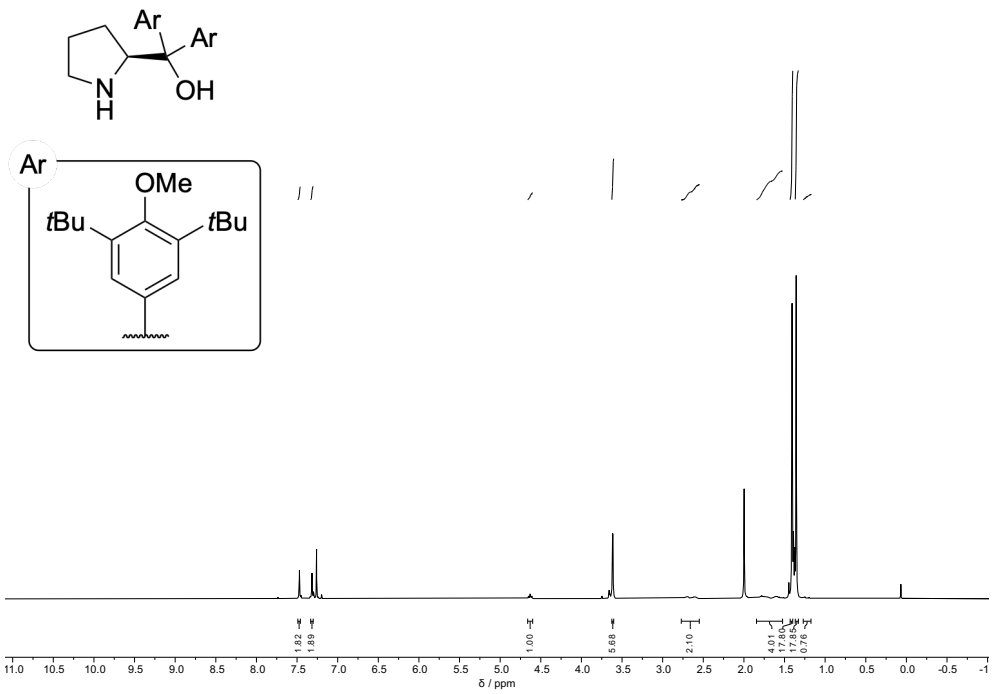


^{13}C-NMR (101 MHz, $CDCl_3$):

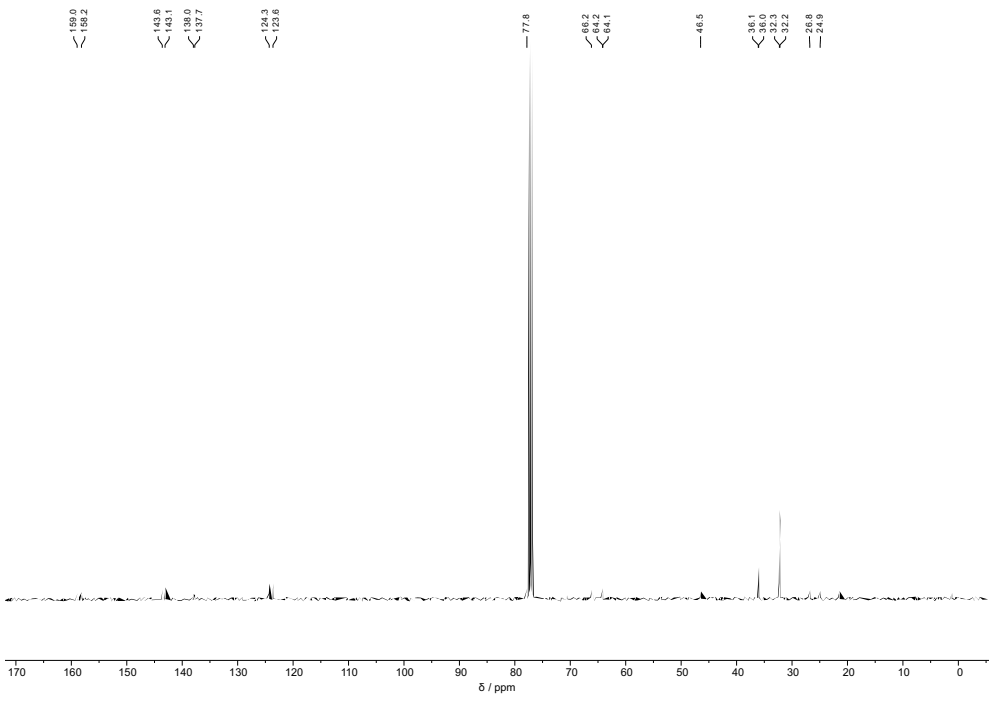


(*S*)-Bis(3,5-di-*t*butyl-4-methoxyphenyl)(pyrrolidin-2-yl)methanol (22f):

^{1}H-NMR (400 MHz, $CDCl_3$):

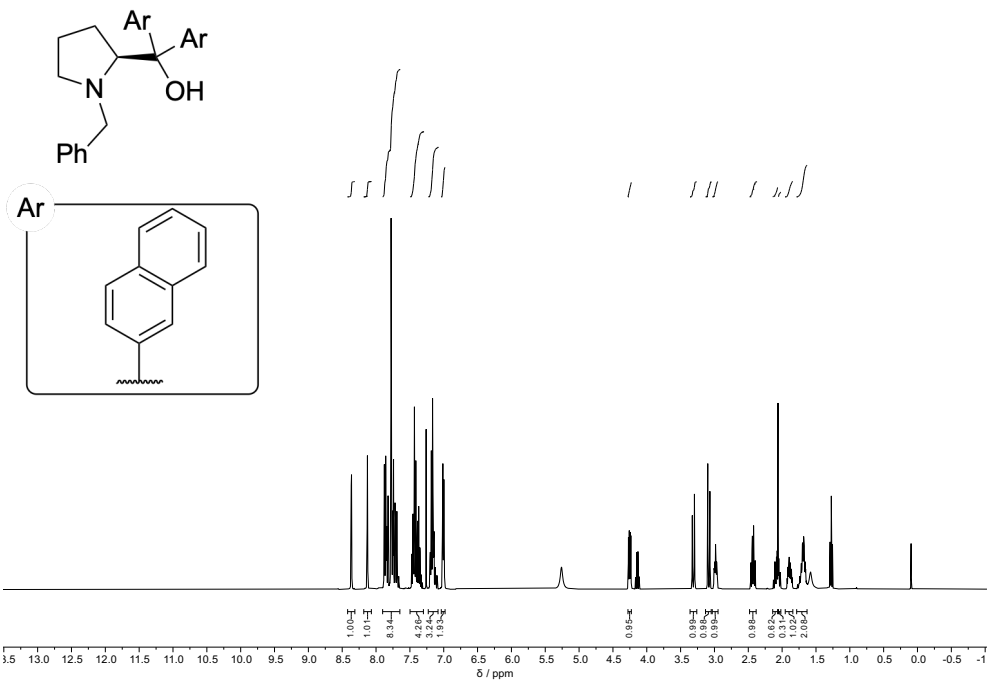


^{13}C-NMR (101 MHz, $CDCl_3$)

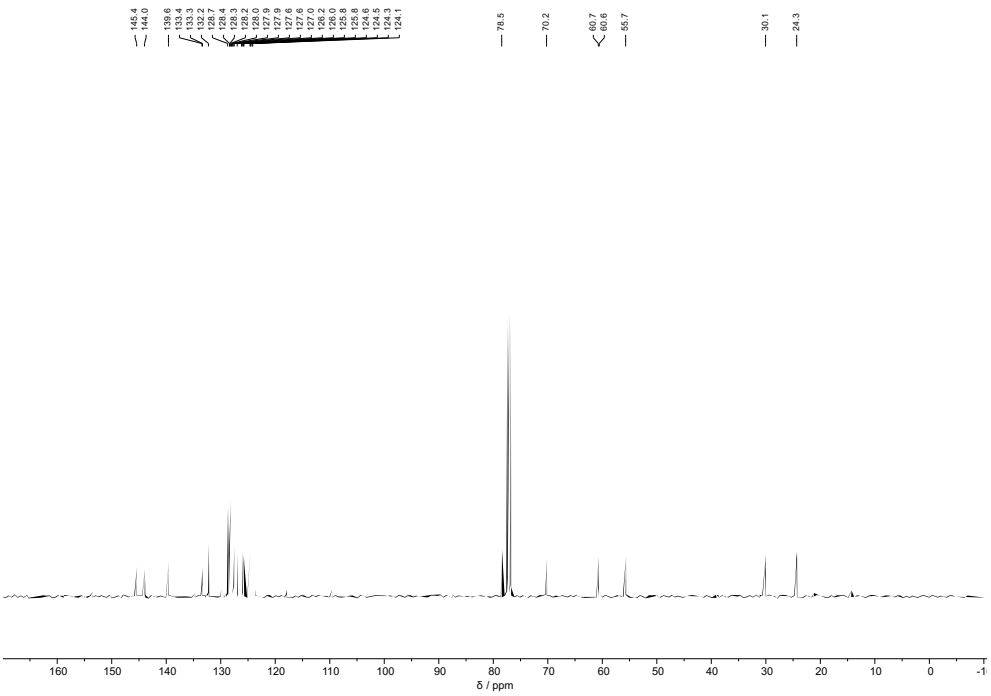


(*S*)-(1-Benzylpyrrolidin-2-yl)dinaphthylmethanol (**53g**):

^{1}H-NMR (400 MHz, $CDCl_3$):

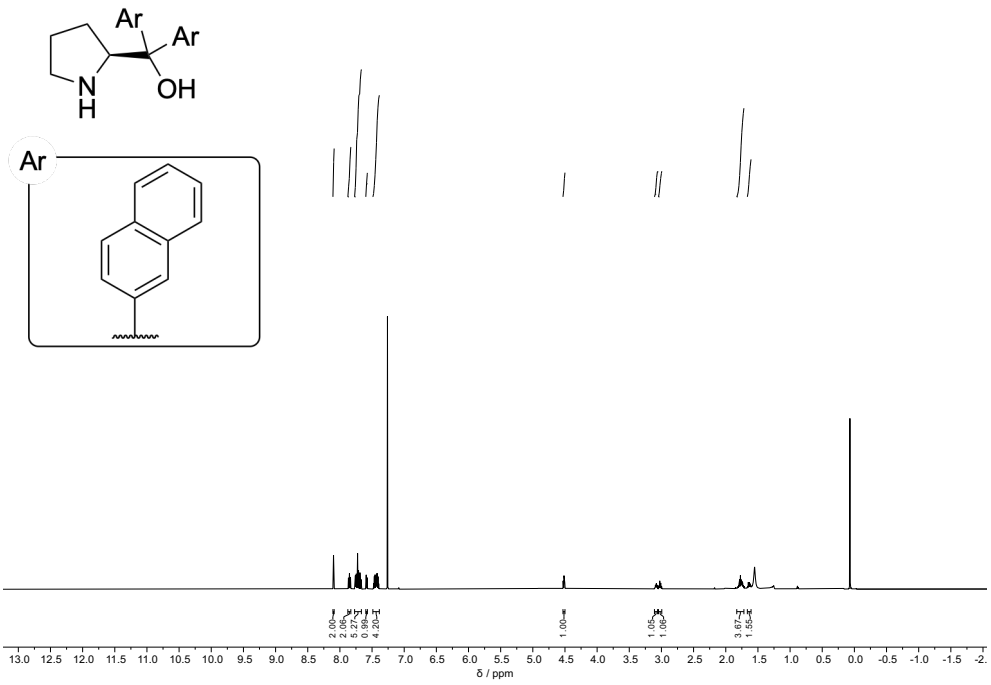


^{13}C-NMR (101 MHz, $CDCl_3$):

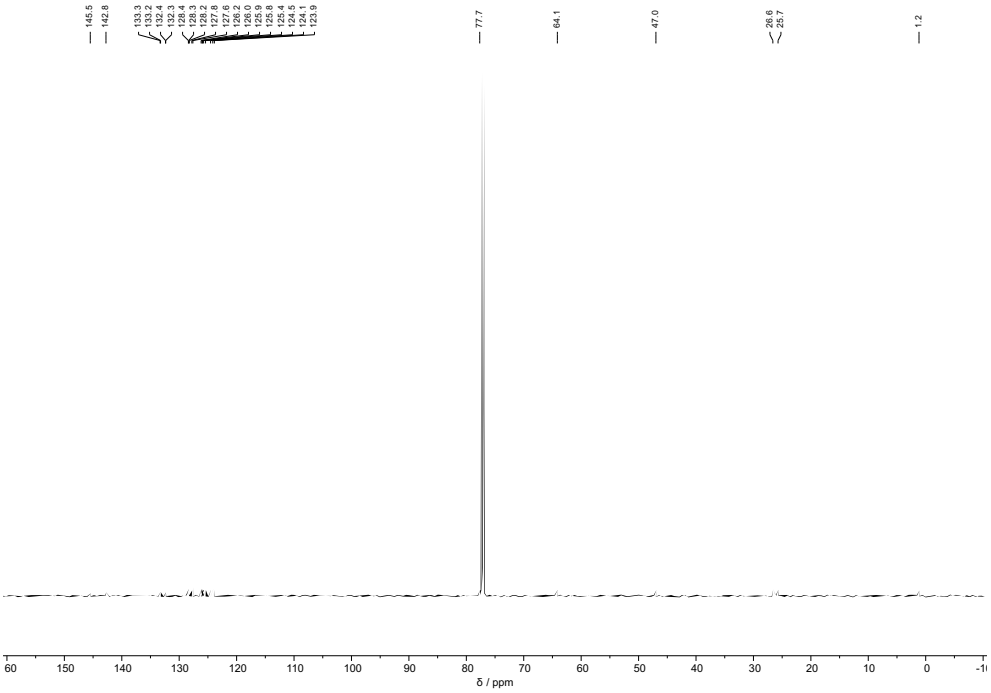


(*S*)-Dinaphthalenyl-2-pyrrolidinemethanol (**22g**):

^{1}H-NMR (400 MHz, $CDCl_3$):

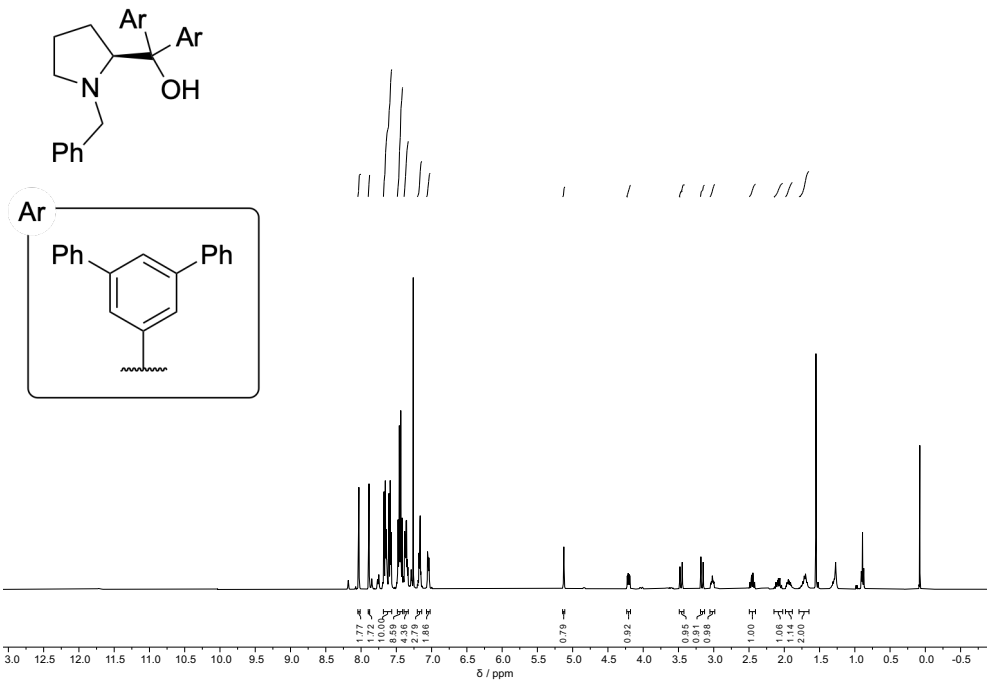


^{13}C-NMR (101 MHz, $CDCl_3$):

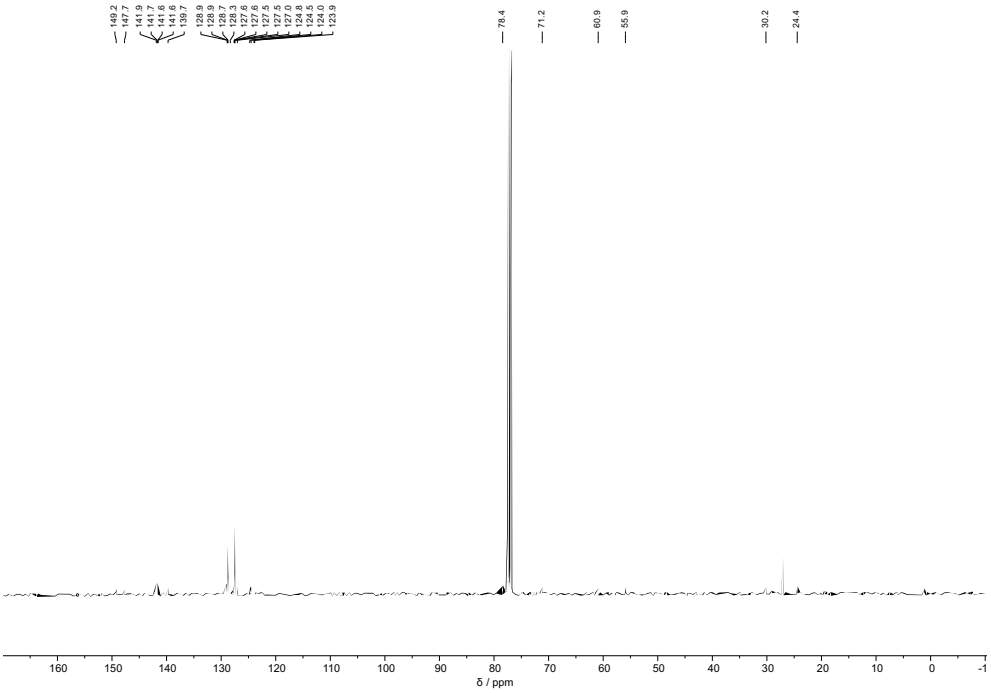


(*S*)-(1-Benzylpyrrolidin-2-yl)bis(3,5-diphenyl)methanol (53i):

^{1}H-NMR (400 MHz, $CDCl_3$):

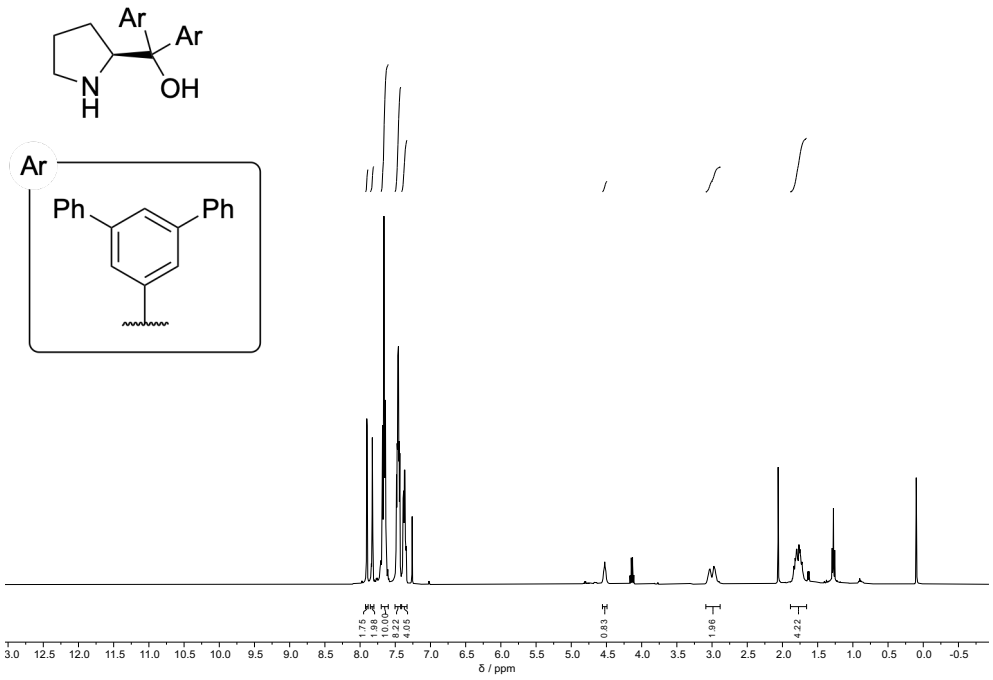


^{13}C-NMR (101 MHz, $CDCl_3$):

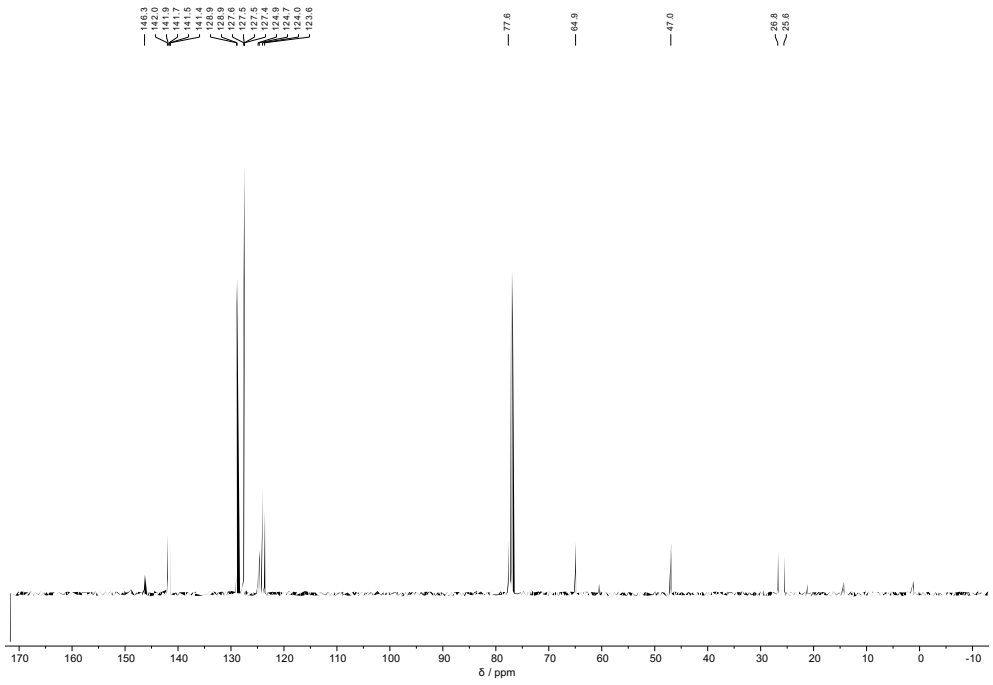


(*S*)-Bis(3,5- diphenyl)(pyrrolidin-2-yl)methanol (**22i**):

^{1}H-NMR (400 MHz, $CDCl_3$):

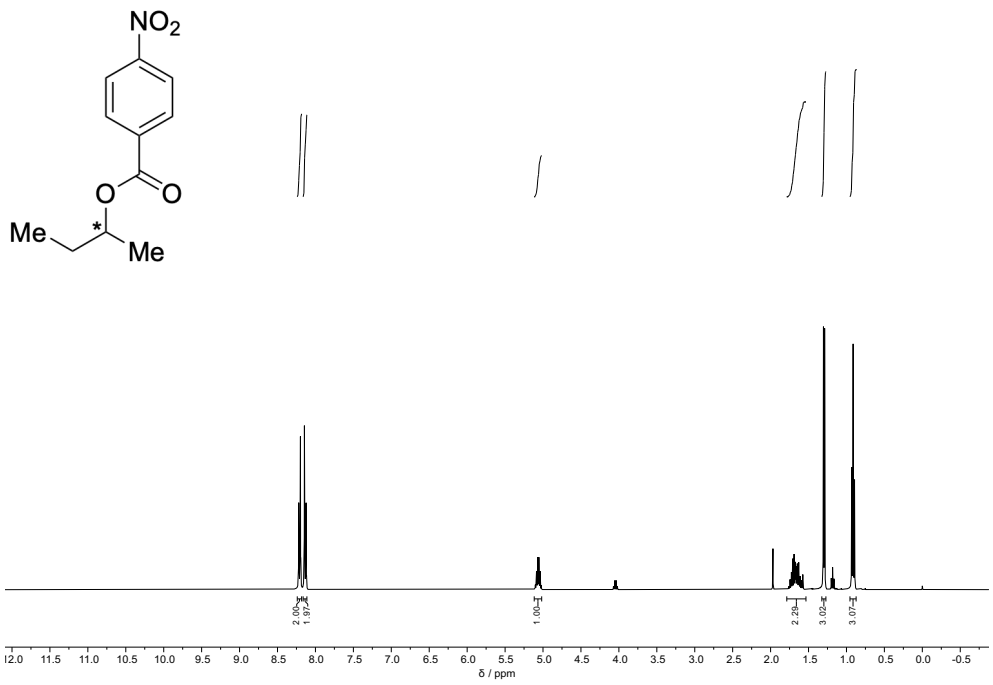


^{13}C-NMR (101 MHz, $CDCl_3$):

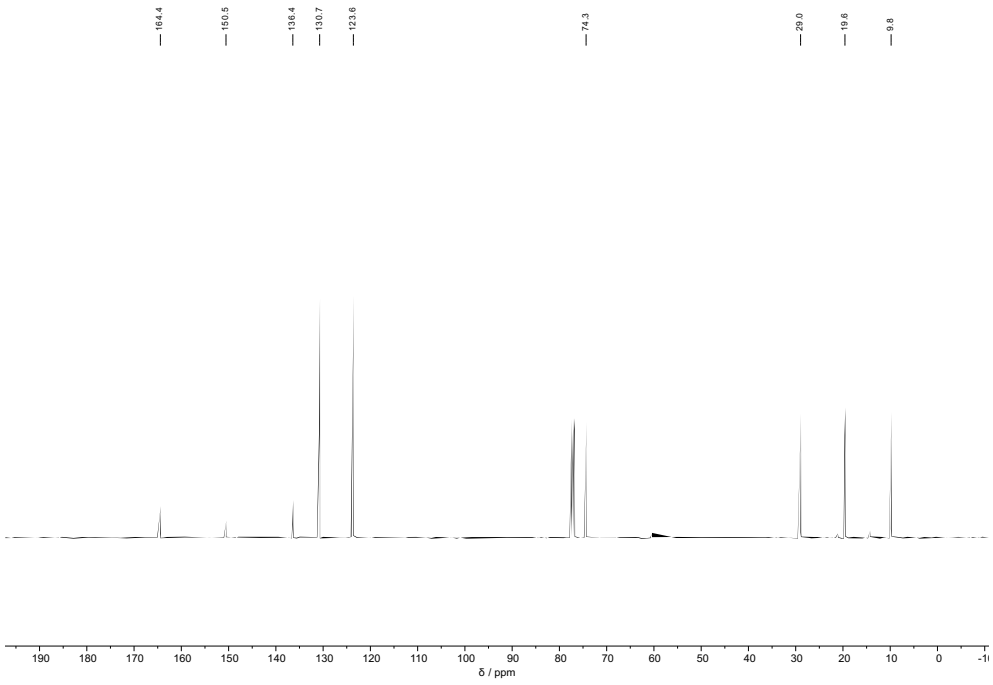


***Sec*-butyl 4-nitrobenzoate** (rac-**85a**):

^{1}H-NMR (400 MHz, $CDCl_3$):

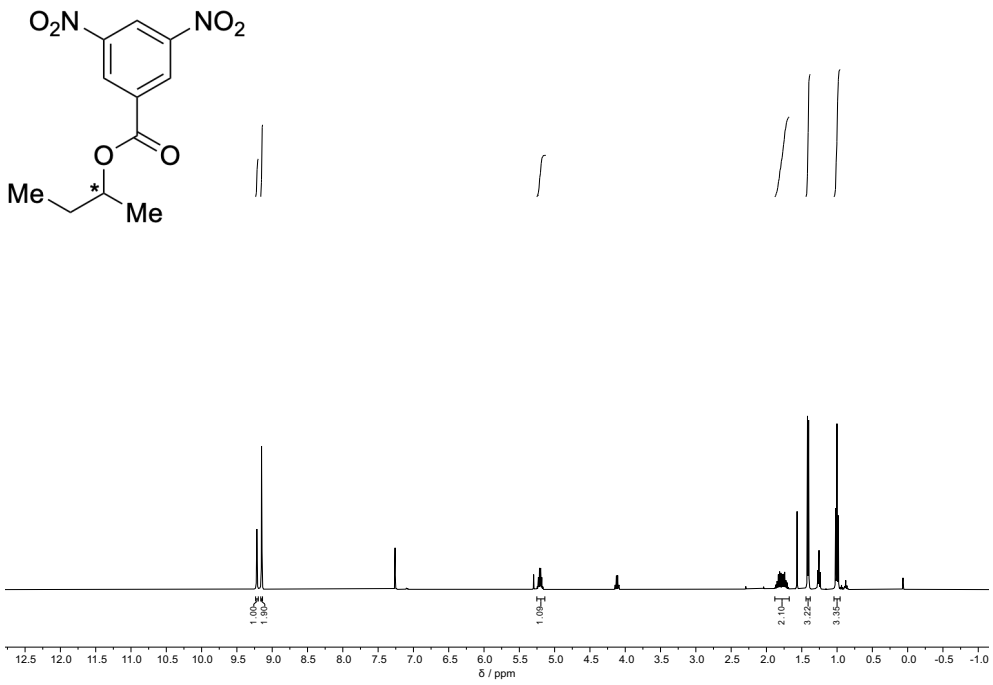


^{13}C-NMR (101 MHz, $CDCl_3$):

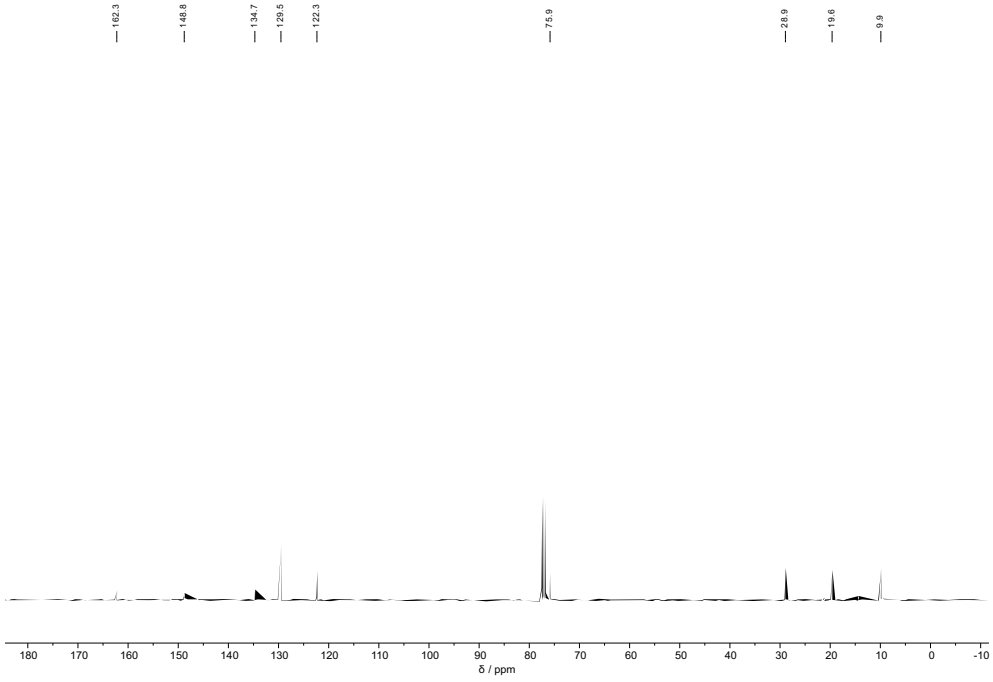


***Sec*-butyl 3,5-dinitrobenzoate** (rac-**85b**):

^{1}H-NMR (400 MHz, $CDCl_3$):

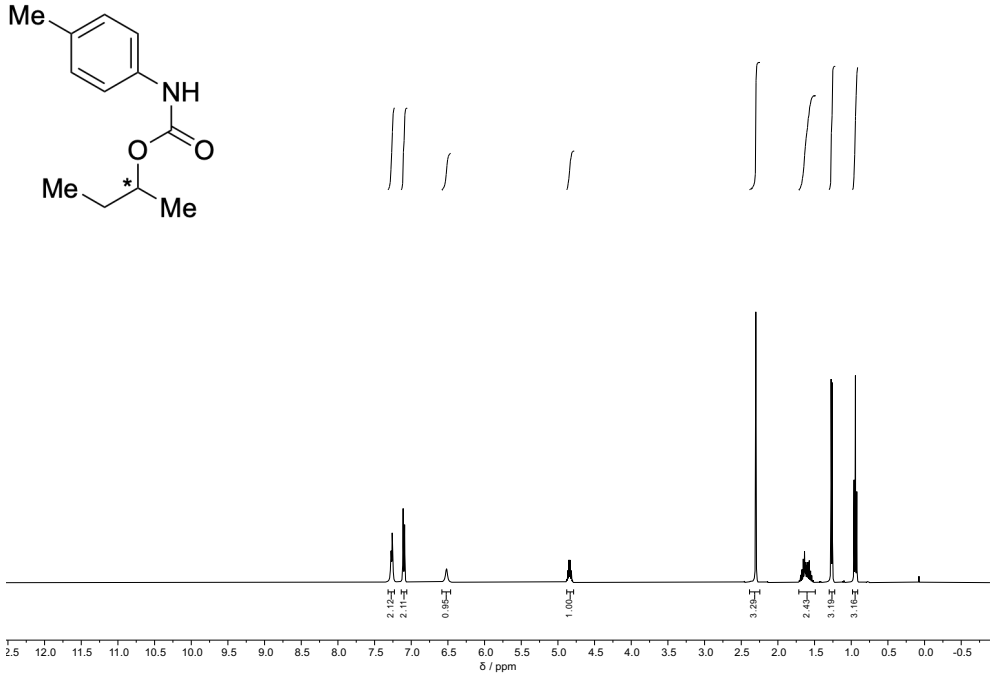


^{13}C-NMR (101 MHz, $CDCl_3$):

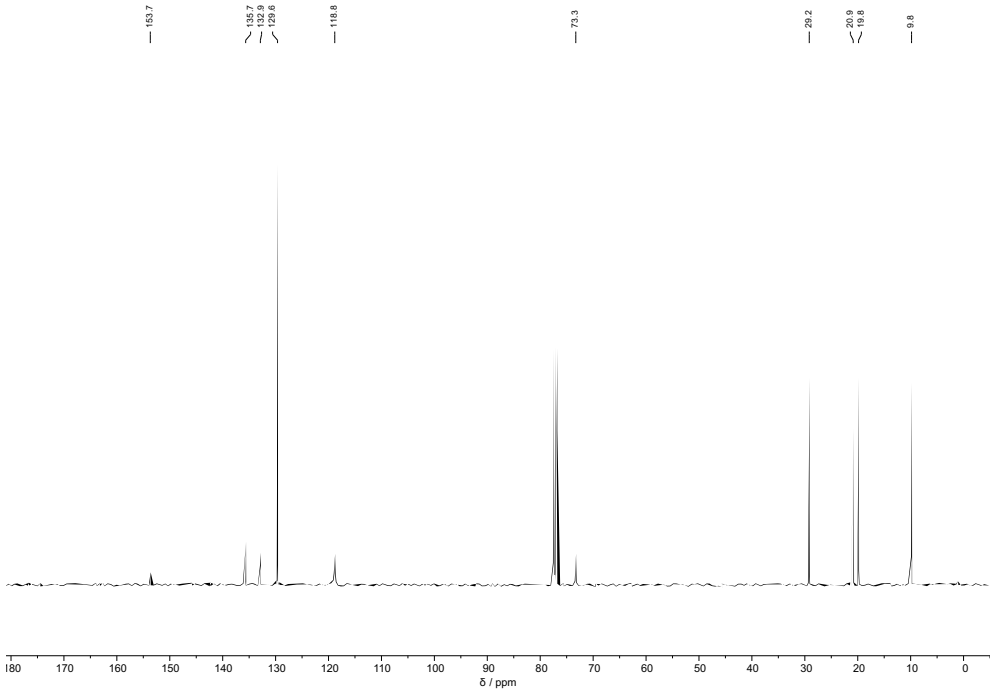


Sec-butyl *p*-tolylcarbamate (rac-**85c**):

^{1}H-NMR (400 MHz, $CDCl_3$):

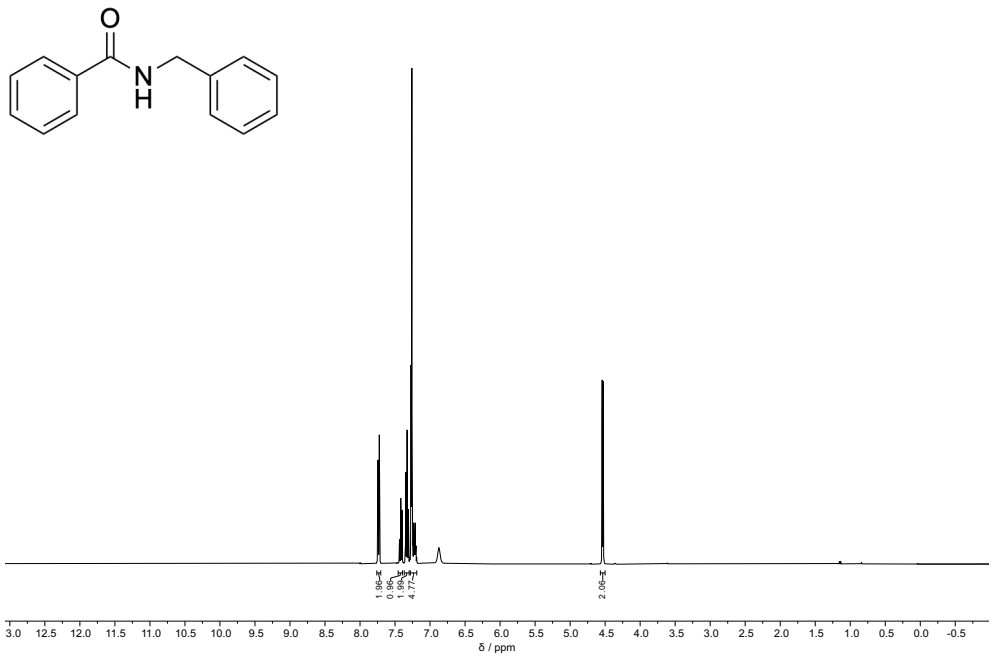


^{13}C-NMR (101 MHz, $CDCl_3$):

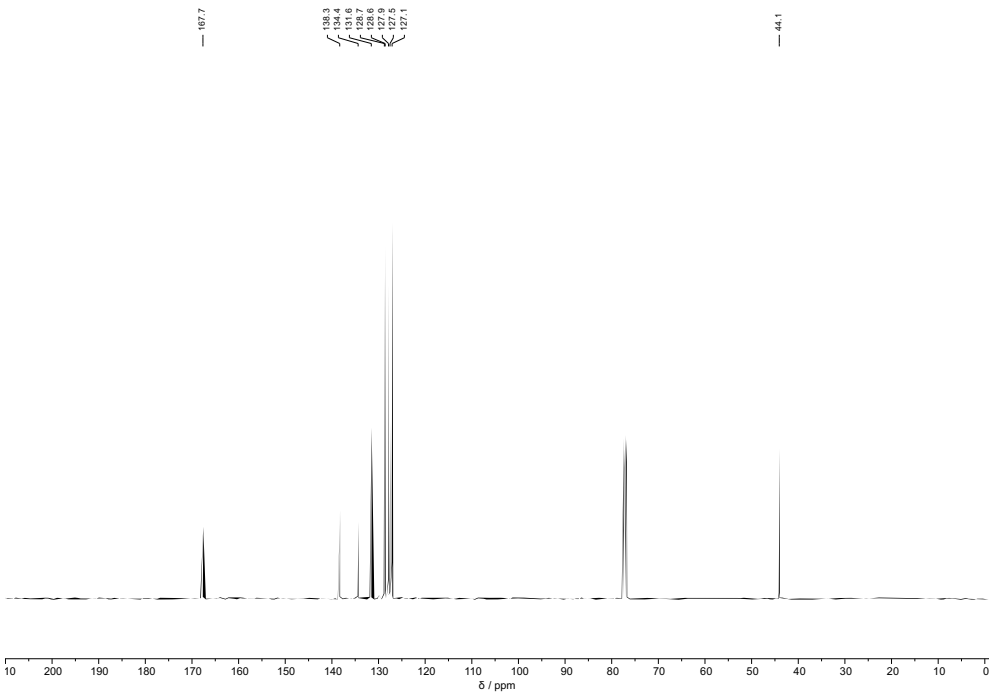


***N*-Benzylbenzamide (143)**:

^{1}H-NMR (400 MHz, $CDCl_3$):

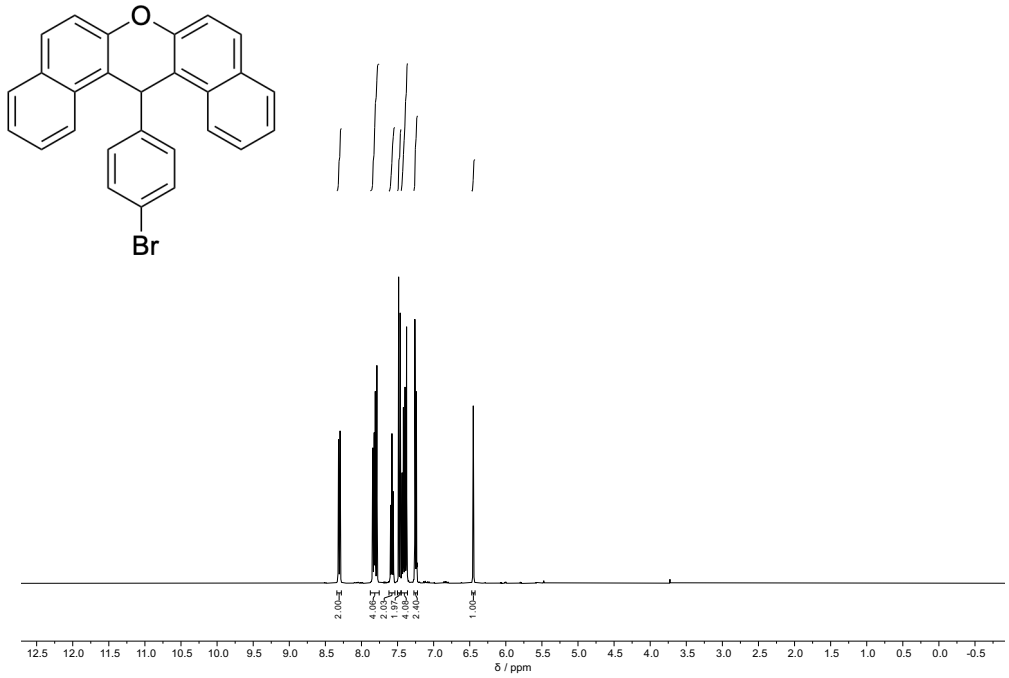


^{13}C-NMR (101 MHz, $CDCl_3$):

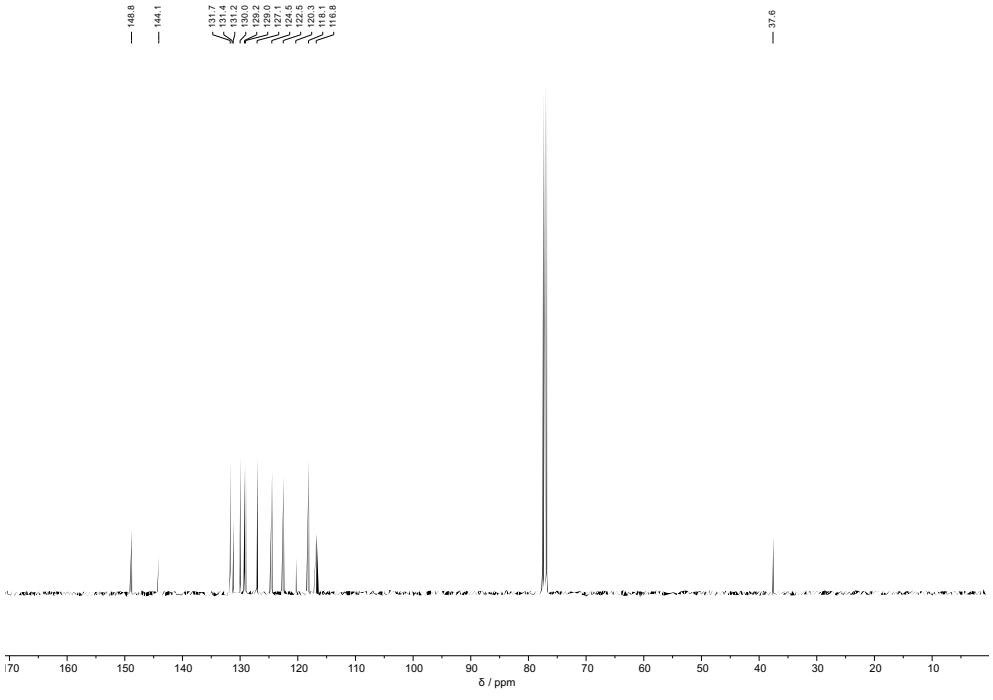


14-(4-Bromophenyl)-14*H*-dibenzo[a,j]xanthene (**69**):

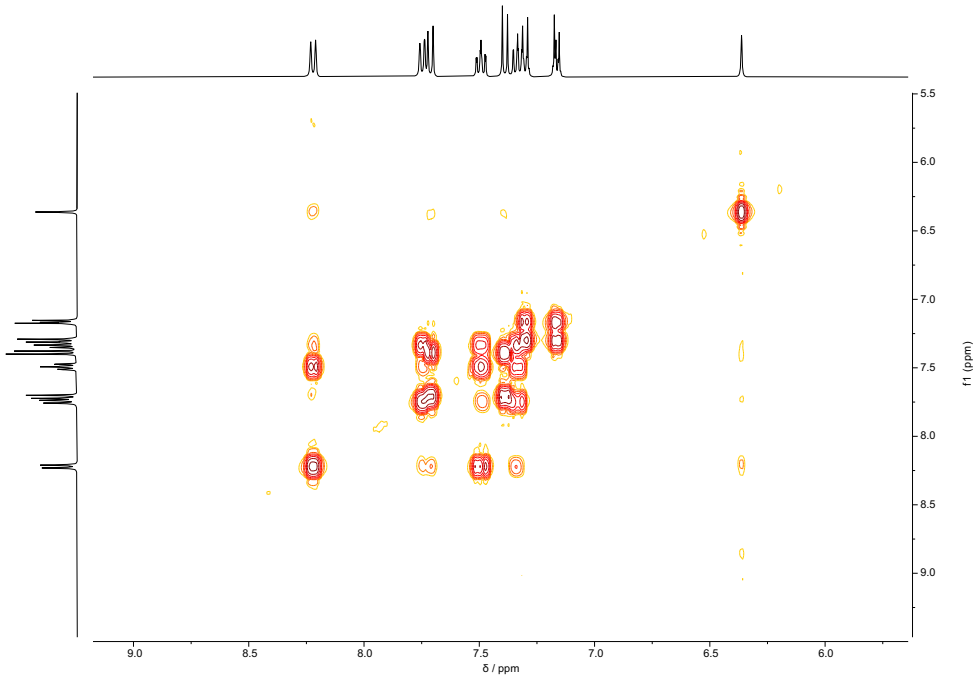
^{1}H-NMR (400 MHz, $CDCl_3$):



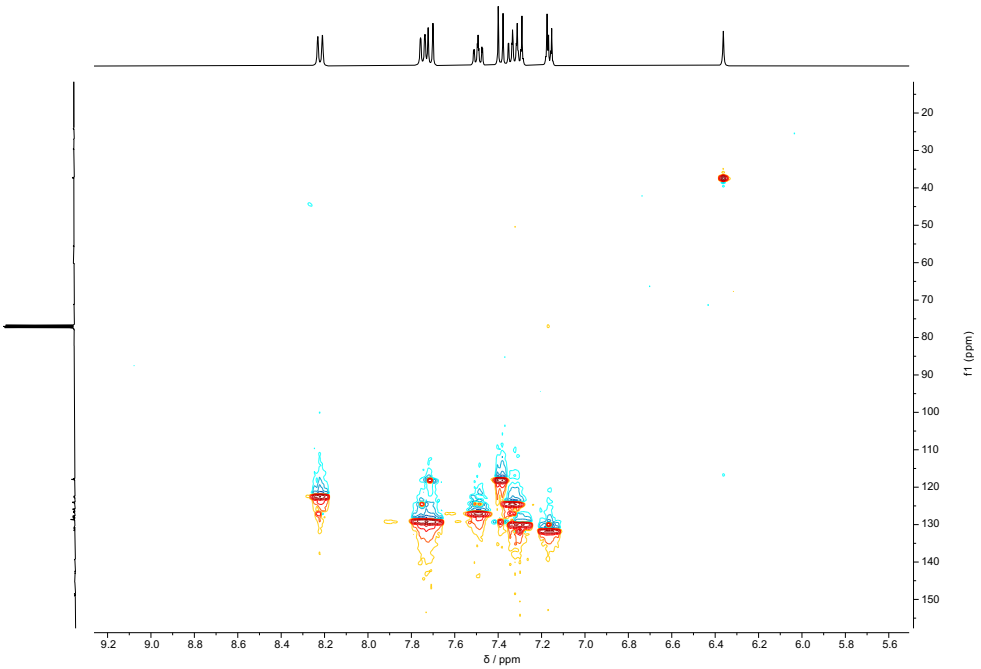
^{13}C-NMR (101 MHz, $CDCl_3$):



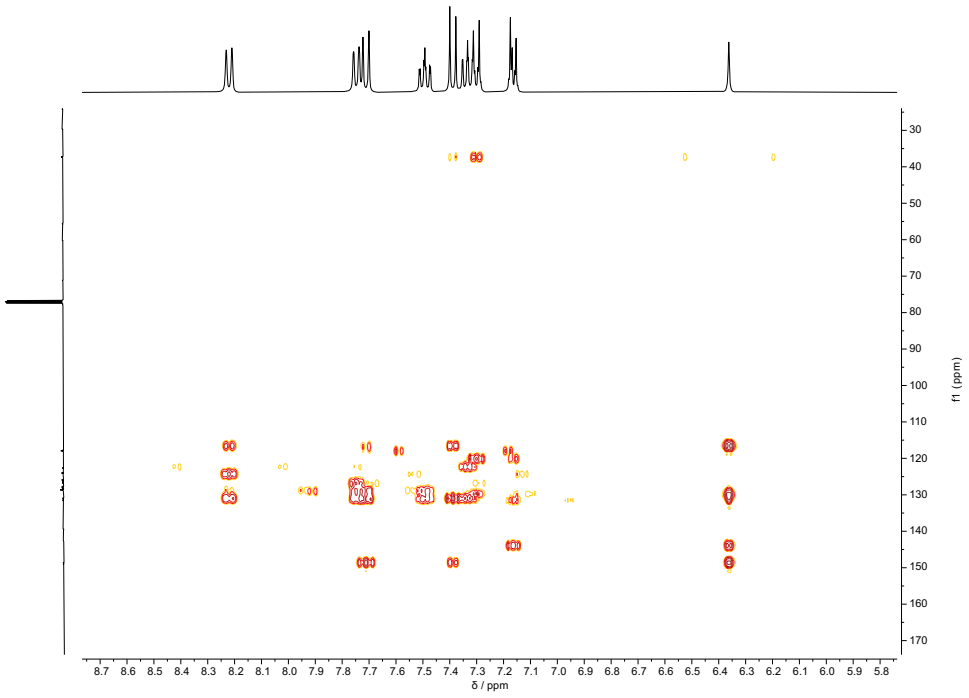
COSY:


5.5
6.0
6.5
7.0
7.5
8.0
8.5
9.0
f1 (ppm)
9.0
8.5
8.0
7.5
7.0
6.5
6.0
δ / ppm

HSQC:

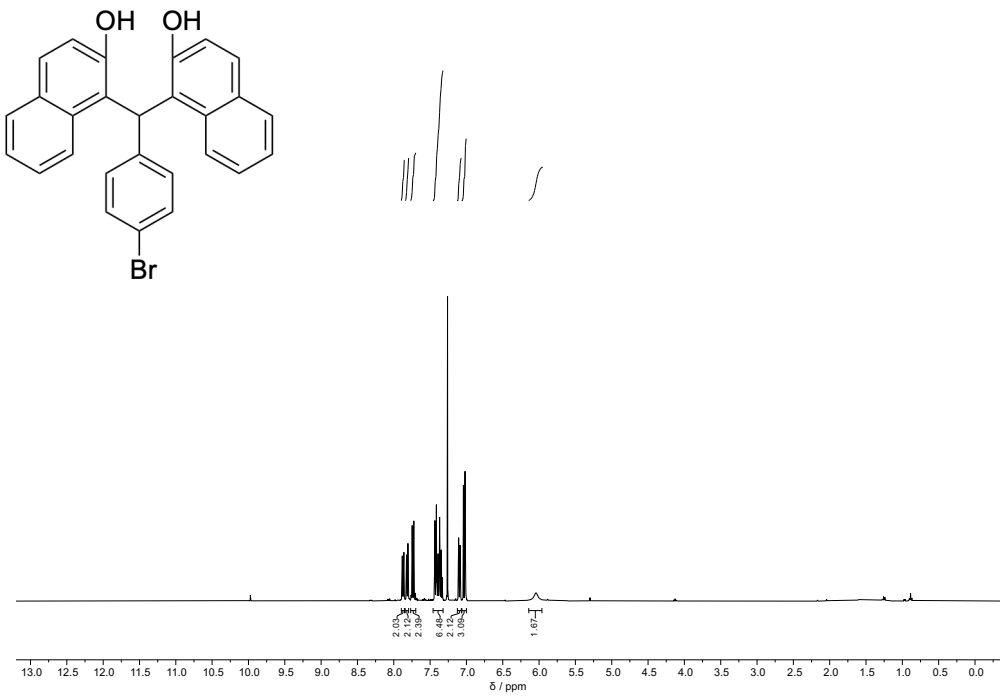

20
30
40
50
60
70
80
90
100
110
120
130
140
150
f1 (ppm)
9.2
9.0
8.8
8.6
8.4
8.2
8.0
7.8
7.6
7.4
7.2
7.0
6.8
6.6
6.4
6.2
6.0
5.8
5.6
δ / ppm

HMBC:

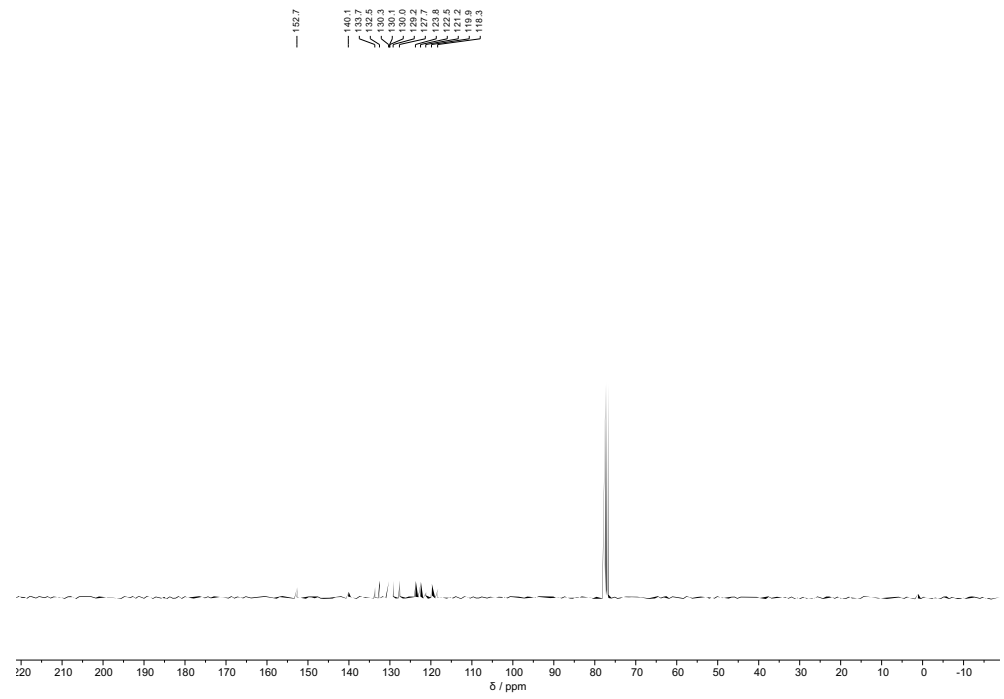

30
40
50
60
70
80
90
100
110
120
130
140
150
160
170
f1 (ppm)
8.7 8.6 8.5 8.4 8.3 8.2 8.1 8.0 7.9 7.8 7.7 7.6 7.5 7.4 7.3 7.2 7.1 7.0 6.9 6.8 6.7 6.6 6.5 6.4 6.3 6.2 6.1 6.0 5.9 5.8
δ / ppm

1,1'-((4-Bromophenyl)methylene)bis(naphthalen-2-ol) (**76**):

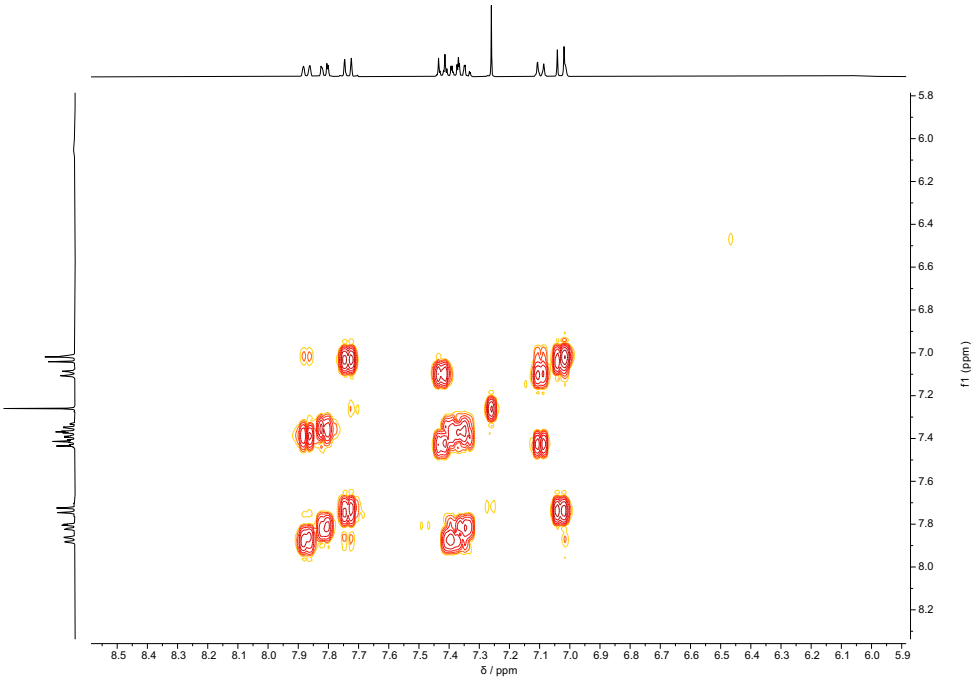
^{1}H-NMR (400 MHz, $CDCl_3$):



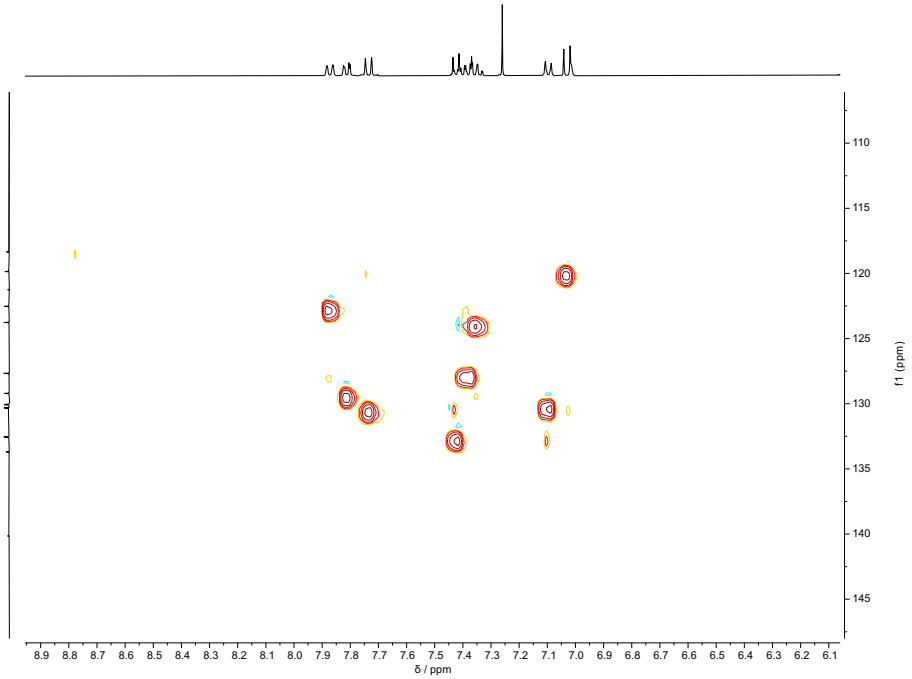
^{13}C-NMR (101 MHz, $CDCl_3$):



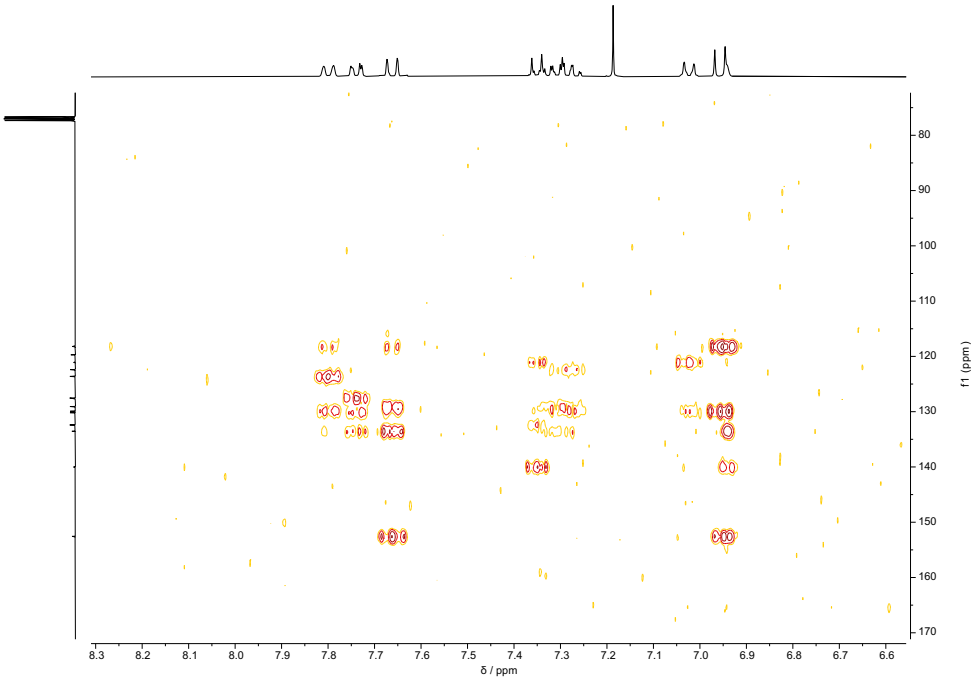
COSY:



HSQC:

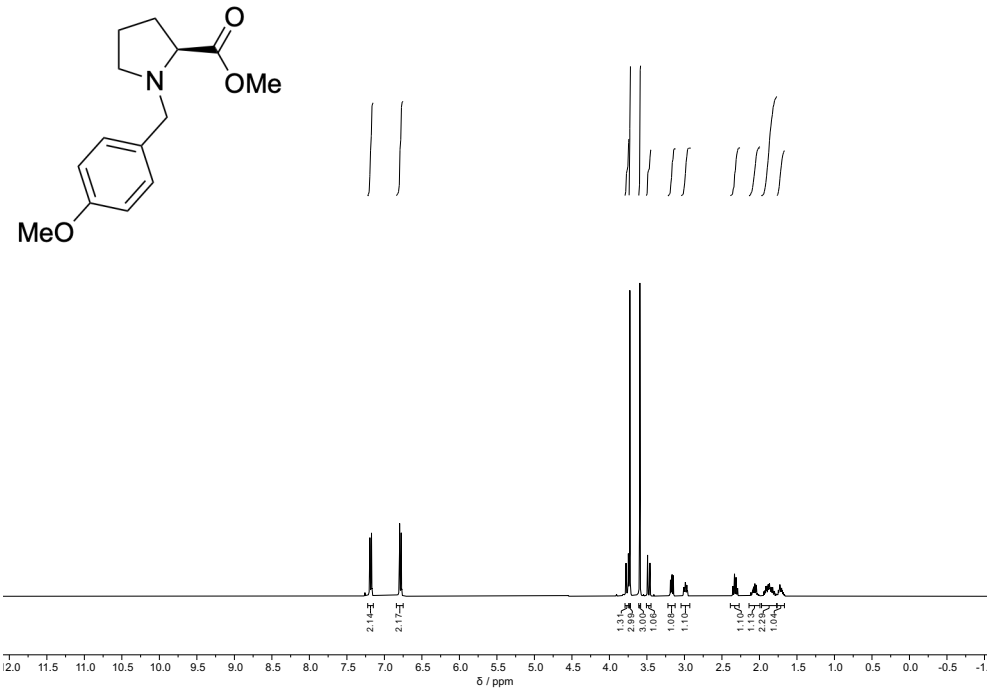


HMBC:

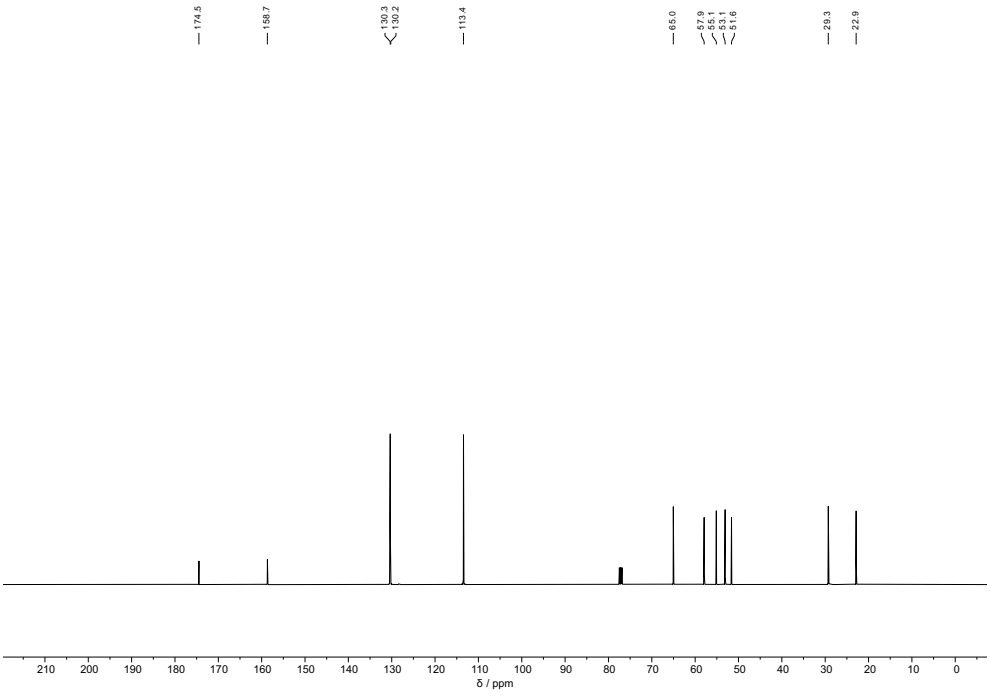

80
90
100
110
120
130
140
150
160
170
f1 (ppm)
8.3
8.2
8.1
8.0
7.9
7.8
7.7
7.6
7.5
7.4
7.3
7.2
7.1
7.0
6.9
6.8
6.7
6.6
δ / ppm

(*S*)-Methyl-1-(4-methoxybenzyl)pyrrolidine-2-carboxylate (**77**):

^{1}H-NMR (400 MHz, $CDCl_3$):

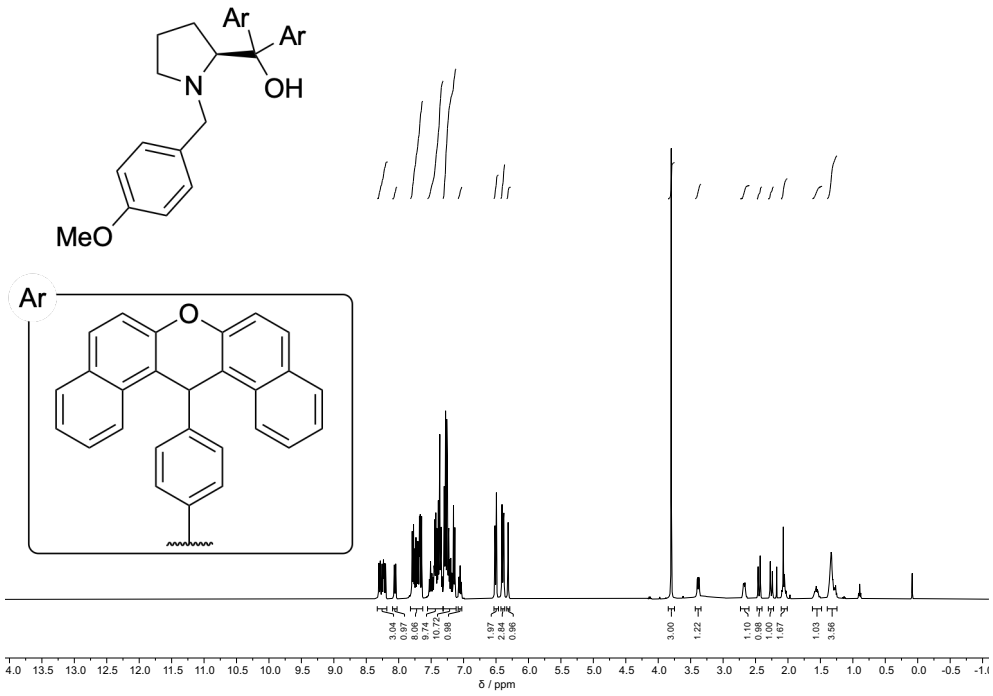


^{13}C-NMR (101 MHz, $CDCl_3$):

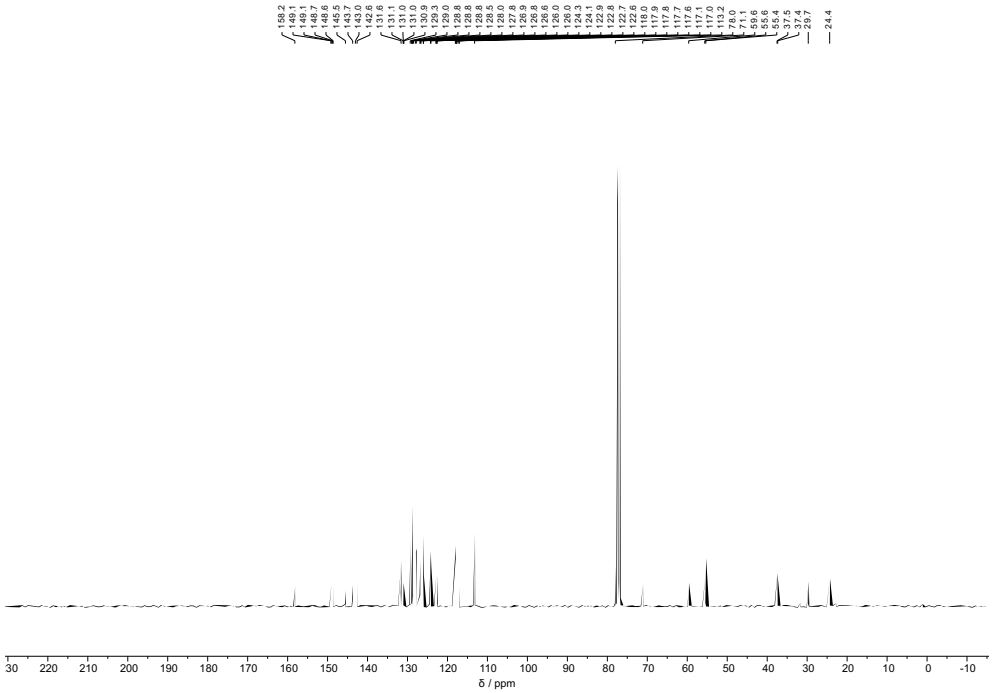


(*S*)-Bis(4-(14*H*-dibenzo[a,j]xanthen-14-yl)phenyl)(1-(4-methoxybenzyl)pyrrolidin-2-yl)methanol (**78k**):

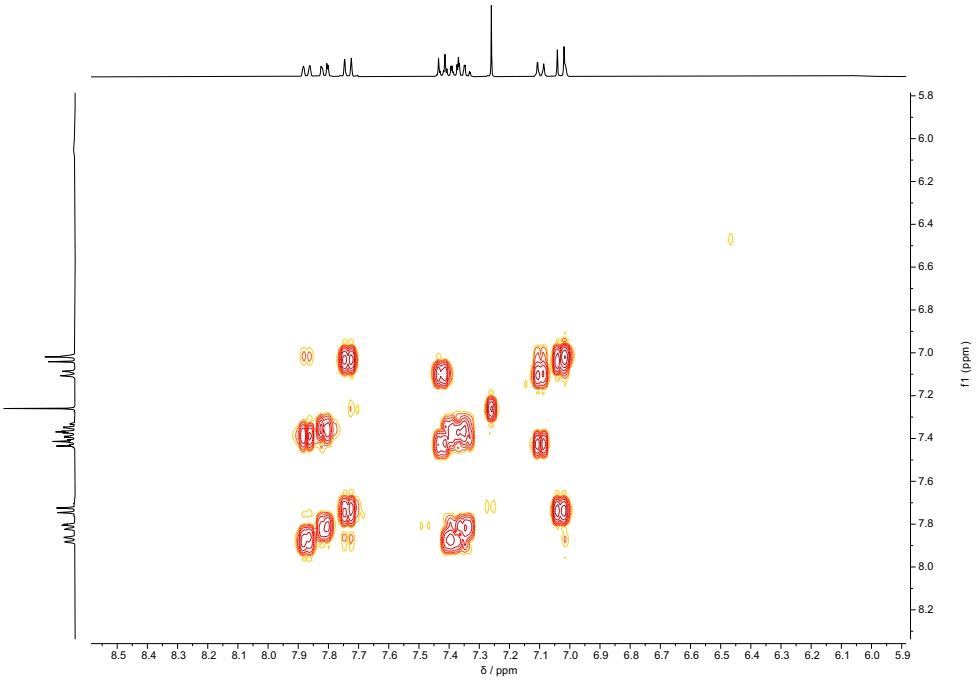
^{1}H-NMR (400 MHz, $CDCl_3$):



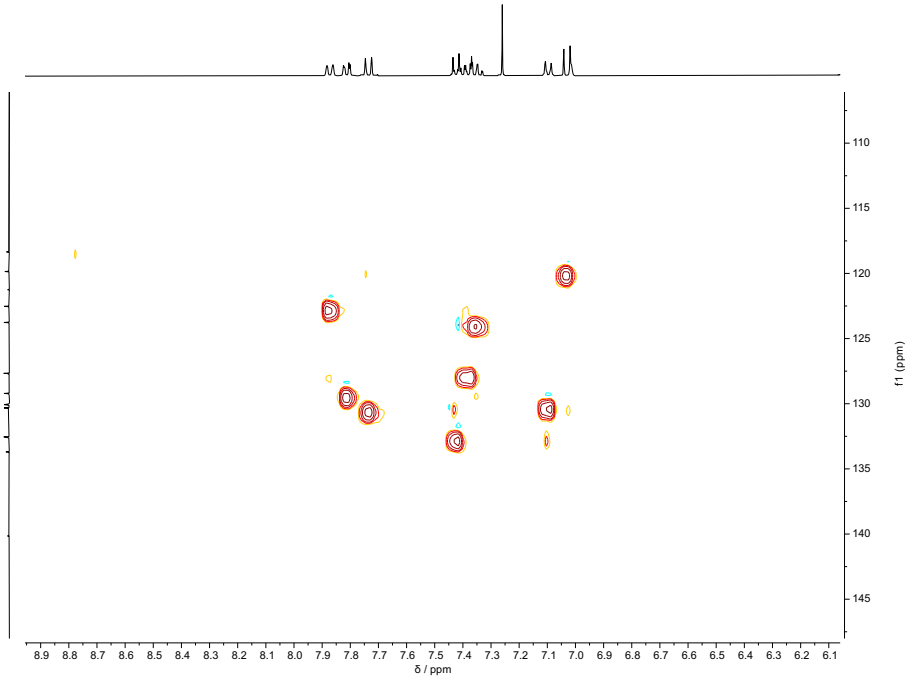
^{13}C-NMR (101 MHz, $CDCl_3$):



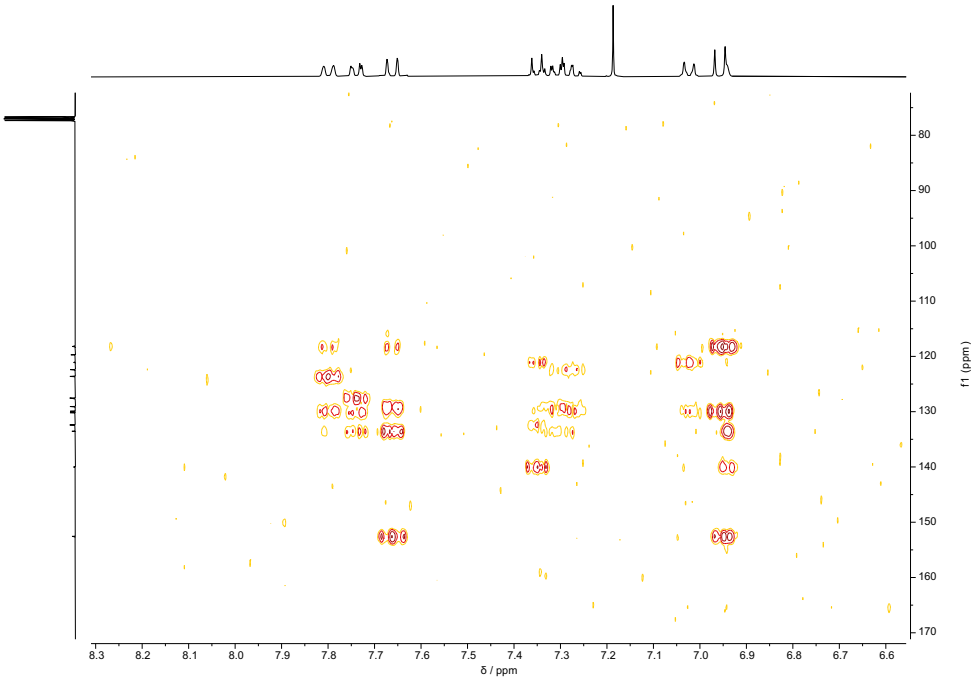
COSY:


5.8
6.0
6.2
6.4
6.6
6.8
7.0
7.2
7.4
7.6
7.8
8.0
8.2
f1 (ppm)
8.5 8.4 8.3 8.2 8.1 8.0 7.9 7.8 7.7 7.6 7.5 7.4 7.3 7.2 7.1 7.0 6.9 6.8 6.7 6.6 6.5 6.4 6.3 6.2 6.1 6.0 5.9
δ / ppm

HSQC:

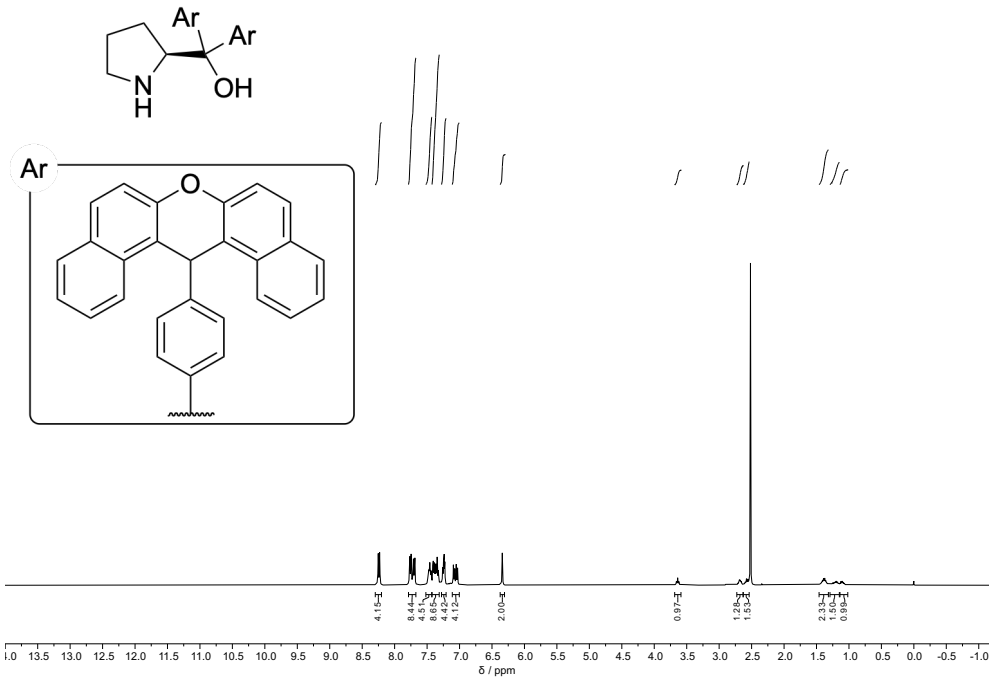

110
115
120
125
130
135
140
145
f1 (ppm)
8.9 8.8 8.7 8.6 8.5 8.4 8.3 8.2 8.1 8.0 7.9 7.8 7.7 7.6 7.5 7.4 7.3 7.2 7.1 7.0 6.9 6.8 6.7 6.6 6.5 6.4 6.3 6.2 6.1
δ / ppm

HMBC:

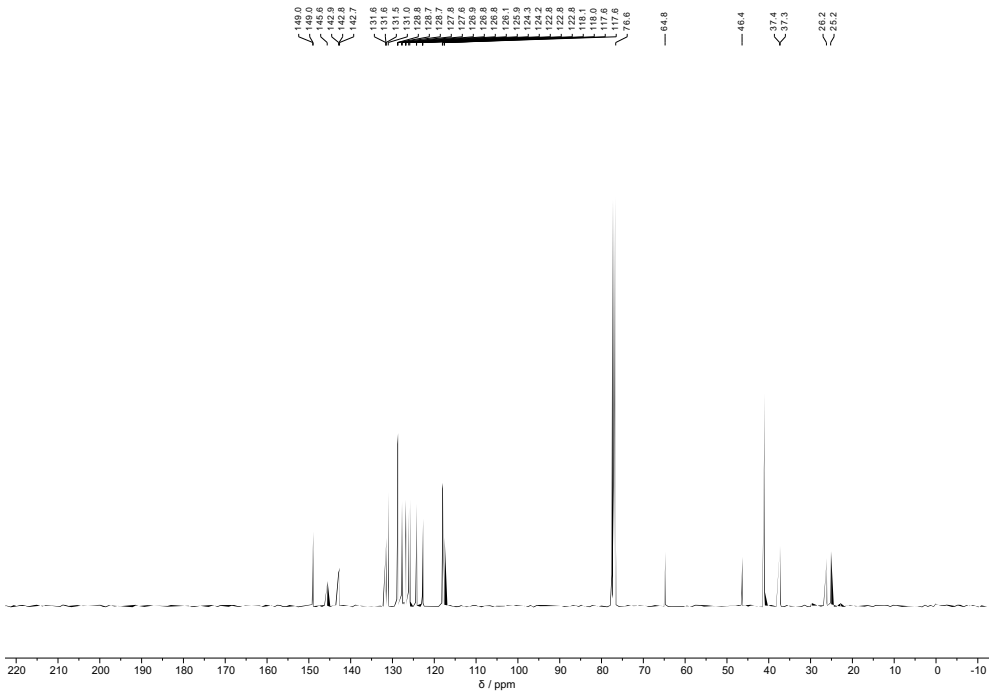

80
90
100
110
120
130
140
150
160
170
f1 (ppm)
8.3
8.2
8.1
8.0
7.9
7.8
7.7
7.6
7.5
7.4
7.3
7.2
7.1
7.0
6.9
6.8
6.7
6.6
δ / ppm

(*S*)-Bis(4-(14*H*-dibenzo9[a,j]xanthen-14-yl)phenyl)8pyrrolidin-2-yl)methanol (22k)

^{1}H-NMR (400 MHz, $CDCl_3$):

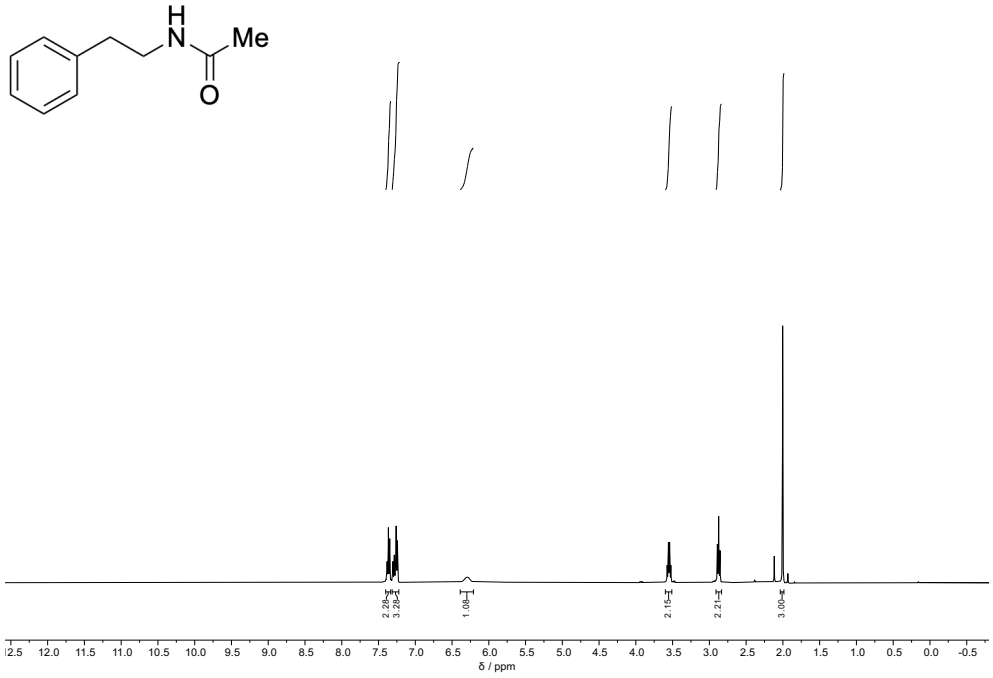


^{13}C-NMR (101 MHz, $CDCl_3$):

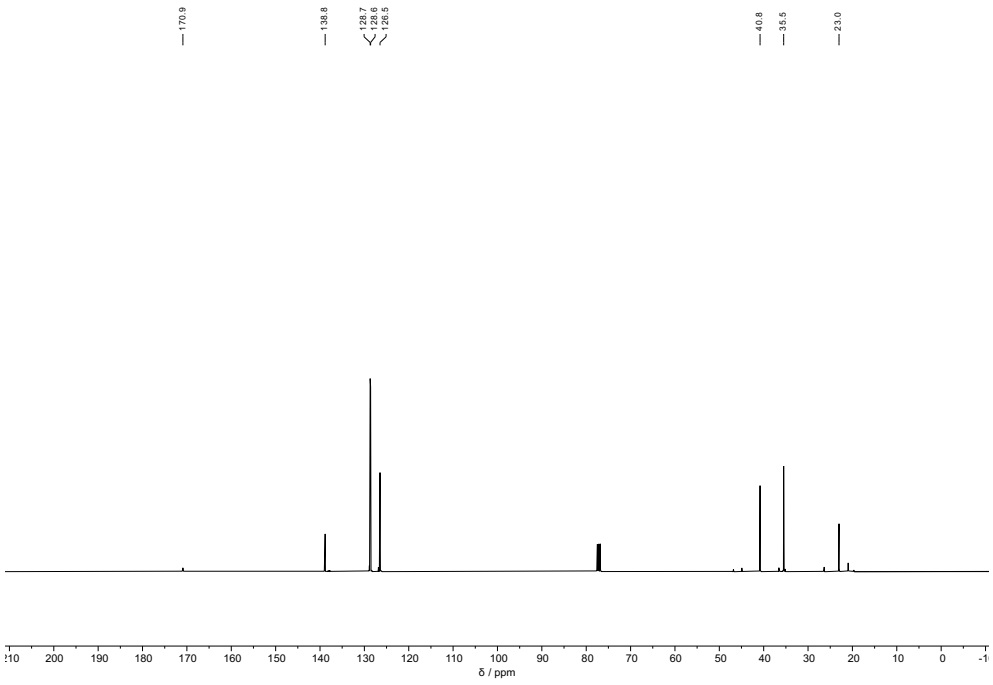


***N*-Phenethylacetamide (89)**:

^{1}H-NMR (400 MHz, $CDCl_3$):

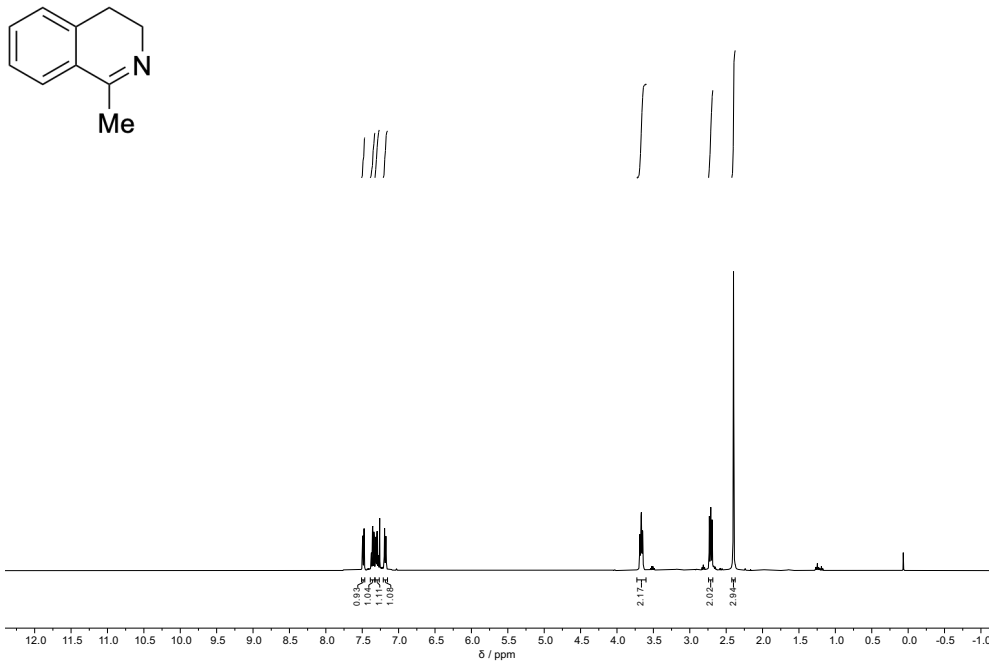


^{13}C-NMR (101 MHz, $CDCl_3$):

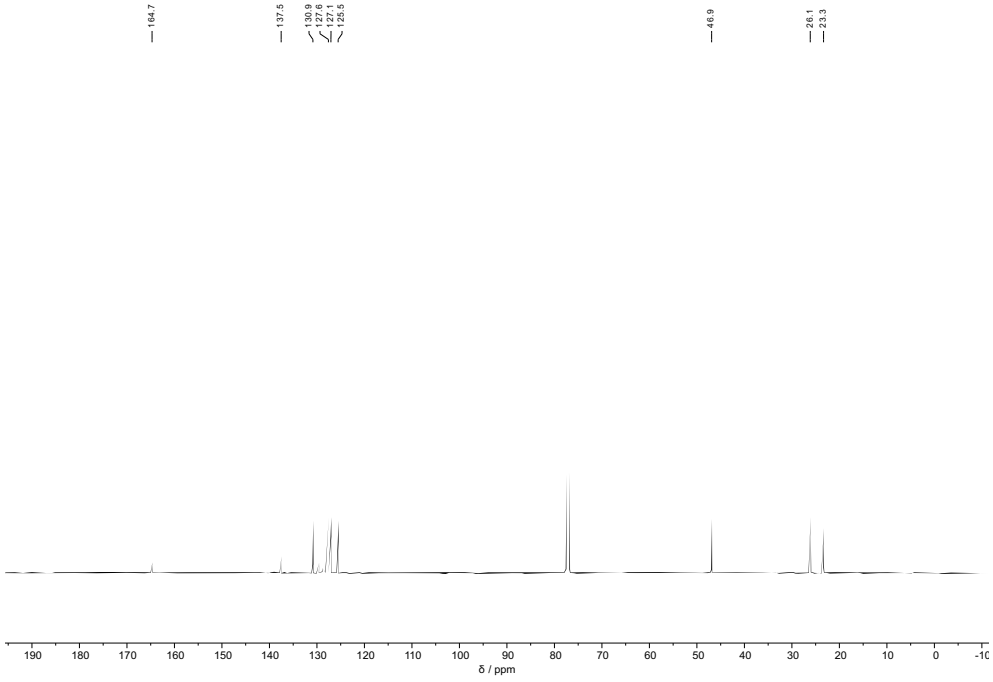


1-Methyl-3,4-dihydroisoquinoline (**87**):

^{1}H-NMR (400 MHz, $CDCl_3$):

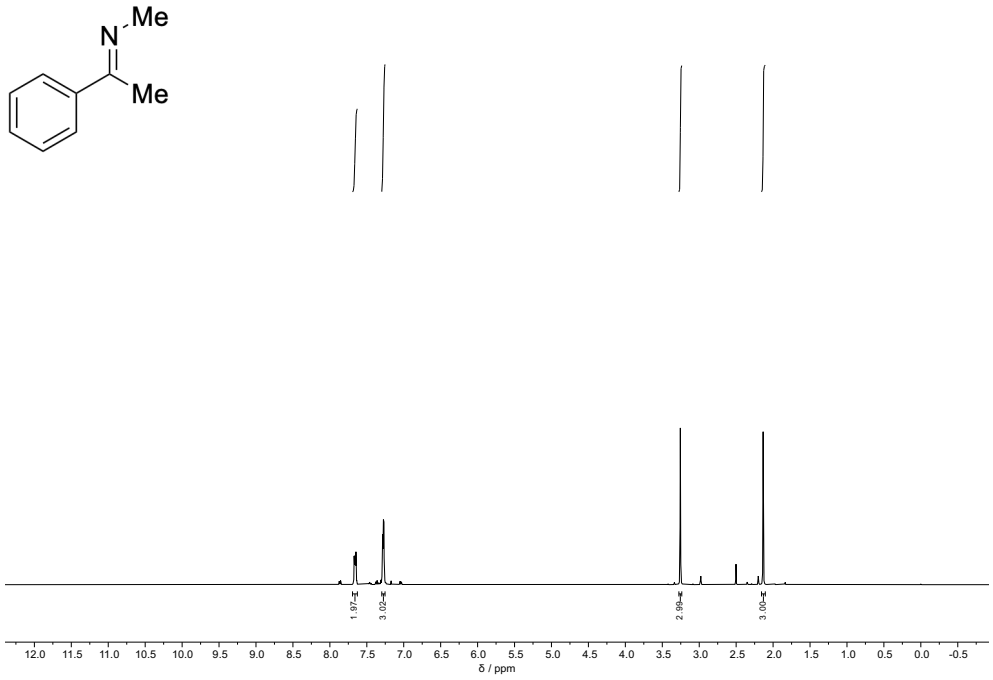


^{13}C-NMR (101 MHz, $CDCl_3$):

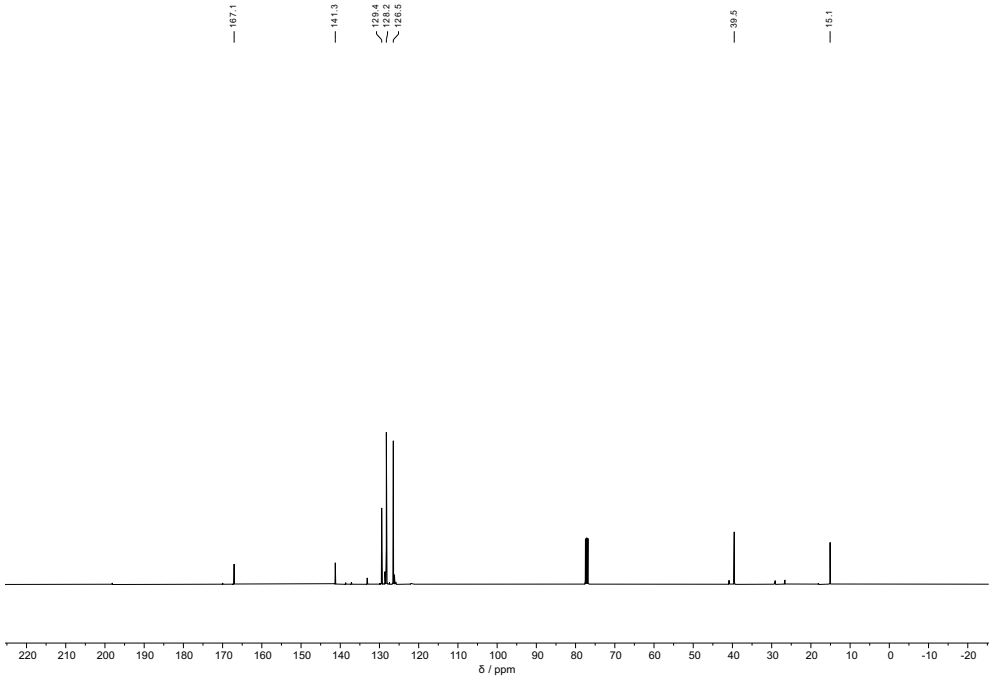


(E)-*N*-(1-Phenylethylidene)methanamine (94):

^{1}H-NMR (400 MHz, $CDCl_3$):

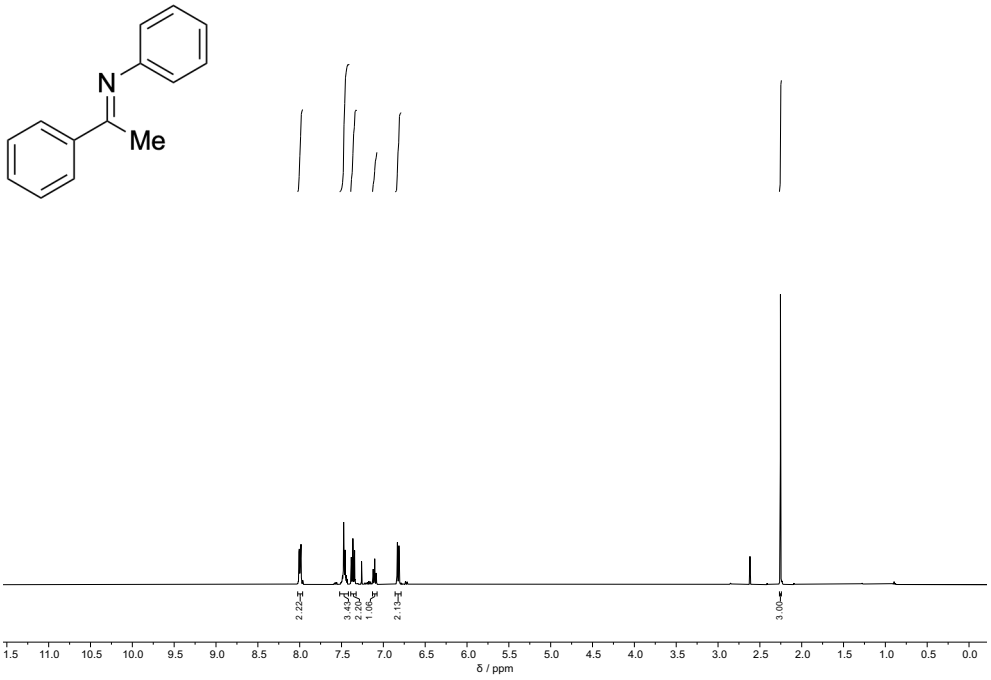


^{13}C-NMR (101 MHz, $CDCl_3$):

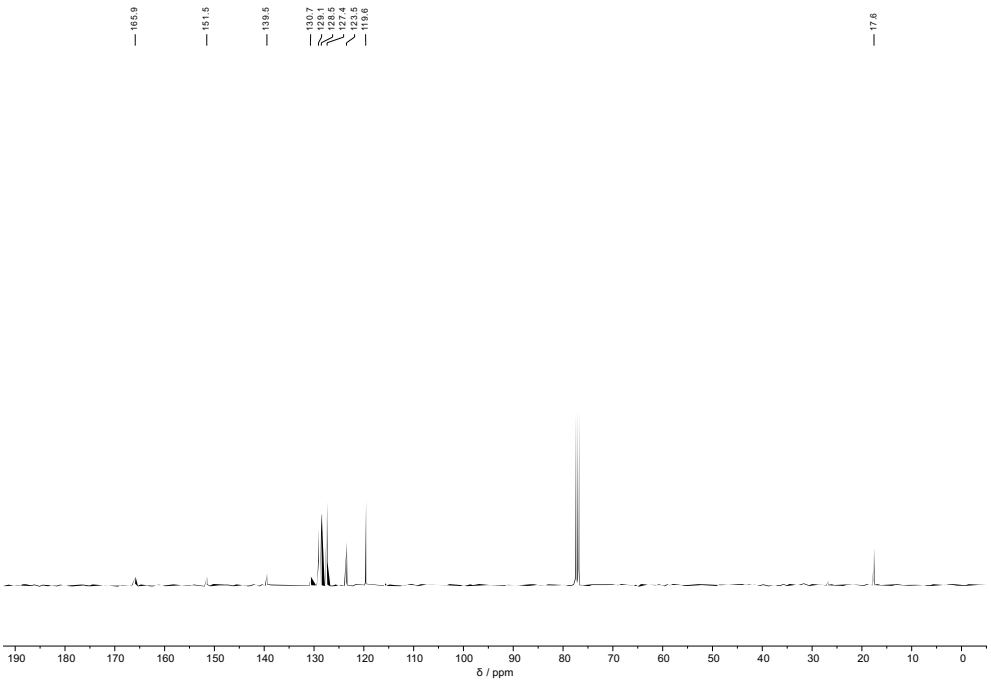


(E)-*N*-(1-Phenylethylidene)aniline (92):

^{1}H-NMR (400 MHz, $CDCl_3$):

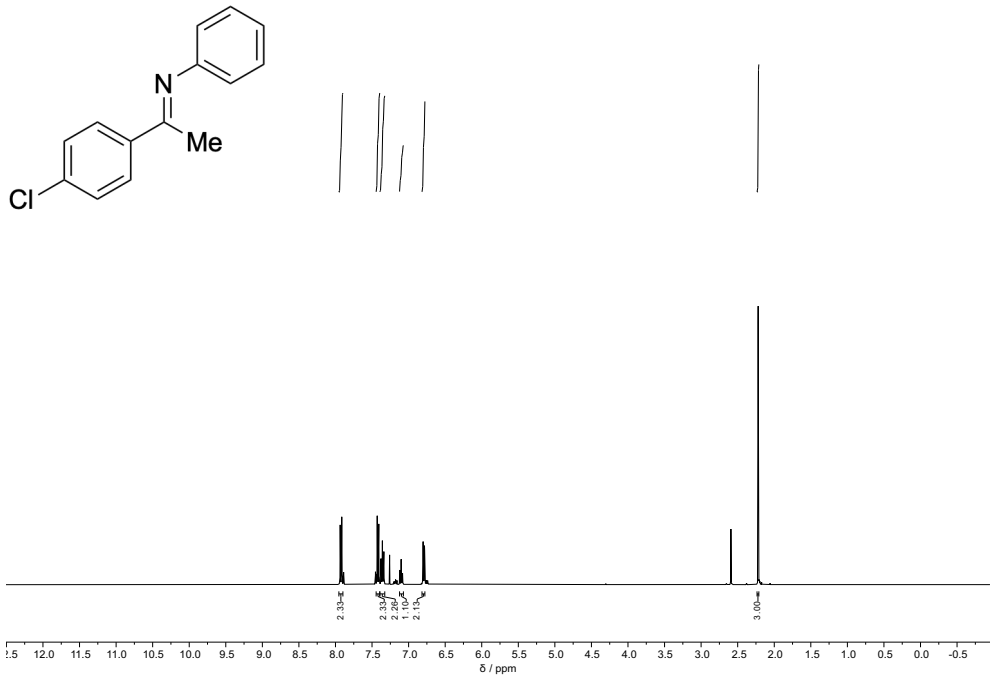


^{13}C-NMR (101 MHz, $CDCl_3$):

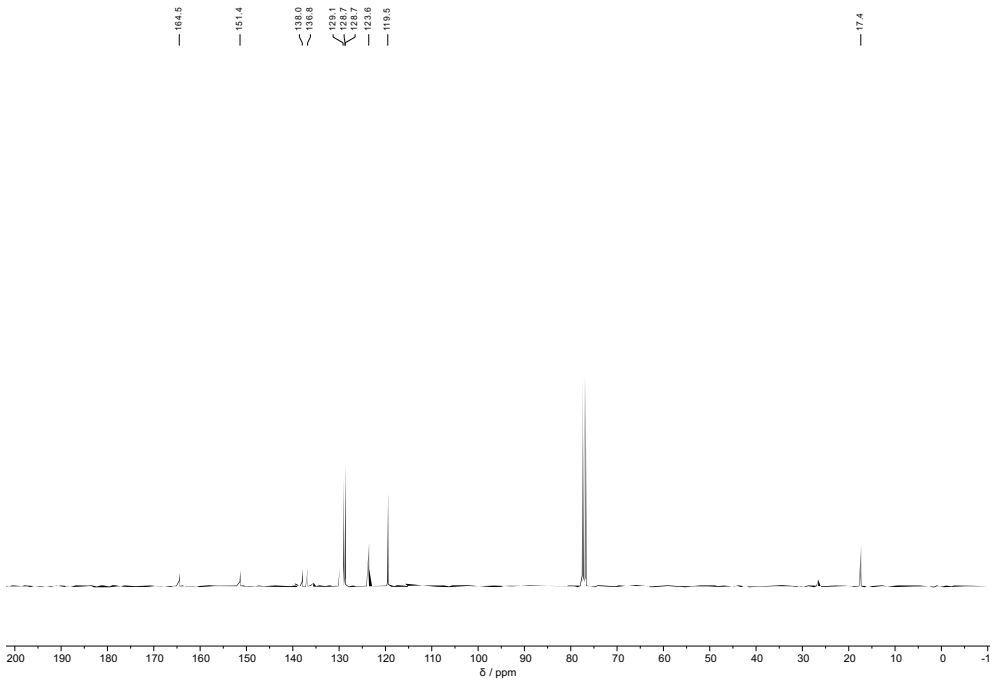


(E)-*N*-(1-4-Chlorophenyl)ethylidene)aniline (96):

^{1}H-NMR (400 MHz, $CDCl_3$):

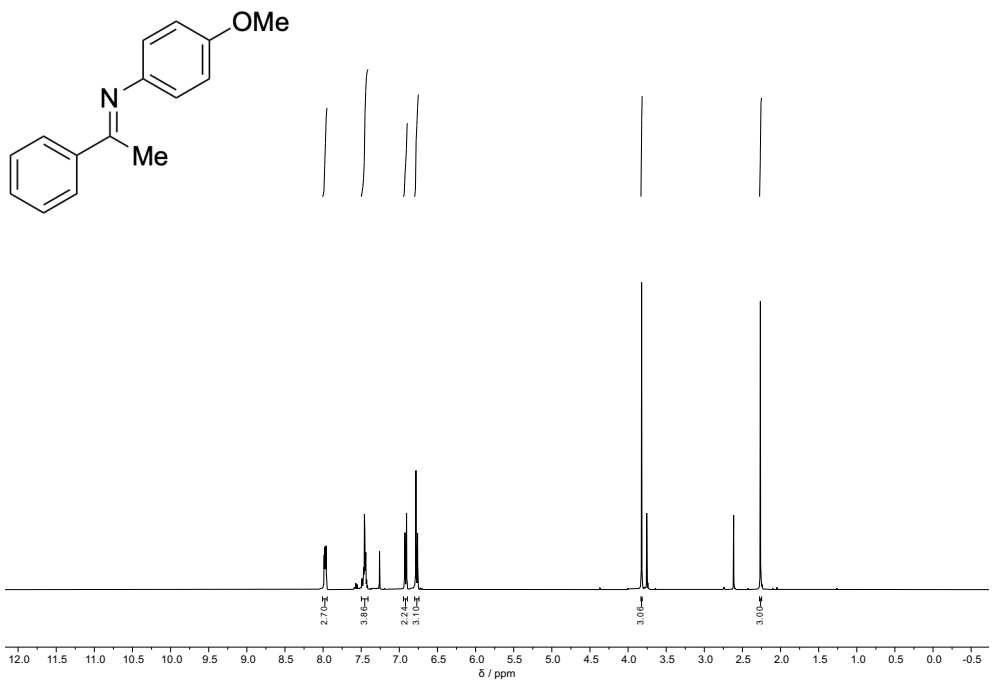


^{13}C-NMR (101 MHz, $CDCl_3$):

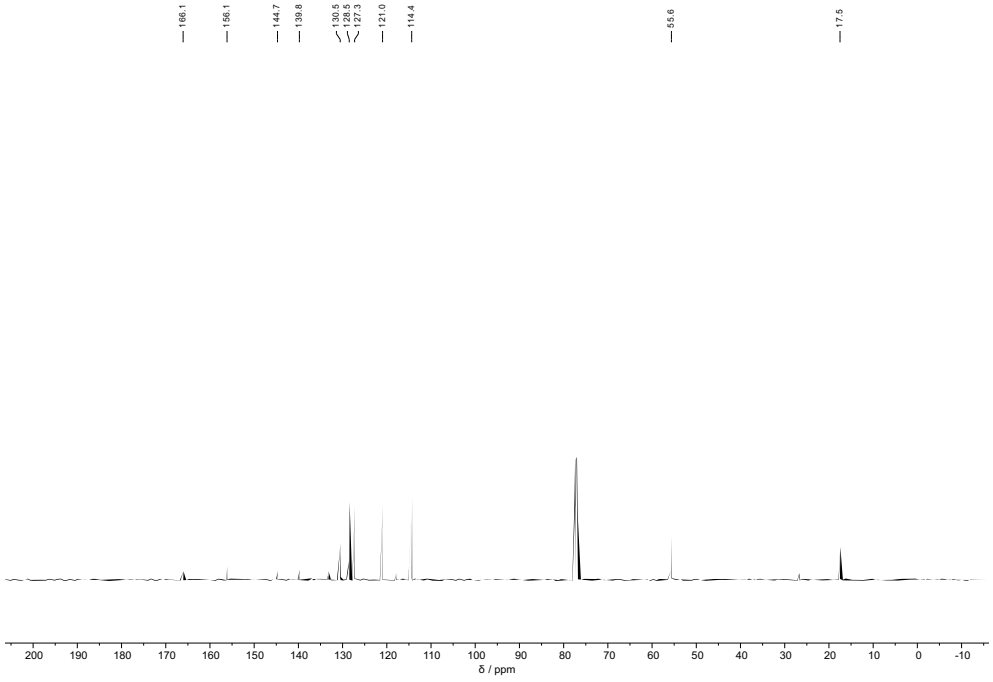


(E)-4-Methoxy-*N*-(1-phenylethylidene)aniline (**97**):

^{1}H-NMR (400 MHz, $CDCl_3$):

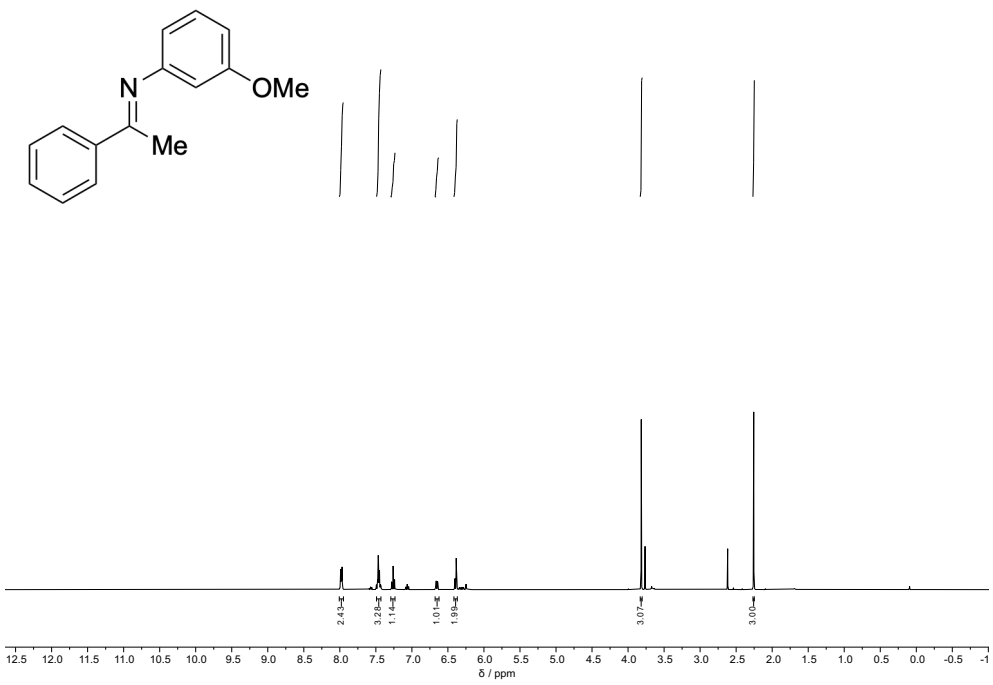


^{13}C-NMR (101 MHz, $CDCl_3$):

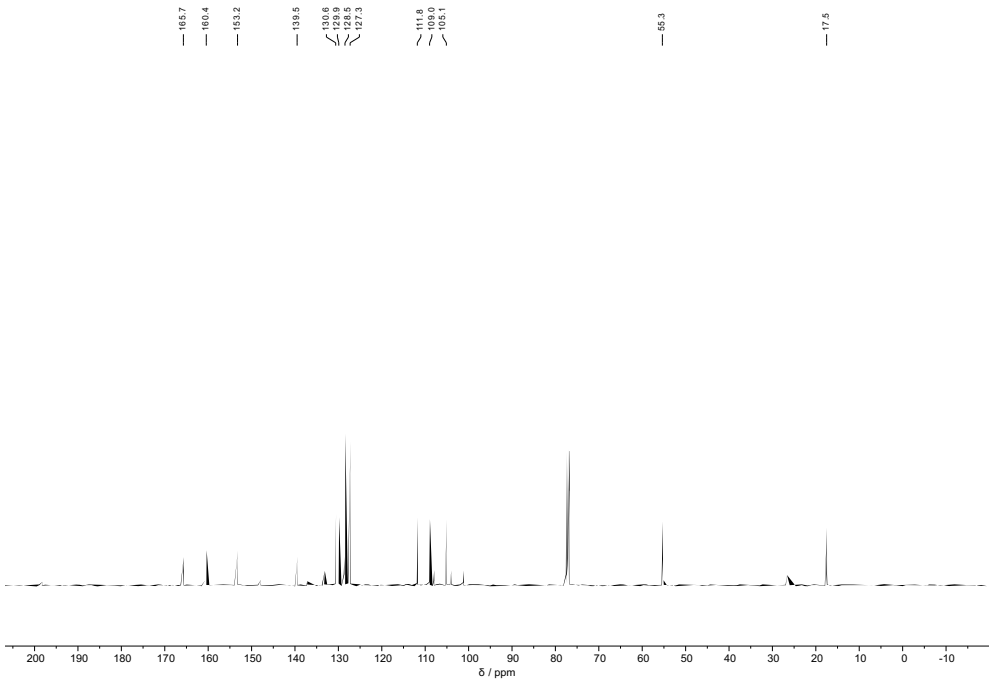


(E)-3-Methoxy-*N*-(1-phenylethylidene)aniline (98):

^{1}H-NMR (400 MHz, $CDCl_3$):

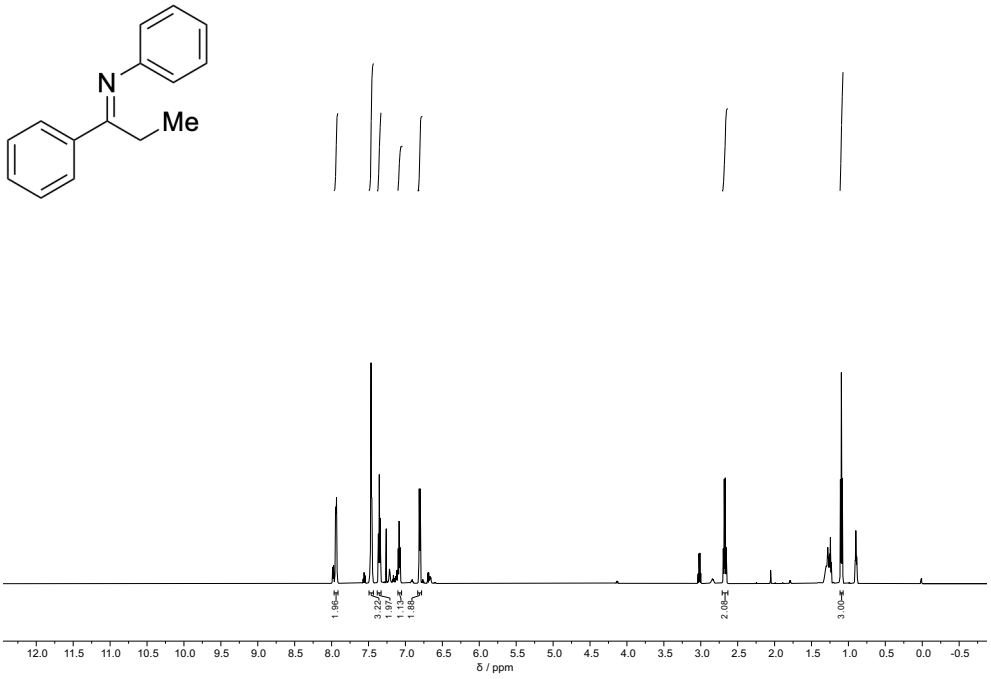


^{13}C-NMR (101 MHz, $CDCl_3$):

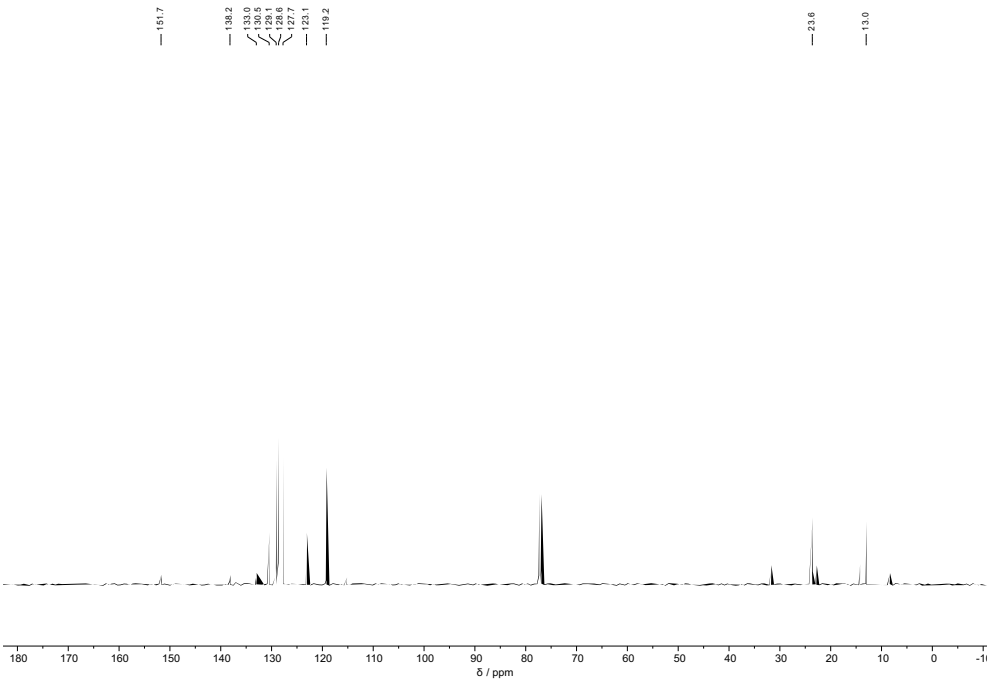


(E)-*N*-(1-Phenylpropylidene)aniline (32b):

^{1}H-NMR (400 MHz, $CDCl_3$):

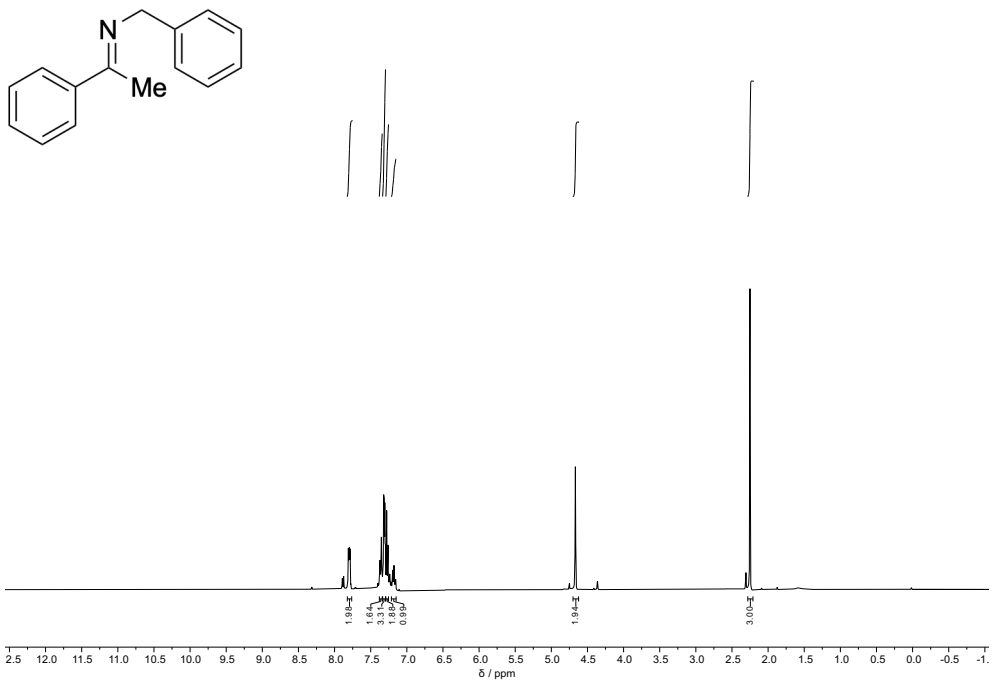


^{13}C-NMR (101 MHz, $CDCl_3$):

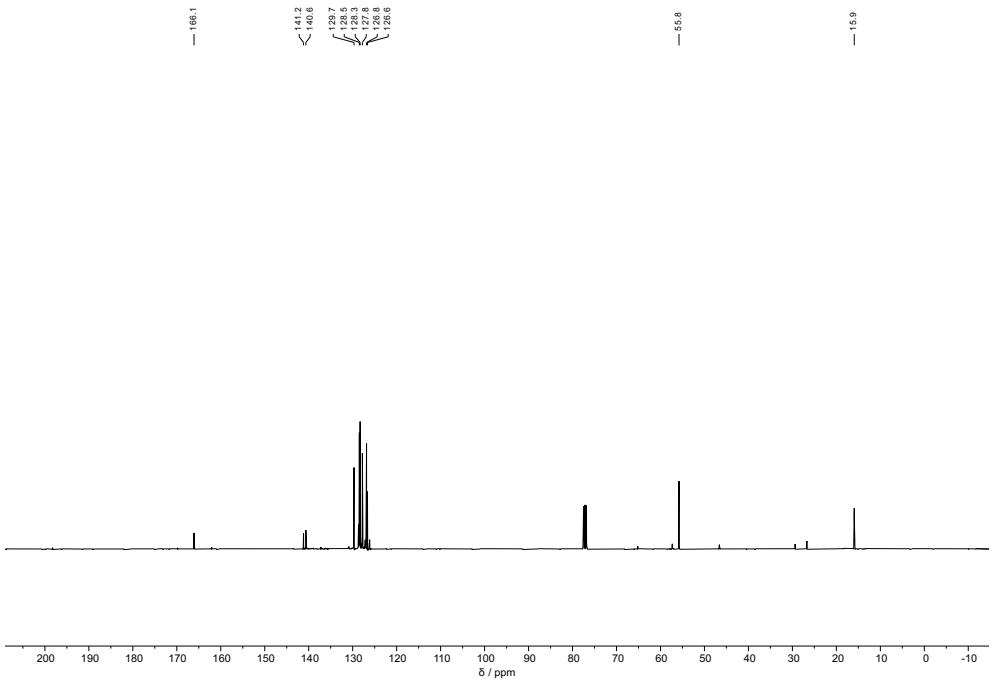


(E)-1-Phenyl-*N*-(1-phenylethylidene)methanamine (95):

^{1}H-NMR (400 MHz, $CDCl_3$):

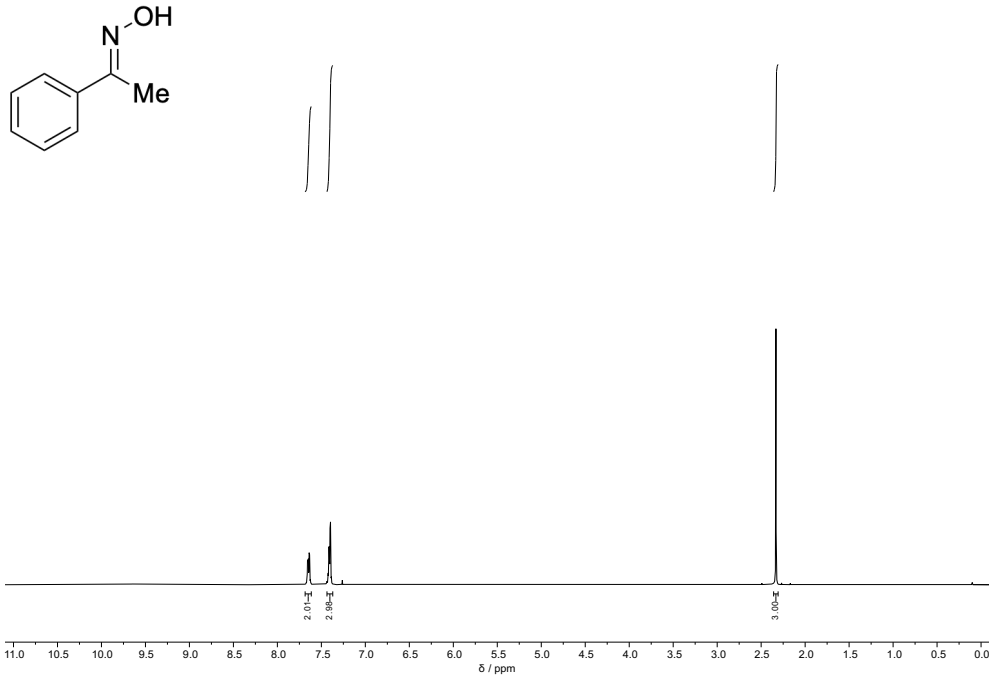


^{13}C-NMR (101 MHz, $CDCl_3$):

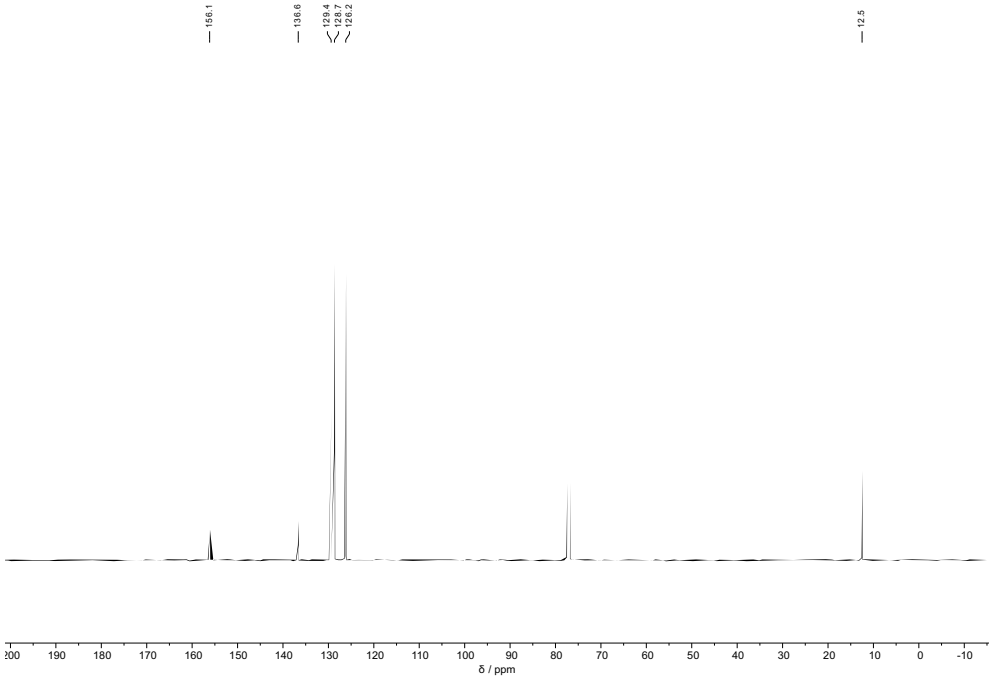


(E)-Acetophenone oxime (**144**):

^{1}H-NMR (400 MHz, $CDCl_3$):

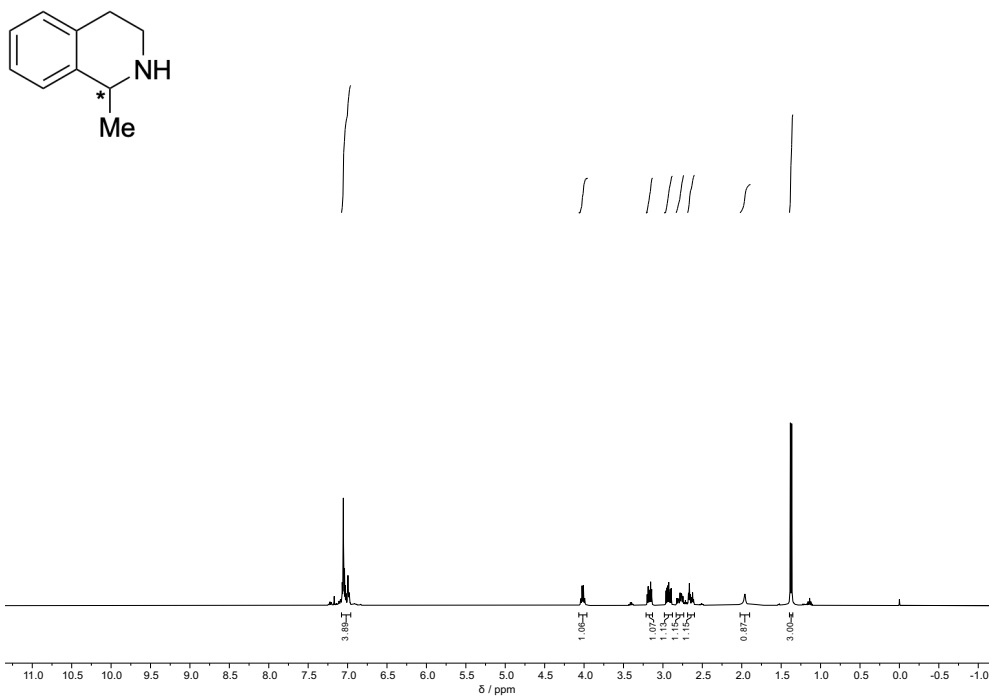


^{13}C-NMR (101 MHz, $CDCl_3$):

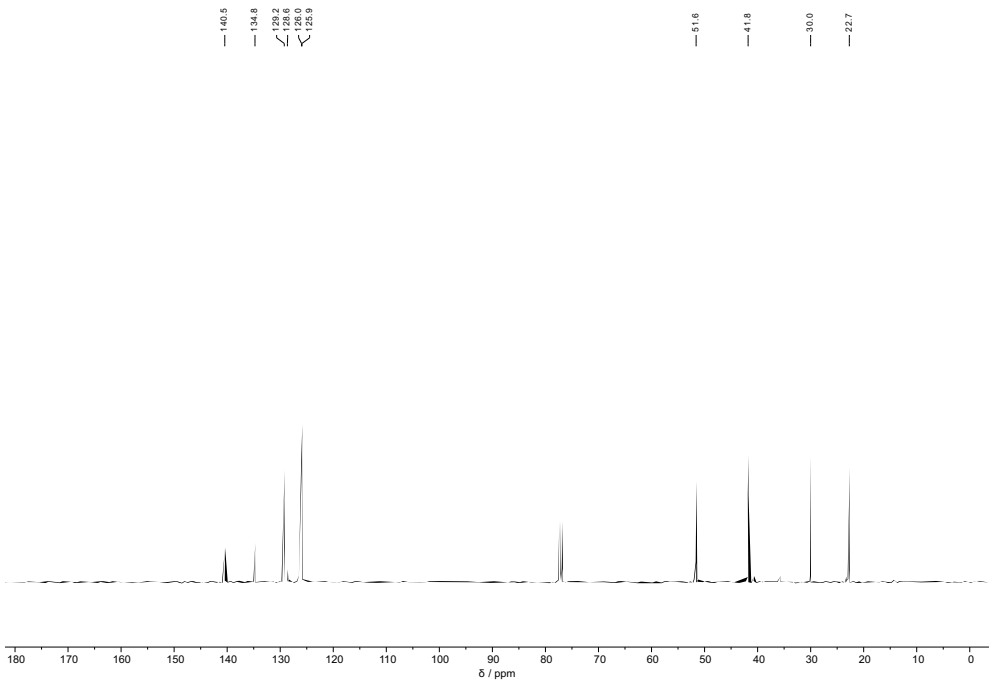


1-Methyl-1,2,3,4-tetrahydroisoquinoline (rac-**91**):

^{1}H-NMR (400 MHz, $CDCl_3$):

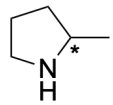


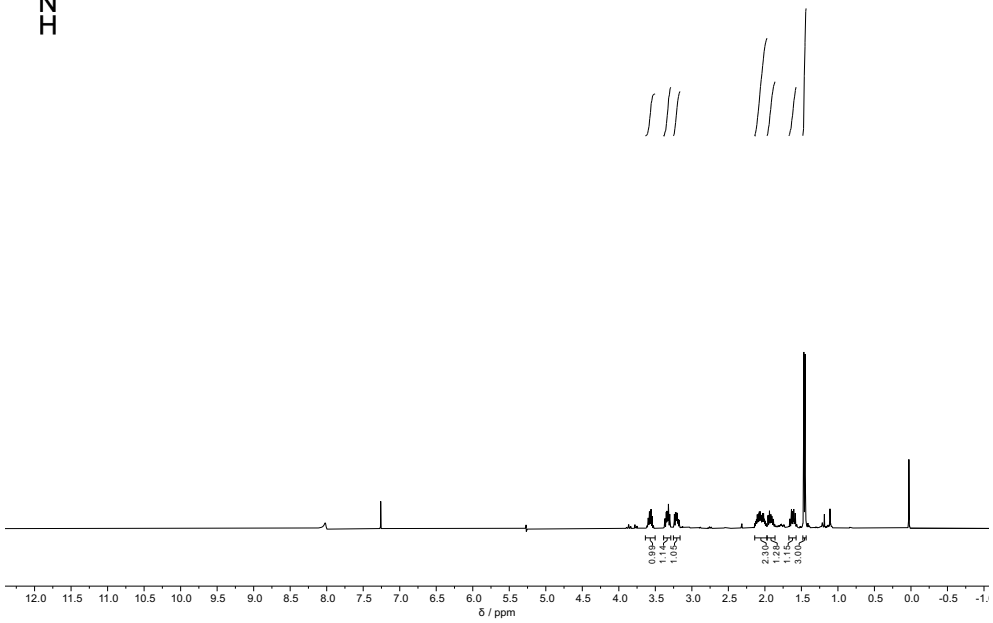
^{13}C-NMR (101 MHz, $CDCl_3$):



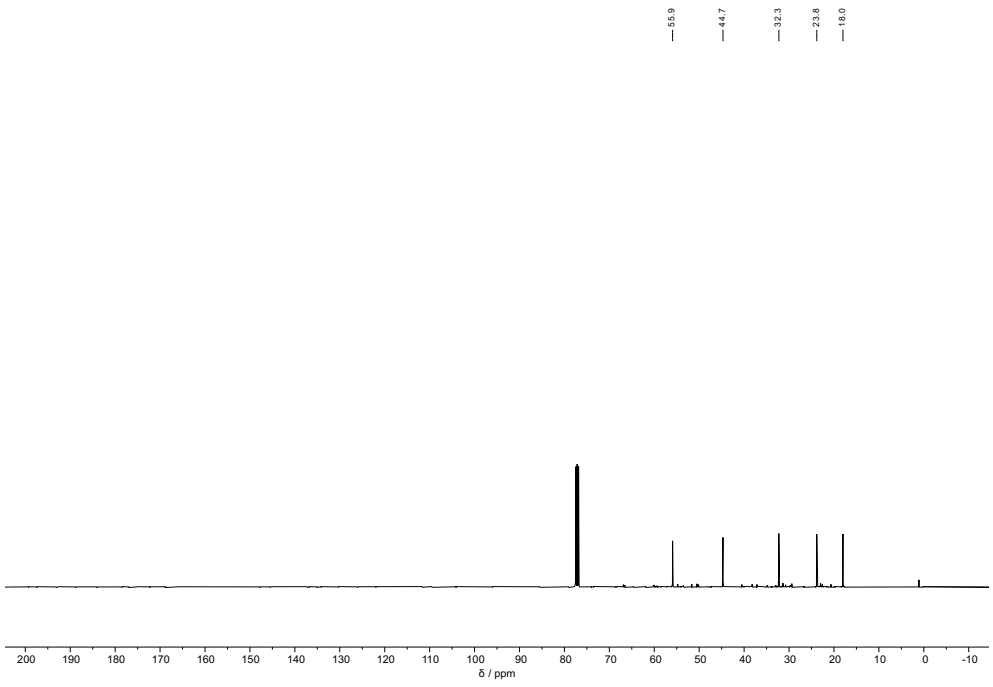
2-Methylpyrrolidine (rac-**90**):

^{1}H-NMR (400 MHz, $CDCl_3$):



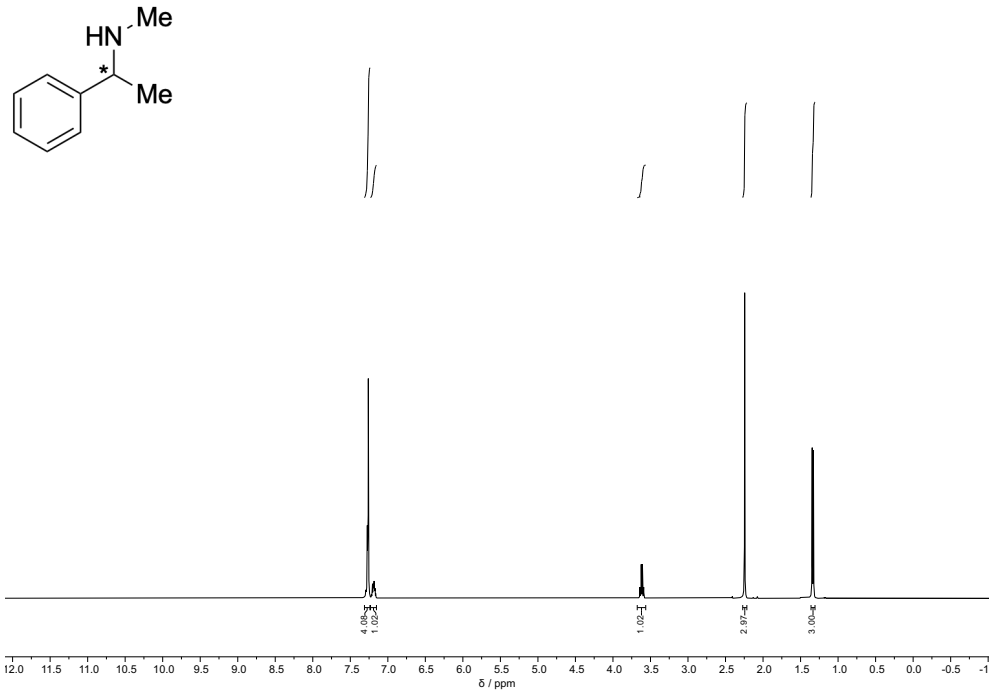


^{13}C-NMR (101 MHz, $CDCl_3$):

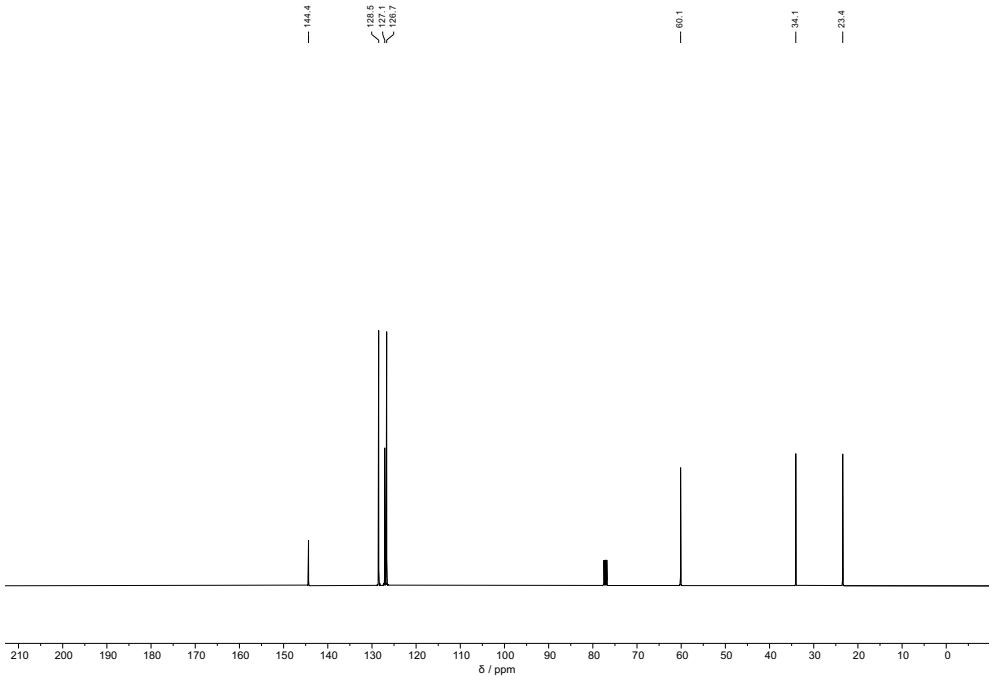


***N*-Methyl-1-phenylethanamine** (rac-**145**):

^{1}H-NMR (400 MHz, $CDCl_3$):

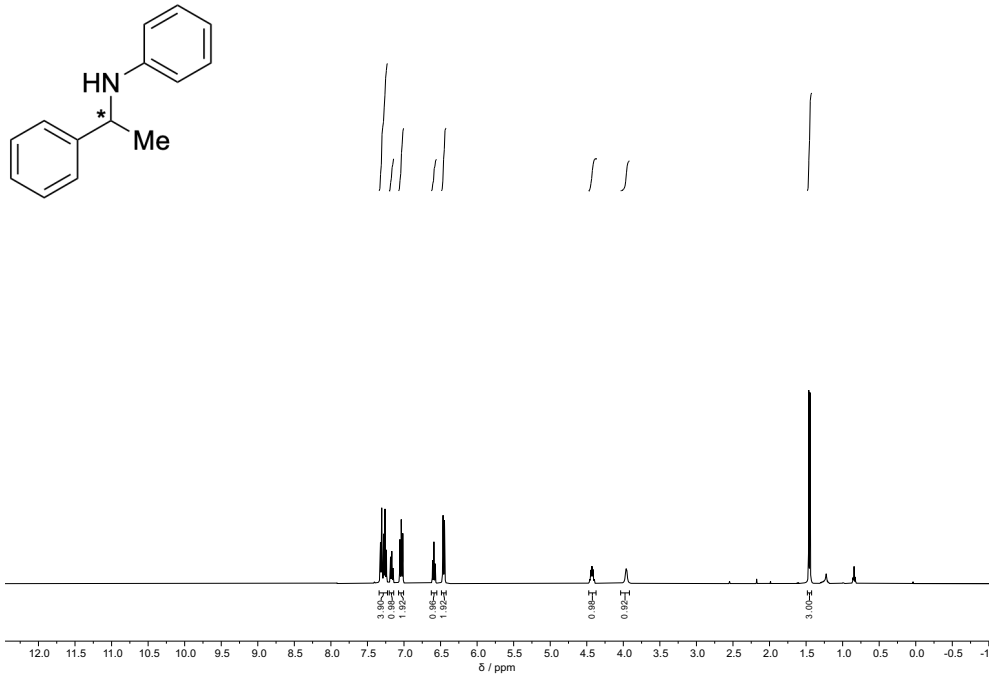


^{13}C-NMR (101 MHz, $CDCl_3$):

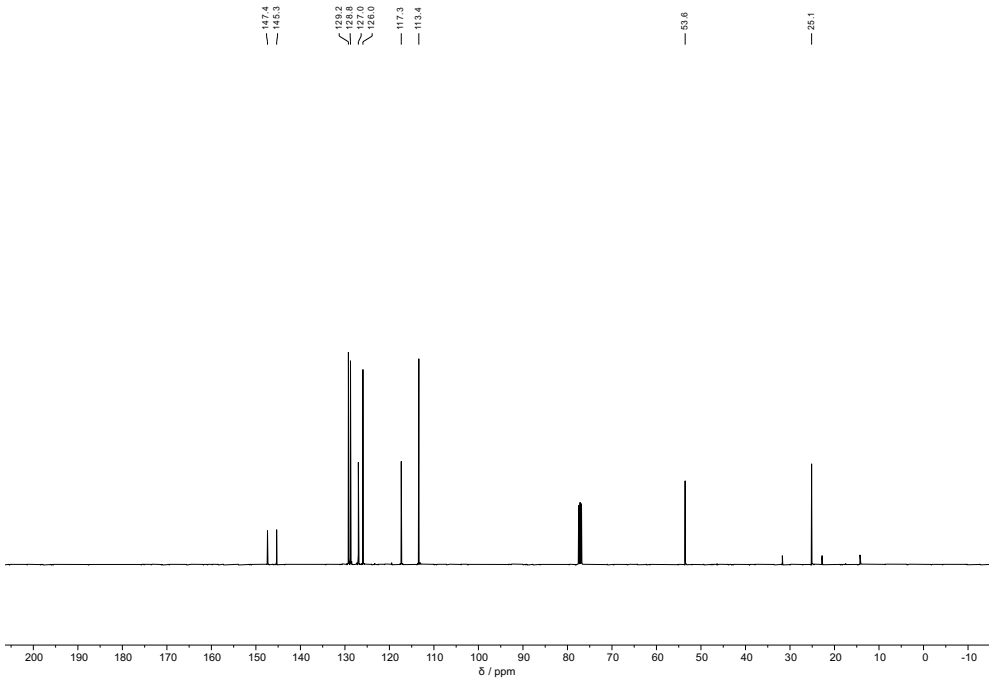


***N*-(1-Phenylethyl)aniline** (rac-**93**):

^{1}H-NMR (400 MHz, $CDCl_3$):

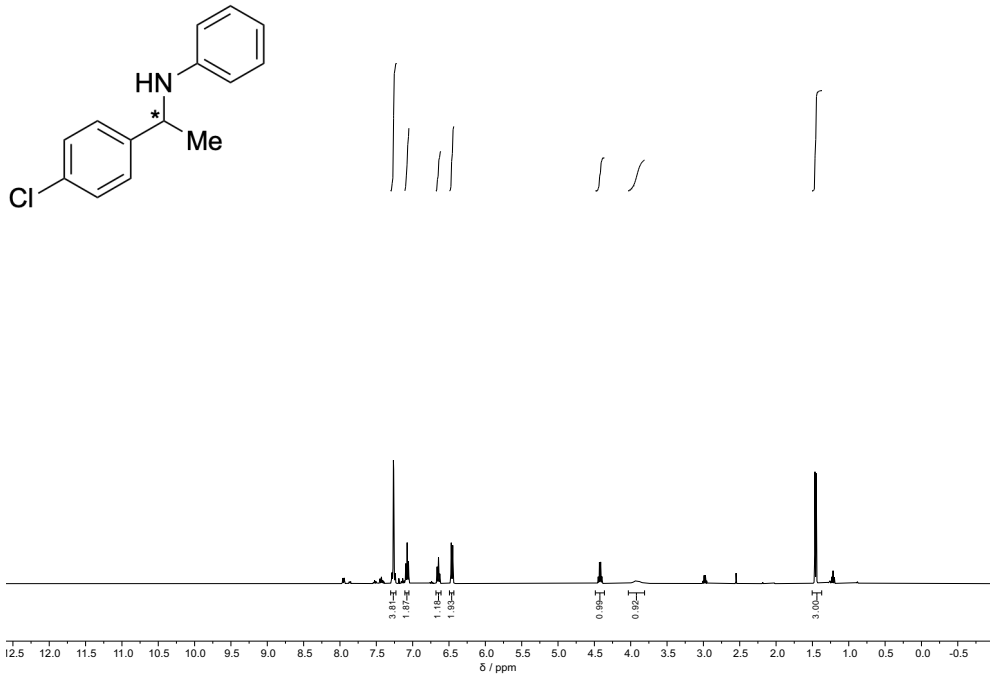


^{13}C-NMR (101 MHz, $CDCl_3$):

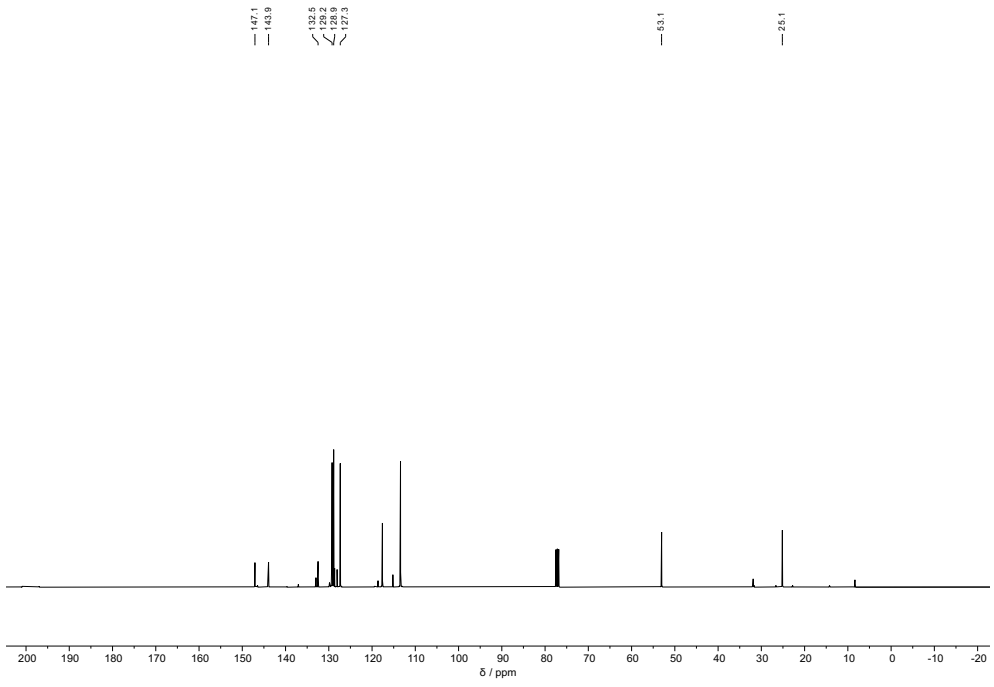


***N*-(1-(4-Chlorophenyl)ethyl)aniline** (rac-**146**)

^{1}H-NMR (400 MHz, $CDCl_3$):

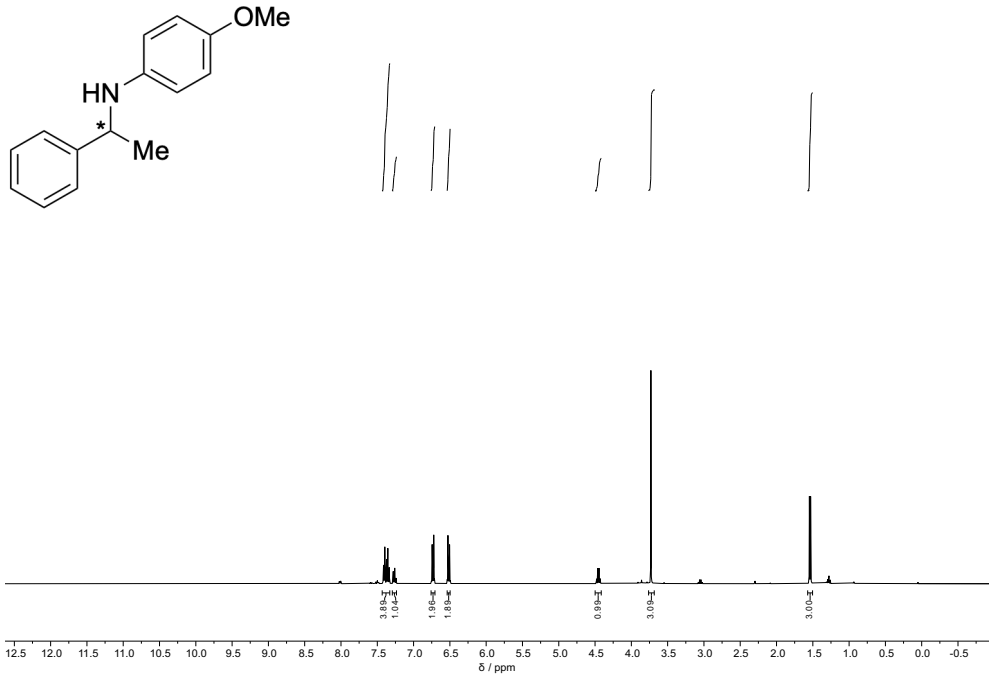


^{13}C-NMR (101 MHz, $CDCl_3$):

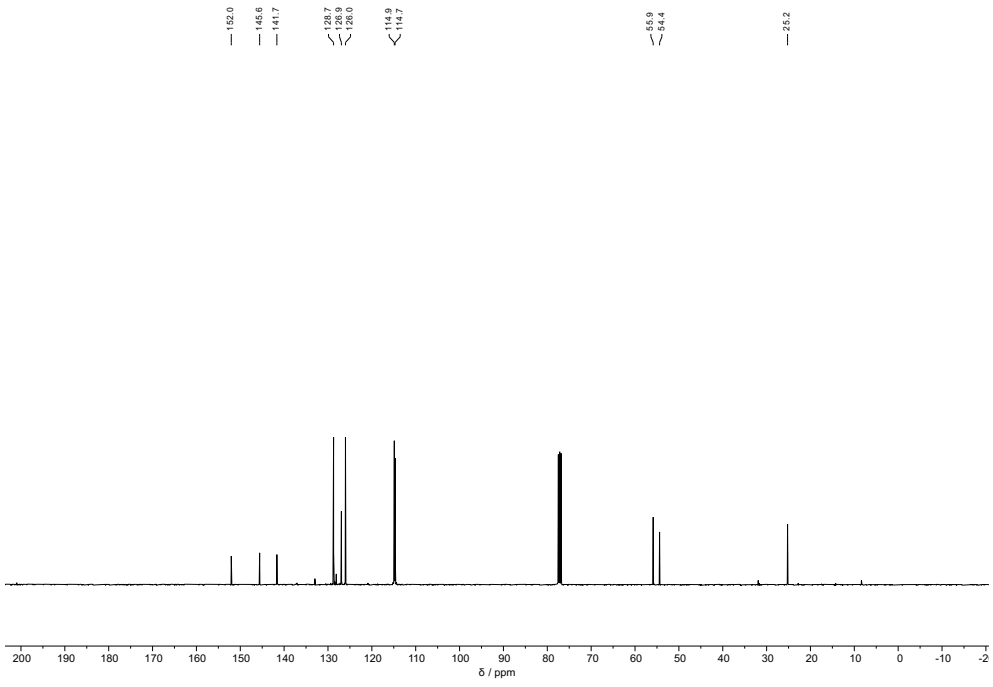


4-Methoxy-*N*-(1-phenylethyl)aniline (rac-**147**):

^{1}H-NMR (400 MHz, $CDCl_3$):

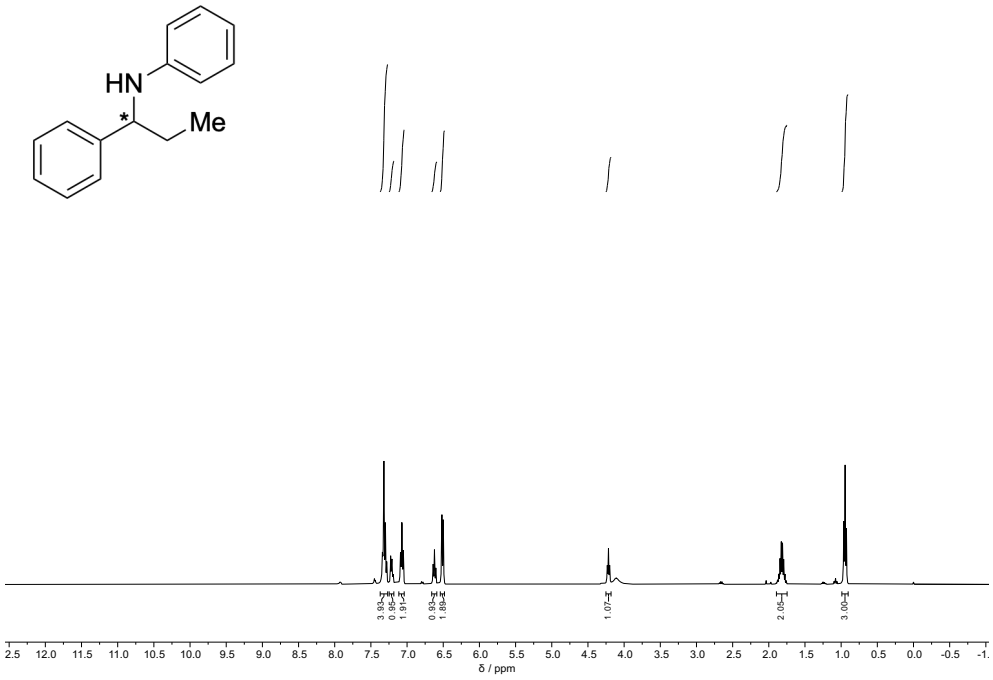


^{13}C-NMR (101 MHz, $CDCl_3$):

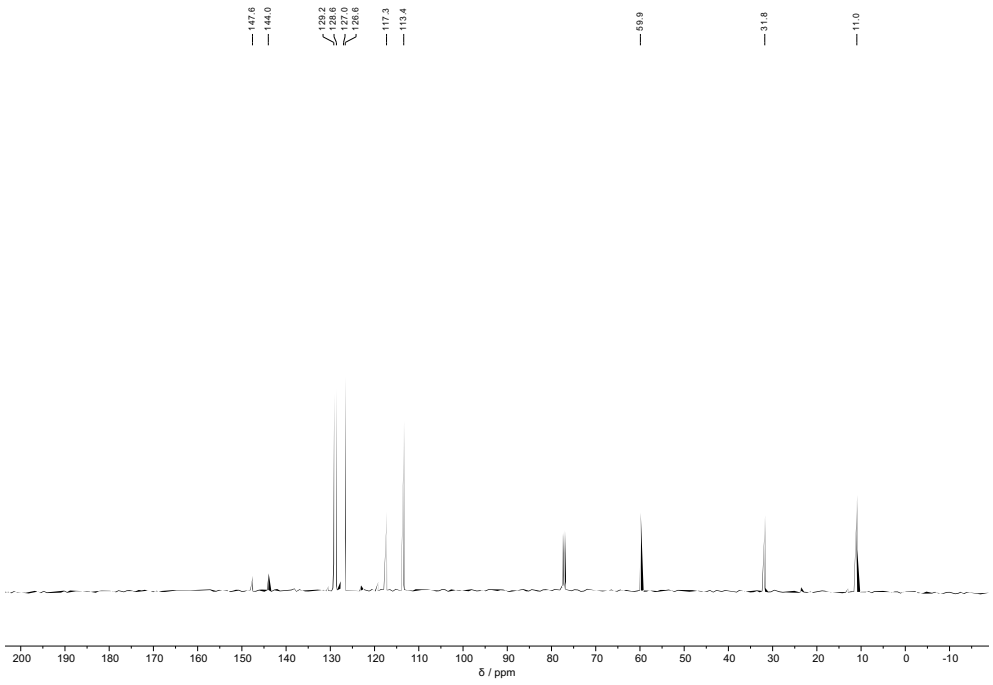


***N*-(1-Phenylpropyl)aniline** (rac-**34b**):

^{1}H-NMR (400 MHz, $CDCl_3$):

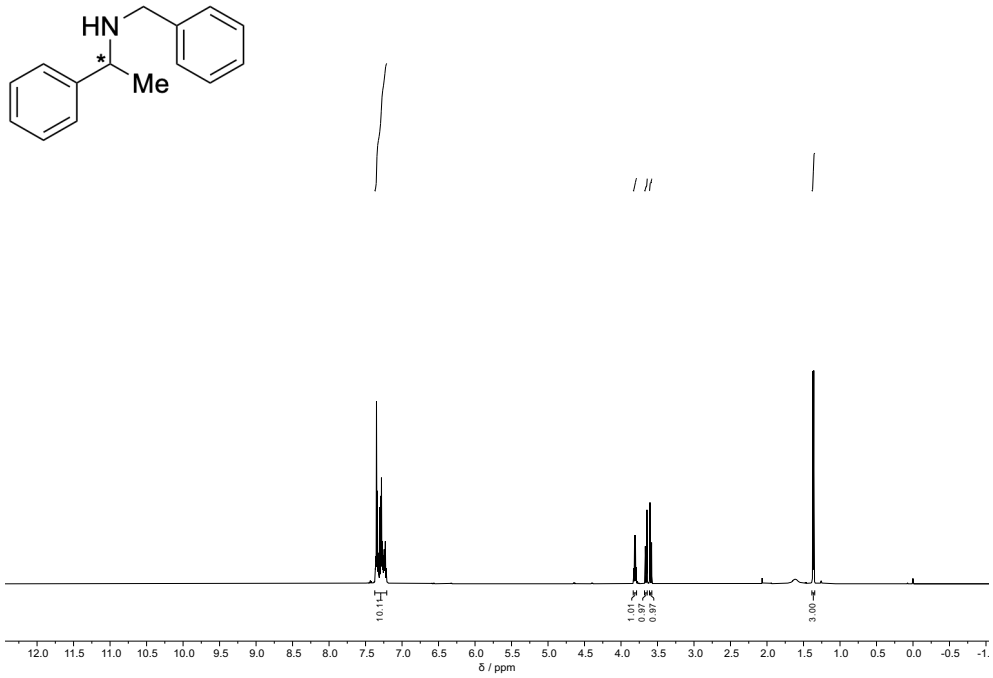


^{13}C-NMR (101 MHz, $CDCl_3$):

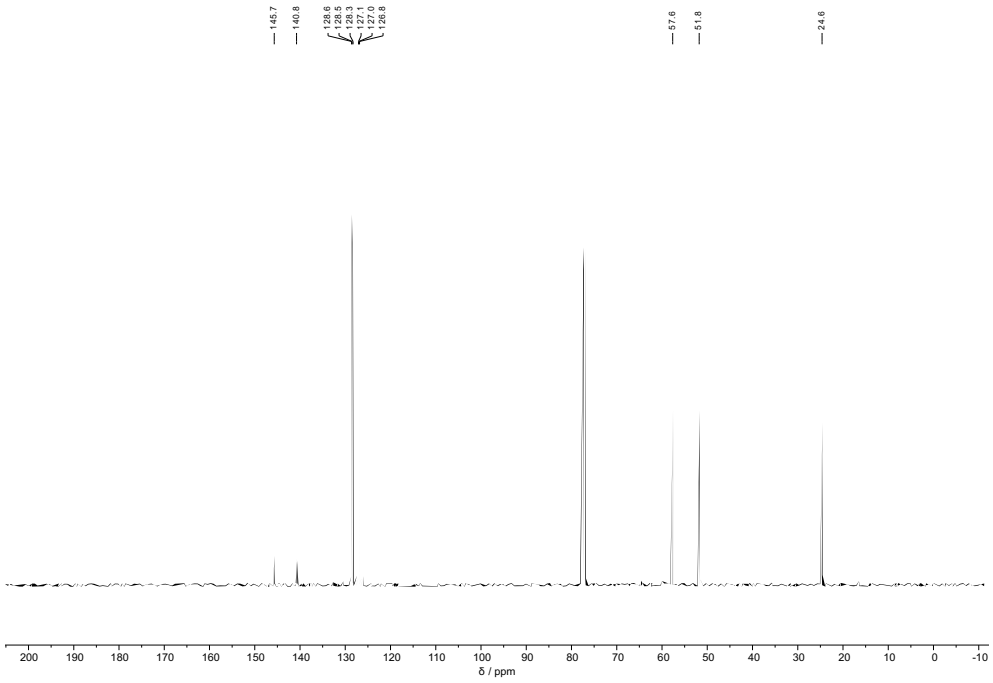


***N*-Benzyl-1-phenylethanamine** (rac-**148**):

^{1}H-NMR (400 MHz, $CDCl_3$):

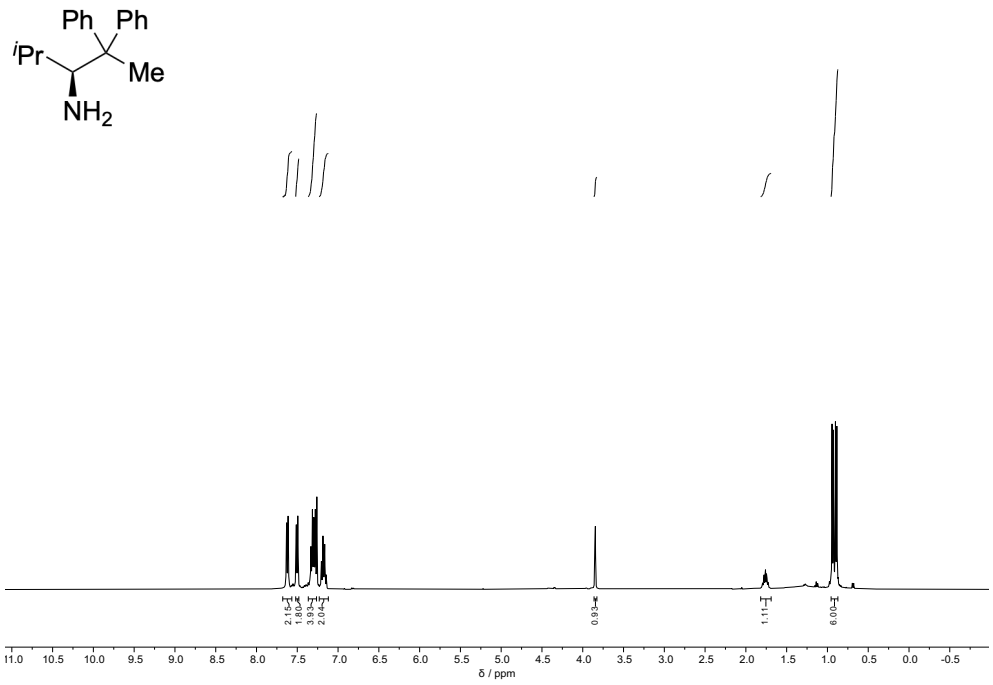


^{13}C-NMR (101 MHz, $CDCl_3$):

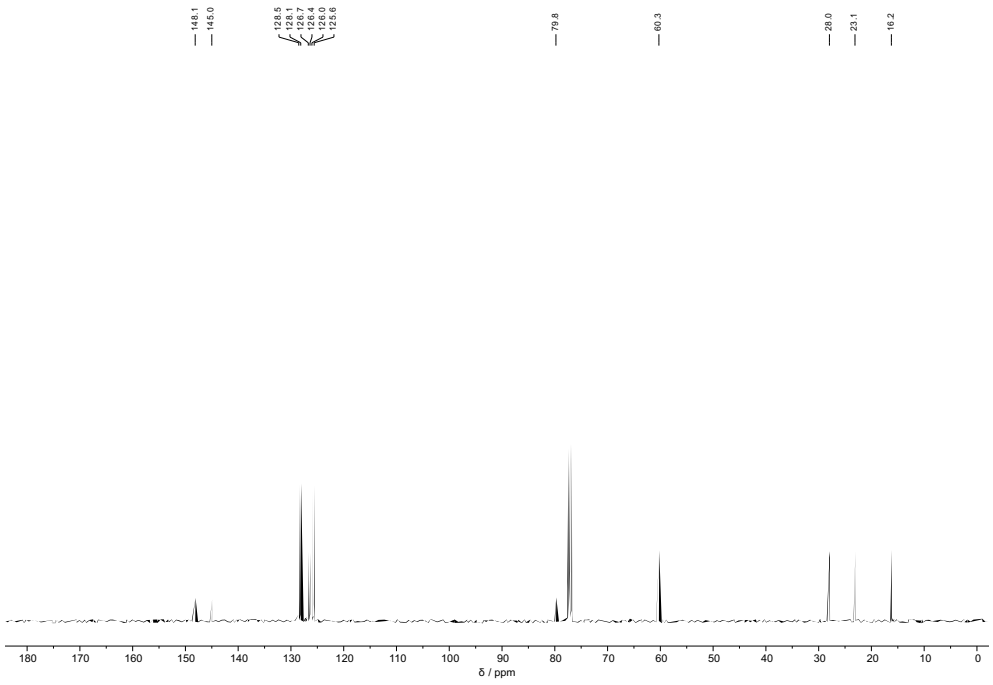


(*S*)-2-Amino-3-methyl-1,1-diphenylbutan-1-ol (**20**):

^{1}H-NMR (400 MHz, $CDCl_3$):

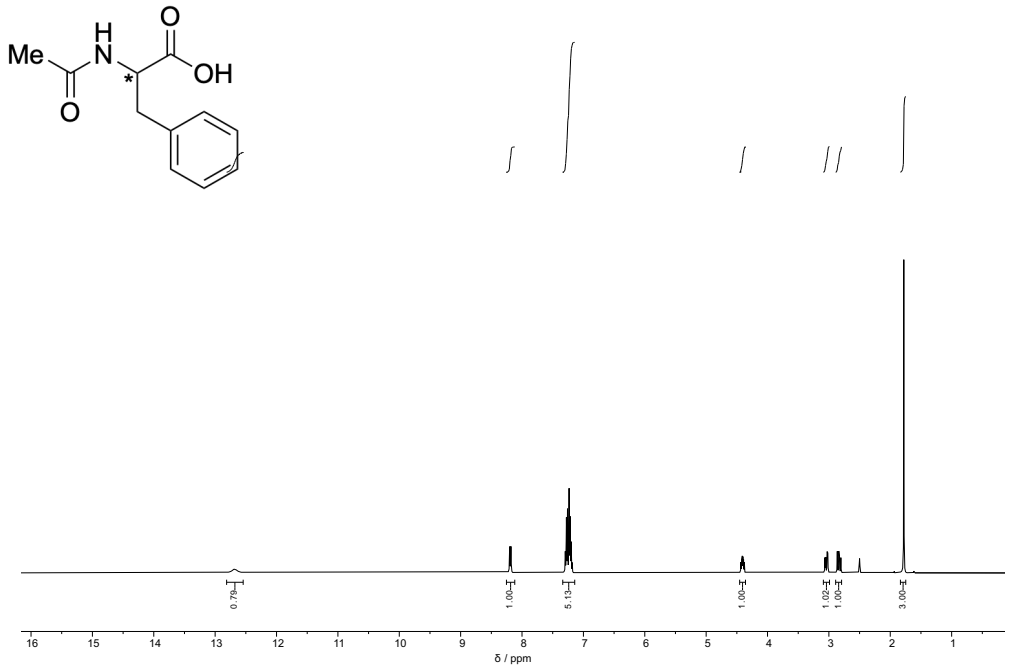


^{13}C-NMR (101 MHz, $CDCl_3$):

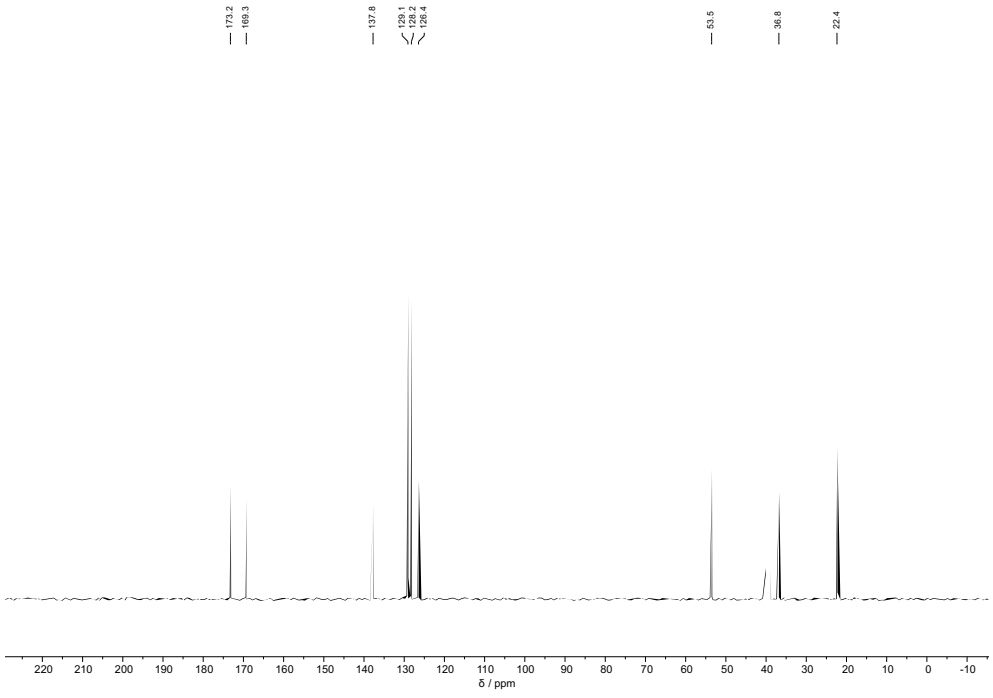


***N*-Acetyl-DL-phenylalanine** (rac-**41a**):

^{1}H-NMR (400 MHz, DMSO-d_6):

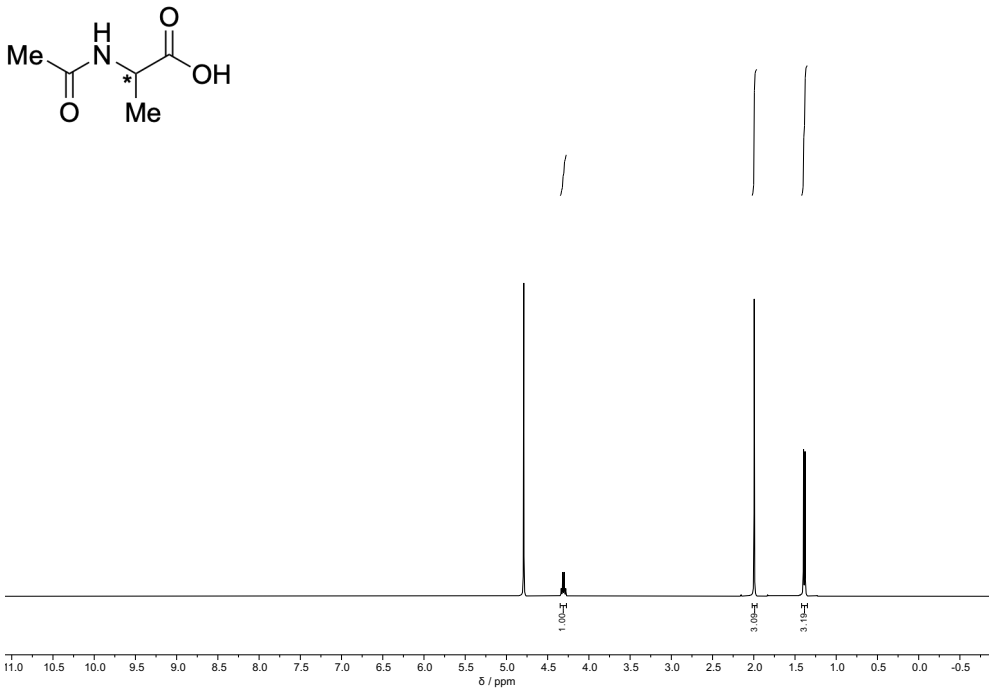


^{13}C-NMR (101 MHz, DMSO-d_6):

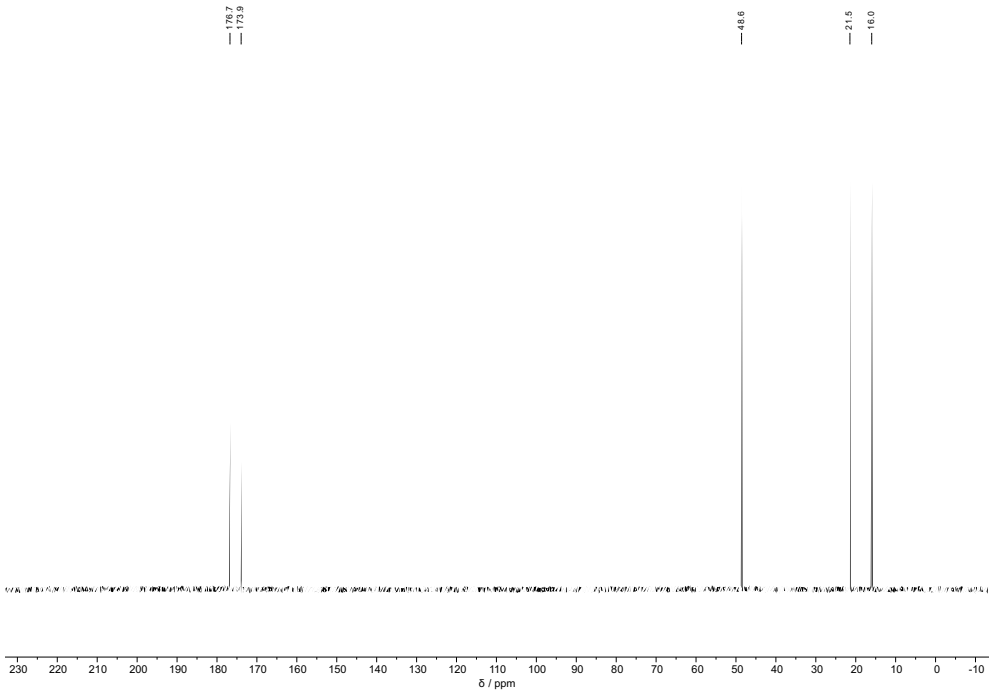


***N*-Acetyl-DL-alanine** (rac-**41b**):

^{1}H-NMR (400 MHz, D_2O):



^{13}C-NMR (101 MHz, D_2O):

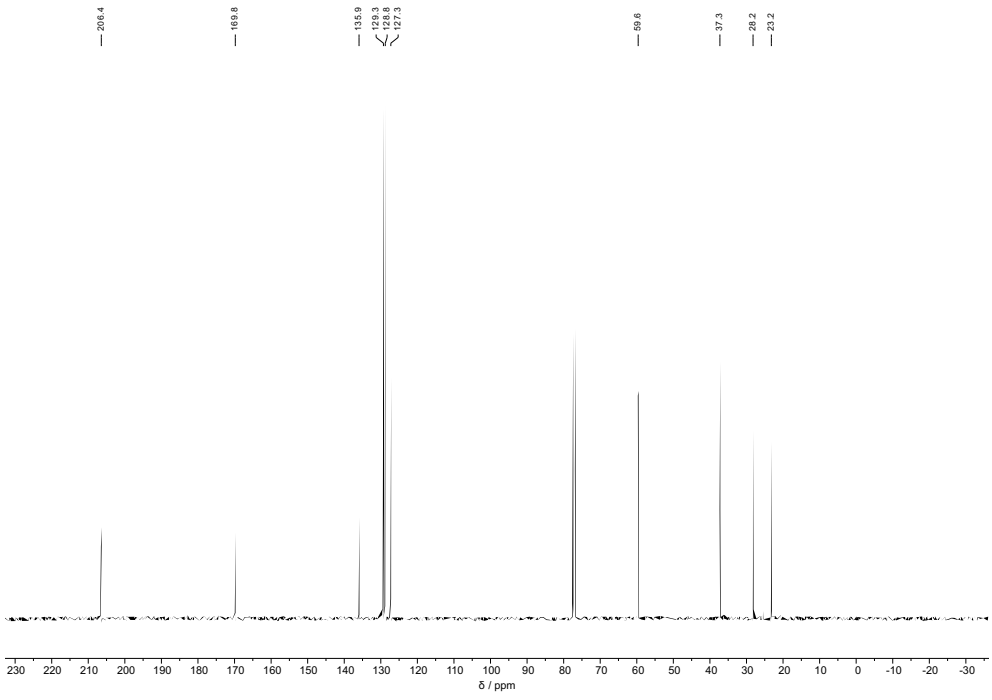


***N*-(3-Oxo-1-phenylbutan-2-yl)acetamide** (rac-**40a**):

^{1}H-NMR (400 MHz, $CDCl_3$):

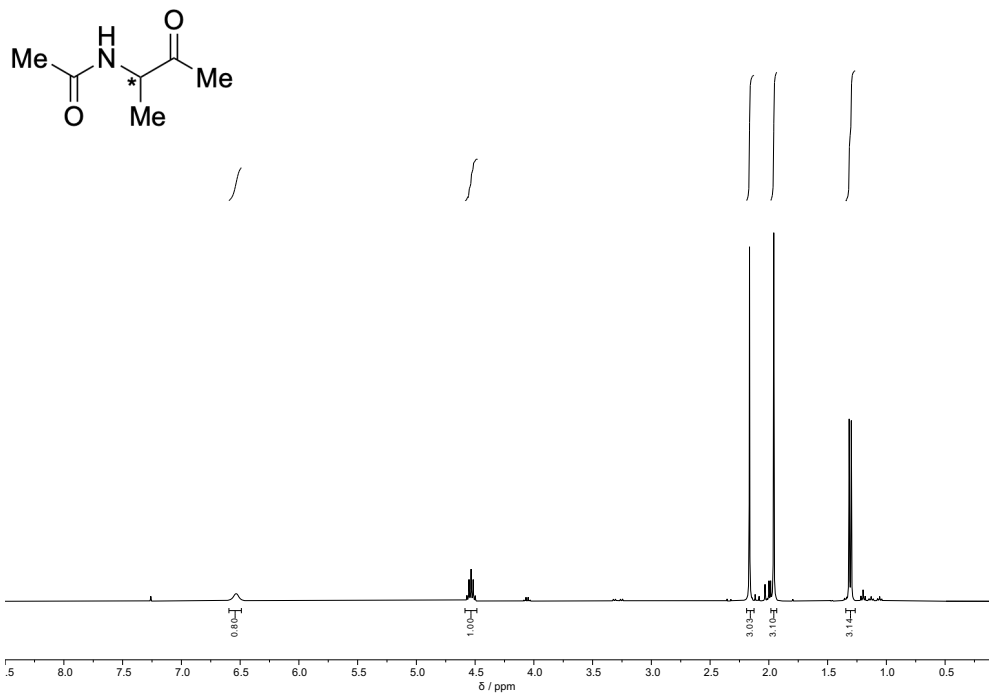


^{13}C-NMR (101 MHz, $CDCl_3$):

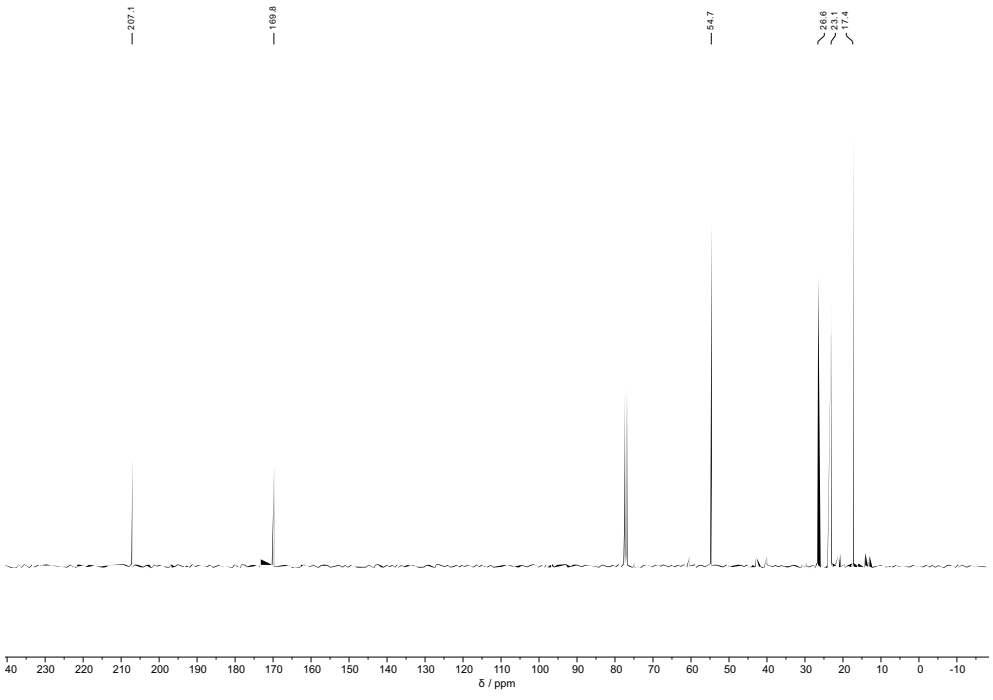


***N*-(3-Oxobutan-2-yl)acetamide** (rac-**40b**):

^{1}H-NMR (400 MHz, $CDCl_3$):

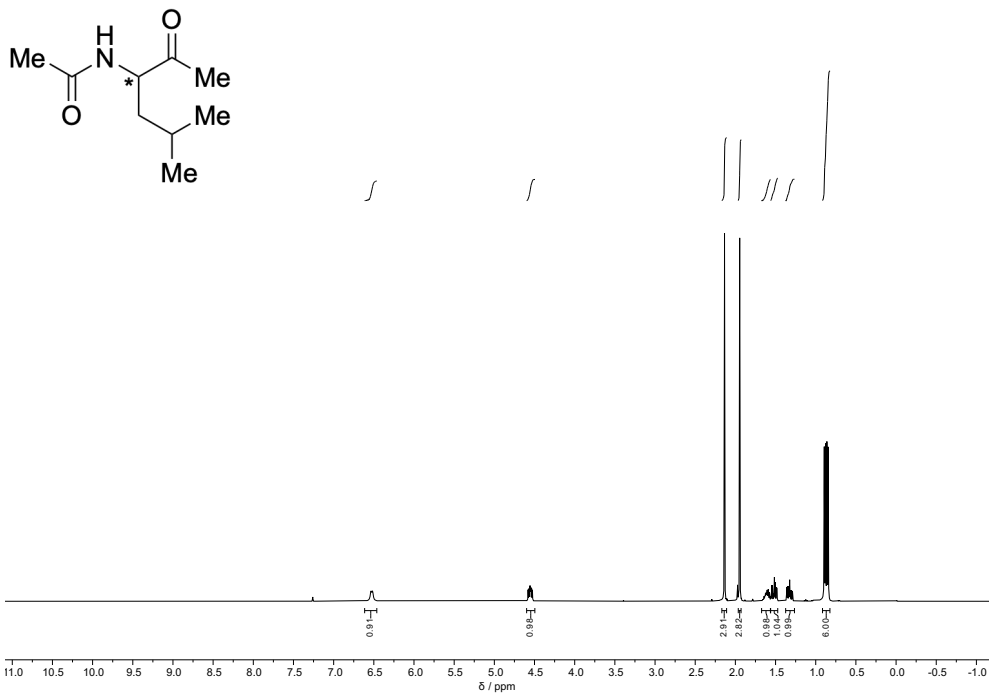


^{13}C-NMR (101 MHz, $CDCl_3$):

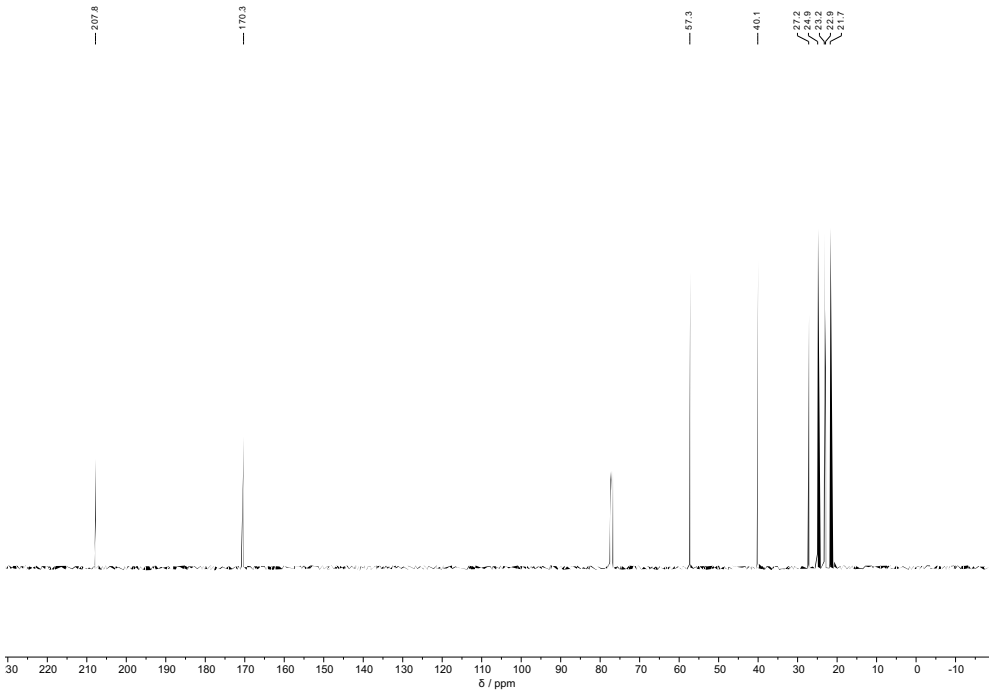


***N*-(5-Methyl-2-oxohexan-3-yl)acetamide** (rac-**40c**):

^{1}H-NMR (400 MHz, $CDCl_3$):

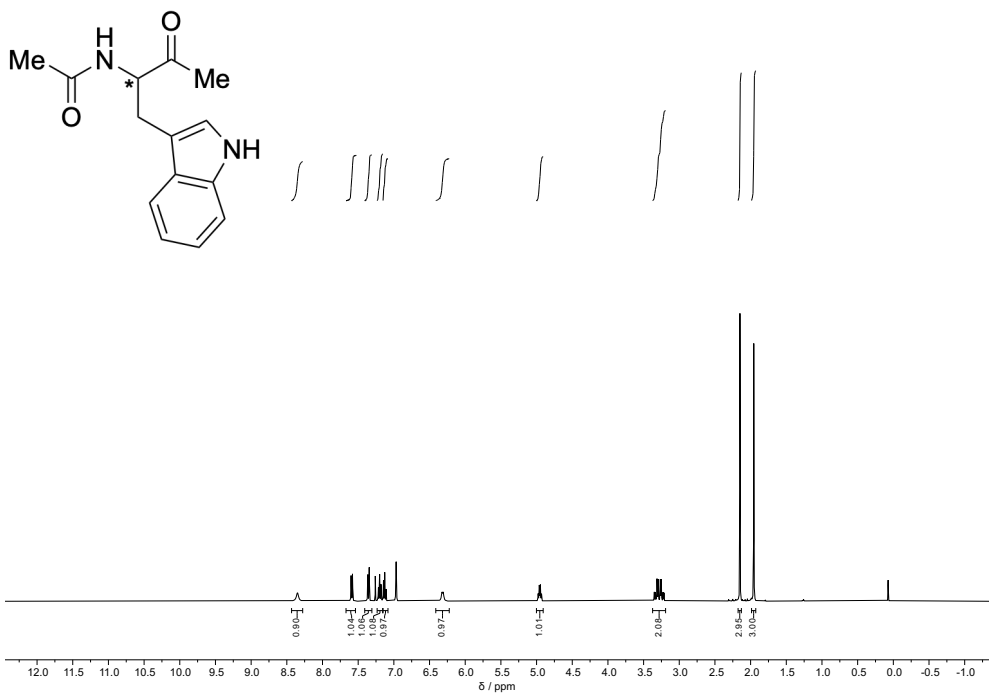


^{13}C-NMR (101 MHz, $CDCl_3$):

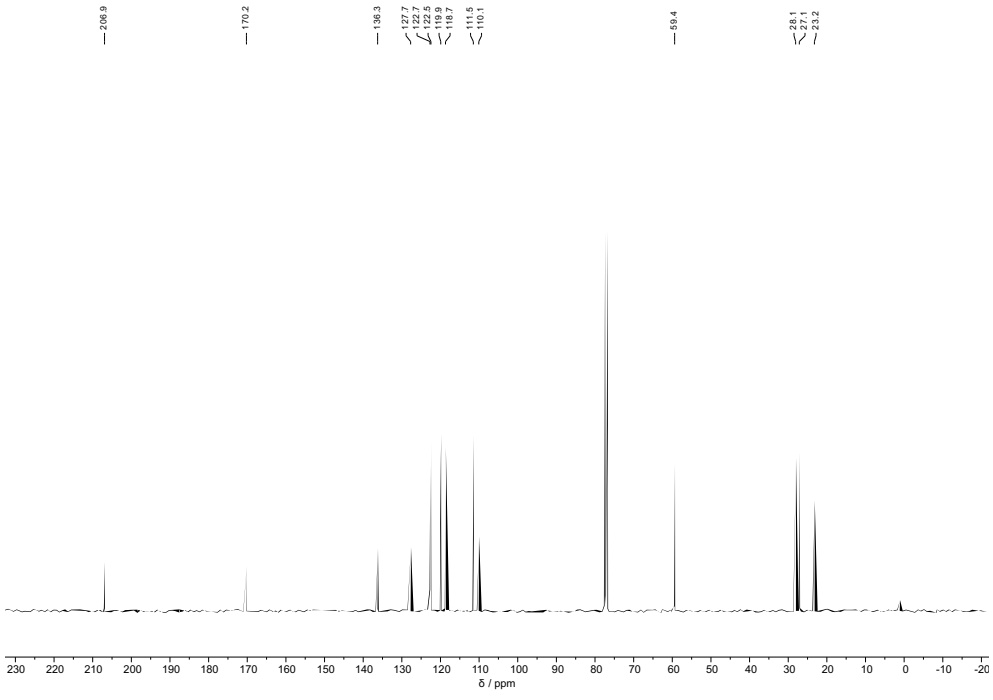


***N*-(1-(1*H*-Indol-3-yl)-3-oxobutan-2-yl)acetamide** (rac-**40d**):

^{1}H-NMR (400 MHz, $CDCl_3$):



^{13}C-NMR (101 MHz, $CDCl_3$):



8 References

[1] W. H. Brooks, W. C. Guida, K. G. Daniel, "The Significance of Chirality in Drug Design and Development" *Curr. Top. Med. Chem.* **2011**, *11*, 760–770.

[2] N. Senkuttuvan, B. Komarasamy, R. Krishnamoorthy, S. Sarkar, S. Dhanasekaran, P. Anaikutti, "The significance of chirality in contemporary drug discovery-a mini review" *RSC Adv.* **2024**, *14*, 33429–33448.

[3] M. M. Coelho, C. Fernandes, F. Remião, M. E. Tiritan, "Enantioselectivity in Drug Pharmacokinetics and Toxicity: Pharmacological Relevance and Analytical Methods" *Molecules* **2021**, *26*, 3113.

[4] B. Kasprzyk-Hordern, "Pharmacologically active compounds in the environment and their chirality" *Chem. Soc. Rev.* **2010**, *39*, 4466–4503.

[5] W. Langenbeck, "Über organische Katalysatoren, I.: Isatin und seine Derivate als Katalysatoren der Dehydrierung von Amino-säuren" *Ber. Deutsch. Chem. Ges.* **1927**, *60 (4)*, 930–934.

[6] P. Vogel, Y. Lam, A. Simon, K. Houk, "Organocatalysis: Fundamentals and Comparisons to Metal and Enzyme Catalysis" *Catalysts* **2016**, *6*, 128.

[7] C. Zhong, X. Shi, "When Organocatalysis Meets Transition-Metal Catalysis" *Eur. J. Org. Chem.* **2010**, *2010*, 2999–3025.

[8] C. A. Busacca, D. R. Fandrick, J. J. Song, C. H. Senanayake, "The Growing Impact of Catalysis in the Pharmaceutical Industry" *Adv. Synth. Catal.* **2011**, *353*, 1825–1864.

[9] M. Ruth, T. Gensch, P. R. Schreiner, "Contrasting Historical and Physical Perspectives in Asymmetric Catalysis: $\Delta\Delta G^{\neq}$ versus Enantiomeric Excess" *Angew. Chem. Int. Ed.* **2024**, *63*, e202410308.

[10] R. Laplaza, J.-G. Sobez, M. D. Wodrich, M. Reiher, C. Corminboeuf, "The (not so) simple prediction of enantioselectivity – a pipeline for high-fidelity computations" *Chem. Sci.* **2022**, *13*, 6858–6864.

[11] R. B. Sunoj, "Transition State Models for Understanding the Origin of Chiral Induction in Asymmetric Catalysis" *Acc. Chem. Res.* **2016**, *49*, 1019–1028.

[12] J. P. Wagner, P. R. Schreiner, "London Dispersion in Molecular Chemistry–Reconsidering Steric Effects" *Angew. Chem. Int. Ed.* **2015**, *54*, 12274–12296.

[13] A. F. Zahrt, J. J. Henle, B. T. Rose, Y. Wang, W. T. Darrow, S. E. Denmark, "Prediction of higher-selectivity catalysts by computer-driven workflow and machine learning" *Science* **2019**, *363*, eaau5631.

[14] S. Gallarati, R. Fabregat, R. Laplaza, S. Bhattacharjee, M. D. Wodrich, C. Corminboeuf, "Reaction-based machine learning representations for predicting the enantioselectivity of organocatalysts" *Chem. Sci.* **2021**, *12*, 6879–6889.

[15] J. P. Reid, M. S. Sigman, "Holistic prediction of enantioselectivity in asymmetric catalysis" *Nature* **2019**, *571*, 343–348.

[16] A. F. Zahrt, S. V. Athavale, S. E. Denmark, "Quantitative Structure–Selectivity Relationships in Enantioselective Catalysis: Past, Present, and Future" *Chem. Rev.* **2020**, *120*, 1620–1689.

[17] E. Casillo, T. Scattolin, S. P. Nolan, "Catalysis meets machine learning: a guide to data-driven discovery and design" *Chem. Commun.* **2025**, *61*, 18247–18272.

[18] B. T. Cho, "Recent advances in the synthetic applications of the oxazaborolidine-mediated asymmetric reduction" *Tetrahedron* **2006**, *62*, 7621–7643.

[19] L. D. Vechia, R. O. M. A. de Souza, L. S. M. Miranda, "The Dakin-West reaction: Past, present and future" *Tetrahedron* **2018**, *74*, 4359–4371.

[20] L. Pasteur, "Sur les relations qui peuvent exister entre la forme cristalline, la composition chimique et le sens de la polarisation rotatoire" *Ann. Chim. Phys.* **1848**, *24*, 442–459.

[21] P. Cintas, "Tracing the Origins and Evolution of Chirality and Handedness in Chemical Language" *Angew. Chem. Int. Ed.* **2007**, *46*, 4016–4024.

[22] L. D. Barron, "Symmetry and molecular chirality" *Chem. Soc. Rev.* **1986**, *15*, 189–223.

[23] V. Prelog, "Chirality in Chemistry" *Science* **1976**, *193*, 17–24.

[24] V. A. Tverdislov, E. V. Malyshko, S. A. Il'chenko, O. A. Zhulyabina, L. V. Yakovenko, "A periodic system of chiral structures in molecular biology" *Biophysics* **2017**, *62*, 331–341.

[25] M. Tang, X. Yang, "Catalytic Enantioselective Synthesis of Inherently Chiral Molecules: Recent Advances" *Eur. J. Org. Chem.* **2023**, *26*, e202300738.

[26] P. Peluso, B. Chankvetadze, "Recognition in the Domain of Molecular Chirality: From Noncovalent Interactions to Separation of Enantiomers" *Chem. Rev.* **2022**, *122*, 13235–13400.

[27] Y. Chen, S. Yekta, A. K. Yudin, "Modified BINOL Ligands in Asymmetric Catalysis" *Chem. Rev.* **2003**, *103*, 3155–3212.

[28] R. Noyori, H. Takaya, “BINAP: an efficient chiral element for asymmetric catalysis” *Acc. Chem. Res.* **1990**, *23*, 345–350.

[29] L. D. Barron, “Chirality and Life” *Space Sci. Rev.* **2008**, *135*, 187–201.

[30] H. Yang, H.-X. Feng, L. Zhou, “Asymmetric Synthesis of Helicenes from Centrally Chiral Precursors” *Eur. J. Org. Chem.* **2024**, *27*, e202400671.

[31] J.-Y. Wang, J. Sun, “Design, Synthesis and Application of Chiral Spirocyclic Bisindoles” *Angew. Chem. Int. Ed.* **2025**, *64*, e202424773.

[32] K. Tomooka, S. Miyasaka, S. Motomura, K. Igawa, “Planar Chiral Dialkoxysilane: Introduction of Inherent Chirality and High Reactivity in Conventional Achiral Alkene” *Chem. Eur. J.* **2014**, *20*, 7598–7602.

[33] G. P. Moss, “Basic terminology of stereochemistry” *Pure Appl. Chem.* **1996**, *68*, 2193–2222.

[34] E. Fogassy, M. Nógrádi, D. Kozma, G. Egri, E. Pálovics, V. Kiss, “Optical resolution methods” *Org. Biomol. Chem.* **2006**, *4*, 3011–3030.

[35] F. W. Lichtenthaler, “Emil Fischer’s Proof of the Configuration of Sugars: A Centennial Tribute” *Angew. Chem. Int. Ed. Engl.* **1992**, *31*, 1541–1556.

[36] E. Fischer, “Ueber die Configuration des Traubenzuckers und seiner Isomere. II.” *Eur. J. Inorg. Chem.* **1891**, *24*, 1836–1845.

[37] R. S. Cahn, C. Ingold, V. Prelog, “Specification of Molecular Chirality” *Angew. Chem. Int. Ed. Engl.* **1966**, *5*, 385–415.

[38] J. Rice, K. Proctor, L. Lopardo, S. Evans, B. Kasprzyk-Hordern, “Stereochemistry of ephedrine and its environmental significance: Exposure and effects directed approach” *J. Hazard. Mater.* **2018**, *348*, 39–46.

[39] A. R. Ribeiro, P. M. L. Castro, M. E. Tiritan, “Chiral pharmaceuticals in the environment” *Environ. Chem. Lett.* **2012**, *10*, 239–253.

[40] S. E. Bahekar, A. A. Aher, S. U. Razvi, M. S. Baig, “The Role of Chirality in Drug Design and Delivery: A Comprehensive Review” *Acta Pharma Rep.* **2024**, *3*, 07–10.

[41] S. Mason, “Biomolecular homochirality” *Chem. Soc. Rev.* **1988**, *17*, 347.

[42] E. Fischer, “Einfluss der Configuration auf die Wirkung der Enzyme” *Ber. Deutsch. Chem. Ges.* **1894**, *27*, 2985–2993.

[43] L. H. Easson, E. Stedman, “Studies on the relationship between chemical constitution and physiological action: Molecular dissymmetry and physiological activity” *Biochem. J.* **1933**, *27*, 1257–1266.

[44] D. D. Boehr, R. Nussinov, P. E. Wright, “The role of dynamic conformational ensembles in biomolecular recognition” *Nat. Chem. Biol.* **2009**, *5*, 789–796.

[45] E. Persch, O. Dumele, F. Diederich, “Molecular Recognition in Chemical and Biological Systems” *Angew. Chem. Int. Ed.* **2015**, *54*, 3290–3327.

[46] G. Diggle, “Thalidomide: 40 years on” *Int. J. Clin. Pract.* **2001**, *55*, 627–631.

[47] T. Eriksson, S. Björkman, P. Höglund, “Clinical pharmacology of thalidomide” *Eur. J. Clin. Pharmacol.* **2001**, *57*, 365–376.

[48] R. A. Hauser, “Levodopa: Past, Present, and Future” *Eur. Neurol.* **2009**, *62*, 1–8.

[49] K. D. Rainsford, “Ibuprofen: pharmacology, efficacy and safety” *Inflammopharmacology* **2009**, *17*, 275–342.

[50] L. Kvittingen, B. J. Sjursnes, R. Schmid, “Limonene in Citrus: A String of Unchecked Literature Citings?” *J. Chem. Educ.* **2021**, *98*, 3600–3607.

[51] R. Eccles, “Menthol and Related Cooling Compounds” *J. Pharm. Pharmacol.* **1994**, *46*, 618–630.

[52] W. D. Nes, “Biosynthesis of Cholesterol and Other Sterols” *Chem. Rev.* **2011**, *111*, 6423–6451.

[53] M. Gates, G. Tschudi, “The Synthesis of Morphine” *J. Am. Chem. Soc.* **1956**, *78*, 1380–1393.

[54] J. A. Le Bel, “Sur les relations qui existent entre les formules atomiques des corps organiques et le pouvoir rotatoire de leurs dissolutions” *Bull. Société Chim. Paris* **1874**, *22*, 337–347.

[55] J. H. van ’t Hoff, “Sur les formules de structure dans l’espace” *Bull. Société Chim. Paris* **1875**, *23*, 295–301.

[56] H. Lu, “Stereoselectivity in drug metabolism” *Expert Opin. Drug Metab. Toxicol.* **2007**, *3*, 149–158.

[57] S. Ross, “Functional foods: the Food and Drug Administration perspective” *Am. J. Clin. Nutr.* **2000**, *71*, 1735S-1738S.

[58] A. Selka, A. Abidli, L. Schiavo, L. Jeanmart, G. Hanquet, W. D. Lubell, “Recent Advances in Sustainable Total Synthesis and Chiral Pool Strategies with Emphasis on (−)-Sclareol in Natural Products Synthesis” *Eur. J. Org. Chem.* **2025**, *28*, e202400983.

[59] D. Seebach, “Organic Synthesis–Where now?” *Angew. Chem. Int. Ed. Engl.* **1990**, *29*, 1320–1367.

[60] Y. Gnas, F. Glorius, “Chiral Auxiliaries - Principles and Recent Applications” *Synthesis* **2006**, *2006*, 1899–1930.

[61] E. J. Corey, H. E. Ensley, “Preparation of an optically active prostaglandin intermediate via asymmetric induction” *J. Am. Chem. Soc.* **2002**, *97*, 6908–6909.

[62] D. A. Evans, J. Bartroli, T. L. Shih, “Enantioselective aldol condensations. 2. Erythro-selective chiral aldol condensations *via* boron enolates” *J. Am. Chem. Soc.* **1981**, *103*, 2127–2129.

[63] R. Noyori, “Asymmetric Catalysis: Science and Opportunities (Nobel Lecture)” *Angew. Chem. Int. Ed.* **2002**, *41*, 2008–2022.

[64] U. T. Bornscheuer, G. W. Huisman, R. J. Kazlauskas, S. Lutz, J. C. Moore, K. Robins, “Engineering the third wave of biocatalysis” *Nature* **2012**, *485*, 185–194.

[65] D. W. C. MacMillan, “The advent and development of organocatalysis” *Nature* **2008**, *455*, 304–308.

[66] M. Silvi, P. Melchiorre, “Enhancing the potential of enantioselective organocatalysis with light” *Nature* **2018**, *554*, 41–49.

[67] M. S. Sigman, E. N. Jacobsen, “Schiff Base Catalysts for the Asymmetric Strecker Reaction Identified and Optimized from Parallel Synthetic Libraries” *J. Am. Chem. Soc.* **1998**, *120*, 4901–4902.

[68] A. Wittkopp, P. R. Schreiner, “Metal-Free, Noncovalent Catalysis of Diels–Alder Reactions by *Neutral* Hydrogen Bond Donors in Organic Solvents and in Water” *Chem. – Eur. J.* **2003**, *9*, 407–414.

[69] T. Akiyama, J. Itoh, K. Yokota, K. Fuchibe, “Enantioselective Mannich-Type Reaction Catalyzed by a Chiral Brønsted Acid” *Angew. Chem. Int. Ed.* **2004**, *43*, 1566–1568.

[70] A. Wittkopp, P. R. Schreiner, “Catalysis of Diels−Alder Reactions in Water and in Hydrogen-Bonding Environments” in *The Chemistry of Dienes Polyenes,* Rappoport, Z., Ed. John Wiley & Sons, Ltd: **2000**, Vol. 2, pp. 1029–1088.

[71] The Nobel Prize Foundation, “Press release: The Nobel Prize in Chemistry 2021,” https://www.nobelprize.org/uploads/2021/10/press-chemistryprize2021.pdf (accessed Aug 12, 2026)

[72] K. A. Ahrendt, C. J. Borths, D. W. C. MacMillan, “New Strategies for Organic Catalysis: The First Highly Enantioselective Organocatalytic Diels−Alder Reaction” *J. Am. Chem. Soc.* **2000**, *122*, 4243–4244.

[73] B. List, R. A. Lerner, C. F. Barbas, “Proline-Catalyzed Direct Asymmetric Aldol Reactions” *J. Am. Chem. Soc.* **2000**, *122*, 2395–2396.

[74] H. Miyamoto, C. Sakumoto, E. Takekoshi, Y. Maeda, N. Hiramoto, T. Itoh, Y. Kato, “Effective Method to Remove Metal Elements from Pharmaceutical Intermediates with Polychelated Resin Scavenger” *Org. Process Res. Dev.* **2015**, *19*, 1054–1061.

[75] V. Oliveira, M. Cardoso, L. Forezi, “Organocatalysis: A Brief Overview on Its Evolution and Applications” *Catalysts* **2018**, *8*, 605.

[76] D. Brenna, R. Porta, E. Massolo, L. Raimondi, M. Benaglia, “A New Class of Low-Loading Catalysts for Highly Enantioselective, Metal-Free Imine Reduction of Wide General Applicability” *ChemCatChem* **2017**, *9*, 941–945.

[77] P. I. Dalko, L. Moisan, “In the Golden Age of Organocatalysis” *Angew. Chem. Int. Ed.* **2004**, *43*, 5138–5175.

[78] S. Mukherjee, J. W. Yang, S. Hoffmann, B. List, “Asymmetric Enamine Catalysis” *Chem. Rev.* **2007**, *107*, 5471–5569.

[79] C. R. Shugrue, S. J. Miller, “Applications of Nonenzymatic Catalysts to the Alteration of Natural Products” *Chem. Rev.* **2017**, *117*, 11894–11951.

[80] H. Eyring, “The Activated Complex in Chemical Reactions” *J. Chem. Phys.* **1935**, *3*, 107–115.

[81] M. G. Evans, M. Polanyi, “Some applications of the transition state method to the calculation of reaction velocities, especially in solution” *Trans. Faraday Soc.* **1935**, *31*, 875–894.

[82] Q. Peng, F. Duarte, R. S. Paton, “Computing organic stereoselectivity – from concepts to quantitative calculations and predictions” *Chem. Soc. Rev.* **2016**, *45*, 6093–6107.

[83] H. Buschmann, H.-D. Scharf, N. Hoffmann, P. Esser, “The Isoinversion Principle–a General Model of Chemical Selectivity” *Angew. Chem. Int. Ed. Engl.* **1991**, *30*, 477–515.

[84] T. Okino, Y. Hoashi, Y. Takemoto, “Enantioselective Michael Reaction of Malonates to Nitroolefins Catalyzed by Bifunctional Organocatalysts” *J. Am. Chem. Soc.* **2003**, *125*, 12672–12673.

[85] E. J. Corey, C. J. Helal, “Reduction of Carbonyl Compounds with Chiral Oxazaborolidine Catalysts: A New Paradigm for Enantioselective Catalysis and a Powerful New Synthetic Method” *Angew. Chem. Int. Ed.* **1998**, *37*, 1986–2012.

[86] H. D. Dakin, R. West, “A General Reaction of Amino Acids” *J. Biol. Chem.* **1928**, *78*, 91–104.

[87] C. Eschmann, L. Song, P. R. Schreiner, “London Dispersion Interactions Rather than Steric Hindrance Determine the Enantioselectivity of the Corey–Bakshi–Shibata Reduction” *Angew. Chem. Int. Ed.* **2021**, *60*, 4823–4832.

[88] H. Liu, K. D. Shimizu, “Contributions of London Dispersion Forces to Solution-Phase Association Processes” *Acc. Chem. Res.* **2023**, *56*, 3572–3580.

[89] M. S. Sigman, K. C. Harper, E. N. Bess, A. Milo, “The Development of Multidimensional Analysis Tools for Asymmetric Catalysis and Beyond” *Acc. Chem. Res.* **2016**, *49*, 1292–1301.

[90] E. J. Corey, R. K. Bakshi, S. Shibata, “Highly enantioselective borane reduction of ketones catalyzed by chiral oxazaborolidines. Mechanism and synthetic implications” *J. Am. Chem. Soc.* **1987**, *109*, 5551–5553.

[91] E. J. Corey, R. K. Bakshi, S. Shibata, C. P. Chen, V. K. Singh, “A stable and easily prepared catalyst for the enantioselective reduction of ketones. Applications to multistep syntheses” *J. Am. Chem. Soc.* **1987**, *109*, 7925–7926.

[92] E. J. Corey, S. Shibata, R. K. Bakshi, “An efficient and catalytically enantioselective route to (*S*)-(–)-phenyloxirane” *J. Org. Chem.* **1988**, *53*, 2861–2863.

[93] E. J. Corey, “New enantioselective routes to biologically interesting compounds” *Pure Appl. Chem.* **1990**, *62*, 1209–1216.

[94] E. J. Corey, “Catalytic Enantioselective Diels–Alder Reactions: Methods, Mechanistic Fundamentals, Pathways, and Applications” *Angew. Chem. Int. Ed.* **2002**, *41*, 1650–1667.

[95] A. R. Nödling, R. Möckel, R. Tonner, G. Hilt, “Lewis Acids as Activators in CBS-Catalysed Diels–Alder Reactions: Distortion Induced Lewis Acidity Enhancement of $SnCl_4$” *Chem. Eur. J.* **2016**, *22*, 13171–13180.

[96] E. Canales, E. J. Corey, “Highly Enantioselective [2+2]-Cycloaddition Reactions Catalyzed by a Chiral Aluminum Bromide Complex” *J. Am. Chem. Soc.* **2007**, *129*, 12686–12687.

[97] J. C. Fiaud, H. B. Kagan, "Réduction de l'acé tophénone par des amines-boranes optiquement actifs" *Bull. Société Chim. Fr.* **1969**, 2742–2743.

[98] A. Hirao, S. Itsuno, S. Nakahama, N. Yamazaki, "Asymmetric reduction of aromatic ketones with chiral alkoxy-amineborane complexes" *J. Chem. Soc. Chem. Commun.* **1981**, 315.

[99] S. Itsuno, K. Ito, A. Hirao, S. Nakahama, "Asymmetric reduction of aliphatic ketones with the reagent prepared from (*S*)-(–)-2-amino-3-methyl-1,1-diphenylbutan-1-ol and borane" *J. Org. Chem.* **1984**, *49*, 555–557.

[100] E. J. Corey, T. Shibata, T. W. Lee, "Asymmetric Diels−Alder Reactions Catalyzed by a Triflic Acid Activated Chiral Oxazaborolidine" *J. Am. Chem. Soc.* **2002**, *124*, 3808–3809.

[101] B. T. Cho, Y. S. Chun, "Asymmetric reduction of *N*-substituted ketimines with the reagent prepared from borane and (*S*)-(–)-2-amino-3-methyl-1,1-diphenylbutan-1-ol (itsuno's reagent): enantioselective synthesis of optically active secondary amines" *J. Chem. Soc. Perkin 1* **1990**, 3200–3201.

[102] B. T. Cho, Y. S. Chun, "Enantioselective synthesis of optically active secondary amines via asymmetric reduction" *Tetrahedron Asymmetry* **1992**, *3*, 1583–1590.

[103] T. Sakai, F. Yan, S. Kashinol, K. Uneyama, "Asymmetric Reduction of 2-(*N*-Arylimino)-3,3,3-trifluoropropanoic Acid Esters Leading to Enantiomerically Enriched 3,3,3-Trifluoroalanine" *Tetrahedron* **1996**, *52*, 233–244.

[104] E. H. M. Kirton, G. Tughan, R. E. Morris, R. A. Field, "Rationalising the effect of reducing agent on the oxazaborolidine-mediated asymmetric reduction of *N*-substituted imines" *Tetrahedron Lett.* **2004**, *45*, 853–855.

[105] M. P. Krzemiński, M. Zaidlewicz, "Asymmetric reduction of ketoxime derivatives and *N*-alkylketimines with borane–oxazaborolidine adducts" *Tetrahedron Asymmetry* **2003**, *14*, 1463–1466.

[106] D. Enders, M. Seppelt, "Catalytic Enantioselective Synthesis of 3-Substituted Benzosultams via Corey-Bakshi-Shibata Reduction of Cyclic *N*-Sulfonylimines" *Synlett* **2011**, *2011*, 402–404.

[107] Z. Lachtar, A. Khorief Nacereddine, A. Djerourou, "Understanding the origin of the enantioselectivity and the mechanism of the asymmetric reduction of ketimine generated from acetophenone with oxazaborolidine catalyst" *Struct. Chem.* **2020**, *31*, 253–261.

[108] A. L. Allred, “Electronegativity values from thermochemical data” *J. Inorg. Nucl. Chem.* **1961**, *17*, 215–221.

[109] S. Kobayashi, H. Ishitani, “Catalytic Enantioselective Addition to Imines” *Chem. Rev.* **1999**, *99*, 1069–1094.

[110] T. C. Nugent, M. El-Shazly, “Chiral Amine Synthesis – Recent Developments and Trends for Enamide Reduction, Reductive Amination, and Imine Reduction” *Adv. Synth. Catal.* **2010**, *352*, 753–819.

[111] G. L. Buchanan, “The Dakin–West reaction” *Chem. Soc. Rev.* **1988**, *17*, 91–109.

[112] R. B. Woodward, M. P. Cava, W. D. Ollis, A. Hunger, H. U. Daeniker, K. Schenker, “The Total Synthesis of Strychnine” *J. Am. Chem. Soc.* **1954**, *76*, 4749–4751.

[113] R. C. Wende, A. Seitz, D. Niedek, S. M. M. Schuler, C. Hofmann, J. Becker, P. R. Schreiner, “The Enantioselective Dakin–West Reaction” *Angew. Chem. Int. Ed.* **2016**, *55*, 2719–2723.

[114] L. Dalla-Vechia, V. G. Santos, M. N. Godoi, D. Cantillo, C. O. Kappe, M. N. Eberlin, R. O. M. A. de Souza, L. S. M. Miranda, “On the mechanism of the Dakin–West reaction” *Org. Biomol. Chem.* **2012**, *10*, 9013–9020.

[115] W. Steglich, G. Höfle, “*N,N* -Dimethyl-4-pyridinamine, a Very Effective Acylation Catalyst” *Angew. Chem. Int. Ed. Engl.* **1969**, *8*, 981–981.

[116] E. R. Jarvo, S. J. Miller, “Amino acids and peptides as asymmetric organocatalysts” *Tetrahedron* **2002**, *58*, 2481–2495.

[117] R. R. Knowles, E. N. Jacobsen, “Attractive noncovalent interactions in asymmetric catalysis: Links between enzymes and small molecule catalysts” *Proc. Natl. Acad. Sci. U. S. A.* **2010**, *107*, 20678–20685.

[118] O. A. von Lilienfeld, “Quantum Machine Learning in Chemical Compound Space” *Angew. Chem. Int. Ed.* **2018**, *57*, 4164–4169.

[119] K. T. Butler, D. W. Davies, H. Cartwright, O. Isayev, A. Walsh, “Machine learning for molecular and materials science” *Nature* **2018**, *559*, 547–555.

[120] M. Soori, B. Arezoo, R. Dastres, “Artificial intelligence, machine learning and deep learning in advanced robotics, a review” *Cogn. Robot.* **2023**, *3*, 54–70.

[121] L. David, A. Thakkar, R. Mercado, O. Engkvist, “Molecular representations in AI-driven drug discovery: a review and practical guide” *J. Cheminformatics* **2020**, *12*, 56.

[122] Y.-C. Lo, S. E. Rensi, W. Torng, R. B. Altman, “Machine learning in chemoinformatics and drug discovery” *Drug Discov. Today* **2018**, *23*, 1538–1546.

[123] D. Weininger, “SMILES, a chemical language and information system. 1. Introduction to methodology and encoding rules” *J. Chem. Inf. Comput. Sci.* **1988**, *28*, 31–36.

[124] H. L. Morgan, “The Generation of a Unique Machine Description for Chemical Structures-A Technique Developed at Chemical Abstracts Service.” *J. Chem. Doc.* **1965**, *5*, 107–113.

[125] D. Rogers, M. Hahn, “Extended-Connectivity Fingerprints” *J. Chem. Inf. Model.* **2010**, *50*, 742–754.

[126] M. Orsi, J.-L. Reymond, “One chiral fingerprint to find them all” *J. Cheminformatics* **2024**, *16*, 53.

[127] J. Gilmer, S. S. Schoenholz, P. F. Riley, O. Vinyals, G. E. Dahl “Neural Message Passing for Quantum Chemistry” in *Proc. 34th Int. Conf. Mach. Learn.*, **2017**, pp. 1263–1272.

[128] P. O. Dral, “Quantum Chemistry in the Age of Machine Learning” *J. Phys. Chem. Lett.* **2020**, *11*, 2336–2347.

[129] F. Strieth-Kalthoff, F. Sandfort, M. H. S. Segler, F. Glorius, “Machine learning the ropes: principles, applications and directions in synthetic chemistry” *Chem. Soc. Rev.* **2020**, *49*, 6154–6168.

[130] I. H. Sarker, “Machine Learning: Algorithms, Real-World Applications and Research Directions” *Sn Comput. Sci.* **2021**, *2*, 160.

[131] J. H. Tanis, C. Giannella, A. V. Mariano, “Introduction to Graph Neural Networks: A Starting Point for Machine Learning Engineers” *ACM Comput. Surv.* **2024**, *58*, 1–37.

[132] S. Salman, X. Liu, “Overfitting Mechanism and Avoidance in Deep Neural Networks” arXiv **2019**, arXiv.1901.06566.

[133] A. Tropsha, “Best Practices for QSAR Model Development, Validation, and Exploitation” *Mol. Inform.* **2010**, *29*, 476–488.

[134] E. N. Muratov, J. Bajorath, R. P. Sheridan, I. V. Tetko, D. Filimonov, V. Poroikov, T. I. Oprea, I. I. Baskin, A. Varnek, A. Roitberg, O. Isayev, S. Curtalolo, D. Fourches, Y. Cohen, A. Aspuru-Guzik, D. A. Winkler, D. Agrafiotis, A. Cherkasov, A. Tropsha, “QSAR without borders” *Chem. Soc. Rev.* **2020**, *49*, 3525–3564.

[135] D. T. Ahneman, J. G. Estrada, S. Lin, S. D. Dreher, A. G. Doyle, “Predicting reaction performance in C-N cross-coupling using machine learning” *Science* **2018**, *360*, 186–190.

[136] P. Raccuglia, K. C. Elbert, P. D. F. Adler, C. Falk, M. B. Wenny, A. Mollo, M. Zeller, S. A. Friedler, J. Schrier, A. J. Norquist, "Machine-learning-assisted materials discovery using failed experiments" *Nature* **2016**, *533*, 73–76.

[137] J. Schummer, "Scientometric studies on chemistry I: The exponential growth of chemical substances, 1800–1995" *Scientometrics* **1997**, *39*, 107–123.

[138] E. J. Llanos, W. Leal, D. H. Luu, J. Jost, P. F. Stadler, G. Restrepo, "Exploration of the chemical space and its three historical regimes" *Proc. Natl. Acad. Sci.* **2019**, *116*, 12660–12665.

[139] S. E. Wheeler, T. J. Seguin, Y. Guan, A. C. Doney, "Noncovalent Interactions in Organocatalysis and the Prospect of Computational Catalyst Design" *Acc. Chem. Res.* **2016**, *49*, 1061–1069.

[140] B. C. Haas, D. Kalyani, M. S. Sigman, "Applying statistical modeling strategies to sparse datasets in synthetic chemistry" *Sci. Adv.* **2025**, *11*, eadt3013.

[141] B. Dou, Z. Zhu, E. Merkurjev, L. Ke, L. Chen, J. Jiang, Y. Zhu, J. Liu, B. Zhang, G.-W. Wei, "Machine Learning Methods for Small Data Challenges in Molecular Science" *Chem. Rev.* **2023**, *123*, 8736–8780.

[142] J. Deng, W. Dong, R. Socher, L.-J. Li, K. Li, L. Fei-Fei, "ImageNet: A Large-Scale Hierarchical Image Database" in *CVPR*, **2009**.

[143] T. B. Brown, B. Mann, N. Ryder, M. Subbiah, J. Kaplan, P. Dhariwal, A. Neelakantan, P. Shyam, G. Sastry, A. Askell, S. Agarwal, A. Herbert-Voss, G. Krueger, T. Henighan, R. Child, A. Ramesh, D. M. Ziegler, J. Wu, C. Winter, C. Hesse, M. Chen, E. Sigler, M. Litwin, S. Gray, B. Chess, J. Clark, C. Berner, S. McCandlish, A. Radford, I. Sutskever, D. Amodei "Language Models are Few-Shot Learners" in *Adv. Neural Inf. Process. Syst.*, **2020**, 1877–1901.

[144] S. M. Kearnes, M. R. Maser, M. Wleklinski, A. Kast, A. G. Doyle, S. D. Dreher, J. M. Hawkins, K. F. Jensen, C. W. Coley, "The Open Reaction Database" *J. Am. Chem. Soc.* **2021**, *143*, 18820–18826.

[145] C. W. Coley, W. H. Green, K. F. Jensen, "Machine Learning in Computer-Aided Synthesis Planning" *Acc. Chem. Res.* **2018**, *51*, 1281–1289.

[146] S. J. Miller, "In Search of Peptide-Based Catalysts for Asymmetric Organic Synthesis" *Acc. Chem. Res.* **2004**, *37*, 601–610.

[147] S. Poplata, T. Bach, “Enantioselective Intermolecular [2+2] Photocycloaddition Reaction of Cyclic Enones and Its Application in a Synthesis of (−)-Grandisol” *J. Am. Chem. Soc.* **2018**, *140*, 3228–3231.

[148] D. J. Mathre, T. K. Jones, L. C. Xavier, T. J. Blacklock, R. A. Reamer, J. J. Mohan, E. T. T. Jones, K. Hoogsteen, M. W. Baum, E. J. J. Grabowski, “A Practical Enantioselective Synthesis of α,α.-Diaryl-2-pyrrolidinemethanol. Preparation and chemistry of the corresponding oxazaborolidines” *J. Org. Chem.* **1991**, *56*, 751–762.

[149] A. Lattanzi, A. Russo, “Diaryl-2-pyrrolidinemethanols catalyzed enantioselective epoxidation of α,β-enones: new insight into the effect of structural modification of the catalyst on reaction efficiency” *Tetrahedron* **2006**, *62*, 12264–12269.

[150] Y. Liu, C. Ma, K. Jiang, T.-Y. Liu, Y.-C. Chen, “Asymmetric Tandem Michael Addition−Wittig Reaction to Cyclohexenone Annulation” *Org. Lett.* **2009**, *11*, 2848–2851.

[151] D. Enders, P. Fey, H. Kipphardt, “Efficient Preparation of the Chiral Auxiliaries SAMP and RAMP. *N*-Amination via Hofmann Degradation” *Org. Prep. Proced. Int.* **1985**, *17*, 1–9.

[152] Y. Yamamoto, E. Shimizu, K. Ban, Y. Wada, T. Mizusaki, M. Yoshimura, Y. Takagi, Y. Sawama, H. Sajiki, “Facile Hydrogenative Deprotection of *N* -Benzyl Groups Using a Mixed Catalyst of Palladium and Niobic Acid-on-Carbon” *ACS Omega* **2020**, *5*, 2699–2709.

[153] C. Zheng, Y. Li, Y. Yang, H. Wang, H. Cui, J. Zhang, G. Zhao, “Highly Efficient Asymmetric Epoxidation of Electron-Deficient α,β-Enones and Related Applications to Organic Synthesis” *Adv. Synth. Catal.* **2009**, *351*, 1685–1691.

[154] D. J. Mathre, A. S. Thompson, A. W. Douglas, K. Hoogsteen, J. D. Carroll, E. G. Corley, E. J. J. Grabowski, “A Practical Process for the Preparation of Tetrahydro-1-methyl-3,3-diphenyl-1*H*,3*H*-pyrrolo[1,2-c][1,3,2]oxazaborole-Borane. A Highly Enantioselective Stoichiometric and Catalytic Reducing Agent” *J. Org. Chem.* **1993**, *58*, 2880–2888.

[155] L. Deloux, M. Srebnik, “Asymmetric boron-catalyzed reactions” *Chem. Rev.* **1993**, *93*, 763–784.

[156] C. W. Coley, W. Jin, L. Rogers, T. F. Jamison, T. S. Jaakkola, W. H. Green, R. Barzilay, K. F. Jensen, “A graph-convolutional neural network model for the prediction of chemical reactivity” *Chem. Sci.* **2019**, *10*, 370–377.

[157] D. Zankov, T. Madzhidov, P. Polishchuk, P. Sidorov, A. Varnek, "Multi-Instance Learning Approach to the Modeling of Enantioselectivity of Conformationally Flexible Organic Catalysts" *J. Chem. Inf. Model.* **2023**, *63*, 6629–6641.

[158] S. Fujita, "A novel approach to systematic classification of organic reactions. Hierarchical subgraphs of imaginary transition structures" *J. Chem. Soc. Perkin Trans. 2* **1988**, 597–616.

[159] P. Veličković, G. Cucurull, A. Casanova, A. Romero, P. Liò, Y. Bengio, "Graph Attention Networks", in *6th Int. Conf. Learn. Represent.*, **2018**.

[160] K. Xu, W. Hu, J. Leskovec, S. Jegelka, "How Powerful are Graph Neural Networks?" in *International Conference on Learning Representations (ICLR)*, **2019**.

[161] D. Duvenaud, D. Maclaurin, J. Aguilera-Iparraguirre, R. Gómez-Bombarelli, T. Hirzel, A. Aspuru-Guzik, R. P. Adams, "Convolutional Networks on Graphs for Learning Molecular Fingerprints" in *Advances in Neural Information Processing Systems (NIPS)*, **2015**, *28*, 2224–2232.

[162] T. Berger, J. Lebon, C. Maichle-Mössmer, R. Anwander, "$CeCl_3$/n-BuLi: Unraveling Imamoto's Organocerium Reagent" *Angew. Chem. Int. Ed.* **2021**, *60*, 15622–15631.

[163] A. Krasovskiy, P. Knochel, "A LiCl-Mediated Br/Mg Exchange Reaction for the Preparation of Functionalized Aryl- and Heteroarylmagnesium Compounds from Organic Bromides" *Angew. Chem. Int. Ed.* **2004**, *43*, 3333–3336.

[164] O. Pereira, M. Ruth, D. Gerbig, R. C. Wende, P. R. Schreiner, "Leveraging Limited Experimental Data with Machine Learning: Differentiating a Methyl from an Ethyl Group in the Corey–Bakshi–Shibata Reduction" *J. Am. Chem. Soc.* **2024**, *146*, 14576–14586.

[165] M. Fuhrmann, N. F. Hacket, P. R. Schreiner, "Streamlined Synthesis of Bulky (Dispersion Energy Donor) Iodobenzenes" *Synthesis* **2026**, *58*, 421–424.

[166] F. K. Behbahani, M. Valiallahi, "Synthesis of 14-aryl-14*H*-dibenzo[a,j]xanthenes using $CuSO_4 \cdot 5H_2O$ as a green and reusable catalyst" *Arab. J. Chem.* **2017**, *10*, 1686–1689.

[167] Y. Cao, C. Yao, B. Qin, H. Zhang, "Solvent-free synthesis of 14-Aryl-14*H*-dibenzo[a,j]xanthenes catalyzed by recyclable and reusable iron(III) triflate" *Res. Chem. Intermed.* **2013**, *39*, 3055–3062.

[168] A. A. Bartolomeu, M. Menezes, L. S. Filho, "Efficient one-pot synthesis of 14-aryl-14*H*-dibenzo[a,j]xanthene derivatives promoted by niobium pentachloride" *Chem. Pap.* **2014**, *68*, 1593–1600.

[169] P. Kulkarni, "Calcium Chloride/HCl an Efficient Co-Catalytic System for Synthesis Xanthene under Microwave Condition" *J. Mex. Chem.* **2018**, *62 (1)*.

[170] Y. Oikawa, T. Yoshioka, O. Yonemitsu, "Specific removal of o-methoxybenzyl protection by DDQ oxidation." *Tetrahedron Lett.* **1982**, *23*, 885–888.

[171] K. Annadi, A. G. H. Wee, "Ceric ammonium nitrate oxidation of *N*-(*p*-methoxybenzyl)lactams: competing formation of *N*-(hydroxymethyl)δ-lactams" *ARKIVOC* **2014**, *2014*, 108–126.

[172] A. L. Williams, S. R. Dandepally, S. V. Kotturi, "A *p*-methoxybenzyl (PMB) protection/deprotection approach toward the synthesis of 5-phenoxy-4-chloro-*N*-(aryl/alkyl) thiophene-2-sulfonamides" *Mol. Divers.* **2010**, *14*, 697–707.

[173] D. B. Alger, "The water solubility of 2-butanol: A widespread error" *J. Chem. Educ.* **1991**, *68*, 939.

[174] O. I. Afanasyev, E. Kuchuk, D. L. Usanov, D. Chusov, "Reductive Amination in the Synthesis of Pharmaceuticals" *Chem. Rev.* **2019**, *119*, 11857–11911.

[175] A. Bischler, B. Napieralski, "Zur Kenntniss einer neuen Isochinolinsynthese" *Ber. Deutsch. Chem. Ges.* **1893**, *26*, 1903–1908.

[176] P. Renzi, J. Hioe, R. M. Gschwind, "Decrypting Transition States by Light: Photoisomerization as a Mechanistic Tool in Brønsted Acid Catalysis" *J. Am. Chem. Soc.* **2017**, *139*, 6752–6760.

[177] K. Maeda, E. Fischer, "Photoformation of '*Z*' (cis) Isomers in Diaryl- and Triaryl-Azomethines, Part II. Electronic and NMR Spectra of Methyl Derivatives of Benzylideneaniline (C_6H_5—CH=N—C_6H_5)" *Isr. J. Chem.* **1977**, *16*, 294–298.

[178] J. Qian, H. Zhao, Q. Gao, L. Chen, Y. Shi, J. Li, Y. Guo, B. Fan, "Enantioselective 1,4-addition of diarylphosphine oxides to α,β-unsaturated ketones catalyzed by oxazaborolidines" *Org. Chem. Front.* **2023**, *10*, 5672–5679.

[179] M. M. Kamal, Z. Liu, S. Zhai, D. Vidović, "Imine Reduction with Me_2S-BH_3" *Molecules* **2021**, *26*, 5443.

[180] C. E. Müller, L. Wanka, K. Jewell, P. R. Schreiner, "Enantioselective Kinetic Resolution of trans-Cycloalkane-1,2-diols" *Angew. Chem. Int. Ed.* **2008**, *47*, 6180–6183.

[181] E. Procházková, A. Kolmer, J. Ilgen, M. Schwab, L. Kaltschnee, M. Fredersdorf, V. Schmidts, R. C. Wende, P. R. Schreiner, C. M. Thiele, "Uncovering Key Structural Features

of an Enantioselective Peptide-Catalyzed Acylation Utilizing Advanced NMR Techniques" *Angew. Chem.* **2016**, *55*, 15754–15759.

[182] P.-G. Echeverria, T. Ayad, P. Phansavath, V. Ratovelomanana-Vidal, "Recent Developments in Asymmetric Hydrogenation and Transfer Hydrogenation of Ketones and Imines through Dynamic Kinetic Resolution" *Synthesis* **2016**, *48*, 2523–2539.

[183] A. M. Salunkhe, E. R. Burkhardt, "Highly enantioselective reduction of prochiral ketones with *N*,*N*-diethylaniline·borane (DEANB) in oxazaborolidine-catalyzed reductions" *Tetrahedron Lett.* **1997**, *38*, 1523–1526.

[184] H. C. Brown, J. V. B. Kanth, P. V. Dalvi, M. Zaidlewicz, "Molecular Addition Compounds. 15. Synthesis, Hydroboration, and Reduction Studies of New, Highly Reactive tert-Butyldialkylamine−Borane Adducts" *J. Org. Chem.* **1999**, *64*, 6263–6274.

[185] H. Drucker, C. Burges, L. Kaufman, A. Smola, V. Vapnik, "Support vector regression machines" *Adv Neural Inf Process Syst* **1997**, *9*, 155–161.

[186] L. Breiman, "Random Forests" *Mach. Learn.* **2001**, *45*, 5–32.

[187] S. Hellberg, M. Sjoestroem, B. Skagerberg, S. Wold, "Peptide quantitative structure-activity relationships, a multivariate approach" *J. Med. Chem.* **1987**, *30*, 1126–1135.

[188] V. L. Deringer, A. P. Bartók, N. Bernstein, D. M. Wilkins, M. Ceriotti, G. Csányi, "Gaussian Process Regression for Materials and Molecules" *Chem. Rev.* **2021**, *121*, 10073–10141.

[189] X. Huang, J. Zhao, Q. Wang, P. Fang, W. Xie, M. Chen, H. Han, L. Zhang, J. Zhang, F. Wang, Z.-Q. Liu, "Comparison of the Effects of Stirring and Standing on Chemical Reactions" *Synlett* **2025**, *36*, 683–688.

[190] Y. Zhu, H.-Y. Huang, Y.-Q. He, M. Wang, X.-Y. Wang, X.-R. Song, Z.-J. Mao, W.-F. Tian, Q. Xiao, "Visible-light enabled photochemical reduction of 1,2-dicarbonyl compounds by Hünig's base" *Org. Chem. Front.* **2022**, *9*, 1924–1931.

[191] S. Hkiri, C. Gourlaouen, S. Touil, A. Samarat, D. Sémeril, "1,3,4-Oxadiazole-functionalized α-amino-phosphonates as ligands for the ruthenium-catalyzed reduction of ketones" *New J. Chem.* **2021**, *45*, 11327–11335.

[192] J. W. Kim, T. Koike, M. Kotani, K. Yamaguchi, N. Mizuno, "Synthetic Scope of $Ru(OH)_x/Al_2O_3$-Catalyzed Hydrogen-Transfer Reactions: An Application to Reduction of Allylic Alcohols by a Sequential Process of Isomerization/Meerwein–Ponndorf–Verley-Type Reduction" *Chem. Eur. J.* **2008**, *14*, 4104–4109.

[193] S. Gaspa, A. Porcheddu, L. De Luca, “Metal-Free Direct Oxidation of Aldehydes to Esters Using TCCA” *Org. Lett.* **2015**, *17*, 3666–3669.

[194] F. Panahi, S. K. Dangolani, A. Khalafi-Nezhad, “Synthesis of a Novel Magnetic Reusable Organocatalyst Based on 4-Dialkylaminopyridines for Acyl Transformations” *ChemistrySelect* **2016**, *1*, 3541–3547.

[195] A. J. Ruddy, O. L. Sydora, B. L. Small, M. Stradiotto, L. Turculet, “(*N*-Phosphinoamidinate)cobalt-Catalyzed Hydroboration: Alkene Isomerization Affords Terminal Selectivity” *Chem. Eur. J.* **2014**, *20*, 13918–13922.

[196] G. Hellner, Z. Boros, A. Tomin, L. Poppe, “Novel Sol-Gel Lipases by Designed Bioimprinting for Continuous-Flow Kinetic Resolutions” *Adv. Synth. Catal.* **2011**, *353*, 2481–2491.

[197] J. Escorihuela, B. Altava, M. I. Burguete, S. V. Luis, “Dual stereocontrolled alkylation of aldehydes with polystyrene-supported nickel complexes derived from α-amino amides” *RSC Adv.* **2015**, *5*, 14653–14662.

[198] A. Taglieber, H. Höbenreich, J. D. Carballeira, R. J. G. Mondière, M. T. Reetz, “Alternate-Site Enzyme Promiscuity” *Angew. Chem. Int. Ed.* **2007**, *46*, 8597–8600.

[199] B. McNerney, B. Whittlesey, D. B. Cordes, C. Krempner, “A Well-Defined Monomeric Aluminum Complex as an Efficient and General Catalyst in the Meerwein–Ponndorf–Verley Reduction” *Chem. Eur. J.* **2014**, *20*, 14959–14964.

[200] T. Ema, N. Ura, M. Yoshii, T. Korenaga, T. Sakai, “Empirical method for predicting enantioselectivity in catalytic reactions: demonstration with lipase and oxazaborolidine” *Tetrahedron* **2009**, *65*, 9583–9591.

[201] J. M. Jr. Favale, E. O. Danilov, J. E. Yarnell, F. N. Castellano, “Photophysical Processes in Rhenium(I) Diiminetricarbonyl Arylisocyanides Featuring Three Interacting Triplet Excited States” *Inorg. Chem.* **2019**, *58*, 8750–8762.

[202] V. Diemer, H. Chaumeil, A. Defoin, A. Fort, A. Boeglin, C. Carré, “Syntheses of Sterically Hindered Pyridinium Phenoxides as Model Compounds in Nonlinear Optics” *Eur. J. Org. Chem.* **2006**, 2727–2738.

[203] L. Shi, C. Tao, Q. Yang, Y. E. Liu, J. Chen, J. Chen, J. Tian, F. Liu, B. Li, Y. Du, B. Zhao, “Chiral Pyridoxal-Catalyzed Asymmetric Biomimetic Transamination of α-Keto Acids” *Org. Lett.* **2015**, *17*, 5784–5787.

[204] E. Ullah, J. McNulty, M. Sliwinski, A. Robertson, "One-step synthesis of reusable, polymer-supported tri-alkyl phosphine ligands. Application in Suzuki–Miyaura and alkoxycarbonylation reactions" *Tetrahedron Lett.* **2012**, *53*, 3990–3993.

[205] A. Rolfe, J. K. Loh, P. K. Maity, P. R. Hanson, "High-Load, Hybrid Si-ROMP Reagents" *Org. Lett.* **2011**, *13*, 4–7.

[206] O.-Y. Lee, K.-L. Law, C.-Y. Ho, D. Yang, "Highly Chemoselective Reductive Amination of Carbonyl Compounds Promoted by InCl3/Et3SiH/MeOH System" *J. Org. Chem.* **2008**, *73*, 8829–8837.

[207] A. Alalla, M. Merabet-Khelassi, L. Aribi-Zouioueche, O. Riant, "Green Synthesis of Benzamides in Solvent- and Activation-Free Conditions" *Synth. Commun.* **2014**, *44*, 2364–2376.

[208] G. P. Perecim, A. Rodrigues, C. Raminelli, "A convenient formation of aporphine core via benzyne chemistry: conformational analysis and synthesis of (*R*)-aporphine" *Tetrahedron Lett.* **2015**, *56*, 6848–6851.

[209] J. S. M. Samec, A. H. Éll, J. B. Åberg, T. Privalov, L. Eriksson, J.-E. Bäckvall, "Mechanistic Study of Hydrogen Transfer to Imines from a Hydroxycyclopentadienyl Ruthenium Hydride. Experimental Support for a Mechanism Involving Coordination of Imine to Ruthenium Prior to Hydrogen Transfer" *J. Am. Chem. Soc.* **2006**, *128*, 14293–14305.

[210] J. Barluenga, A. Jiménez-Aquino, F. Aznar, C. Valdés, "Modular Synthesis of Indoles from Imines and o-Dihaloarenes or o-Chlorosulfonates by a Pd-Catalyzed Cascade Process" *J. Am. Chem. Soc.* **2009**, *131*, 4031–4041.

[211] J. Chen, Z. Zhang, Z. Bao, Y. Su, H. Xing, Q. Yang, Q. Ren, "Functionalized Metal–Organic Framework as a Biomimetic Heterogeneous Catalyst for Transfer Hydrogenation of Imines" *ACS Appl. Mater. Interfaces* **2017**, *9*, 9772–9777.

[212] R. U. Gutiérrez, H. C. Correa, R. Bautista, J. L. Vargas, A. V. Jerezano, F. Delgado, J. Tamariz, "Regioselective Synthesis of 1,2-Dihydroquinolines by a Solvent-Free $MgBr_2$-Catalyzed Multicomponent Reaction" *J. Org. Chem.* **2013**, *78*, 9614–9626.

[213] B. P. Jacobs, P. T. Wolczanski, E. B. Lobkovsky, "Oxidatively Triggered Carbon–Carbon Bond Formation in Ene-amide Complexes" *Inorg. Chem.* **2016**, *55*, 4223–4232.

[214] P. Eisenberger, A. M. Bailey, C. M. Crudden, "Taking the F out of FLP: Simple Lewis Acid–Base Pairs for Mild Reductions with Neutral Boranes via Borenium Ion Catalysis" *J. Am. Chem. Soc.* **2012**, *134*, 17384–17387.

[215] Z. Han, J. Lv, J. Zhang, "One-pot synthesis of 2-amino-3,4-dicyanopyridines from ketoximes and tetracyanoethylene via Cu(I)-catalyzed cyclization" *Tetrahedron* **2019**, *75*, 2162–2168.

[216] T. Huber, L. Schneider, A. Präg, S. Gerhardt, O. Einsle, M. Müller, "Direct Reductive Amination of Ketones: Structure and Activity of S-Selective Imine Reductases from Streptomyces" *ChemCatChem* **2014**, *6*, 2248–2252.

[217] C. Bauer, F. Müller, S. Keskin, M. Zobel, R. Kempe, "A Highly Active Cobalt Catalyst for the General and Selective Hydrogenation of Aromatic Heterocycles" *Chem. Eur. J.* **2023**, *29*, e202300561.

[218] P. Ji, K. Manna, Z. Lin, X. Feng, A. Urban, Y. Song, W. Lin, "Single-Site Cobalt Catalysts at New $Zr_{12}(\mu_3\text{-}O)_8(\mu_3\text{-}OH)_8(\mu_2\text{-}OH)_6$ Metal–Organic Framework Nodes for Highly Active Hydrogenation of Nitroarenes, Nitriles, and Isocyanides" *J. Am. Chem. Soc.* **2017**, *139*, 7004–7011.

[219] Y. Chen, S. Liu, P. Cui, Y. Zhang, Q. Liu, H. Zhou, "Metal-free one-pot three-step process for the direct conversion of aryl alkynes into secondary amines with $TfOH/B_2(OH)_4$" *Tetrahedron Lett.* **2019**, *60*, 327–330.

[220] A. Abdukader, H. Jin, Y. Cheng, C. Zhu, "Rhenium-catalyzed amination of alcohols by hydrogen transfer process" *Tetrahedron Lett.* **2014**, *55*, 4172–4174.

[221] M. Hatano, S. Suzuki, K. Ishihara, "Highly Efficient Alkylation to Ketones and Aldimines with Grignard Reagents Catalyzed by Zinc(II) Chloride" *J. Am. Chem. Soc.* **2006**, *128*, 9998–9999.

[222] J. Aziz, J.-D. Brion, A. Hamze, M. Alami, "Copper Acetoacetonate $[Cu(acac)_2]$/BINAP-Promoted Csp^3–N Bond Formation *via* Reductive Coupling of *N*-Tosylhydrazones with Anilines" *Adv. Synth. Catal.* **2013**, *355*, 2417–2429.

[223] R. R. Mittapalli, S. J. J. Guesné, R. J. Parker, W. T. Klooster, S. J. Coles, J. Skidmore, A. P. Dobbs, "The Asymmetric Aza-silyl-Prins Reaction: Synthesis of Enantiopure Piperidines" *Org. Lett.* **2019**, *21*, 350–355.

9 Acknowledgments

An dieser Stelle möchte ich mich ganz herzlich bei all den Menschen bedanken, die mich auf meinem bisherigen Weg motiviert und unterstützt haben. Diese Arbeit wäre ohne die Begegnungen, Erfahrungen und den Rückhalt vieler besonderer Menschen nicht möglich gewesen.

Mein erster und größter Dank gilt Herrn Prof. Dr. Schreiner für die Möglichkeit, in seiner Arbeitsgruppe zu promovieren. Vielen Dank für das Vertrauen, das Sie mir entgegengebracht haben, als Sie mich trotz meines Wechsels von einer anderen Universität und aus einem anderen chemischen Fachbereich in Ihre Gruppe aufnahmen. Die wissenschaftliche Freiheit, die Sie mir gegeben haben, und Ihre konstruktive Kritik haben wesentlich zur Entstehung dieser Arbeit beigetragen und mich sowohl fachlich als auch persönlich geprägt. Darüber hinaus danke ich meinem Zweitgutachter, Herrn Prof. Dr. Wegner, sowie den weiteren Mitgliedern der Prüfungskommission, Herrn Prof. Dr. Smarsly und Herrn Prof. Dr. Schindler, herzlich für ihre Bereitschaft und die Zeit, diese Arbeit zu begutachten.

Von ganzem Herzen danke ich ebenso Dr. Raffael Wende und Dr. Dennis Gerbig für das Korrekturlesen dieser Arbeit, die vielen hilfreichen Ratschläge, die lustigen Gespräche und eure ständige Offenheit mir gegenüber. Dass ich nach meinem Wechsel so schnell in Gießen angekommen bin, verdanke ich den ehemaligen sowie gegenwärtigen Kolleginnen und Kollegen der Arbeitsgruppe Schreiner. Besonders bedanken möchte ich mich bei Akkad Danho, Marvin Domanski, Charlotte Lauter, Jan Metzler, Nikolaos Vagkidis und Benito Marrazi. Ihr habt nicht nur dazu beigetragen, dass ich mich fachlich schnell zurechtgefunden habe, sondern auch für jede Menge Freude im Arbeitsalltag gesorgt. Ebenso möchte ich Caio Porto nennen, der zwar nur kurz in der Arbeitsgruppe war, aber dennoch großen Einfluss auf mich und diese Arbeit nahm. Allen anderen Arbeitsgruppen der JLU danke ich für die vielen schönen Momente in den Praktika und die lustigen Gespräche während gemeinsamer Veranstaltungen. Ein weiterer Dank gilt meinen Studenten Lukas Meyer und Albert Lautenbach, die durch ihr Engagement und ihre praktische Mitarbeit ebenfalls einen wesentlichen Beitrag zu dieser Arbeit geleistet haben.

Neben dem wissenschaftlichen Diskurs sind es vor allem die vielen helfenden Hände im Hintergrund, die den Laboralltag überhaupt erst möglich machen. Ohne die festangestellten Mitarbeiterinnen und Mitarbeiter des Instituts wäre diese Arbeit schlichtweg nicht realisierbar gewesen. Für die großartige Unterstützung danke ich daher Michaella Richter, Mario Dauber, Eike

Santowski, Lisa Wiegand, Steffen Wagner, Stefan Bernhardt, Anja Benekenstein, Jana Küchenmeister, Edgar Reitz, Anika Bernhardt, Anja Platt, Inna Klein, Dr. Heike Hausmann und Dr. Jörg Neudert.

Abseits der Universität Gießen richtet sich mein Blick auch auf die wertvollen Wegbegleiter meines bisherigen Lebensweges. Mein herzlicher Dank gilt daher meinem Bachelorbetreuer Frank Kaiser sowie meiner Masterbetreuerin Anja Blümler, die mich in meiner frühen akademischen Entwicklung maßgeblich gefördert haben. Ein ebenso großes Dankeschön gebührt meinen Freunden aus der Frankfurter Unizeit und all jenen, mit denen ich in den letzten Jahren so viel Schönes erleben durfte. Speziell danke ich Matthias Becker, Adrian Zebisch, Ben Ehis Obhafuoso, Nicklas Schulz Eickhorst, Patrick Lotz, Zita Hille, Thomas Osburg, Thomas Pottmeyer, Kay Hammen, Jonas Kubitza, Jakub Golanski und Kostantinos Stamatakis. Wahre Freunde findet man im Leben selten, daher schätze ich mich unglaublich glücklich, dass ihr mich auf meinem Weg begleitet, mich geprägt und mir so wundervolle Erinnerungen geschenkt habt.

Zu guter Letzt möchte ich mich den Menschen widmen, die mir privat am wichtigsten sind. Meiner Freundin Lorena danke ich von ganzem Herzen für ihre Liebe und unendliche Unterstützung. Eine Promotion ist oft auch für die Partnerin eine echte Geduldsprobe, weshalb ich jeden Tag dankbar bin, dich an meiner Seite zu wissen. Danke, dass du mein Ruhepol bist, mich stets wieder aufgebaut und mir in jeder Phase dieser Arbeit den Rücken gestärkt hast. Ebenso danke ich meinem Cousin Joel, der für mich nicht einfach nur Familie, sondern ein echter Bruder ist. Ich genieße jede Minute, die wir miteinander verbringen, und danke dir dafür, dass du mir durch deinen eigenen Weg zeigst, dass man seine Träume erreichen kann, wenn man an sie glaubt. Für deine Zukunft als Pilot drücke ich dir weiterhin ganz fest die Daumen. Ein großes Dankeschön gilt auch meiner Tante Carla und meinem Onkel Paulo, die seit meiner Kindheit an mich geglaubt haben und immer für mich da waren. Nicht unerwähnt bleiben dürfen meine Großeltern, sowohl väterlicherseits als auch mütterlicherseits, die das Fundament unserer wunderbaren Familie gebildet haben.

Der tiefste und allerwichtigste Dank gilt schließlich meinen Eltern. Ihr habt mich all die Jahre bedingungslos unterstützt und mir eine behütete Kindheit voller schöner Erinnerungen geschenkt. Ihr habt nie aufgehört, an mich zu glauben, und seid meine absolut größten Vorbilder. Diese Arbeit ist euch gewidmet als kleines Zeichen meiner unendlichen Dankbarkeit für alles, was ihr jemals für mich getan habt. Ihr seid die besten Eltern der Welt und ich liebe euch von ganzem Herzen.